Les Rencontres de Physique de la Vallée d'Aoste

Results and Perspectives in Particle Physics

edited by M. Greco

La Thuile, Aosta Valley *February 26th - March 3rd, 2012*

ISTITUTO NAZIONALE DI FISICA NUCLEARE
Laboratori Nazionali di Frascati

Les Rencontres de Physique de la Vallée d'Aoste

Results and Perspectives in Particle Physics

INFN
Istituto Nazionale
di Fisica Nucleare

Società Italiana di Fisica

FRASCATI PHYSICS SERIES

Series Editor
Danilo Babusci

Technical Editor
Marcella Missiroli

Volume LVII - Special Issue

Jointly published by:

Istituto Nazionale di Fisica Nucleare - Laboratori Nazionali di Frascati
Divisione Ricerca - SIDS - Ufficio Biblioteca e Pubblicazioni
Via Enrico Fermi 40, I-00044 Frascati (Roma), Italy
e-mail: sis.publications@lnf.infn.it

Società Italiana di Fisica
Via Saragozza 12, I-40123 Bologna, Italy
http://www.sif.it

FRASCATI PHYSICS SERIES

Les Rencontres de Physique de la Vallée d'Aoste

RESULTS AND PERSPECTIVES IN PARTICLE PHYSICS

ISBN: 978-88-7438-077-0

Printed in Italy by Compositori Industrie Grafiche
Via Stalingrado 97/2
40128 Bologna

FRASCATI PHYSICS SERIES

Volume LVII

Les Rencontres de Physique de la Vallée d'Aoste

Results and Perspectives in Particle Physics

Editor
Mario Greco

La Thuile, Aosta Valley, February 26^{th} - March 3^{rd}, 2012

Conference Organizers

Giorgio Bellettini	Pisa
Giorgio Chiarelli	Pisa
Mario Greco	Roma Tre
Gino Isidori	Laboratori Nazionali di Frascati

Chairpersons

Riccardo Barbieri	Pisa
Giorgio Bellettini	Pisa
Giorgio Chiarelli	Pisa
Alvaro De Rújula	CERN
Mario Greco	Roma Tre
Gino Isidori	Laboratori Nazionali di Frascati
Andrey Korytov	University of Florida
Victor Novikov	ITEP
Giovanni Punzi	Pisa
Gigi Rolandi	CERN
Alexander Studenikin	JINR
Roberto Tenchini	Pisa

CONTENTS

FLAVOUR PHYSICS, *CP* VIOLATION AND RARE DECAYS

ELECTROWEAK AND TOP PHYSICS

HIGGS SEARCHES

SEARCHING FOR NEW PHYSICS

YOUNG SCIENTIST FORUM

PERSPECTIVES

IL NUOVO CIMENTO Vol. 35 C, N. 6 Novembre-Dicembre 2012
DOI 10.1393/ncc/i2012-11343-1

Colloquia: LaThuile12

Preface

M. Greco
Dipartimento di Fisica, Università di Roma Tre - Via della Vasca Navale 84, 00146 Roma, Italy

The 2012 Rencontres de Physique de la Vallée d'Aoste were held at the Planibel Hotel of La Thuile, Aosta Valley, on February 26th - March 3rd, featuring the twenty-sixth edition of "Results and Perspectives in Particle Physics".

The physics programme included various topics in particle physics, also in connection with present and future experimental facilities, as cosmology and astrophysics, neutrino physics, CP violation and rare decays, electroweak and hadron physics with e^+e^- and hadron colliders, heavy flavours, search for new physics and prospects at future facilities.

The session on "Physics and Society" included special colloquia on "Thorium Reactors", and "Physics in Latin America". We are very grateful to Stuart Henderson and Luciano Maiani for their participation and contribution.

Giorgio Bellettini, Giorgio Chiarelli, Gino Isidori and I would like to warmly thank the session chairpersons and the speakers for their contribution to the success of the meeting.

The regional government of the Aosta Valley, in particular through the Minister of Public Education and Culture Laurent Vierin, has been very pleased to offer its financial support and hospitality to the Rencontres of La Thuile. Also on behalf of the participants, representatives of some major Laboratories and Institutes in the world, we would like to thank all the Regional Authorities. Special thanks are also due to Bruno Baschiera, local coordinator of the Rencontres.

We are grateful to the President of INFN Fernando Ferroni, the Directors of INFN Laboratori Nazionali di Frascati, Umberto Dosselli and INFN Sezione di Pisa, Giovanni Batignani, for the support in the organization of the Rencontres. We would like to thank also Lucia Lilli, Claudia Tofani and Paolo Villani for their help in both planning and running the meeting. We are also grateful to Alessandra Miletto for her valuable contribution to the local organization of the meeting. The excellent assistance provided by Mauro Giannini made it possible to set up the computer link to the international network.

Finally we would like to thank the Mayor Gilberto Roullet and the local authorities of La Thuile and the "Azienda di Promozione Turistica del Monte Bianco" for their warm hospitality, and the Planibel Hotel staff for providing us with an enjoyable atmosphere.

SESSION I - COSMOLOGY AND ASTROPHYSICS

IL NUOVO CIMENTO Vol. 35 C, N. 6 Novembre-Dicembre 2012
DOI 10.1393/ncc/i2012-11344-0

Colloquia: LaThuile12

The Planck mission: From first results to cosmology

P. Natoli([1])([2])([3]), A. Gruppuso([3]) and N. Mandolesi([3])

([1]) *Dipartimento di Fisica e Sezione INFN, Università degli Studi di Ferrara via Giuseppe Saragat 1, I-44100 Ferrara, Italy*
([2]) *Agenzia Spaziale Italiana Science Data Center, c/o ESRIN - via Galileo Galilei Frascati, Italy*
([3]) *INAF-IASF Bologna, Istituto di Astrofisica Spaziale e Fisica Cosmica di Bologna Istituto Nazionale di Astrofisica - via Piero Gobetti 101, I-40129 Bologna, Italy*

ricevuto il 7 Settembre 2012

Summary. — *Planck* is an ESA satellite launched in May 2009, whose main objective is to image the anisotropies of the Cosmic Microwave Background Radiation and their linear polarizartion with unprecedented sensitivity, angular resolution and frequency leverage. *Planck* is providing high-quality data to be mined for decades to come. Planck results have been released starting January 2011 ("early results") and February 2012 ("intermediate results") and are limited to Galactic and extragalactic science. The first cosmological data products are awaited for early 2013. *Planck* has a wide list of scientific targets. Here we focus on constraining constraints about parity-violating models that go beyond Maxwell's electromagnetism. We focus first on the *in vacuo* cosmological birefringence angle that constraints the rotation of the polarization plane of last scattered background photons. The latter can be non-null only if there is a parity-violating coupling in the Maxwell Lagrangian. We also discuss the so-called parity anomaly claimed in the anisotropy intensity spectrum of the WMAP data (Kim and Naselsky, 2010). We describe the basic formalism, the relevant estimators and the overall analysis strategy. We finally forecast the capabilities of Planck in tightening the present constraints.

PACS `98.80.-k` – Cosmology.

1. – Introduction

The statistical properties of the Cosmic Microwave Background (hereafter, CMB) pattern may be used to constrain parity (P) symmetry. Parity violations arise in several models: as modification of electromagnetism [1-3] (hence deviations from the particle physics Standard Model) or as modification of the standard picture of the Inflationary mechanism (where P is broken due to primordial gravitational waves). In the latter case, we refer to chiral gravity [4-7] and in the former we generally talk of cosmological birefringence. Both of these classes of models predict non-vanishing cross-correlations between E and B modes and T and B modes. However, chiral gravity induces such correlations at the CMB last scattering surface whereas cosmological birefringence induces them by rotating the polarization plane during the CMB photon journey from its last scattering to us [8]. We focus here only on cosmic birefringence case, reporting mainly findings from [9]. In addition, we review the claimed P anomaly found at large angular scaless in the anisotropy intensity (temperature or "TT") spectrum of the WMAP data, first claimed by Kim and Naselsky in 2010 [10-13]. The latter is dubbed a parity anomaly in view of an observed discrepancy (in power) among even and odd multipoles, which behave differently under P transformation (see sect. **2**, below). However, there is no sound theoretical framework that could explain such a mismatch. it is commonly use such terminology, *i.e.* TT parity anomaly. It is not known yet whether the effect arises due to fundamental physics or it is due to some spurious sources, *i.e.* instrumental systematics or poorly removed astrophysical foregrounds [14]. If the effect is indeed due to fundamental physics, its appearance at large angular scales naturally suggests the possibility that a P-violating mechanism is involved during an early phase of the universe. Other explanations exist: for a more conservative approach see [11] where it is assumed that the early universe evolution obeys the standard inflationary mechanism, and concluded that we must then live in a special location of the universe. Translational invariance would thus be violated for scales larger than $\sim 4\,\mathrm{Gpc}$ leading some sort of breaking of the Copernican principle.

2. – Parity symmetry in CMB

All-sky temperature maps, $T(\hat{n})$, are usually expanded in terms of spherical harmonics $Y_{\ell m}(\hat{n})$, with $\hat{n}$ being a unit vector or direction on the sky, completely specified by a couple of angles (θ, ϕ). The quantities $a_{T,\ell m} = \int \mathrm{d}\Omega\, Y^{\star}_{\ell m}(\hat{n})\, T(\hat{n})$, are coefficients of the spherical harmonics expansion, and $\mathrm{d}\Omega = \mathrm{d}\theta \mathrm{d}\phi \sin\theta$. Under reflection (or P) symmetry ($\hat{n} \to -\hat{n}$), these coefficients behave as $a_{T,\ell m} \to (-1)^{\ell}\, a_{T,\ell m}$. Analogously, for polarization, one may consider the linear polarization maps([1]) ($Q(\hat{n})$ and $U(\hat{n})$). The latter are not scalar, but rather components of a rank-two tensor [15] and are decomposed by the appropriate spin harmonics:

$$a_{\pm 2,\ell m} = \int \mathrm{d}\Omega\, Y^{\star}_{\pm 2,\ell m}(\hat{n})\, (Q(\hat{n}) \pm iU(\hat{n})), \tag{1}$$

where $Y_{\pm 2,\ell m}(\hat{n})$ are precisely Spherical Harmonics of spin 2 and $a_{\pm 2,\ell m}$ are the corresponding coefficients. It is then useful to introduce new coefficients as linear combinations of the previous:

$$a_{E,\ell m} = -(a_{2,\ell m} + a_{-2,\ell m})/2, \tag{2}$$

$$\text{and} \quad a_{B,\ell m} = -(a_{2,\ell m} - a_{-2,\ell m})/2i. \tag{3}$$

([1]) Due to the polarization dependence of the Compton cross section the CMB does not display circular polarization, at least in a standard scenario. Hence we do not consider the Stokes parameter V in what follows.

These have opposite behaviors under a P transofrmation:

$$a_{E,\ell m} \to (-1)^{\ell}\, a_{E,\ell m}, \tag{4}$$

$$a_{B,\ell m} \to (-1)^{\ell+1}\, a_{B,\ell m}. \tag{5}$$

If P is conserved, by combining the previous transformation one immediately derives that the cross-correlations $C_\ell^{TB} = \langle a^\star_{T,\ell m} a_{B,\ell' m'}\rangle$ and $C_\ell^{EB} = \langle a^\star_{E,\ell m} a_{B,\ell' m'}\rangle$ must vanish. Further details can be found in [15, 16] and explicit algebra is set forth in the Appendix of [12].

3. – Cosmological birefringence

The CMB is a powerful probe of cosmological birefringence and, hence, of the parity behavior of the electromagnetic Lagrangian for two main reasons. First, it is generated in the early universe, when the physics at the stake was not obviously identical to present. Secondly, the long look-back time of CMB photons may render tiny violations to the electromagnetic Lagrangian observable, since such effects usually accumulate during propagation. CMB polarization arises at two distinct cosmological times: the recombination epoch ($z \sim 1100$) and the reionization era ($z \sim 11$ or less [17]). When the CMB field is expanded in spherical harmonics, the first signal mostly shows up at high multipoles, since polarization is generated through a causal process and the Hubble horizon at last scattering only subtends a degree sized angle. The later reionization of the cosmic fluid at lower redshift impacts the low ℓ instead. These two regimes need to be taken into account when probing for cosmological birefringence, since they can be ascribed to different epochs and, hence, physical conditions. For other cosmological observations about the Cosmological Birefringence effect see [1, 2, 18, 19].

For instance, the presence of a primordial homogeneous [20] or helical [21] magnetic field would induce Faraday rotation and non-zero TB correlations. Parity-asymmetric gravity dynamics during inflation could cause unbalance in left and right-handed gravitational waves, which impacts TB and EB [4]. In general, models in high energy physics with non-standard parity-violating interactions also predict TB and EB signals different from zero [8]. A popular model for which parity is broken in the photon sector is the Chern-Simons perturbation to the Maxwell Lagrangian [1]:

$$\Delta\mathcal{L} = -\frac{1}{4}\, p_\mu \epsilon^{\mu\nu\rho\sigma} F_{\rho\sigma} A_\nu,$$

where $F^{\mu\nu}$ is the Maxwell tensor and A^μ the four-potential. The four-vector p_μ can be interpreted in several ways, *e.g.*, the derivative of the quintessence field or the gradient of a function of the Ricci scalar [22]. In any case a P violation always arises provided that the timelike component of p_μ does not vanish. C and T symmetries are then unbroken so CP and CPT are not conserved. Given that p^μ selects a preferred direction in spacetime, Lorenz invariance cannot be preserved.

Historically, the effect has been first constrained by measuring polarized light from high redshift radio galaxies and quasars [1, 2, 19, 23], see [24] for an analysis on ultraviolet polarization of distant radio galaxies. Recent polarization oriented CMB observations [25-28] have been capable to measure TB and EB correlations, other than TT, TE and EE correlations. While no detection has been claimed to date, polarization data have been used to derive constraints on the birefringence angle [26, 29-31].

In the limit of constant birefringence angle, α, the angular power spectra of CMB anisotropies, assuming $C_\ell^{TB} = C_\ell^{EB} = 0$, are given by [4, 29, 32, 33](2). The polarization rotation can be parametrized by the angle α, namely the birefringence angle, that, in the limit of constant α, impacts the angular power spectra of CMB anisotropies as follows [4, 29, 32, 33]:

$$C_\ell^{TE,obs} = C_\ell^{TE} \cos(2\alpha), \tag{6}$$

$$C_\ell^{TB,obs} = C_\ell^{TE} \sin(2\alpha), \tag{7}$$

$$C_\ell^{EE,obs} = C_\ell^{EE} \cos^2(2\alpha) + C_\ell^{BB} \sin^2(2\alpha), \tag{8}$$

$$C_\ell^{BB,obs} = C_\ell^{BB}\rangle \cos^2(2\alpha) + C_\ell^{EE} \sin^2(2\alpha), \tag{9}$$

$$C_\ell^{EB,obs} = \frac{1}{2} \left(C_\ell^{EE} + C_\ell^{BB} \right) \sin(4\alpha). \tag{10}$$

The WMAP team [26], using a Markov Chain Monte Carlo (MCMC) method, at high ℓ (from 24 to 800) find $\alpha^{\mathrm{WMAP}\,7yr} = -0.9^\circ \pm 1.4^\circ$ at 68% CL. Our constraint, obtained at low resolution [9] and considering the same estimator that has been used in [31], reads $\alpha = -1.6^\circ \pm 1.7^\circ\,(3.4^\circ)$ at 68% (95%) CL for $\Delta\ell = 2 - 47$. Considering $\Delta\ell = 2 - 23$ we obtain $\alpha = -3.0^\circ{}^{+2.6^\circ}_{-2.5^\circ}$ at 68% CL and $\alpha = -3.0^\circ{}^{+6.9^\circ}_{-4.7^\circ}$ at 95% CL. This is the same multipole range considered by the WMAP team at low resolution in [26] (the only other result available in the literature at these large angular scales) where with a pixel-based likelihood analysis they obtain $\alpha^{\mathrm{WMAP}\,7yr} = -3.8^\circ \pm 5.2^\circ$ at 68% CL. In [39] it is claimed that the improvement expected for the Planck satellite [40] in terms of sensitivity [41] is around 15. Almost the same number is obtained in [9]. Both forecasts are provided considering just the nominal sensitivity whereas the uncertainties coming from the systematic effects are not taken into account.

4. – TT parity anomaly

The starting consideration for this analysis is that CMB physics does not distinguish between even and odd multipoles [10, 11]. Therefore the power contained in even and odd multipoles must be statistically the same. We define the following quantities:

$$C^X_{+/-} \equiv \frac{1}{(\ell_{max} - 1)} \sum_{\ell=2,\ell_{max}}^{+/-} \frac{\ell(\ell+1)}{2\pi} \hat{C}^X_\ell , \tag{11}$$

where $\hat{C}^X_\ell$ are the estimated APS obtained with *BolPol* for the power spectrum $X = TT$, TE, EE and BB. The sum is meant only over the even or odd ℓ and this is represented respectively by the symbol $+$ or $-$. Therefore, two estimators can be built from eq. (11): the "ratio" $R^X = C^X_+/C^X_-$ (see [10-12]) and the "difference" $D^X = C^X_+ - C^X_-$, (see [12, 42]), where $C^X_\pm$ is the band power average contained in the even $(+)$ or odd $(-)$ multipoles with X standing for one of the six CMB spectra. See [13] for other estimators.

---

(2) See [34, 35] as an example of computation that takes into account the time dependence of α in a specific model of pseudoscalar fields coupled to photons. See [36-38] as examples of non-isotropic birefringence effect.

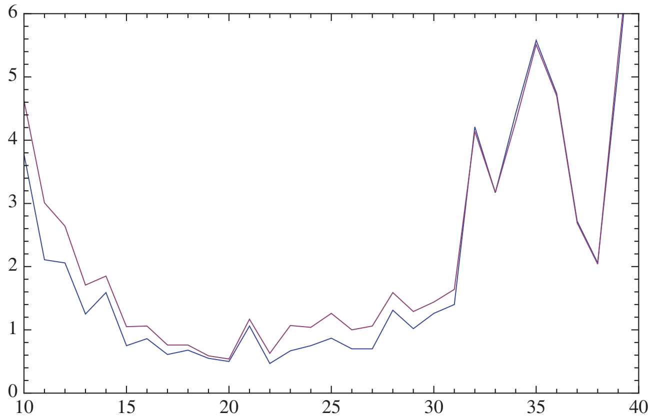

Fig. 1. – TT. Percentage of the WMAP 7 year value (y-axis) *vs.* ℓ_{max} (x-axis). The blue line is for the ratio and the red line for the difference.

In fig. 1 we plot the percentage related to the WMAP 7 year P anomaly for TT *versus* ℓ_{max} in the range 10–40 for the two considered estimators. As evident there is not a single ℓ_{max} for which the TT anomaly shows up, but rather a characteristic scale in the ℓ range $[16, 32]$. We confirm the previously reported P anomaly in TT in the range $\Delta\ell = [2, 22]$ at $> 99.5\%$ CL. Planck will not improve the signal-to-noise ratio in this range for the TT spectrum, since it is already cosmic variance dominated in the WMAP data. However Planck has a wider frequency coverage and this will improve the component separation layer in the data analysis pipeline. Moreover Planck is observing the sky with a totally different scanning strategy and this represents a benefit from the systematic effects analysis point of view.

* * *

This work has been done in the framework of the Planck LFI activities. In particular we acknowledge the use of the Planck LFI DPC code, BolPol, described in [9, 12]. We acknowledge support by ASI through ASI/INAF agreement I/072/09/0 for the Planck LFI activity of Phase E2. We acknowledge the use of computing facilities at NERSC. We acknowledge the use of the Legacy Archive for Microwave Background Data Analysis (LAMBDA([3])). Support for LAMBDA is provided by the NASA Office of Space Science. Some of the results in this paper have been derived using the HEALPix [43] package([4]).

REFERENCES

[1] Carroll S. M., Field G. B. and Jackiw R., *Phys. Rev. D*, **41** (1990) 1231.
[2] Carroll S. M. and Field G. B., *Phys. Rev. D*, **43** (1991) 3789.
[3] Carroll S. M., *Phys. Rev. Lett.*, **81** (1998) 3067.
[4] Lue A., Wang L.-M. and Kamionkowski M., *Phys. Rev. Lett.*, **83** (1999) 1506.
[5] Contaldi C. R., Magueijo J. and Smolin L., *Phys. Rev. Lett.*, **101** (2008) 141101.

([3]) `http://lambda.gsfc.nasa.gov/`
([4]) `http://healpix.jpl.nasa.gov/`

[6] Saito S., Ichiki K. and Taruya A., *JCAP*, **09** (2007) 002.
[7] Sorbo L., *JCAP*, **06** (2011) 003.
[8] Gluscevic V. and Kamionkowski M., *Phys. Rev. D*, **81** (2010) 123529.
[9] Gruppuso A., Natoli P., Mandolesi N., De Rosa A., Finelli F. and Paci F., *JCAP*, **02** (2012) 023.
[10] Kim J. and Naselsky P., *Astrophys. J.*, **714** (2010) L265.
[11] Kim J. and Naselsky P., *Phys. Rev. D*, **82** (2010) 063002.
[12] Gruppuso A., Finelli F., Natoli P., Paci F., Cabella P., De Rosa A. and Mandolesi N., *Mon. Not. R. Astron. Soc.*, **411** (2011) 1445.
[13] Aluri P. K. and Jain P., *Mon. Not. R. Astron. Soc.*, **419** (2012) 3378.
[14] Maris M., Burigana C., Gruppuso A., Finelli F. and Diego J. M., *Mon. Not. R. Astron. Soc.*, **415** (2011) 2546.
[15] Zaldarriaga M. and Seljak U., *Phys. Rev. D*, **55** (1997) 1830.
[16] Zaldarriaga M., *Astrophys. J.*, **503** (1998) 1.
[17] Dodelson S., *Modern Cosmology* (Academic Press, Elsevier) 2003.
[18] Amelino-Camelia G. *et al.*, *Nature*, **393** (1998) 763.
[19] Alighieri S. d. S., arXiv:1011.4865 [astro-ph.CO].
[20] Scannapieco E. S. and Ferreira P. G., *Phys. Rev. D*, **56** (1997) 7493.
[21] Pogosian L., Vachaspati T. and Winitzki S., *Phys. Rev. D*, **65** (2002) 083502; Giovannini M., *Phys. Rev. D*, **71** (2005) 021301.
[22] Davoudiasl H. *et al.*, *Phys. Rev. Lett.*, **93** (2004) 201301; Li H., Li M. and Zhang X., *Phys. Rev. D*, **70** (2004) 047302.
[23] Carroll S. M. and Field G. B., *Phys. Rev. Lett.*, **79** (1997) 2394; Carroll S. M., *Phys. Rev. Lett.*, **81** (1998) 3067; Nodland B. and Ralston J. P., *Phys. Rev. Lett.*, **78** (1997) 3043; Eisenstein D. J. and Bunn E. F., *Phys. Rev. Lett.*, **79** (1997) 1957; Leahy J. P., astro-ph/9704285, 1997.
[24] Alighieri S. d. S., Finelli F. and Galaverni M., *Astrophys. J.*, **715** (2010) 33 (arXiv:1003.4823 [astro-ph.CO]).
[25] Pryke C. *et al.* (QUaD Collaboration), *Astrophys. J.*, **692** (2009) 1247.
[26] Komatsu E. *et al.* (WMAP Collaboration), *Astrophys. J. Suppl.*, **192** (2011) 18.
[27] Piacentini F. *et al.*, *Astrophys. J.*, **647** (2006) 833.
[28] Montroy T. E. *et al.*, *Astrophys. J.*, **647** (2006) 813.
[29] Feng B., Li M., Xia J.-Q., Chen X. and Zhang X., *Phys. Rev. Lett.*, **96** (2006) 221302.
[30] Cabella P., Natoli P. and Silk J., *Phys. Rev. D*, **76** (2007) 123014.
[31] Wu E. Y. S. *et al.* (QUaD Collaboration), *Phys. Rev. Lett.*, **102** (2009) 161302.
[32] Feng B., Li H., Li M.-z. and Zhang X.-m., *Phys. Lett. B*, **620** (2005) 27.
[33] Komatsu E. *et al.* (WMAP Collaboration), *Astrophys. J. Suppl.*, **180** (2009) 330.
[34] Galaverni M. and Finelli F., *Nucl. Phys. Proc. Suppl.*, **194** (2009) 51.
[35] Finelli F. and Galaverni M., *Phys. Rev. D*, **79** (2009) 063002.
[36] Li M. and Zhang X., *Phys. Rev. D*, **78** (2008) 103516.
[37] Kamionkowski M., *Phys. Rev. D*, **82** (2010) 047302.
[38] Gubitosi G. *et al.*, (arXiv:1106.6049 [astro-ph.CO]).
[39] Gubitosi G. *et al.*, *JCAP*, **08** (2009) 021.
[40] Ade P. A. R. *et al.* (Planck Collaboration), *Astron. Astrophys.*, **536** (2011) A1.
[41] Planck Collaboration, *ESA publication* ESA-SCI (2005)/1 (arXiv:astro-ph/0604069).
[42] Paci F. *et al.*, *Mon. Not. R. Astron. Soc.*, **407** (2010) 399.
[43] Gorski K. M., Hivon E., Banday A. J., Wandelt B. D., Hansen F. K., Reinecke M. and Bartelmann M., *Astrophys. J.*, **622** (2005) 759.

IL NUOVO CIMENTO Vol. 35 C, N. 6 Novembre-Dicembre 2012
DOI 10.1393/ncc/i2012-11345-y

Colloquia: LaThuile12

Recent results from Fermi-LAT

F. de Palma on behalf of the Fermi LAT Collaboration
INFN, Sezione di Bari - Bari, Italy

ricevuto il 7 Settembre 2012

Summary. — We highlight the most important recent results from the Fermi Large Area Telescope (LAT). The latest source catalog (2FGL) is briefly discussed and several recent results on DM indirect searches from different targets are summarized. Finally, various results on the cosmic rays direct detection are presented.

PACS 95.85.Pw – γ-ray.
PACS 95.80.+p – Astronomical catalogs, atlases, sky surveys, databases, retrieval systems, archives, etc.
PACS 95.35.+d – Dark matter (stellar, interstellar, galactic, and cosmological).
PACS 96.50.S- – Cosmic rays.

1. – The LAT instrument

The LAT is a pair conversion detector on board the Fermi Gamma-ray Space Telescope. It began its nominal science operations on August 4, 2008. It is designed to measure the directions, energies, and arrival times of γ-rays incident over a wide Field of View (FoV ~ 2.4 sr), while rejecting background from charged cosmic rays. To take full advantage of the LAT large FoV, the primary observing mode of Fermi is the so-called scanning mode that ensures an almost uniform sky coverage every two orbits (~ 3 hours). In case of particularly interesting targets of opportunity, the observatory can be inertially pointed either by issuing a command from the ground, or autonomously in the occurrence of a Gamma-ray Burst (GRB).

The LAT is composed by a precision converter-tracker and a calorimeter, each consisting of a 4×4 array of towers. A segmented anti coincidence detector (ACD), for the rejection of the charged-particle background, covers the tracker array [1-3]. Different event selections were developed for the various analysis that can be done with the LAT data and three different cuts were applied to select public data samples with increasing levels of purity, see [3] and the LAT performace web page(1).

(1) http://www.slac.stanford.edu/exp/glast/groups/canda/archive/pass7v6/lat_Performance.htm

2. – The 2FGL source catalog

The second Fermi LAT source catalog (2FGL) [4] represents the most complete catalog of γ-ray sources in the 100 MeV–100 GeV energy range. Source detection is based on the average flux over the 24 month period. The 2FGL includes source locations and spectral fits in terms of power-law, power-law with exponential cutoff, or log-normal forms. Also included are flux measurements and statistical significance in five energy bands, light curves on monthly intervals for each source and a variability index. Twelve sources in the catalog are modeled as spatially extended with different shapes and sizes. The analysis was performed applying the new event P7SOURCE_V6 [3] selections and using a new and highly-resolved model of the diffuse Galactic and isotropic emissions. All the results are summarized in FITS files(2) and are publicly available from the FSSC web page(3). The sources reported in the 2FGL have a statistical significance of at least 4 σ above the background (see [4]).

As in the two previous LAT source catalogs [5,6], in the 2FGL the distinction between associations and firm identifications is kept. Although many associations, particularly those for AGNs, have very high probability of being true, a firm identification is based on one of the following three criteria:

1. Periodic Variability and Pulsations. Pulsars are the larger class in this category but binaries are also included.
2. Spatial Morphology. Spatially extended sources whose morphology can be related to the shape seen at other wavelengths include SNR, PWNe, and galaxies.
3. Correlated Variability. Variable sources, primarily AGNs, whose γ-ray variability can be matched to that seen at one or more other wavelengths, are considered to be firm identifications.

In total, we firmly identify 127 out of the 1873 2FGL sources. The algorithm for the associations is described in [4] and in [6]. In summary, we use a Bayesian approach that trades the positional coincidence of possible counterparts with 2FGL sources against the expected number of chance coincidences to estimate the probability that a specific counterpart association (in other catalogs) is indeed real (*i.e.*, a physical association). We retain counterparts as associations if they reach a posterior probability of at least 80%.

Among the 1873 sources in the 2FGL catalog, 575 (31%) remain unassociated. This could be due to both a incomplete catalog coverage at $|b| < 10°$ and to some systematic uncertainties in the galactic model. 162 sources are flagged to indicate possible confusion with residual imperfections in the diffuse model.

The next years will allow to detect and observe even fainter sources and increase the statistics for population studies, allowing us to better constrain different emission models of the various sources. Above 10 GeV, Fermi is starting to detect large-scale regions of excess high-energy emission not predicted by interstellar emission models, including the *"Fermi lobes"* [7] and other large-scale hard-spectrum diffuse features. At these energies more than 500 sources have been detected, and around 170 of these sources are still unassociated and are not observed at other energies. Since the photon statistics are still

(2) `http://fits.gsfc.nasa.gov/`
(3) `http://fermi.gsfc.nasa.gov/ssc/data/access/lat/2yr_catalog/`

low in this energy range, we will likely continue to find new sources during the next years of observations.

Using a 36 months data sample 101 pulsars have been found and 16 SNRs have been studied. With the forthcoming SNR LAT catalog more sources could be found and studied and a better understanding of the emission region and mechanism will follow. The study and identification of nearby sources of photons and possibly of cosmic rays is of fundamental importance also for other analysis of the LAT data that will be described in the following sections.

3. – Dark Matter search strategy

In the following subsections some of the main targets for the indirect Dark Matter (DM) signal search with the Fermi data will be shown.

3˙1. *Dwarfs satellites*. – Milky Way dwarf spheroidal (dSph) galaxies are good candidate targets for DM studies through annihilation signatures, because their mass-to-light ratio is predicted to be of the order of 10–10^3 [8], implying that they could be largely DM dominated. Moreover, since no significant γ-ray emission of astrophysical origin is expected (these systems host few stars and no hot gas), the detection of a γ-ray signal could provide a clean DM signature. Weakly Interacting Massive Particles (WIMPs) have long been consideredas well-motivated candidates for DM that could contribute to the 80% of the non-baryonic mass density in the universe. At a given energy E, the differential γ-ray flux $\Phi_\gamma(E, \Delta\Omega)$ from WIMP annihilation in a region covering a solid angle $\Delta\Omega$ and centered on a DM source, can be factorized as [9]

$$\Phi_\gamma(E, \Delta\Omega) = J(\Delta\Omega) \times \Phi^{PP}(E), \tag{1}$$

where $J(\Delta\Omega)$ is the *"astrophysical factor"* or J-factor, *i.e.* the line of sight (l.o.s.) integral of the DM density squared in the direction of observation over the solid angle $\Delta\Omega$. The term $\Phi^{PP}(E)$ is the *"particle physics factor"*, that encodes the particle physics properties of the DM as the mass of the WIMP (m_χ) and various parameters that describe the annihilation. $\Phi^{PP}(E)$ depends linearly to $\langle\sigma v\rangle$, *i.e.* the WIMP pair annihilation cross-section times the relative velocity of the two annihilating particles.

Even if the J-factor is different for each dSph, the characteristics of the WIMP candidate (m_W, $\langle\sigma_{\mathrm{ann}} v\rangle$, annihilation channels and their branching ratios) can be assumed to be universal and so different sources can be studied together.

In [10] 24 months of P6V3 *diffuse* class events [3] between 200 MeV and 100 GeV are analyzed. Using the newly developed *composite2* likelihood technique, the DM signals across 10 Regions of Interest (ROIs), each associated to a different dSph, are combined while the other diffuse models and point sources are fitted separately. Uncertainties on the J-factor are taken into account in the fit procedure by adding a proper term to the likelihood that represents the measurement uncertainties. As no significant signal is found, upper limits were reported (see fig. 1). These upper limits allow us to rule out WIMP annihilation with cross-sections predicted by the most generic cosmological calculations up to a mass of ~ 27 GeV for the $b\bar{b}$ channel and up to a mass of ~ 37 GeV for the $\tau^+\tau^-$ channel. More stringent upper limits could be obtained in the future with more data (in 10 years an improvement of a factor of 5) and with new dSphs. In [11] these limits are compared with the predictions of a large number of different models.

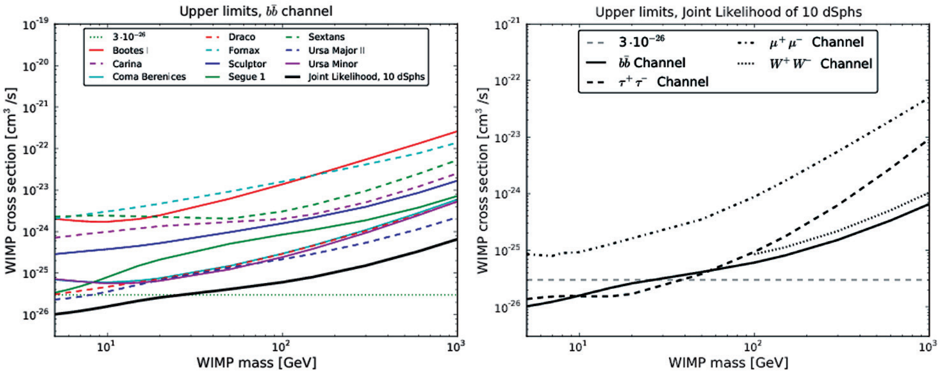

Fig. 1. – Left panel: derived 95% CL upper limits on a WIMP annihilation cross-section for all selected dSphs and for the joint likelihood analysis for annihilation into the $b\bar{b}$ final state. Right panel: derived 95% CL upper limits on the WIMP annihilation cross-section for all the four channels studied in [10] $b\bar{b}$, $\tau^+\tau^-$, $\mu^+\mu^-$ and W^+W^-. The most generic cross-section ($\sim 3 \cdot 10^{-26}\,\mathrm{cm}^3\,\mathrm{s}^{-1}$ for a purely s-wave cross-section) is shown as a reference in both plots. Uncertainties in the J-factor are included in all the analyses. Taken from [10].

Another approach to this analysis is described in [9]. In this case the same set of dSphs were used, but the analysis was performed with 3 years of P7SOURCE_V6 data [3] in the energy range from 562 MeV to 562 GeV implementing a model independent approach. A signal region of 0.5° and a background region consisting of an annulus between 5° and 6° around each dSph were selected. The upper limits were evaluated with a Bayesian technique on each dSph and for all the ten sources with two different procedures, using the average J-factor or the proper J-factors of each source. The upper limits on the signal counts were finally converted into upper limits on the flux by means of an unfolding procedure (see [9] and references therein). These results, even though obtained with a different event reconstruction and a different technique are similar and consistent with the previous ones.

3˙2. *Clusters.* – Clusters of galaxies are the most massive objects in the Universe that have had time to virialize by the present epoch, making nearby clusters attractive targets for searches for a signature from DM annihilation. Clusters are more distant, but also more massive than dSph galaxies, and like dSphs, they are very DM dominated, and typically lie at high galactic latitudes where the contamination from Galactic γ-ray background is low. Unlike in dSphs, DM annihilation is not the only potential source of γ-ray emission because several astrophysical mechanisms can occur. Significant γ-ray, emission has not been detected from local clusters by the Fermi-LAT in the first 11 months of observation [12] and a recent preliminary analysis on 24 months of data for 6 clusters did not show any excess in the stacked residual maps. These results provided some tight limits on DM models, even though in literature there are different analysis that show the possibility of a faint signal (*e.g.*, [13]).

3˙3. *Milky Way.* – The DM annihilation in the Milky Way halo is another target for DM search due to the large DM density expected in the vicinity of the Galactic Center and the proximity of the region. The analysis in this region is done with both the profile likelihood technique [14] and the Bayesian technique [10]. In the first approach, various

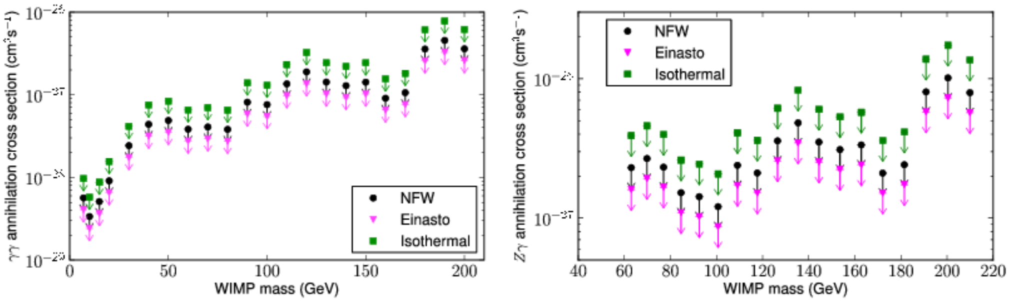

Fig. 2. – Dark matter annihilation 95% CL cross-section upper limits into $\gamma\gamma$ (left) and $Z\gamma$ (right) for the NFW, Einasto, and isothermal profiles for the region $|b| > 10^\circ$ plus a $20^\circ \times 20^\circ$ square centered on the Galactic center. γZ limits below $E_\gamma < 30\,\text{GeV}$ are not shown. Taken from [17].

limits are evaluated, from the most conservative one (assuming that all the detected photons from the halo are produced by annihilating/decaying WIMPs), to the deepest one (using GALPROP [15] simulations to model the astrophysical diffuse background). The limits derived for leptonic models challenge the interpretation of the PAMELA and Fermi cosmic rays anomalies (see sect. **4**) as annihilation of DM in the Galactic Halo, while they are not enough constraining to exclude the interpretation in terms of decaying DM. In [10] just the most conservative approach is used, and 1000 random locations are selected to set upper limits that are consistent with the previous.

The Galactic center is also a good candidate to observe the DM annihilation signal due to the large quantity of DM that should be located in that region, even though it is one of the most crowded and complex region in the sky. A preliminary analysis with 3 years of P7 data [3] has shown that the galactic diffuse component and some point sources can account for the observed emission and no strong structures are found in residuals maps.

3˙4. *Spectral lines from WIMPs*. – In [16] and [17] a search for monochromatic γ-rays from WIMPs annihilation or decay is preformed. If a WIMP annihilates or decays directly into a photon (γ) and another particle (X), the photons are approximately monochromatic. Detection of one or more striking spectral lines would be convincing evidence for DM. Using a set of 2 years P6 DATACLEAN [3] data no evidence for photon lines was found. Starting from the evaluated upper limits at 95% CL on the spectral line and assuming three different spatial distribution of DM, it is possible to evaluate the upper limits on the annihilation cross-section on both the $\gamma\gamma$ channel and the $Z\gamma$ channel (see bottom panel of fig. 2 and for a complete discussion see [17]). Theoretical predictions for γ-ray line intensity are highly model dependent, so that only some models are constrained by this results. In literature (*e.g.*, [18]) some analyses that have found a hint of a possible detection can be found.

3˙5. *Isotropic diffuse background*. – In [19] and [20] the full-sky γ-ray survey is performed for searching a possible isotropic DM signal, originating from annihilations summed over halos at all redshifts. Most cosmological halos are individually unresolved and will contribute to an approximately isotropic γ-ray background radiation (IGRB). The difficulty of estimating the isotropic background to the cosmological DM annihilation signal further increases the uncertainty in these limits. Blazars, radio galaxies and star-forming galaxies account from 50% to 80% of the observed extragalactic background light spectra. Given these uncertainties, in [19] the most conservative and most optimistic limits on cross-sections span three orders of magnitude. While the most conservative constraints barely reach exclusion of theoretically discussed DM cross-sections, more optimistic descriptions of the DM halos and subhalos would instead allow to exclude several models.

4. – The LAT as an electron detector

Since electromagnetic (EM) cascades are generated during both electron and photon interactions in matter, the LAT is also by its nature a detector for electrons and positrons. For event reconstruction (track identification, energy and direction measurement, ACD analysis) and calculation of variables used in event classification we use the same reconstruction algorithms as for photons. The selections are of course different and specific to the electron analysis. The high flux of cosmic-rays (CRs) protons and helium compared to that of electrons and positrons dictates that the hadron rejection must be 10^3–10^4, increasing with energy, which can be reached analysing the shape of the shower.

4˙1. *Electron and positron combined spectra.* – The observed spectra in [21], from 7 GeV to 1 TeV can be fitted by a power law with spectral index in the interval 3.03–3.13 (best fit 3.08), similar to that given in [22]. The spectrum is significantly harder than that reported by previous experiments with the absence of any evident feature. In any case, some spectral flattening at 70–200 GeV and a noticeable excess above 200 GeV are suggested, as compared to the power-law spectral fit. The gentle features of the spectrum can be explained within a conventional model by adjusting the injection spectra. Another possibility that provides a good overall agreement with our spectrum is the introduction of an additional leptonic component with a hard spectrum. Such an additional component is motivated by the rise in the positron fraction reported by PAMELA [23] and the LAT (see sect. **4˙2**). Different kinds of models can explain this component, from nearby sources (such as pulsars) to the annihilation of DM particles (see [21] for more references).

4˙2. *Electron and positron separate spectra.* – The LAT can also measure separately the spectra of CR electrons (CREs) and positrons from 20 GeV to 200 GeV, taking advantage of the Earth shadow and the offset direction for electrons and positrons due to the geomagnetic field, as fully described in [24]. This is the first time that the absolute CR positron spectrum has been measured above 50 GeV and that the fraction has been determined above 100 GeV, as shown in fig. 3. We find that the positron fraction increases with energy between 20 and 200 GeV, in agreement with the results reported by PAMELA [23]. The best established mechanism for producing CR positrons is secondary production. Such secondary production will result in a positron fraction that decreases with energy. The origin of the rising positron fraction at high energy is unknown and has been ascribed to a variety of mechanisms including additional contribution from pulsars and SNRs, CRs interacting with giant molecular clouds, and DM (see [24] and references therein). Future measurements with greater sensitivity and energy reach, such as those by AMS-02, are necessary to distinguish between the many possible explanations of this increase.

4˙3. *Cosmic-ray electron anisotropy.* – In [25] the arrival directions of the reconstructed cosmic-ray electrons and positrons were searched for anisotropies at angular scales extending from $\sim 10^\circ$ up to 90°. Any anisotropy in the arrival directions of

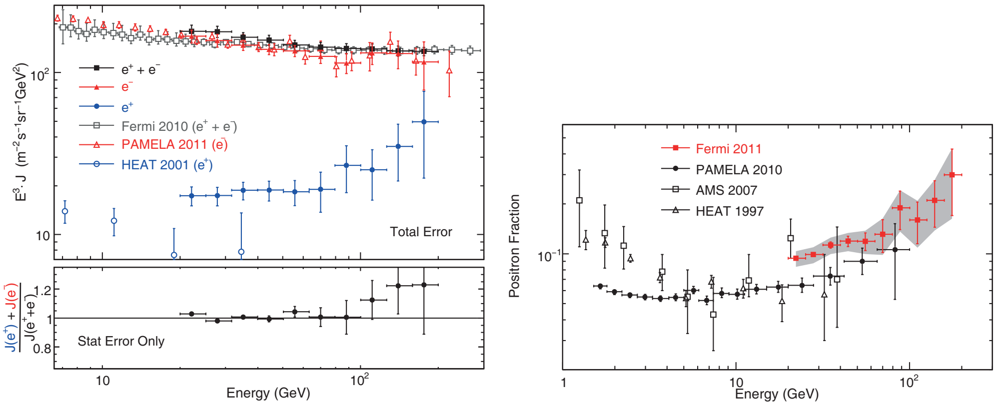

Fig. 3. – On the left: energy spectra for e^+, e^-, and $e^+ + e^-$ (control region). In the control region where both species are allowed, this analysis reproduces the Fermi LAT results reported previously for the total electron plus positron spectrum [22,21] (gray). The bottom panel shows that the ratio between the sum and the control flux is consistent with 1 as expected. On the right: positron fraction measured by the Fermi LAT and by other experiments. The Fermi statistical uncertainty is shown with error bars and the total (statistical plus systematic uncertainty) is shown as a shaded band. For the full list of reference and for more details see [24].

cosmic-ray electrons (CREs) detected by the LAT would be a powerful tool to discriminate between a DM origin and an astrophysical one. In particular, since Galactic DM is denser towards the direction of the Galactic center, the generic expectation in the DM annihilation or decay scenario is a dipole with an excess towards the center of the Galaxy and a deficit towards the anti-center. Also, both the Monogem and the Geminga pulsars, likely some of the most significant CRE sources, are both roughly placed opposite to the direction of the Galactic Center, making a search for anisotropy an effective distinguishing diagnostic. Two independent techniques were applied, both resulting in null results. Upper limits on the degree of the anisotropy were set, for different energy ranges and angular scale. The upper limits for a dipole anisotropy ranged from $\sim 0.5\%$ to $\sim 10\%$. These limits were compared with the predicted anisotropies from individual nearby pulsars and from DM annihilations, in all cases, they lie roughly above the predicted anisotropies.

4·4. *High-energy cosmic-ray electrons from the Sun.* – In [26] we use the high-energy cosmic-ray electron and positron (CRE) data set to search for flux variations correlated with the Sun direction. No known astrophysical mechanisms are expected to generate a significant high-energy CRE ($> 100\,\text{GeV}$) excess associated with the Sun, while several classes of DM models could generate this kind of emission.

In some scenarios DM particles captured by the Sun through elastic scattering interactions would annihilate to ϕ (a new light intermediate state) pairs in the Sun's core, and if the ϕ could escape the surface of the Sun before decaying to CREs, these can be detected by the LAT. In other scenarios DM is captured by the Sun only through inelastic scattering (iDM), this could lead to a non-negligible fraction of DM annihilating outside the Sun's surface. For models in which iDM annihilates to CREs, an observable flux at energies above a few tens of GeV could be produced.

In the case of annihilation of DM through an intermediate state and subsequent decay to $e^{\pm}$, the upper limits on solar CRE fluxes provide significantly stronger constraints on the DM scattering cross-section than limits previously derived by constraining the final state radiation emission associated with this decay channel using solar γ-ray measurements. For the iDM scenario, the solar CRE flux upper limits exclude the range of models which can reconcile the data from DAMA/LIBRA and CDMS for $m_\chi \gtrsim 70\,\mathrm{GeV}$, assuming DM annihilates predominantly to $e^{\pm}$. Since direct detection experiments are not sensitive to the dominant annihilation channels of the DM particles, other data, *e.g.*, solar γ-ray measurements and neutrino searches, may be able to further constrain these models by excluding regions of parameter space for alternative annihilation channels.

* * *

The *Fermi* LAT Collaboration acknowledges support from a number of agencies and institutes for both development and the operation of the LAT as well as scientific data analysis. These include NASA and DOE in the United States, CEA/Irfu and IN2P3/CNRS in France, ASI and INFN in Italy, MEXT, KEK, and JAXA in Japan, and the K. A. Wallenberg Foundation, the Swedish Research Council and the National Space Board in Sweden. Additional support from INAF in Italy and CNES in France for science analysis during the operations phase is also gratefully acknowledged.

REFERENCES

[1] Atwood W. B. *et al.*, *Astrophys. J.*, **697** (2009) 1071.
[2] Abdo A. A. *et al.*, *Astropart. Phys.*, **32** (2009) 193.
[3] Fermi-LAT Collaboration, *Astrophys. J. Suppl. S.*, **203** (2012) 4.
[4] Nolan P. L. *et al.*, *Astrophys. J. Suppl. S.*, **199** (2012) 31.
[5] Abdo A. A. *et al.*, *Astrophys. J. Suppl. S.*, **183** (2009) 46.
[6] Abdo A. A. *et al.*, *Astrophys. J. Suppl. S.*, **188** (2010) 405.
[7] Su M., Slatyer T. R. and Finkbeiner D. P., *Astrophys. J.*, **724** (2010) 1044.
[8] Strigari L. E. *et al.*, *Nature*, **454** (2008) 1096.
[9] Mazziotta M. N. *et al.*, *Astropart. Phys.*, **37** (2012) 26.
[10] Ackermann M. *et al.*, *Phys. Rev. Lett.*, **107** (2011) 241302.
[11] Cotta R. C. *et al.*, *J. Cosm. Astropart. Phys.*, **4** (2012) 16.
[12] Ackermann M. *et al.*, *J. Cosm. Astropart. Phys.*, **5** (2010) 25.
[13] Han J. *et al.*, arXiv:1201.1003 (2012).
[14] Ackermann M. *et al.*, arXiv:1205.6474 (2012).
[15] Strong A. W., Moskalenko I. V. and Reimer O., *Astrophys. J.*, **537** (2000) 763.
[16] Abdo A. A. *et al.*, *Phys. Rev. Lett.*, **104** (2010) 091302.
[17] Ackermann M. *et al.*, *Phys. Rev. D*, **86** (2012) 022002.
[18] Weniger C., arXiv:1204.2797 (2012).
[19] Abdo A. A. *et al.*, *J. Cosm. Astropart. Phys.*, **4** (2010) 14.
[20] Ackermann M., *Talk at the TeVPA 2011 conference, 1-5 Aug. 2011, Stockholm, Sweden.*
[21] Ackermann M. *et al.*, *Phys. Rev. D*, **82** (2010) 092004.
[22] Abdo A. A. *et al.*, *Phys. Rev. Lett.*, **102** (2009) 181101.
[23] Adriani O. *et al.*, *Nature*, **458** (2009) 607.
[24] Ackermann M. *et al.*, *Phys. Rev. Lett.*, **108** (2012) 011103.
[25] Ackermann M. *et al.*, *Phys. Rev. D*, **82** (2010) 092003.
[26] Ajello M. *et al.*, *Phys. Rev. D*, **84** (2011) 032007.

IL NUOVO CIMENTO Vol. 35 C, N. 6 Novembre-Dicembre 2012
DOI 10.1393/ncc/i2012-11346-x

Colloquia: LaThuile12

KLOE searches on dark forces

S. Giovannella for the KLOE-2 Collaboration
INFN, Laboratori Nazionali di Frascati - via Enrico Fermi 40, Frascati, Italy

ricevuto il 7 Settembre 2012

Summary. — The existence of a secluded gauge sector could explain at the same time several unexpected astrophysical observations. This hypothesis can be tested at low energy e^+e^- colliders by searching for a light vector gauge boson, called U, mediating dark forces. At DAΦNE, the Frascati e^+e^- ϕ-factory, three different U boson production channels can be studied. Results obtained with KLOE data and perpectives for the KLOE-2 run, where a larger data sample is expected, are discussed.

PACS `14.70.Pw` – Other gauge bosons.

1. – Dark matter and dark forces

Several recent astrophysical observations produced unexpected results, as the 511 keV gamma-ray signal from the galactic center observed by the INTEGRAL satellite [1], the excess in the cosmic ray positrons reported by PAMELA [2], the total electron and positron flux measured by ATIC [3], Fermi [4] and HESS [5, 6], the annual modulation of the DAMA/LIBRA signal [7, 8] and the low energy spectrum of nuclear recoil candidate events observed by CoGeNT [9]. These anomalies could be all explained with the existence of a dark matter weakly interacting massive particle, belonging to a secluded gauge sector under which the Standard Model (SM) particles are uncharged [10-19]. An abelian gauge field, the U boson with mass near the GeV scale, couples the secluded sector to the SM through its kinetic mixing with the SM hyper-charge gauge field. The kinetic mixing parameter, ϵ, is expected to be of the order 10^{-4}–10^{-2} [11, 21], so that observable effects can be induced in $\mathcal{O}$(GeV)–energy e^+e^- colliders [20-24] and fixed target experiments [25-28]. The possible existence of a new light boson gauging a new symmetry with a small coupling was in fact already introduced on general grounds in [29], and rediscussed in models postulating also the existence of light spin 0 or 1/2 dark matter particles [30, 31]. This boson can have both vector and axial-vector couplings to quark and leptons, however axial couplings are strongly constrained by data, leaving room to vector couplings only.

2. – Searches for dark forces at KLOE

The KLOE experiment operates at DAΦNE, the e^+e^- Frascati ϕ-factory. From 2000 to 2006, KLOE collected $2.5\,\mathrm{fb}^{-1}$ of collisions at the ϕ meson peak and about $240\,\mathrm{pb}^{-1}$ below the ϕ resonance ($\sqrt{s} = 1\,\mathrm{GeV}$). The ϕ meson predominantly decays into charged and neutral kaons, thus allowing KLOE to make precision studies in the fields of flavor physics, low-energy QCD and test of discrete symmetries [32].

A new beam crossing scheme allowing a reduced beam size and increased luminosity is operating at DAΦNE [33]. The KLOE-2 detector was successfully installed in this new interaction region and has been upgraded with small angle tagging devices to detect both high- and low-energy electrons or positrons in $e^+e^- \to e^+e^- X$ events. An inner tracker and small angle calorimeters are scheduled to be installed in a subsequent step, providing larger acceptance both for charged particles and photons. A detailed description of the KLOE-2 physics program can be found in ref. [34].

The U boson can be produced at DAΦNE through radiative decays of neutral mesons, such as $\phi \to \eta U$. With the statistics already collected at KLOE, this decay can potentially probe couplings down to $\epsilon \sim 10^{-3}$ [22], covering most of the parameter's range of interest for the theory. The U boson can be observed by its decay into a lepton pair, while the η can be tagged by one of its not-rare decays.

Assuming also the existence of a secluded Higgs boson, the h', both the U and the h' can be produced at DAΦNE if their masses are smaller than M_ϕ. The mass of the U and h' are both free parameters, and the possible decay channels can be very different depending on which particle is heavier. In both cases, an interesting production channel is the h'-strahlung, $e^+e^- \to Uh'$ [20]. Assuming the h' to be lighter than the U boson, it turns out to be very long-lived, so that the signature process will be a lepton pair, generated by the U boson decay, plus missing energy. In the case $m_{h'} > m_U$, the dark Higgs frequently decays to a pair of real or virtual U's. In this case one can observe events with 6 leptons in the final state, due to the h'-strahlung process, or 4 leptons and a photon, due to the $e^+e^- \to h'\gamma$ reaction.

Another possible channel to look for the existence of the U boson is the $e^+e^- \to U\gamma$ process [20]. The expected cross-section can be as high as $\mathcal{O}(\mathrm{pb})$ at DAΦNE energies. The on-shell boson can decay into a lepton pair, giving rise to a $\ell^+\ell^-\gamma$ signal of few MeV mass resolution. About 10^3 events/fb^{-1} are expected to be produced for $\epsilon \sim 10^{-3}$.

In the following sections, results from the analyes of $\phi \to \eta U$ and $e^+e^- \to Uh'$ channels are reported, together with perspectives for the new KLOE-2 run.

3. – The $\phi \to \eta U$ decay

As discussed above, the search of the U boson can be performed at KLOE using the decay chain $\phi \to \eta U$, $U \to \ell^+\ell^-$. An irreducible background due to the Dalitz decay of the ϕ meson, $\phi \to \eta\,\ell^+\ell^-$, is present. This decay has been studied by the SND and CMD-2 experiments, which measured a branching fraction of $\mathrm{BR}(\phi \to \eta\, e^+e^-) = (1.19 \pm 0.19 \pm 0.07) \times 10^{-4}$ and $\mathrm{BR}(\phi \to \eta\, e^+e^-) = (1.14 \pm 0.10 \pm 0.06) \times 10^{-4}$, respectively [35,36]. This corresponds to a cross-section of $\sigma(\phi \to \eta\,\ell^+\ell^-) \sim 0.7\,\mathrm{nb}$, with a di-lepton mass range $M_{\ell\ell} < 470\,\mathrm{MeV}$. For the signal, the expected cross-section is expressed by [22]

$$\sigma(\phi \to \eta\, U) = \epsilon^2\, |F_{\phi\eta}(m_U^2)|^2\, \frac{\lambda^{3/2}(m_\phi^2, m_\eta^2, m_U^2)}{\lambda^{3/2}(m_\phi^2, m_\eta^2, 0)}\, \sigma(\phi \to \eta\gamma), \tag{1}$$

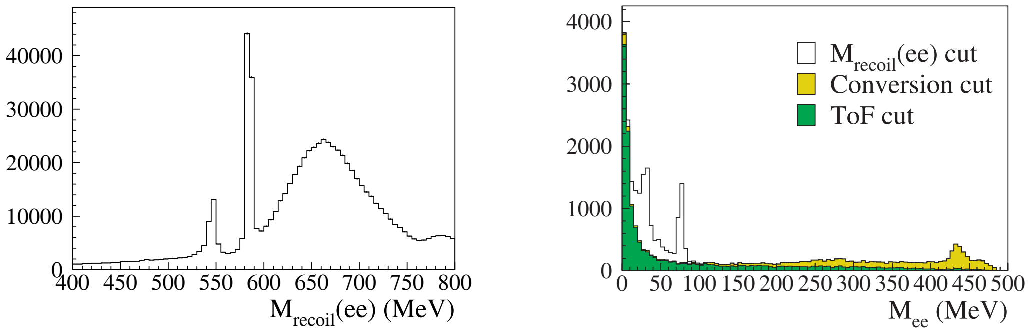

Fig. 1. – Left: Recoiling mass against the e^+e^- pair for data sample after preselection cuts. The $\phi \to \eta\, e^+e^-$ signal is clearly visible in the peak corresponding to η mass. The second peak at $\sim 590\,\text{MeV}$ is due to $K_S \to \pi^+\pi^-$ events with wrong mass assignment. Right: M_{ee} distribution for data at different analysis steps.

where $F_{\phi\eta}(m_U^2)$ is the $\phi\eta\gamma^*$ transition form factor evaluated at the U mass while the following term represents the ratio of the kinematic functions of the involved decays, with $\lambda(m_1^2, m_2^2, m_3^2) = [1 + m_3^2/(m_1^2 - m_2^2)]^2 - 4m_1^2 m_3^2/(m_1^2 - m_2^2)^2$. Using $\epsilon = 10^{-3}$ and $|F_{\phi\eta}(m_U^2)|^2 = 1$, a cross-section $\sigma(\phi \to \eta\, U) \sim 40\,\text{fb}$ is obtained. Despite the small ratio between the overall cross-section of $\phi \to \eta\, U$ and $\phi \to \eta\, \ell^+\ell^-$, their different di-lepton invariant mass distributions allow to test the ϵ parameter down to 10^{-3} with the KLOE data set.

The best U decay channel to search for the $\phi \to \eta\, U$ process at KLOE is in e^+e^-, since a wider range of U boson masses can be tested and $e^\pm$ are easily identified using a time-of-flight (ToF) technique. The η can be tagged by the three-pion or two-photon final state, which represent $\sim 95\%$ of the total decay rate. We have performed a search using the $\eta \to \pi^+\pi^-\pi^0$ channel, which provide a clean signal with four charged tracks and two photon in the final state. Studies are under way also for the $\eta \to \pi^0\pi^0\pi^0$ and $\eta \to \gamma\gamma$ samples.

3·1. *The* $\eta \to \pi^+\pi^-\pi^0$ *final state*. – The analysis of the $\eta \to \pi^+\pi^-\pi^0$ final state has been performed on $1.5\,\text{fb}^{-1}$. The Monte Carlo (MC) simulation of the irreducible background $\phi \to \eta\, e^+e^-$, $\eta \to \pi^+\pi^-\pi^0$ has been produced with $\mathrm{d}\Gamma(\phi \to \eta\, e^+e^-)/\mathrm{d}m_{ee}$ weighted according to Vector Meson Dominance model [37], using the form factor parametrization from the SND experiment [35]. The MC simulation for the $\phi \to \eta\, U$ decay has been developed according to [22], with a flat distribution in M_{ee}. All MC productions, including all other ϕ decays, take into account changes in DAΦNE operation and background conditions on a run-by-run basis. Data-MC corrections for cluster energies and tracking efficiency, evaluated with radiative Bhabha events and $\phi \to \rho\pi$ samples, respectively, have been applied.

Preselection cuts require: i) four tracks in a cylinder around the interaction point (IP) plus two photon candidates; ii) best $\pi^+\pi^-\gamma\gamma$ match to the η mass using the pion hypothesis for tracks; iii) other two tracks assigned to e^+e^-; iv) loose cuts on η and π^0 invariant masses ($495 < M_{\pi^+\pi^-\gamma\gamma} < 600\,\text{MeV}$, $70 < M_{\gamma\gamma} < 200\,\text{MeV}$). These simple cuts allow to clearly see the peak due to $\phi \to \eta\, e^+e^-$ events in the distribution of the recoil mass to the e^+e^- pair, $M_{\text{recoil}}(ee)$ (see fig. 1, left). A cut $535 < M_{\text{recoil}}(ee) < 560\,\text{MeV}$ is then applied.

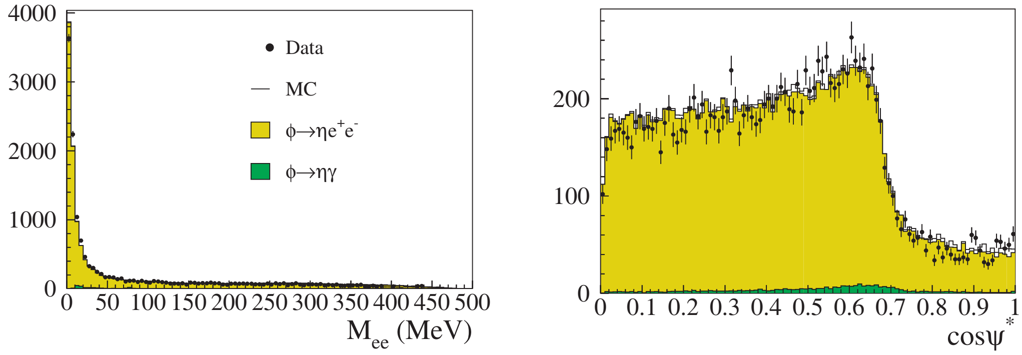

Fig. 2. – Invariant mass of the e^+e^- pair (left) and $\cos\psi^*$ distribution (right) for $\phi \to \eta\, e^+e^-$, $\eta \to \pi^+\pi^-\pi^0$ events.

A residual background contamination, due to $\phi \to \eta\gamma$ events with photon conversion on beam pipe (BP) or drift chamber walls (DCW), is rejected by tracing back the tracks of the two e^+, e^- candidates and reconstructing their invariant mass (M_{ee}) and distance (D_{ee}) at the BP/DCW surfaces. As both quantities are small in case of photon conversions, $\phi \to \eta\gamma$ background is removed by rejecting events with: $M_{ee}(BP) < 10\,\text{MeV}$ and $D_{ee}(BP) < 2\,\text{cm}$, $M_{ee}(DCW) < 80\,\text{MeV}$ and $D_{ee}(DCW) < 10\,\text{cm}$. A further relevant background, originated by $\phi \to K\bar{K}$ and wrongly reconstructed $\phi \to \pi^+\pi^-\pi^0$ decays surviving analysis cuts, have more than two charged pions in the final state and are suppressed using time-of-flight (ToF) to the calorimeter. When an energy cluster is connected to a track, the arrival time to the calorimeter is evaluated both using the calorimeter timing (T_{cluster}) and the track trajectory ($T_{\text{track}} = L_{\text{track}}/\beta c$). The $\Delta T = T_{\text{track}} - T_{\text{cluster}}$ variable is then evaluated in both electron (ΔT_e) and pion (ΔT_π) hypotheses. Events with an e^+, e^- candidate outside a $3\,\sigma$'s window on the ΔT_e variables are rejected. In fig. 1, right, the M_{ee} distribution evaluated at different steps of the analysis is shown. The peaks at $\sim 30\,\text{MeV}$ and $\sim 80\,\text{MeV}$ are due to photon conversions on BP and DCW, respectively. The ToF cut reduces the tail at high M_{ee} values while the conversion cut removes events in the low invariant mass region. The analysis efficiency as a function of M_{ee} ranges between 10% and 20%, increasing for high M_{ee} values.

In fig. 2 the comparison between data and Monte Carlo events for M_{ee} and $\cos\psi^*$ distributions is shown. The second variable is the angle between the η and the e^+ in the e^+e^- rest frame. About 14000 $\phi \to \eta\, e^+e^-$, $\eta \to \pi^+\pi^-\pi^0$ candidates are present in the analyzed data set, with a negligible residual background contamination. As an accurate description of the background is crucial for the search of the U boson, its shape is extracted directly from our data. A fit is performed to the M_{ee} distribution, after applying a bin-by-bin subtraction of the $\phi \to \eta\gamma$ background and efficiency correction. The parametrization of the fitting function has been taken from ref. [37]:

$$\frac{\mathrm{d}\Gamma(\phi \to \eta\, e^+e^-)}{\mathrm{d}q^2} = \frac{\alpha}{3\pi}\,\frac{|F_{\phi\eta}(q^2)|^2}{q^2}\sqrt{1-\frac{4m^2}{q^2}}\left(1+\frac{2m^2}{q^2}\right)\lambda^{3/2}(m_\phi^2, m_\eta^2, m_U^2) \tag{2}$$

with $q = M_{ee}$ and the transition form factor described by $F_{\phi\eta}(q^2) = 1/(1-q^2/\Lambda^2)$. Free parameters of the fit are Λ and an overall normalization factor. A good description of

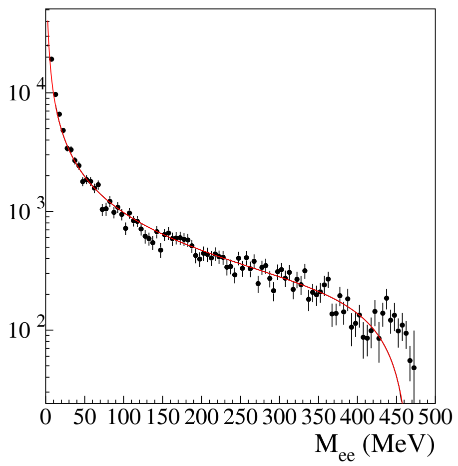

Fig. 3. – Fit to the M_{ee} spectrum for the Dalitz decays $\phi \to \eta\, e^+e^-$, using the $\eta \to \pi^+\pi^-\pi^0$ final state.

the M_{ee} shape is obtained, except at the high end of the spectrum (see fig. 3), where a residual background contamination from multi-pion events is still present.

As mentioned before, the $\phi \to \eta U$ MC signal has been produced according to ref. [22], with a flat distribution of the U boson invariant mass. Events are then divided in subsamples of 1 MeV width. For each M_{ee} value, signal hypothesis has been excluded at 90% CL using the $\mathrm{CL_S}$ technique [38]. For the $\phi \to \eta U$ signal, the opening of the $U \to \mu^+\mu^-$ threshold has been included, in the hypothesis that the U boson decays only to lepton pairs and assuming equal coupling to e^+e^- and $\mu^+\mu^-$. The expected shape for the irreducible background $\phi \to \eta\, e^+e^-$ is obtained from our fit to the M_{ee} distribution, taking also into account the error on number of background events as a function of M_{ee}. In fig. 4 the exclusion plot on $\alpha'/\alpha = \epsilon^2$ variable is compared with existing limits from the muon anomalous magnetic moment a_μ [39] and from recent measurements of the MAMI/A1 [40] and APEX [41] experiments. The gray line is where the U boson parameters should lay to account for the observed discrepancy between measured and calculated a_μ values. Our result greatly improves existing limits in a wide mass range, resulting in an upper limit on the α'/α parameter of $\leq 2 \times 10^{-5}$ at 90% CL for $50 < M_U < 420\,\mathrm{MeV}$.

3˙2. *The* $\eta \to \pi^0\pi^0\pi^0$, $\eta \to \gamma\gamma$ *final states*. – Other two analyses devoted to the search of the $\phi \to \eta U$, $U \to e^+e^-$, decay are in progress, using fully neutral η decay channels.

The analysis strategy for the $\eta \to \pi^0\pi^0\pi^0$ decay is similar to the previous one. After preselection cuts based on event topology, the background is reduced to negligible levels by cutting on the e^+e^- recoil mass, ToF variables and rejecting events due to conversions. The preliminary di-lepton invariant mass using $1.7\,\mathrm{fb}^{-1}$ is shown in fig. 5, left. Evaluation of the exclusion plot is in progress.

For the $\eta \to \gamma\gamma$ final state, the most severe background is generated by double radiative Bhabha scattering events and it is strongly reduced by cutting on the opening angle between the charged tracks and the photons. Residual non-Bhabha background is rejected by using further electron identification, based on the E/p ratio for the e^+e^-

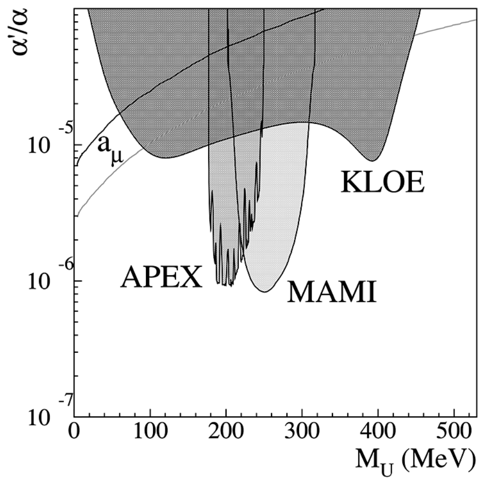

Fig. 4. – Exclusion plot at 90% CL for the parameter $\alpha'/\alpha = \epsilon^2$, compared with existing limits in our region of interest.

candidates. The resulting background reduction is still not enough for the search of $\phi \to \eta U$ events. The M_{ee} spectrum obtained with $1.7\,\mathrm{fb}^{-1}$ (fig. 5, right) shows a clear evidence of $\phi \to \eta\, e^+e^-$ Dalitz decays at low values and a residual background contamination at high M_{ee} due to Bhabha events. Work is in progress to further improve the signal-to-background ratio.

4. – The Higgs′-strahlung channel

The feasibility of the search for the process $e^+e^- \to Uh'$ has been done considering the $m_{h'} < m_U$ case. At DAΦNE energies, for $\epsilon \sim 10^{-3}$, a production cross-section of $\approx 20\,\mathrm{fb}$ is expected and the h' has $\tau_{h'} > 10\,\mu\mathrm{s}$, escaping the detection. The signature is therefore a lepton pair from the U boson plus missing energy.

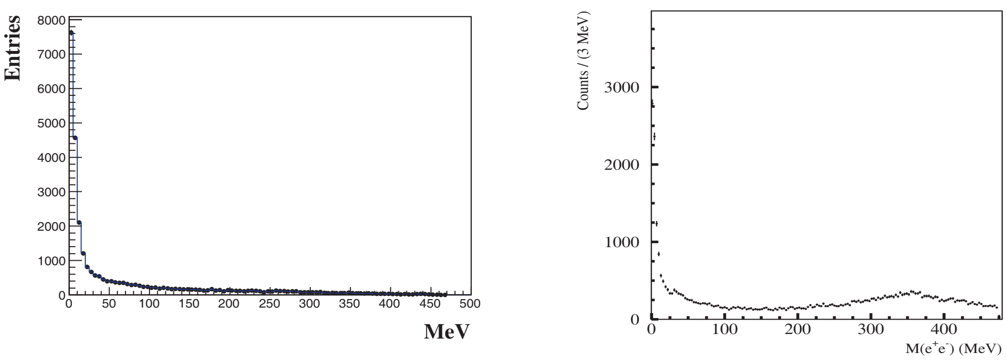

Fig. 5. – Invariant mass of the e^+e^- pair for $\eta \to \pi^0\pi^0\pi^0$ (left) and $\eta \to \gamma\gamma$ (right) channels.

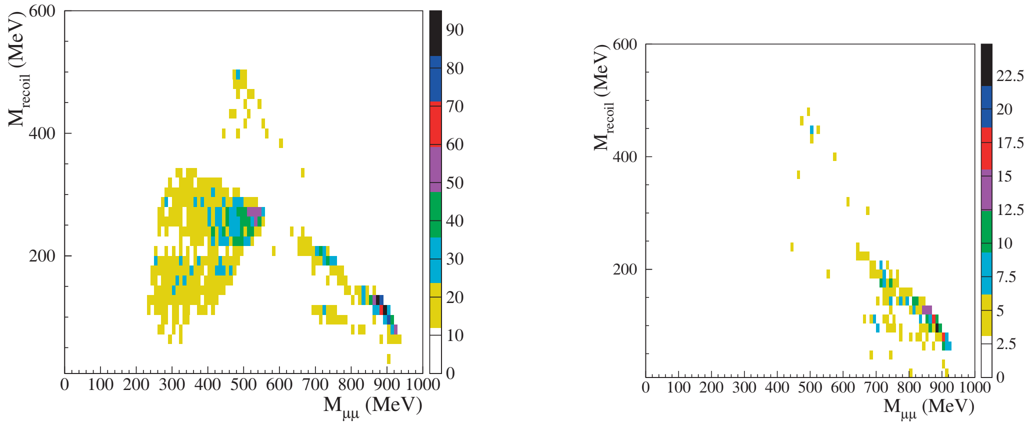

Fig. 6. – Search for $e^+e^- \to h'U$, $U \to \mu^+\mu^-$, $h' \to$ "*invisible*" events: recoil mass to the $\mu^+\mu^-$ pair as a function of the di-muon invariant mass for data taken at the ϕ mass (left) and at $\sqrt{s} = 1\,\text{GeV}$ (right).

The selection strategy has been optimized using Monte Carlo events. The signal has been generated according to ref. [20] in a discrete set of mass values in the range $m_U \leq 900\,\text{MeV}$, $m_{h'} \leq 400\,\text{MeV}$. The $U \to e^+e^-$ events are not selected by any official KLOE event classification (ECL) algorithms, which divide the events on the basis of topological information and provide reconstructed data to be used for different analyses. On the contrary, ECL is fully efficient for $U \to \mu^+\mu^-$ events when $m_{h'} < 300\,\text{MeV}$. We therefore considered the $\mu^+\mu^-$ final state only.

Muons are identified and separated from electrons and pions using a neural network algorithm based on energy depositions along the shower depth in the calorimeter and E/p, β variables. The other relevant cuts to reduce background contamination are: i) missing momentum direction in the barrel calorimeter; ii) a tight cut on vertex-IP distance and iii) no clusters in the calorimeter, with the exception of the two associated to tracks. The residual background contamination is due to $e^+e^- \to \pi^+\pi^-\gamma/\mu^-\mu^-\gamma$ continuum events with an undetected photon, and to $\phi \to K^+K^- \to \mu + \mu^-\nu\bar{\nu}$ with early decaying kaons.

In fig. 6, left the distribution of the recoil mass to the $\mu^+\mu^-$ pair (M_{recoil}) as a function of the di-muon invariant mass obtained with $1.65\,\text{fb}^{-1}$ is reported. M_{recoil} is evaluated using the center-of-mass energy of each run measured with Bhabha scattering events and the momenta of the muons. Continuum background, which can be further reduced tuning the π/μ identification algorithm, is concentrated in the band at $M_{\mu^+\mu^-} > 700\,\text{MeV}$. The $\phi \to K^+K^-$ channel covers a wider region of the plane ($M_{\mu^+\mu^-} < 600\,\text{MeV}$, $M_{\text{recoil}} < 300\,\text{MeV}$). This background, having only two muons in the final state and missing energy due to neutrinos, has the same signature of the signal. The efficiency for $e^+e^- \to Uh'$ events is 15–40%, depending on m_U, $m_{h'}$ masses. Taking into account the total integrated luminosity, a signal would show up as a sharp peak with ≤ 10 events in the M_{recoil}-$M_{\mu\mu}$ plane for $\epsilon \sim 10^{-3}$.

Being the $\phi \to K^+K^-$ background a nasty background source, we repeated the analysis using the off-peak sample, $0.2\,\text{fb}^{-1}$ taken at a center-of-mass energy of 1 GeV. As can be seen in fig. 6, right, the contribution from resonant background is not present anymore, providing a much cleaner sample for the search of $e^+e^- \to Uh'$ candidates.

5. – Summary and perspectives for KLOE-2

The search for $\phi \to \eta U$ with $U \to e^+e^-$, $\eta \to \pi^+\pi^-\pi^0$, using $1.5\,\mathrm{fb}^{-1}$ of KLOE data, results in an upper limit on the $\alpha'/\alpha = \epsilon^2$ parameter of $\leq 2 \times 10^{-5}$ at 90% CL for $50 < M_U < 420\,\mathrm{MeV}$. The inclusion of the the $\eta \to \pi^0\pi^0\pi^0$ and $\eta \to \gamma\gamma$ channels, already under study, will cover 95% of the η decay channels. Due to larger branching ratio and analysis efficiency, an improvement of ≈ 2 on the upper limit is expected. With the new data sample expected at KLOE-2, this value can be further improved. An integrated luminosity $10\,\mathrm{fb}^{-1}$ will provide another factor 2 improvement on the upper limit evaluation.

The search of the Higgs$'$-strahlung channel, $e^+e^- \to Uh'$ with $U \to \mu^+\mu^-$ plus missing energy, is limited by a non-negligible $\phi \to K^+K^-$ background in a wide region of the $M_{\mu^+\mu^-}$, M_{recoil} plane. Work is in progress to reduce this contribution on the KLOE data sample. At KLOE-2, the improvement on the vertex resolution, achievable with the insertion of the inner tracker, will provide a higher rejection factor. The feasibility of a high statistics run at 1 GeV, where the resonant background contribution is naturally reduced, is also under discussion.

* * *

I would like to warmly thank the organizers for their invitation and for the kind hospitality. This work was supported in part by the EU Integrated Infrastructure Initiative HadronPhysics Project under contract number RII3-CT-2004-506078; by the European Commission under the 7th Framework Programme through the "Research Infrastructures" action of the "Capacities" Programme, Call: FP7-INFRASTRUCTURES-2008-1, Grant Agreement N. 227431; by the Polish Ministery of Science and Higher Education through the Grant No. 0469/B/H03/2009/37.

REFERENCES

[1] Jean P. *et al.*, *Astron. Astrophys.*, **407** (2003) L55.
[2] Adriani O. *et al.*, *Nature*, **458** (2009) 607.
[3] Chang J. *et al.*, *Nature*, **456** (2008) 362.
[4] Abdo A. A. *et al.*, *Phys. Rev. Lett.*, **102** (2009) 181101.
[5] Aharonian F. *et al.*, *Phys. Rev. Lett.*, **101** (2008) 261104.
[6] Aharonian F. *et al.*, *Astron. Astrophys.*, **508** (2009) 561.
[7] Bernabei R. *et al.*, *Int. J. Mod. Phys. D*, **13** (2004) 2127.
[8] Bernabei R. *et al.*, *Eur. Phys. J. C*, **56** (2008) 333.
[9] Aalseth C. E. *et al.*, *Phys. Rev. Lett.*, **107** (2011) 141301.
[10] Pospelov M., Ritz A. and Voloshin M. B., *Phys. Lett. B*, **662** (2008) 53.
[11] Arkani-Hamed N., Finkbeiner D. P., Slatyer T. R. and Weiner N., *Phys. Rev. D*, **79** (2009) 015014.
[12] Alves D. S. M., Behbahani S. R., Schuster P. and Wacker J. G., *Phys. Lett. B*, **692** (2010) 323.
[13] Pospelov M. and Ritz A., *Phys. Lett. B*, **671** (2009) 391.
[14] Hisano J., Matsumoto S. and Nojiri M. M., *Phys. Rev. Lett.*, **92** (2004) 031303.
[15] Cirelli M., Kadastik M., Raidal M. and Strumia A., *Nucl. Phys. B*, **813** (2009) 1.
[16] March-Russell J., West S. M., Cumberbatch D. and Hooper D., *JHEP*, **07** (2008) 058.
[17] Cholis I., Dobler G., Finkbeiner D. P., Goodenough L. and Weiner N., *Phys. Rev. D*, **80** (2009) 123518.
[18] Cholis I., Finkbeiner D. P., Goodenough L. and Weiner N., *JCAP*, **12** (2009) 007.

[19] Arkani-Hamed N. and Weiner N., *JHEP*, **12** (2008) 104.
[20] Batell B., Pospelov M. and Ritz A., *Phys. Rev. D*, **79** (2009) 115008.
[21] Essig R., Schuster P. and Toro N., *Phys. Rev. D*, **80** (2009) 015003.
[22] Reece M. and Wang L. T., *JHEP*, **07** (2009) 051.
[23] Borodatchenkova N., Choudhury D. and Drees M., *Phys. Rev. Lett.*, **96** (2006) 141802.
[24] Yin P. F., Liu J. and Zhu S. H., *Phys. Lett. B*, **679** (2009) 362.
[25] Bjorken J. D., Essig R., Schuster P. and Toro N., *Phys. Rev. D*, **80** (2009) 075018.
[26] Batell B., Pospelov M. and Ritz A., *Phys. Rev. D*, **80** (2009) 095024.
[27] Essig R., Schuster P., Toro N. and Wojtsekhowski B., *JHEP*, **02** (2011) 009.
[28] Freytsis M., Ovanesyan G. and Thaler J., *JHEP*, **01** (2010) 111.
[29] Fayet P., *Phys. Lett. B*, **95** (1980) 285; **187** (1981) 184.
[30] Boehm C. and Fayet P., *Nucl. Phys. B*, **683** (2004) 219.
[31] Fayet P., *Phys. Rev. D*, **70** (2004) 023514.
[32] Bossi F. *et al.*, *Riv. Nuovo Cimento*, **031** (2008) 531.
[33] Milardi C. *et al.*, *ICFA Beam Dyn. Newslett.*, **48** (2009) 23.
[34] Amelino-Camelia G. *et al.*, *Eur. Phys. J. C*, **68** (2010) 619.
[35] Achasov M. N. *et al.*, *Phys. Lett. B*, **504** (2001) 275.
[36] Akhmetshin R. R. *et al.*, *Phys. Lett. B*, **501** (2001) 191.
[37] Landsberg L. G., *Phys. Rep.*, **128** (1985) 301.
[38] Junk T., *Nucl. Instrum. Methods A*, **434** (1999) 435.
[39] Pospelov M., *Phys. Rev. D*, **80** (2009) 095002.
[40] Merkel H. *et al.*, *Phys. Rev. Lett.*, **106** (2011) 251802.
[41] Abrahamyan S. *et al.*, *Phys. Rev. Lett.*, **107** (2011) 191804.

IL NUOVO CIMENTO Vol. 35 C, N. 6 Novembre-Dicembre 2012
DOI 10.1393/ncc/i2012-11347-9

Colloquia: LaThuile12

Dark Matter searches: A theoretical perspective

M. Cirelli

CERN Theory Division, CH-1211 Genève, Switzerland
Institut de Physique Théorique, CNRS, URA 2306 & CEA/Saclay
F-91191 Gif-sur-Yvette, France

ricevuto il 7 Settembre 2012

Summary. — In an era of promising experimental searches, Dark Matter theorists are diversifying their portfolio, adding assets different from the time-honored SuperSymmetric neutralino. I pick and briefly discuss a few new directions in model building and in phenomenology: Minimal Dark Matter, Asymmetric Dark Matter and Secluded Dark Matter (Report numbers: CERN-PH-TH/2012-081, SACLAY–T12/026).

PACS `95.35.+d` – Dark matter (stellar, interstellar, galactic, and cosmological).
PACS `12.60.-i` – Models beyond the standard model.
PACS `98.80.Cq` – Particle-theory and field-theory models of the early Universe (including cosmic pancakes, cosmic strings, chaotic phenomena, inflationary universe, etc.).

1. – Introduction

At the cost of oversimplifying history, I shall claim that the latest 30 years or so, in the field of particle Dark Matter (DM) phenomenology, have been dominated by one single dispotic ruler: the SuperSymmetric neutralino. Sure, challengers have tried to emerge, sometimes with force (*e.g.*, Kaluza-Klein DM), and a somewhat clandestine subculture has continued to pursue its goals in the dark (axion or sterile neutrino workshippers, for instance). But there is little doubt that SuSy DM is perceived by most of the community as a point of reference and veneration. *E.g.*, it is not uncommon to hear experimentalists or astronomers confuse (or identify in their minds, in a sort of revealing giveaway) the concepts of "particle DM", "WIMP" and "neutralino".

Of course, there is nothing surprising in this state of affairs, given that the theoretical community has insisted for decades that i) the neutralino is such a well motivated DM candidate which ii) is just around the corner in your favorite energy/scattering strength/sensitivity scale. And indeed the neutralino *is* such a well-motivated DM candidate, if SuSy is true, and it *is* around the corner, if naturalness motivated and naïve SuSy parameters hold.

However, other possibilities exist.

TABLE I. – *A tentative categorization of some popular DM candidates. In **bold**, those picked for an additional discussion in the text, in italic, naturalness-inspired candidates.*

Charge	Candidates	Production	Stability
~~electromagnetic~~	–	–	–
weak	*neutralino...*	thermal freeze-out	R-parity
	Kaluza-Klein DM		KK-parity
	Little Higgs DM		T-parity
	Minimal DM	thermal freeze-out	gauge symmetry
	Inert Doublet DM		$\mathbb{Z}_2$ symmetry
strong(ish)	*Technicolor DM* } **asym DM**	'exhaustion'	T-baryon number
	mirror DM } **asym DM**		$\mathbb{Z}_2$ symmetry
other	"**secluded DM**"	sort of freeze-out	some symmetry
	Wimpless DM		some symmetry
none	singlet scalar	thermal freeze-out	$\mathbb{Z}_2$ symmetry
	sterile ν	mixing	just long lived
	gravitino	thermal or decay	R-parity or long lived
	axion	misalignment?	just long lived

2. – The current panorama and an attempt at widening the perspective

Many DM candidates (including the neutralino, my strawman) arise within the context of comprehensive theories (such as supersymmetry), often aiming at explaining some problem in particle physics (such as the hierarchy problem) other than the DM problem itself. For this reason it is often customary to classify them in terms of the theory in which they originate (SuperSymmetric DM, Kaluza-Klein DM, Technicolor DM...). However, this is not necessarily the only way to proceed. An arguably more democratic and revealing classification could be made in terms of the quantum numbers under which the DM candidate is charged, or in terms of the production mechanism that assures its correct abundance today, or yet in terms of the reason which guarantees its stability (or meta-stability) on cosmological time-scales.

Table I presents such a classification. Bear in mind that it is only partial and that no classification I can come up with would be totally satisfactory (at least to me). This is as good as an attempt can be.

Starting from the left of the table: DM can be charged under different forces. The first possibility is electromagnetism, but this is immediately excluded by the very name of *Dark* Matter (more technically: there exist very stringent constraints on ChaMPs, Charge Massive Particles [1]).

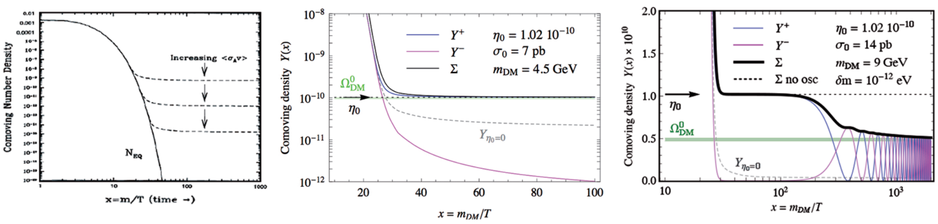

Fig. 1. – Three typical histories of DM abundance production mechanisms: thermal WIMP freeze-out (left, from [2]), asymmetric DM "exhaustion" (center) and talantogenesis (oscillating asymmetric DM, right).

Next come weak interactions (in the sense of the Standard Model $SU(2)$): this is the well known class of WIMPs, Weakly Interacting Massive Particles. In this class lie the candidates which arise within SuSy, extradimensions, Little Higgs, *i.e.* as a byproduct of a more ambitious and comprehensive theory, often addressing the naturalness issue. Here also lie, however, models loosely identified by the fact that they aim at providing a viable DM candidate insisting on introducing the minimal set of new particles beyond the Standard Model, somewhat in opposition to the mainstream direction just discussed. The namesake Minimal Dark Matter (MDM) [7] falls in this class, as well as less fundamentalist theories such as the model in [12], the hidden vector [13], the Inert Doublet Model (IDM) [14, 15] and others. I will discuss MDM in sect. **3**˙1.

One of the main compelling features of WIMP candidates is that it is automatically produced in the correct amount in cosmology, thanks to the so called "WIMP miracle", a realization of the thermal freeze-out mechanism which works in the following way. DM particles were as abundant as photons in the beginning, being freely created and destructed in pairs when the temperature of the hot plasma was larger then their mass. Their relative number density started then being suppressed as annihilations proceeded but the temperature dropped below their mass, due to the cooling of the Universe. Finally the annihilation processes also froze out as the Universe expanded further. The remaining, diluted abundance of stable particles constitutes the DM today. As it turns out, particles with weak scale mass ($\sim 100\,\mathrm{GeV}$–$1\,\mathrm{TeV}$) and weak interactions could play the above story remarkably well, and their final abundance would automatically (miraculously?) be the observed Ω_{DM}. This is an enchanting story, but it is certainly not the only possibility, as we will also see below. (See fig. 1.)

Dark Matter can also be subject to strong or simil-strong interactions, such as in Technicolor or Mirror DM motivated models. Here the emphasis is on the existence of some large interaction cross section similar to that of baryons. In this case the production mechanism is completely different from thermal freeze-out and it relies instead on the existence of a primordial asymmetry, as I will discuss in sect. **3**˙2. For this reason, these kinds of models are accomunated in the category of asymmetric DM for my purposes.

Apart from the ordinary interactions discussed so far (and of course apart from gravity), it could be that other new forces exist, under which DM is charged. This is the basic idea underlying models such as "secluded DM" and WIMPless DM (named of course in opposition to weakly interacting DM), which I will briefly discuss in sect. **3**˙3.

Finally, DM could have no charge at all. This does not mean that it needs not interact with ordinary matter at all. It just means that it is sterile under all gauge groups. In this class of candidates one finds singlet scalar DM [3], sterile neutrino DM [4], gravitino DM [5], the axion [6].

The reason by which the DM particle is stable constitutes another aspect of difference among candidates. The most popular solution is to invoke the existence of a (possibly discrete) symmetry that forbids its decay. This symmetry may be imposed in the theory for other purposes (or be the remnant of a larger broken one imposed for other purposes) so that DM "benefits" from it somewhat by chance. Alternatively, it can be put there by hand just to keep DM stable. A notable example in the first class is R-parity in SuSY, while in the second class one can mention KK-parity in ExtraDimensional DM, T-parity in Little Higgs DM etc. The "stabilization symmetry" has become such a household tool for the model builder that often he/she does not even spend time arguing about it: when in a hurry, just say you add a $\mathbb{Z}_2$ symmetry and move on. Recently, however, a couple of different options have emerged. The first one is that DM might be stabilized by the ordinary gauge symmetries of the Standard Model: this is the idea underlying the MDM model, discussed in sect. **3**˙1. The second one is the realization that, after all, DM need not be absolutely stable but just long lived enough to still be around on cosmological timescales: decaying DM has been the subject of much interest lately.

3. – A few new directions

3˙1. *Minimal Dark Matter: the most economical model?* – The MDM model [7-11] is constructed by simply adding on top of the Standard Model a single fermionic or scalar multiplet $\mathcal{X}$ charged under the usual SM $SU_L(2) \times U_Y(1)$ electroweak interactions (that is: a WIMP). Its conjugate $\bar{\mathcal{X}}$ belongs to the same representation, so that the theory is vector-like with respect to $SU_L(2)$ and anomaly-free. The Lagrangian is "minimal":

$$\mathscr{L} = \mathscr{L}_{\rm SM} + \frac{1}{2}\begin{cases} \bar{\mathcal{X}}(i\not{D} + M)\mathcal{X}, & \text{for fermionic } \mathcal{X}, \\ |D_\mu \mathcal{X}|^2 - M^2|\mathcal{X}|^2, & \text{for scalar } \mathcal{X}. \end{cases} \tag{1}$$

The gauge-covariant derivative D_μ contains the known electroweak gauge couplings to the vectors bosons of the SM (Z, $W^\pm$ and γ) and M is a tree level mass term (the only free parameter of the theory). A host of additional terms (such as Yukawa couplings with SM fields) would in principle be present, but for successful candidates they will be forbidden by gauge and Lorentz invariance, as detailed below. $\mathcal{X}$ is fully determined by the assignments of its quantum numbers under the gauge group: the number of its $SU(2)_L$ components, $n = \{2, 3, 4, 5 \ldots\}$ and the hypercharge Y.

For a given assignment of n there are a few choices of the hypercharge Y such that one component of the $\mathcal{X}$ multiplet has electric charge $Q = T_3 + Y = 0$ (where T_3 is the usual "diagonal" generator of $SU(2)_L$), as needed for a DM candidate. For instance, for the doublet $n = 2$, since $T_3 = \pm 1/2$, the only possibility is $Y = \mp 1/2$. For $n = 5$ one can have $Y = \{0, \pm 1, \pm 2\}$, and so on. The list of possible candidates has to stop at $n \leq 5$ (8) for fermions (scalars) because larger multiplets would accelerate the running of the $SU(2)_L$ coupling g_2: demanding that the perturbativity of $\alpha_2^{-1}(E)$ is mantained all the way up to $E \sim M_{\rm Pl}$ (since the Planck scale $M_{\rm Pl}$ is the cutoff scale of the theory) imposes the bound.

The candidates with $Y \neq 0$ have vector-like interactions with the Z boson that produce a tree-level spin-independent elastic cross sections which are 2–3 orders of magnitude above the present bounds from direct detection searches. Unless minimality is abandoned in an appropriate way, such MDM candidates are therefore excluded and I will focus in the following on those with $Y = 0$.

Next I need to inspect which of the remaining candidates are stable against decay into SM particles. For instance, the fermionic 3-plet with hypercharge $Y = 0$ would couple through a Yukawa operator $\mathcal{X}LH$ with a SM lepton doublet L and a Higgs field H and decay in a very short time. This is not a viable DM candidate, unless the operator is eliminated by some *ad hoc* symmetry. For another instance, the scalar 5-plet with $Y = 0$ would couple to four Higgs fields with a dimension 5 operator $\mathcal{X}HHH^*H^*/M_{\rm Pl}$, suppressed by one power of the Planck scale. Despite the suppression, the resulting typical life-time $\tau \sim M_{\rm Pl}^2\,{\rm TeV}^{-3}$ is shorter than the age of the Universe, so that this is not a viable DM candidate.

Now, the crucial observation is that, given the known SM particle content, the large n multiplets cannot couple to SM fields and are therefore automatically stable DM candidates. This is the same reason why known massive stable particles (like the proton) are stable: decay modes consistent with renormalizability and gauge symmetry do not exist. In other words, for these candidates DM stability is explained by an "accidental symmetry", like proton stability. Among the candidates that survived all the previous constraints, only two possibilities then emerge: a $n = 5$ fermion, or a $n = 7$ scalar. But scalar states may have non-minimal quartic couplings with the Higgs field. I will then set the 7-plet aside and focus on the fermionic 5-plet for minimality.

In summary, the "Minimal Dark Matter" construction singles out a

$$\text{fermionic } SU(2)_L \text{ 5-plet with hypercharge } Y = 0$$

as providing a fully viable, automatically stable DM particle. It is called "Minimal DM" since it is described by the minimal gauge-covariant Lagrangian that one obtains adding the minimal amount of new physics to the SM in order to explain the DM problem.

Assuming that DM arises as a thermal relic in the Early Universe, via the standard freeze-out process, we can compute the abundance of MDM as a function of its mass M. In turn, requiring that MDM makes all the observed DM, $\Omega_{\rm DM}h^2 = 0.110 \pm 0.005$, we can univocally determine M. Not surprisingly, its value turns out to be broadly in the TeV range, because MDM is a pure WIMP model for which the "WIMP miracle" applies. The actual value turns out to be $9.6 \pm 0.2\,$TeV, somewhat on the high side because the 5-plet has many components so that coannihilations are important *and* because Sommerfeld corrections (not discussed here) enhance the annihilation cross section.

3$\dot{}$2. *Asymmetric Dark Matter: a new production paradigm?* – I briefly presented above the thermal freeze-out mechanism, which plays a prominent role for WIMP candidates, including MDM. I now discuss another possibility, which is to assume that DM particles were once in thermal equilibrium *with an initial asymmetry* between particles and antiparticles. This was originally considered in Technicolor-like constructions [16-20] or mirror models [21-27], but also in other contexts [28-33]. In the latest two years, there has been a revival of interest for this scenario, dubbed Asymmetric Dark Matter (aDM) [34-58], with the aim in particular of connecting the DM abundance to the abundance of baryons, *i.e.* to understand the origin of the ratio $\Omega_{\rm B}/\Omega_{\rm DM} \sim 1/5$. A common production history for the dark and visible matter, in fact, provides an elegant explanation of why the two densities are so close to each other. This approach, in its simplest realizations, suggests a rather light particle, $\mathcal{O}(5\,{\rm GeV})$: this does not match the expected scale of new physics, but part of the community has seen in it intriguing connections with some recent hints of signals in various direct detection experiments. Like for the baryonic abundance, if there is an asymmetry in the dark sector, as soon as annihilations have wiped out the density of (say) antiparticles, the number density of particles remains frozen for lack of targets, and is entirely controlled by the primordial asymmetry rather than by the value of the annihilation cross section. This is why this scenario appears rather constraining on the value of the DM mass.

This conclusion changes in the presence of oscillations between DM and anti-DM particles [59,60]. Such oscillations can indeed replenish the depleted population of "targets". Annihilations, if strong enough, can then re-couple and deplete further the DM/anti-DM abundance. The final DM relic abundance is therefore attained through a more complex history than in the standard case of aDM, and in closer similarity to the freeze-out one. So this is an instructive setup in the sense that it fills a gap between the standard thermal freeze out prediction (where $\Omega_{\rm DM}$ does not depend explicitly on the DM mass but only on the annihilation cross section $\langle\sigma v\rangle$), and the aDM prediction where $\Omega_{\rm DM}h^2$ does not depend on $\langle\sigma v\rangle$ but only on the primordial DM asymmetry.

3˙3. *Secluded Dark Matter: new dark forces?* – A model building line which has attracted a *huge* interest in recent years is the one of models with new dark forces or, more generically, a rich Dark Sector. Most of them have been directly stimulated by the rather ephemeral desire of explaining the charged CR excesses in PAMELA, FERMI and HESS [61], but nevertheless they have taught us to look into new interesting directions, and this is a part that will most probably stay.

The model which undoubtedly has most attracted attention and has best spelled out the ingredients is presented in [62], although similar ideas have been proposed before or around the same time [63-69]. The model in [62] features a TeV-ish DM particle which is sterile under the SM gauge group but which interacts with itself via a new force-carrying boson ϕ (with the strength of typical gauge couplings). The DM annihilation therefore proceeds through DM DM $\to \phi\phi$. A small mixing between ϕ and the electromagnetic current assures that ϕ eventually decays. Therefore the process of DM annihilation occurs in 2 steps: first two DMs go into two ϕ's and then each ϕ's, thanks to its mixing with a photon, goes into a couple of SM particles. The crucial ingredient is that the mass of ϕ is chosen to be light, of the order of $\lesssim 1\,\mathrm{GeV}$. This simple assumption, remarkably, kills two birds with a stone. On one side, the exchange of ϕ realizes a Sommerfeld enhancement, thus providing a very large annihilation cross section today but preserving the thermal production of DM in the Early Universe. On the other side, ϕ can only decay into SM particles lighter than a GeV, *i.e.* electrons, muons and possibly pions, but not protons: this assures that the annihilation is leptophilic, for a simple kinematical reason. The model therefore fulfils all the requirements needed to explain charged CR anomalies [61]. The construction can then be complicated *ad libitum*, *e.g.* assuming that the dark gauge group is non-Abelian and the DM sits in a multiplet of such group, with small splitting between the components. This allows to accommodate other experimental anomalies, not discussed here.

The kinematical argument is not the only one available to justify a leptophilic nature for DM. In the literature, variations have been proposed in which DM is coupled preferentially to leptons because it carries a lepton number [70], because it shares a quantum number with a lepton [61, 71], because quarks live on another brane [72] or... "because I say so" [73].

4. – Conclusions

At a historical moment in which conventional DM candidates are facing their "moment of truth" [74], I argue that new alternative directions are gaining momentum. In sect. **2**

I tried to categorize many DM candidates in terms of their "charge", production process or stability mechanism, pointing out that there is a whole panorama outside of the ordinary, naturalness motivated, thermal WIMP candidates. I then picked three ideas for some further discussion: Minimal Dark Matter (sect. **3**˙1, one of the most economic modesl), Asymmetric DM (sect. **3**˙2, an example of alternative production mechanism) and secluded DM (sect. **3**˙3, advocating new dark forces).

* * *

I would like to thank the organizers of the Rencontres for the kind ospitality. This work is supported by the French National Research Agency ANR under contract ANR 2010 BLANC 041301 and by the EU ITN network UNILHC.

REFERENCES

[1] Sanchez-Salcedo F., Martinez-Gomez E. and Magana J., *JCAP*, **02** (2010) 031, 1002.3145.
[2] Kolb E. and Turner M., *The Early Universe* (Westview Press) 1994.
[3] Silveira V. and Zee A., *Phys. Lett. B*, **161** (1985) 136; McDonald J., *Phys. Rev. D*, **50** (1994) 3637, hep-ph/0702143; Burgess C., Pospelov M. and ter Veldhuis T., *Nucl. Phys. B*, **619** (2001) 709, hep-ph/0011335.
[4] Dodelson S. and Widrow L. M., *Phys. Rev. Lett.*, **72** (1994) 17 [hep-ph/9303287].
[5] Pagels H. and Primack J. R., *Phys. Rev. Lett.*, **48** (1982) 223; Bolz M., Buchmuller W. and Plumacher M., *Phys. Lett. B*, **443** (1998) 209, hep-ph/9809381.
[6] Preskill J., Wise M. B. and Wilczek F., *Phys. Lett. B*, **120** (1983) 127; Abbott L. F. and Sikivie P., *Phys. Lett. B*, **120** (1983) 133; Dine M. and Fischler W., *Phys. Lett. B*, **120** (1983) 137.
[7] Cirelli M., Fornengo N. and Strumia A., *Nucl. Phys. B*, **753** (2006) 178, hep-ph/0512090.
[8] Cirelli M., Strumia A. and Tamburini M., *Nucl. Phys. B*, **787** (2007) 152, 0706.4071.
[9] Cirelli M., Franceschini R. and Strumia A., *Nucl. Phys. B*, **800** (2008) 204, 0802.3378.
[10] Cirelli M. and Strumia A., *PoS IDM*, **2008** (2008) 089, 0808.3867 [astro-ph].
[11] Cirelli M. and Strumia A., *New J. Phys.*, **11** (2009) 105005, 0903.3381 [hep-ph].
[12] Mahbubani R. and Senatore L., *Phys. Rev. D*, **73** (2006) 043510, hep-ph/0510064.
[13] Hambye T., *JHEP*, **01** (2009) 028, 0811.0172 [hep-ph].
[14] Barbieri R., Hall L. J. and Rychkov V. S., *Phys. Rev. D*, **74** (2006) 015007, hep-ph/0603188; See also Deshpande N. G. and Ma E., *Phys. Rev. D*, **18** (1978) 2574, where the model is introduced, but without explicitly addressing the DM problem.
[15] Hambye T. and Tytgat M., *Phys. Lett. B*, **659** (2008) 651, 0707.0633 [hep-ph].
[16] Nussinov S., *Phys. Lett. B*, **165** (1985) 55.
[17] Barr S. M., Chivukula R. S. and Farhi E., *Phys. Lett. B*, **241** (1990) 387.
[18] Barr S. M., *Phys. Rev. D*, **44** (1991) 3062.
[19] Kaplan D. B., *Phys. Rev. Lett.*, **68** (1992) 741.
[20] Gudnason S., Kouvaris C. and Sannino F., *Phys. Rev. D*, **73** (2006) 115003, hep-ph/0603014; Gudnason S., Kouvaris C. and Sannino F., *Phys. Rev. D*, **74** (2006) 095008 [hep-ph/0608055].
[21] Hodges H. M., *Phys. Rev. D*, **47** (1993) 456.
[22] Foot R. and Volkas R. R., *Phys. Rev. D*, **52** (1995) 6595 [hep-ph/9505359].
[23] Berezhiani Z. and Mohapatra R., *Phys. Rev. D*, **52** (1995) 6607 [hep-ph/9505385].
[24] Berezhiani Z., Dolgov A. and Mohapatra R., *Phys. Lett. B*, **375** (1996) 26, hep-ph/9511221.
[25] Bento L. and Berezhiani Z., hep-ph/0111116.

[26] Berezhiani Z., *Through the Looking-Glass: Alice's Adventures in Mirror World*, in Shifman M. *et al.* (Editor), *From fields to strings*, Vol. **3**, 2147-2195 [hep-ph/0508233].
[27] Foot R. and Volkas R. R., *Phys. Rev. D*, **68** (2003) 021304, [hep-ph/0304261]; Foot R. and Volkas R. R., *Phys. Rev. D*, **69** (2004) 123510 [hep-ph/0402267].
[28] Farrar G. R. and Zaharijas G., *Phys. Rev. Lett.*, **96** (2006) 041302 [hep-ph/0510079].
[29] Hooper D., March-Russell J. and West S., *Phys. Lett. B*, **605** (2005) 228, hep-ph/0410114.
[30] Kitano R. and Low I., *Phys. Rev. D*, **71** (2005) 023510 [hep-ph/0411133].
[31] Agashe K. and Servant G., *JCAP*, **02** (2005) 002 [hep-ph/0411254].
[32] Cosme N., LopezHonorez L. and Tytgat M., *Phys. Rev. D*, **72** (2005) 043505, hep-ph/0506320.
[33] Belotsky K., Fargion D., Khlopov M. and Konoplich R. V., *Phys. At. Nucl.*, **71** (2008) 147-161 [hep-ph/0411093]; Khlopov M. Y., *Pisma Zh. Eksp. Teor. Fiz.*, **83** (2006) 3 [astro-ph/0511796].
[34] Kaplan D. E., Luty M. and Zurek K., *Phys. Rev. D*, **79** (2009) 115016, 0901.4117 [hep-ph].
[35] Cohen T. and Zurek K. M., *Phys. Rev. Lett.*, **104** (2010) 101301, 0909.2035 [hep-ph].
[36] Cai Y., Luty M. A. and Kaplan D. E., 0909.5499 [hep-ph].
[37] An H., Chen S.-L., Mohapatra R. and Zhang Y., *JHEP*, **03** (2010) 124, 0911.4463 [hep-ph].
[38] Shelton J. and Zurek K. M., *Phys. Rev. D*, **82** (2010) 123512, 1008.1997 [hep-ph].
[39] Buckley M. R. and Randall L., *JHEP*, **09** (2011) 009, 1009.0270 [hep-ph].
[40] Davoudiasl H., Morrissey D. E., Sigurdson K. and Tulin S., *Phys. Rev. Lett.*, **105** (2010) 211304, 1008.2399 [hep-ph].
[41] Haba N. and Matsumoto S., *Prog. Theor. Phys.*, **125** (2011) 1311, 1008.2487 [hep-ph].
[42] Chun E. J., *Phys. Rev. D*, **83** (2011) 053004, 1009.0983 [hep-ph].
[43] Gu P.-H., Lindner M., Sarkar U. and Zhang X., *Phys. Rev. D*, **83** (2011) 055008, 1009.2690.
[44] Blennow M., Dasgupta B., Fernandez-Martinez E. and Rius N., *JHEP*, **03** (2011) 014, 1009.3159 [hep-ph].
[45] McDonald J., 1009.3227 [hep-ph].
[46] Allahverdi R., Dutta B. and Sinha K., *Phys. Rev. D*, **83** (2011) 083502, 1011.1286 [hep-ph].
[47] Dutta B. and Kumar J., *Phys. Lett. B*, **699** (2011) 364, 1012.1341 [hep-ph].
[48] Falkowski A., Ruderman J. and Volansky T., *JHEP*, **05** (2011) 106, 1101.4936 [hep-ph].
[49] Cheung C. and Zurek K. M., *Phys. Rev. D*, **84** (2011) 035007, 1105.4612 [hep-ph].
[50] Del Nobile E., Kouvaris C. and Sannino F., *Phys. Rev. D*, **84** (2011) 027301, 1105.5431.
[51] Cui Y., Randall L. and Shuve B., 1106.4834 [hep-ph].
[52] March-Russell J. and McCullough M., 1106.4319 [hep-ph].
[53] Frandsen M., Sarkar S. and Schmidt-Hoberg K., *Phys. Rev. D*, **84** (2011) 051703, 1103.4350.
[54] Davoudiasl H., Morrissey D. E., Sigurdson K. and Tulin S., 1106.4320 [hep-ph].
[55] Graesser M. L., Shoemaker I. M. and Vecchi L., 1107.2666 [hep-ph].
[56] Arina C. and Sahu N., 1108.3967 [hep-ph].
[57] McDonald J., 1108.4653 [hep-ph].
[58] Barr S. M., 1109.2562 [hep-ph].
[59] Cirelli M., Panci P., Servant G. and Zaharijas G., *JCAP*, **03** (2012) 015, arXiv:1110.3809 [hep-ph].
[60] Tulin S., Yu H.-B. and Zurek K. M., 1202.0283 [hep-ph].
[61] Cirelli M., Kadastik M., Raidal M. and Strumia A., *Nucl. Phys. B*, **813** (2009) 1, 0809.2409.
[62] Arkani-Hamed N., Finkbeiner D. P., Slatyer T. R. and Weiner N., *Phys. Rev. D*, **79** (2009) 015014, 0810.0713 [hep-ph].

[63] Pospelov M., Ritz A. and Voloshin M. B., *Phys. Lett. B*, **662** (2008) 53, 0711.4866 [hep-ph].
[64] Feldman D., Liu Z. and Nath P., *Phys. Rev. D*, **79** (2009) 063509, 0810.5762 [hep-ph].
[65] Cholis I., Goodenough L. and Weiner N., *Phys. Rev. D*, **79** (2009) 123505, 0802.2922.
[66] Nelson A. E. and Spitzer C., *JHEP*, **10** (2010) 066, 0810.5167 [hep-ph].
[67] Cholis I., Finkbeiner D., Goodenough L. and Weiner N., *JCAP*, **12** (2009) 007, 0810.5344.
[68] Nomura Y. and Thaler J., *Phys. Rev. D*, **79** (2009) 075008, 0810.5397 [hep-ph].
[69] Bai Y. and Han Z., *Phys. Rev. D*, **79** (2009) 095023, 0811.0387 [hep-ph].
[70] Phalen D. J., Pierce A. and Weiner N., *Phys. Rev. D*, **80** (2009) 063513, 0901.3165 [hep-ph].
[71] Fox P. J. and Poppitz E., *Phys. Rev. D*, **79** (2009) 083528, 0811.0399 [hep-ph].
[72] Park S. C. and Shu J., *Phys. Rev. D*, **79** (2009) 091702, 0901.0720 [hep-ph].
[73] Harnik R. and Kribs G. D., *Phys. Rev. D*, **79** (2009) 095007, 0810.5557 [hep-ph].
[74] Bertone G., *Nature*, **468** (2010) 389, 1011.3532 [astro-ph.CO].

IL NUOVO CIMENTO Vol. 35 C, N. 6 Novembre-Dicembre 2012
DOI 10.1393/ncc/i2012-11348-8

Colloquia: LaThuile12

Modified gravity: Problems and observational manifestations

E. V. Arbuzova

Department of Higher Mathematics, University "Dubna" - 141980 Dubna, Russia

ricevuto il 7 Settembre 2012

Summary. — Some models of modified gravity and their observational manifestations are considered. It is shown, that gravitating systems with mass density rising with time evolve to a singular state with infinite curvature scalar. The universe evolution during the radiation-dominated epoch is studied in R^2-extended gravity theory. Particle production rate by the oscillating curvature is calculated. Possible implications of the model for cosmological creation of non-thermal dark matter are discussed.

PACS `98.80.Cq` – Particle-theory and field-theory models of the early Universe (including cosmic pancakes, cosmic strings, chaotic phenomena, inflationary universe, etc.).
PACS `95.35.+d` – Dark matter (stellar, interstellar, galactic, and cosmological).
PACS `95.30.Sf` – Relativity and gravitation.

1. – Introduction

Discovering of the cosmic antigravity based on the accumulated astronomical data, such as observation of the large-scale structure of the universe, measurements of the angular fluctuations of the cosmic microwave background radiation, determination of the universe age (for a review see [1]), and especially discovery of the dimming of distant Supernovae [2], is the most attractive event in cosmology of the last quarter of century. It was established and unambiguously proved that the universe expansion is accelerated, but the driving force behind this accelerated expansion in still unknown.

Among possible explanations, the most popular is probably the assumption of a new (unknown) form of cosmological energy density with large negative pressure, $P < -\rho/3$, the so-called dark energy, for a review see, *e.g.*, [3].

A competing mechanism to describe the accelerated expansion is represented by gravity modifications at small curvature, the so-called $f(R)$-gravity theories, as suggested in ref. [4]. In these theories the standard Einstein-Hilbert Lagrangian density, proportional to the scalar curvature R, is replaced by a function $f(R)$, so the usual action of General

Relativity acquires an additional term:

$$S = -\frac{m_{Pl}^2}{16\pi}\int \mathrm{d}^4x\sqrt{-g}\, f(R) + S_m = -\frac{m_{Pl}^2}{16\pi}\int \mathrm{d}^4x\sqrt{-g}\,\left[R + F(R)\right] + S_m, \tag{1}$$

where $m_{Pl} = 1.22\cdot 10^{19}\,\mathrm{GeV}$ is the Planck mass and S_m is the matter action.

The original version of such models [4] suffers from a strong instability in the presence of gravitating bodies [5] and because of that more complicated functions $F(R)$ have been proposed [6-9], which are free from the mentioned exponential instability.

Though free of instability [5], the models proposed in [6-8] possess another troublesome feature, namely in a cosmological situation they should evolve from a singular state in the past [10]. Moreover, it was found in refs. [11,12] that in presence of matter, a singularity may arise in the future if the matter density rises with time; such future singularity is unavoidable, regardless of the initial conditions, and is reached in a time which is much shorter than the cosmological one.

2. – Explosive phenomena in modified gravity

In paper [12] the model of modified gravity with $F(R)$ function suggested in ref. [6] was considered:

$$F(R) = \lambda R_0\left[\left(1+\frac{R^2}{R_0^2}\right)^{-n} - 1\right]. \tag{2}$$

Here constant λ is chosen to be positive to produce an accelerated cosmological expansion, n is a positive integer, and R_0 is a constant with dimension of the curvature scalar. The latter is assumed to be of the order of the present day average curvature of the universe, *i.e.* $R_0 \sim 1/t_U^2$, where $t_U \approx 4\cdot 10^{17}\,\mathrm{s}$ is the universe age.

The corresponding equations of motion have the form

$$(1+F')\,R_{\mu\nu} - \frac{1}{2}\,(R+F)\,g_{\mu\nu} + (g_{\mu\nu}D_\alpha D^\alpha - D_\mu D_\nu)\,F' = \frac{8\pi T_{\mu\nu}^{(m)}}{m_{Pl}^2}, \tag{3}$$

where $F' = \mathrm{d}F/\mathrm{d}R$, D_μ is the covariant derivative, and $T_{\mu\nu}^{(m)}$ is the energy-momentum tensor of matter.

By taking trace over μ and ν in eq. (3) we obtain the equation of motion which contains only the curvature scalar R and the trace of the energy-momentum tensor of matter:

$$3D^2F' - R + RF' - 2F = T, \tag{4}$$

where $T = 8\pi T_\mu^\mu/m_{Pl}^2$.

We analyze the evolution of R in massive objects with time-varying mass density, $\rho_m \gg \rho_c$. The cosmological energy density at the present time is $\rho_c \approx 10^{-29}\,\mathrm{g/cm^3}$, while matter density of, say, a dust cloud in a galaxy could be about $\rho_m \sim 10^{-24}\,\mathrm{g/cm^3}$. Since the magnitude of the curvature scalar is proportional to the mass density of a non-relativistic system, we find $R \gg R_0$. In this limit:

$$F(R) \approx -\lambda R_0\left[1 - \left(\frac{R_0}{R}\right)^{2n}\right]. \tag{5}$$

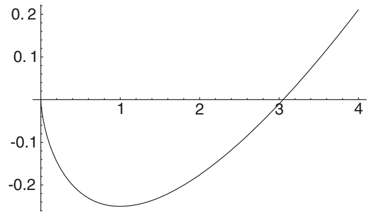

Fig. 1. – Potential $U(z) = z(1+\kappa\tau) - z^{1-\nu}/(1-\nu)$, $\nu = \frac{1}{5}$, $\tau = 0$.

The equation of motion is very much simplified if we introduce the new notation

$$w = -F' = 2n\lambda \left(\frac{R_0}{R}\right)^{2n+1}. \tag{6}$$

Evolution of w is governed by a simple equation of unharmonic oscillator:

$$(\partial_t^2 - \Delta)w + U'(w) = 0. \tag{7}$$

Potential $U(w)$ is equal to

$$U(w) = \frac{1}{3}\left(T - 2\lambda R_0\right) w + \frac{R_0}{3}\left[\frac{q^\nu}{2n\nu} w^{2n\nu} + \left(q^\nu + \frac{2\lambda}{q^{2n\nu}}\right)\frac{w^{1+2n\nu}}{1+2n\nu}\right], \tag{8}$$

where $\nu = 1/(2n+1)$, $q = 2n\lambda$, and in eq. (7) $U'(w) = \mathrm{d}U/\mathrm{d}w$.

Notice that infinite R corresponds to $w = -F' = 0$, so if F' reaches zero, it would mean that R becomes infinitely large.

Potential U would depend upon time, if the mass density of the object under scrutiny changes with time, $T = T(t)$. If only the dominant terms are retained and if the space derivatives are neglected, eqs. (7), (8) simplify to

$$z'' - z^{-\nu} + (1+\kappa\tau) = 0. \tag{9}$$

Here we introduced dimensionless quantities

$$\begin{aligned} t &= \gamma\tau, \qquad \gamma^2 = \frac{3q}{(-R_0)}\left(-\frac{R_0}{T_0}\right)^{2(n+1)}, \\ w &= \beta z, \qquad \beta = \gamma^2 T_0/3 = q\left(-\frac{R_0}{T_0}\right)^{2n+1}. \end{aligned} \tag{10}$$

The minimum of the potential $U(z)$ (fig. 1) sits at $z_{min} = (1+\kappa\tau)^{-1/\nu}$. When the mass density rises, the minimum moves towards zero and becomes less deep. If at the process of "lifting" of the potential $z(\tau)$ happens to be at $U > 0$ it would overjump potential which is equal to zero at $z = 0$. In other words, $z(\tau)$ would reach zero, which corresponds to infinite R, and so the singularity can be reached in finite time (see fig. 2).

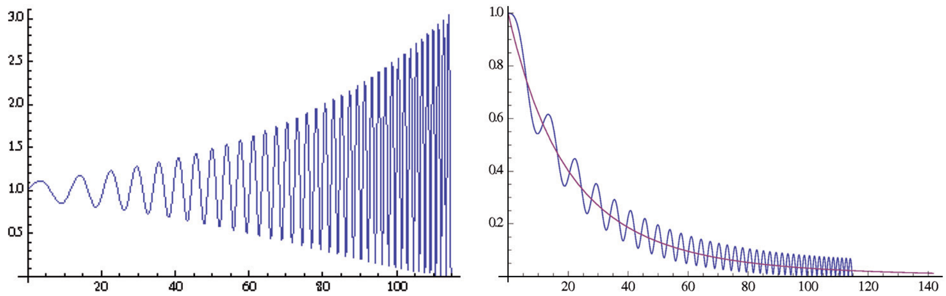

Fig. 2. – Ratio $z(\tau)/z_{min}(\tau)$ (left) and functions $z(\tau)$ and $z_{min}(\tau)$ (right) for $n = 2$, $\kappa = 0.01$, $\rho_m/\rho_c = 10^5$. Initial conditions: $z(0) = 1$ and $z'(0) = 0$.

The simplest way to avoid singularity is to introduce the R^2-term into the gravitational action,

$$\delta F(R) = -R^2/6m^2\,, \tag{11}$$

where m is a constant parameter with dimension of mass.

In the homogeneous case and in the limit of large ratio R/R_0 equation of motion for R is modified as

$$\left[1 - \frac{R^{2n+2}}{6\lambda n(2n+1)R_0^{2n+1}m^2}\right]\ddot{R} - (2n+2)\frac{\dot{R}^2}{R} - \frac{R^{2n+2}(R+T)}{6\lambda n(2n+1)R_0^{2n+1}} = 0. \tag{12}$$

With dimensionless curvature and time

$$y = -\frac{R}{T_0}\,, \qquad \tau_1 = t\left[-\frac{T_0^{2n+2}}{6\lambda n(2n+1)R_0^{2n+1}}\right]^{1/2} \tag{13}$$

the equation for R is transformed into

$$\left(1 + gy^{2n+2}\right)y'' - 2(n+1)\frac{(y')^2}{y} + y^{2n+2}\left[y - (1+\kappa_1\tau_1)\right] = 0, \tag{14}$$

where the prime means derivative with respect to τ_1.

We introduced here the new parameter, g, which can prevent from the approach to infinity and is equal to

$$g = -\frac{T_0^{2n+2}}{6\lambda n(2n+1)m^2 R_0^{2n+1}} > 0. \tag{15}$$

For very large m, or small g, when the second term in the coefficient of the second derivatives in eqs. (12) and (14) can be neglected, the numerical solution demonstrates that R would reach infinity in finite time in accordance with the results presented above (see fig. 3, left panel). Non-zero g would terminate the unbounded rise of R. To avoid too large deviation of R from the usual gravity coefficient g should be larger than or of the order of unity. In the right panel of fig. 3 it is clearly seen, that for $g = 1$ the amplitude

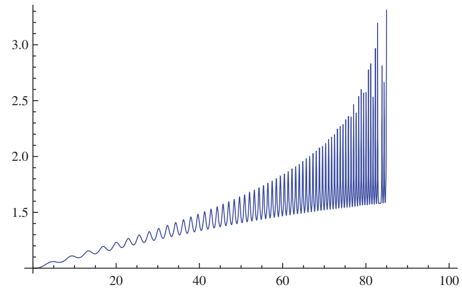

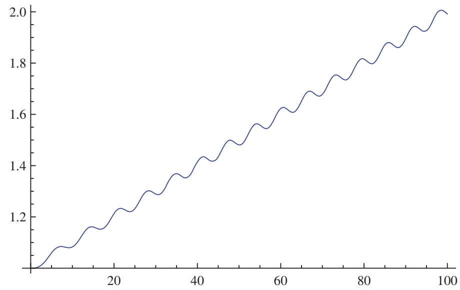

Fig. 3. – Numerical solutions of eq. (14) for $n = 3$, $\kappa_1 = 0.01$, $y(\tau_{in}) = 1 + \kappa_1\tau_{in}$, $y'(\tau_{in}) = 0$. Left panel: $g = 0$. Right panel: $g = 1$.

of oscillations remains constant whereas the average value of R increases with time. As follows from eq. (14), the frequency of small oscillations of y around $y_0 = 1 + \kappa_1\tau_1$ in dimensionless time τ_1 is

$$\omega_\tau^2 = \frac{1}{g}\,\frac{g y_0^{2n+2}}{1 + g y_0^{2n+2}} \le \frac{1}{g}\,. \tag{16}$$

It means that in physical time the frequency would be

$$\omega \sim \frac{1}{t_U}\left(\frac{T_0}{R_0}\right)^{n+1}\frac{y_0^{n+1}}{\sqrt{1 + g y_0^{2n+2}}} \le m. \tag{17}$$

In particular, for $n = 5$ and for a galactic gas cloud with $T_0/R_0 = 10^5$, the oscillation frequency would be 10^{12} Hz $\approx 10^{-3}$ eV. Higher density objects, *e.g.*, those with $\rho = 1\,\mathrm{g/cm^3}$ would oscillate with much higher frequency, saturating bound (17), *i.e.* $\omega \sim m$. All kinds of particles with masses smaller than m might be created by such oscillating field.

3. – Cosmological evolution and particle production in R^2 gravity

In the present section we study the cosmological evolution of the Universe in a theory with only an additional R^2 term in the action, neglecting other terms which have been introduced to generate the accelerated expansion in the contemporary universe [13]. The impact of such terms is negligible in the limit of sufficiently large curvature, $|R| \gg |R_0|$, where R_0 is the cosmological curvature at the present time.

In other words, we study here the cosmological evolution of the early and not so early universe in the model with the action

$$S = -\frac{m_{Pl}^2}{16\pi}\int \mathrm{d}^4x\sqrt{-g}\left(R - \frac{R^2}{6m^2}\right) + S_m. \tag{18}$$

The modified Einstein equations for this theory read

$$R_{\mu\nu} - \frac{1}{2}g_{\mu\nu}R - \frac{1}{3m^2}\left(R_{\mu\nu} - \frac{1}{4}Rg_{\mu\nu} + g_{\mu\nu}D_\alpha D^\alpha - D_\mu D_\nu\right)R = \frac{8\pi}{m_{Pl}^2}T_{\mu\nu}. \tag{19}$$

Expressing the curvature scalar R through the Hubble parameter $H = \dot{a}/a$ as $R = -6\dot{H} - 12H^2$, we get the time-time component of eq. (19):

$$\ddot{H} + 3H\dot{H} - \frac{\dot{H}^2}{2H} + \frac{m^2 H}{2} = \frac{4\pi m^2}{3m_{Pl}^2 H}\rho, \tag{20}$$

where over-dots denote derivative with respect to the physical time t.

Taking the trace of eq. (19) yields

$$\ddot{R} + 3H\dot{R} + m^2\left(R + \frac{8\pi}{m_{Pl}^2}T_\mu^\mu\right) = 0. \tag{21}$$

In what follows, we study the cosmological evolution in the R^2-theory assuming rather general initial conditions for R and H and dominance of relativistic matter with the following equation for the matter content:

$$\dot{\rho} + 4H\rho = 0. \tag{22}$$

It is convenient to rewrite the equations in terms of the dimensionless quantities $\tau = H_0\, t$, $h = H/H_0$, $r = R/H_0^2$, $y = 8\pi\rho/(3m_{Pl}^2 H_0^2)$, and $\omega = m/H_0$,where H_0 is the value of the Hubble parameter at some initial time t_0. Thus the following system of equations for dimensionless Hubble parameter is obtained:

$$h'' + 3hh' - \frac{h'^2}{2h} + \frac{\omega^2}{2}\frac{h^2 - y}{h} = 0, \tag{23a}$$

$$y' + 4hy = 0. \tag{23b}$$

First we assume that the deviations from General Relativity (GR) are small and expand $h = 1/(2\tau) + h_1$ and $y = 1/(4\tau^2) + y_1$, assuming that $h_1/h \ll 1$ and $y_1/y \ll 1$, and solve the linearized system of equations.

The complete asymptotic solution for h has the form

$$h(\tau) \simeq \frac{1}{2\tau} + \frac{c_1 \sin(\omega\tau + \varphi)}{\tau^{3/4}}. \tag{24}$$

The Hubble parameter oscillates around GR value, $h_0 \sim 1/(2\tau)$ with rising amplitude, $h_1/h_0 \sim \tau^{1/4}$, and for sufficiently large τ the second term would start to dominate and the linear approximation would no longer hold. Using trancated Fourier expansion it is possible to obtain approximate analytical solutions of the full non-linear system in the high-frequency limit $\omega\tau \gg 1$. The same results are found numerically for the initial conditions $h_0 = 1 + \delta h_0$, $h_0' = -2 + \delta h_0'\, y_0 = 1 + \delta y_0$ (see fig. 4).

Gravitational particle production may non-trivially affect the solutions of the above equations. Below we consider particle production by the external oscillating gravitational field and present the equation of motion for the evolution of R with the account of the back-reaction from particle production. This leads to an exponential damping of the oscillating part of R, while the non-oscillating “Friedmann” part remains practically

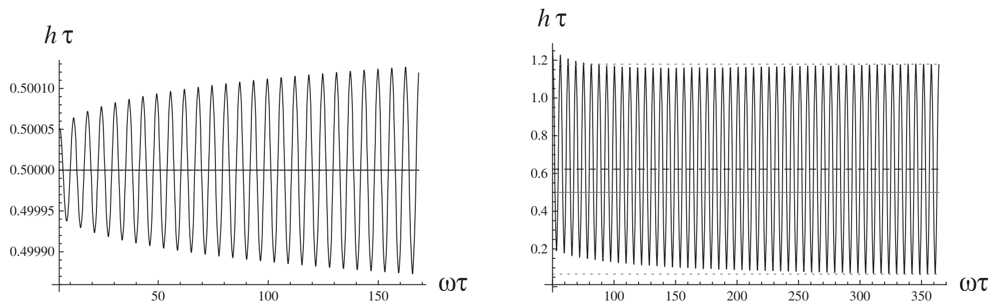

Fig. 4. – Numerical solution of eqs. (23). Left panel: linear regime with $\delta h_0 = 10^{-4}$, $\delta h_0' = 0$, $y_0 = 1$, $\omega = 10$. Right panel: high-frequency limit with $\delta h_0 = 1.5$, $\delta h_0' = 0$, $y_0 = 0$, $\omega = 100$. Initial conditions are different from GR, the central value $h\tau = 0.6$ is shifted from GR value 0.5.

undisturbed. The particle production influx into the cosmological plasma is estimated in the case of a massless, minimally-coupled to gravity scalar field with the action

$$S_\phi = \frac{1}{2}\int \mathrm{d}^4x\,\sqrt{-g}\,g^{\mu\nu}\partial_\mu\phi\,\partial_\nu\phi. \tag{25}$$

It terms of the conformally rescaled field, $\chi \equiv a(t)\phi$, and conformal time η, such that $a\,\mathrm{d}\eta = \mathrm{d}t$, we can rewrite the equations of motion as

$$R'' + 2\frac{a'}{a}R' + m^2a^2R = 8\pi\frac{m^2}{m_{Pl}^2}\frac{1}{a^2}\left[\chi'^2 - (\vec{\nabla}\chi)^2 + \frac{a'^2}{a^2}\chi^2 - \frac{a'}{a}(\chi\chi' + \chi'\chi)\right], \tag{26a}$$

$$R = -6a''/a^3, \tag{26b}$$

$$\chi'' - \Delta\chi + \frac{1}{6}\,a^2R\,\chi = 0, \tag{26c}$$

We derive a closed equation for R taking the average value of the χ-dependent quantum operators in the r.h.s. of eq. (26a) over vacuum, in presence of an external classical gravitational field R following the procedure described in ref. [14], where such equation was obtained in one-loop approximation.

The dominant contribution of particle production is given by the equation

$$\ddot{R} + 3H\dot{R} + m^2R \simeq \frac{1}{12\pi}\frac{m^2}{m_{Pl}^2}\int_{t_0}^{t}\mathrm{d}t'\,\frac{\ddot{R}(t')}{t-t'}\,. \tag{27}$$

This equation is linear in R and naturally non-local in time since the impact of particle production depends upon all the history of the evolution of the system.

Using again the procedure of truncated Fourier expansion including the back-reaction effects in the form of eq. (27), we obtain the decay rate

$$\Gamma_R = \frac{m^3}{48m_{Pl}^2}\,. \tag{28}$$

This result is in agreement with ref. [15]. The characteristic decay time of the oscillating curvature is

$$\tau_R = \frac{1}{2\Gamma_R} = \frac{24 m_{Pl}^2}{m^3} \simeq 2 \left(\frac{10^5\,\mathrm{GeV}}{m} \right)^3 \mathrm{s}. \tag{29}$$

The contribution of the produced particles into the total cosmological energy density reaches its maximum value at approximately this time.

The influx of energetic protons and antiprotons could have an impact on BBN. Thus this would either allow to obtain some bounds on m or even to improve the agreement between the theoretical predictions for BBN and the measurements of the primordial abundances of light nuclei.

The oscillating curvature might be a source of dark matter in the form of heavy supersymmetric (SUSY) particles. Since the expected light SUSY particles have not yet been discovered at LHC, to some people supersymmetry somewhat lost its attractiveness. The contribution of the stable lightest SUSY particle into the cosmological energy is proportional to

$$\Omega \sim m_{SUSY}^2 / m_{Pl} \tag{30}$$

and for m_{SUSY} in the range 100–1000 GeV the cosmological fraction of these particles would be of order unity. It is exactly what is necessary for dark matter. However, it excludes thermally produced LSP's if they are much heavier. If LSP's came from the decay of R and their mass is larger than the "mass" of R, *i.e.* m, the LSP production could be sufficiently suppressed to make a reasonable contribution to dark matter.

In contemporary astronomical objects oscillation frequency could vary from m down to very low frequency. The oscillations may produce radiation from high-energy cosmic rays down to radio waves.

* * *

I thank my coauthors, A. D. Dolgov and L. Reverberi, for cooperation. I am especially grateful to A. D. Dolgov for help and fruitful discussions during the entire period of collaboration. This work was supported by the Grant of the Government of Russian Federation, No. 11.G34.31.0047.

REFERENCES

[1] Nakamura K. *et al.* (Particle Data Group), *J. Phys. G*, **37** (2010) 075021.

[2] Riess A. G. *et al.*, *Astron. J.*, **116** (1998) 1009; *Astrophys. J.*, **607** (2004) 665; Perlmutter S. *et al.*, *Nature*, **391** (1998) 51; *Astrophys. J.*, **517** (1999) 565; Schmidt B. P. *et al.*, *Astrophys. J.*, **507** (1998) 46.

[3] Peebles P. J. E. and Bharat Ratra, *Rev. Mod. Phys.*, **75** (2003) 559; Copeland E. J., Sami M. and Tsujikawa S., *Int. J. Mod. Phys. D*, **15** (2006) 1753.

[4] Capozziello S., Carloni S. and Troisi A., *Recent Res. Dev. Astron. Astrophys.*, **1** (2003) 625; Carroll S. M., Duvvuri V., Trodden M. and Turner M. S., *Phys. Rev. D*, **70** (2004) 043528.

[5] Dolgov A. D. and Kawasaki M., *Phys. Lett. B*, **573** (2003) 1.

[6] Starobinsky A. A., *JETP Lett.*, **86** (2007) 157.

[7] Hu W. and Sawicki I., *Phys. Rev. D*, **76** (2007) 064004.

[8] Appleby A. and Battye R., *Phys. Lett. B*, **654** (2007) 7.

[9] Nojiri S. and Odintsov S. D., *Phys. Lett. B*, **657** (2007) 238.
[10] Appleby S. A. and Battye R. A., *JCAP*, **05** (2008) 019.
[11] Frolov A. V., *Phys. Rev. Lett.*, **101** (2008) 061103; Thongkool I., Sami M., Gannouji R. and Jhingan S., *Phys. Rev. D*, **80** (2009) 043523; Thongkool I., Sami M. and Rai Choudhury S., *Phys. Rev. D*, **80** (2009) 127501.
[12] Arbuzova E. V. and Dolgov A. D., *Phys. Lett. B*, **700** (2011) 289.
[13] Arbuzova E. V., Dolgov A. D. and Reverberi L., *JCAP*, **02** (2012) 049.
[14] Dolgov A. D. and Hansen S. H., *Nucl. Phys. B*, **548** (1999) 408.
[15] Vilenkin A., *Phys. Rev. D*, **32** (1985) 2511.

SESSION II - NEUTRINO PHYSICS AND LEPTON FLAVOUR VIOLATION

IL NUOVO CIMENTO Vol. 35 C, N. 6 Novembre-Dicembre 2012
DOI 10.1393/ncc/i2012-11349-7

Colloquia: LaThuile12

OPERA neutrino oscillation results

A. M. Guler on behalf of the OPERA Collaboration
Middle East Technical University - 06800 Ankara, Turkey

ricevuto il 7 Settembre 2012

Summary. — The OPERA experiment was designed to perform the first detection of $\nu_\mu \to \nu_\tau$ neutrino oscillations in a direct appearance mode. We present the analysis results of the 2008–2009 statistics corresponding to 4.88×10^{19} p.o.t. In this sample, one ν_τ candidate event has been observed in the $\tau \to h$ channel. The statistical significance of this observation is estimated to be 95%.

PACS 14.60.Pq – Neutrino mass and mixing.
PACS 25.30.Pt – Neutrino-induced reactions.

1. – Introduction

Neutrino oscillations were first observed by the Super-Kamiokande experiment [1] in 1998. In recent years, several other experiments [2] using atmospheric, solar, reactor and accelerator neutrinos have confirmed the existence of neutrino oscillations and measured the mixing parameters. However, the direct observation of the appearance of ν_τ from an oscillated ν_μ is still missing. The observation of ν_τ appearance in an accelerator neutrino experiment will unambiguously prove that $\nu_\mu \to \nu_\tau$ is the dominant channel for the neutrino atmospheric sector. This is the main goal of the OPERA experiment [3]. In particular, the aim is to find the signal events coming from ν_τ charged-current interactions:

$$\nu_\tau N \to \tau^- X, \tag{1}$$

followed by one of the following decay topologies:

$$\begin{aligned} \tau^- &\to \mu^- \bar{\nu}_\mu \nu_\tau \\ &\to e^- \bar{\nu}_e \nu_\tau \\ &\to h^- (n\pi^0) \nu_\tau \\ &\to h^- h^- h^+ (n\pi^0) \nu_\tau . \end{aligned} \tag{2}$$

The oscillation parameters and very short decay length ($87\,\mu$m) of the tau require i) a long baseline, ii) high-energy neutrino beam and iii) a massive detector with a high spatial resolution. OPERA is exposed to the long-baseline CNGS ν_μ beam, 732 km away from its neutrino source at CERN. The average neutrino energy is $\sim 17\,\text{GeV}$ well above the production threshold for the tau. The $\bar{\nu}_\mu$ contamination in terms of interactions is 2.1%, the ν_e and $\bar{\nu}_e$ contaminations are lower than 1% while the prompt ν_τ in the beam is negligible. The challenge of the OPERA experiment is to achieve the very high spatial accuracy required for the detection of the tau inside a large-mass active target. The technology chosen for this challenge are emulsion films interleaved with lead plates, historically called Emulsion Cloud Chamber (ECC). The submicrometer spatial resolution of the nuclear emulsion allows a precise three-dimensional reconstruction of the neutrino vertex as well as of the decay vertex associated short-lived particles, including the tau. The large target mass given by the lead plates allows to collect enough statistics.

2. – The detector

OPERA is a hybrid detector made of two identical Super Modules (SM) each consists of a target section, of a scintillator tracker detector (TT) and a spectrometer. The total mass is 1250 kTons. A target section is a succession of walls filled with elements called bricks, interleaved with planes of scintillator strips composing the Target Tracker (TT) that provide real time detection of the outgoing charged particles.

The target sections consist of about 150000 ECC bricks and each of them is made of 56 lead plates and 57 emulsion films for a total weight of 8.3 kg. An OPERA emulsion film has two layers each 44 μm on both sides of base. The total thickness is about 290 μm. The transverse size is $12.5 \times 10.0\,\text{cm}^2$. A pair of nuclear emulsion films are used as interface between electronic detector and ECC brick. Tightly packed doublets of emulsion films are glued to the downstream face of each brick and can be removed without opening the brick.

The electronic detectors trigger the readout, identify and measure the trajectory of charged particles and locate the brick where the interaction occurred. The momentum of muons are measured by the spectrometers which consist of a dipolar magnet made of two iron arms. The trajectory of muons are traced back through the scintillator planes up to brick where the track originates. When no muons are observed, the scintillator signals produced by electrons or hadronic showers are used to predict the location of the brick that contains the primary neutrino interaction vertex. A detailed description of the OPERA detector is given in [4].

The scanning of the emulsion films is performed with two different types of automatic microscope, the European Scanning System (ESS) and Japanese S-UTS. The European scanning system makes use of commercial subsystems in a software based framework. The horizontal stage movable in XY coordinates with a CMOS camera mounted on the optical axis along which it can be moved to change the focal plane. The control workstation hosts a motion control unit that directs the stage to the area to be scanned and drives the camera along the Z-axis to produce optical tomographic image sequences. Then, the images are enhanced by means of a vision processing board in the control workstation. The reconstructed clusters in an emulsion layer is called micro-tracks. The linking of two matching micro-tracks produces the base-track. The system can work at a speed of $20\,\text{cm}^2$/h/layer. The Japanese system has been developed in Nagoya and is based on highly customized components. The feature of this system is removal of the stop and go process of the stage in the data taking stage. The optical system is moved by a piezo-electric device. The dedicated board make the track recognition, building micro-tracks. The system can reach the speed of $72\,\text{cm}^2$/h/layer.

3. – Event location and decay search

During years 2008–2009, OPERA has collected 31576 triggers corresponding to 5.13×10^{19} protons on target. Among these events 5255 events reconstructed as occurring inside the OPERA target.

The first step of event location is the extraction of the brick from the target wall. Then the CS is detached and its films are searched for compatible with the electronic data to verify the brick selection. In the case this search is unsuccessful, the brick is equipped with a fresh CS and inserted back into the target. All tracks measured in the CS are searched in the most downstream films of the brick and followed back until they are not found in three consecutive films. The stopping point is considered as the signature either for a primary of a secondary vertex. The vertex is then confirmed by scanning a volume with a transverse size of $1\,\text{cm}^2$ on at least 6 films downstream and 2 films upstream of the stopping plate is scanned around each stopping point. The data are processed by an offline program to reconstruct all tracks originating inside the volume. These tracks are input for a vertex reconstruction algorithm which is tuned to find also decay topologies.

The mean efficiency of event location is found to be $74 \pm 2\%$ and $48 \pm 4\%$ for ν_μ charged-current(CC) and neutral-current(NC) events, respectively. The expected number of located events in the 2008–2009 data sample is 2978 ± 75. But the result presented in this paper comes from the decay search analysis of 2738 events corresponding to 92% of the located sample.

When a secondary vertex is found the kinematical analysis of the whole event is done using the ECC brick data. The momentum of charged particles are determined by multiple coulomb scattering [5] measured in the ECC brick. The energy of γ-rays and electrons is estimated by a Neural Network algorithm that uses the combination of the number of track segments in the emulsion films and the shape of the electromagnetic shower, together with the multiple Coulomb scattering of the leading tracks.

4. – The candidate event

By applying decay search procedure, one ν_τ candidate was observed in the 2008–2009 data sample. The candidate event has 7 prongs at primary vertex out of which 4 are identified as originating from a hadron and 3 have a probability lower than 0.1% of being caused by a muon. The parent track exhibits a kink topology and the daughter track is identified as produced by a hadron through its interaction. Its impact parameter with respect to the primary is $55 \pm 4\,\mu$m, the impact parameter for other tracks is smaller than $7\,\mu$m. Two γ-rays point to the secondary vertex. The event passes all selection criteria described in [3] and summarized in table I. The invariant mass of two γ-rays is $120 \pm 20(\text{stat.}) \pm 35(\text{syst.})\,\text{MeV}/c$. If we assume the secondary hadron is π^- the invariant mass becomes $640^{+125}_{-80}(\text{stat.})^{+100}_{-90}(\text{syst.})\ \text{MeV}/c^2$ the decay mode is compatible therefore with being $\tau^- \to \rho^-(777)\nu_\tau$ whose branching ratio is about 25%. A detailed description of the candidate event can be found in [6].

5. – Background estimation

The charmed particles have lifetimes similar to that of the tau and have similar topologies. The finding efficiency of the decay vertices is therefore also similar to that of tau decays. Comparing the observed charm event sample with simulation would be a test for corresponding efficiencies and backgrounds. Table II shows the

Table I. – *Selection criteria for* ν_τ *candidate event.*

Varibale	Cut-off	Candidate Event
Missing P_T at Primary Vertex (GeV/c)	< 1.0	$0.57^{+0.32}_{-0.17}$
Angle between parent track and primary hadronic shower in the transverse plane	$\frac{\pi}{2}$	3.01 ± 0.03
Kink angle (mrad)	> 20	41 ± 2
Daughter momentum (GeV/c)	> 2	12^{+6}_{-3}
Daughter P_T when γ-ray at the decay vertex (GeV/c)	> 0.3	$0.47^{+0.24}_{-0.12}$
Decay length (μm)	< 2000	1335 ± 35

Table II. – *The observed and expected charm topologies in the* 2008–2009 *sample.*

Topology	Observed charm events	Expected charm events with background
C1	13	17.8
V2	18	16.5
C3	5	5.8
V4	3	2.1
Total	39	42.2 ± 8.3

comparison between observed charm events and expected from simulation. There is a good agreement between them.

The main background source to all τ decay channels is constituted by charmed particle production in ν_μCC interactions where the primary lepton is not identified. The charm background was evaluated using charm cross-sections measured by the CHORUS Collaboration [7].

Table III. – *Expected number of signal and background events in the* 2008–2009 *sample.*

Decay channel	Number of signal for 4.88×10^{19} p.o.t	Number of background for 4.88×10^{19} p.o.t
$\tau \to \mu$	0.39	0.02 ± 0.01
$\tau \to e$	0.63	0.05 ± 0.01
$\tau \to h$	0.49	0.05 ± 0.01
$\tau \to 3h$	0.15	0.04 ± 0.01
Total	1.65	0.16 ± 0.03

The second main source of background in $\tau \to h$ decay channel comes from one-prong inelastic interactions of primary hadrons produced in ν_μNC interactions or in ν_μCC interactions where the primary lepton is not identified and in which no nuclear fragments can be associated with secondary interaction. This background has been evaluated with Monte Carlo simulation based on FLUKA [8] and cross-checked with data.

6. – Conclusion

The OPERA experiment, aiming at the first detection of neutrino oscillations in direct appearance mode where the oscillated neutrino is identified. The analysis of the 2008–2009 data corresponding to 4.88×10^{19} p.o.t. intensity has been completed and a single ν_τ candidate event which is compatible with the expectation was observed. All background sources and expected number of tau events are summarized in table III. The significance of the observation of one decay in the $\tau \to h$ channel is found to be 95%. Considering all decay channels, the number of expected signal and background events are respectively 1.65 ± 0.41 and 0.16 ± 0.03(syst.), the probability for the event to be background being 15%.

The analysis of 2010–2011 data samples is in progress.

* * *

This work is supported by TUBITAK under Grant No. 108T324.

REFERENCES

[1] Fukuda Y. *et al.* (Super-Kamiokande Collaboration), *Phys. Rev. Lett.*, **81** (1998) 1562.
[2] Ahn M. H. *et al.* (K2K Collaboration), *Phys. Rev. D*, **74** (2006) 072003; Michael D. G. *et al.* (MINOS Collaboration), *Phys. Rev. Lett.*, **97** (2006) 191801; Michael D. G. *et al.* (CHOOZ Collaboration), *Eur. Phys. J. C*, **27** (2003) 331; Ahmad Q. R. *et al.* (SNO Collaboration), *Phys. Rev. Lett.*, **89** (2002) 011301.
[3] Guler M. *et al.* (OPERA Collaboration), CERN-SPSC-2000-028.
[4] Acquafredda R. *et al.* (OPERA Collaboration), *JINST*, **4** (2009) P04018.
[5] Agafonova N. *et al.* (OPERA Collaboration), *New J. Phys.*, **14** (2012) 13026.
[6] Agafonova N. *et al.* (OPERA Collaboration), *Phys. Lett. B*, **691** (2010) 138; Agafonova N. *et al.* (OPERA Collaboration), *New J. Phys.*, **14** (2012) 33017.
[7] Kayis-Topaksu A. *et al.* (CHORUS Collaboration), *New J. Phys.*, **13** (2011) 093002.
[8] FLUKA package, `http://www.fluka.org/fluka.php`.

IL NUOVO CIMENTO Vol. 35 C, N. 6 Novembre-Dicembre 2012
DOI 10.1393/ncc/i2012-11350-2

Colloquia: LaThuile12

Solar-neutrino physics with Borexino

M. G. Giammarchi(*) on behalf of the Borexino Collaboration
INFN, Sezione di Milano - Milano, Italy

ricevuto il 7 Settembre 2012

Summary. — The Borexino solar-neutrino detector is a high-radiopurity low-threshold liquid scintillator that detects solar neutrinos by means of the elastic scattering $\nu e \rightarrow \nu e$ reaction. The detector, located at the Laboratori Nazionali del Gran Sasso (LNGS, Italy) and has now measured solar neutrinos from the ^{7}Be, ^{8}B and pep components. Terrestrial neutrinos (geoneutrinos) have also been observed.

PACS 26.65.+t – Solar neutrinos.
PACS 29.40.Mc – Scintillation detectors.
PACS 14.60.Pq – Neutrino mass and mixing.

1. – Introduction

Solar-neutrino physics originally started from the study of the basic working principle of the core of the Sun, with nuclear-fusion reactions producing energy and emitting neutrinos. The pioneering Davis experiment [1] was the first one to detect (with radiochemical methods) solar neutrinos and to measure a deficit with respect to the flux predicted by theoretical models. Additional experiments were performed starting from the end of the 80's both in radiochemical mode [2-4] and in real-time mode [5-7], while theoretical models of the sun evolved into what is now known as the Standard Solar Model [8, 9]. Figure 1 shows the prediction of the flux of solar neutrinos according to the Standard Solar Model.

In general, real-time experiments have been performed with water Cerenkov detectors with an energy threshold of about 5 MeV, mainly due to natural radioactivity. Therefore, only $\sim 0.001\%$ of the total neutrino flux has been observed in real time before 2007.

Measuring low energy (sub-MeV) solar neutrinos has been the subject of an intensive research and development program carried out in Borexino since the beginning of the 90's.

(*) E-mail: marco.giammarchi@mi.infn.it

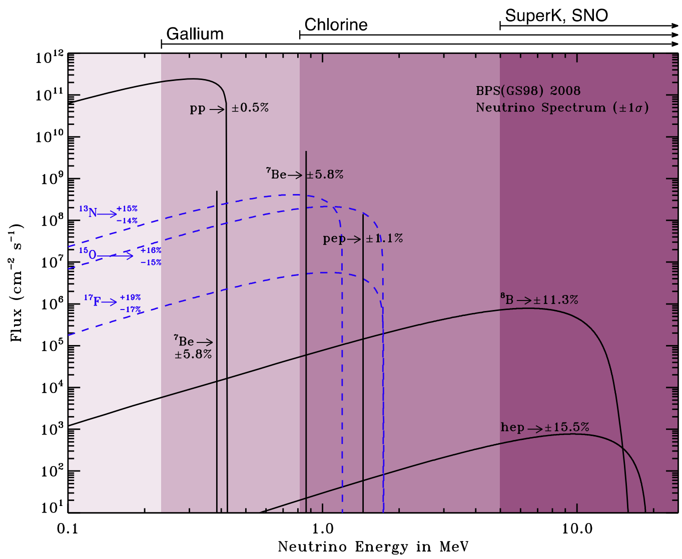

Fig. 1. – Solar-neutrino energy spectrum as predicted by the Sandard Solar Model. Typical detection thresholds of solar-neutrino experiments are shown as well as model uncertainties on the solar fluxes.

Borexino [10] is a real time experiment to study low-energy solar neutrinos and other rare phenomena, based on the $\nu e^- \to \nu e^-$ elastic scattering reaction. The experimental design threshold is of 50 keV while the analysis threshold is ~ 200 keV; these values make it possible to study solar-neutrino components such as the 0.862 MeV ^{7}Be solar neutrino line, generating a recoil electron with 664 keV maximum energy. The detection reaction is observed in a large mass (100 tons) of ultrapure and well-shielded liquid scintillator.

The predictions of solar fluxes depend both on the Standard Solar Model and the value of the parameters of the LMA solution of neutrino oscillations [11, 12]. The Borexino experimental program makes it possible to directly test this prediction by measuring solar neutrinos on a wide energy range.

The main challenge of an experiment with such a low energy threshold is the background coming from natural sources such as cosmic rays or radioactivity. Studies have been made on low radioactivity materials and purification techniques with a comparable effort devoted to detection and measurement of very low activity levels [13]. As a part of this program, a prototype of the Borexino detector, called Counting Test Facility [14], was built and operated at LNGS to demonstrate very low radioactive contamination levels (10^{-16} g/g of ^{238}U equivalent or less [15]) in a ton scale scintillator detector. This research culminated into the construction, filling and operation of the full-scale Borexino detector.

2. – The Borexino detector

Borexino [16] is an unsegmented scintillation detector featuring ~ 300 tonnes of well-shielded liquid ultrapure scintillator viewed by 2200 photomultipliers (fig. 2). The detector core is a transparent spherical vessel (Nylon Sphere, 100 μm thick), 8.5 m diameter, filled with 300 tonnes of liquid scintillator and surrounded by 100 tonnes of high-purity

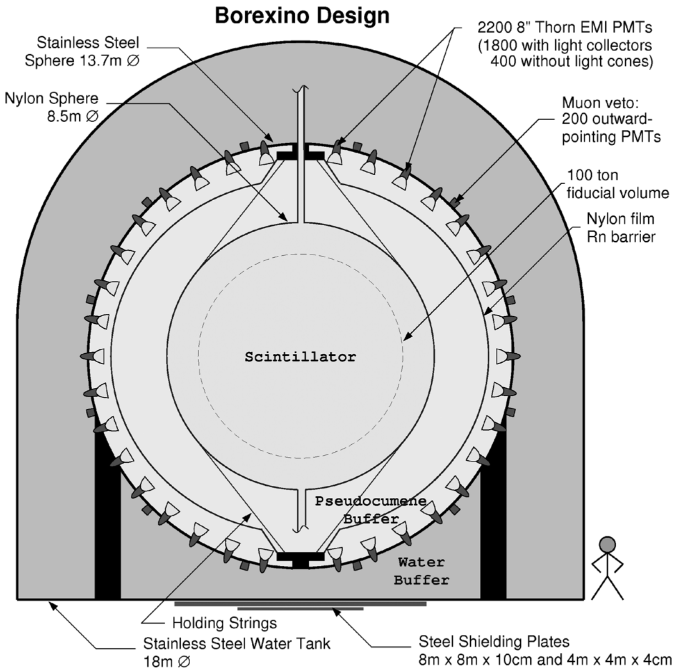

Fig. 2. – Schematics of the Borexino detector at Gran Sasso (see text).

buffer liquid. The scintillator mixture is pseudocumene (PC) and PPO (1.5 g/l) as a fluor, while the buffer liquid consists of PC alone (with the addition of DMP as light quencher). The photomultipliers are supported by a Stainless Steel Sphere, which also separates the inner part of the detector from the external shielding, provided by 2400 tonnes of pure water (Water Buffer). An additional containment vessel (Nylon film Radon barrier) is interposed between the Scintillator Nylon Sphere and the photomultipliers, with the goal of reducing radon diffusion towards the internal part of the detector.

The outer water shield is instrumented with 200 outward-pointing photomultipliers serving as a veto for penetrating muons, the only significant remaining cosmic-ray related background at the Gran Sasso depth (about 3700 m of water equivalent). The innermost 2200 photomultipliers are divided into a set of 1800 devices equipped with light cones (so that they collect light only from the Nylon Sphere region) and a set of 400 PMT's without light cones, sensitive to light originated in the whole Stainless Steel Sphere volume. This design greatly increases the capability of the system to identify muons crossing the PC buffer (and not the scintillator).

The Borexino design is based on the concept of a graded shield of progressively lower intrinsic radioactivity as one approaches the sensitive volume of the detector; this culminates in the use of the 200 tonnes of the low background scintillator to shield the 100 tonnes innermost Fiducial Volume. In these conditions, the ultimate background will be dominated by the intrinsic contamination of the scintillator, while all backgrounds from the construction materials and external shieldings will be neglible.

Borexino also features several external systems conceived to purify the experimental fluids (water, nitrogen, scintillator) used in the experiment (see, *e.g.* [17]).

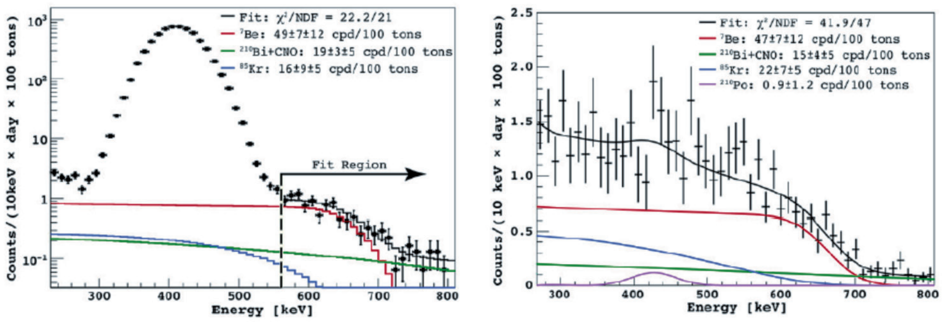

Fig. 3. – The fit to the Be-7 region can be made without (left) or with (right) the statistical α/β discrimination (left). The results of the Be-7 fits in both cases is consistent. The fit is done by including the signal as well as the $^{210}\mathrm{Bi} + \mathrm{CNO}$ and the $^{85}\mathrm{Kr}$ background.

3. – Borexino and solar neutrinos

The filling of the detector started in January 2007, with scintillator displacing the purified water from inside the detector volumes. The data taking started in May 2007.

The detection reaction of Borexino, $\nu e^- \to \nu e^-$, is sensitive to all neutrino flavors while having a higher cross section for electron neutrinos. The energy deposited in the active target produces scintillation light which is collected in the photomultipliers. The energy of the event can be reconstructed from the detected number of photoelectrons (~ 500/MeV), while the position of the event is calculated from the photoelectron arrival times. The radiopurity of the detector has been found to be better than the specifications. In particular, ^{14}C contamination of the scintillator was found to be $\sim 2\times 10^{-18}$ $^{14}\mathrm{C}/^{12}\mathrm{C}$, which is important in the low-energy part of the spectrum (200 keV or less). The Th-232 and U-238 contaminations were found to be $\sim 4.6 \times 10^{-18}$ and $\sim 2 \times 10^{-17}$ g/g respectively. Finally the Kr-85 contamination (of considerable importance for the Be-7 measurement) was limited to 30 counts/day in the Fiducial Volume.

The Borexino main trigger fires when at least 30 PMT's each detect at least a photoelectron within a time window of 60 ns, corresponding approximately to an energy threshold of 60 keV for electrons. The main cuts that are performed in the analysis are the muon cut and the pulse-shape alpha/beta discrimination. Additional cuts involve event quality, delayed coincidences to remove Rn daughters as well as spatial (fiducial) cuts. In all the analyses reported below, only the general characteristics will be given, leaving the interested reader to the full description in the relevant bibliography.

4. – The detection of the Be-7 solar neutrinos

Borexino reported the first detection of solar neutrinos [18] a few months after the start of the data taking. The evidence was based on detecting the recoil spectrum of the electron due to the $\nu e^- \to \nu e^-$ scattering. Figure 3 shows the relevant part of the spectrum after the cuts (quality, muons, space, and Rn daughter cuts, with or without α/β discrimination), with the presence of the ^{210}Po quenched alpha out of equilibrium with the other isotopes of the ^{222}Rn sequence. The ^{210}Po peak is effectively removed by the pulse-shape discrimination cut and the ^{7}Be shoulder (located at 664 keV for a neutrino energy of 861 keV) is evident in the 560–800 keV energy region. This constituted the first experimental evidence of the ^{7}Be nuclear reaction inside the Sun.

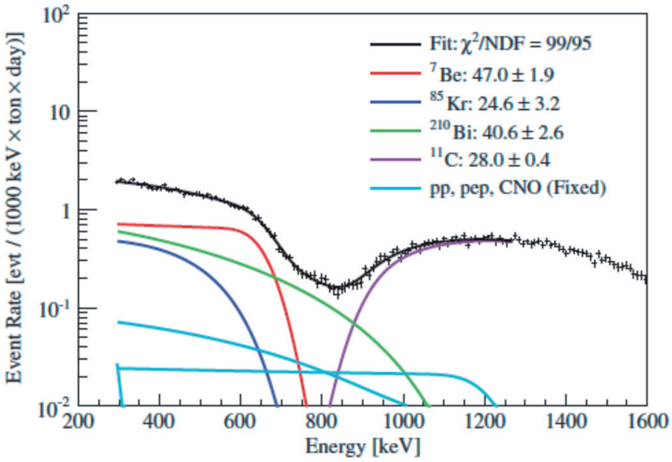

Fig. 4. – Analitically fitted spectrum of recoil electrons in the Be-7 spectral region showing different fit components, given in units of (counts/(day 100 ton)).

During the fit procedures, the backgrounds were left as free parameters, including the ^{85}Kr component, whose spectral shape is similar to the signal and whose uncertainty substantially contributes to the systematic error. We have verified that the ^{85}Kr result from the fit is consistent with the direct measurement of the ^{85}Kr delayed coincidence rate([1]).

Subsequent analyses have profited from better statistics [19] and a subsequent intensive calibration campaign [20] (see below). An example of a fitted spectrum is shown in fig. 4. Again, the Kr-85 fit results was cross-checked with the delayed coincidence measurement. The result obtained for the solar neutrino Be-7 rate is of $46.0 \pm 1.5(\text{stat})^{+1.5}_{-1.6}(\text{syst})$ counts/(day 100 ton), in agreement with the Standard Solar Model and the Mikheyev-Smirnov-Wolfenstein large mixing angle neutrino oscillation mechanism.

As a part of the Borexino solar neutrino data, a study was made to look for day-night asymmetry in the ^{7}Be neutrino rate [21]. The presence of this effect could be indicative of the so-called LOW region of parameters for solar-neutrino oscillations ($\delta m^2 \sim 10^{-7}\,\text{eV}^2$), which was previously strongly disfavored only the KamLAND antineutrino measurement, thereby relying on the CPT assumption. The obtained results, of

$$A_{dn} = 2\,\frac{N-D}{N+D} = 0.01 \pm 0.012(\text{stat}) \pm 0.007(\text{syst}) \tag{1}$$

agrees with the MSW-LMA solution for neutrino oscillations and disagrees with the LOW solution at more than 8.5 σ CL.

([1]) The decay sequence $^{85}\text{Kr} \to {}^{85m}\text{Rb} + \text{e}^+ + \bar{\nu}_\text{e}$, $^{85m}\text{Rb} \to {}^{85}\text{Rb} + \gamma$ ($\tau = 1.5\,\mu$s, BR $= 0.43\%$) was used to tag the content of Kr-85.

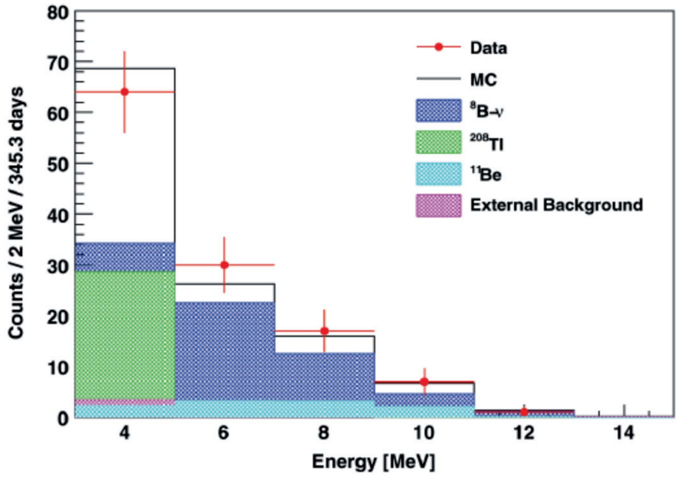

Fig. 5. – ^{8}B neutrino spectrum and remaining background after data selection. The black line is the Monte Carlo simulation.

5. – The calibration campaign

In order to better understand the performance of the detector and minimize systematic error on the ^{7}Be and other measurements, during 2010 an intense calibration campaign was performed. Sources such as ^{57}Co, ^{139}Ce, ^{203}Hg, ^{85}Sr, ^{54}Mn, ^{65}Zn, ^{60}Co, and ^{40}K were used for gamma calibration, while ^{14}C, ^{214}Bi, and ^{214}Po were used to understand the response of the detector to β's and α's. Finally, an AmBe source was used for neutrons and high-energy gammas. These studies allowed a significant reduction of the systematic error on the determination of the Fiducial Volume and the energy scale. Several parameters of the simulation codes (such as the light yield and the quenching factor) could be determined with greater accuracy. External sources were also deployed in several positions around the detector.

In addition, purification campaigns were conducted (water extraction, distillation, nitrogen stripping) that have significantly reduced two of the most important backgrounds, ^{85}Kr and ^{210}Bi.

6. – The B-8 measurement

Solar neutrinos from ^{8}B are measured in Borexino [22] by studying the high-energy part of the spectrum, starting from 3 MeV; this limit is imposed by the presence of the ^{208}Tl contamination. For this analysis, muon and cosmogenic background had to be treated with special care. ^{214}Bi and ^{208}Tl removal were performed together with neutron rejection. Figure 5 shows the final spectrum obtained after the cuts. The fitted number of ^{8}B events, $0.22 \pm 0.04(\text{stat}) \pm 0.01(\text{syst})$ (counts/day 100 t) is in good agreement with the Standard Solar Model (both high and low metallicity) and the MSW-LMA oscilaltion mechanism for neutrinos.

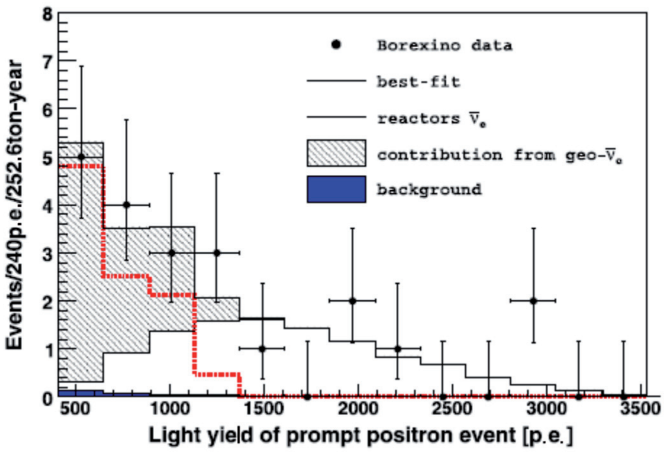

Fig. 6. – Light-yield spectrum for the positron prompt events showing the remaining background, the nuclear reactor component and the geoneutrino signals. The conversion form p.e. to energy is approximately 500 p.e./MeV.

7. – The observation of geoneutrinos

Geoneutrinos, electron antineutrinos produced in β decays of naturally occurring radioactive isotopes in the Earth, are a direct probe of our planet's interior. They are produced in the decays of ^{40}K and in the chains of radioactive isotopes ^{238}U and ^{232}Th. The detection reaction in the Borexino scintillator, $\bar{\nu}_e + p \rightarrow e^+ + n$ (with a 1.806 MeV threshold) makes it possible to detect only a part of the ^{238}U and ^{232}Th antineutrinos. The positron in the final state comes promptly to rest in the scintillator and annihilates by emitting two 511 keV gamma rays, giving a prompt event with a visible energy of $E(\bar{\nu}_e) - 0.782$ MeV, while the free neutron is typically captured on protons with a mean time of 256 μs, resulting in the emission of a 2.22 MeV de-excitation γ-ray which provides a coincident delayed event. Background rejection was performed with special emphasis on accidental coincidences, primary muons producing a secondary neutron and cosmogenically-produced neutron emitters (such as ^{9}Li or ^{8}He).

Thanks to the high radiopurity of the Borexino scintillator, the (α, n) background was small, so the final dominant background after cuts was the one due to European nuclear power reactors, producing antineutrinos up to 10 MeV.

Figure 6 shows the positron spectrum remaining after the cuts, showing the contribution of geo-neutrinos and reactor neutrinos. The geo-neutrino rate was found, though a maximum-likelihhod fit, to be of $3.9^{+1.6}_{-1.3}$ events/100 ton y [23].

8. – The pep first observation and the CNO limit

Observation of solar neutrinos in the 1.0–1.5 MeV energy range poses a special experimental challenge. First of all, ^{11}C background, of cosmogenic origin, is a β^+ emitter that is copiously produced even at the Gran Sasso depth ($\sim$ 30 events/day 100 tons). Secondly, other cosmogenic isotopes like ^{10}C need to be considered. Thirdly, the ^{210}Bi contamination on the low side of the range, needs to be addressed.

This spectral energy range is of great interest for two reasons. First, the pep component of the solar neutrino spectra —a monochromatic 1.44 MeV neutrino line— can be

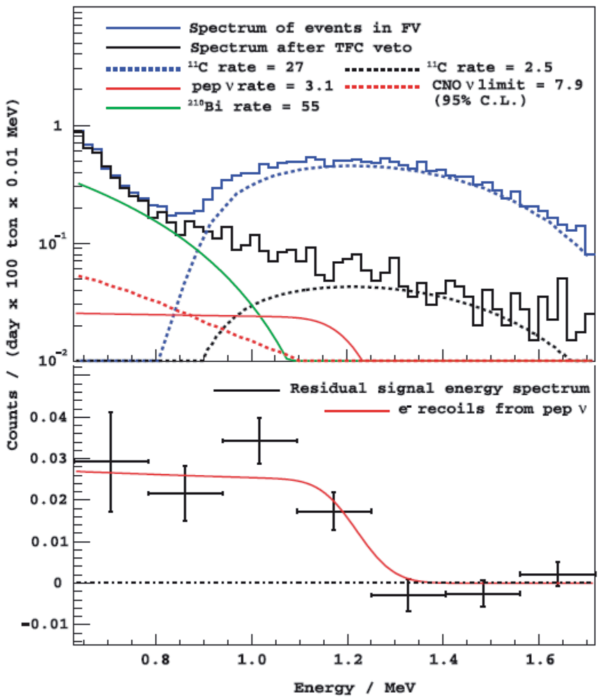

Fig. 7. – Top: energy spectra of events in the Fiducial Volume in the pep region before and after the threefold coincidence. The solid and dashed blue lines show the data and estimated ^{11}C rate before any veto is applied. The solid black line shows the data after the C-11 removal procedure, whose contribution (dashed black line) has been suppressed. The rate values are integrated over all energies and are quoted in units of counts/(day 100 ton). Bottom: residual energy spectrum after best-fit rates of all considered backgrounds are subtracted. The recoil spectrum from pep ν at the best fit rate is also shown.

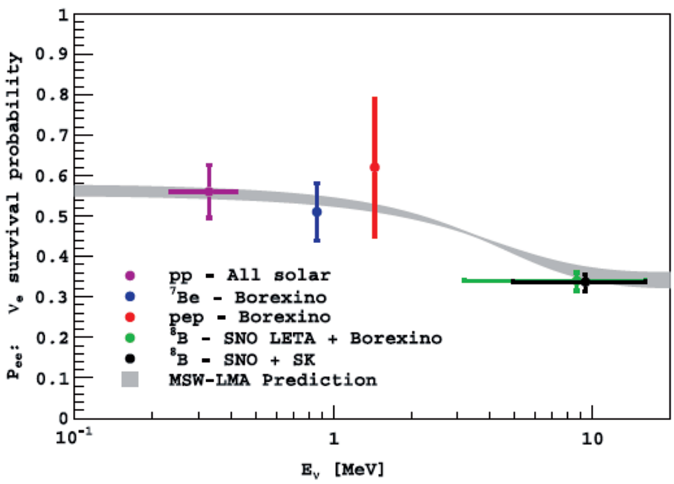

Fig. 8. – Probability that an electron neutrino produced in the Sun will be detected as an eletron neutrino on Earth. The gray band shows the MSW-LMA oscillation prediction.

found in this region; this component is interesting because it occurs at the very beginning of the pp production cycle in the Sun and is therefore well constrained by solar models. Secondly, this range offers the possibility to look for CNO production in the Sun, which is predicted to be $\sim 1\%$ of the pp cycle and has never been observed before.

Similarly to the case of the B-8 analysis, ^{11}C background was reduced by using the threefold coincidence (between the parent muon, a spallation neutron and the ^{11}C beta-plus decay itself). In addition, the pulse-shape difference between e^- and e^+ (from ^{11}C) were measured in organic liquid scintillators; a small difference in the time distribution of the scintillation signals arises in fact from the finite lifetime of the orthopositronium (formed only by the e^+) [25]. This effect was taken into account in the final fit.

Figure 7 shows the spectra before and after the final residual subtraction, with the observation of the pep solar component [24] at 3.1 ± 0.6(stat) $\pm$ 0.3(syst) counts/(day 100 ton) which agrees with the solar models and the MSW-LMA solution. A pep-CNO correlated analysis was made to study the robustness of the pep result; a CNO flux upper limit was found at < 7.9 counts/(day 100 ton) at 95% CL (pep fixed at the Standard Model value), which is the best upper limit to date.

9. – Conclusions

Borexino has measured the ^{7}Be, pep and ^{8}B solar-neutrino components, therefore decisively contributing to the measurement of the survival probability of solar neutrinos. The survival probability as a function of energy, fig. 8, clearly shows the transition between the vacuum and the matter-dominated energy range. In addition, the detector has measured geoneutrinos at Gran Sasso and imposed upper limits on the day-night asymmetry of the ^{7}Be flux and the CNO component in the Sun.

Finally, the excellent sensitivity of the Borexino detector has been exploited to study additional low-background physics topics [26-28].

Appendix A.

The Borexino Collaboration

G. Bellini, J. Benziger, D. Bick, S. Bonetti, G. Bonfini, M. Buizza Avanzini, B. Caccianiga, L. Cadonati, F. Calaprice, C. Carraro, P. Cavalcante, A. Chavarria, D. D'Angelo, S. Davini, A. Derbin, A. Etenko, K. Fomenko, D. Franco, C. Galbiati, S. Gazzana, C. Ghiano, M. Giammarchi, M. Goeger-Neff, A. Goretti, L. Grandi, E. Guardincerri, S. Hardy, Aldo Ianni, Andrea Ianni, V. Kobychev, D. Korablev, G. Korga, Y. Koshio, D. Kryn, M. Laubenstein, T. Lewke, E. Litvinovich, B. Loer, F. Lombardi, P. Lombardi, L. Ludhova, I. Machulin, S. Manecki, W. Maneschg, G. Manuzio, Q. Meindl, E. Meroni, L. Miramonti, M. Misiaszek, D. Montanari, P. Mosteiro, V. Muratova, L. Oberauer, M. Obolensky, F. Ortica, M. Pallavicini, L. Papp, L. Perasso, S. Perasso, A. Pocar, R. S. Raghavan, G. Ranucci, A. Razeto, A. Re, A. Romani, A. Sabelnikov, R. Saldanha, C. Salvo, S. Schönert, H. Simgen, M. Skorokhvatov, O. Smirnov, A. Sotnikov, S. Sukhotin, Y. Suvorov, R. Tartaglia, G. Testera, D. Vignaud, R. B. Vogelaar, F. von Feilitzsch, J. Winter, M. Wojcik, A. Wright, M. Wurm, J. Xu, O. Zaimidoroga, S. Zavatarelli, and G. Zuzel.

REFERENCES

[1] Davis R., *Nobel Prize Lecture* (2002).
[2] Hampel W. *et al.*, *Phys. Lett. B*, **447** (1999) 127.
[3] Abdurashitov J. N. *et al.*, *Phys. Rev. Lett.*, **83** (1999) 4686.
[4] Altmann M. *et al.*, *Phys. Lett. B*, **616** (2005) 174.
[5] Fukuda S. *et al.*, *Phys. Rev. Lett.*, **86** (2001) 5651.
[6] Fukuda S. *et al.*, *Phys. Rev. Lett.*, **539** (2002) 179.
[7] Ahmad Q. R. *et al.*, *Phys. Rev. Lett.*, **87** (2001) 071301.
[8] Bahcall J. N. and Pinsonneault M. H., *Phys. Rev. Lett.*, **92** (2004) 121301.
[9] Serenelli A. *et al.*, *Astrophys. J. Lett.*, **705** (2009) L123.
[10] Alimonti G. *et al.*, *Astropart. Phys.*, **16** (2002) 205.
[11] Bahcall J. N. *et al.*, *JHEP*, **0408** (2004) 016.
[12] Fogli G. L. *et al.*, *Progr. Nucl. Phys.*, **57** (2006) 742.
[13] Arpesella C. *et al.*, *Astropart. Phys.*, **18** (2002) 1.
[14] Alimonti G. *et al.*, *Nucl. Instrum. Methods A*, **406** (1998) 411.
[15] Alimonti G. *et al.*, *Astropart. Phys.*, **8** (1998) 141.
[16] Alimonti G. *et al.*, *Nucl. Instrum. Methods A*, **600** (2009) 568.
[17] Alimonti G. *et al.*, *Nucl. Instrum. Methods A*, **609** (2009) 58.
[18] Arpesella C. *et al.*, *Phys. Lett. B*, **658** (2008) 101.
[19] Arpesella C. *et al.*, *Phys. Rev. Lett.*, **101** (2008) 091302.
[20] Bellini G. *et al.*, *Phys. Rev. Lett.*, **107** (2011) 141302.
[21] Bellini G. *et al.*, *Phys. Lett. B*, **707** (2012) 22.
[22] Bellini G. *et al.*, *Phys. Rev. D*, **82** (2010) 033006.
[23] Bellini G. *et al.*, *Phys. Lett. B*, **687** (2010) 299.
[24] Bellini G. *et al.*, *Phys. Rev. Lett.*, **108** (2012) 051302.
[25] Franco D. *et al.*, *Phys. Rev. C*, **83** (2011) 015504.
[26] Bellini G. *et al.*, *Phys. Lett. B*, **696** (2011) 191.
[27] Bellini G. *et al.*, *JINST*, **6** (2011) P05005.
[28] Bellini G. *et al.*, *Phys. Rev. D*, **85** (2012) 092003.

IL NUOVO CIMENTO Vol. 35 C, N. 6 Novembre-Dicembre 2012
DOI 10.1393/ncc/i2012-11351-1

Colloquia: LaThuile12

Theoretical models for neutrino masses

L. Merlo(*)

Physik-Department, Technische Universität München
James-Franck-Strasse, D-85748 Garching, Germany and
TUM Institute for Advanced Study, Technische Universität München
Lichtenbergstrasse 2a, D-85748 Garching, Germany

ricevuto il 7 Settembre 2012

Summary. — The recent measurements of the neutrino reactor angle require a re-examination of flavour models based on discrete groups. Indeed, when these models deal with the Tri-Bimaximal, the Bimaximal and the Golden Ratio mixing patterns, some tensions arise in order to accommodate the reactor angle. In particular, strong constraints come from lepton-flavour–violating processes, like $\mu \to e\gamma$. We present the analysis and the main results.

PACS 14.60.Pq – Neutrino mass and mixing.
PACS 11.30.Hv – Flavor symmetries.
PACS 12.60.Jv – Supersymmetric models.

1. – Neutrino data and predictive mass patterns

Solar- and atmospheric-neutrino experiments have established the appearance and the disappearance of specific flavour neutrinos, that finds the best explanation in the oscillation of active neutrinos. Even if the issue of the presence of one or more sterile neutrinos must still be clarified, global fits with only three oscillating active neutrinos well reproduce the data. Nowadays, the most recent results(1) on the oscillation data can be summarized in table I.

More recently, T2K data [1] showed evidences for a non-vanishing reactor angle at the 3σ level. Subsequently also MINOS [2] and Double Chooz [3] presented their results, in agreement with T2K one. In the last months the Daya Bay [4] and RENO [5] experiments have released their results on the observation of electron antineutrino disappearance,

(*) E-mail: luca.merlo@ph.tum.de
(1) Notice that the best-fit values for the reactor angle differ for a factor of 2 in the two fits, due to the exclusion (Fogli *et al.* [7]) or the inclusion (Schwetz *et al.* [6]) of the data from SBL neutrino experiments with a baseline < 100 m.

TABLE I. – *Fits to neutrino oscillation data. For the fit of Schwetz et al.* [6]*, different results have been found for the two hierarchies: the IH is shown in the brackets. In both the fits, the results correspond to the new reactor fluxes, accounting for the T2K* [1] *and MINOS* [2] *data on the reactor angle.*

	Fogli *et al.* [7]	Schwetz *et al.* [6]
Δm^2_{sun} ($10^{-5}\,\mathrm{eV}^2$)	$7.58^{+0.22}_{-0.26}$	$7.59^{+0.20}_{-0.18}$
Δm^2_{atm} ($10^{-3}\,\mathrm{eV}^2$)	$2.35^{+0.12}_{-0.09}$	$2.50^{+0.09}_{-0.16}\,[2.40^{+0.08}_{-0.09}]$
$\sin^2\theta_{12}$	$0.312^{+0.017}_{-0.016}$	$0.312^{+0.017}_{-0.015}$
$\sin^2\theta_{23}$	$0.42^{+0.08}_{-0.03}$	$0.52^{+0.06}_{-0.07}\,[0.52\pm 0.06]$
$\sin^2\theta_{13}$	0.025 ± 0.007	$0.013^{+0.007}_{-0.005}[0.016^{+0.008}_{-0.006}]$

providing at more than 5σ and 6σ, respectively, the evidence for a non-vanishing reactor angle:

$$\sin^2\theta_{13} = 0.024 \pm 0.005 \qquad [\text{Daya Bay}]\,, \qquad \sin^2\theta_{13} = 0.029 \pm 0.006 \qquad [\text{RENO}]\,. \tag{1}$$

The average of the results for the reactor angle from the cited experiments, for normal (inverted) hierarchy, is given by

$$\sin^2\theta_{13} = 0.022 \pm 0.004\,(0.023 \pm 0.004)\,. \tag{2}$$

From the theoretical side, a great effort has been put to construct flavour models that are able to describe and explain the experimental results. Before the new data on the reactor angle, the attention was focussed on a particular class of mixing patterns, for their high predictive power. In the following we will concentrate of the Tri-Bimaximal [8, 9] (TB), the Golden Ratio [10-14] (GR) and the Bimaximal [15-18] (BM) schemes. All these mixing schemes predict a maximal atmospheric angle and a vanishing reactor angle,

$$\sin^2\theta_{23} = \frac{1}{2}\,, \qquad \sin^2\theta_{13} = 0\,, \tag{3}$$

while they differ for the prediction of the solar angle:

$$\sin^2\theta_{12}^{TB} = \frac{1}{3}\,, \qquad \sin^2\theta_{12}^{GR} = \frac{2}{5+\sqrt{5}} \equiv \frac{1}{\sqrt{5}\phi}\,, \qquad \sin^2\theta_{12}^{BM} = \frac{1}{2}\,. \tag{4}$$

Considering the predicted value of the solar angle for the three mixing schemes, while the TB and the GR patterns agree well with the data, the BM one does not at more than 5σ. The interest in the BM pattern is mainly due to its relation with the so-called Quark-Lepton complementarity [19-21] (QLC): the QLC consists in a numerical relation such that the sum of the experimental values of the lepton solar angle and of the Cabibbo angle is roughly $\pi/4$. From here the idea to revert this expression and write $\theta_{12}^{exp} \approx \theta_{12}^{BM} - \theta_C$, where the BM prediction for the solar angle enters [22-24].

Entering more into the details of the these predictive patterns, the unitary matrices corresponding to the mixing angles listed in eqs. (3) and (4) are the following:

$$(5)\quad U_{TB}=\begin{pmatrix} 2/\sqrt{6} & 1/\sqrt{3} & 0\\ -1/\sqrt{6} & 1/\sqrt{3} & -1/\sqrt{2}\\ -1/\sqrt{6} & 1/\sqrt{3} & 1/\sqrt{2}\end{pmatrix},\quad U_{BM}=\begin{pmatrix} 1/\sqrt{2} & -1/\sqrt{2} & 0\\ 1/2 & 1/2 & -1/\sqrt{2}\\ 1/2 & 1/2 & 1/\sqrt{2}\end{pmatrix},$$

$$U_{GR}=\begin{pmatrix} \cos\theta_{12}^{GR} & \sin\theta_{12}^{GR} & 0\\ \sin\theta_{12}^{GR}/\sqrt{2} & -\cos\theta_{12}^{GR}/\sqrt{2} & 1/\sqrt{2}\\ \sin\theta_{12}^{GR}/\sqrt{2} & -\cos\theta_{12}^{GR}/\sqrt{2} & -1/\sqrt{2}\end{pmatrix}.$$

In all the three mixing matrices the 13 entry is zero, corresponding to a vanishing reactor angle and to an undetermined Dirac CP phase. Moreover, all the entries are pure numbers and ensure the independence of the mixing angles from the specific neutrino spectrum: this feature is commonly linked to neutrino mass matrices that are form-diagonalizable [25] (FD).

2. – Neutrino flavour models and the reactor angle

The predictive patterns described in the previous section have been considered as a starting point to reproduce the experimental data. To this aim discrete non-Abelian flavour symmetries are extremely successful and have been implemented in different approaches. In the following we will concentrate on models where the flavour symmetry is: global, in order to avoid the presence of a new force, the corresponding gauge bosons and their flavour violating effects [26-28] (a gauged discrete symmetry should be considered as a remnant of a gauged continuous symmetry breaking); spontaneously broken at the high-energy, in order to prevent strong flavour-violating effects common in the low-energy flavour breaking mechanism [29-31]; broken by a set of scalar fields, called flavons, that transform only under the flavour symmetry, for which a well-defined vacuum alignment mechanism can be constructed (this is one of the main advantages with respect to continuous symmetries [32,33]). In models that fulfill the previous description, the Yukawa Lagrangian is usually written in terms of non-renormalizable operators [34] suppressed by suitable powers of the cut-off scale $\Lambda_f \approx \Lambda_L \approx \Lambda_{GUT}$, where Λ_L is the scale of lepton-number–violation and Λ_{GUT} the GUT scale:

$$(6)\qquad \mathcal{L}_Y=\frac{(Y_e[\varphi^n])_{ij}}{\Lambda_f^n}\,e_i^c\,H^\dagger\,\ell_j+\frac{(Y_\nu[\varphi^m])_{ij}}{\Lambda_f^m}\,\frac{(\ell_i\,\tilde{H}^*)(\tilde{H}^\dagger\,\ell_j)}{2\Lambda_L}\,.$$

Here the Weinberg operators describes the neutrinos, but a completely similar Yukawa Lagrangian can be written for the See-Saw mechanisms. When the flavour and the electroweak symmetries are broken, the charged lepton and neutrino mass matrices are generated. In these models, considering only the lowest-dimensional operators, the TB, GR and BM patterns could naturally arise as the lepton mixing matrix U_{PMNS}. Considering also the higher-dimensional operators, new contributions correct the LO PMNS matrix and are responsible for deviations from the TB, GR and BM predicted mixing angles.

The main ingredient that allows to recover these mixing patterns and their corrections is the flavour-breaking mechanism: the flavons develop vacuum expectation values

(VEVs) in specific directions of the flavour space, such that the starting flavour symmetry G_f is broken down to two distinct subgroup, G_ν and G_ℓ in the neutrino and charged lepton sectors, respectively. We will indicate the set of flavons that lead to G_ν (G_ℓ) as Φ_ν (Φ_ℓ). G_ν and G_ℓ represent the low energy symmetries of the neutrino and charged lepton mass matrices: some examples are $G_\nu = Z_2 \times Z_2$(2) and $G_\ell = Z_n$, with $n > 3$.

Furthermore, the existence of such symmetry-breaking mechanism is usually enforced in a supersymmetric context, even if other possibilities have been studied [39, 40]: in the following we will consider only supersymmetry flavour models.

Whether the final PMNS reproduces the experimental data depends on specific features of the models: in the following we identify three major classes that well represent the present situation in model building [43-45]. The GR models can be associate with the TB ones for what concerns the results of the present analysis.

2˙1. *Typical A_4 models for the TB mixing pattern.* – For this class, we consider for definiteness the model in refs. [39, 41, 42], but the analysis applies to a broader range of models based on A_4 (see ref. [43-45] for details) or on other symmetries (*i.e.* refs. [46-48]). The neutrino and charged lepton mass matrices can be written as

$$m_e = m_e^{(0)} + \delta m_e^{(1)}\,, \qquad\qquad m_\nu = m_\nu^{(0)} + \delta m_\nu^{(1)}\,, \tag{7}$$

where $m_e^{(0)} = \mathrm{diag}(y_e,\, y_\mu,\, y_\tau)\, v_d\, \eta$, with v_d the VEV of H_d and $\eta = \langle\Phi_\ell\rangle/\Lambda_f$ a small parameter that breaks A_4 down to G_ℓ, and $m_\nu^{(0)}$ is diagonalized by the TB mixing matrix.

In a typical model, the NLO contributions to both the mass matrices correct all the entries and are of the same order of magnitude, that we can parametrise with $\xi = \langle\Phi_\ell\rangle/\Lambda_f \approx \langle\Phi_\nu\rangle/\Lambda_f$, a small parameter that breaks also the subgroups G_ℓ and G_ν. In this case, the mixing angles receive deviations from the initial TB values and we can write

$$\begin{aligned}
\sin^2\theta_{23} &= \frac{1}{2} + \mathcal{R}e(c^e_{23})\,\xi + \frac{1}{\sqrt{3}}\left(\mathcal{R}e(c^\nu_{13}) - \sqrt{2}\,\mathcal{R}e(c^\nu_{23})\right)\,\xi,\\
\sin^2\theta_{12} &= \frac{1}{3} - \frac{2}{3}\mathcal{R}e(c^e_{12} + c^e_{13})\,\xi + \frac{2\sqrt{2}}{3}\,\mathcal{R}e(c^\nu_{12})\,\xi,\\
\sin\theta_{13} &= \frac{1}{6}\left|3\sqrt{2}\,(c^e_{12} - c^e_{13}) + 2\sqrt{3}\left(\sqrt{2}\,c^\nu_{13} + c^\nu_{23}\right)\right|\,\xi\,,
\end{aligned} \tag{8}$$

where $c^{e,\nu}_{ij}$, complex random number with absolute value of order 1, is the ij entry of unitary matrices that diagonalize the charged lepton and neutrino mass matrices at the NLO. Accordingly with these expressions, the success rate to reproduce all the three mixing angles inside the corresponding 3σ ranges is maximized for $\xi = 0.07$ for both the NH and IH. We analyze quantitatively the expressions in eq. (8) and their correlations in fig. 1. The $c^{e,\nu}_{ij}$ parameters are treated as complex complex numbers with absolute values following a Gaussian distribution around 1 with variance 0.5. In the plots we show only the NH case. The IH case is similar.

(2) In some cases, G_f it broken down to $G_\nu = Z_2$, but an additional accidental Z_2 symmetry is also present in this sector [35-38].

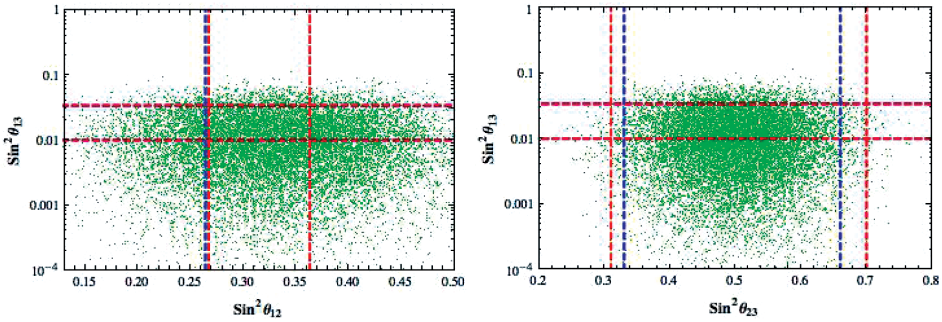

Fig. 1. – Typical A_4 Models. $\sin^2\theta_{13}$ as a function of $\sin^2\theta_{12}$ ($\sin^2\theta_{23}$) is plotted on the left (right), following eq. (8). The vertical lines represent the 3σ values for $\sin^2\theta_{12}$ and $\sin^2\theta_{23}$, following the Fogli *et al.* [7] fit, in blue, and the Schwetz *et al.* [6] fit, in red. The horizontal lines refers to the 3σ values for $\sin^2\theta_{13}$ as in eq. (2).

As we can see, the plots are representing the general behaviour of this class of models: $\sin^2\theta_{13}$ increases with ξ, but correspondingly also the deviation of $\sin^2\theta_{12}$ from 1/3 does. As a result, even for the value of ξ that maximizes the success rate, the requirement for having a reactor angle inside its 3σ error range corresponds to a prediction for the solar angle that is no more in good agreement with data.

2˙2. *Special A_4 models for the TB mixing pattern.* – There are some special models based on the group A_4 [49], in which the LO predictions for the mass matrices are the same as in the previous section, but the corrections are not completely generic. In the specific case of the model in ref. [49], the charged lepton mass matrix still receive generic corrections proportional to $\xi = \langle\Phi_\ell\rangle/\Lambda_f$, but the neutrino mass matrix is corrected only in determined directions: the unitary matrix that digitalize the final neutrino mass matrix is given by

$$(9) \qquad U_\nu = U_{TB}\,V\,, \qquad \text{with} \qquad V = \begin{pmatrix} \alpha & 0 & \xi' \\ 0 & 1 & 0 \\ -\xi'^* & 0 & \alpha^* \end{pmatrix},$$

where $|\alpha|^2 + |\xi'|^2 = 1$, where $\xi' = \langle\Phi_\nu\rangle/\Lambda_f$. In this specific model $\xi' > \xi$. The final expressions for the neutrino mixing angles after the inclusion of all these corrections are given by

$$(10) \qquad \sin\theta_{13} = \left|\sqrt{\frac{2}{3}}\,\xi' + \frac{c^e_{12} - c^e_{13}}{\sqrt{2}}\,\xi\right|, \qquad \delta \approx \arg\xi'\,,$$

$$(11) \qquad \sin^2\theta_{12} = \frac{1}{3} + \frac{2}{9}\,|\xi'|^2 - \frac{2}{3}\,\mathcal{R}e(c^e_{12} + c^e_{13})\,\xi\,,$$

$$(12) \qquad \sin^2\theta_{23} = \frac{1}{2} + \frac{1}{\sqrt{3}}\,|\xi'|\,\cos\delta + \mathcal{R}e(c^e_{23})\,\xi\,.$$

The success rate to reproduce all the three mixing angles inside their corresponding 3σ error ranges is maximized by $|\xi'| = 0.166(0.171)$ for the NH (IH). The parameters have been chosen such that ξ is a real number in [0.005, 0.06] and c^e_{ij} are random complex

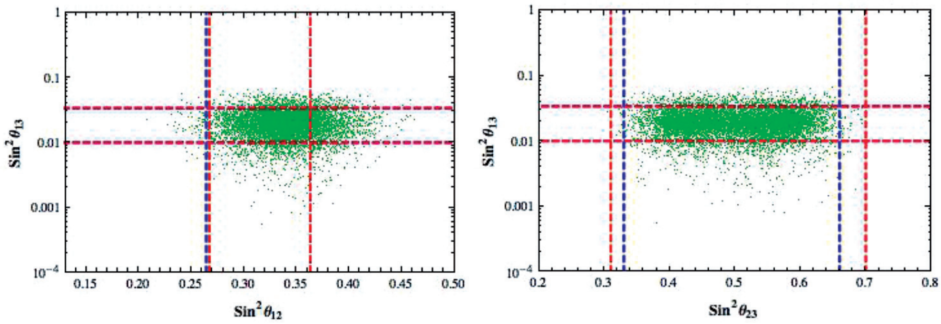

Fig. 2. – Special A_4 Models. $\sin^2\theta_{13}$ as a function of $\sin^2\theta_{12}$ ($\sin^2\theta_{23}$) is plotted on the left (right), following eqs. (11) and (12). The vertical and the horizontal lines are as in fig. 1.

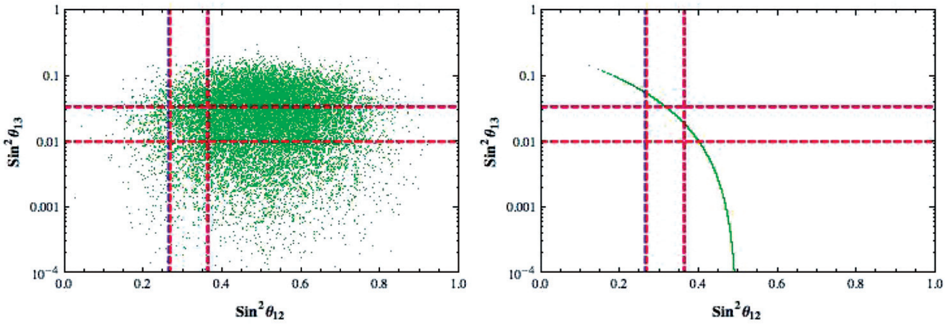

Fig. 3. – S_4 Models. Left: $\sin^2\theta_{13}$ as a function of $\sin^2\theta_{12}$ is plotted, following eq. (13); right: Correlation with $\sin^2\theta_{12}$ with $c_{13} = 0$.

numbers with absolute values following a Gaussian distribution around 1 with variance 0.5. We analyze quantitatively the deviations in eqs. (11) and (12) and their correlations in fig. 2: in the plots on the left (right) column, we show the correlations in eqs. (11) and (12) between $\sin^2\theta_{13}$ and $\sin^2\theta_{12}$ or $\sin^2\theta_{23}$, respectively: ξ' is a complex number with absolute values equal to 0.166. In the plots we show only the NH case. The IH case is similar. For this choice of the parameters, the model can well describe all three angles inside the corresponding 3σ interval, and its success rate is much larger than that of the typical TB models.

2˙3. *S_4 models for the BM mixing pattern.* – For the last class, we focus on a representative model based on the S_4 discrete group [22]. In this case, $m_e^{(0)}$ is still the diagonal matrix with the charged lepton masses, but $m_\nu^{(0)}$ is diagonalized by the BM mixing matrix. At the higher orders, the neutrino mass matrix preserves the same LO flavour structure up to the NNLO level. On the contrary, the changed lepton mass matrix is corrected at the NLO in all the entries, but not in the 23 and 32 ones. As a result, the final neutrino mixing angles at the NLO are given by

$$\sin\theta_{13} = \frac{1}{\sqrt{2}}\,|c^e_{12} - c^e_{13}|\,\xi\,, \qquad \sin^2\theta_{12} = \frac{1}{2} - \frac{1}{\sqrt{2}}\,\mathcal{R}e(c^e_{12}+c^e_{13})\,\xi\,, \qquad \sin^2\theta_{23} = \frac{1}{2}\,. \tag{13}$$

To properly correct the BM value of the solar angle to agree with the data, ξ is expected to be $\mathcal{O}(\lambda_C)$. Studying the success rate to have all the three mixing angles inside the corresponding 3σ ranges, we find that it is maximized for both the NH and IH when $\xi = 0.163$. We analyze quantitatively the expressions in eq. (13) and their predictions in fig. 3, where $c_{12,13}$ have been taken as random complex numbers with absolute value following a Gaussian distribution around 1 with variance 0.5, while $\xi = 0.185(0.194)$. A value close $\cos\delta^{CP}$ close to -1 is favoured in order to maximize the success rate [43-45]. In fig. 3, only for the NH case is shown. The IH case is similar.

Considering the results for the success rates of all the three classes of models, these S_4 models are strongly disfavoured with respect to the special S_4 ones, while are comparable with respect to the typical A_4 models.

3. – Conclusions

Discrete symmetries can well accommodate the neutrino mixing pattern, especially considering an approach in which the PMNS matrix is given in first approximation by the TB, the GR or the BM patterns. With the new results on the reactor angle, however, it appears suspicious that one of these mixing schemes could be a fundamental structure of nature, while it is getting stronger the feeling that they are simply numerical accidents. Indeed, the type and the size of the corrections necessary to bring these mixing patterns in agreement with the data put severe doubts on their naturalness.

Furthermore, as discussed in a series of papers [50-55] and updated in ref. [43-45], the analysis of lepton flavour violating transitions is fundamental to test flavour models. In particular, with the new results on the reactor angle and the large size of the NLO corrections, the bounds on the supersymmetric parameters space coming from the $\ell_i \to \ell_j\gamma$ decays are strong, even for small $\tan\beta$, and if light supersymmetric particles are found then these models are disfavoured. Moreover, it appears impossible to satisfy the MEG bound and, at the same time, to reproduce the muon $g-2$ discrepancy.

Even though the huge effort of these years in constructing flavour models to describe masses and mixings for the neutrinos, and more in general for all the fermions, it is discouraging that no illuminating strategy arise form this scenario. On the other hand, this is partially related to the large uncertainties still present in the flavour sector. The hope is that with a better determination of the lepton mixing angles and with the knowledge of the CP phases, the neutrino mass scale, the type of the neutrino nature and spectrum, it will be finally possible to shed light on the origin of the fermion masses and mixings.

* * *

I warmly thank G. Altarelli, F. Feruglio and E. Stamou for the fruitful collaboration that leaded to the results presented in this talk. I recognise that this work has been partly supported by the TUM-IAS, funded by the German Excellence Initiative. Finally I thank the organizers of the La Thuile conference for the kind invitation and for their efforts in organizing this enjoyable meeting.

REFERENCES

[1] Abe K. *et al.*, *Phys. Rev. Lett.*, **107** (2011) 041801.
[2] Adamson P. *et al.*, *Phys. Rev. Lett.*, **107** (2011) 181802.
[3] Abe Y. *et al.*, arXiv:1112.6353.
[4] An F. P. *et al.*, *Phys. Rev. Lett.*, **108** (2012) 171803.

[5] Ahn J. K. *et al.*, arXiv:1204.0626.
[6] Schwetz T., Tortola M. and Valle J. W. F., *New J. Phys.*, **13** (2011) 109401.
[7] Fogli G. L. *et al.*, *Phys. Rev. D*, **84** (2011) 053007.
[8] Harrison P. F., Perkins D. H. and Scott W. G., *Phys. Lett. B*, **530** (2002) 167.
[9] Xing Z.-z., *Phys. Lett. B*, **533** (2002) 85.
[10] Kajiyama Y., Raidal M. and Strumia A., *Phys. Rev. D*, **76** (2007) 117301.
[11] Rodejohann W., *Phys. Lett. B*, **671** (2009) 267.
[12] Adulpravitchai A., Blum A. and Rodejohann W., *New J. Phys.*, **11** (2009) 063026.
[13] Everett L. L. and Stuart A. J., *Phys. Rev. D*, **79** (2009) 085005.
[14] Feruglio F. and Paris A., *JHEP*, **03** (2011) 101.
[15] Vissani F., arXiv: hep-ph/9708483.
[16] Barger V. D. *et al.*, *Phys. Lett. B*, **437** (1998) 107.
[17] Nomura Y. and Yanagida T., *Phys. Rev. D*, **59** (1999) 017303.
[18] Altarelli G. and Feruglio F., *JHEP*, **11** (1998) 021.
[19] Altarelli G., Feruglio F. and Masina I., *Nucl. Phys. B*, **689** (2004) 157.
[20] Raidal M., *Phys. Rev. Lett.*, **93** (2004) 161801.
[21] Minakata H. and Smirnov A. Y., *Phys. Rev. D*, **70** (2004) 073009.
[22] Altarelli G., Feruglio F. and Merlo L., *JHEP*, **05** (2009) 020.
[23] de Adelhart R., Bazzocchi F. and Merlo L., *JHEP*, **08** (2010) 001.
[24] Meloni D., *JHEP*, **10** (2011) 010.
[25] Low C. I. and Volkas R. R., *Phys. Rev. D*, **68** (2003) 033007.
[26] Grinstein B., Redi M. and Villadoro G., *JHEP*, **11** (2010) 067.
[27] Buras A. J., Merlo L. and Stamou E., *JHEP*, **08** (2011) 124.
[28] Buras A. J., Carlucci M. V., Merlo L. and Stamou E., *JHEP*, **03** (2012) 088.
[29] de Adelhart R., Bazzocchi F., Merlo L. and Paris A., *JHEP*, **03** (2011) 035.
[30] de Adelhart R., Bazzocchi F., Merlo L. and Paris A., *JHEP*, **03** (2011) 040.
[31] Branco G. C. *et al.*, *Phys. Rep.*, **516** (2012) 1.
[32] Feldmann T., Jung M. and Mannel T., *Phys. Rev. D*, **80** (2009) 033003.
[33] Alonso R., Gavela M. B., Merlo L. and Rigolin S., *JHEP*, **07** (2011) 012.
[34] de Medeiros I. and Merlo L., *JHEP*, **02** (2011) 062.
[35] de Adelhart R., Feruglio F. and Hagedorn C., *Phys. Lett. B*, **703** (2011) 447.
[36] de Adelhart R., Feruglio F. and Hagedorn C., *Nucl. Phys. B*, **858** (2012) 437.
[37] Ge S. F., Dicus D. A. and Repko W. W., *Phys. Lett. B*, **702** (2011) 220.
[38] Hernandez D. and Smirnov A. Y., *Phys. Rev. D*, **86** (2012) 053014.
[39] Altarelli G. and Feruglio F., *Nucl. Phys. B*, **720** (2005) 64.
[40] Bazzocchi F. and Morisi S., *Phys. Rev. D*, **80** (2009) 096005.
[41] Altarelli G. and Feruglio F., *Nucl. Phys. B*, **741** (2006) 215.
[42] Altarelli G. and Meloni D., *J. Phys. G*, **36** (2009) 085005.
[43] Altarelli G., Feruglio F., Merlo L. and Stamou E., *JHEP*, **08** (2012) 021.
[44] Altarelli G., Feruglio F. and Merlo L., arXiv:1205.5133, to be published in *Fortschr. Phys.* (2012).
[45] Bazzocchi F. and Merlo L., arXiv:1205.5135, to be published in *Fortschr. Phys.* (2012).
[46] Feruglio F., Hagedorn C., Lin Y. and Merlo L., *Nucl. Phys. B*, **775** (2007) 120.
[47] Bazzocchi F., Merlo L. and Morisi S., *Nucl. Phys. B*, **816** (2009) 204.
[48] Bazzocchi F., Merlo L. and Morisi S., *Phys. Rev. D*, **80** (2009) 053003.
[49] Lin Y., *Nucl. Phys. B*, **824** (2010) 95.
[50] Feruglio F., Hagedorn C., Lin Y. and Merlo L., *Nucl. Phys. B*, **809** (2009) 218.
[51] Ishimori H. *et al.*, *JHEP*, **12** (2008) 082.
[52] Ishimori H. *et al.*, *JHEP*, **12** (2009) 054.
[53] Feruglio F., Hagedorn C. and Merlo L., *JHEP*, **03** (2010) 084.
[54] Feruglio F., Hagedorn C., Lin Y. and Merlo L., *Nucl. Phys. B*, **832** (2010) 251.
[55] Merlo L., Rigolin S. and Zaldivar B., *JHEP*, **11** (2011) 047.

IL NUOVO CIMENTO Vol. 35 C, N. 6 Novembre-Dicembre 2012
DOI 10.1393/ncc/i2012-11352-0

Colloquia: LaThuile12

Searching for double-beta decays with the GERDA experiment

S. Hemmer(*) for the GERDA Collaboration

Dipartimento di Fisica e Astronomia, Università di Padova and INFN, Sezione di Padova Via Marzolo 8, 35131 Padova, Italy

ricevuto il 7 Settembre 2012

Summary. — The search for neutrinoless double-beta decay ($0\nu\beta\beta$) is presently the only feasible way to approach the fundamental question regarding the Majorana or Dirac nature of the neutrino. The observation of $0\nu\beta\beta$ would be the proof that the neutrino is a Majorana particle, *i.e.* that it is its own antiparticle. The measurement of the half-life of $0\nu\beta\beta$ would give direct access to a determination of the effective Majorana mass of the neutrino. The Germanium Detector Array (GERDA) experiment at the LNGS underground laboratories uses high-purity germanium detectors to search for $0\nu\beta\beta$ of ^{76}Ge. The experiment started Phase I in November 2011, using 15 kg of enriched germanium crystals with the goal of a background index of 10^{-2} counts/(keV·kg·y). A second, later phase will double the mass of the enriched detectors and aim at a background at the level of 10^{-3} counts/(keV·kg·y). This contribution presents the status of the GERDA Phase I data taking. A short outlook is given on the ongoing preparations for Phase II.

PACS `14.60.Pq` – Neutrinos mass and mixing.
PACS `14.60.St` – Nonstandard model neutrinos, right-handed neutrinos, etc.
PACS `29.40.Wk` – Solid-state detectors.

1. – Neutrinoless double-beta decay

Oscillation measurements have established that the neutrinos are massive particles. The two squared mass differences have been measured, one in absolute value, one also in sign. There are, however, still many open questions: Is the neutrino a Majorana particle, that is its own antiparticle? Is the neutrino mass hierarchy normal or inverted? What is the absolute neutrino mass scale?

The only practical way to experimentally test the nature of the neutrino is the search for neutrinoless double-beta decay ($0\nu\beta\beta$). The observation of this process would be the proof that the neutrino has at least a Majorana component with a non-zero mass [1].

(*) E-mail: `sabine.hemmer@pd.infn.it`

Neutrino-accompanied double-beta decay ($2\nu\beta\beta$) has been observed for several nuclei [2] that cannot decay via single beta decay. In this standard-model allowed decay, the nucleus undergoes double-beta decay under emission of two electrons and two antineutrinos $\overline{\nu}_e$. Due to the presence of the $\overline{\nu}_e$, the combined energy spectrum of the two electrons is continuous. If neutrinos are Majorana particles, the $\overline{\nu}_e$ emitted in one beta decay can be absorbed in the other, leading to $0\nu\beta\beta$. This process is not allowed by the Standard Model and the lepton number is violated by two units. Since all energy released in the decay is carried by the outgoing electrons, the experimental signature is a sharp peak at the Q-value of the decay, $Q_{\beta\beta}$, in their combined energy spectrum. From the half-life $T_{1/2}$ of $0\nu\beta\beta$ the effective Majorana mass, $\langle m_{\beta\beta}\rangle$, can be deduced:

$$T_{1/2}^{-1} = G^{0\nu}(Q_{\beta\beta}, Z) \cdot \left|M^{0\nu}\right|^2 \cdot \langle m_{\beta\beta}\rangle^2,$$

$$\langle m_{\beta\beta}\rangle = \left|\sum_{i=1}^{3} {U_{e_i}}^2 m_i\right|,$$

where the U_{e_i} are the electron-neutrino elements from the mixing matrix, m_i are the neutrino mass eigenvalues, $G^{0\nu}(Q_{\beta\beta}, Z)$ is the phase-space factor of the decay of a nucleus with atomic number Z and Q-value $Q_{\beta\beta}$, and $\left|M^{0\nu}\right|^2$ is the nuclear matrix element. Assuming the neutrino exchange to be the dominant mechanism of the process it provides also information on the absolute mass scale.

2. – Search for $0\nu\beta\beta$ in ^{76}Ge

If it exists, $0\nu\beta\beta$ is an extremely rare process. If the number of signal events, N_S, is larger than the standard fluctuation expected for the number of background events, N_b, the sensitivity S on $T_{1/2}$ of an experiment scales as

$$S \sim \epsilon \cdot a \cdot \sqrt{\frac{M \cdot t}{b \cdot \Delta E}},$$

where ϵ is the detection efficiency, a the abundance of the $2\nu\beta\beta$ isotope, M the detector mass, t the measurement time, $b = N_b/(M \cdot t \cdot \Delta E)$ the background index, and ΔE the energy region of interest, ROI, which scales with the resolution of the detector. From this, the requirements on the experiment can be deduced: large ϵ, good energy resolution, small b, long t, and large $a \cdot M$.

These demands make germanium detectors an attractive option for the search for $0\nu\beta\beta$. Since ^{76}Ge is an isotope that undergoes double-beta decay, the detector is also the source. Germanium can be produced very radio-pure, guaranteeing a small intrinsic b and the typical energy resolution is of the order of (0.1–0.2)%.

There are also some disadvantages, though. The Q-value of ^{76}Ge is only 2039 keV, and thus the external b is rather large. In addition, a of ^{76}Ge in natural germanium is only 7.8%, so that costly enrichment is needed.

Table I shows the exposure, b, and the derived lower limits on $T_{1/2}$ for two former experiments that deployed germanium detectors to search for $0\nu\beta\beta$, the Heidelberg-Mowscow (HdM) experiment [3], and the IGEX experiment [4].

The corresponding upper limits on $\langle m_{\beta\beta}\rangle$ are of the order of 0.1 to 1 eV. The large uncertainties on $\langle m_{\beta\beta}\rangle$ are due to the uncertainties in the calculation of $\left|M^{0\nu}\right|^2$ [5].

TABLE I. – *Previous* ^{76}Ge *experiments.*

	HdM	IGEX
Exposure [kg·y]	71.1	8.9
b [counts/(keV·kg·y)]	0.11	0.17
$T_{1/2}$ limit (90% CL) [y]	$1.9 \cdot 10^{25}$	$1.6 \cdot 10^{25}$
Reference	[3]	[4]

There has been the claim of a signal by a part of the HdM collaboration [6] with $T_{1/2} = (0.69–4.18) \cdot 10^{25}$ y (3σ range), corresponding to $\langle m_{\beta\beta} \rangle = (0.24–0.58)$ eV.

3. – The GERDA experiment

3$\cdot$1. *The experiment.* – GERDA is an experiment [7] designed for the search for $0\nu\beta\beta$ of ^{76}Ge. GERDA will be operated in two phases. In the first phase, germanium detectors from the IGEX and HdM experiments are reused. There are about 15 kg of germanium detectors which have been enriched in ^{76}Ge to a level of about 86% and an additional 15 kg of natural germanium detectors. The design goal for the background index is of the order of 10^{-2} counts/(keV·kg·y). An exposure of 15 kg·y will allow to reach $\langle m_{\beta\beta} \rangle \leq (0.23–0.39)$ eV [5] and thus to check the signal claim. In the second phase, an additional 20 kg of new enriched germanium detectors will be added and the background will be further reduced down to 10^{-3} counts/keV·kg·y. With an exposure of 100 kg·y, it will be possible to measure half-lives of the order of $1.5 \cdot 10^{26}$ y, corresponding to measuring $\langle m_{\beta\beta} \rangle$ down to (0.09–0.15) eV [5].

The sensitivity of the GERDA experiment is limited by the background. A large contribution to the background comes from cosmic radiation. To avoid it, the experiment was built in the INFN Gran Sasso underground laboratories. The overlaying rock provides in average 3400 m of water equivalent shielding, suppressing the cosmic-ray muon flux by a factor 10^6 (1 muon/(m^2·h)).

The environmental background component is reduced by graded shielding: The germanium detectors are submerged in a stainless-steel cryostat with a diameter of 4.2 m, filled with 64 m^3 of liquid Argon (LAr). Material close to the detectors is minimized: the bare germanium detectors are directly submerged in the LAr, using minimal support and cabling. Figure 1a shows a string with three Phase I detectors in their low-mass holders. The cryostat is surrounded by a water tank with a diameter of 10 m and a height of 9 m, containing 580 m^3 of ultra-pure water. The water serves as shielding for photons and spallation neutrons from outside the water tank. The water tank is equipped with photomultiplier tubes to detect the Čerenkov light of remaining cosmic muons. All materials used to build the experiment were screened to guarantee their radio-purity. On top of the water tank, a class 10 000 clean room is located and the detector strings are inserted into the cryoliquid through a lock system. The exposure for the detectors above ground is avoided as far as possible to reduce cosmogenic activation to a minimum. A sketch of the GERDA experiment is depicted in fig. 1b.

Several techniques have been developed to reject remaining background events. In general, background events have a different topology than $0\nu\beta\beta$ events. Most $0\nu\beta\beta$

(a) (b) (c)

Fig. 1. – (a) A detector string. (b) A sketch of the GERDA experiment. (c) The mini-shrouds.

events will deposit their energy locally within a sphere with a radius of $\leq 1\,\mathrm{mm}$ due to the limited range of electrons in germanium. These are so-called single-site events. The main background contribution comes from Compton-scattered photons. Their energy deposits are usually separated by centimeters, producing so-called multi-site events. It is therefore very unlikely that more than one detector in the array has an energy deposit in the case of a signal event. So, an anticoincidence cut between different detectors allows for further reduction of the background.

Background events can additionally be reduced using pulse shape analysis (PSA) [8,9]. In this case, the pulses generated by the detectors in response to the energy depositions are analyzed. This allows to distinguish between different event topologies and thus to discard background events.

3˙2. *Phase I data taking.* – In November 2011, the first phase of the GERDA experiment started. All eight enriched germanium detectors (five from the HdM experiment and three from the IGEX experiment) with a total mass of 14.6 kg and three natural germanium detectors with a total mass of 7.6 kg were deployed in GERDA. Due to instabilities and high leakage currents, two of the enriched detectors are not used for analysis.

The energy spectra for the enriched and natural detectors with a lifetime of 95 days are shown in fig. 2a and fig. 2b, respectively. The exposures are 3.80 kg·y and 1.97 kg·y. The contribution from $2\nu\beta\beta$ dominates the spectrum between 400 and 1400 keV for the enriched detectors.

In the energy region below 500 keV, the spectrum is dominated by the decays of ^{39}Ar. Since ^{39}Ar is a pure beta emitter with a Q-value of 565 keV, these decays do not add any background in the ROI around 2039 keV.

Another background that is easily distinguishable in the spectra is a line at 1525 keV. The spectrum around this energy is depicted in fig. 3a. The line can be attributed to decays of ^{42}Ar to ^{42}K (Q-value = 600 keV) and the subsequent decays to ^{42}Ca [10]. In 82% of the cases, ^{42}K decays directly to the ^{42}Ca ground state. In the other 18% of the cases, ^{42}K decays to an excited level of ^{42}Ca which de-excites under emission of a 1524.7 keV photon, explaining the line in the GERDA energy spectrum. The Q-value

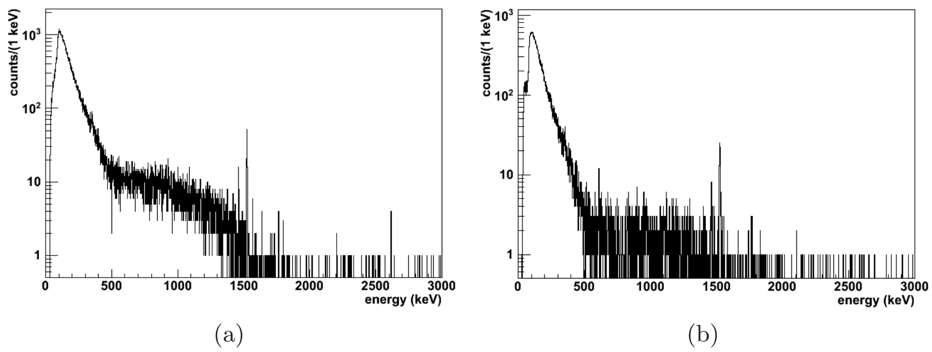

Fig. 2. – (a) The energy spectrum of the enriched germanium detectors. (b) The energy spectrum of the natural germanium detectors. The lifetime is 95 d, corresponding to an exposure of 3.80 kg·y and 1.97 kg·y, respectively.

of the decay of ^{42}K is 3525.4 keV, well above the ROI. The electron which is released in the decay can deposit energy in one of the germanium detectors. Since it loses energy in the LAr as well as in the deadlayer of the detector, the energy deposited in the active volume of the detector can be close to the Q-value of $0\nu\beta\beta$. Thus, the decays of ^{42}K add background in the ROI. During the commissioning of GERDA it was found that the line strength at 1525 keV was significantly higher than expected from previous limits [11]. It could be considerably reduced by putting the detectors in a field-free configuration, that is by avoiding electrical fields in their proximity. This minimizes the attraction of positively charged ^{42}K ions to the detector vicinity. The field-free configuration was achieved by closing the electrical field lines originating from the voltage-biased surfaces of the detectors on a thin copper layer closely surrounding each detector string. These so-

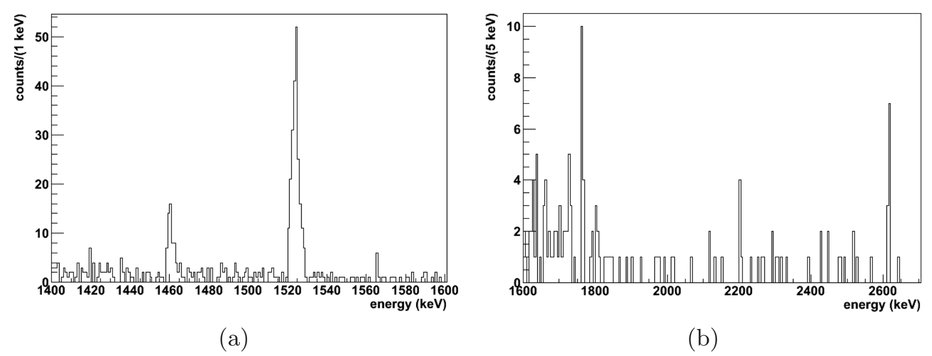

Fig. 3. – (a) The energy spectrum of the enriched germanium detectors around 1525 keV in the field-free configuration. The peak at 1460 keV can be accounted to ^{40}K background decays. (Its two decay modes have Q-values of 1311 keV and 1504 keV, respectively, and therefore cannot contribute to the background in the ROI.) (b) The energy spectrum of the enriched detectors around the ROI. The lifetime is 95 d, corresponding to an exposure of 3.80 kg·y.

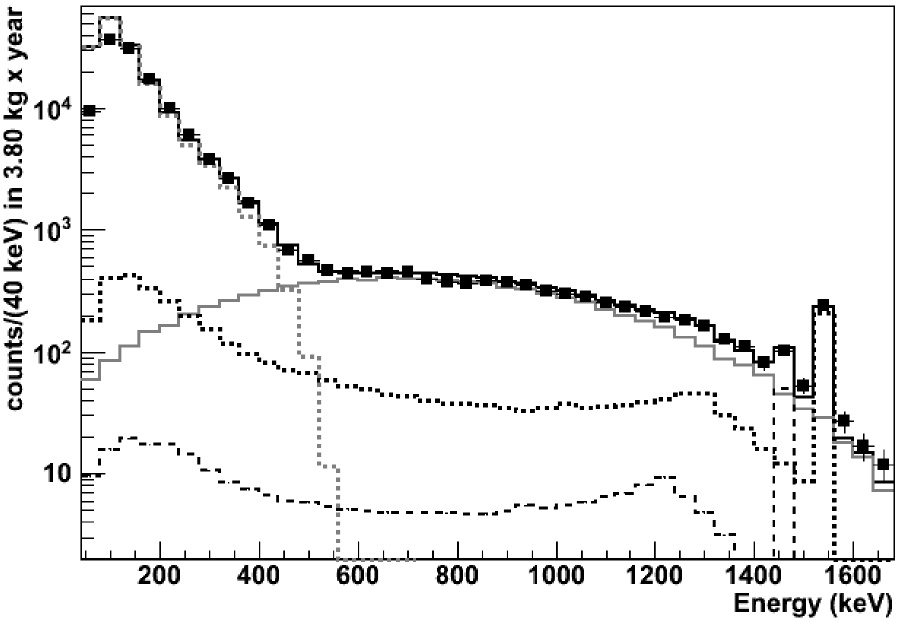

Fig. 4. – Comparison of the energy spectrum of the enriched detectors with MC. The single contributions are from ^{42}K (black dotted line), ^{40}K (black dashed line), ^{39}Ar (grey dotted line) and $2\nu\beta\beta$ of ^{76}Ge (grey continuous line). The black squares are the data for an exposure of 3.80 kg·y (lifetime = 95 d). They are well reproduced by the sum of all MC contributions shown with the black continuous line.

called mini-shrouds can be seen in fig. 1c. Nevertheless, also in the field-free configuration the count rate at 1525 keV remains approximately two times the expectation. The subject is still under investigation.

To quantify the background in the ROI, the events are counted that have an energy deposit in only one detector and no signal from the muon veto and that fall in the 200 keV energy window centered at 2039 keV, the Q-value of $0\nu\beta\beta$. No information about the events in the region between 2019 keV and 2059 keV is available since this region is subject to blinding. From the number of events in the ROI and excluding the blinded window, the background index is determined. It is $0.017^{+0.009}_{-0.005}$ counts/(keV·kg·y) for the enriched detectors, using the first GERDA runs with an exposure of 3.80 kg·y. For the natural germanium detectors it is $0.049^{+0.015}_{-0.013}$ counts/(keV·kg·y) with an exposure of 1.97 kg·y. The energy spectrum around the ROI for the enriched detectors is depicted in fig. 3b.

The background is most likely a combination of several contributions: photons and degraded α's from decays of isotopes present in the ^{232}Th- and ^{238}U-chains, ^{42}K beta decays, and decays of cosmogenic isotopes like ^{60}Co and ^{68}Ge. The achieved background index for the enriched detectors is slightly higher than the design goal of 10^{-2} counts/keV·kg·y. It is, however, a factor ten smaller than that of the previous experiments mentioned in sect. **2**. Also note that no pulse shape analysis has been applied yet.

Figure 4 shows a comparison of the data energy spectrum of the enriched detectors with Monte Carlo simulations (MC) of the various contributions in the energy region up to 1700 keV. The contributions that are considered are the following:

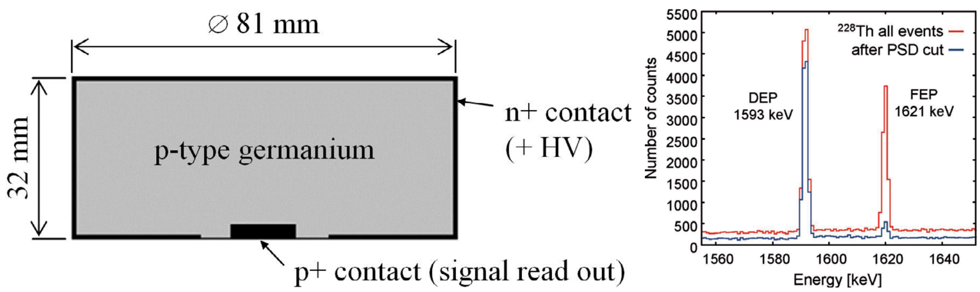

(a) (b)

Fig. 5. – (a) Sketch of a BEGe detector. (b) The energy spectrum of a ^{228}Th source before (red) and after (black) PSA. Both graphics were taken from ref. [14].

- ^{42}K: The decays were simulated homogeneously distributed in the LAr surrounding the detectors. The peak at 1525 keV was used to normalize the MC.
- ^{40}K: The decays were simulated in the detector holders and normalized using the peak at 1460 keV.
- ^{39}Ar: The decays were simulated homogenously distributed in the LAr surrounding the detectors. The specific activity used to normalize the MC was taken from ref. [12].
- ^{76}Ge: To normalize the MC of $2\nu\beta\beta$ to the data, the result for $T_{1/2}$ from HdM [13] was used.

All contributions were simply added up without performing a fit. They describe the data very well.

3˙3. *Phase II preparations*. – For the second phase of the GERDA experiment about 20 kg of additional enriched germanium detectors will be deployed. To achieve the goal of a background index of 10^{-3} counts/(keV·kg·y), it is crucial to fully exploit the potential of PSA. Therefore, so-called broad-energy germanium (BEGe) detectors will be used. These p-type germanium detectors have an n^+-contact covering the whole outer surface and a small p^+-contact on the bottom. A sketch of such a detector can be seen in fig. 5a.

Thanks to their geometry, BEGe detectors allow for an excellent PSA performance which can be exploited to reduce the background [14]. In fig. 5b an example of an energy spectrum of a ^{228}Th source measured with a BEGe detector is shown. The double-escape peak (DEP) events at 1593 keV are mainly single-site events and have thus a topology which is very similar to the $0\nu\beta\beta$ signal events. The peak at 1621 keV originates predominantly from Compton-scattered photons and thus contains mainly multi-site events. With PSA, this background peak can be reduced to about 10% of its original height, while 90% of the signal-like events in the DEP remain [14]. This powerful tool will be a decisive factor for reaching the Phase II background goal.

Seven of the new enriched BEGe detectors have already been produced and are currently being tested in the HADES underground laboratory in Mol, Belgium.

Another ongoing effort regarding the preparations for the second phase of the GERDA experiment is the possibility to read out scintillation light from LAr. As LAr is a scintillator material, particles crossing this medium can be detected by detecting the scintillation light they produce. This is a very effective method to significantly reduce the external background contribution. The LArGe [15] test facility at the Gran Sasso laboratories was built to investigate this strategy.

4. – Conclusions

The observation of $0\nu\beta\beta$ is at present the only experimentally feasible way to test the Majorana-nature of the neutrino. Previous experiments have set limits on the half-life of this decay on the order of 10^{25} y and a claim of evidence has been made by a subgroup of the HdM experiment.

GERDA is a new-generation $0\nu\beta\beta$ experiment. In a first phase, the claim will be checked. In a second phase, limits on the half-life of the order of $1.5 \cdot 10^{26}$ y will be reached.

The experiment started Phase I data taking in November 2011. A background measurement based on the first data taken with enriched detectors with an exposure of 3.80 kg·y gives a background index of $0.017^{+0.009}_{-0.005}$ counts/(keV·kg·y), very close to the design goal of 10^{-2} counts/(keV·kg·y). The experiment is running smoothly and first results on $2\nu\beta\beta$ are expected very soon.

REFERENCES

[1] Schechter J. and Valle J., *Phys. Rev. D*, **25** (1982) 2951.
[2] Barabash A. S., *Phys. At. Nucl.*, **74** (2011) 603.
[3] Klapdor-Kleingrothaus H. V. *et al.*, *Eur. Phys. J. A*, **12** (2001) 147.
[4] Aalseth C. E. *et al.*, *Phys. Rev. D*, **65** (2002) 092007.
[5] Smolnikov A. and Grabmayr P., *Phys. Rev. C*, **81** (2010) 028502.
[6] Klapdor-Kleingrothaus H. V. *et al.*, *Phys. Lett. B*, **586** (2004) 198.
[7] Abt I. *et al.*, arXiv:hep-ex/0404039 (2004).
[8] Majorovits B. and Klapdor-Kleingrothaus H. V., *Eur. Phys. J. A*, **6** (1999) 463.
[9] González D. *et al.*, *Nucl. Instrum. Methods A*, **515** (2003) 634.
[10] Firestone R. B. *et al.*, *Table of Isotopes*, 8th edition (Wiley) 1996.
[11] Ashitkov V. D. *et al.*, arXiv:nucl-ex/0309001 (2003).
[12] Benetti P. *et al.*, *Nucl. Instrum. Methods A*, **574** (2007) 83.
[13] Dörr C. and Klapdor-Kleingrothaus H. V., *Nucl. Instrum. Methods A*, **513** (2003) 596.
[14] Budjáš D. *et al.*, *JINST*, **4** (2009) P10007.
[15] Heisel M., *LArGe - A liquid argon scintillation veto for GERDA*, PhD thesis, Ruperto-Carola Universität Heidelberg (2011).

IL NUOVO CIMENTO Vol. 35 C, N. 6 Novembre-Dicembre 2012
DOI 10.1393/ncc/i2012-11353-y

Colloquia: LaThuile12

First results on Θ_{13} from the Double Chooz reactor antineutrino experiment

B. Reinhold(*) for the Double Chooz Collaboration
MPIK Heidelberg - Saupfercheckweg 1, D-69117 Heidelberg, Germany

ricevuto il 7 Settembre 2012

Summary. — Double Chooz is an electron antineutrino disappearance experiment observing neutrinos originating from the Chooz nuclear power plant and interacting in our detector. The flux of electron anti-neutrinos is altered through neutrino oscillations and thereby allows to measure Θ_{13}. The Double Chooz Collaboration published first results on its search for the neutrino mixing angle Θ_{13} in 2011. The current analysis comprises about 100 days of data taken since April 2011. Performing a so-called rate+shape analysis, a best-fit value for $\sin^2 2\Theta_{13} = 0.086$ is reported with uncertainties of ± 0.041 (stat) ± 0.030 (syst) using $\Delta m^2_{13} = 2.4 \cdot 10^{-3}\,\text{eV}^2$. This article provides details about the analysis that lead to this result.

PACS `14.60.Pq` – Neutrino mass and mixing.
PACS `13.15.+g` – Neutrino interactions.
PACS `25.30.Pt` – Neutrino-induced reactions.
PACS `95.55.Vj` – Neutrino, muon, pion, and other elementary particle detectors; cosmic ray detectors.

1. – Introduction

Neutrino oscillations are by now a well-established model to explain experimental data from a wide variety of experiments. Be it solar- or atmospheric-neutrino experiments or experiments observing man made neutrinos from dedicated beams or reactors. Neutrino oscillations originate from the fact that neutrino flavour eigenstates are different from mass eigenstates. The flavour eigenstates are related to the mass eigenstates through the so-called PMNS([1]) mixing matrix which can be parameterized by three mixing angles Θ_{12}, Θ_{23}, Θ_{13} and a CP-violating phase δ. Additionally, neutrino oscillations require non-zero differences of neutrino masses squared: Δm^2_{13} and Δm^2_{23}. Two of the three mixing angles are found to be large or even close to maximal whereas until recently

(*) E-mail: `Bernd.Reinhold@mpi-hd.mpg.de`
([1]) PMNS: Pontecorvo, Maki, Nakagata, Sakawa.

only upper limits existed for the third mixing angle Θ_{13}. δ-CP is hardly constrained by experimental data. This was still the situation at the beginning of 2011. Then indications for a finite Θ_{13} were reported by both the MINOS and T2K experiments in the $\nu_\mu \rightarrow \nu_e$ appearance channel [1, 2].

End of 2011 Double Chooz was the first of a second generation of reactor antineutrino experiments to report its results in the search of Θ_{13} [3]. In early 2012 both the Daya Bay and RENO reactor antineutrino experiments found similar best fit results for $\sin^2 2\Theta_{13}$ with higher significance [4,5]. A finite Θ_{13} opens the possibility to measure CP violation in the neutrino sector and the mass hierarchy in the near future.

2. – Oscillation probability

The survival probability $\mathcal{P}_{\overline{\nu}_e \rightarrow \overline{\nu}_e}$ for electron antineutrino is

$$\mathcal{P}_{\overline{\nu}_e \rightarrow \overline{\nu}_e}(L, E) = 1 - \sin^2(2\Theta_{13}) \sin^2 \left(1.27 \Delta m^2_{13}[eV^2] \frac{L[m]}{E[MeV]} \right), \tag{1}$$

in the approximation of small $\frac{L}{E}$, with L being the distance between reactor and detector and E is the energy of the antineutrino $\overline{\nu}_e$. As the neutrino energy spectrum coming from the reactor is known to have its maximum at around 3 MeV and $\Delta m^2_{13} = 2.4 \cdot 10^{-3}\,\mathrm{eV}^2$, one can calculate from formula (1) that a detector, located at 1.05 km from the two reactor cores is close to the oscillation maximum and is thereby sensitive to Θ_{13}.

3. – The Double Chooz detector

3$\cdot$1. *Two-detectors concept.* – The current generation of reactor neutrino experiments all adopt a two or multi detector concept in order to reduce systematic uncertainties. In case of Double Chooz the Near Detector will be placed at 410 m distance from the two reactor cores and the Far Detector is located at 1.05 km from the antineutrino source.

While the neutrino flux and spectrum at the Far Detector is altered through neutrino oscillations, namely by Δm^2_{13} and Θ_{13}, the Near Detector observes an almost unoscillated spectrum regardless of the actual value of Θ_{13} and so the ratio of the Far and Near Detector spectrum allow to extract Θ_{13}. Systematic uncertainties in the antineutrino flux coming from the reactors cancel. Absolute systematic uncertainties in the estimation of backgrounds, efficiencies or in the detector response reduce, so that only relative uncertainties remain. These relative uncertainties are substantially smaller than the absolute uncertainties.

Since the Near Detector is still under construction, for the current analysis only data of the Far Detector has been used and the analysis has been performed by comparing a measured neutrino spectrum to a predicted spectrum, which was calculated from reactor data and propagated through a detailed Monte Carlo (MC) simulation of the detector. The Monte Carlo simulation of the detector is based on GEANT4 [6] and has been tuned using calibration data. Many of the systematic uncertainties are estimated from remaining discrepancies between data and MC simulations.

3$\cdot$2. *Detection principle.* – The electron anti-neutrinos are detected via the Inverse Beta Decay (IBD) interaction on proton: $\bar{\nu_e} + p \rightarrow n + e^+$ ($E_{threshold} = 1.8\,\mathrm{MeV}$). The positron, which receives basically all the kinetic energy of the neutrino (minus the threshold energy), deposits its energy in the scintillator and eventually annihilates with

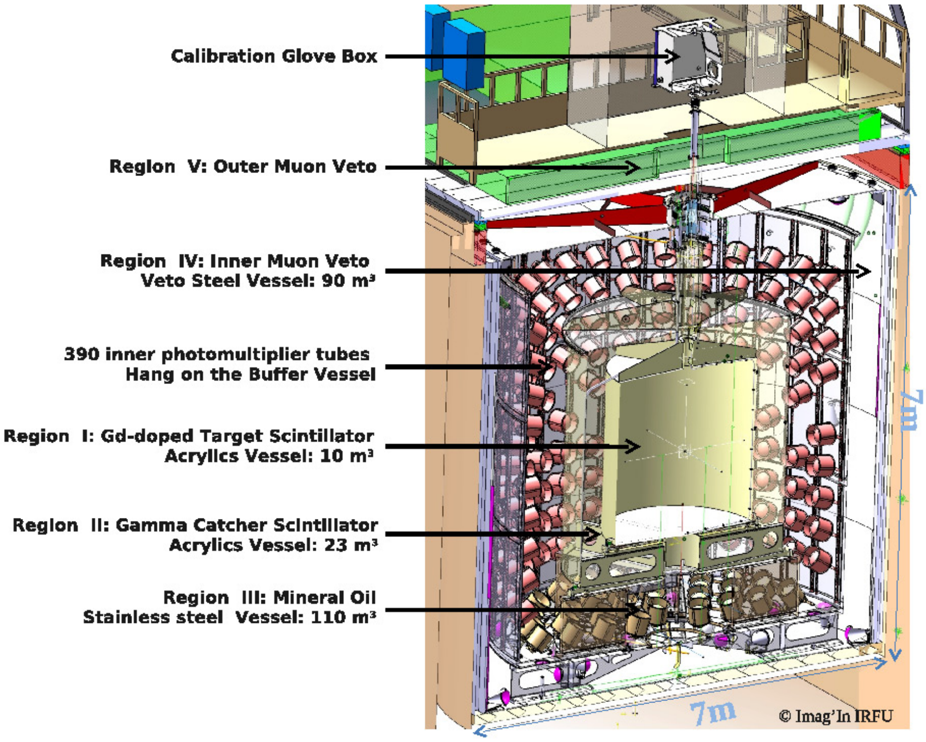

Fig. 1. – The Double Chooz detector design.

an electron. This prompt signal is followed by a delayed signal from the capture of the neutron on hydrogen or gadolinium (Gd). While the prompt signal of the positron can be considered instantaneous, the neutron capture has a time constant of about 30 μs.

3˙3. *The Far Detector*. – Figure 1 shows the composition of the Far Detector. In the center there is the ν*-Target* (Region I) consisting of 10.3 m^3 of gadolinium-loaded liquid scintillator at 1 g/l Gd-loading [7]. It is contained in a 8 mm thick cylindrical acrylic vessel and forms the fiducial volume for the search for Θ_{13}. The Target volume is surrounded by more than 22 m^3 of the so-called γ-catcher (GC) enclosed in a second acrylic vessel of 12 mm thickness (Region II). Gammas originating from the prompt and delayed event of a neutrino interaction in the Target, travel macroscopic distances while loosing their energy. The γ-catcher ensures a complete deposition of the gammas' energies and helps to reduce systematic uncertainties on the neutrino detection efficiency.

The next volume contains 114 m^3 of non-scintillating buffer liquid in a 3 mm thick stainless steel vessel (Region III). The *Buffer* volume decreases the background rates both in the prompt and delayed event originating in the ambient rock or residual radioactivity of the PMT glass. At the inner wall of the Buffer volume 390 10$''$ PMTs are mounted providing a coverage of about 13% [8, 9]. Finally, there is a 0.5 m thick stainless steel vessel, filled with organic liquid scintillator based on LAB (linear alkyl benzene), the so-called *Inner Veto* (Region IV). Muons and muon-induced particles entering the detector from outside produce light in the scintillator, which is then detected by 78 8$''$ PMTs. The cylindrical Inner Veto vessel has a diameter of 6.5 m and a height of about 7 m, which corresponds to 90 m^3 of active muon veto. Outside the Inner Veto there are 15 cm of steel as an additional shielding to reduce background due to external gammas coming from the surrounding rock. The PMT signals are readout by 500 MHz flash-ADC hardware. The Trigger System is custom made, it forms trigger signals mainly based on the integrated charge information. Together they form a deadtime free data acquisition system [10].

On top of the cylindrical detector (Regions I-IV) a plastic scintillator strip detector serves as an additional Muon tracker, the so-called *Outer Veto* (Region V). It is superior in its vertex reconstruction capabilities compared to the Inner Veto and extends beyond the edges of it and thereby allows to veto muons, that would otherwise go undetected. The Outer Veto will help to understand and reduce the uncertainties due to muon induced backgrounds. As it has been installed slightly later than the main detector, the Outer Veto data has not been used in this analysis yet, but will be in the upcoming analysis upgrades.

4. – Calibration

Double Chooz uses the total sum of photo electrons (PE) as estimator for the deposited energy of a given event. The PEs per PMT are calculated from the charge collected in a given Inner Detector PMT, which is then multiplied by a gain factor, that has been determined from single PEs recorded with dedicated LED, that are permanently installed in the Inner Detector. The sum of PEs is calibrated with the hydrogen capture peak of the neutron source ^{252}Cf in the Target center, corresponding to 2.223 MeV. The corresponding calibration factor is about 200 PE/MeV. ^{252}Cf and γ-sources (^{137}Cs, ^{68}Ge and ^{60}Co), deployed at the Target center, have been used to study the non-linearity in energy response. A function has been determined to correct for remaining differences between data and MC, and is applied to MC on a per event basis. The same calibration sources have been deployed also at various positions in the ν-Target and in the γ-Catcher to study and correct for the variation of the detector response with position. In a similar fashion as for the non-linearity correction function, a position correction function has been determined and is also applied to the Monte Carlo data sets.

The LEDs are used to inject light into the detector on a regular basis (daily and weekly) and so this data set is used to monitor the stability of the detector response over time. The stability *vs.* time is also monitored using Spallation Neutrons capturing on H and Gd, signals induced by ambient radioactivity and Gd-captures of IBD events, see fig. 2. The stability is within 1% and in particular no degradation of the Target scintillator *vs.* time has been found.

5. – Neutrino Selection

Neutrino candidates are selected as a coincidence of a *prompt* energy deposition E_{prompt} between 0.7 and 12.2 MeV, followed by a *delayed* energy deposition $E_{delayed}$ between 6 and 12 MeV within a time difference Δt between prompt and delayed of $[2, 100]\,\mu$s. In order to avoid events from accidentally light emitting PMT bases the following cuts are applied: $Q_{max}/Q_{tot} < 0.09$ (0.06) for the prompt (delayed) energy and rms(T_{start}) < 40 ns, where Q_{max} is the charge seen by the PMT with maximum charge, Q_{tot} is the total charge of all PMTs and rms(T_{start}) is the standard deviation of the distribution of arrival times of pulses per PMT (and event).

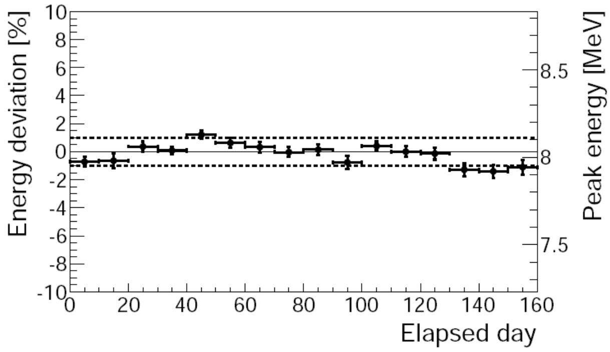

Fig. 2. – Gd peak position of IBD events *vs.* time since start of data taking (April 2011). Stability within 1% is found and in particular no degradation of the scintillators is observed [3].

To avoid neutrino-like coincidences originating from muon induced secondaries a 1 ms veto is applied after each muon interacting in the Inner Veto or Inner Detector, which results in an after muon deadtime of 4.5%. The following multiplicity cut is applied to avoid correlated background: There may not be any Trigger 100 μs before and 400 μs after the prompt energy deposition of a coincidence.

6. – Reactor prediction

The predicted number of electron anti-neutrinos interacting in the detector is proportional to the thermal power of each reactor core $P_{th}(t)$, the average energy released per fission $\langle E_f \rangle$ and the mean cross-section per fission $\langle \sigma_f \rangle$:

$$N_\nu^{pred}(E,t) = \frac{N_p \epsilon}{4\pi L^2} \cdot \frac{P_{th}(t)}{\langle E_f \rangle} \cdot \langle \sigma_f \rangle, \tag{2}$$

where N_p is the proton number in the ν-Target, ϵ is the neutrino detection efficiency and L is the distance from reactor to detector. The relative fraction of the isotopes ^{235}U, ^{239}Pu, ^{238}U, ^{241}Pu in the total fuel content enters both in $\langle E_f \rangle$ and $\langle \sigma_f \rangle$. Since the composition of the cores change with time ("burn-up"), $\langle E_f \rangle$ and $\langle \sigma_f \rangle$ are time dependent as well. Detailed simulations of the core evolution have been undertaken with two independent codes, MURE [11] and DRAGON [12] and the fission rates have been calculated. For the mean cross-section per fission improved spectra from [13] are used, while the normalisation is taken from the Bugey-4 measurement [14], with a correction to the composition of the Chooz reactors. Overall the systematic uncertainties related to the reactor amount to 1.8%.

7. – Backgrounds

The following classes of background can induce neutrino-like coincidences at the order of a few neutrino candidates per day in total.

There is *accidental background* at a rate of 0.33 ± 0.03 day^{-1}, where the prompt and delayed energy depositions are not causally linked. The prompt stems from remaining radioactivity in the scintillator, PMTs or from the ambient rock, the delayed is a neutron-like energy deposition. The accidental background can be estimated using the off-time technique, in which the coincidence time window between prompt and delayed is shifted in time.

Three classes of *correlated background* are distinguished: ^{9}Li, *Fast Neutrons* and *Stopping Muons*. Some decay branches of ^{9}Li are β-n emitters, which can mimic IBD candidates([2]). Due to the long halflife (178 ms) of ^{9}Li it is hard to veto, given a muon rate of 46 Bq in the Inner Veto. As the ^{9}Li is being produced mainly during high-energy depositions, the ^{9}Li rate is studied using neutrino like coincidences following an energy deposition $> 600\,\text{MeV}$. The resulting Δt_μ distribution is fitted with a constant + exponential, using the ^{9}Li halflife as time constant. Varying the muon energy cut to lower values provides an estimate of the central value and the uncertainty of the ^{9}Li rate: 2.3 ± 1.2 events/day. A shape uncertainty of 20% is coming from a MC study using variations in decay branches of ^{9}Li.

Fast Neutrons are also muon-induced background, where the prompt event is mimicked by recoil protons while the neutron is thermalizing in the γ-Catcher and Target and eventually capturing on Gd, which then forms the delayed event. Such a coincidence only is contributing to the neutrino candidates, if the muon does not pass through the Inner Veto. The rate and shape of the fast neutrons is estimated by applying the neutrino selection cuts, but expanding the prompt energy window from $[0.7, 12.2]$ MeV up to 30 MeV. Above 12 MeV one has a background only data sample, which sets the normalisation of the Fast Neutrons. The prompt energy spectrum of Fast Neutrons is taken as flat across the whole energy spectrum, including $[0.7, 12.2]$ MeV. The extrapolation of the spectral shape into the neutrino energy region has been validated using a subclass of Fast Neutron candidates, which also leave a signal in the Inner Veto and therefore allow to tag them as background even below 12 MeV. The sample of Fast Neutrons also contains a set of stopping muons, that enter the detector through the chimney region at the top of the detector. The fast neutrons (+ stopping muon component) have an estimated rate of $0.83 \pm 0.38\,\text{d}^{-1}$.

The overall background rate from accidentals, fast neutrons + stopping muons and ^{9}Li adds up to $3.46 \pm 1.26\,\text{d}^{-1}$. During one day in October 2011 both reactor cores were off, which allowed to perform a background-only measurement. Two neutrino-like candidates have been found, which is in good agreement with the overall background rate.

The signal to background ratio of better than 11 is illustrated in fig. 3: the selected neutrino rate contains both signal and background and still follows nicely the neutrino rate predicted from the reactor power. For the 100 days of data 4121 neutrino candidates have been selected. Taking into account for the after muon deadtime a rate of 42.6 ± 0.7 neutrinos/day is observed.

8. – Efficiencies

The Trigger Efficiency above 0.7 MeV is $100^{+0}_{-0.4}\%$. The Neutron detection efficiency has been estimated with ^{252}Cf and comprises the cut efficiency of the delayed energy cut at 6 MeV (94.5% in data), the fraction of neutron captures on Gd (86.0%) and

([2]) Actually this type of background contains also a fraction of ^{8}He, which cannot be disentangled from ^{9}Li due to the low statistics and similar decay characteristics. For brevity only ^{9}Li is quoted below.

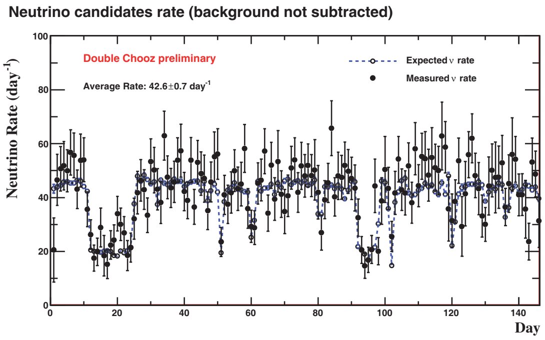

Fig. 3. – Selected and predicted neutrino rate per day *vs.* days since start of data taking. The predicted neutrino rate is calculated from the reactor data, the selected neutrino rate includes background events.

the efficiency of the ΔT_{e^+n} cut (96.5%). Uncertainties of the detection efficiency are estimated from remaining differences between data and MC and summarized in table I. A normalisation correction is applied to account for a net "Spill-In" current of 1.4%.

9. – Θ_{13} analysis

Θ_{13} is extracted using a χ^2 analysis. A "Rate-Only" (1 energy bin) and a "Rate+Shape" analysis using 17 energy bins between 0.7 and 12.2 MeV have been undertaken. In order to account for bin-to-bin correlations, four covariance matrices are used to include uncertainties from reactor, statistics, detector and background spectral shape. Both analyses give consistent results, with the "Rate+Shape" analysis being most sensitive to Θ_{13}. Our best fit result is $\sin^2(2\Theta_{13}) = 0.086 \pm 0.041$ (stat) ± 0.030 (syst) with $\chi^2/\text{n.d.f.} = 23.7/17$. A summary of systematic uncertainties *w.r.t.* the signal is given in table I. Observed and predicted positron energy spectra for no oscillation and the best fit are shown in fig. 4.

Using a frequentist analysis, the no oscillation hypothesis is ruled out at the 94.6% CL, which can be interpreted as an indication of non-zero Θ_{13}. A combined analysis with the T2K and MINOS accelerator experimental results on θ_{13} excludes θ_{13} being equal at more than 3σ.

Table I. – *Systematic uncertainties on the absolute normalisation of the signal due to the detector, the reactor and backgrounds as well as the statistical uncertainty are summarized below.*

Detector	2.1%	*Reactor*	1.8%
- Energy response	1.7%	- Bugey4 measurement	1.4%
- E_{delay} containment	0.6%	- Fuel composition	0.9%
- Gd Fraction	0.6%	- Thermal power	0.5%
- ΔT_{e+n}	0.5%	- Reference spectra	0.5%
- Spill in/out	0.4%	- Energy per fission	0.2%
- Trigger efficiency	0.4%	- IBD cross-section	0.2%
- Target H	0.3%	- Baseline	0.2%
Statistics	1.6%	*Backgrounds*	3.0%

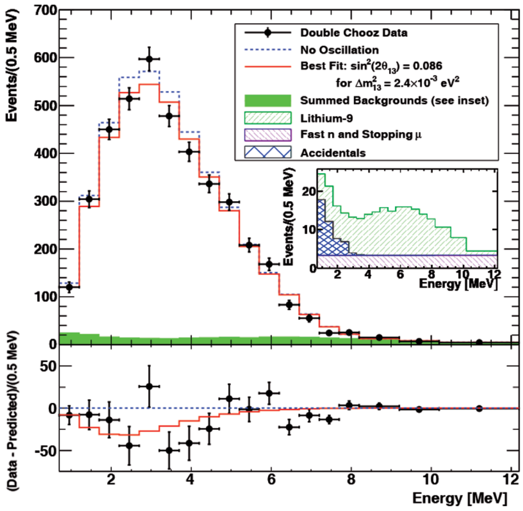

Fig. 4. – Observed (black dots) and predicted positron energy spectrum for the no-oscillation case (blue dotted line) and for the best fit value of $\sin^2 2\Theta_{13}$ (red line). The backgrounds are shown in green and the individual contributions (accidentals, ^{9}Li, Fast-n+ stopping μ) are shown in the inset. At the bottom the difference between data and the predicted no-oscillation spectrum is shown.

10. – Conclusions and outlook

A first analysis searching for Θ_{13} has been performed using data taken since April 13th, 2011. Approximately 100 days of data give a best fit of $\sin^2(2\Theta_{13}) = 0.086 \pm 0.051$ from a fit of a rate deficit and taking into account the prompt spectrum's spectral shape information. An indication of non-zero Θ_{13} is found.

Analysis improvements are already underway and the Double Chooz Near Detector will be operational soon to lead to an estimated 1σ precision of $\sin^2(2\Theta_{13}) \sim 0.02$.

REFERENCES

[1] Adamson P. *et al.*, *Phys. Rev. Lett.*, **107** (2011) 181802; arXiv:1108.0015.
[2] Abe K. *et al.*, *Phys. Rev. Lett.*, **107** (2011) 041801.
[3] Abe Y. *et al.*, *Phys. Rev. Lett.*, **108** (2012) 131801; arXiv:1112.6353.
[4] An F. P. *et al.*, *Phys. Rev. Lett.*, **108** (2012) 171803; arXiv:1203.1669.
[5] Ahn J. K. *et al.*, *Phys. Rev. Lett.*, **108** (2012) 191802; arXiv:1204.0626.
[6] Agostinelli S. *et al.*, *Nucl. Instrum. Methods A*, **506** (2003) 250.
[7] Aberle C. *et al.*, *JINST*, **7** (2012) 6008.
[8] Matsubara T. *et al.*, arXiv:1104.0786, to be published in *Nucl. Instrum. Methods A* (2012).
[9] Bauer C. *et al.*, *JINST*, **6** (2011) P06008; arXiv:1104.0758.
[10] Cabrera A., *Nucl. Instrum. Methods A*, **617** (2010) 473.
[11] *MURE, MCNP utility for reactor evolution*, 2009. `http://www.nea.fr/tools/abstract/detail/nea-1845`.
[12] Jones C. L. *et al.*, *Phys. Rev. D*, **86** (2012) 012001.
[13] Mueller Th. A. *et al.*, *Phys. Rev. C*, **83** (2011) 054615; arXiv:1101.2663.
[14] Declais Y. *et al.*, *Phys. Lett. B*, **338** (1994) 383.

IL NUOVO CIMENTO Vol. 35 C, N. 6 Novembre-Dicembre 2012
DOI 10.1393/ncc/i2012-11354-x

Colloquia: LaThuile12

Phenomenological review of Lepton Flavour Violation

S. Davidson

IPNL, Université de Lyon, Université Lyon 1, CNRS/IN2P3
4 rue E. Fermi 69622 Villeurbanne cedex, France

ricevuto il 7 Settembre 2012

Summary. — This is a review of current bounds on Lepton Flavour Violation (LFV), and some discussion of what could be learned about New Physics from an observation of LFV. There are no model predictions (see, for instance, T. Feldmann, *PoS BEAUTY* **2011** (2011) 017; P. Paradisi, *PoS HQL* **2010** (2010) 052; G. F. Giudice and O. Lebedev, *Nucl. Phys. Proc. Suppl.* **217** (2011) 318).

PACS `11.30.Hv` – Flavor symmetries.
PACS `12.60.-i` – Models beyond the standard model.
PACS `14.60.-z` – Leptons.

For the purposes of this review, a lepton is a Standard Model fermion without strong interactions, such as the electron or its neutrino. Lepton flavour, or generation, is a quantum number distinguishing the three copies e, μ, and τ of a massive electrically charged lepton plus its neutrino. Finally, Lepton Flavour Violation (LFV), is a flavour-changing point interaction of charged leptons. By this definition, LFV is equivalent to a Flavour-Changing Neutral Current (FCNC) contact interaction among the charged leptons, such as $\tau \to \mu\gamma$. Neutrino oscillations do not qualify.

The relation of LFV to New Physics, is fundamentally different from the relation between quark flavour and New Physics (NP). In the Standard Model, neutrinos are massless, and lepton flavour is conserved. So the observation of LFV is a signal of Beyond-the-Standard-Model (BSM)(1) Physics. But we know that there is BSM in the lepton sector, because neutrinos oscillate and therefore have mass. So LFV happens, due to the New Physics responsable for neutrino masses — but the rate is unknown. This situation can be constrasted with the quark sector, where the SM predicts FCNC, and most observations are in such good agreement with the SM, that quark flavour bounds are perceived as a hurdle for New Physics models, introduced to address some other issue.

The amplitudes for LFV induced by the neutrino masses, treated as Dirac masses, are $\propto m_\nu^2/m_W^2 \sim 20^{-24}$. So observable LFV requires dynamics other than m_ν. A variety

(1) I use BSM and NP interchangeably.

TABLE I. – *A selection of LFV processes and current bounds. The third colomn gives the mass scale of New Particles which could induce the process at dimension 6 via a loop with couplings of $\mathcal{O}(1)$. For such scenarios, μ searches are sensitive to higher scales than τ searches.Similarly, LFV is more likely to be found in Ks than in Bs. The last colomn gives the mass scale of New Particles which induce the process via a loop with two extra Higgs legs (saturated by Higgs vevs) and couplings of $\mathcal{O}(1)$. All channels are promising to search for such New Physics scenarios. The New particles in such scenarios could be accessible to the LHC.*

Process	Bound	Scale (dim 6, loop)	Scale (dim 8, loop)
$BR(\mu \to e\gamma)$	$< 2.4 \times 10^{-12}$	48 TeV	2.9 TeV
$BR(\mu \to e\bar{e}e)$	$< 1.0 \times 10^{-12}$	170 TeV (tree)	5.5 TeV (tree)
		14 TeV	1.5 TeV
$\frac{\sigma(\mu+Ti\to e+Ti)}{\sigma(\mu\ \text{capture})}$	$< 4.3 \times 10^{-12}$	40 TeV	2.6 TeV
$BR(\tau \to \ell\gamma)$	$< 3.3, 4.4 \times 10^{-8}$	2.8 TeV	0.7 TeV
$BR(\tau \to 3\ell)$	$< 1.5 - 2.7 \times 10^{-8}$	9 TeV (tree)	1 TeV (tree)
$BR(\tau \to e\pi)$	$< 8.1 \times 10^{-8}$	0.5 TeV	0.3 TeV
$BR(\overline{K_L^0} \to \mu\bar{e})$	$< 4.7 \times 10^{-12}$	25 TeV$(V \pm A)$	2.1 TeV$(V \pm A)$
		140 TeV$(S \pm P)$	5 TeV$(S \pm P)$
$BR(B \to e^{\pm}\mu^{\mp})$	$< 6.4 \times 10^{-8}$	3 TeV $(S \pm P)$	

of models fit oscillation data and current LFV bounds, but give different predictions for LFV rates. This wide diversity can be parametrised via the Effective Lagrangian.

The scale(s) of the New Physics in the lepton sector are unknown. I assume here that the New Particles are heavier than the Higgs vev $v = 175\,\text{GeV}$, so that the only "light" fields in the Effective Lagrangian are the known SM fields.

1. – Current bounds and where to look?

Experimentally, we know that LFV rates are below current sensitivities(for refernces, see for instance [1]). A selection of bounds is presented in the second colomn of table I. An interesting question is therefore "where is the most promising place to look?"

New particles can have escaped detection to date because they are heavy (*e.g.* SUSY, etc.), or because they interact weakly (like axions, majorons, or sterile neutrinos). Here, I only consider heavy New Particles. At SM scales, footprints of heavy NP are encoded an the "effective Lagrangian" $\mathcal{L}_{eff} = \mathcal{L}_{SM} + \Delta\mathcal{L}_{eff}^{LFV} + \Delta\mathcal{L}_{eff}^{other}$. It has the SM particle content, SM gauge symmetries, and all (mass) dimension > 4 operators are allowed. If the new particles masses are of order a (fuzzy) mass scale Λ, the interactions they induce among SM particles can be described, at energies $\ll \Lambda$, via

$$\Delta\mathcal{L}_{eff}^{LFV} = \sum_{d\geq 5}\sum_{n} \frac{C^n}{\Lambda^{d-4}} O_n(H, \{\psi\}, A_\mu, \ldots) + \text{h.c.} \tag{1}$$

where the operators $\{O_n\}$ are built with SM fields, respect SM gauge symmetries, and, more intuitively, describe the legs of LFV diagrams (including Higgs vevs). See fig. 1. From the New Physics perspective, the (dimensionless) coefficients C^n contain SM and NP coupling constants and loop factors; it can be convenient to factor out the SM

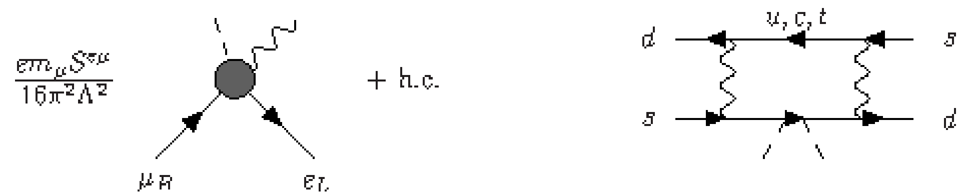

Fig. 1. – On the left, the diagram and "effective coupling" corresponding to the dipole operator of eq. (2). Notice that the normalisation of the coefficient assumes that the chirality flip is due to the heaviest lepton Yukawa coupling, and that the NP contributes via a loop. Only the combination $S^{\alpha\beta}/\Lambda^2$ is measurable, but it is intuitive to separate it into the dimensionless $S^{\alpha\beta}$ which contains New Physics couplings, and the New Physics mass scale Λ. On the right, a GIM-suppressed FCNC diagram in the SM. Since two quark mass insertions are required, the diagram has two Higgs legs and is of dimension 8.

coupling constants and $1/(16\pi^2)$, so that C appears to be a product of New Physics couplings. For instance the dipole operator, which describes $g-2$ and $\ell_\alpha \to \ell_\beta \gamma$, in this review is normalised:

$$\frac{em_\alpha}{16\pi^2\Lambda^2}[S_L]_{\alpha\beta}\overline{e_R}_\beta \sigma^{\mu\nu} e_{L\alpha} F_{\mu\nu} + \frac{em_\alpha}{16\pi^2\Lambda^2}[S_R]_{\alpha\beta}\overline{e}_\beta \sigma^{\mu\nu} e_{R\alpha} F_{\mu\nu}. \tag{2}$$

$\mathcal{L}_{eff}$ can provide a useful bridge between data and theories. From data, the operator coefficients can be constrained. From a theory, the operator coefficients can be calculated. From the perspective that data should identify the correct theory, it is interesting to ask to what degree "the" theory can be reconstructed from the coefficients of $\mathcal{L}_{eff}$. However, we make no progress on this question here.

A lower bound on the mass scale Λ of perturbative New Physics can be obtained from the experimental bounds as follows. First, find the lowest dimension operator/diagram corresponding to a process(usually dimension 6 for LFV), set the New Couplings to 1 (on the assuption that perturbative couplings are ≤ 1), and compute the rate. Notice that the bound obtained will depend on what loop or SM coupling factors are scaled out of C in eq. (1). In table I, the New Phyics is assumed to contribute via loop diagrams, as if New Particles had a conserved quantum number, so $C/(\Lambda^2)$ was taken to be $1/(16\pi^2\Lambda^2)$.

In the SM, quark FCNC are suppressed by the quadratic GIM mechanism. The additional m_q^2/m_W^2 factor can be interpreted as placing SM FCNC at dimension 8, with 4 fermion legs and two Higgs legs (see fig. 1 on the right). From a phenomenological bottom-up perspective, one can ask if this might also occur in New Physics scenarios [2].

Bounds on the scale of New Physics that contributes to LFV at one loop via dimension-8 operators, can be obtained following a similar recipe to the dimension-6 bounds. The coefficients $\frac{C^{(6)}}{\Lambda^2}$ of the dimension-6 operators contributing to a process are set to 0, and replaced by the coefficients $\frac{C^{(8)}v^2}{16\pi^2\Lambda^4}$ of the dimension-8 operators/diagrams which have similar fermion legs and two additional Higgs legs (vevs). The lower bounds on Λ at dimension 8, given in table I, are obtained by setting $C^8 \simeq 1$.

An objection to the bounds of table I is that the flavoured couplings we know in the SM are not 1. Bounds that take into account a possible hierarchy in flavoured New Physics couplings can be obtained by following the Cheng-Sher ansätz [3], which is that

TABLE II. – *Expected Branching Ratios due to tree level TeV-scale New Particles with hierarchical couplings, as in eq.* (3). *In meson decays, the chiral structure of the matrix element is indicated. The "long-distance loop" estimates correspond to an a dipole operator, where the off-shell photon decays to a charged lepton pair.*

Process	Bound	Expectation
$BR(\mu \to e\gamma)$	$< 2.4 \times 10^{-12}$	$\sim 2 \times 10^{-14}$ (with mass insertion)
$BR(\mu \to e\bar{e}e)$	$< 1.0 \times 10^{-12}$	$\sim 10^{-17}$ (long-distance loop)
$BR(\tau \to \mu\gamma)$	$< 4.4 \times 10^{-8}$	$\sim 8 \times 10^{-11}$ (with mass insertion)
$BR(\tau \to 3\ell)$	$< 2.1 \times 10^{-8}$	$\sim\ 0^{-14}$ (long-distance loop)
$BR(\overline{K_L^0} \to \mu\bar{e})$	$< 4.7 \times 10^{-12}$	$\sim 5 \times 10^{-15}$ $(S \pm P)$
		$\sim 10^{-17}$ $(V \pm A)$
$BR(B \to \tau^{\pm}e^{\mp})$	$< 2.8 \times 10^{-5}$	$\sim 4 \times 10^{-15}$ $(S \pm P)$
$BR(B_s \to \tau^{\pm}\mu^{\mp})$		$\sim 10^{-11}$ $(S \pm P)$
$BR(B \to e^{\pm}\mu^{\mp})$	$< 6.4 \times 10^{-8}$	$\sim 4 \times 10^{-16}$ $(S \pm P)$
$BR(B \to K^0\mu^{\pm}e^{\mp})$	$< 2.7 \times 10^{-7}$	$\sim 10^{-15}$ $(V \pm A)$
$BR(B^+ \to K^+\tau\bar{\mu})$	$< 7.7 \times 10^{-5}$	$\sim 10^{-11}$

flavoured fermion couplings are $\propto$ SM fermion masses

$$\lambda_{ij} \simeq \sqrt{\frac{m_i m_j}{v^2}}\,, \quad i,j \text{ any SM fermion.} \tag{3}$$

Such patterns arise, for instance, in Randall-Sundrum extra-dimensional models. To obtain the rate estimates given in table II (see also [4]), I assume that new particles with masses $\sim$ TeV and couplings like eq. (3) contribute via tree diagrams (when possible) to the various processes. The $\ell_\alpha \to \ell_\beta\gamma$ branching ratios are estimated with a $1/(16\pi^2)$ loop factor, and chirality flip due to a Higgs insertion on an external leg, as in fig. 1. Without this factor, the prediction exceeds the current upper bounds.

In summary, neutrino masses imply that there *is* New Physics dedicated to Lepton Flavour. However, no flavour-changing processes have yet been observed among charged leptons. Current bounds are consistent with various patterns of New Physics. Most new flavoured particles with masses $\gtrsim$ few $\to 10\,\text{TeV}$, and $\mathcal{O}(1)$ couplings are allowed if they contribute to LFV via loops. New flavoured particles with masses $\sim$ TeV and hierarchical couplings can contribute at the tree level. Most importantly, the three classes of BSM scenarios considered here (in loops at dimension 6 or 8, with hierarchical couplings), can most readily be found in different processes (μ decays, τ decays, K decays,...). This means that improving the sensitivity of all LFV modes is interesting, because there is no model independent "golden mode" which is the "best place" to look.

2. – What can we learn?

Some anticipated sensitivities to various LFV processes([2]) are listed in table III. In this section, we suppose that some LFV is observed, and discuss an example of what

([2]) NA62 will have K^+'s, and could explore $BR(K^+ \to \pi^+\mu^+e^-) \sim 10^{-12}$. However, for LFV, its not clear this is more sensitive that the current bounds from $K \to \mu^+e^-$

TABLE III. – *Future sensitivities of various experiments to LFV processes.*

Some processes	Current sensitivities	Future sensitivity
$BR(\mu \to e\gamma)$	$< 2.4 \times 10^{-12}$	$\sim 10^{-13}(10^{-14}$ (MEG)
$BR(\mu \to e\bar{e}e)$	$< 1.0 \times 10^{-12}$	
$\frac{\sigma(\mu+Au\to e+Au)}{\sigma(\mu \text{ capture})}$	$< 7 \times 10^{-13}$	$10^{-16} - 10^{-18}$(J-PARC)
$BR(\tau \to \ell\gamma)$	$< 3.3, 4.4 \times 10^{-8}$	few $\times 10^{-9}$ (S-B fact)
$BR(\tau \to 3\ell)$	$< 1.5 - 2.7 \times 10^{-8}$	$\lesssim 10^{-9}$ (S-B fact)
$BR(\tau \to e\phi)$	$< 3.1 \times 10^{-8}$	$\lesssim 10^{-9}$ (S-B fact)
$BR(\overline{K_L^0} \to \mu\bar{e})$	$< 4.7 \times 10^{-12}$	
$BR(K^+ \to \pi^+\bar{\nu}\nu)$	$= 1.7 \pm 1.1 \times 10^{-10}$	100 evts (NA62)

such data could tell us about New Physics. An early discussion in this perspective is [5]. There are two steps to learning about NP: first, determining the coefficients of the effective Lagrangian, then, in principle, it would be interesting to "reconstruct" the New Physics Lagrangian from the Effective Lagrangian.

One way to learn about New Physics is to combine various observables. In many processes, such as $\tau \to 3\ell$ or $\mu - e$ conversion, there are several operators of the same dimension which can contribute to the rate, so experimental observables depend on combinations of operator coefficients. Interesting studies [6] have shown that these coefficients could be disentangled with additional observables, such as angular correlations in $\tau \to 3\ell$, or nucleus-dependance in $\mu - e$ conversion. Knowing the various coefficients in the Effective Lagrangian can give some information on the properties of New mediating Particles, such as their colour or spin.

Measuring the same process for different flavours (*e.g.*: $\mu \to e\gamma$, $\tau \to e\gamma$, $\tau \to \mu\gamma$) tells about the flavour structure of the Effective Lagrangian coefficient, and, possibly also of the New couplings. Consider $\tau \to \ell\gamma$ and $\mu \to e\gamma$, which constrain the flavour structure

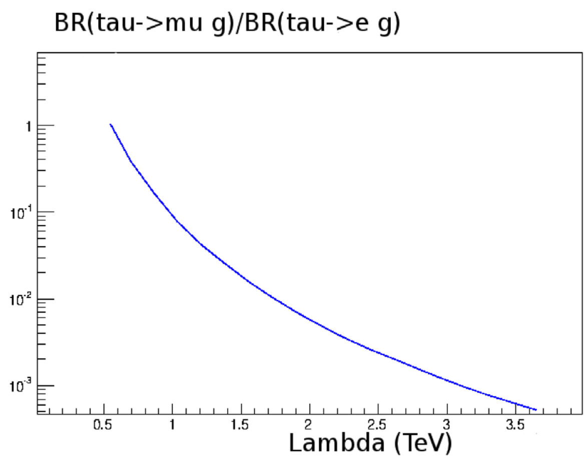

Fig. 2. – The hierarchy predicts $BR(\tau \to \mu\gamma)$ below anticipated Super B fact sensitivities.

of the dipole coefficient. Only one operator contributes, although it is convenient to separate it in two according to fermion chirality (as in eq. (2)), rather than write the operator +h.c. For simplicity, I assume chirality flip on an external leg.

Recall that $BR(\mu \to e\gamma) \leq 10^{-12}$. And suppose we see $BR(\tau \to e\gamma) \sim 10^{-8}$ at a Super-B factory. This is an interesting scenario for learning about flavour structure, because we have two pieces of information: the $\tau \to e\gamma$ rate, and the "approximate zero" from $\mu \to e\gamma$. However, S_L and S_R combine to an arbitrary complex three by three matrix, which cannot be reconstructed from two observations.

So I make one more assumption, which is common in hierarchical flavour physics: suppose that the dipole coefficient $em_\alpha S_{\alpha\beta}/16\pi^2\Lambda^2$ is dominated by its largest eigenvalue (this is like taking $[\mathbf{Y}_u^\dagger \mathbf{Y}_u]_{bs} \simeq V_{tb}^* y_t^2 V_{ts}$). Then there are three parameters, $\Lambda, |V_{3e}|$, and $|V_{3\mu}|$, to parametrise $\mu \to e\gamma, \tau \to e\gamma, \tau \to \mu\gamma$. If one allows that the LHC can give a lower bound on Λ, an upper bound on the remaining rate $\tau \to \mu\gamma$ can be predicted. This bound is shown in fig. 2. It arises because V_{3e} must be large, if "sufficiently heavy" NP induces $\tau \to e\gamma$:

$$\widetilde{BR}(\tau \to e\gamma) \simeq 10^{-8} \left(\frac{500\,\mathrm{GeV}}{\Lambda}\right)^4 \frac{|V_{3e}|^2}{10^{-4}} \gtrsim 10^{-8}.$$

Then $\widetilde{BR}(\mu \to e\gamma) \propto |V_{3\mu}V_{3e}^*|^2 \lesssim 10^{-12}$ imposes that $|V_{3\mu}|$ is "approximately zero" (assuming $|V_{3e}^*|$ is large). This argument is relevant for the experimental scenario where the LHC puts a lower bound on the mass of LFV mediators, and a Super-B factory sees a $\tau \to \ell\gamma$ decay. Then the argument says that: if the New Physics couplings are hierarchical, then only one of $\tau \to \mu\gamma$ or $\tau \to e\gamma$ should be seen. Notice that this upper bound arises irrespective of whether $\mu \to e\gamma$ is observed or not. See [7] for caveats to this argument.

In summary, it is the author's opinion that it is interesting to explore how much of the fundamental New Physics Lagrangian can be reconstructed from coefficients of the Effective Lagrangian. I described here a simple example (with some hidden assumptions) where measuring one rare τ decay allows to learn whether the New couplings are hierarchical. This example also illustrates that discovering an LFV process in τ's is arguably more interesting than discovering it in μ's, because combining a τ detection at $BR \sim 10^{-8}$ with a μ bound at $BR \lesssim 10^{-12}$ gives information about both the New Physics flavour structure and scale.

* * *

I thank the organisers for inviting me to La Thuile in the year of the first LHC results.

REFERENCES

[1] Nakamura K. *et al.* (Particle Data Group), *J. Phys. G*, **37** (2010) 075021.
[2] Goudelis A., Lebedev O. and Park J.-h., *Phys. Lett. B*, **707** (2012) 369 [arXiv:1111.1715 [hep-ph]]; Giudice G. F. and Lebedev O., *Phys. Lett. B*, **665** (2008) 79 [arXiv:0804.1753 [hep-ph]]; Babu K. S. and Nandi S., *Phys. Rev. D*, **62** (2000) 033002 [hep-ph/9907213].
[3] Cheng T. P. and Sher M., *Phys. Rev. D*, **35** (1987) 3484.
[4] Carpentier M. and Davidson S., *Eur. Phys. J. C*, **70** (2010) 1071 [arXiv:1008.0280 [hep-ph]].
[5] Brignole A. and Rossi A., *Nucl. Phys. B*, **701** (2004) 3 [hep-ph/0404211].
[6] Cirigliano V., Kitano R., Okada Y. and Tuzon P., *Phys. Rev. D*, **80** (2009) 013002 [arXiv:0904.0957 [hep-ph]]; Kitano R., Koike M. and Okada Y., *Phys. Rev. D*, **66** (2002) 096002 (Erratum-ibid. D **76** (2007) 059902) [hep-ph/0203110]; Kitano R. and Okada Y., *Phys. Rev. D*, **63** (2001) 113003 [hep-ph/0012040].
[7] Davidson S., *Eur. Phys. J. C*, **72** (2012) 1897 [arXiv:1112.2956 [hep-ph]].

IL NUOVO CIMENTO Vol. 35 C, N. 6 Novembre-Dicembre 2012
DOI 10.1393/ncc/i2012-11355-9

Colloquia: LaThuile12

Searching for $\mu \to e\gamma$ with MEG

G. Cavoto
Istituto Nazionale di Fisica Nucleare, Sezione di Roma
Piazzale A.Moro, 2 00185 Roma, Italy

ricevuto il 7 Settembre 2012

Summary. — New results of a search for the ultra-rare decay $\mu \to e\gamma$ by the MEG Collaboration at the Paul Scherrer Institut (PSI) continuous muon beam are reported here. The data were taken during 2009 and 2010 and correspond to approximately 1.8×10^{14} muon stopped on target. A maximum-likelihood fit analysis sets an upper limit at 90% CL on the branching ratio, $\mathcal{B}(\mu \to e\gamma) < 2.4\ 10^{-12}$, the best limit ever achieved for this process.

PACS 13.35.Bv – Decays of muons.
PACS 11.30.Hv – Flavor symmetries.
PACS 12.10.Dm – Unified theories and models of strong and electroweak interactions.

1. – Description

The standard model of elementary particles (SM) forbids processes with violation of the lepton flavour accidental symmetry (LFV). The process $\mu \to e\gamma$ is highly suppressed even with the introduction of neutrino masses and mixing in the SM [1,2]. An immeasurably small branching ratio ($\mathcal{B} \lesssim 10^{-51}$) for this decay would be allowed. On the contrary, new physics scenarios beyond SM, such as supersymmetric grand unified theories or theories with extra dimensions, predict branching ratios in the 10^{-12} to 10^{-14} range [3-5]. This is close to the present limit set by the MEGA experiment [6], $\mathcal{B} \leq 1.2 \times 10^{-11}$, which places one of the most stringent constraints on the formulation of such theories. Observation of $\mu \to e\gamma$ therefore would be an unambiguous signature of new physics, while improvements on the existing limit would stringently constrain many of the new physics scenarios beyond SM.

2. – The MEG experiment

The $\mu \to e\gamma$ process has simple two-body kinematics with well-defined photon and positron energies. An experiment devoted to search for this process should be carefully optimized to fight the background by obtaining the best experimental resolution with some trade-off on the detection efficiency. Positive muons are not captured on target nuclei and they must be preferred for this search. The background to $\mu^+ \to e^+\gamma$ decay comes either from radiative muon decays $\mu^+ \to e^+\nu\bar{\nu}\gamma$ (RMD) in which the neutrinos carry away little energy or from an accidental coincidence of an energetic positron from a normal Michel decay with a γ-ray coming from RMD, Bremsstrahlung or positron annihilation-in-flight. The accidental coincidences are by more than one order of magnitude the dominant background. Given the possibly tiny $\mathcal{B}$ value a high beam rate is necessary. The PSI πE5 beam line is used to stop 3×10^7 positive muons per second in the target. The residual polarization of the decaying muons along the beam axis was measured to be $\langle P \rangle = -0.89 \pm 0.04$.

The MEG detector [7, 8] provides an asymmetric coverage (10% solid angle in total) of the thin muon stopping target (205 μm thick polyethylene) in order to minimize the material crossed by the photon before being detected. It is composed of a positron spectrometer and a photon detector in search of back-to-back and time coincident photons and positrons. The positron spectrometer consists of a set of drift chambers (DC) [9] and scintillation timing counters (TC) [10] located inside a superconducting solenoid with a gradient field [11] along the beam axis, ranging from 1.27 Tesla at the centre to 0.49 Tesla at either end. Such B field efficiently sweeps out the low-energy positrons from the spectrometer volume. The photon detector [12], located outside of the solenoid, is a homogeneous volume (900 ℓ) of liquid xenon (LXe) viewed by 846 UV-sensitive photo-multiplier tubes (PMTs) submerged in the liquid. The spectrometer measures the positron momentum vector and timing, while the LXe detector is used to reconstruct the γ-ray energy as well as the position and time of its first interaction in LXe. All the signals are individually digitized by in-house designed waveform digitizers based on the multi-GHz domino ring sampler chip (DRS) [13].

The MEG detector response, resolutions and stability are constantly monitored and calibrated. The PMTs of the LXe detector are calibrated by LEDs and α-sources immersed in the liquid [14] during physics data acquisition. The energy scale and resolutions of the LXe detector are measured over the energy range of 4.43 to 129.4 MeV using various γ-rays sources. Photons from a radioactive Am/Be source and from (p, γ)-reaction using a dedicated Cockcroft-Walton accelerator (CW) [15] are injected twice a week in the LXe detector, while once a year a $\pi^- p$ charge exchange and radiative capture reactions (CEX) are used to produce monochromatic photons in an energy range very close to the signal photon energy. A 9 MeV-γ line from the capture in nickel of neutrons from a pulsed and triggerable deuteron-deuteron neutron generator allows to check the stability of the LXe detector even during data-taking. The relative time between the TC and LXe detector is monitored using RMD and 2γ-events from ${}^{11}_{5}\mathrm{B}(p, 2\gamma){}^{12}_{6}\mathrm{C}$ reactions.

The $\mu^+ \to e^+\gamma$ trigger requires the presence of a high-energy γ-ray in the LXe detector and a hit on the timing counters within a 20 ns window together with an approximate back-to-back topology. Pre-scaled monitoring and calibration triggers are also recorded. A more detailed description of the MEG detector can be found in ref. [8].

3. – Data analysis

The results presented here are based on data collected in 2009 and 2010 (for a total of 1.8×10^{14} μ^+-decays in the target). The 2010 statistics are about twice that of 2009. All sub-detectors were running stably during these periods.

In 2010 a DRS upgrade resulted in an improvement in the time resolution while an increase in noise in the DC, due to a deterioration of the HV power supplies, and some unusable DC modules caused a slightly worse positron tracking performances.

A blind analysis procedure was adopted such that events close to the signal region were kept hidden (blind region) until all the analysis procedures had been completely defined. A maximum likelihood analysis fit method was used to extract the signal and background yields. Therefore, the probability density functions (PDFs) needed for the likelihood analysis were constructed using the only events outside of the blind region (side-bands) or calibration samples.

3˙1. *Observables reconstruction and resolutions.* – The kinematic variables used to identify the $\mu^+ \to e^+\gamma$ decays are the γ-ray and e^+ energies (E_γ, E_e), their relative directions ($\theta_{e\gamma}$, $\phi_{e\gamma}$) and relative emission time ($t_{e\gamma}$). The relative directions are defined as $\theta_{e\gamma} = (\pi - \theta_e) - \theta_\gamma$ and $\phi_{e\gamma} = (\pi + \phi_e) - \phi_\gamma$, θ and ϕ being the polar angle and the azimuthal angle, respectively, taking the z-axis as the beam-axis. The offline event selection requires at least one e^+-track reconstructed in the spectrometer and pointing to the target, with minimal quality cuts applied. The blind region is defined by $48 < E_\gamma < 58\,\mathrm{MeV}$ and $|t_{e\gamma}| < 1\,\mathrm{ns}$.

The positron track reconstruction in the spectrometer is based on a Kalman filter technique [16]. Effects of multiple scattering and energy loss in the detector materials in the presence of the non-uniform magnetic field are taken into account. The gradient magnetic field was measured with Hall probes in 2006 and compared with the prediction from the coil currents showing good agreement (within 0.2%). Only the major component along the beam axis of the measured field is used in the analysis to avoid possible misalignment errors from the Hall probes. The other minor components are deduced from Maxwell equations with boundary conditions at a symmetry plane at the magnet centre. Internal alignment of the DC is obtained by tracking cosmic-ray muons without a magnetic field and by minimizing the measured residuals in a manner independent of the initially assumed alignment [17]. The absolute position of the DC system is based on an optical survey.

The resolutions of the positron track direction are estimated by exploiting tracks with two full turns in the DC sensitive volume Each turn is treated as an independent sub-track and the resolutions are extracted from the difference between the fitted parameters of the two reconstructed sub-tracks. Monte Carlo (MC) simulations demonstrate that the RMS of such differences (fig. 1) are good estimates of the angular resolutions at the target. Small corrections (at the level of 10%) account for a dependence on positron momentum.

The reference energy resolution is evaluated by fitting the kinematic edge of the Michel decays with a convolution of the theoretical Michel spectrum with a resolution function represented by a sum of three Gaussians. The core Gaussian component describes about 80% of the events with a tail ($\sigma_{tail} = 3\sigma_{core}$) and an outlier ($\sigma_{out} = 6\sigma_{core}$) components being approximately 15% and 5% of the total.

The decay vertex coordinates and the positron direction at the vertex are determined by extrapolating the reconstructed track back to the target with the constraint given by the target plane. Given this constraint, a geometrical correlation is generated between ϕ_e at the vertex position and E_e, that can be parametrized as $\sigma_{\phi_e} = \sqrt{\sigma_0^2 + (k \tan\phi_e)^2}$ where σ_0 is the ϕ_e resolution for $\phi_e = 0$, *i.e.* the direction orthogonal to the target plane, and $k \sim 10\,\mathrm{mrad}$ is a parameter that can be determined experimentally by using the two-turn method. This effect is perfectly reproduced by the MC simulation.

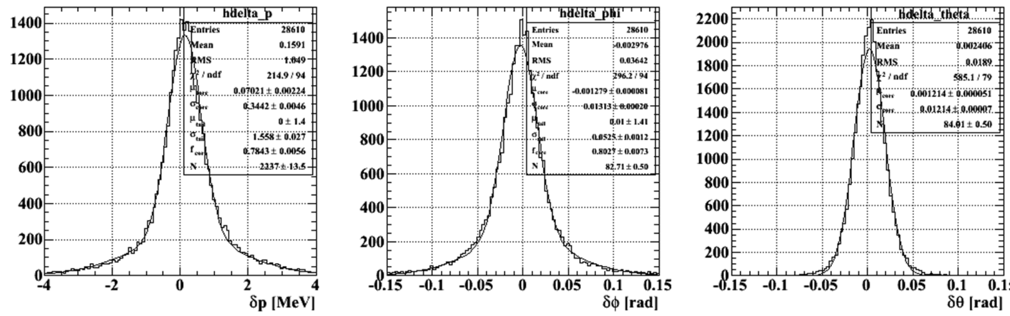

Fig. 1. – Double turn tracks momentum (left) and angle (center and right) distribution. The plots shows the difference of the sub-tracks parameters, obtained with independent fits to each sub-track.

The resolution on the decay vertex coordinates is also determined by the two-turn method; along the beam axis it is described by a Gaussian while in the vertical direction it is described by the sum of two Gaussians (core component approximately 85%).

The determination of the photon energy E_γ in the LXe detector is based on the sum of the number of scintillation photons detected by the PMTs; correction factors take into account the different PMT geometrical acceptances. Due to its geometry the detector response is not totally uniform over the photon entrance window; this is corrected for by using γ-lines from CW and CEX reactions. The absolute energy scale and resolution at the signal energy $E_\gamma = 52.8\,\mathrm{MeV}$ are determined by the CEX measurement; the resolution σ_R, extracted from a Gaussian fit to the high energy side of the spectrum, depends also on the depth (w) of the γ-ray conversion point from the photon entrance surface of the LXe detector. Events with shallow conversion point ($w < 2\,\mathrm{cm}$) represents the 37% of the total and have a resolution about 20% worse than the events with $w > 2\,\mathrm{cm}$. The 3D-map of the measured resolutions is incorporated into the PDFs for the likelihood analysis.

The photon energy scale and the resolutions are cross-checked by fitting the background spectra measured in the side-bands with the theoretical RMD spectrum folded with the detector resolutions. This allows to monitor the resolutions during the run and confirms that they are well represented by the CEX evaluations. The systematic uncertainty of the E_γ-scale is estimated to be $\simeq 0.3\%$.

Since MEG operates at a high beam intensity, it is important to recognize and unfold pile-up photons. For each event the spatial and temporal distributions of the PMT charge are studied to identify photon pile-up in the LXe detector; in case of positive identification, corrections to the PMT charges are applied. Cosmic ray events are rejected using their topological characteristics.

The position of the first interaction of the γ-ray in the LXe detector is derived from the light distribution measured by the PMTs close to the region of the energy deposition by fitting the distribution with the expectation. The position resolution in the plane of the photon entrance window is measured in a dedicated CEX run with a lead slit-collimator placed in front of the LXe detector, while the w resolution and the position dependence of the resolutions are evaluated by a MC simulation.

The γ-ray direction (θ_γ and ϕ_γ) is defined by the line connecting the decay vertex to the γ-ray conversion point measured by the LXe detector.

The relative time $t_{e\gamma}$ is derived from the two time measurements by the LXe detector

TABLE I. – *Resolution (Gaussian σ) and efficiencies for* 2009 *and* 2010 *data.*

PDF parameters	2009	2010
Core $\frac{\sigma_{E_{e^+}}}{E_{e^+}}$	0.74%	0.74%
Core Gaussian fraction	83%	79%
e^+ σ_θ	9.4 mrad	11.0 mrad
e^+ σ_ϕ ($\phi = 0$)	6.7 mrad	7.2 mrad
e^+ σ_Z / $\sigma_Y(core)$	1.5/1.1 mm	2.0/1.1 mm
$\frac{\sigma_{E_\gamma}}{E_\gamma}$ $w > 2$ cm	1.9%	1.9%
γ position at LXe $\sigma_{(u,v)}$-σ_w	5–6 mm	5–6 mm
$\theta_{e\gamma}$	14.5 mrad	17.1 mrad
$\phi_{e\gamma}$	13.1 mrad	14.0 mrad
γ-e^+ timing	150 ps	130 ps
Efficiency		
Trigger	91%	92%
γ reconstruction	58%	59%
e^+ reconstruction	40%	34%

and the TC, after correcting for the length of the particles flight-paths. The associated resolutions at the signal energy are evaluated from the RMD peak observed in the E_γ side-band; a small correction takes into account the E_γ-dependence measured in the CEX calibration runs. The position of the RMD-peak corresponding to $t_{e\gamma} = 0$ was monitored constantly during the physics data-taking period and found to be stable to within 15 ps.

All the mentioned resolutions are collected in table I for 2009 and 2010 data separately. Reconstruction efficiency for positron and photon within the detector acceptance are also reported in table I.

3˙2. *Maximum-likelihood analysis.* – A likelihood analysis is carried out for events in a portion of the blind region (analysis region) defined by $48 < E_\gamma < 58$ MeV, $50 < E_e < 56$ MeV, $|t_{e\gamma}| < 0.7$ ns, $|\theta_{e\gamma}| < 50$ mrad and $|\phi_{e\gamma}| < 50$ mrad. These intervals in the analysis variables are between five and twenty sigmas wide to fully contain the signal events and also retain some background events. The best estimates of the numbers of signal, RMD and accidental background (BG) events in the analysis region are obtained by maximizing the following likelihood function:

$$\begin{aligned}
&\mathcal{L}\left(N_{\text{sig}}, N_{\text{RMD}}, N_{\text{BG}}\right) = \\
&\quad \frac{e^{-N}}{N_{\text{obs}}!} e^{-\frac{(N_{\text{RMD}} - \langle N_{\text{RMD}} \rangle)^2}{2\sigma^2_{\text{RMD}}}} e^{-\frac{(N_{\text{BG}} - \langle N_{\text{BG}} \rangle)^2}{2\sigma^2_{\text{BG}}}} \\
&\quad \times \prod_{i=1}^{N_{\text{obs}}} \left(N_{\text{sig}} S(\vec{x}_i) + N_{\text{RMD}} R(\vec{x}_i) + N_{\text{BG}} B(\vec{x}_i)\right),
\end{aligned}$$

where $\vec{x}_i = \{E_\gamma, E_e, t_{e\gamma}, \theta_{e\gamma}, \phi_{e\gamma}\}$ is the vector of observables for the i-th event, N_{sig}, N_{RMD} and N_{BG} are the fitted numbers of signal, RMD and BG events, while S, R and B are their corresponding PDFs. $N = N_{\text{sig}} + N_{\text{RMD}} + N_{\text{BG}}$ and N_{obs} is the observed total number of events in the analysis window. $\langle N_{\text{RMD}} \rangle = 27.2$ (52.2) and $\langle N_{\text{BG}} \rangle = 270.9$ (610.8) are the numbers of RMD and BG events extrapolated from the side-bands

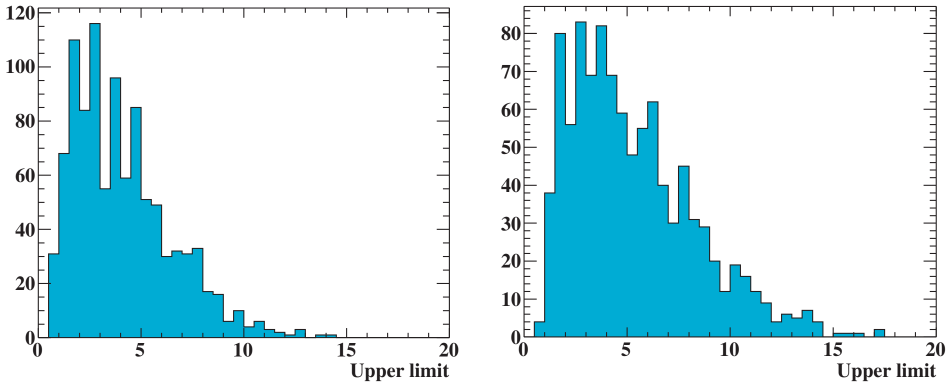

Fig. 2. – Distribution of 90% upper limit on N_{sig} in two ensembles of toy MC experiments corresponding to 2009 (left) and 2010 (rigth) dataset.

together with their uncertainties $\sigma_{\mathrm{RMD}} = 2.8$ (6.0) and $\sigma_{\mathrm{BG}} = 8.3$ (12.6), respectively for 2009 (2010) data.

The signal PDF $S(\vec{x_i})$ is the product of the PDFs for E_e, $\theta_{e\gamma}$, $\phi_{e\gamma}$ and $t_{e\gamma}$, which are correlated variables, as explained above, and the E_γ PDF. The PDFs properly incorporate the measured resolutions and correlations among $E_e, \theta_{e\gamma}$, $\phi_{e\gamma}$ and $t_{e\gamma}$ on an event-by-event basis. The RMD PDF $R(\vec{x_i})$ is the product of the same $t_{e\gamma}$-PDF as that of the signal and the PDF of the other four correlated observables, which is formed by folding the theoretical spectrum with the detector response functions. The BG PDF $B(\vec{x_i})$ is the product of the five PDFs, each of which is defined by the single background spectrum, precisely measured in the side-bands. The dependence of the resolutions on the position of the γ-ray interaction point and on the positron tracking quality is taken into account in the PDFs.

A frequentist approach with a profile likelihood-ratio ordering [18, 19] is used to compute the confidence intervals on N_{sig}. Other, independent analysis schemes based on averaged PDFs without event-by-event information or Bayesian approach were also used and found to be compatible with the analysis presented here to within 10 to 20% difference in the obtained branching ratio upper limits.

In order to convert N_{sig} into a branching ratio value the normalization relative to the Michel decay is computed [8] by counting the number of Michel positrons passing the same analysis cuts. This is accomplished by means of a pre-scaled Michel positron trigger enabled during the physics data-taking. A correction to the pre-scaling factor due to positron pile-up in the TC is taken into account. Another method for computing the normalization uses RMD events in the E_γ side-band and the theoretical branching ratio of the RMD. The normalizations calculated by these two independent methods are in good agreement and are combined to give the normalization factor with a 7% uncertainty.

The sensitivity ($\mathcal{S}$) of the experiment with a null signal hypothesis is evaluated by taking the median of the distribution of the upper limit on the branching ratio obtained over an ensemble of toy MC experiments. The rates of RMD and BG events, as measured in the side-bands, are assumed in the simulated experiments. In fig. 2 the distribution of the upper limit on N_{sig} on these ensembles are reported for the 2009 and 2010 data sets separately. It must be emphasized that these sensitivities are consistent with the upper limits obtained by the likelihood analyses in several comparable analysis regions of the $t_{e\gamma}$ side-bands demonstrating a good control over the background description.

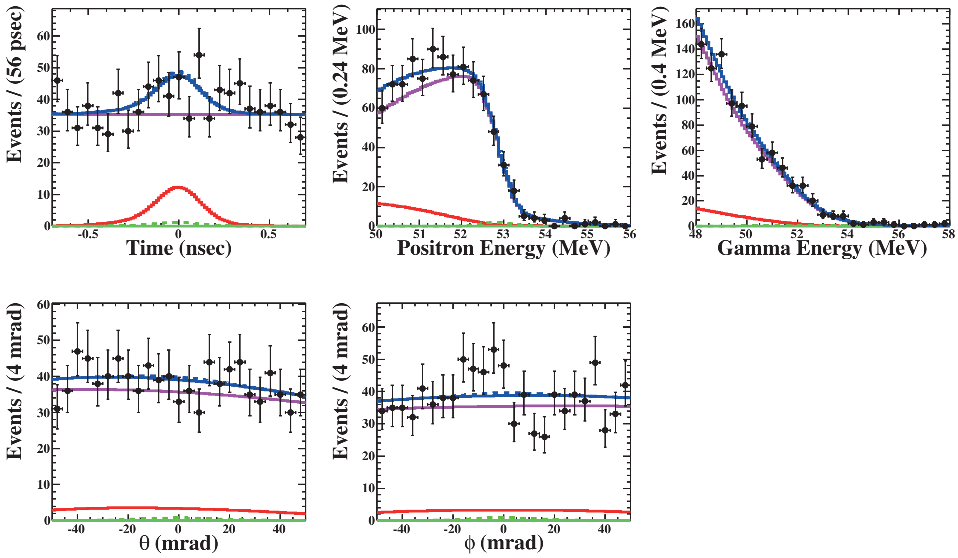

Fig. 3. – Distributions of events for the various observables, $t_{e\gamma}$, E_e, and E_γ on the top row, $\theta_{e\gamma}$ and $\phi_{e\gamma}$ on the bottom row. The projected PDF total, S, R and B (blue, green, red, and magenta) are superimposed. The dotted lines includes the 90% CL upper limit on $N_{\rm sig}$ for comparison.

After calibrations, optimization of the analysis algorithms and background studies in the side-bands are completed, the likelihood analysis in the analysis region is performed. In fig. 3 the event distribution for the various observables is shown with the superimposed PDF.

The analysis of the full data sample gives a 90% CL upper limit of 2.4×10^{-12} on $\mathcal{B}\ (\mu \to e\gamma)$. The 90% CL intervals as well as the best estimate of the branching ratio for 2009 and 2010 data separately are also given in table II. The 2009 data set, which gives a positive best estimate for the branching ratio, is consistent with the hypothesis $\mathcal{B} = 0$ with an 8% probability.

The systematic uncertainties for the parameters of the PDFs and the normalization factor are taken into account in the calculation of the confidence intervals by fluctuating the PDFs according to the uncertainties. The largest contributions to the systematic

Table II. – *Single event sensitivity (SES), sensitivity ($\mathcal{S}$), best fit ($\mathcal{B}_{fit}$),and upper limits (UL) at the* 90% *CL of the branching ratio (given in* $\times 10^{-12}$ *unit) for the* 2009, 2010 *and combined* 2009 + 2010 *data sets. Best fit* ($N_{\rm sig}$) *events and* $N_{\rm obs}$ *are also reported.*

Data set	SES	$\mathcal{S}$	$N_{\rm obs}$	$N_{\rm sig}$	$\mathcal{B}_{\rm fit}$	UL
2009	0.9	3.3	311	3.4	3.2	9.6
2010	0.4	2.2	645	−2.2	−1.0	1.7
2009 + 2010	–	1.6	–	–	−0.2	2.4

uncertainty, which amount to a shift of about 2% in total in the branching ratio upper limit, come from the uncertainties of the offsets of the relative angles, the correlations in the positron observables and the normalization.

4. – Conclusions and perspectives

In this contribution the results of 2009 and 2010 data analysis collected by the MEG experiment has been presented, leading to a 90% CL upper limit of 2.4×10^{-12} on $\mathcal{B}\ (\mu \to e\gamma)$, which constitutes the most stringent limit on the existence of the $\mu \to e\gamma$ decay, superseding the previous limit by a factor of 5. In 2011 the MEG experiment has already doubled the collected data and plans to add more data in 2012. The detector performances are expected to be similar. The predicted sensitivity at the end of 2012 would be in the range 10^{-13} challenging several model of new physics. An upgrade of the system is under discussion and could further bring down the sensitivity to less than 10^{-13}.

* * *

The author thanks his collaborators of the MEG experiment. He acknowledges the support of INFN (Italy).

REFERENCES

[1] Cheng T. P. and Li L.-F., *Phys. Rev. Lett.*, **45** (1980) 1908.
[2] Barbieri R. and Hall L. J., *Phys. Lett. B*, **338** (1994) 212 [hep-ph/9408406].
[3] Barbieri R., Hall L. and Strumia A., *Nucl. Phys. B*, **455** (1995) 219.
[4] Hisano J., Nomura D. and Yanagida T., *Phys. Lett. B*, **437** (1998) 351.
[5] Raidal M. *et al.*, *Eur. Phys. J. C*, **57** (2008) 13.
[6] Brooks M. L. *et al.* (MEGA Collaboration), *Phys. Rev. Lett.*, **83** (1999) 1521.
[7] Baldini A., Mori T. *et al.*, "The MEG experiment: search for the $\mu \to e\gamma$ decay at PSI", available at `http://meg.psi.ch/docs`.
[8] Adam J. *et al.* (MEG Collaboration), *Nucl. Phys. B*, **834** (2010) 1.
[9] Hildebrandt M. *et al.* (MEG Collaboration), *Nucl. Instrum. Methods A*, **623** (2010) 111.
[10] De Gerone M. *et al.*, *Nucl. Instrum. Methods A*, **638** (2010) 41.
[11] Ootani W. *et al.*, *IEEE Trans. Appl. Supercond.*, **14** (2004) 568.
[12] Mihara S. *et al.* (MEG Collaboration), *J. Phys.: Conf. Ser.*, **308** (2011) 012009.
[13] Ritt S. *et al.*, *Nucl. Instrum. Methods A*, **623** (2010) 486.
[14] Baldini A. *et al.*, *Nucl. Instrum. Methods A*, **565** (2006) 589.
[15] Adam J. *et al.* (MEG Collaboration), *Nucl. Instrum. Methods A*, **641** (2011) 19.
[16] Frühwirt R. *et al.*, *Data Analysis Techniques for High Energy Physics*, second edition (Cambridge University Press, Cambridge) 2000.
[17] CMS Collaboration, *JINST*, **5** (2010) T03009.
[18] Nakamura K. *et al.* (Particle Data Group), *J. Phys. G*, **37** (2010) 075021.
[19] Feldman G. J. and Cousins R. D., *Phys. Rev. D*, **57** (1998) 3873.

SESSION III - QCD PHYSICS / HADRONIC INTERACTIONS

IL NUOVO CIMENTO Vol. 35 C, N. 6 Novembre-Dicembre 2012
DOI 10.1393/ncc/i2012-11356-8

Colloquia: LaThuile12

ALICE results on heavy-ion physics at the LHC

L. Ramello for the ALICE Collaboration

Dipartimento di Scienze e Innovazione Tecnologica
Università del Piemonte Orientale and INFN - Alessandria, Italy

ricevuto il 7 Settembre 2012

Summary. — ALICE is a multipurpose detector for high-energy nucleus-nucleus physics at the CERN Large Hadron Collider. In November 2010, ALICE took its first Pb-Pb data at the center-of-mass energy of 2.76 TeV per nucleon pair; reference data in proton-proton collisions at the same energy were collected in 2011. This paper gives an overview of the main physics results obtained with these data. In particular, I will present results on identified charged and strange particle transverse momentum spectra, on anisotropic flow of charged particles, on open heavy flavour and quarkonia production in Pb-Pb collisions, compared to pp collisions. These first Pb-Pb results from ALICE at LHC are broadly consistent with expectations based on lower energy RHIC and SPS data. They indicate that matter created in these collisions, while initially much larger and hotter, still behaves like a very strongly interacting, almost perfect liquid. A brief outlook on the expected results from the second, higher statistics Pb-Pb run of Fall 2011 will be given as well.

PACS 25.75.Ld – Collective flow.
PACS 25.75.Gz – Particle correlations and fluctuations.

1. – The ALICE experiment

The ALICE experiment [1] was designed for the study of the Quark-Gluon Plasma produced in Pb-Pb collisions at the CERN Large Hadron Collider, at a center-of-mass energy which is presently (2010-2011 runs) about 14 times the energy attained previously at the Relativistic Heavy Ion Collider (RHIC). For a general overview of LHC results from Pb-Pb collisions see, *e.g.*, [2]. The experiment is fully described in [1]; results presented in the following are based on the central barrel detectors, namely the Internal Tracking System (ITS), the Time Projection Chamber (TPC) and the Time of Flight system (TOF), as well as on the Muon Spectrometer and on the Electromagnetic Calorimeter (EMCal). In addition, the Zero-Degree Calorimeters (ZDC) and the VZERO scintillator hodoscopes have been used for centrality determination. Two triggers have been used, namely the Minimum Bias (MB) trigger based on signals from the Silicon Pixel Detector

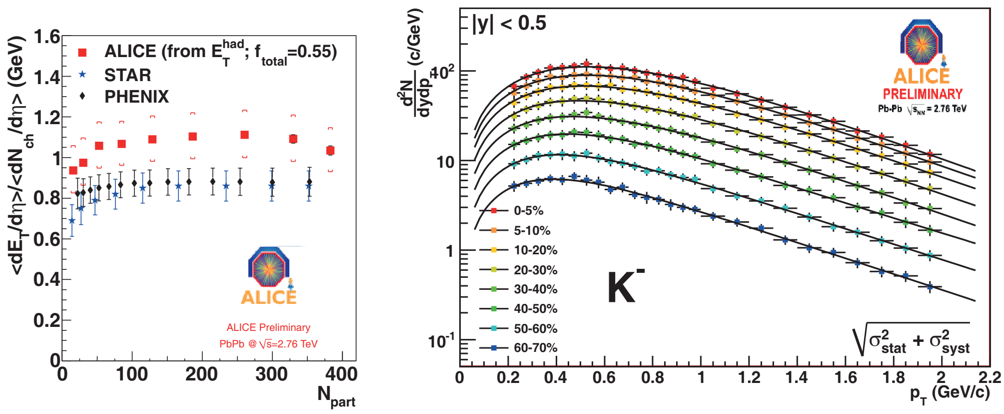

Fig. 1. – Left: transverse energy $\mathrm{d}E_t/\mathrm{d}\eta$ over charged track density $\mathrm{d}N_{ch}/\mathrm{d}\eta$ per participant pair *vs.* number of participants. Right: preliminary transverse momentum spectra of K^- in Pb-Pb collisions of different centralities ranging from 0–5% to 60–70%; lines represent blast-wave fits.

and the VZERO scintillator hodoscopes (see, *e.g.*, [3]), and the MUON trigger given by a muon signal in the trigger chambers of the Muon Spectrometer in coincidence with the MB trigger.

2. – ALICE results from Pb-Pb collisions at 2.76 TeV

Published and preliminary results from Pb-Pb collisions collected in the first Pb-Pb run (Fall 2010) at the LHC energy of 2.76 TeV per nucleon pair are presented in the following. The integrated luminosity in the 2010 run is $2.9\,\mu\mathrm{b}^{-1}$ corresponding to 17.7 million Minimum Bias events. Reference to pp runs at 2.76 and 7 TeV has been made when necessary, in particular to establish the nuclear modification factors described in the following. The higher statistics 2011 Pb-Pb run is briefly described in the final section.

2˙1. *Global event features*. – The main centrality observables used in ALICE are the multiplicity in the VZERO scintillator array and the forward energy in the ZDCs. Using a Glauber fit to the cross-section, centrality classes corresponding to given fractions of the inelastic Pb-Pb cross-section are defined (see, *e.g.*, [4]). For the most central class 0–5%, a charged multiplicity density of 1584 ± 76 at midrapidity has been measured [3]; normalizing to the number of participant nucleon pairs this corresponds to $(\mathrm{d}N_{ch}/\mathrm{d}\eta)/(N_{part}/2) = 8.3 \pm 0.4$, *i.e.* about 2.1 times the value measured at RHIC in central Au-Au collisions at 0.2 TeV center-of-mass energy, a stronger rise than the one predicted by a $\log(\sqrt{s_{NN}})$ extrapolation from lower energies. The dependence on centrality of charged multiplicity density is very similar [4] to the one observed at RHIC. The energy density obtained in the most central collisions has been estimated via the Bjorken formula $\epsilon_{Bj} = \frac{1}{\tau\pi R^2}\mathrm{d}E_T/\mathrm{d}\eta$ (see, *e.g.*, fig. 1(left)); the product of energy density and formation time, $\epsilon\tau$, is at the LHC about 2.5 larger than the one measured at RHIC. Assuming an upper limit on the formation time of $1\,\mathrm{fm}/c$, an energy density of at least $15\,\mathrm{GeV}/\mathrm{fm}^3$ is obtained.

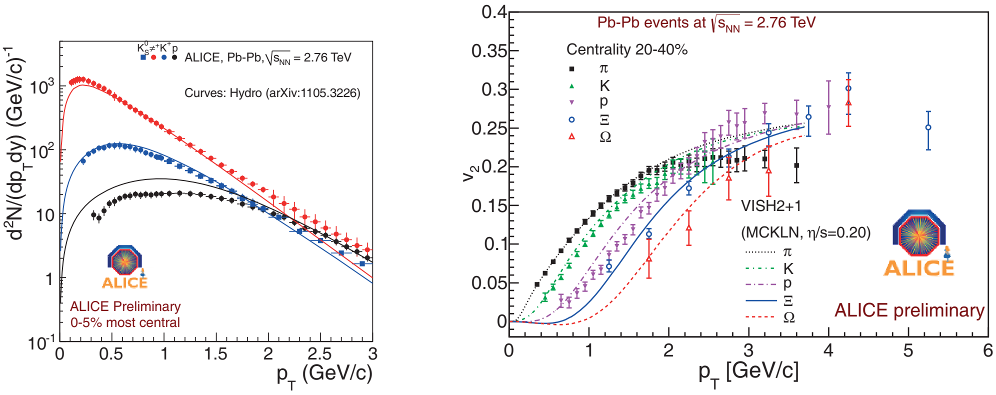

Fig. 2. – Left: Comparison of transverse momentum spectra of positively charged hadrons (and K_s^0) in Pb-Pb central collisions with a hydrodynamical calculation. Right: Elliptic flow coefficient *vs.* p_t for identified hadrons measured in Pb-Pb collisions in the 20–40% centrality class.

The spatial extent and the temporal duration of the particle emitting source is extracted from Hanbury-Brown Twiss interferometry of identical bosons (pions in this case) [5]: the HBT radii thus obtained indicate a volume of about 5000 fm^3, which is twice the one observed at RHIC, and a lifetime about 40% longer.

2·2. *Collective expansion and anisotropic flow.* – Detailed informations on the expansion of the source can be obtained by the transverse momentum spectra and by the azimuthal anisotropy (in particular the elliptic flow coefficient v_2) of identified hadrons. An example of transverse momentum spectra as a function of centrality is given in fig. 1(right). Lines represent blast-wave [6] fits, from which one obtains integrated yields dN/dy, average p_t and (by performing a simultaneous fit to different hadrons at given centrality) the parameters of the system at kinematic freeze out: temperature T_{fo} and average radial flow velocity β (in units of c). A strong radial flow, $\beta \simeq 0.66$, is observed in the most central collisions, *i.e.* about 10% higher than at RHIC; the estimated T_{fo} is slightly below 100 MeV for the same central collisions. The mean p_t of identified hadrons is correspondingly higher at LHC.

The preliminary p_t spectra of positively charged hadrons (and K_S^0, which extend the p_t range towards higher values) are shown in fig. 2(left) for the most central Pb-Pb collisions. Feed-down from weak decays has been subtracted. Lines represent a recent hydrodynamical calculation [7] which reproduces well the shape and the absolute value of the spectra, with the exception of protons whose yield appears to be overestimated.

The initial spatial anisotropy of the hot and dense medium formed in a Pb-Pb collision gives rise during the expansion to a momentum space anisotropy which is quantified by a Fourier expansion in the transverse plane. The p_t-integrated elliptic flow coefficient v_2 for charged particles measured [8] at LHC is about 30% higher than at RHIC, which is attributed to the harder p_t spectrum at LHC, since the differential flow coefficient $v_2(p_t)$ at LHC is very similar to the RHIC one. More insight is gained by measuring $v_2(p_t)$ for identified hadrons: fig. 2(right) shows preliminary measurements for several identified hadrons including hyperons in 20–40% central Pb-Pb collisions. The mass splitting induced by radial flow is evident, pions being the least affected by radial flow.

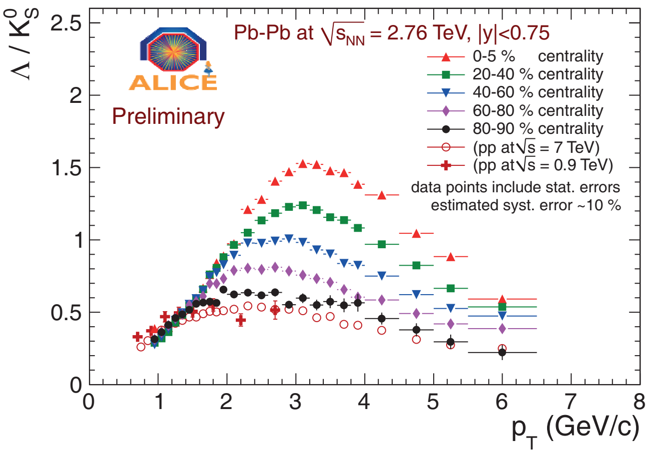

Fig. 3. – Λ/K_s^0 ratio *vs.* p_t for 5 centrality classes in Pb-Pb collisions at $\sqrt{s_{NN}} = 2.76\,\mathrm{TeV}$, as well as in pp collisions at 0.9 and 7 TeV.

A comparison with recent hydrodynamical calculation with shear-viscosity–to–entropy-density ratio $\eta/s = 0.20$ [7] (in units $\hbar = k_B = 1$) shows good agreement also for hyperons.

2˙3. *Strangeness and chemical composition.* – The mid-rapidity yields of identified hadrons provide information on the temperature T_{ch} of the so-called chemical freeze out, after which only elastic interactions occur, which can alter the p_t distributions but not any more the particle ratios. Additional information can be obtained by the p_t dependence of some of the ratios, like, *e.g.*, the strange baryon/meson ratio shown in fig. 3. Strange baryons are more abundant than mesons at higher p_t, and the baryon/meson ratio increases with centrality. The rise with p_t at fixed centrality is consistent with the quark recombination scenario, while the interplay between soft and hard production results in the subsequent decrease with p_t. The maximum value of the ratio is slightly higher at LHC than at RHIC (as measured by the STAR collaboration in central Au-Au collisions at 0.2 TeV, see [9]) and the maximum occurs at higher p_t. The enhancement of this ratio with respect to pp persists up to at least 6 GeV/c.

Another important piece of information comes from the strangeness enhancement, already observed at SPS and RHIC, as obtained from ratios of multi-strange baryon yields in ion-ion and pp interactions. ALICE results on multi-strange baryon production in pp interactions at 7 TeV have been recently released [10]. Figure 4 shows that the enhancement in Pb-Pb collisions (with respect to pp ones) at LHC increases with the number of strange quarks and with centrality, confirming the SPS/RHIC trend; however, the enhancement decreases with increasing center-of-mass energy.

The temperature of chemical freeze out can be extracted combining several particle ratios (including the ones derived from yields of multi-strange baryons), as shown in fig. 5(left) for 0–20% central Pb-Pb collisions at the LHC. The comparison with thermal model [11] calculations indicates a rather low T_{ch} if protons are included, but this appears to be ruled out by the ratios involving multi-strange baryons. If these are included and protons are excluded, a chemical freeze out temperature of 164 MeV (with a chemical

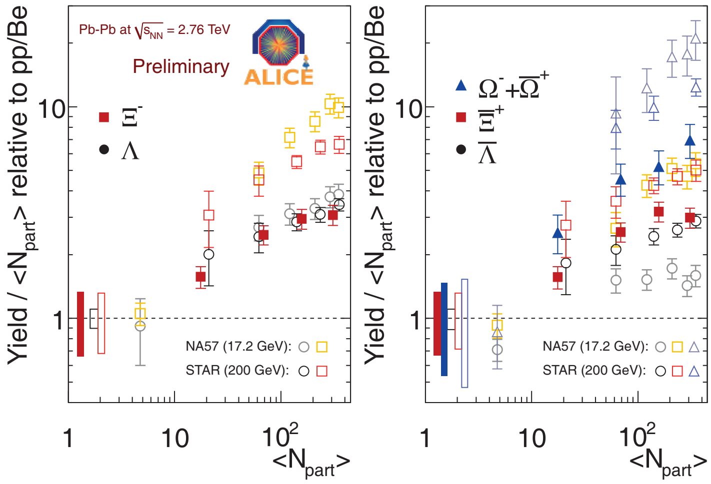

Fig. 4. – Enhancement of multi-strange (anti-)baryon production in Pb-Pb (Au-Au) collisions with respect to pp collisions at SPS, RHIC and LHC.

potential $\mu = 1\,\text{MeV}$) is obtained at LHC, which is close both to the one measured at RHIC and to the critical temperature T_c from Lattice QCD calculations.

2·4. *Parton energy loss in the medium.* – The nuclear modification factor $R_{AA} = \frac{1}{T_{AA}}(\mathrm{d}N_{AA}/\mathrm{d}p_t)/(\mathrm{d}N_{pp}/\mathrm{d}p_t)$ of charged hadrons (see, *e.g.*, [12]), heavy flavour mesons [13] and jets is a powerful tool to test the predicted dependence of the parton energy loss in the medium on their color charge and mass. ALICE has observed a larger suppression of charged hadrons with respect to the one measured at RHIC, with the strongest suppression occurring at $p_t \simeq 6$–$7\,\text{GeV}/c$; R_{AA} then increases for $p_t > 10\,\text{GeV}/c$, with hints of flattening above $30\,\text{GeV}/c$, see fig. 5(right).

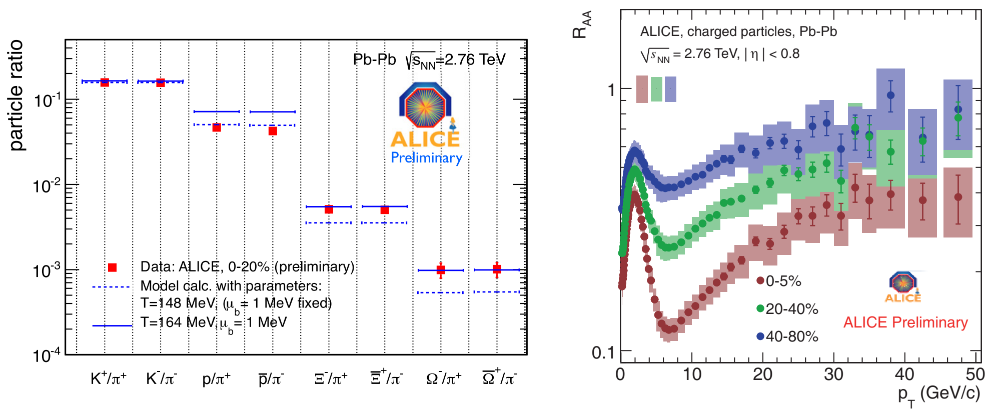

Fig. 5. – Left: Preliminary mid-rapidity particle ratios in 0–20% central Pb-Pb collisions, compared to thermal model calculations. Right: Nuclear modification factor *vs.* p_t for charged hadrons in Pb-Pb collisions, in three centrality classes.

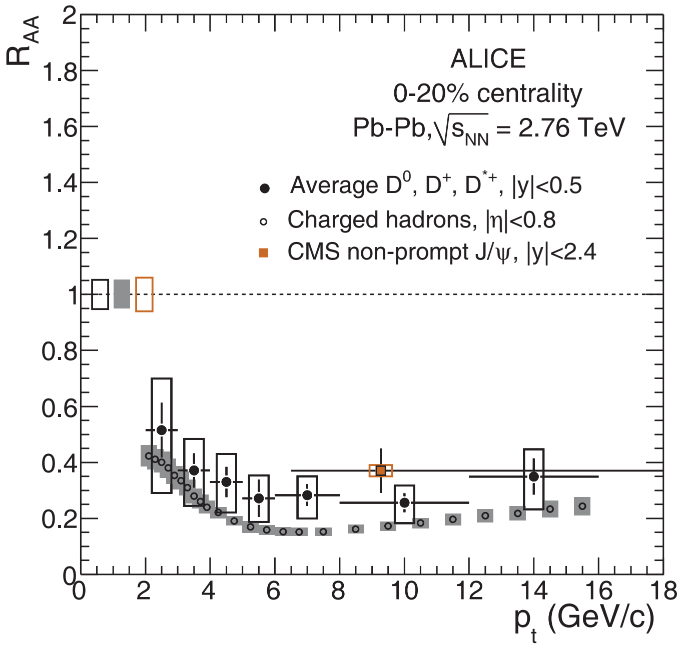

Fig. 6. – D-meson nuclear modification factor (averaged over three species) *vs.* p_t for Pb-Pb collisions, in the 0–20% centrality class. The R_{AA} for charged mesons (dominated by pions) is also shown. The nuclear modification factor for non-prompt J/ψ's at high p_t as obtained by the CMS Collaboration is shown for comparison.

ALICE has recently measured the nuclear modification factor of prompt D mesons [13] in central (0–20%) Pb-Pb collisions, see fig. 6. For $p_t > 5\,\mathrm{GeV}/c$, a suppression of a factor 3-4 is observed for the three species measured (D^0, D^+ and D^{*+} with the respective antiparticles). Comparing to charged hadrons, which in the measured p_t range are dominated by pions, there is an indication for $R^D_{AA} > R^{charged}_{AA}$, in line with models for the radiative energy loss of partons in the hot and dense medium: gluons (which are the main source of pions) are expected to be more suppressed than light quarks, which in turn are expected to be more suppressed than heavy quarks. The result obtained by CMS [14] on non-prompt J/ψ's from B decays is also shown, indicating a lesser suppression for the heavier b quark.

2˙5. *Quarkonia dissociation and regeneration in the medium.* – The J/ψ suppression (already observed at SPS and RHIC energies) and its possible regeneration at LHC energies (due to the much greater number of c quarks produced) is perhaps the most important signature for Quark Gluon Plasma formation in heavy-ion collisions. ALICE has recently released the results [15] on the J/ψ nuclear modification factor as a function of p_t down to $p_t = 0$ in the forward rapidity range ($2.5 < y < 4.0$). The nuclear modification factor, integrated over the 0–80% most central collisions, is $0.545 \pm 0.032(\mathrm{stat.}) \pm 0.084(\mathrm{syst.})$ and does not exhibit a significant dependence on the collision centrality. These features appear significantly different from lower energy measurements. More details are given in [15].

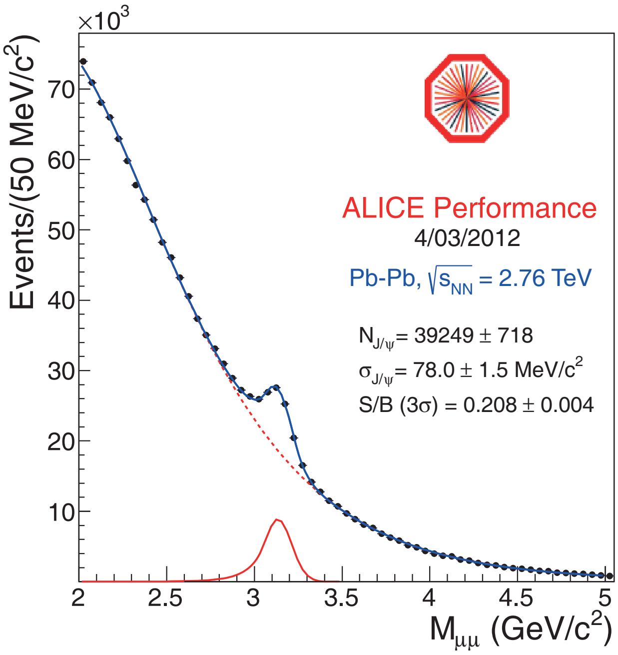

Fig. 7. – J/ψ in the opposite-sign dimuon invariant mass spectra from the 2011 Pb-Pb run.

3. – Conclusions and outlook

The ALICE Collaboration focused in 2011 on the analysis of the first Pb-Pb run at 2.76 TeV of 2010 as well as on the vast amount of pp data collected at 2.76 TeV and 7 TeV in 2010 and early 2011. The main results obtained so far can be summarized as follows: i) a medium with 3 times higher-energy density than RHIC has been observed; ii) a smooth evolution with center-of-mass energy of global events observables has been found, now the Collaboration is looking more differentially into (*e.g.*) higher flow harmonics with identified hadrons and an extended p_t range; iii) a strong suppression of high p_t hadrons with respect to *pp* collisions has been found; iv) the nuclear modification factor R_{AA} of light and heavy quarks is similar; v) the J/ψ at low p_t is less suppressed than at RHIC.

The second Pb-Pb run (Fall 2011) was very successful with an increase of a factor 15 in the collected statistics with respect to the previous year; now the ALICE Collaboration is focusing on analysis of new data (see, *e.g.*, fig. 7, showing the quality of the J/ψ signal collected in the Muon Spectrometer), preparation of the p-Pb run—which in particular will provide a measurement of the cold matter effects relevant for heavy flavours—and on the upgrade programme.

* * *

I am grateful to the organizers of the Rencontres de Physique for giving me the opportunity to present ALICE results on heavy-ion physics and to the ALICE collaborators for their continuous effort in running the experiment and analyzing our data.

REFERENCES

[1] Aamodt K. *et al.* (ALICE Collaboration), *JINST*, **3** (2008) S08002.
[2] Müller B., Schukraft J. and Wyslouch B., *Annu. Rev. Nucl. Part. Sci.*, **62** (2012) 361.
[3] Aamodt K. *et al.* (ALICE Collaboration), *Phys. Rev. Lett.*, **105** (2010) 252301.
[4] Aamodt K. *et al.* (ALICE Collaboration), *Phys. Rev. Lett.*, **106** (2011) 032301.
[5] Aamodt K. *et al.* (ALICE Collaboration), *Phys. Lett. B*, **696** (2011) 328.
[6] Schnedermann E. *et al.*, *Phys. Rev. C*, **48** (1993) 2462.
[7] Shen C. *et al.*, *Phys. Rev. C*, **84** (2011) 044903; see also `arXiv.org:1105.3226` preprint (2011).
[8] Aamodt K. *et al.* (ALICE Collaboration), *Phys. Rev. Lett.*, **105** (2010) 252302.
[9] Abelev B. *et al.* (STAR Collaboration), *Phys. Rev. Lett.*, **97** (2006) 152301.
[10] Abelev B. *et al.* (ALICE Collaboration), *Phys. Lett. B*, **712** (2012) 309.
[11] Andronic A. *et al.*, *Phys. Lett. B*, **673** (2009) 142.
[12] Aamodt K. *et al.* (ALICE Collaboration), *Phys. Lett. B*, **696** (2011) 30.
[13] Abelev B. *et al.* (ALICE Collaboration), *JHEP*, **09** (2012) 112.
[14] Chatrchyan S. *et al.* (CMS Collaboration), *JHEP*, **05** (2012) 063.
[15] Abelev B. *et al.* (ALICE Collaboration), *Phys. Rev. Lett.*, **109** (2012) 072301.

IL NUOVO CIMENTO Vol. 35 C, N. 6 Novembre-Dicembre 2012
DOI 10.1393/ncc/i2012-11357-7

Colloquia: LaThuile12

Heavy-ion physics results from CMS

G. I. Veres(*)
CERN - European Organization for Nuclear Research - Geneva, Switzerland

ricevuto il 7 Settembre 2012

Summary. — This paper summarizes recent experimental results related to heavy-ion collisions from the CMS Collaboration. Global features, like charged particle and transverse-energy density as a function of pseudorapidity, as well as correlations, elliptic flow, and the production of hard probes like isolated photons, Z and W bosons, jets, J/ψ and Υ particles will be presented. Many of these observations are possible for the first time at the LHC, and the CMS experimental apparatus is well suited to conduct detailed studies of hard probes in the recently collected high-luminosity Pb + Pb data.

PACS 25.75.-q – Relativistic heavy-ion collisions.
PACS 25.75.Ag – Global features in relativistic heavy-ion collisions.
PACS 25.75.Bh – Hard scattering in relativistic heavy-ion collisions.
PACS 25.75.Cj – Photon, lepton, and heavy quark production in relativistic heavy-ion collisions.

1. – Introduction

The strong interaction—described by the theory of Quantum Chromodynamics, QCD—is one of the fundamental forces in Nature. At the extremely high energy density of about 1 GeV/fm^3 and at a temperature of 150–180 MeV/k_B, the nuclear matter is predicted to undergo a phase transition, beyond which the relevant degrees of freedom are the quarks and gluons. The only available experimental tools to create these conditions in the laboratory are the collisions of heavy ions, such as Pb nuclei. The present paper is a brief overview of recent results from the CMS Collaboration at the Large Hadron Collider (LHC), based on the first two heavy-ion data-taking periods in 2010 and 2011.

The first indications of the QCD phase transition appeared at the CERN SPS accelerator. The Relativistic Heavy Ion Collider (RHIC) has extended the experimental investigations at the center-of-mass energy per nucleon pair of $\sqrt{s_{NN}} = 0.2$ TeV. At the LHC, in PbPb collisions at $\sqrt{s_{NN}} = 2.76$ TeV it has become possible to use fully

(*) On leave from the Eötvös Loránd University, Budapest.

reconstructed energetic jets, Z and W bosons, isolated high-p_T photons, and Υ mesons, so-called "hard probes" to study the characteristics of the high energy density medium.

The CMS detector is well adapted to measure these hard probes, with its strong, 3.8 T magnetic field, electromagnetic and hadronic calorimeters covering a large pseudorapidity range $|\eta| < 5.2$, high-precision silicon tracking system ($|\eta| < 2.4$), large muon detectors outside the superconducting solenoid and the calorimeter layers and the flexible, two-level trigger system [4]. At very small angles with respect to the beam line, the CASTOR calorimeter and the Zero-Degree Calorimeters (ZDCs) complement the central apparatus.

The high center-of-mass energy and the experimental capabilities make it possible to study a variety of observables, among them the η-distributions of charged particles and transverse energy; the Fourier spectrum of single-particle azimuthal-angle distributions and two-particle correlations; electroweak "candles" like isolated photons and the Z and W bosons. Furthermore, the good dimuon-mass resolution allows one to reconstruct the members of the J/ψ and Υ families separately. Finally, various aspects of the energy loss of hard-scattered partons as they traverse the created medium can be studied: the suppression of high-p_T charged particles, the p_T-imbalance of reconstructed jet pairs as a function of p_T and centrality, and a comparison of jet fragmentation functions in PbPb and pp collisions. Many of these results already utilize the data set collected in 2011.

2. – Bulk observables

The CMS apparatus is capable of detecting particles in a very wide kinematic range. At the low transverse momentum end, charged hadrons down to $p_T \approx 30\,\mathrm{MeV}/c$ have been measured without magnetic field with the pixel layers of the inner tracker system. Simple counting of pixel clusters and reconstructing two-point tracklets were in agreement at the percent level. The measured number of charged particles per unit of pseudorapidity is normalized by the number of nucleons participating in the collision according to the Glauber-model, N_{part}, in each centrality class. The results can be seen in the left panel of fig. 1 [5], compared to various model predictions, including the HIJING event generator with two different gluon shadowing parameters [1], a calculation based on the gluon saturation approach [2], and the DPMJET-III model [3]. The number of particles created in the collision per participant nucleon increases with the total volume of the overlap zone, and the measured particle densities provide constraints on the initial conditions of the quark-gluon matter in any hydrodynamical approach.

The wide pseudorapidity coverage of the CMS calorimeters can be utilized to measure the transverse energy produced in heavy-ion collisions, after corrections for calorimeter energy scale, acceptance, and low-energy particles deflected by the magnetic field.

The collision energy dependence of the normalized transverse-energy distribution, $(\mathrm{d}E_T/\mathrm{d}\eta)/(\langle N_{part}\rangle/2)$ is plotted in the right panel of fig. 1 for central PbPb collisions at $\eta = 0$. Between the RHIC and LHC energies, the amount of transverse energy created in the collision increases more quickly than the logarithm of $s_{_{NN}}$ used to describe data at lower energies. Similarly to the charged particle multiplicity, the energy dependence is better described by $s^n_{_{NN}}$ with $n \approx 2$. Between the top RHIC and LHC energies, the normalized transverse-energy density increases by a factor of 3.3 ± 0.3, while the same increase for the charged particle multiplicity is only 2.35 ± 0.15 [11].

The energy density per unit volume in a central PbPb collision is estimated using the Bjorken-formula [12] to be $15\,\mathrm{GeV/fm}^3$, for a formation time of $1\,\mathrm{fm}/c$ and transverse radius of 7 fm, which is hundred times more than the normal nuclear density.

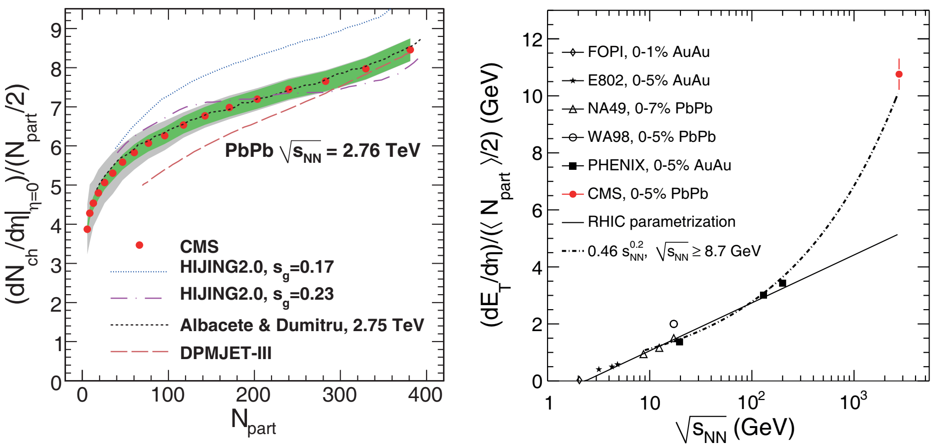

Fig. 1. – Left: normalized charged particle density, $\mathrm{d}N_{ch}/\mathrm{d}\eta/(N_{part}/2)$, compared with model predictions [1-3] as a function of the number of participants, N_{part}, in 2.76 TeV PbPb collisions. Right: normalized transverse-energy density for central collisions at $\eta = 0$ as a function of the center-of-mass energy, compared to data at lower $\sqrt{s_{NN}}$.

The azimuthal anisotropy of the final state charged particles, characterized by the second Fourier coefficient, v_2, was measured as a function of p_T, η and centrality using various methods. The v_2/ϵ ratio, where ϵ is the initial geometrical eccentricity of the set of interacting (participating) nucleons, is expected to scale with the charged particle density normalized by the transverse overlap area. Indeed, the left panel of fig. 2 shows that the relation between the two quantities, that is thought to be related to the shear viscosity to the entropy density ratio of the hydrodynamically evolving system, does not depend on the collision energy between $\sqrt{s_{NN}} = 62.4$ and 2760 GeV [13].

Asymmetries in the azimuthal angle (ϕ) distributions of single particles lead to non-uniform $\Delta\phi$ distributions of particle pairs. If the two particles are distant in terms of pseudorapidity, the latter can be derived from the single-particle distributions using a simple factorization. This observation allows for the extraction of the Fourier-coefficients, $v_2 - v_5$ of the single-particle distributions from long-range ($2 < |\Delta\eta| < 4$) two-particle correlations [14]. These coefficients measured in a given p_T bin of selected particle pairs is presented in the right panel of fig. 2.

3. – Hard probes

Hard scattering processes creating electroweak bosons play an important reference role in the heavy-ion research at LHC, because these particles (γ, Z, W) can be observed without modification by the strongly interacting colored medium. Measurements of the cross sections of isolated photons at high p_T [15], as well as $Z \to \mu^+\mu^-$ [16] and $W^\pm \to \mu^\pm\nu$ [17] processes in PbPb collisions were completed using the CMS electromagnetic calorimeters, tracker and muon systems and the capabilities of measuring the missing transverse momentum, respectively. The production yields of these three particles, normalized by the nuclear overlap function, is consistent with that measured or calculated for pp collisions at the same center-of-mass energy, as can be seen in fig. 3

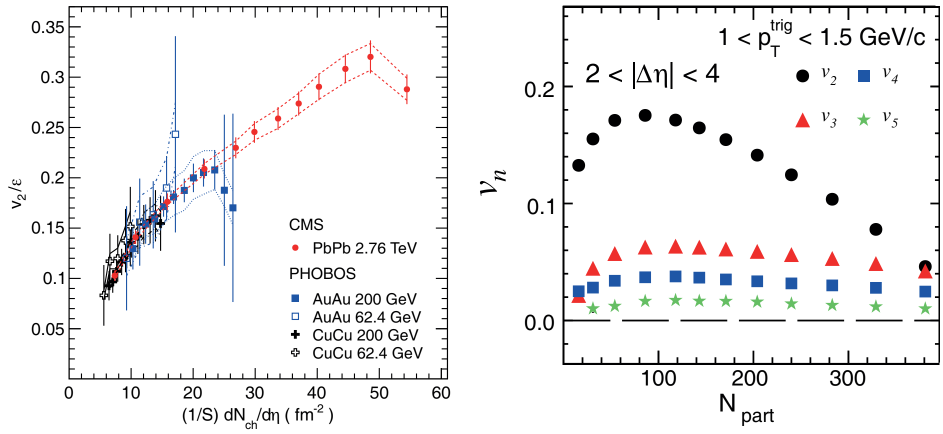

Fig. 2. – Left: eccentricity-scaled v_2 as a function of charged particle density from CMS and PHOBOS. The error bars include both statistical and systematic uncertainties of v_2. The dashed lines represent the systematic uncertainties in the eccentricity determination. Right: the single-particle azimuthal anisotropy harmonics, $v_2 - v_5$, extracted from the long-range ($2 < |\Delta\eta| < 4$) azimuthal dihadron correlations as a function of N_{part} in PbPb collisions at $\sqrt{s} = 2.76\,\mathrm{TeV}$ for $1 < p_T^{assoc} < 3\,\mathrm{GeV}/c$ and $1 < p_T^{trig} < 1.5\,\mathrm{GeV}/c$.

and fig. 5. Different yields of W^+ and W^- particles were observed in PbPb with respect to that in pp collisions, reflecting the different u and d quark content in the proton and neutron and the Z/A ratio of the Pb ion.

The good momentum resolution and precise vertexing capabilities of the CMS tracking system make it possible to statistically separate the promptly produced J/ψ particles, observed via their dimuon decay, from those originating from b-hadron decays, based on the decay length distribution [18]. These particles are expected to be suppressed

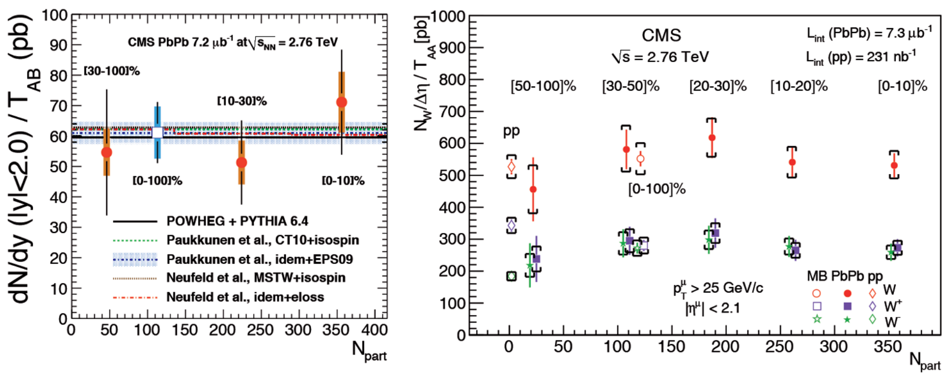

Fig. 3. – Left: the dN/dy of $Z \to \mu^+\mu^-$ per event divided by the nuclear overlap function T_{AB} as a function of N_{part}, compared to theoretical predictions [6-10]. Right: centrality dependence of the $W^\pm \to \mu^\pm\nu$ yields in PbPb and pp collisions. Yields are given for events where the muon falls in the region $|\eta| < 2.1$ and $p_T > 25\,\mathrm{GeV}/c$.

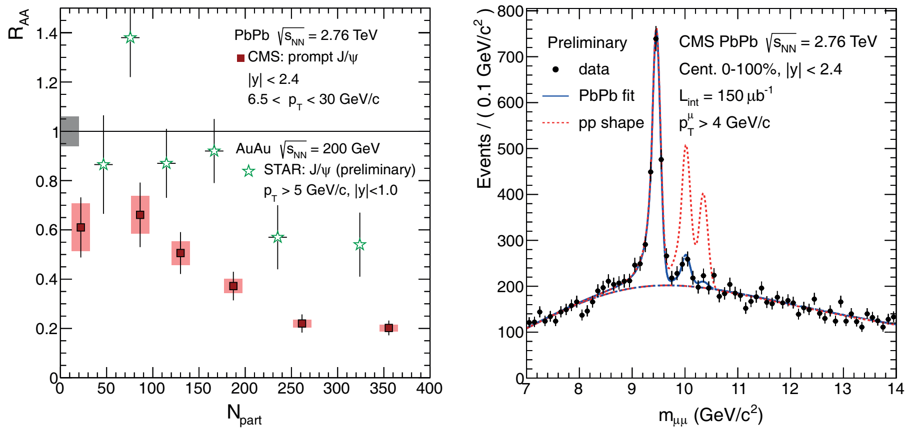

Fig. 4. – Left: R_{AA} of prompt J/ψ *vs.* N_{part} compared to STAR. Right: dimuon invariant-mass distribution from the PbPb data at $\sqrt{s_{NN}} = 2.76\,\mathrm{TeV}$. The blue solid line shows the fit to the PbPb data. The red dashed line shows the shape obtained from the fit to the *pp* data.

in a high-temperature environment due to Debye-screening, as a direct consequence of deconfinement. The J/ψ yield, normalized by the nuclear overlap function and the yield measured in *pp* collisions, which is called the nuclear modification factor, R_{AA}, is presented on the left panel of fig. 4 as a function of N_{part}. The strongest suppression is observed in central PbPb events, exceeding that measured at RHIC in a somewhat different p_T and η range.

The other spectacular observation of quarkonium suppression is illustrated in the right panel of fig. 4, where the $\Upsilon(1S)$, $\Upsilon(2S)$ and $\Upsilon(3S)$ mass peaks are shown in the $\mu^+\mu^-$ invariant mass distribution for both PbPb and *pp* collisions, with the $\Upsilon(1S)$ yields nomalized between the two systems. In PbPb events the excited Υ states are suppressed with respect to *pp* collisions, leading to a similar interpretation as for the J/ψ particles.

Summarizing the present knowledge on the single particle suppression, we can conclude that the production of charged hadrons [19] and J/ψ particles created from b-quark decays are strongly suppressed in central PbPb collisions compared to the *pp* reference, as demonstrated in fig. 5. The left panel compares the CMS measurement of charged particle R_{AA}, extending to $p_T = 100\,\mathrm{GeV}/c$ to lower energy data and various model predictions [20-25], while the right panel summarizes the results on γ, Z, and W production, including b quarks [15-19].

The suppression of particle production at a given p_T is thought to be a consequence of the steeply decreasing p_T distribution of particles combined with the energy loss of hard-scattered partons which fragment into hadrons, as they traverse the hot and dense medium created in the heavy-ion collision. Since this medium inherits an elongated geometrical shape from the nuclear overlap zone in the plane perpendicular to the beam line, the azimuthal asymmetry of high-p_T hadrons should be sensitive to the above mentioned energy loss as a function of path length covered in the hot plasma. Most of the high-p_T hadrons originate from the fragmentation of energetic jets, and thus their azimuthal asymmetry stems from completely different physical processes compared to low p_T, where the hydrodynamical evolution of the system plays a key role.

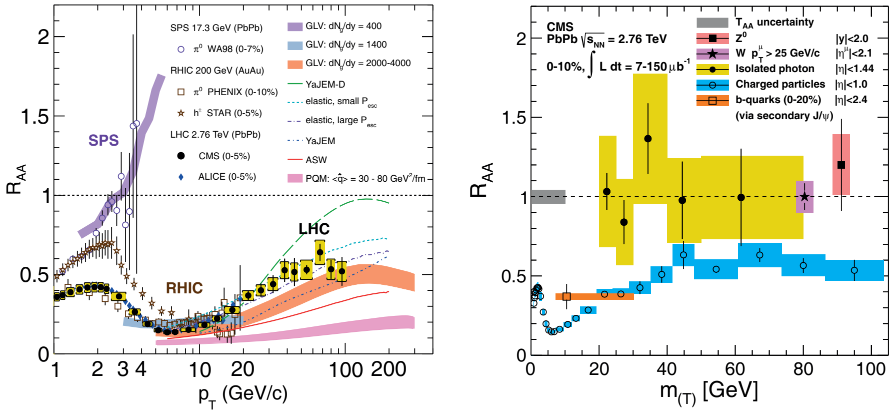

Fig. 5. – Left: the nuclear modification factor R_{AA} in central heavy-ion collisions at three different center-of-mass energies, as a function of p_T, for neutral pions and charged hadrons, compared to theoretical predictions [20-25]. Right: R_{AA} for charged particles in central collisions, along with R_{AA} measurements for photons, Z, W and non-prompt J/ψ particles. For the Z and W results, the data point is plotted at the rest mass of the particle, otherwise they are plotted at the $m_T = \sqrt{m^2 + p_T^2}$ (transverse mass) value. For charged hadrons, pion mass is assumed.

The flexibility of the CMS trigger system allowed for the design and utilization of a unique high-p_T trigger, which selects events that contain a charged particle in the tracker system above a given p_T-threshold. Sufficient number of such collisions were recorded to make the measurement of the v_2 Fourier-coefficient possible up to $p_T \approx 60\,\text{GeV}/c$ [26]. The result is presented in fig. 6 as a function of p_T in six centrality classes, proving that the azimuthal asymmetry stays larger than zero up to about $40\,\text{GeV}/c$.

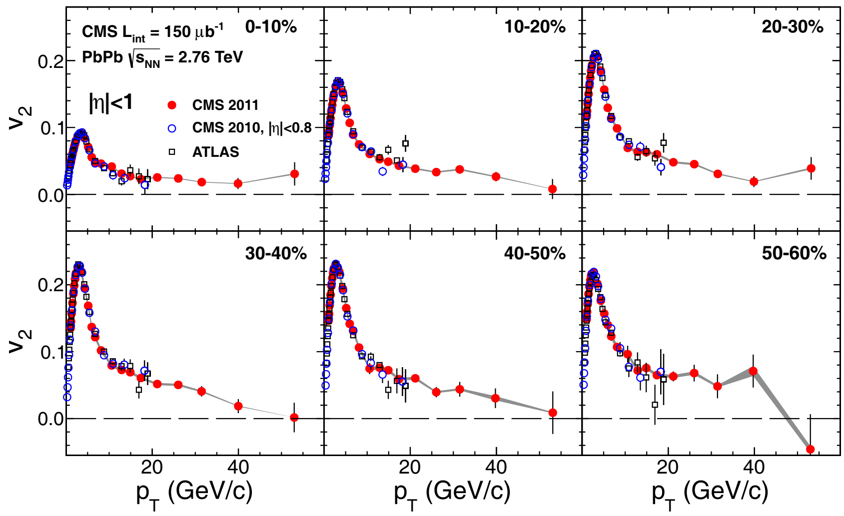

Fig. 6. – The anisotropy harmonics, v_2, as a function of p_T for six centrality ranges in PbPb collisions at $\sqrt{s_{NN}} = 2.76\,\text{TeV}$, measured by the CMS experiment (solid markers). Comparison to results from the ATLAS (open squares) and CMS (open circles) experiments using data collected in 2010 is also shown.

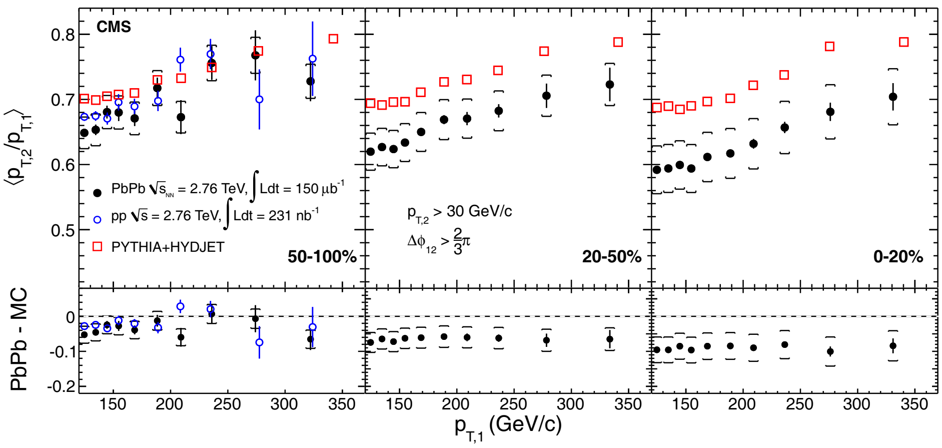

Fig. 7. – Average dijet momentum ratio, $\langle p_{T,2}/p_{T,1}\rangle$, as a function of leading jet p_T for three bins of collision centrality. PbPb data are shown as points, while predictions from the PYTHIA+HYDJET model are shown as squares. In the most peripheral bin, results are compared with pp data (open circles). The difference between the PbPb measurement and the expectations from PYTHIA+HYDJET is shown in the bottom panels.

The CMS calorimeter and tracking system is highly segmented and has a wide η-coverage, and capable to deliver enough detail for jet reconstruction even in the high multiplicity environment of central PbPb collisions. The energy contribution from the underlying event is subtracted using a suitably designed algorithm [27]. This way, experimental investigations of the parton energy loss can be taken to the next, deeper level, bypassing the complications of the jet fragmentation process. Large imbalance between the transverse momenta of the fully reconstructed leading (highest-p_T) and subleading (second highest p_T) jets was observed, as compared to pp collisions, which is the direct consequence of parton energy loss in the medium. The mean transverse-momentum ratio, $\langle p_{T,2}/p_{T,1}\rangle$, of subleading and leading jets reconstructed back-to-back in azimuth (requiring $\Delta\Phi_{1,2} > 2\pi/3$), is plotted in fig. 7, as a function of the transverse momentum of the leading jet, $p_{T,1}$, in three centrality classes. With increasing centrality, the imbalance grows, while the difference between the measured ratio in PbPb collisions and the reference (pp simulation embedded in simulated heavy-ion events) is independent of transverse momentum. On the other hand, the sharp back-to-back correlation of the leading and subleading jet in azimuthal angle, similar to jets in pp collisions, is preserved also in PbPb collisions.

The CMS Collaboration investigated several further aspects of the jet momentum imbalance. The momentum missing from the cone of the subleading jet was found back, carried by low-p_T particles and by particles outside of the jet cone [28]. Furthermore, jet fragmentation functions were studied and compared between heavy-ion and pp collisions, and the hard part of the fragmentation pattern was found to be remarkably similar between jets created in the medium and those propagating in vacuum [29], independently of the imbalance between the two jets. Recently, further evidence for parton energy loss was presented in form of the momentum imbalance of γ-jet events [30]. The high-energy frontier at the LHC has clearly opened up a new set of possibilities to carry out detailed studies of the strongly interacting matter in an extended volume under extreme conditions.

4. – Summary

The CMS experiment has measured the particle and transverse-energy density created in heavy-ion collisions, indicating the presence of strongly interacting medium with an extremely high energy density, and various effects of collective motion, influenced by the geometrical asymmetries of the initial nuclear overlap zone at the moment of the collision. It was shown that the high-p_T photons, Z and W bosons are not modified by the strongly interacting medium created in high-energy heavy-ion collisions. These measurements served as the first steps of the first gamma-jet correlation study at the LHC. On the other hand, a strong suppression of charged hadrons, J/ψ and Υ particles and their excited states was observed. The J/ψ mesons originating from b-quark decays were separated from the prompt ones, and an indirect evidence for b-quark energy loss was provided. The transverse-momentum imbalance of dijet events was studied in detail, indicating a strong parton energy loss in the medium, with no significant modification of the angular correlation between the jets. The momentum imbalance of jets is compensated by low-p_T particles over a large spread in angle with respect to the jet axis, while the fragmentation functions observed in PbPb and pp collisions are similar, and independent of the parton energy loss.

REFERENCES

[1] Deng W.-T., Wang X.-N. and Xu R., *Phys. Lett. B*, **701** (2011) 133.
[2] Albacete J. L. and Dumitru A., arXiv:1101.5161 [hep-ph] (2011).
[3] Bopp F. W., Engel R., Ranft J. and Roesler S., arXiv:0706.3875 [hep-ph] (2007).
[4] Chatrchyan S. *et al.* (CMS Collaboration), *JINST*, **3** (2008) S08004.
[5] Chatrchyan S. *et al.* (CMS Collaboration), *JHEP*, **08** (2011) 141.
[6] Paukkunen H. and Salgado C. A., *JHEP*, **03** (2011) 071.
[7] Eskola K. J., Paukkunen H. and Salgado C. A., *JHEP*, **04** (2009) 065.
[8] Neufeld R. B., Vitev I. and Zhang B. W., *Phys. Rev. C*, **83** (2011) 034902.
[9] Martin A., Stirling W. and Thorne R., *Eur. Phys. J. C*, **63** (2009) 189.
[10] Alioli S., Nason P., Oleari C. *et al.*, *JHEP*, **07** (2008) 060.
[11] Chatrchyan S. *et al.* (CMS Collaboration),
[12] Bjorken J. D. *et al.* (CMS Collaboration), *Phys. Rev. D*, **27** (1983) 140.
[13] Chatrchyan S. *et al.* (CMS Collaboration), arXiv:1204.1409 [nucl-ex] (2012).
[14] Chatrchyan S. *et al.* (CMS Collaboration), arXiv:1201.3158 [nucl-ex] (2012).
[15] Chatrchyan S. *et al.* (CMS Collaboration), *Phys. Lett. B*, **710** (2012) 256.
[16] Chatrchyan S. *et al.* (CMS Collaboration), *Phys. Rev. Lett.*, **106** (2011) 212301.
[17] Chatrchyan S. *et al.* (CMS Collaboration), arXiv:1205.6334 [nucl-ex] (2012).
[18] Chatrchyan S. *et al.* (CMS Collaboration), *JHEP*, **05** (2012) 063.
[19] Chatrchyan S. *et al.* (CMS Collaboration), *Eur. Phys. J. C*, **72** (2012) 1945.
[20] Dainese A., Loizides C. and Paic G., *Eur. Phys. J. C*, **38** (2005) 461.
[21] Vitev I. and Gyulassy M., *Phys. Rev. Lett.*, **89** (2002) 252301.
[22] Vitev I., *J. Phys. G*, **30** (2004) S791.
[23] Salgado C. A. and Wiedemann U. A., *Phys. Rev. D*, **68** (2003) 014008.
[24] Armesto N., Dainese A., Salgado C. A. *et al.*, *Phys. Rev. D*, **71** (2005) 054027.
[25] Renk T. *et al.*, *Phys. Rev. C*, **84** (2011) 014906.
[26] Chatrchyan S. *et al.* (CMS Collaboration), arXiv:1204.1850 [nucl-ex] (2012).
[27] Chatrchyan S. *et al.* (CMS Collaboration), *Phys. Lett. B*, **712** (2012) 176.
[28] Chatrchyan S. *et al.* (CMS Collaboration), *Phys. Rev. C*, **84** (2011) 024906.
[29] Chatrchyan S. *et al.* (CMS Collaboration), arXiv:1205.5872 [nucl-ex] (2012).
[30] Chatrchyan S. *et al.* (CMS Collaboration), arXiv:1205.0206 [nucl-ex] (2012).

IL NUOVO CIMENTO Vol. 35 C, N. 6 Novembre-Dicembre 2012
DOI 10.1393/ncc/i2012-11358-6

Colloquia: LaThuile12

Recent results on QCD and forward physics from the CMS Collaboration

R. Arcidiacono on behalf of the CMS Collaboration
Università del Piemonte Orientale and INFN - Torino, Italy

ricevuto il 7 Settembre 2012

Summary. — A selection of recent results on QCD, diffraction and exclusive processes from the CMS experiment at LHC are here presented. The measurements refer to data which have been collected in 2010, during proton-proton collisions at the center-of-mass energy of $\sqrt{s} = 7\,\text{TeV}$. The results rely on excellent performance of the tracking systems as well as on unprecedented calorimetry pseudo-rapidity coverage.

PACS `12.38.Qk` – Quantum chromodynamics: Experimental tests.
PACS `13.85.-t` – Hadron-induced high- and super-high-energy interactions (energy $> 10\,\text{GeV}$).

1. – Introduction

LHC is the highest-energy proton-proton collider and, at the same time, the machine where the lowest parton momentum fraction, ξ, can be achieved, allowing the exploration of new regions of the parton dynamics phase space. This machine provides excellent and unique opportunities to tune Monte Carlo generators and test the validity of QCD and Standard Model predictions at high energy, as well as the possibility to study rare processes. All the measurements here presented make use of the data collected in 2010, during proton-proton collisions at the center of mass energy of $\sqrt{s} = 7\,\text{TeV}$. For most of them, the low pile-up conditions characterizing the 2010 data taking represent the best environment to perform precision tests of QCD observables and forward physics processes.

2. – The CMS detector

The CMS detector main component is a 6 m diameter, 13 m long solenoidal magnet, operated to generate a 3.8 T magnetic field. Pixel and silicon strips tracking detectors are located inside the solenoid, with a pseudo-rapidity $|\eta| < 2.5$ coverage. Always inside the solenoid and surrounding the tracking systems, there are a lead tungstate crystal electromagnetic calorimeter (ECAL), and a brass-scintillator hadronic calorimeter (HCAL), covering $|\eta| < 2.9$ and < 3.0 regions, respectively. The pseudo-rapidity is defined as $\eta = -\log[\tan(\theta/2)]$, where θ is the polar angle of the particle with respect to the beam axis.

Outside the solenoid and embedded in the return yoke of the magnet, there are several layers of muon chambers composed by drift tubes, resistive plate chambers and cathode strip chambers. They form a high resolution and redundant muon detection system.

CMS is also equipped with Cerenkov calorimeters in the forward region, characterized by a challenging environment due to the limited space and high radiation levels. The hadronic forward calorimeter covers the range $2.9 < |\eta| < 5.2$, the CASTOR calorimeter, located on the minus side, covers the range from 6.6 to 5.2, and the Zero-Degree calorimeter extends the rapidity coverage beyond 8.1 (for neutral particles).

A detailed description of CMS can be found in [1].

3. – QCD results

Among the several measurements which are of great interest as QCD tests and QCD model tunings, we presents the results obtained for the total (visible) proton-proton (pp) inelastic cross section at $\sqrt{s} = 7\,\text{TeV}$, measured with two independent methods covering different phase space, and for the Underlying Event (UE) activity. Both measurements are important for precision tests of Standard Model processes and new physics searches.

3˙1. *Inelastic proton-proton cross section measurement.* – CMS has performed the measurement of the visible inelastic proton-proton cross section with two independent methods that make use of the central tracking system and of the hadronic forward calorimeters [2, 3]. The calorimeter-based technique is especially sensitive to low-mass states, boosted along the beam line, but might miss central diffractive events, while the track method accounts for the events with central activity and does not cover high rapidity events.

The track-based method makes use of the pile-up events (interactions which occur at the same time of a given triggered bunch crossing) distributions, present during standard 2010 data taking, and relies on the high performance of the tracking system. The technique is the following: in single-μ events, the distribution of extra vertexes is measured, in bins of instantaneous luminosity, separately for events having between one and nine vertexes; the distributions obtained are corrected for the vertex reconstruction efficiency; the visible cross section σ_{pp} is derived by fitting the corrected vertex distributions, assuming that the probability of having n pile-up events is given by the Poisson law:

$$P(n) = \frac{(L \cdot \sigma_{pp})^n}{n!} e^{-L\cdot\sigma} \tag{1}$$

as a function of the instantaneous luminosity L.

This technique is repeated for three different categories of visible events, characterized by having at least 2, 3 or 4 tracks with $|\eta| < 2.4$ and $p_T > 200\,\text{MeV}$. For each category, the visible cross section measurement is referred to the corresponding hadron-level definition which requires at least 2, 3 or 4 generated charged particles with $|\eta| < 2.4$ and $p_T > 200\,\text{MeV}$. The acceptance and reconstruction efficiency correction is derived from the CMS detector simulation and it is totally model-independent. Figure 1 shows

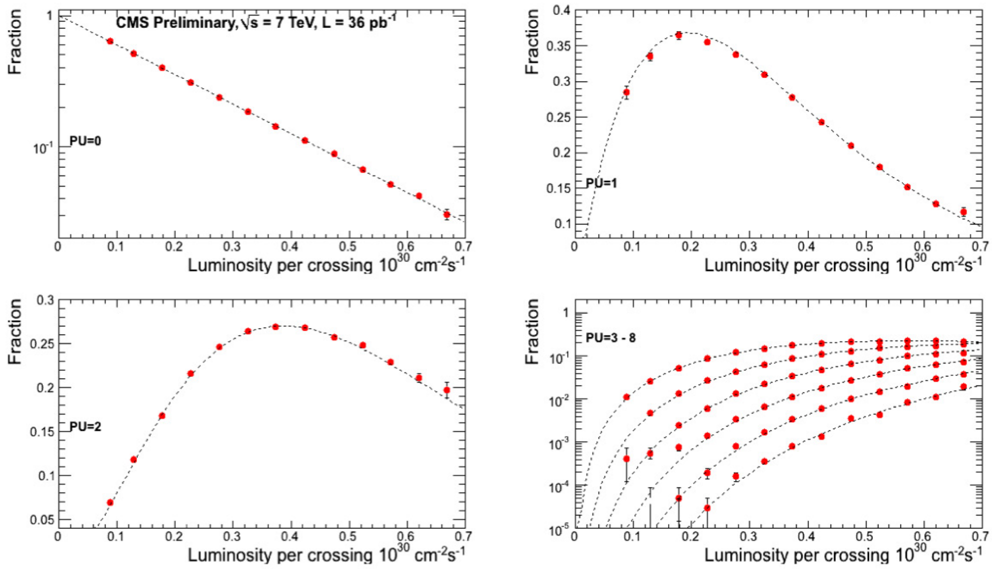

Fig. 1. – Fraction of events with > 1 track with pile-up events $= 0$–8 as a function of luminosity. The dotted lines are Poisson fits.

the comparison of the distribution of vertexes in the data (for events with at least two tracks) and in the MC, as a function of the instantaneous luminosity, for pile up from 0 to 8. The main source of systematic uncertainty is the error on the CMS luminosity determination, which is 4%. The systematic checks performed include the usage of a different dataset, the study of dependency upon the fit parameters, vertex reconstruction quality and efficiency corrections.

The measured values of σ_{pp}, for events with at least 2, 3 or 4 charged particles with $|\eta| < 2.4$ and $p_T > 200\,\text{MeV}$, and their systematic errors are

$$\begin{aligned}\sigma_{pp}(> 1\text{track}) &= [58.7 \pm 2.0\ (\text{syst}) \pm 2.4\ (\text{lum})]\ \text{mb},\\ \sigma_{pp}(> 2\text{tracks}) &= [57.2 \pm 2.0\ (\text{syst}) \pm 2.4\ (\text{lum})]\ \text{mb},\\ \sigma_{pp}(> 3\text{tracks}) &= [55.4 \pm 2.0\ (\text{syst}) \pm 2.4\ (\text{lum})]\ \text{mb}.\end{aligned}$$

In the HF-based method, the number of pp collisions which deposit at least $E = 5\,\text{GeV}$ in either of the HF calorimeters are counted. The threshold of 5 GeV is used to reject a large part of the detector noise still selecting pp collisions with high efficiency. The analysis is performed using events triggered by the Zero-Bias condition (LHC colliding beams in the given bunch crossing), collected during the low luminosity runs with pile up probability ranging between 0.7% and 12%. The number of true pp collisions, which are proportional to the cross section to be measured, are obtained by correcting the measured counting for the selection efficiency, evaluated with Monte Carlo studies, the pile up probability and the detector noise, measured in data with dedicated triggers.

At generator level, the HF activity requirements correspond to selecting events where at least one proton looses more than a fraction $\xi = 5 \times 10^{-6}$ of its momentum. The variable ξ is also defined as $\xi = M_X^2/s$, where s is the squared center-of-mass energy and

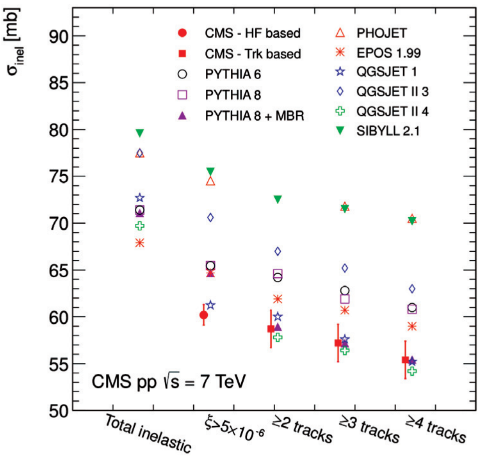

Fig. 2. – Comparison between the CMS measurements of the inelastic *pp* cross section for the four different final states and the predictions of several Monte Carlo models. Monte Carlo predictions have a common uncertainty of 1 mb (not shown).

M_X is the mass of the higher system in the collision products, which is separated from the rest by the largest rapidity gap in the event (for diffractive events ξ is the fraction of momentum lost by the outgoing proton).

The measured visible cross section for events with $\xi > 5 \times 10^{-6}$ is

$$\sigma_{pp}(\xi > 5 \times 10^{-6}) = [60.2 \pm 0.2 \text{ (stat)} \pm 1.1 \text{ (syst)} \pm 2.4 \text{ (lum)}] \text{ mb},$$

where the systematic uncertainty takes into account the studies performed on selection efficiency, contamination from lower ξ region, HF energy threshold, detector noise effects.

Figure 2 compares the four CMS results with the predictions of several models, from Pythia6, Pythia8 tand Phojet as well as three models, based on the same Regge-Gribov phenomenology as Phojet but with different implementations of various model ingredients, commonly used in cosmic ray physics (Qgsjet, Sybill and Epos).

Phojet and Sybill overestimate the cross section by more than 20%, Epos, Qgsjet (Q-II-03), Pythia6 and Pythia8 tunes are 10% above the measured cross sections, while Qgs01 and Qgsjet (Q-II-04) agree within one standard deviation of the data points.

3˙2. *Underlying event measurements*. – In hadron-hadron scattering the underlying event (UE) is defined as all the processes which can be attributed to the hadronization of the partons involved in the hardest scatter. The underlying event is thus composed by initial- and final-state radiations, the particles produced by the multiple parton interactions (MPI) and the beam-beam-remnants (BBR) resulting from the hadronization of the partonic constituents that did not participate in other scatterings. It is important to measure and model correctly the underlying event for the precision measurements of Standard Model processes and the search for new physics at high energies.

To define observables which are sensitive to the UE activity, after having identified the direction of the leading track or jet (reflecting the hard scatter parton direction), charged particles are categorized according to their azimuthal distance $\Delta\phi$ w.r.t the leading object. The particle production in the away region ($|\Delta\phi| > 120°$) is expected to be dominated by the recoiling partons balancing the hard scatter whereas the transverse region ($60° < |\Delta\phi| < 120°$) should be the best for the study of the underlying event. The strength of the UE activity is measured in terms of the average charged-particle multiplicity and the average scalar sum of p_T of the charged particles, expressed as density dividing by the area of the considered $\eta \times \phi$ space.

CMS has performed the measurement of the underlying event activity at $\sqrt{s} = 0.9$ and 7 TeV [4,5], in minimum bias events where the hard scatter direction is identified by the leading track-jet (highest p_T object formed using a jet algorithm applied to reconstructed tracks). The track-jet p_T also defines the scale of the event. A strong increase of the UE activity in the transverse region is observed with increasing leading track-jet p_T. In the 7 TeV data, the fast rise is followed by a plateau region, above 8 GeV/c, with nearly constant multiplicity and small Σp_T^{CH} increase, indicating that particle production due to MPI saturates. A strong growth in hadronic activity is also observed as a function of the center-of-mass energy. Several tunes of Pythia6 and Pythia8 have been compared to the measurements, with a good description of most distributions at 7 TeV and of the dependence from 0.9 to 7 TeV provided by the Z1 tune.

A complementary method to study the underlying event is the one using the well-known Drell-Yan di-muon final state $q\bar{q} \to \mu\mu$, with the di-muon invariant mass in the Z mass range ($60\,\mathrm{GeV} < m_{\mu\mu} < 120\,\mathrm{GeV}$) [6]. In this process it is possible to separate very well the contribution due to the primary hard scatter and the background contamination level is very low. The average charged-particle multiplicity density and the average Σp_T^{CH} density are studied in the three distinct topological regions, away, transverse and towards, defined with respect to the resulting direction of the di-muons system, as a function of di-muon invariant mass and transverse p_T. After excluding the muons of the DY event, the activity in the transverse region is found to be higher than the activity in the towards region due to the spill-over contribution from the hadronic recoil activity in the away region, as shown in fig. 3. The UE activity shows a small growth as a function of $p_T^{\mu\mu}$ mainly due to the increase of radiations, combined with a saturated MPI contribution as the scale of the hard process is high ($\sim M_Z$). These measurements have been compared to predictions of various Pythia tunes, Pythia6 Z1, Pythia6 DW and Pythia8 4C. These models differ in the PDF description, in the implementation of initial and final state radiations, fragmentation and the MPI. The average Σp_T^{CH} density is described well by the Pythia6 Z1 tune with a maximum discrepancy of 10% at small values of $p_T^{\mu\mu}$, whereas the average charged particle density is in agreement with the prediction of Pythia6 Z1 and DW. Pythia8 4C predictions show good agreement with the data only at small $p_T^{\mu\mu}$.

4. – Measurement of hard diffraction at LHC

Evidence of hard diffraction at the LHC has been observed in events associated to W and Z boson production with large rapidity gaps (LRG) [7]. In particular, a large asymmetry in the signed pseudo-rapidity (particle charge $\times|\eta|$ distribution) of the W and Z-decay leptons is observed. This asymmetry is well described by the prediction of the POMPYT generator. The diffractive component is determined to be $50.0 \pm 9.3(\mathrm{stat.}) \pm 5.2(\mathrm{syst.})\%$ and provides the first evidence of diffractive W/Z production at the LHC.

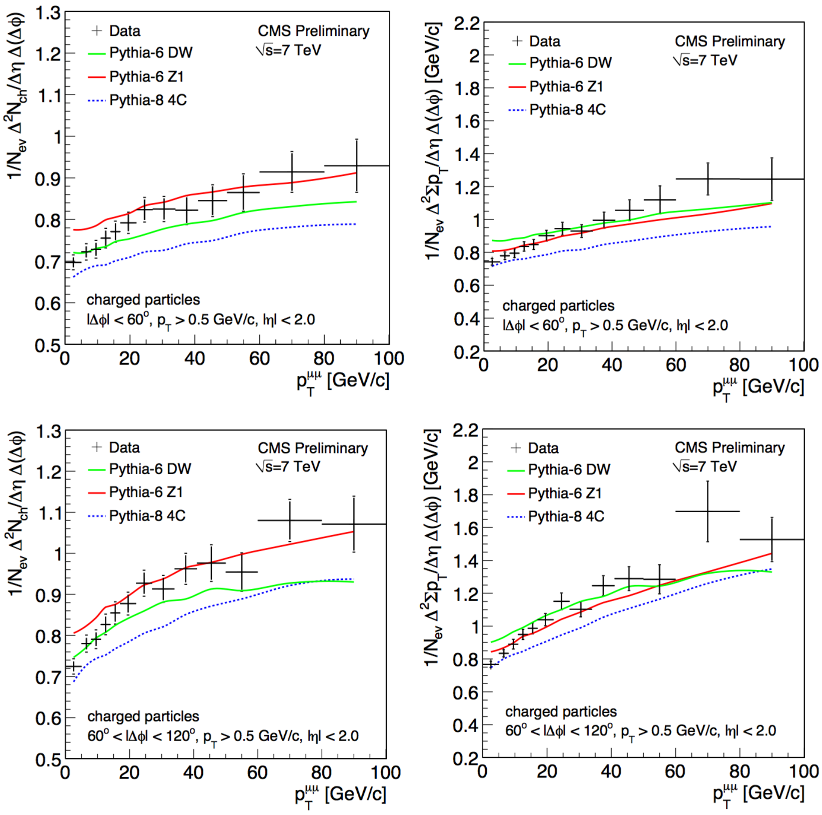

Fig. 3. – Plots on the top (bottom) row show the average charged particle multiplicity and Σp_T^{CH} densities as a function of $p_T^{\mu\mu}$ in the towards (transverse) region, as measured in DY di-muon events after having excluded the two muons.

Another recent result, based on an integrated luminosity of $2.7\,\mathrm{nb}^{-1}$ collected in 2010 with very low pile up conditions, refers to the measurement of single-diffractive di-jet events [8]. The events are selected requiring two jets with transverse momentum $p_T > 20\,\mathrm{GeV}$ in the range $|\eta| < 4.4$. The differential cross section for di-jet production is shown in fig. 4 as a function of the reconstructed ξ, a variable that approximates the fractional momentum loss of one of the scattered protons in single diffractive pp collisions. The results are compared to the predictions of diffractive and non-diffractive Monte Carlo models. The low-ξ events are dominated by diffractive di-jet production.

5. – Exclusive processes at LHC

In central exclusive productions, *i.e.* $pp \to p + X + p$, the colliding protons remain intact with small transverse momentum after an interaction and all the transferred energy goes into a central color singlet system, which is fully measured. No other particles are produced in the interaction and large rapidity gaps are present. Three main types of exclusive process are QED $\gamma\gamma$ interaction (*e.g.*, exclusive $\mu^+\mu^-$, e^+e^- production), γIP fusion (*e.g.*, exclusive Υ production) and IPIP exchange (*e.g.*, exclusive $\gamma\gamma$ or Higgs boson

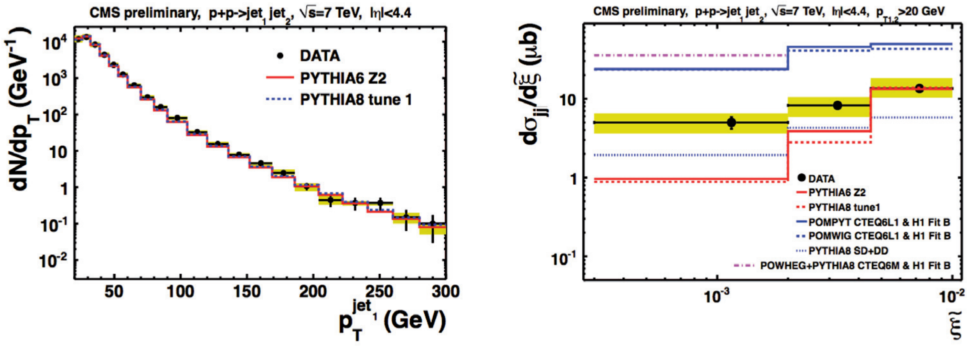

Fig. 4. – On the left: transverse-momentum distribution of the first—highest p_T—jet for data (black points) and non-diffractive MC generators (PYTHIA6 Z2 and PYTHIA8 tune 1). On the right: differential cross section for di-jet events as a function of reconstructed ξ. The predictions of non-diffractive (PYTHIA6 Z2 and PYTHIA8 tune 1) and diffractive (POMPYT SD, POMWIG SD and PYTHIA8 SD+DD) MC generators are also shown.

production), where IP denotes a pomeron. Recent results on exclusive $\gamma\gamma$ production of $\mu^+\mu^-$, e^+e^-, and on the double Pomeron exchange production of $\gamma\gamma$ final states are here presented.

5˙1. *Exlcusive di-muon events.* – A measurement of the exclusive two-photon production of muon pairs, $pp \to p + \mu^+\mu^- + p$ has been performed on the complete 2010 dataset of $40\,\mathrm{pb}^{-1}$ [9]. This QED process has small theoretical uncertainties and striking kinematic distributions, which make it an attractive candidate for absolute calibration of luminosity of pp collisions. Events are selected requiring to have one vertex with only two tracks (muons) associated, within 2 mm; both muons transverse momentum $p_T > 4\,\mathrm{GeV}$ and located in the pseudo-rapidity region $|\eta| < 2.1$. Moreover the di-muon invariant mass has to be greater than 11.5 GeV, to remove the contribution from exclusive photoproduction of upsilon mesons. The exclusivity condition is imposed only on the primary vertex, using the tracking system only. For muon pairs thus selected, a fit to the $p_T(\mu^+\mu^-)$ distribution results in a measured partial cross section of $\sigma = [3.38^{0.58}_{-0.55}(\mathrm{stat.}) \pm 0.16(\mathrm{syst.}) \pm 0.14(\mathrm{lumi})]$ pb. The ratio to the predicted value is $0.83^{0.14}_{0.13}(\mathrm{stat.}) \pm 0.04(\mathrm{syst.})$. The characteristic distributions of the muon pairs produced via $\gamma\gamma$ fusion, such as the muon acoplanarity, the muon pair invariant mass and transverse momentum, are well described by the full detector simulation using the LPAIR event generator.

5˙2. *Search for exclusive di-photon/di-electron events.* – Central exclusive $\gamma\gamma$ and e^+e^- events have been studied in a data sample corresponding to an integrated luminosity of $36\,\mathrm{pb}^{-1}$ [10]. Since an overlapping inelastic pp interaction, in the same beam crossing, would spoil the exclusivity condition and make the exclusive interaction unobservable, only beam crossings with single interactions (no pile-up) are used in this analysis.

The exclusive $\gamma\gamma$ (e^+e^-) event signature requires two reconstructed photon candidates (one positron and one electron candidates), each with transverse energy $E_T > 5.5\,\mathrm{GeV}$ and pseudo-rapidity $|\eta| < 2.5$, and no other particles detected in the range $|\eta| < 5.2$. The incident protons stay intact, or diffractively dissociate, escaping along the beam direction

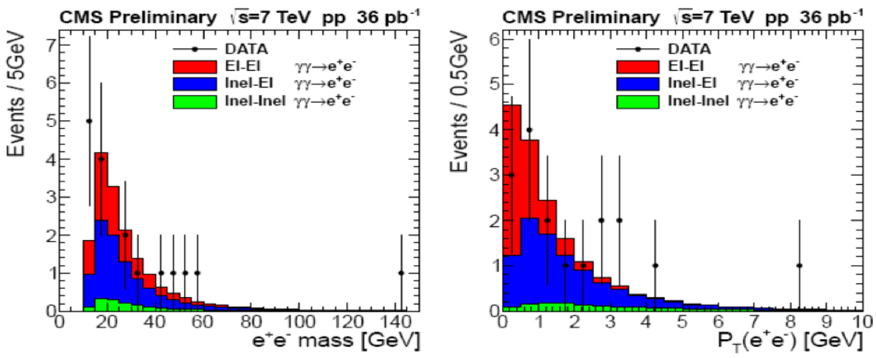

Fig. 5. – Di-electron invariant mass (left) and p_T distributions (right) for the exclusive e^+e^- events, compared to the LPAIR Monte Carlo predictions for the exclusive (El-El) and semi-exclusive (Inel-El, Inel-Inel) categories.

without being detected. The detector noise and beam background have been studied in zerobias and unpaired bunches events.

No di-photon candidate satisfies all the selection criteria. An upper limit on the cross section of $pp \to p + \gamma\gamma + p$ with $E_T(\gamma) > 5.5\,\text{GeV}$ and $|\eta| < 2.5$ is set at 1.30 pb with 95% confidence level.

For the di-electron channel, 17 e^+e^- candidates on a background of 0.84 ± 0.28 (stat.) events are observed. The theoretical QED prediction evaluated with the event generator LPAIR is 16.5 ± 1.7(theo.) $\pm\, 1.2$(syst.) events. The semi-exclusive e^+e^- having one or both protons dissociated and escape undetected are here considered as signal. Figure 5 shows the di-electron invariant mass and the p_T distributions, in good agreement with the QED predictions.

REFERENCES

[1] CMS Collaboration, *JINST*, **03** (2008) S08004.
[2] CMS Collaboration, *Measurement of the inelastic pp cross section at* $\sqrt{s} = 7\,\text{TeV}$ *with the CMS detector, Physics Analysis Summary* FWD-11-001 (2011).
[3] CMS Collaboration, *Measurement of the inelastic pp cross section at* $\sqrt{s} = 7\,\text{TeV}$, *Physics Analysis Summary* QCD-11-002 (2011).
[4] CMS Collaboration, *Eur. Phys. J. C*, **70** (2010) 555.
[5] CMS Collaboration, *JHEP*, **09** (2011) 109.
[6] CMS Collaboration, *Measurement of the Underlying Event activity in the Drell-Yan process in proton-proton collisions at* $\sqrt{s} = 7\,\text{TeV}$, *Physics Analysis Summary* QCD-10-040 (2010).
[7] CMS Collaboration, *Forward energy flow and central track multiplicities in W and Z boson events at* $\sqrt{s} = 7\,\text{TeV}$ *pp collisions, Physics Analysis Summary* FWD-10-008 (2010).
[8] CMS Collaboration, *Evidence for hard-diffractive dijet production in pp collisions at* $\sqrt{s} = 7\,\text{TeV}$, *Physics Analysis Summary* FWD-10-004 (2010).
[9] CMS Collaboration, *Measurement of exclusive* $\gamma\gamma \to \mu^+\mu^-$ *production at* $\sqrt{s} = 7\,\text{TeV}$, *Physics Analysis Summary* FWD-10-005 (2011).
[10] CMS Collaboration, *Search for central exclusive* $\gamma\gamma$ *production and observation of central exclusive* e^+e^- *production in pp collisions at* $\sqrt{s} = 7\,\text{TeV}$, *Physics Analysis Summary* FWD-11-004 (2011).

IL NUOVO CIMENTO Vol. 35 C, N. 6 Novembre-Dicembre 2012
DOI 10.1393/ncc/i2012-11359-5

Colloquia: LaThuile12

QCD results using jets and photons in ATLAS

D. López Mateos on behalf of the ATLAS Collaboration
Harvard University - Cambridge, MA 02138, USA

ricevuto il 7 Settembre 2012

Summary. — Measurements of jet and photon production performed with data collected during 2010 with the ATLAS detector at the LHC are surveyed. They are compared to leading-order and next-to-leading-order calculations, providing a breadth of tests of QCD at a new energy regime. Agreement is generally found with the most sophisticated calculations, except in regions of phase space where the calculations are expected to reach certain limitations. For those observables for which they are available, next-to-leading-order calculations matched to parton showers are shown to exhibit a large dependence on the choice of parton shower tune, comparable in size to the estimated uncertainties of the perturbative calculations.

PACS 12.38.Qk – Quantum chromodynamics: Experimental tests.
PACS 13.85.Qk – Inclusive production with identified leptons, photons or other non-hadronic particles.
PACS 13.87.-a – Jets in large-Q^2 scattering.

1. – Introduction

The study of the production of jets and photons in proton-proton collisions encompasses a wide variety of key observables in high-energy physics. Photon and jet production can be used to measure the strong coupling constant, obtain information about the proton and photon structures, and provide constraints and develop tools for searches of physics beyond the Standard Model. In what follows, some of the measurements of photon and jet production performed up to date with the ATLAS detector at the LHC are shown and discussed, as well as comparisons to a variety of perturbative QCD calculations combined with models of non-perturbative effects. Photon and jet reconstruction are also discussed, since they constitute a large component of the experimental uncertainties in the measurements presented.

2. – Photon and jet reconstruction and performance

The ATLAS calorimeters are used primarily in the reconstruction and identification of photons and jets [1]. A liquid-argon/lead electromagnetic (EM) calorimeter with fine segmentation in pseudorapidity (η) and ϕ, and additional segmentation along the direction of the shower development, covers the pseudorapidity range of $|\eta| < 3.2$. Hadronic calorimeters, built using scintillating tiles and iron for $|\eta| < 1.7$ and liquid argon and copper in the end-cap ($1.5 < |\eta| < 3.2$), complement the EM calorimeter. Forward calorimeters extend the coverage to $|\eta| = 4.9$, and are used only for jet reconstruction in this document.

2·1. *Photon reconstruction and identification.* – Photons are reconstructed using the full longitudinal segmentation of the EM calorimeter. Photon identification is performed using properties of the longitudinal and transverse shower development, and includes the rejection of showers that leak into the hadronic calorimeter. For the tight identification used in the measurements presented, cuts are performed on nine shower shape variables. Observed differences between these variables in data and Monte Carlo simulation are considered in the estimation of the systematic uncertainties in purity and efficiency measurements. An additional isolation cut is performed on the energy deposited in a cone of radius 0.4 in $[\eta, \phi]$ around the photon candidate to reduce fakes in the analyses discussed in this document.

One of the dominant systematic uncertainties in measurements with photons arises from uncertainties in the measurement of photon purities. One of the methods used for this measurement is illustrated at the top of fig. 1a. The measurement exploits the isolation cut and the removal of some of the tight selection requirements to build three control regions with enhanced background contributions. The estimate of the number of background events in the signal region is obtained as the ratio of events in regions C to D, normalized by the number of background events found in region B. The method includes corrections for signal contamination in the control regions. The bottom of the figure represents an extension of the method needed for diphoton measurements, where the purity of the subleading photon is estimated with a similar approach when the leading photon falls in the signal region.

Measured purities have been cross-checked with several methods, including one illustrated in fig. 1b, where the isolation variable across regions A and B is considered as a continuous variable and a template fit is performed to obtain the background and signal contributions. The background templates are obtained in regions C and D. Results are consistent for all methods used.

Systematic uncertainties in the purity estimates arise from the degree of correlations between the different regions, differences in the shower shapes between data and Monte Carlo simulations, and definition of the C and D regions, among other less significant effects. The purity estimate obtained for one of the prompt photon measurements presented is shown in fig. 1c with its associated systematic uncertainties.

2·2. *Jet reconstruction and systematic uncertainties in the jet energy scale.* – Calorimeter jets are reconstructed using the anti-k_t jet algorithm [4] with resolution parameters $R = 0.4, 0.6$ and a four-momentum recombination scheme. Jets are constructed with topological clusters at the electromagnetic scale and calibrated with a scheme designed to bring the calorimeter jet energy to the energy of the truth particle jets on average [5]. Truth particle jets are reconstructed using the same algorithm as calorimeter jets but using as input stable particles with a lifetime longer than 10 ps after hadronization.

Systematic uncertainties in the jet energy scale are estimated propagating to jets measurements of the response of single particles. The measurements have been performed

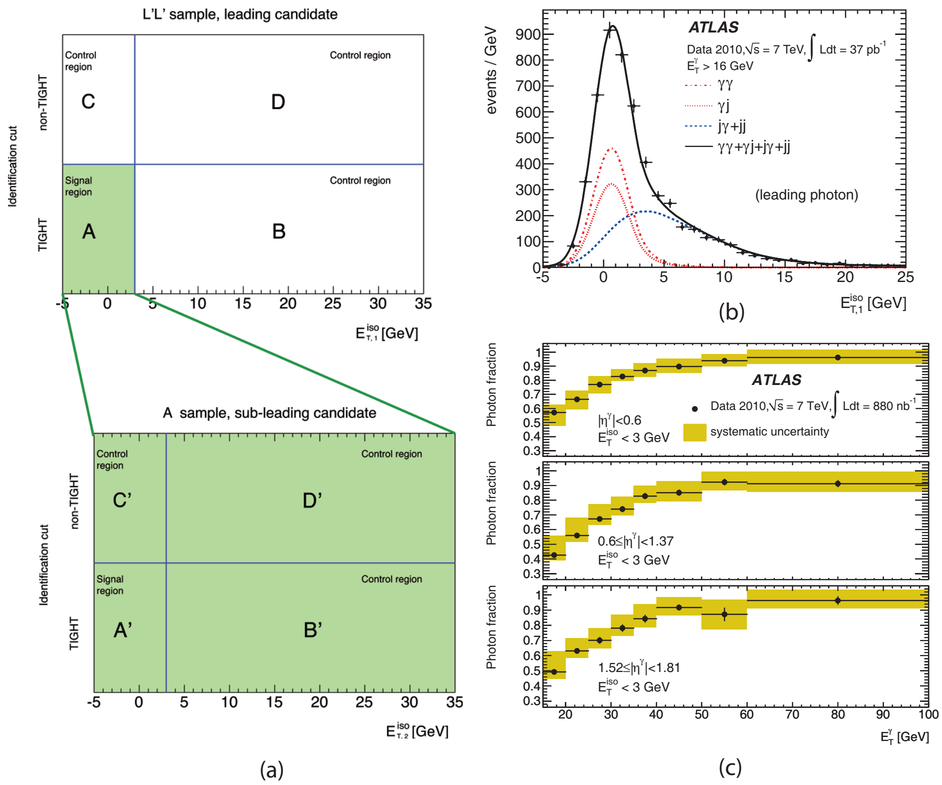

Fig. 1. – (a): Illustration of control regions built to estimate the purity of the photon selection in the diphoton analysis [2]. (b): Template fit to the photon isolation in the tight region for the diphoton cross section measurement [2]. Note that the isolation energy can be negative due to detector resolution effects. (c): Measured purities for different photon rapidity regions as a function of the photon p_{T} for the prompt photon production measurement [3]. Systematic uncertainties in the purity are shown as shaded error bands.

using test beams [6] and collision data [7]. The response of certain neutral particles has not been measured, and a conservative systematic uncertainty is estimated using different models of the hadronic shower in the detector simulation [5]. Additional systematic uncertainties are considered to account for fragmentation effects in the particle p_{T} spectrum inside the jet, the limited knowledge of the dead material in the final detector configuration, and the impact of threshold effects for particles showering in the dense environment inside a jet. The total systematic uncertainty and these individual components are shown in fig. 2 (left).

Since the single particle analysis can only be performed in the central region of the detector that was represented in the test beam measurements, an additional systematic uncertainty is added to account for differences in the calibration as a function of η. This uncertainty is estimated *in situ* using the p_{T} balance of jets in a dijet system, and it is dominated by limitations in the *in situ* method that make it sensitive to the modeling of the physics in dijet events. This is illustrated in fig. 2 (right), where different models of the underlying physics are represented by different Monte Carlo simulations.

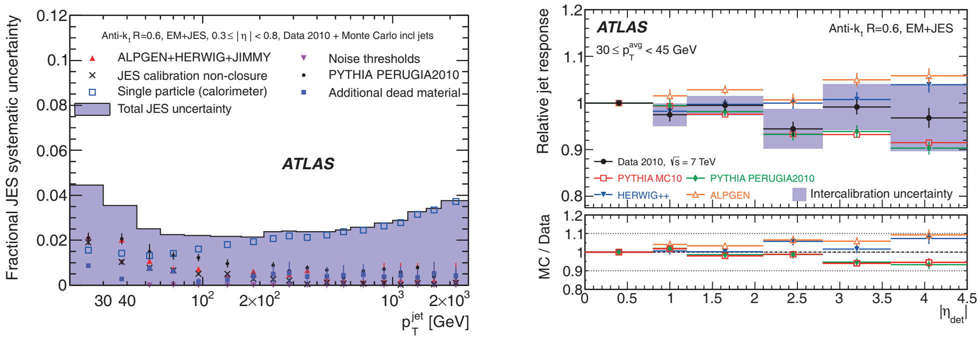

Fig. 2. – Left: Systematic uncertainties in the jet energy scale as a function of jet p_T for jets in the barrel. Right: Relative response of jets measured using dijet p_T balance (solid markers) and results obtained with different Monte Carlo simulations (open markers). The resulting η-dependent systematic uncertainty is shown as a shaded error band around the data points [5].

3. – Benchmark measurements

Photon and diphoton production measurements, as well as inclusive jet and dijet production measurements, have been performed at lower energies in a variety of colliders, and constitute the basic, yet insightful, building blocks of the jet and photon physics program with the ATLAS detector.

3˙1. *Prompt photon and photon+jet production measurements.* – Figure 3 (left) shows a measurement of the differential cross section for isolated photon production as a function of photon E_T. Two measurements are shown, one covering the low-E_T region, performed with early data, and another one performed with the full 2010 dataset. Only

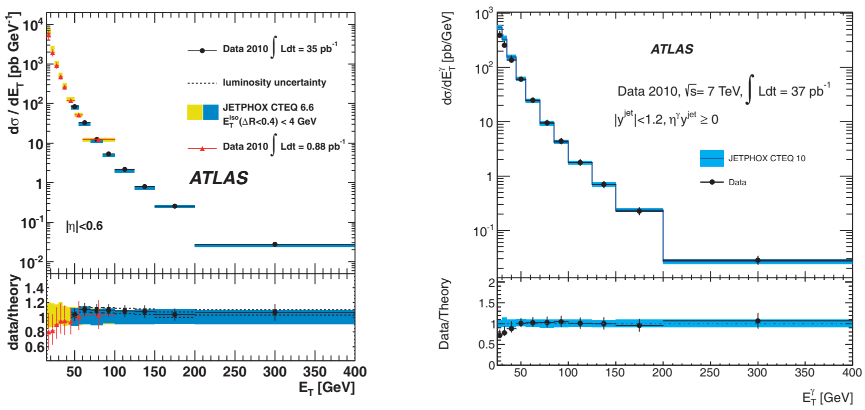

Fig. 3. – Left: Prompt photon production cross section as a function of photon E_T for isolated photons falling in the central region of the detector ($|\eta| < 0.6$) [8]. Right: Photon production cross section for photons produced in association with a jet in the same rapidity hemisphere and when the jet falls in the central region of the detector ($|y| < 1.2$). Data results are shown as solid points and the next-to-leading-order calculation and associated systematic uncertainties are shown as shaded error bands [9].

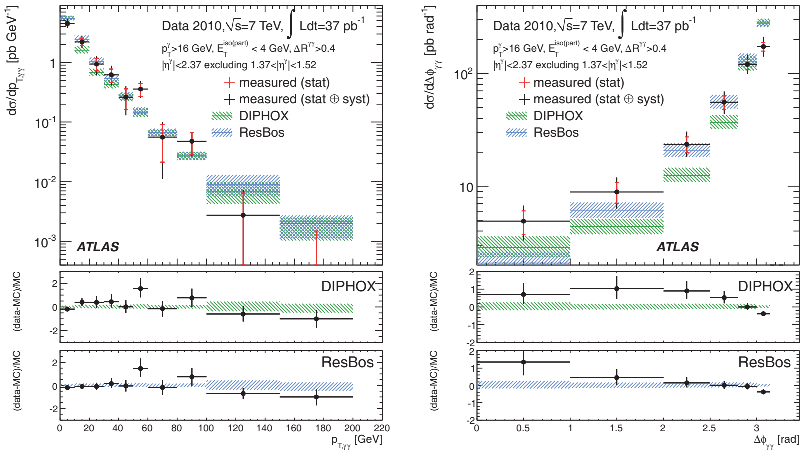

Fig. 4. – Measured differential cross section for diphoton production as a function of p_T of the diphoton system (left) and opening angle in ϕ of the diphoton system (right) for isolated photons compared to a next-to-leading-order calculation and a calculation including resummation of next-to-next-to-leading logarithms [2].

the measurement in the central rapidity bin is shown. The result is compared to a next-to-leading-order calculation and shows differences at low E_T which are, however, consistent with the calculation within systematic uncertainties.

In hadron colliders, prompt photon production happens primarily in association with a jet. Explicit study of the correlations between the photon and the jet allows for further understanding of the details of parameters entering theoretical calculations such as the proton structure functions. Figure 3 (right) shows a measurement of the differential cross section for isolated photon production as a function of photon E_T when the photon is produced in the same rapidity hemisphere as an associated jet with $p_T > 20$ GeV. Similar agreement with theory as in the prompt photon production measurement is found, and no significant dependence on the hemisphere correlations has been observed.

3·2. *Diphoton production measurement.* – Figure 4 shows differential cross section measurements as a function of diphoton p_T (left) and opening angle in ϕ between the photons (right) for isolated photons. Comparisons are performed to a next-to-leading order calculation (DIPHOX) and a next-to-leading-order calculation with a parameterized treatment of photon fragmentation and resummation of next-to-next-to-leading logarithms (ResBos). The differential cross section as a function of p_T is well described by both calculations, as well as the differential cross section as a function of the invariant mass (not shown). Both calculations, however, fail to predict a $\Delta\phi$ distribution that is less strongly peaked for back-to-back configurations. The prediction provided by ResBos is closer to the data, as expected, due to the impact of large logarithms on event shape variables.

3·3. *Inclusive and dijet production measurements.* – Figure 5 shows the ratio of the measured inclusive jet cross section to a baseline next-to-leading-order calculation corrected for non-perturbative effects. The ratios of different predictions of a next-to-leading-order calculation matched with different parton showers to the baseline calculation

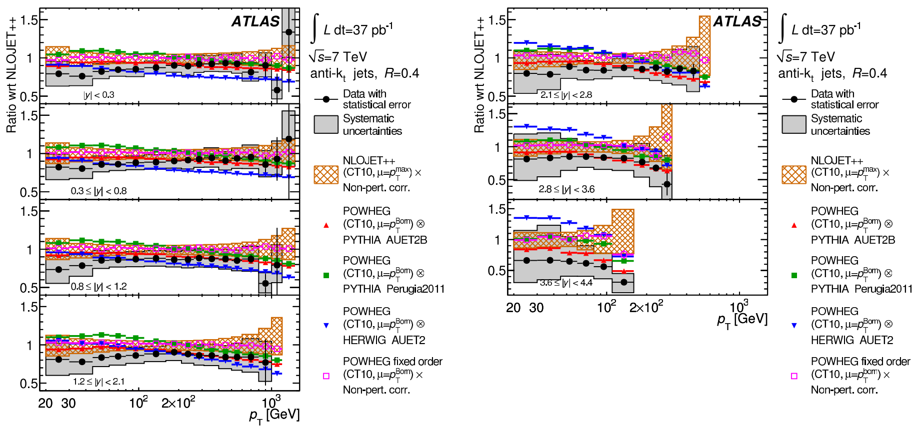

Fig. 5. – Ratio of measured inclusive jet cross section to next-to-leading-order calculation using NLOJet++ and the CT10 parton distribution functions (solid points). Different rapidity bins are shown and jets built with $R = 0.4$ are used. The shaded area around the data points represent the systematic uncertainty in the measurement. The hatched area around 1 represents the systematic uncertainty in the next-to-leading-order calculation. The other markers represent the next-to-leading-order calculation matched to parton showers implemented in POWHEG with different tunes and implementations [10].

are also shown. The measurement agrees within systematic uncertainties with the fixed-order prediction, except in the highest p_T and rapidity bins. The measurement is, however, systematically lower than the prediction. This effect has been shown to become significantly smaller when using jets built with $R = 0.6$ [10]. The predictions from calculations with different parton showers show a large spread, of size comparable to that of the uncertainties in the perturbative calculation.

Figure 6 presents the dijet cross section measurement as a function of the dijet invariant mass compared to theoretical calculations as in fig 5. The measurement is binned in y^*, the rapidity of the dijet system in its center of mass. The results show similar features to those observed in the inclusive jet measurement.

4. – Further measurements and insight into QCD

The availability of a higher center-of-mass energy at the LHC, and new theoretical tools allows for additional measurements that provide further insight into QCD. A small selection of such measurements is discussed in what follows.

4·1. *b-jet cross section measurements.* – Figure 7 shows the ratio of the measured inclusive b-jet cross section to two next-to-leading-order predictions matched to parton showers. Agreement is found between data and the prediction obtained with POWHEG, and it has been shown to not depend on whether POWHEG is interfaced to Pythia or Herwig/Jimmy. A significant disagreement is, however, found in comparisons with MC@NLO, demonstrating the importance of the details of the matching of the next-to-leading-order calculations to the parton shower.

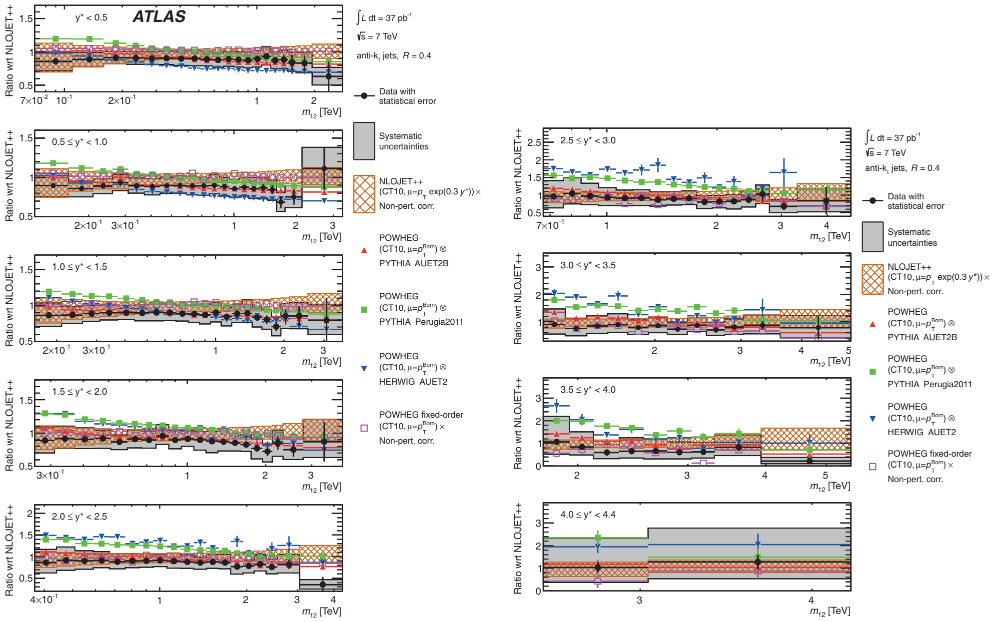

Fig. 6. – Ratio of measured dijet cross section to next-to-leading-order calculation using NLO-Jet++ and the CT10 parton distribution functions (solid points). Different y^* bins are shown and jets built with $R = 0.4$ are used. The different curves shown are as in fig. 5 [10].

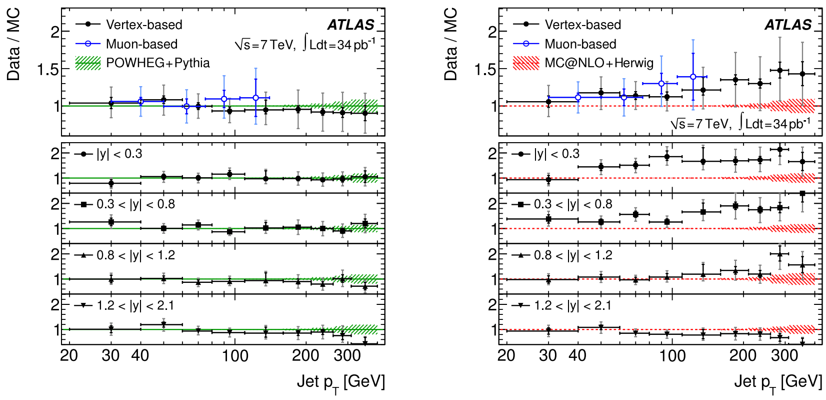

Fig. 7. – Ratio of measured inclusive b-jet cross section to next-to-leading-order calculations interfaced to parton showers. Measured cross sections are shown as calculated through fits to vertex properties and to properties of a muon associated to the jet when enough events were available. Theory predictions correspond to those obtained with POWHEG+Pythia (left) and MC@NLO+Herwig/Jimmy (right). Results are shown in the full rapidity range studied (top figures) and for different rapidity ranges. Statistical uncertainties are shown as dark error bars and the total uncertainty as lighter error bands [11]. The shaded band around 1 represents the statistical uncertainties in the theoretical calculation, scale and proton structure function uncertainties being small compared to the uncertainties in the measurement.

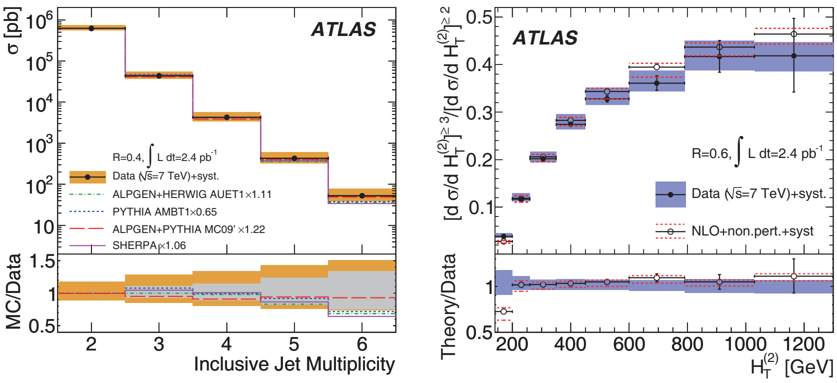

Fig. 8. – Left: Measured inclusive jet multiplicity cross section compared to different leading-order calculations, normalized to the inclusive 2-jet cross section. The systematic uncertainty in the measurement is shown as a shaded error band around the data. The ratios of the different Monte Carlo simulations to the data are shown on the bottom plot. The light-shaded band on the bottom plot shows the systematic uncertainties in the measurement of the shape of the distribution. Right: Measured ratio of 3-jet to 2-jet cross section as a function of $H_T^{(2)}$ (solid points) compared to a next-to-leading-order calculation (open points) using NLOJet++. The bands around the data represent the systematic uncertainty in the measurement, and the dashed lines around the calculation bracket the systematic uncertainty in the calculation [12].

4·2. *Multijet cross section measurements*. – Figure 8 shows the measurement of the production cross section as a function of the inclusive jet multiplicity and the measurement of the ratio of the 3-jet to 2-jet cross sections as a function of the sum of the p_T of the two leading jets ($H_T^{(2)}$). The shape of the inclusive jet multiplicity distribution depends largely on the parton shower tune used, and does not agree with the measurement for the highest multiplicities for most tunes.

The cross section ratio measurement compares well to the next-to-leading-order calculation, except in the lowest bin, where kinematic cuts in the selection are likely to constrain the phase space to regions where the next-to-leading-order calculation reaches its limitations. Systematic uncertainties in the ratio measurement are comparable to theoretical uncertainties in the calculation. Jets built with $R = 0.6$ are used in this comparison. Results using $R = 0.4$ show larger uncertainties in the perturbative calculation [12].

5. – Conclusions and future prospects

Comparisons have been shown for a variety of measurements and next-to-leading-order calculations, including calculations matched to parton showers. Generally, agreement is found between data and the theoretical calculations, and the uncertainties in the measurement are of comparable in size to those in the perturbative calculations. Comparisons with different parton shower tunes interfaced to matrix-element calculations have revealed the importance of the choice of tune when attempting to understand systematic effects in the predictions. Work to understand the differences between the tunes will help future measurements and searches for physics beyond the Standard Model. In addition, new analyses are being performed that will use the current measurements to constrain the parameters entering QCD calculations and gain the fundamental understanding that will allow for a comprehensive physics program using jet substructure [13].

REFERENCES

[1] ATLAS Collaboration, *JINST*, **3** (2008) S08003.
[2] ATLAS Collaboration, *Phys. Rev. D*, **85** (2012) 012003.
[3] ATLAS Collaboration, *Phys. Rev. D*, **83** (2011) 052005.
[4] Cacciari M., Salam G. P. and Soyez G., *JHEP*, **04** (2008) 063.
[5] ATLAS Collaboration, arXiv:1112.6426; to be published in *Eur. Phys. J. C*.
[6] Aharrouche M. *et al.*, *Nucl. Instrum. Methods A*, **614** (2010) 400.
[7] ATLAS Collaboration, arXiv:1203.1302; to be published in *Eur. Phys. J. C*.
[8] ATLAS Collaboration, *Phys. Lett. B*, **706** (2011) 150.
[9] ATLAS Collaboration, *Phys. Rev. D*, **85** (2012) 092014.
[10] ATLAS Collaboration, *Phys. Rev. D*, **86** (2012) 014022.
[11] ATLAS Collaboration, *Eur. Phys. J. C*, **71** (2011) 1846.
[12] ATLAS Collaboration, *Eur. Phys. J. C*, **71** (2011) 1763.
[13] ATLAS Collaboration, *JHEP*, **05** (2012) 128.

IL NUOVO CIMENTO Vol. 35 C, N. 6 Novembre-Dicembre 2012
DOI 10.1393/ncc/i2012-11360-0

Colloquia: LaThuile12

Recent QCD studies at the Tevatron

S. Moed Sher
Fermilab - Batavia, IL, USA

ricevuto il 7 Settembre 2012

Summary. — Since the beginning of Run II at the Fermilab Tevatron, the QCD physics groups of the CDF and D0 Collaborations have worked to reach unprecendented levels of precision for many QCD observables. This note summarizes important recent measurements with dataset corresponding to up to $8\,\mathrm{fb}^{-1}$ of total integrated luminosity.

PACS 12.38.-t – Quantum chromodynamics.

1. – Introduction

The Tevatron collider at Fermilab provides collisions of protons with anti-protons at a center-of-mass evergy of 1.96 TeV. By the end of the Tevatron Run II, the multipurpose detectors of the CDF [1] and D0 [2] experiments were delivered a total integrated luminosity of about $12\,\mathrm{fb}^{-1}$. This large amount of data is exploit in order to make important progress in constraining and confirming the calculations of quantum chromodymanics (QCD) theory. Precise measurements of QCD observables in hadron-hadron collisions, such as jet cross sections, constrain parton density functions (PDFs) and confirms the predictive power of theory. This results in a better control of the standard QCD production calculations, which are used to predict major backgrounds for many important physical processes. In addition, the specific QCD processes which pose challanges to New Physics searches such a supersymmetry and Higgs production can be measured directly with the increased size of available datasets.

In this note some of the recent measurements from the CDF and D0 Collaborations are reviewed. These measurements are related to QCD hard scattering processes. A brief introduction to the structure of hadronic collisions is useful as a motivation for jet definition. Hadronic collision may be factorized into perturbative components (hard scattering and initial and final state radiation) and non-perturbative components (beam remnants and multiple parton interactions). These components are illustrated in fig. 1.

This simple picture is an example of processes which are modeled by Monte Carlo generating programs to simulate hadronic collisions. The picture becomes more complicated when the properties of QCD color confinement and detector effects are included.

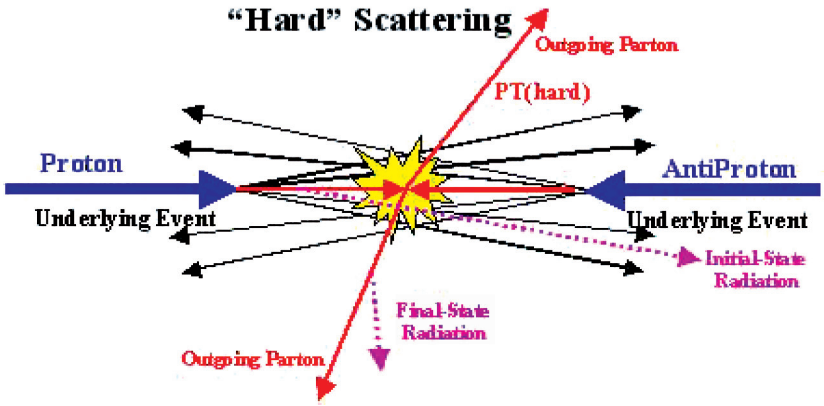

Fig. 1. – Simple model for hadronic collisions.

The colored partons must hadronize into color neutral hadrons. These particles are then clustered into jets by jets algorithms. Jets may be clustered at the parton (quarks and gluons), particle (hadrons) or detector (calorimeter towers) level. Measurements are made at the detector level, but it is useful to use the parton and particle level jets from Monte Carlo simulations to derive corrections to the measured quantities.

The analyses discussed in this note focus on the perturbative component of the collision and do not include studies of the non-perturbative regime (where pQCD fails), such as the "soft" interactions generating the underlying event which accompanies the "hard" collision.

2. – Angular decorrelatoins in $\gamma + 2(3)$ jets

The D0 Collaboration used inclusive $\gamma+2$ jets and $\gamma+3$ jets events with an integrated luminosity of about $1\,\mathrm{fb}^{-1}$ to measure cross sections as a function of the angle in the plane transverse to the beam direction between the transverse momentum (P_T) of the $\gamma+$ leading jet system (jets are ordered in P_T) and the P_T of the other jet for the $\gamma+2$ jet events, or P_T sum of the two other jets for the $\gamma+3$ jet events, [3]. Differential cross sections were studies in three bins of the second jet P_T. The results are compared to different Multiple Particle Intercation (MPI) models and demonstrate that the prediction of the Single Particle (SP) models do not describe the measurements, and an additional contribution from Double Parton (DP) events is required to describe the data. The data favors the predictions of the new PYTHIA MPI models with P_T-ordered showers, implemented in the Perugia and and S0 tunes, and also SHERPA with its default MPI model. Predictions from previous PYTHIA MPI models with tunes A and DW are disfavored. The results of these measurements are shown in fig. 2.

3. – Three jet mass cross section

Using about $0.7\,\mathrm{fb}^{-1}$ of integrated luminosity collected by the D0 experiment, differential cross sections for three jet mass were measured, [4]. In this measurement jets are defined by the midpoint cone algorithm with cone size $R = 0.7$. Five scenarios were considered, where the rapidities of the three leading P_T jets are restricted to $|y| < 0.8$, $|y| < 1.6$, $|y| < 2.4$. The transverse momentum selection required $P_{T1} > 150\,\mathrm{GeV}/c$, and

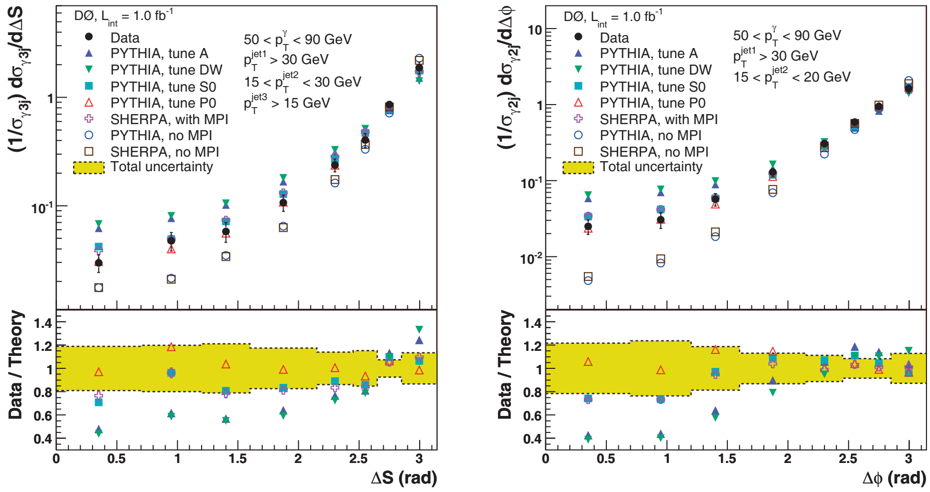

Fig. 2. – On the left: normalized differential cross section in γ+3 jet events, $(1/\sigma_{\gamma 3j})\mathrm{d}\sigma_{\gamma 3j}/\mathrm{d}\Delta S$, in data compared to MC models, and the ratio of data over theory, only for models including MPI, in the range $15 < P_T^{jet2} < 30\,\mathrm{GeV}$. On the right: normalized differential cross section in $\gamma + 2$ jet events, $(1/\sigma_{\gamma 2j})\mathrm{d}\sigma_{\gamma 2j}/\mathrm{d}\Delta S$, in data compared to MC models, and the ratio of data over theory, only for models including MPI, in the range $15 < P_T^{jet2} < 20\,\mathrm{GeV}$.

$P_{T3} > 40\,\mathrm{GeV}/c$. For $|y| < 2.4$ additional measurements are made for $P_{T3} > 70\,\mathrm{GeV}$ and $P_{T3} > 100\,\mathrm{GeV}$. Figure 3 shows results for the differential three jet cross section in M_{3j}, for different rapidity ranges and for different P_T criteria. The data are compared to theoretical models of NLO pQCD and non-perturbative corrections. The renormalization and factorization scales are set to the average P_T of the three leading P_T jets: $\mu_R = \mu_F = \mu_0 = (P_{T1}+P_{T2}+P_{T3})/3$. Figure 4 shows the ratio between data and theory

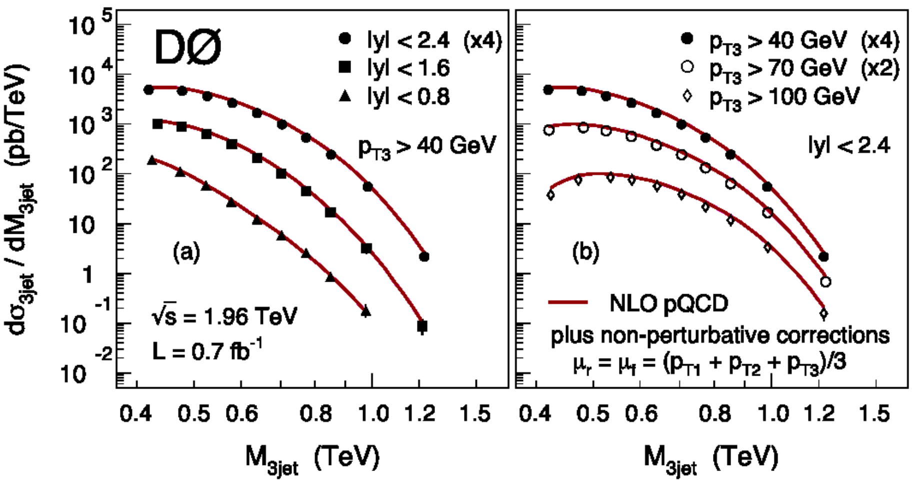

Fig. 3. – D0 measurement of the three-jet cross section as a function of the three-jet invariant mass in different rapidity regions (left) and for different P_{T3} requirements (right).

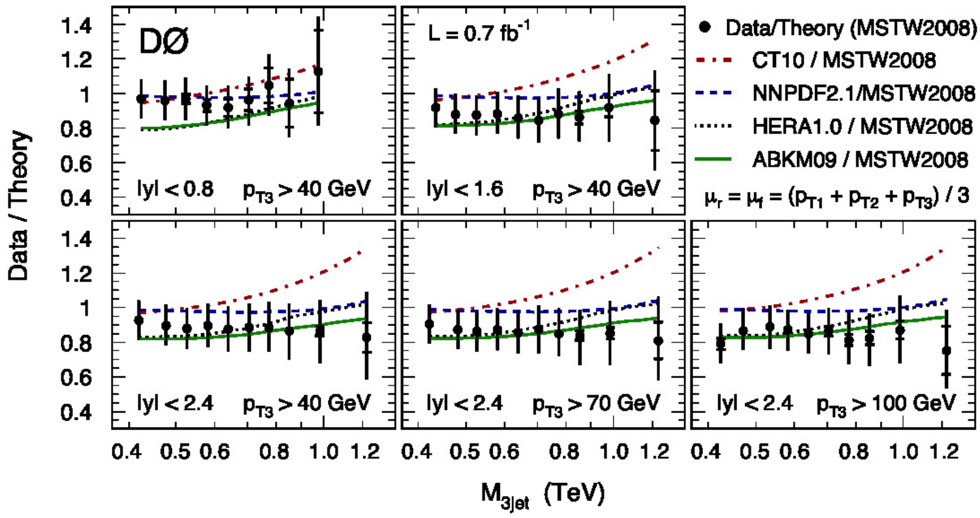

Fig. 4. – Ratios between data and theory for the D0 three-jet cross section measurement. The ratios are comupted for different PDFs and are shown as a function of the three-jet invariant mass in different rapidity regions and for different P_{T3} requirements.

for different PFDs. The data are reasonably well described by the next-to-leading order calculation done with NLOJET++ and the MSTW2008NLO PDFs.

4. – W + jets production

The measurements of inclusive $W(\rightarrow e\nu) + n$ jets cross sections ($n = 1, 2, 3, 4$), presented as total inclusive cross sections and differentially in the n-th jet transverse momentum was done by the D0 Collaboration [5]. The measurements are made using data corresponding to an integrated luminosity of $4.2\,\text{fb}^{-1}$. The selection for $W + n$ jet events include the following criteria: presence of a central electron with $P_T > 15\,\text{Gev}$, missing transverse energy $> 20\,\text{GeV}$, transverse mass of the W boson candidate $> 40\,\text{GeV}/c$, and the jet transverse momentum $> 20\,\text{GeV}$. The spatial distance between the cone and the nearest jet is required to be $\Delta R > 0.5$. Acceptance corrections and background contributions from $Z+$jets, top pair production, diboson and single top production are estimated using different MC events generators [5]. The backgrounds from multijet production are determined using aa data driven method. Figure 5 shows these cross section results as a function of P_T of the first, second, third and forth jet, and compared to pQCD predictions in NLO (for $n_{jet} < 3$) or LO (for $n_{jet} = 4$). Within their uncertainties, the NLO pQCD predictions agree pretty well with the data, except for the low P_T region for $W + 1$ jet and high-P_T region for $W + 3$ jets. The LO predictions for $W + 4$ jets agree with the data, but have very large uncertainties from the renormalization scale dependence.

5. – Observation of W boson + single-charm production

Calculations of $W +$ heavy quark production are available at leading order (LO) and next-to-leading order (NLO) QCD [6], with the NLO cross section about 50% larger than

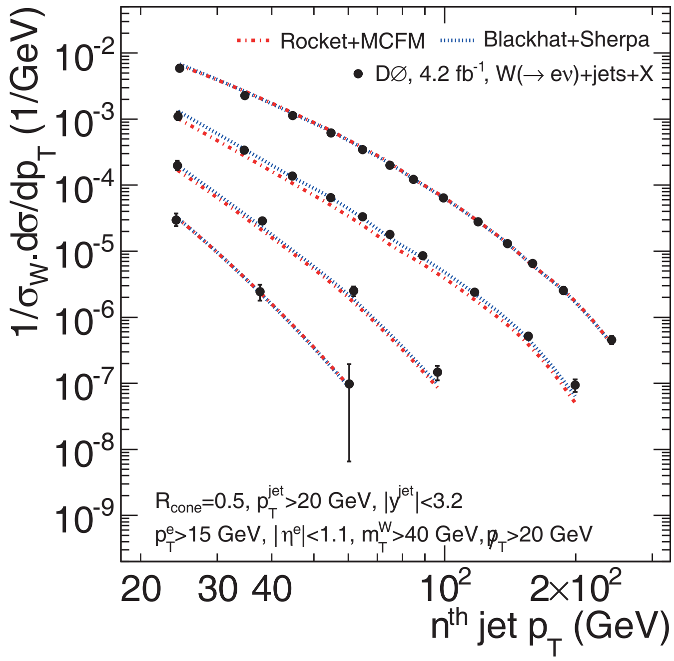

Fig. 5. – Measured $W + n$ jet differential cross section as a function of n-th jet P_T for jet multiplicities $n = 14$, normalized to the inclusive $W \to e$ cross section. $W + 1$ jet inclusive spectra are shown by the top curve, the $W + 4$ jet inclusive spectra by the bottom curve. The measurements are compared to the fixed-order NLO predictions for the jet multiplicities $n = 13$, and to LO predictions for $n = 4$.

at LO. Overall, the uncertainty on the NLO theoretical expectation for W boson + single-charm quark production at the Tevatron is about 1020%, depending on the charm phase space, with the largest uncertainties due to the choice of factorization and renormalization scales and the shape of the s quark PDF.

The CDF Collaboration performed the first observation of the $p\bar{p} \to Wc$ production cross section at the Tevatron collider [7]. The charm quark is identified through the semileptonic decay of the charm hadron into an electron or muon (soft leptons). The Wc production cross section is determined first separately using soft electrons and soft muons, and then the two measurements are combined. The analysis exploits the correlation between the charge of the W boson and the charge of the soft lepton from the semileptonic decay of the charmed hadron. Charge conservation in the process $gq \to Wc$ $(q = d, s)$ allows as final states only the pairings $W^+\bar{c}$ and Wc; as a result, the charge of the lepton from the semileptonic decay of the c quark and the charge of the W boson are always of opposite sign. In practice, this correlation is diluted in the reconstructed events due to hadronic decays in flight and hadrons misidentified as soft leptons. These contaminations in the signal selection and other background contributions, such as $W +$ jets and $Z +$ jets production, top pair production and single top, as well as diboson and multijet production, are considered in the analysis. The W is identified through its leptonic decay. The measured production cross section $\sigma_{Wc}(P_{Tc} > 20\,\mathrm{GeV}/c, |\eta_c| < 1.5) - B(W \to l\nu) = 13.3 + 3.3\,\mathrm{pb}$, in agreement with theoretical expectations, with a significance for the Wc signal of 6.4σ.

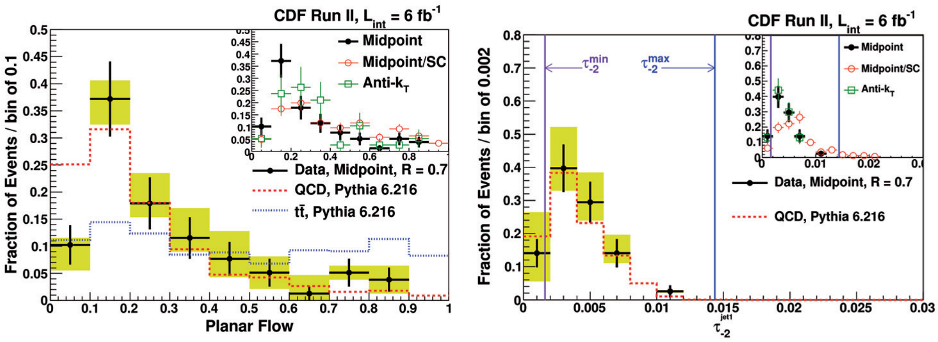

Fig. 6. – The angularity distribution for midpoint jets with $P_T > 400\,\mathrm{GeV}/c$. The $t\bar{t}$ rejection cuts and requirement for $90\,\mathrm{GeV} < m_{j1} < 120\,\mathrm{GeV}$ are applied. The PYTHIA calculation (red dashed line) and the pQCD kinematic endpoints are shown (left); The planar flow distributions after applying the top rejection cuts and requiring $130\,\mathrm{GeV} < m_{j1} < 210\,\mathrm{GeV}$. PYTHIA QCD (red dashed line) and $t\bar{t}$ (blue dotted line) jets are shown (right).

6. – Jet substructure

The study of high-transverse-momentum massive jets provides an important test of pQCD and gives an insight into the parton showering mechanism. In addition, massive boosted jets compose an important background in searches for various new physics models, the Higgs boson, and highly boosted top quark pair production. Particularly relevant is the case where the decay of a heavy resonance produces high-P_T top quarks that decay hadronically. In all these cases, the hadronic decay products can be detected as a single jet with substructure that differs from pQCD jets once the jet P_T is greater than 400–500 GeV/c. The CDF Collaboration performed a measurement of substructure of jets with $P_T > 400\,\mathrm{GeV}/c$ by studing distributions of the jet mass and measuring angularity, the variable describing the energy distribution inside the jet, and planar flow, the variable differentiating between two-prong and three-prong decays [8]. At small cone sizes and large jet mass, these variables are expected to be quite robust against soft radiation and allow, in principle, a comparison with theoretical predictions in addition to comparison with MC results. Jets are reconstructed with the midpoint cone algorithm (cone radii $R = 0.4$, 0.7, and 1.0) and with the antikt algorithm [9] (with distance parameter $R = 0.7$). Events are selected in a sample with $6\,\mathrm{fb}^{-1}$ based on the inclusive jet trigger. There is a good agreement between the measurement and the analytic predictions and with PYTHIA MC predictions. The midpoint and antikt algorithms have very similar jet substructure distributions for high mass jets, see fig. 6. The angularity distribution shown on fig. 6 (left) in addition to reasonable agreement data and PYTHIA MC also demonstrates that the high-mass jets coming from light quark and gluon production are consistent with two-body final states and that further rejection against high mass QCD jets can be obtained by using the planar flow variable, fig. 6 (right).

7. – Conclusions

Measurements from the Tevatron Run II defined a new level of QCD precision measurements in hadron-hadron collisions. Several results from the Tevatron were reviewed in this note mostly showing nice agreement with NLO predictions. The QCD programs of the CDF and D0 Collaborations have been dedicated to testing and constraining pQCD and also measuring cross sections of important background processes. These studies are important for many searches at the Large Hadron Collider (LHC), where measurements of this type are among the first to be made using LHC data [10, 11].

REFERENCES

[1] Acosta D. E. *et al.* (CDF Collaboration), *Phys. Rev. D*, **71** (2005) 032001.
[2] LeCompte T. and Diehl H. T., *Ann. Rev. Nucl. Part. Sci.*, **50** (2000) 71.
[3] Abazov V. M. *et al.* (D0 Collaboration), *Phys. Rev. D*, **83** (2011) 052008.
[4] Abazov V. M. *et al.* (D0 Collaboration), arXiv:1104.1986v2 [hep-ex] (2011).
[5] Abazov V. M. *et al.* (D0 Collaboration), *Phys. Lett. B*, **705** (2011) 200.
[6] Keller S., Giele W. T. and Laenen E., *Phys. Lett. B*, **372** (1996) 141.
[7] CDF Collaboration, *Public note*, `http://www-cdf.fnal.gov/physics/new/qcd/QCD.html` (2012).
[8] Aaltonen T. *et al.* (CDF Collaboration), arXiv:1106.5952v2 [hep-ex] (2011).
[9] Cacciari S. G. P. and Soyez G., *JHEP*, **04** (2008) 063.
[10] CMS Collaboration, *CERN-CMS-NOTE-2006*, **067** (2007) .
[11] Skands P. Z., *Contribution to Les Houches Workshop on Physics at TeV Colliders* FERMILAB-CONF-07-706-T (2007).

IL NUOVO CIMENTO Vol. 35 C, N. 6 Novembre-Dicembre 2012
DOI 10.1393/ncc/i2012-11361-y

Colloquia: LaThuile12

Probes of soft and hard QCD at LHCb

E. Santovetti on behalf of the LHCb Collaboration
Università di Roma "Tor Vergata" and INFN, Sezione di Roma 2 - Roma, Italy

ricevuto il 7 Settembre 2012

Summary. — The LHCb experiment is instrumented in the forward region. Due to this, it can provide QCD and electroweak measurements complementary to the other LHC experiments. The W and Z production cross-sections have been measured in proton-proton collisions at $\sqrt{s} = 7\,\text{TeV}$. The measurements of the production cross-section of the $\Psi(2S)$ meson and the Υ mesons are reported. The observation of double-charm production is also discussed.

PACS 14.70.Fm – W bosons.
PACS 14.70.Hp – Z bosons.
PACS 14.40.Pq – Heavy quarkonia.

1. – Introduction

The LHCb experiment is designed to investigate the properties of the heavy-quark sector and aims to study CP-violation processes and rare decays involving b and c hadrons. It can also be used to study QCD and electroweak processes. The bb pair production are strongly correlated at small angle with respect to the beam line, therefore the LHCb detector [1] has been designed as a single-arm forward spectrometer covering a pseudorapidity range $2 < \eta < 5$. The detector consists of a silicon vertex detector, a dipole magnet, a tracking system, two ring-imaging Cherenkov (RICH) detectors, a calorimeter system and a muon system.

The LHCb experiments made several measurements in the soft QCD sector (baryon number transport, strange baryon suppression, charged track multiplicity, inclusive ϕ cross-section, etc. . .) as well as in the quarkonium physics. In these proceedings we will present some of the latest results on electroweak physics (sect. **2**) and quarkonia (sect. **3**).

2. – Electroweak measurements

The W and Z production cross-sections at $\sqrt{s} = 7\,\text{TeV}$ energy are measured using the decays $W \to \mu\nu$, $Z \to \mu\mu$ and $Z \to \tau\tau$. The W production charge asymmetry has been also measured as a function of the lepton pseudorapidity.

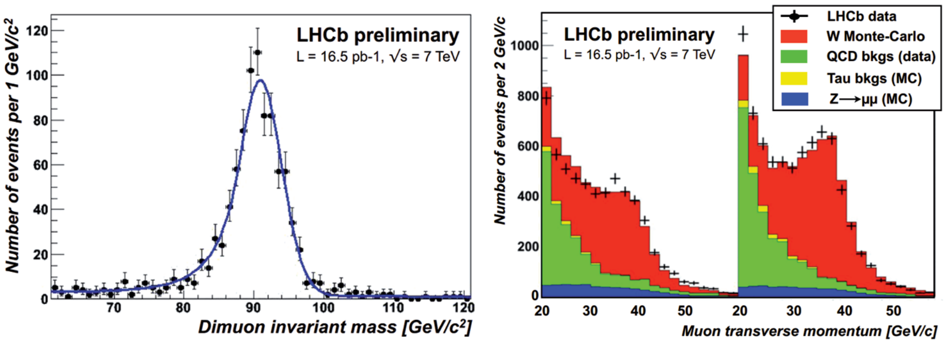

Fig. 1. – Left: Di-muon invariant mass of Z candidates: data points are fitted to a Crystal Ball function (signal) on an exponential (background). Right: p_T distribution for negative (left) and positive (right) charged muons.

This analysis uses $\int \mathcal{L} = (16.5 \pm 1.7)\,\mathrm{pb}^{-1}$ of data, collected during 2010 [2]. This results are recently updated with a larger statistic sample [3].

$Z \to \mu^+\mu^-$ selection. – Concerning the $Z \to \mu\mu$, the events are selected by requiring two well reconstructed muons with a transverse momentum, p_T, greater than $20\,\mathrm{GeV}/c$ and lying in the pseudorapidity (η) range between 2.0 and 4.5. To further identify $Z \to \mu^+\mu^-$ events, the invariant mass is required to be consistent with Z production by imposing the mass constraint $81\,\mathrm{GeV}/c^2$, $M_{\mu\mu} < 101\,\mathrm{GeV}/c^2$. 833 candidate events satisfy these criteria.

$W \to \mu\nu$ selection. – The signature for a W boson is a single isolated high-transverse-momentum lepton and minimal other activity in the event. As the background contamination is expected to be larger than in Z events, additional criteria to the $p_T > 20\,\mathrm{GeV}/c$ and $2.0 < \eta < 4.5$ requirements are imposed; consistency with the primary vertex and muon isolation. Semi-leptonic B and D meson decays are suppressed by requiring the impact parameter significance of the muon with respect to the primary vertex to be less than 2. Isolation is imposed by demanding that the summed transverse energy in a cone of radius $\sqrt{\Delta\eta^2 + \Delta\phi^2} = 0.5$ around the muon is less than $2\,\mathrm{GeV}/c$. 7624 $W^+ \to \mu^+\nu$ and 5732 $W^- \to \mu^-\nu$ candidates pass these requirements.

A detailed background study is performed: $Z \to \mu^+\mu^-$ where one of the muons goes outside the LHCb geometrical acceptance; $W \to \tau\nu$ and $Z \to \tau\tau$ where one tau decays leptonically inside the detector to a muon; b and c events containing semi-leptonic decays with a muon in the final state; generic QCD events where pions or kaons are misidentified as muons (decay in flight or punch-through).

The signal yield is estimated by fitting the lepton p_T spectrum to the shapes expected for signal (simulation) and each background class (simulation and data-driven by anti-cuts) in 5 bins of the lepton pseudorapidity. The W selected candidates and the result of the fit are shown in fig. 1 (right). The fit estimates that $(34 \pm 1)\%$ of the sample is composed by $W^+ \to \mu^+\nu$, $(26 \pm 1)\%$ by $W^- \to \mu^-\nu$ and $(31 \pm 1)\%$ is due to the QCD background.

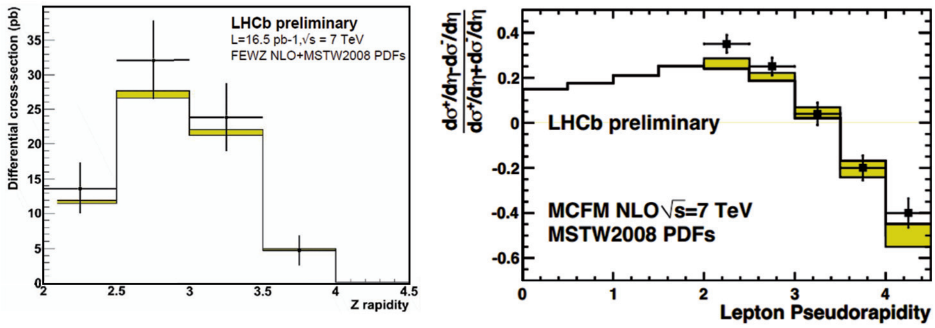

Fig. 2. – Left: Differential cross-section for Z production in bins of boson rapidity. Right: W charge asymmetry in bins of lepton pseudorapidity. The points are the measured data (statistical and systematic errors combined) compared to the NLO prediction with the MSTW084 PDF set; the yellow band is the theoretical uncertainty.

Results. – The Z and W production cross-sections are measured, with the kinematic requirements above specified, according to the formula:

$$\sigma = \frac{N_{Candidates} - N_{Background}}{\epsilon_{Trigger} \cdot \epsilon_{Tracking} \cdot \epsilon_{\mu-ID} \cdot \epsilon_{Selection} \cdot \int \mathrm{L}}, \tag{1a}$$

where all involved efficiencies (trigger, tracking, muon identification and selection) are measured directly from data and cross-checked with simulation. Background estimates, efficiency measurements and luminosity determination are considered as sources of systematic error. Inclusive production cross-sections for Z, W^+ and W^- bosons are determined to be

$$\sigma(W^+ \to \mu^+\nu) = (1007 \pm 48 \pm 101)\ \text{pb}, \tag{2a}$$
$$\sigma(W^- \to \mu^-\nu) = (680 \pm 40 \pm 68)\ \text{pb}, \tag{2b}$$
$$\sigma(Z \to \mu\mu) = (73 \pm 4 \pm 7)\ \text{pb}. \tag{2c}$$

The differential Z cross-section in 5 bins of the boson rapidity and the W charge asymmetry in 5 bins of lepton pseudorapidity are shown in fig. 2. This measurements can be used to probe the PDF's and test the QCD predictions.

3. – Quarkonium results

The measurement of $\Psi(2S)$ *meson production at* $\sqrt{s} = 7\,\text{TeV}$. – The differential cross-section for the inclusive production of $\Psi(2S)$ mesons in pp collisions at $\sqrt{s} = 7\,\text{TeV}$ has been measured [4] using an integrated luminosity of $36\,\text{pb}^{-1}$. The decay channels $\Psi(2S) \to \mu^+\mu^-$ and $\Psi(2S) \to (J/\Psi \to \mu^+\mu^-)\pi^+\pi^-$ are reconstructed using prompt $\Psi(2S)$ and $\Psi(2S)$ decaying from a b-hadron (delayed). The separation between the two samples is done using a pseudo-decay-time distribution defined as $t = d_z(M/p_z)$, where d_z is the separation along the beam axis between the $\Psi(2S)$ decay vertex and the primary vertex, M is the nominal $\Psi(2S)$ mass and p_z is the component of its momentum along the beam axis. The polarization of promptly reconstructed $\Psi(2S)$'s is not measured

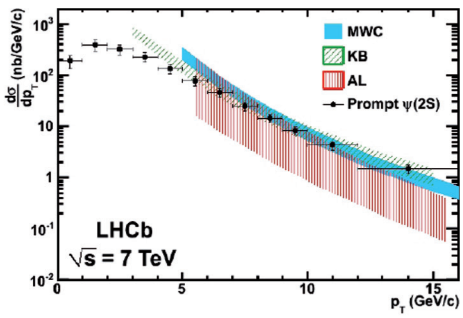

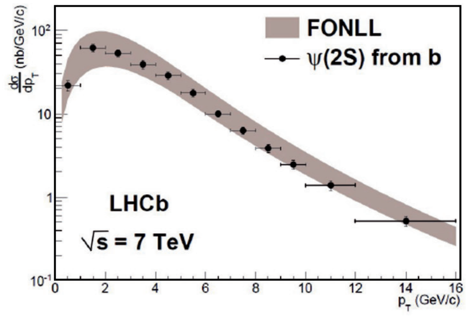

Fig. 3. – Left: Differential production cross-section *vs.* p_T for prompt $\Psi(2S)$. The predictions of three non-relativistic QCD models are also shown for comparison. MWC [6] and KB [7] are NLO calculations including colour-singlet and colour-octet contributions. AL [8] is a colour-singlet model including the dominant NNLO terms. Right: Differential production cross-section *vs.* p_T for delayed $\Psi(2S)$. The shaded band is the prediction of a FONLL calculation [9].

here, therefore a systematic uncertainty is computed separately for the unknown state of the polarization. This does not effect the delayed $\Psi(2S)$. The differential cross-sections for prompt $\Psi(2S)$ and delayed $\Psi(2S)$ mesons are measured in the kinematic range $p_T(\Psi(2S)) < 16\,\mathrm{GeV}/c$ and $2 < y(\Psi(2S)) < 4.5$:

$$(3a)\qquad \sigma_{prompt}(\Psi(2S)) = 1.44 \pm 0.01(\mathrm{stat}) \pm 0.12(\mathrm{syst})^{+0.20}_{-0:40}(\mathrm{pol})\ \mu\mathrm{b},$$

$$(3b)\qquad \sigma_b(\Psi(2S)) = 0.25 \pm 0.01(\mathrm{stat}) \pm 0.02(\mathrm{sys})\ \mu\mathrm{b}.$$

Recent QCD calculation on the differential cross-sections are found to be in a good agreement with these results as shown in fig. 3. Combining this result with the LHCb measurement of the J/Ψ cross-section (from b decay) in the same fiducial range [5], the inclusive branching ratio has been determined to be

$$(4a)\qquad \mathcal{B}(b \to \Psi(2S)\ X) = (2.73 \pm 0.06(\mathrm{stat}) \pm 0.16(\mathrm{syst}) \pm 0.24(\mathrm{BR})) \times 10^{-3},$$

where the last uncertainty is due to the $\mathcal{B}(b \to J/\Psi\ X)$, $\mathcal{B}(J/\Psi \to \mu^+\mu^-)$ and $\mathcal{B}(\Psi(2S) \to e^+e^-)$ branching fraction uncertainties. The later branching fraction is used and justified by the leptons universalities.

$\Upsilon(1S)$ *production cross-section.* – The $\Upsilon(1S)$, $\Upsilon(2S)$ and $\Upsilon(3S)$ states have been observed via their decays into two muons with sufficient resolution to separate fully the $\Upsilon(2S)$ and $\Upsilon(3S)$ invariant mass peaks (see fig. 4 (left)). The $\Upsilon(1S)$ differential production cross-section as a function of $\Upsilon(1S)$ y and p_T has been measured [10] in the fiducial region $pT < 15\,\mathrm{GeV}/c$ and $2.0 < y < 4.5$. The fiducial region has been divided into bins of width $1\,\mathrm{GeV}/c$ in p_T and one unit of rapidity (y) and a dataset corresponding to an integrated luminosity of $32.4\,\mathrm{pb}^{-1}$ has been used. The $\Upsilon(1S)$ yield has been extracted from a fit to the di-muon invariant mass distribution using a Crystal Ball to model the signal shape and an exponential to model the background shape (see fig. 4 (left)). The results have been reported under the assumption of unpolarized $\Upsilon(1S)$ and the largest systematic uncertainty comes from this assumption. The measured $\Upsilon(1S)$ production cross-section, integrated over the fiducial region, assuming unpolarized $\Upsilon(1S)$

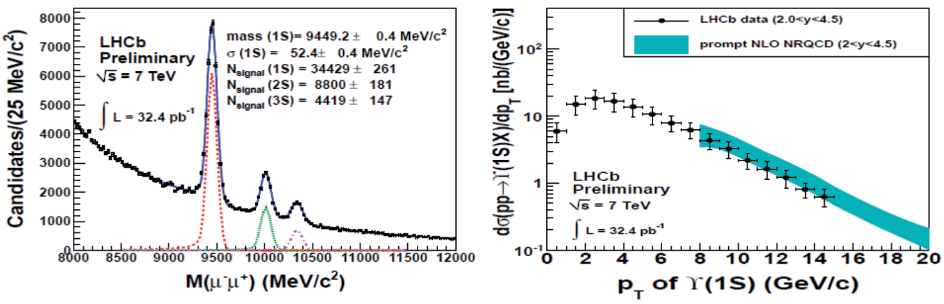

Fig. 4. – Left: The invariant-mass distribution of the selected $\Upsilon \to \mu^+\mu^-$ candidates. The three peaks correspond to the $\Upsilon(1S)$, $\Upsilon(2S)$, and $\Upsilon(3S)$ signals (from left to right). The superimposed curves and the signal yields are the result of the fit. Right: The measured differential $\Upsilon(1S)$ production cross-section as a function of p_T integrated over y (black dots) compared to the prediction calculated from NRQCD at NLO, including contributions from χ_b and $\Upsilon(2S)$ decays, summing the colour-singlet and colour-octet contributions [11] (coloured band).

is $\sigma_{\Upsilon(1S)} = 108.3 \pm 0.7^{+30.9}_{-25.8}$ nb where the first uncertainty is statistical and the second is systematic. The measured $\Upsilon(1S)$ differential production cross-section as a function of $\Upsilon(1S) p_T$ ($\mathrm{d}\sigma/\mathrm{d}p_T$) has been compared with LO and NLO NRQCD, and with NLO and NNLO CS theoretical predictions. The predictions take into account the $\Upsilon(1S)$ feed down from χ_b and $\Upsilon(2S)$ and are in good agreement with data (see, for example, fig. 4 (right)). The results are allowing for the different rapidity range in good agreement with those obtained by the CMS Collaboration [12].

Observation of double-charm production involving open charm. – The production of a J/Ψ accompanied by open charm and pairs of open-charm (C) hadrons are observed [13] in pp collisions at $\sqrt{s} = 7\,\mathrm{TeV}$ using an integrated luminosity of $355\,\mathrm{pb}^{-1}$. Leading-order calculation in perturbative QCD and a model including Double-Parton Scattering (DPS) [14, 15] give significantly different prediction, $\sigma(J/\Psi\, C) + J/\Psi\bar{C} \sim 18\,\mathrm{nb}$ and $\sim 280\,\mathrm{nb}$, respectively. The DPS predictions can also be tested through the ratios of cross-sections of the charm hadrons involved: in a DPS scenario $\sigma(C_1) \times \sigma(C_2)/\sigma(C_1C_2)$ should be equal (twice bigger if $C_1 \neq C_2$) to the effective DPS cross-section measured at the Tevatron [16]. The open charm hadrons considered here are: D^0, D^+, D_s^+ and Λ_c^+, while the $C\bar{C}$ are used as control channels. Selected charged tracks are combined to form $J/\Psi \to \mu^+\mu^-$, $D^0 \to K^-\pi^+$, $D^+ \to K^-\pi^+\pi^+$, $D_s^+ \to K^-K^+\pi^+$ and $\Lambda_c^+ \to pK^+\pi^+$. Subsequently these candidates are combined into $J/\Psi C$, CC and $C\bar{C}$. The combinations are requested to come from the same primary vertex and lie in the rapidity range $2 < y(J/\Psi, C) < 4$ and the p_T range $p_T(J/\Psi) < 12\,\mathrm{GeV}/c$ and $3\,\mathrm{GeV}/c < p_T(C) < 12\,\mathrm{GeV}/c$. In addition a flight distance $c\tau > 100\,\mu\mathrm{m}$ is required for the C.

Signals with a statistical significance over five standard deviations have been observed for the four $J/\Psi\, C$, for six CC modes: D^0D^0, D^0D^+, $D^0D_s^+$, $D^0\Lambda_C^+$, D^+D^+ and $D^+D_s^+$, and for seven $C\bar{C}$ channels: $D^0\bar{D}0$, D^0D^-, $D^0D_s^-$, $D^0\bar{\lambda}_c^-$, D^+D^-, $D^+D_s^-$ and $D^+\bar{\Lambda}_c^-$. In fig. 5 the cross-sections are shown on the left and the DPS fraction on the right. Results favour the DPS model using the effective cross-section measured at Tevatron, which is also favoured with the absence of azimuthal and rapidity correlations. The transverse momentum of these events has also been studied. In the $J/\Psi C$ case we can see an harder $p_T^{J/\Psi}$ spectra compared to the prompt J/Ψ production.

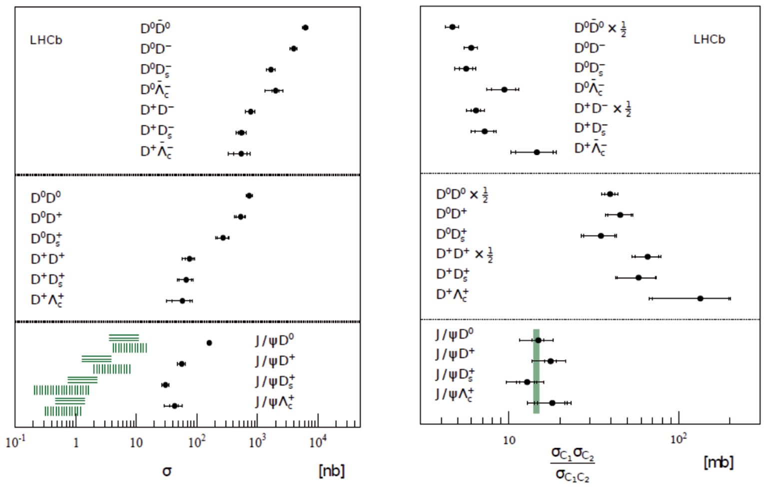

Fig. 5. – Left: Measured cross-sections $\sigma_{J/\Psi C}$, σ_{CC} and $\sigma_{C\bar{C}}$ (points with error bars) compared, in $J/\Psi C$ channels, to the calculations in refs. [17] (vertical hatched areas) and ref. [18] (horizontal hatched areas). The inner error bars show the statistical uncertainty whilst the outer error bars show the sum of the statistical and systematic uncertainties in quadrature. Right: Measured ratios $\sigma(C_1) \times \sigma(C_2)/\sigma(C_1C_2)$ (points with error bars) in comparison with the expectations from DPS using the cross-section measured at Tevatron for multi-jet events (light green shaded area). For the D^0D^0, $D^0\bar{D}^0$, D^+D^+ and D^+D^- cases the ratios are rescaled with the symmetry factor of one half. The inner error bars show the statistical uncertainty whilst the outer error bars show the sum of the statistical and systematic uncertainties in quadrature. For the $J/\Psi C$ case the outermost error bars correspond to the total uncertainties including the uncertainties due to the unknown polarization of the prompt J/Ψ mesons.

REFERENCES

[1] Alves A. A. *et al.* (The LHCb Collaboration), *JINST 3*, **13** (2008) s08005.
[2] LHCb Collaboration, *JHEP*, **06** (2012) 058.
[3] LHCb Collaboration, LHCb-CONF-2011-039.
[4] LHCb Collaboration, *Eur. Phys. J. C*, **72** (2012) 2100.
[5] LHCb Collaboration, *Eur. Phys. J. C*, **71** (2011) 1645; *Eur. Phys. J. C*, **71** (2011) 1645.
[6] Ma Y. Q., Wang K. and Chao K. T., arXiv:hep-ph/1012.1030.
[7] Kniehl B. and Butenschön M., *Phys. Rev. Lett.*, **106** (2011) .
[8] Artoisenet P. *et al.*, *Phys. Rev. Lett.*, **101** (2008) 152001; *Eur. Phys. J. C*, **61** (2009) 693.
[9] Cacciari M., Greco M. and Nasou P., *JHEP*, **9805** (1998) 007; *JHEP*, **07** (2004) 033.
[10] LHCb Collaboration, *Eur. Phys. J. C*, **72** (2012) 2025.
[11] Wang K., Ma Y. Q. and Chao K. T., private communication.
[12] CMS Collaboration, arXiv:1012.5545v1.
[13] LHCb Collaboration, *JHEP*, **06** (2012) 141.
[14] Berezhnoy A. V. *et al.*, *Phys. Rev. D*, **57** (1998) 4385.
[15] Kom C. H., Kulesza A. and Stirling W. J., *Phys. Rev. Lett.*, **107** (2011) 082002; *Phys. Rev. B*, **705** (2011) 116 and arXiv:1106.2184.
[16] CDF Collaboration, *Phys. Rev. D*, **56** (1997) 3811.
[17] Baranov S. P., *Phys. Rev. D*, **73** (2006) 074021.
[18] Lansberg J. P., *Eur. Phys. J. C*, **61** (2009) 693.

IL NUOVO CIMENTO Vol. 35 C, N. 6 Novembre-Dicembre 2012
DOI 10.1393/ncc/i2012-11362-x

Colloquia: LaThuile12

QCD in hadron collisions

G. P. Salam

CERN - PH-TH, CH-1211 Geneva 23, Switzerland
Department of Physics, Princeton University - Princeton, NJ 08544, USA
LPTHE; CNRS UMR 7589; UPMC University Paris 6 - Paris, France

ricevuto il 7 Settembre 2012

Summary. — This paper examines recent progress in collider QCD and some facets of the interplay between these developments and searches for new particles and phenomena at the Tevatron and LHC.

PACS 12.38.-t – Quantum chromodynamics.
PACS 12.38.Bx – Perturbative calculations.
PACS 13.85.-t – Hadron-induced high- and super-high-energy interactions (energy > 10 GeV).
PACS 13.87.-a – Jets in large-Q^2 scattering.

1. – Introduction

The past 18 months have seen considerable excitement in the field of collider particle physics. Among the topics that deserve a mention, one might include the measurement of an unexpectedly large $t\bar{t}$ forward-backward asymmetry at the Tevatron [1, 2], CDF's anomalous bump in W + dijet production [3], the LHC's exclusion of huge swathes of supersymmetric parameter space [4, 5] and hints of the Higgs boson from both the Tevatron and the LHC [6-8].

The purpose of this talk is to examine a selection of the past years' collider-QCD developments, attempting to place them in the context of the above "headline" developments. To guide us through this exercise, let us start by recalling that hard collider events can be broken up into various components: the non-perturbative structure of the proton, *e.g.* encoded in parton distribution functions and as relevant also to multiple semi-soft interactions; the "hard" process, amenable to fixed-order perturbative calculation, usually involving at most a handful of partons; the fragmentation of those partons, often implemented as a parton shower; and the hadronisation process, by which partons turn into the hadrons that are observed experimentally. All of these elements must be dealt with correctly (and together) if one is to fully predict the properties of events at hadron colliders. We start our examination of recent QCD progress by considering the element that has seen the most concerted effort, namely the hard process.

2. – The hard process at next-to-leading order

The hard process is where we make use of a perturbative expansion in the strong-coupling constant, α_s. Given that $\alpha_s \sim 0.1$ at the scales of relevance, one might expect that a leading-order (LO) calculation should generally be accurate to within about 10%. It is quite straightforward to check whether this is the case across a range of processes with the help of a tool such as NLOJet++ [9], MCFM [10] and VBFNLO [11]. While there are cases where next-to-leading order corrections are modest, for example for the inclusive jet spectrum, quite often one finds that the NLO terms are large: the Z-boson p_t spectrum sees a 50% correction at NLO; and the jet p_t spectrum in events with a Z-boson sees a NLO correction of several hundred percent. Sometimes these large corrections can be understood based on simple physical considerations, for example the appearance of new, enhanced topologies at NLO. There is, however, no general understanding of the different sizes of the NLO corrections and so, to obtain a reasonable degree of accuracy for hadron collider predictions, one must usually explicitly calculate the NLO terms.

In recent years, guidance as to which NLO calculations to carry out has come from the many different searches that are being performed. A classic example comes from SUSY searches: gluinos can decay to a squark and antiquark, with the squark then decaying to a quark and unobserved neutralino, so the signature for pair production of gluinos is the presence of four jets and missing energy; an important background is then Z plus 4-jets, where the Z-boson decays to neutrinos. One would like to know this background to NLO.

A measure of the difficulty of such a calculation is the number of external legs: Z plus 4-jet production is a $2 \to 5$ process. The first hadron-collider NLO calculation was for the Drell-Yan process in 1979, *i.e.* essentially a $2 \to 1$ process [12]. It was not until 1987 that $2 \to 2$ processes started to be calculated, including photon+jet [13], heavy-quark pair production [14] and dijet production [15, 16]. $2 \to 3$ processes started to follow ten years later, notably $Wb\bar{b}$ production [17]. Extrapolating, it should come as no surprise that it was around 2009 that $2 \to 4$ processes began to appear, with two calculations for $W + 3$ jets [18] and three for the production of two heavy $q\bar{q}$ pairs [19].

One might deduce that one should then wait until around 2019 for the background process that we mentioned above, $Z + 4$ jets, a $2 \to 5$ process. Yet, remarkably, its calculation appeared 8 years ahead of schedule, in 2011 [20] (another $2 \to 5$ process, $W + 4$ jets, came out earlier, in 2010 [21], and is in excellent agreement with data, cf. fig. 1 left). There have even been first calculations of processes with a complexity equivalent to that of a $2 \to 6$ process [22]. While it is beyond the scope of this review to describe the many ingenious innovations behind this progress, it should be said that a number have benefited from recent progress in understanding how to fully carry out a 20-year old dream [23] of sewing together tree amplitudes to obtain loop graphs (for more details see [24]).

Given this progress, it is natural to ask if it is being used by the experiments. At first sight, when opening one of the many SUSY search papers from ATLAS or CMS one is initially disappointed: nearly all the results rely either on matrix-element (tree level) calculations supplemented with parton showers (ME+PS) or "data-driven" estimates of backgrounds. Part of the reason is that pure NLO calculations provide information about partons, whereas experiments can only sensibly input hadrons to their detector simulations. Yet, digging deeper, there are cases where cutting-edge NLO results are

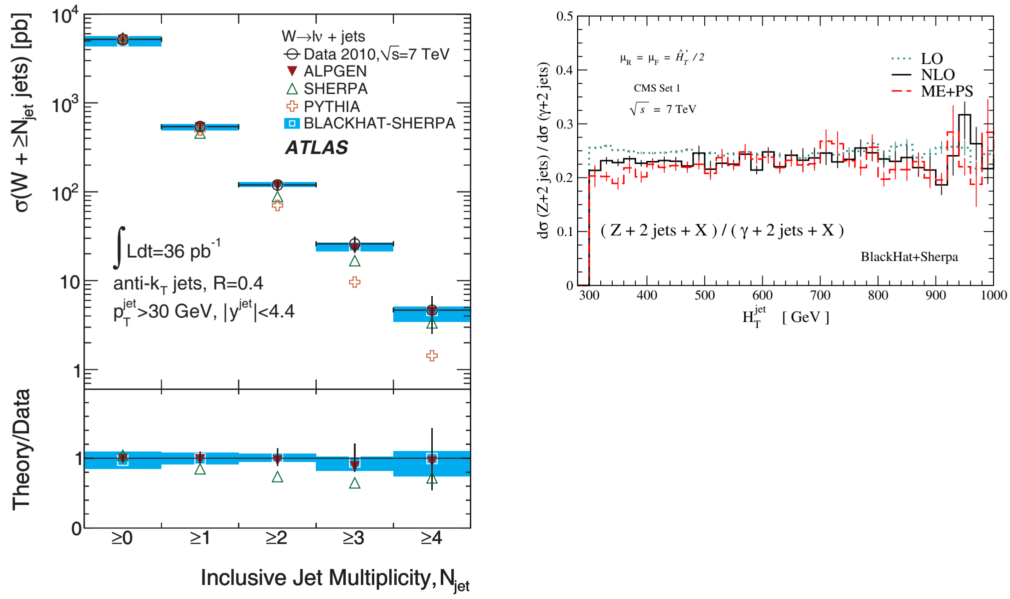

Fig. 1. – Left: comparison of measurements and NLO (Blackhat-Sherpa) predictions of $W+n$-jet cross sections *vs.* n [25]. Right: ratio of the $Z+2$-jet to $\gamma+2$-jet cross sections at LO, NLO and with parton showers matched to tree level calculations, showing excellent stability [26].

already having an impact. An example is [27], which compares data both to ME+PS and to data-driven background estimates, relying on the latter for its final SUSY exclusion limits. "Data-driven" sounds as if it is altogether independent of theorists. In this specific case, for estimating the $Z+$jets background the idea is to measure the $\gamma+$jets cross section (instead of a direct measurements of Z's, which suffers from the low $Z \to \ell^+\ell^-$ branching ratio) and then to use NLO predictions for the ratio of $\gamma+$jets to $Z+$jets to deduce the expected measured $Z+$jets background. Many experimental systematics such as jet-energy scale are common to both and therefore cancel in the ratio; meanwhile the theoretical prediction is extremely stable, fig. 1 (right). So, the data-driven method here is actually a clever way of exploiting precisely known aspects both theory and experiment, while minimising the impact of their intrinsic limitations. More generally, data-driven methods do not always (or even often) use NLO, but they do quite often involve this idea of finding a way to combine the best of theory and experiment.

3. – Systematically matching showers and NLO

Despite the power of data-driven methods, there remain many cases where the experiments do need a direct, quality prediction of hadron-collider processes. This is crucial in many Higgs searches, which nearly always rely on precise hadron level predictions of the signal, and also often of the backgrounds. And it was the case also for the analysis that led to the $W+2$-jet anomaly reported by CDF [3], but not found by D0 [28]. One of the standards for collider predictions involves the matching of tree level matrix-element calculations with parton showers and it is to such predictions, passed through detector simulations, that the CDF and D0 W + 2j results were compared.

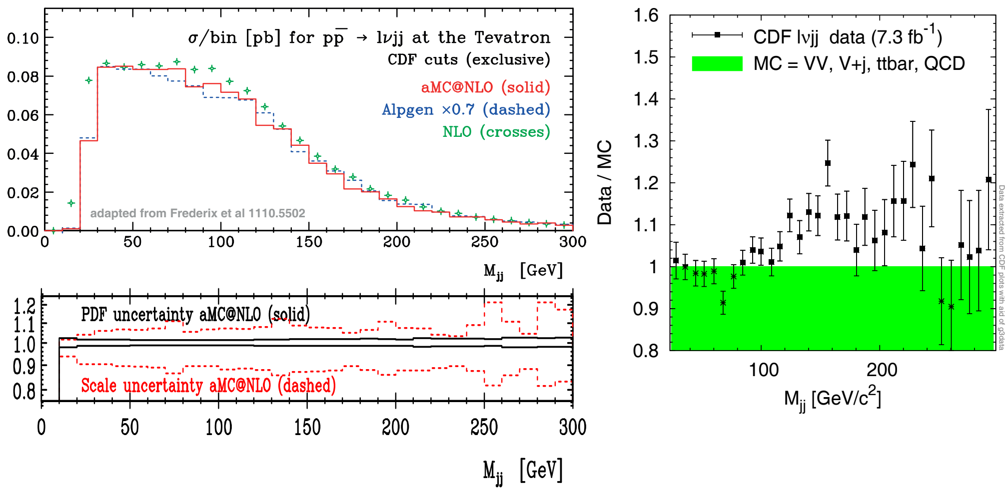

Fig. 2. – Left: aMC@NLO calculation of the dijet mass spectrum in $W + 2j$ events, compared to Alpgen (ME+PS) and pure NLO; also shown are the PDF and scale uncertainties. Right: the CDF data as read from the plots of [3], shown as a ratio to the expected background (also read from the plots), instead of the usual difference between data and background.

Combining tree level (*i.e.* LO) calculations and parton showers is relatively easy nowadays thanks to automated tools for tree-level predictions of essentially any standard-model process (*e.g.* MadGraph [29], Alpgen [30], Sherpa [31]) and methods such as MLM [32] and CKKW [33] matching, which address the issue of combining tree level calculations for different multiplicities, while avoiding the double counting that would be caused by the fact that parton-showers themselves generate extra emissions (for a recent review see [34]).

A concern with any calculation based on tree-level methods is that it is essentially a leading-order calculation, yet we know that NLO corrections can be large. NLO calculations can also be combined with parton showers, through the MC@NLO [35] or POWHEG [36] methods (see also [37]), generally with a significant improvement in precision; this is less straightforward than for tree-level calculations, because of the need for 1-loop matrix-elements and because of extra issues of double counting that arise at NLO. Until recently it had always been done on a case-by-case basis, usually limited to cases with low multiplicities (*e.g.*, just W production, with no jets other than that from the NLO radiation). A major development of the past couple of years has been that a huge number of extra processes has become available. Two approaches have been taken: one is the POWHEG-Box [38], which provides well-documented infrastructure for taking existing NLO calculations and turning them into a POWHEG type calculation (a related approach been taken in Sherpa [39]); the other is the aMC@NLO [40] approach, which builds on MadGraph so as to automatically calculate NLO (loop and tree-level) matrix elements and combine them with parton showers with the MC@NLO method.

A calculation of the $W + 2j$ process with the CDF cuts has been one of the headline applications of the aMC@NLO method, with results shown in fig. 2 (left)([1]). The

([1]) Showered NLO $W + 3$-jet results have since then become available with the MC@NLO method in Sherpa [41].

aMC@NLO and Alpgen results (the latter after a rescaling to account for an overall NLO K-factor) agree remarkably well in this case, suggesting that predictions are relatively stable. Interestingly, aMC@NLO and Alpgen bear more similarity to each other than either does to the pure NLO results, highlighting the importance of showering effects.

One advantage of NLO calculations (whether with a shower or not) is that scale variations can offer a reasonable way of estimating uncertainties. These uncertainties are shown also in fig. 2 (left) and are of the order of 10–15%. For comparison, the right-hand plot of fig. 2 shows the CDF data as a *ratio* to the expected background. What appears as a peak around 150 GeV in the usual plots of (data − background), here appears as the start of a broad 10% excess starting around 140 GeV, with only the barest hints of a peak around 150 GeV. It is not my intention to claim that background uncertainties are responsible for CDF's anomaly, but simply to provide a reminder that when looking at effects of the order of 10%, we enter a region where our ability to predict backgrounds sufficiently accurately can start to become a serious issue. Of course, a number of explanations have been proposed to explain the anomaly (beyond the scope of this paper). Ultimately, however, it is almost certainly impossible for outsiders to resolve this issue, and one can only hope that the CDF and D0 experiments will at some point have the means to bring closure to the question.

4. – Going beyond the limitations of NLO

There are at least two avenues to go beyond the limitations of NLO calculations. On the one hand one can aim for high precision, for example with NNLO. On the other, in the context of searches, one can try to make signals emerge more clearly.

4·1. *Next-to-next-to-leading order*. – NNLO is available for all processes involving the production of a single vector or Higgs boson, but until recently was mostly inexistent for processes with two bosons or with coloured particles in the final state. It is crucial not just in prediction backgrounds, but also in deriving information from "signals"—for example for extracting parton distribution functions from W and Z production differential cross sections; and, once (if) the Higgs boson is discovered, for determining its couplings to the rest of the standard model.

The past couple of years has seen several new NNLO calculations and they can roughly be divided into two classes: one class is that where NNLO delivers its promise of high precision, for example the inclusive calculation of vector-boson fusion Higgs production [42] or the differential calculation of WH production [43]. The former is shown in fig. 3 and, for once, the convergence is just as one would expect with a coupling ~ 0.1.

A second class of processes has more sobering results: fig. 3 (right) shows the recent NNLO $\gamma\gamma$ [44] prediction where one sees 50% corrections in going from NLO to NNLO. Yet another case where NNLO appears to face difficulties and that has seen extensive discussion is for the prediction of the efficiency of jet vetoes in Higgs production [45].

Various physics mechanisms can lead to this poor behaviour of the perturbative series: Sudakov logarithms when one puts excessively stringent cuts on the final state; threshold logarithms when one is limited by the available partonic centre of mass energy; and the appearance of partonic scattering channels at NLO or NNLO that were not possible at lower order (*e.g.*, $qq \to qq\gamma\gamma$). Still despite progress on individual aspects (*e.g.*, Higgs Sudakov boson [46, 47] and jet [48-51] p_t resummations, Higgs threshold resummations [52-54], or the combination of processes with different multiplicities [55]), one

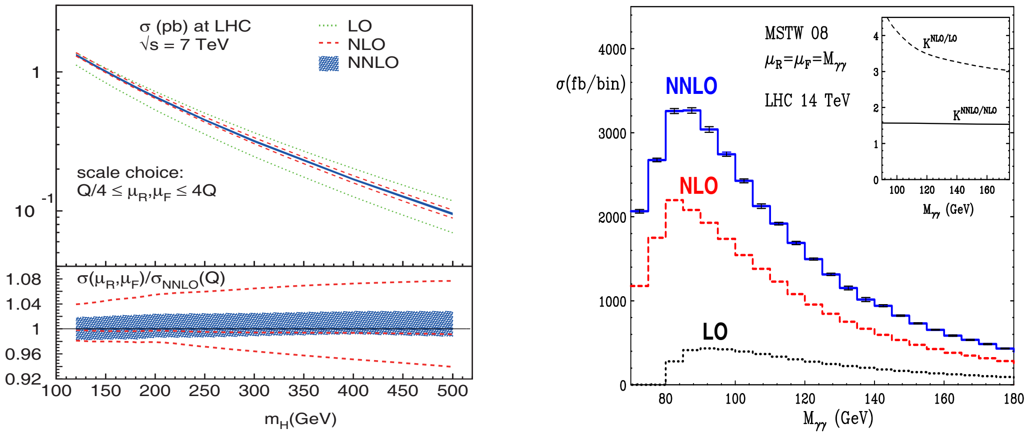

Fig. 3. – Recent NNLO predictions for inclusive vector-boson fusion [42] (left) and differential $\gamma\gamma$ production [44] (right).

cannot help but wonder whether with more insight we might not obtain predictions that just systematically converge better.

I cannot close this section without mentioning a result that appeared only after my presentation at the La Thuile meeting, the NNLO corrections to $q\bar{q} \to t\bar{t}$ [56]. It is the first time that a NNLO calculation appears for a process involving coloured particles in both initial and final states and as such is a groundbreaking achievement. It brings significantly improved precision, at the 3% level (roughly a factor of 3 improvement over NLO), to the prediction of the Tevatron $t\bar{t}$ cross section(^{2}).

4·2. *Rethinking searches*. – It can be tempting to say that if only we knew collider backgrounds better we would significantly improve the reach of a range of searches. But I believe it is just as important to ask the question of whether using our understanding of QCD can help us to find better analysis techniques, techniques that improve signal-to-background (S/B) ratios (and sometimes also $S/\sqrt{B}$) and so reduce the impact of background uncertainties.

One example of this is in the search for $b\bar{b}$ decays of a light Higgs boson when produced in association with a W or Z. Long thought to be inaccessible due to huge backgrounds, this channel became possible again after the results of [57], which showed how to improve signal-to-background ratios by going to high p_t (backgrounds drop faster than signal) and developing appropriate "boosted-Higgs" jet-substructure reconstruction methods. Since then, the idea of going to high p_t has been adopted in [58,59], though there are insufficient data so far to truly benefit from the new jet substructure methods. In parallel, this and other early work has spurred a whole new field of investigation into event-topologies with boosted tops, vector and Higgs bosons, and BSM particles, together with extensive further developments on the jet-substructure analysis techniques. Several reviews cover this progress in detail [60-62].

(^{2}) It is also interesting because there were a number of predictions for the $t\bar{t}$ cross section based on threshold resummation, even though Tevatron $t\bar{t}$ production is not strictly at threshold. A verification of how well these performed can provide useful insight into the applicability of different approaches to threshold resummation, possibly also in other not-really-threshold contexts such as LHC Higgs production.

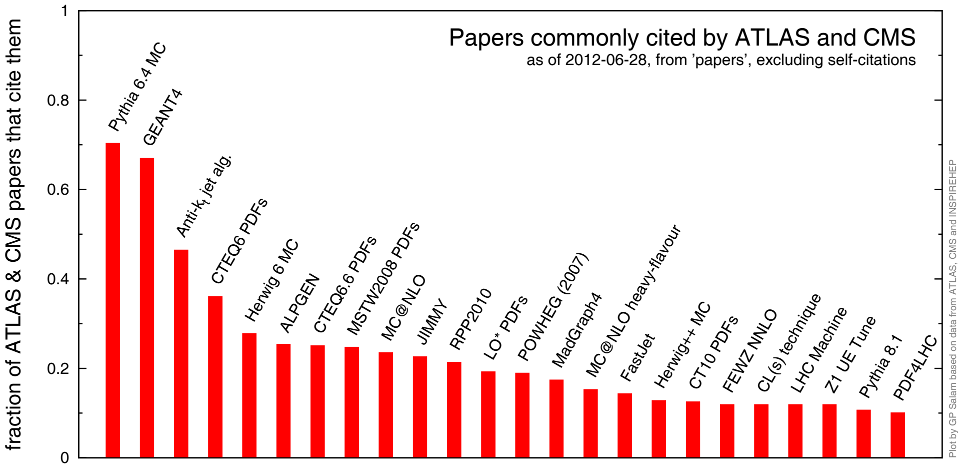

Fig. 4. – The papers most frequently cited by the ATLAS and CMS collaborations (excluding citations to ATLAS and CMS), showing the fraction of ATLAS and CMS papers that refer to each one.

While "boosted-object" searches have garnered much of the attention recently, progress is also being made in better signal detection in other areas too: quark/gluon discrimination has recently seen a renewal of interest [63] and may have applications in many searches; and there is clearly scope for novel methods even in "standard" SUSY searches [64].

A general question that remains open here is whether such improvements will continue to come mainly from an intuitive understanding of QCD *vs.* BSM differences, as has largely been the case so far, or whether there is a benefit to be had also from more quantitative, analytical insight into how signals and backgrounds differ.

5. – Conclusions

Many of the cutting-edge QCD research results discussed here have come with an initial focus on one or the other specific class of search or application. It is interesting to look also at what the LHC experiments use across the board, on a day-to-day basis. Figure 4 shows the papers most commonly referred to by ATLAS and CMS and, for each, the fraction of the collaborations' articles that refer to them. Some aspects of this graph are unsurprising, such as the overwhelming role played by Pythia. Other aspects provide a reminder that such citations data should be interpreted with an abundance of caution: one cannot help but notice the position of the "LHC Machine" relative to Pythia([3]). Still, it is striking that of the 24 articles shown (those cited by more than 10% of the collaborations' papers), 20 stem from the QCD community, a tribute to the key role being played by QCD at the LHC.

([3]) Of course, Pythia is easier to run.

* * *

I am grateful to V. Cavaliere, J. Winter and W. Zhu for numerous discussions related to the CDF $W +$ dijet anomaly. I also wish to thank the organisers for the stimulating environment provided during the workshop and both the organisers and the French Agence Nationale de la Recherche (grant ANR-BLAN-2009-060) for financial support.

REFERENCES

[1] Aaltonen T. *et al.* (CDF Collaboration), *Phys. Rev. D*, **83** (2011) 112003.
[2] Abazov V. M. *et al.* (D0 Collaboration), *Phys. Rev. D*, **84** (2011) 112005.
[3] Aaltonen T. *et al.* (CDF Collaboration), *Phys. Rev. Lett.*, **106** (2011) 171801.
[4] Aad G. *et al.* (ATLAS Collaboration), *Phys. Lett. B*, **710** (2012) 67.
[5] Chatrchyan S. *et al.* (CMS Collaboration), *Phys. Rev. Lett.*, **107** (2011) 221804.
[6] Aad G. *et al.* (ATLAS Collaboration), *Phys. Lett. B*, **710** (2012) 49.
[7] Chatrchyan S. *et al.* (CMS Collaboration), *Phys. Lett. B*, **710** (2012) 26.
[8] TEVNPH and CDF and D0 Collaborations, arXiv:1203.3774 [hep-ex].
[9] Nagy Z., *Phys. Rev. D*, **68** (2003) 094002.
[10] Campbell J. M. and Ellis R. K., *Phys. Rev. D*, **65** (2002) 113007.
[11] Arnold K. *et al.*, *Comput. Phys. Commun.*, **180** (2009) 1661.
[12] Altarelli G., Ellis R. K. and Martinelli G., *Nucl. Phys. B*, **157** (1979) 461.
[13] Aurenche P. *et al.*, *Nucl. Phys. B*, **286** (1987) 553.
[14] Nason P., Dawson S. and Ellis R. K., *Nucl. Phys. B*, **303** (1988) 607; Beenakker W., Kuijf H., van Neerven W. L. and Smith J., *Phys. Rev. D*, **40** (1989) 54.
[15] Aversa F., Chiappetta P., Greco M. and Guillet J. P., *Nucl. Phys. B*, **327** (1989) 105.
[16] Giele W. T., Glover E. W. N. and Kosower D. A., *Nucl. Phys. B*, **403** (1993) 633.
[17] Ellis R. K. and Veseli S., *Phys. Rev. D*, **60** (1999) 011501.
[18] Ellis R. K., Melnikov K. and Zanderighi G., *JHEP*, **04** (2009) 077; Berger C. F. *et al.*, *Phys. Rev. Lett.*, **102** (2009) 222001.
[19] Bredenstein A., Denner A., Dittmaier S. and Pozzorini S., *Phys. Rev. Lett.*, **103** (2009) 012002; Bevilacqua G., Czakon M., Papadopoulos C. G., Pittau R. and Worek M., *JHEP*, **09** (2009) 109; Binoth T. *et al.*, *Phys. Lett. B*, **685** (2010) 293.
[20] Ita H. *et al.*, *Phys. Rev. D*, **85** (2012) 031501.
[21] Berger C. F. *et al.*, *Phys. Rev. Lett.*, **106** (2011) 092001.
[22] Becker S. *et al.*, *Phys. Rev. Lett.*, **108** (2012) 032005.
[23] Bern Z., Dixon L. J., Dunbar D. C. and Kosower D. A., *Nucl. Phys. B*, **425** (1994) 217; *Nucl. Phys. B*, **435** (1995) 59.
[24] Ellis R. K., Kunszt Z., Melnikov K. and Zanderighi G., arXiv:1105.4319 [hep-ph].
[25] Aad G. *et al.* (ATLAS Collaboration), *Phys. Rev. D*, **85** (2012) 092002.
[26] Bern Z. *et al.*, *Phys. Rev. D*, **84** (2011) 114002.
[27] CMS Collaboration, CMS-PAS-SUS-1104.
[28] Abazov V. M. *et al.* (D0 Collaboration), *Phys. Rev. Lett.*, **107** (2011) 011804.
[29] Alwall J. *et al.*, *JHEP*, **09** (2007) 028.
[30] Mangano M. L. *et al.*, *JHEP*, **07** (2003) 001 [hep-ph/0206293].
[31] Gleisberg T. *et al.*, *JHEP*, **02** (2009) 007.
[32] Alwall J. *et al.*, *Eur. Phys. J. C*, **53** (2008) 473.
[33] Catani S., Krauss F., Kuhn R. and Webber B. R., *JHEP*, **11** (2001) 063 [hep-ph/0109231].
[34] Buckley A. *et al.*, *Phys. Rep.*, **504** (2011) 145.
[35] Frixione S. and Webber B. R., *JHEP*, **06** (2002) 029.
[36] Nason P., *JHEP*, **11** (2004) 040.

[37] Nason P. and Webber B., arXiv:1202.1251 [hep-ph].
[38] Alioli S., Nason P., Oleari C. and Re E., *JHEP*, **06** (2010) 043.
[39] Hoche S., Krauss F., Schonherr M. and Siegert F., *JHEP*, **04** (2011) 024.
[40] Hirschi V. *et al.*, *JHEP*, **05** (2011) 044.
[41] Hoeche S., Krauss F., Schonherr M. and Siegert F., [arXiv:1201.5882 [hep-ph]].
[42] Bolzoni P., Maltoni F., Moch S.-O. and Zaro M., *Phys. Rev. Lett.*, **105** (2010) 011801.
[43] Ferrera G., Grazzini M. and Tramontano F., *Phys. Rev. Lett.*, **107** (2011) 152003.
[44] Catani S. *et al.*, *Phys. Rev. Lett.*, **108** (2012) 072001.
[45] Dittmaier S. *et al.*, arXiv:1201.3084 [hep-ph].
[46] Bozzi G., Catani S., de Florian D. and Grazzini M., *Nucl. Phys. B*, **737** (2006) 73.
[47] Cao Q.-H., Chen C.-R., Schmidt C. and Yuan C.-P., arXiv:0909.2305 [hep-ph].
[48] Banfi A., Monni P. F., Salam G. P. and Zanderighi G., arXiv:1206.4998 [hep-ph].
[49] Becher T. and Neubert M., arXiv:1205.3806 [hep-ph].
[50] Tackmann F. J., Walsh J. R. and Zuberi S., arXiv:1206.4312 [hep-ph].
[51] Banfi A., Salam G. P. and Zanderighi G., arXiv:1203.5773 [hep-ph].
[52] Catani S., de Florian D., Grazzini M. and Nason P., *JHEP*, **07** (2003) 028.
[53] Kidonakis N., *Phys. Rev. D*, **77** (2008) 053008.
[54] Ahrens V., Becher T., Neubert M. and Yang L. L., *Phys. Rev. D*, **79** (2009) 033013.
[55] Rubin M., Salam G. P. and Sapeta S., *JHEP*, **09** (2010) 084.
[56] Baernreuther P., Czakon M. and Mitov A., arXiv:1204.5201 [hep-ph].
[57] Butterworth J. M., Davison A. R., Rubin M. and Salam G. P., *Phys. Rev. Lett.*, **100** (2008) 242001.
[58] ATLAS Collaboration, ATLAS-CONF-2012-015.
[59] Chatrchyan S. *et al.* (CMS Collaboration), *Phys. Lett. B*, **710** (2012) 284.
[60] Abdesselam A. *et al.*, *Eur. Phys. J. C*, **71** (2011) 1661.
[61] Altheimer A. *et al.*, *J. Phys. G*, **39** (2012) 063001.
[62] Plehn T. and Spannowsky M., arXiv:1112.4441 [hep-ph].
[63] Gallicchio J. and Schwartz M. D., *Phys. Rev. Lett.*, **107** (2011) 172001.
[64] Hook A., Izaguirre E., Lisanti M. and Wacker J. G., *Phys. Rev. D*, **85** (2012) 055029.

SESSION IV - FLAVOUR PHYSICS, CP VIOLATION AND RARE DECAYS

IL NUOVO CIMENTO Vol. 35 C, N. 6 Novembre-Dicembre 2012
DOI 10.1393/ncc/i2012-11363-9

Colloquia: LaThuile12

Study of CPV in b and charm systems at LHCb

E. Maurice on behalf of the LHCb Collaboration
CPPM, Université Aix-Marseille, CNRS/IN2P3 - France

ricevuto il 7 Settembre 2012

Summary. — The LHCb experiment is a single-arm spectrometer designed to pursue an extensive study of CP violation in b and charm systems. In this contribution, three recent measurements are presented. First, the difference between CP asymmetries of $D^0 \to K^-K^+$ and $D^0 \to \pi^-\pi^+$ decays using $0.6\,\mathrm{pb}^{-1}$ of 2011 data is detailled. Then an important milestones towards the measurement of the γ angle is presented with the study of $B^\pm \to DK^\pm$ decays using $1\,\mathrm{fb}^{-1}$. Third, the measurement of the CP-violating phase ϕ_s in $B_s^0 \to J/\psi\phi$ and $B_s^0 \to J/\psi f_0$ is reported.

PACS 12.15.Ff – Quark and lepton masses and mixing.
PACS 12.15.Hh – Determination of Cabibbo-Kobayashi & Maskawa (CKM) matrix elements.

1. – Introduction

The LHCb experiment is dedicated to the study of charm and beauty flavour physics. Precise measurements in these sectors allow to test the CKM paradigm of flavour structure and CP violation. More precisely, LHCb investigate the possible New Physics effects in the loop-mediated processes. In this document, we present three recent LHCb results about CP violation in charm and beauty sectors. In sect. **2**, we present the difference in time-integrated CP asymmetries between $D^0 \to K^-K^+$ and $D^0 \to \pi^-\pi^+$, using $0.6\,\mathrm{pb}^{-1}$ of 2011 data. In sect. **3**, we detail the CP violation in $B^\pm \to DK^\pm$. In sect. **4**, we report on the measurement of the CP-violating phase ϕ_s.

2. – CP violation in charm

In the Standard Model, CP violation in charm sector is expected to be small [1, 2]. New Physics could enhance the rate of CP violation [3]. LHCb measures the difference in time-integrated CP asymmetries between $D^0 \to K^-K^+$ and $D^0 \to \pi^-\pi^+$, using $0.6\,\mathrm{pb}^{-1}$ of data collected in 2011 [4]. By requiring a $D^{*+} \to D^0\pi^+$ decay, the initial state, D^0 or $\overline{D}^0$, is tagged using the sign of the “slow” pion $\pi^\pm$.

The raw asymmetry for tagged D^0 decays to a final state f is defined as

$$A_{raw}(f) = \frac{N(D^{*+} \to D^0(f)\pi^+) - N(D^{*-} \to \overline{D}^0(\overline{f})\pi^-)}{N(D^{*+} \to D^0(f)\pi^+) + N(D^{*-} \to \overline{D}^0(\overline{f})\pi^-)},$$

with $N(X)$ the number of reconstructed events of decays X, and f the final state. This raw asymmetry can be written as the sum of various asymmetries,

$$A_{raw}(f) = A_{CP}(f) + A_D(f) + A_D(\pi_s) + A_P(D^{*+}),$$

where $A_{CP}(f)$ is the intrinsic physics CP asymmetry, $A_D(f)$ the asymmetry to select the D^0 decay into the final state f, $A_D(\pi_s)$ the detection asymmetry of the slow pion coming from the D^{*+} decay chain, and $A_P(D^{*+})$ the production asymmetry for prompt D^{*+} mesons.

For a two-body decay of a spin-0 particle to a self-conjugate final state there can be no D^0 detection asymmetry: $A_D(K^-K^+) = A_D(\pi^-\pi^+) = 0$. At first order, $A_D(\pi_s)$ and $A_P(D^{*+})$ cancel out in the difference $A_{raw}(K^-K^+) - A_{raw}(\pi^-\pi^+)$. Finally, the measurement of ΔA_{CP} corresponds to the difference of physics asymmetries:

$$\Delta A_{CP} = A_{CP}(K^-K^+) - A_{CP}(\pi^-\pi^+) = A_{raw}(K^-K^+) - A_{raw}(\pi^-\pi^+).$$

In order to minimize second-order effects, the analysis is done in bins of kinematic variables, magnet polarity and running periods. In total, 216 independent measurements are made for each decay mode. The χ^2/ndf of these measurements is 211/215. The final time-integrated difference in CP asymmetry between $D^0 \to K^-K^+$ and $D^0 \to \pi^-\pi^+$ decays is the weighted average over 216 bins:

$$\Delta A_{CP} = [-0.82 \pm 0.21(\text{stat}) \pm 0.11(\text{syst})]\,\%.$$

It is the first evidence of CP violation in charm sector, with a significance of 3.5σ. This measurement is consistent with the current HFAG world average [5].

ΔA_{CP} can be written at first order as the sum of CP asymmetries:

$$\Delta A_{CP} = \left(a_{CP}^{dir}(K^-K^+) - a_{CP}^{dir}(\pi^-\pi^+)\right) + \frac{\Delta\langle t\rangle}{\tau} a_{CP}^{ind},$$

with a_{CP}^{dir} the asymmetry coming from direct CP violation for the decay, $\langle\Delta t\rangle$ the difference in average decay time of the D^0 mesons in the K^-K^+ and $\pi^-\pi^+$ sample, τ the true D^0 lifetime, a_{CP}^{ind} the asymmetry from CP violation in the mixing. Using this result, the HFAG world-average combination in the plan $(\Delta a_{CP}^{dir}, a_{CP}^{ind})$ represented by the fig. 1 gives

$$a_{CP}^{ind} = (-0.019 \pm 0.232)\%, \qquad \text{and} \qquad \Delta a_{CP}^{dir} = (-0.645 \pm 0.180)\%.$$

This combination is consistent with no CP violation at 0.128%. To understand this 3.5σ effect, further analyses are ongoing at LHCb, and more theoretical precision is needed.

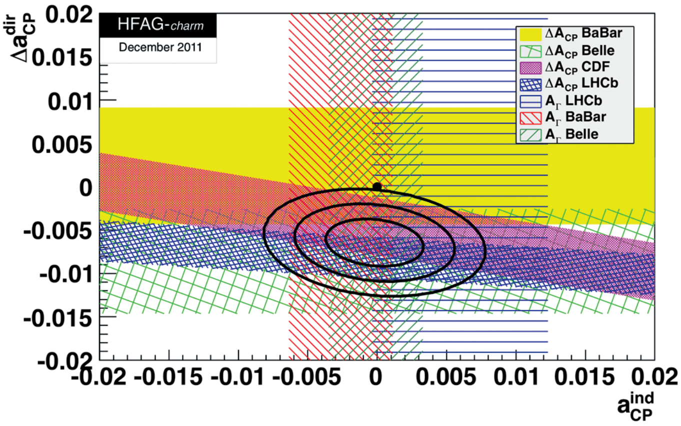

Fig. 1. – HFAG combination of the ΔA_{CP} and A_Γ measurements [5]. The bands represent $\pm 1\sigma$ intervals. No CP violation correspond to the black point at $(0,0)$, and the two dimensional 68% CL, 95% CL and 99.7% CL regions are the black ellipses.

3. – Toward a measurement of the CKM angle γ

The γ angle is the least accurately known parameter of the CKM unitarity triangle. In terms of CKM elements, γ is defined as: $\gamma = \arg(-\frac{V_{ud}V_{ub}^\star}{V_{cd}V_{cb}^\star})$. The indirect determination via global fits to experimental data gives $\gamma = (67.1^{+4.6}_{-3.7})$ [6]. One of the main goals of the LHCb experiment is to perform a precise direct measurement of this angle. It is extracted from the interference between $b \to u$ and $b \to c$ transitions. LHCb experiment has passed many milestones towards γ measurement with [7]. This contribution focuses on the first LHCb paper using the whole 2011 data: the direct CP violation in $B^\pm \to D^0 K^\pm$ decays with $1\,\text{fb}^{-1}$ [8].

The analyses of direct CP violation in $B^\pm \to D^0 K^\pm$ are time-integrated measurements, using only the self-tagging modes. The interference between decays to the same final products $(K^-K^+\pi^-)$ by different intermediate states (D^0K^- or $\overline{D}^0K^-$) gives access to γ. Depending of the D^0 decay, different measurement methods are avaiblable. The sensitivity to γ is given by the asymmetries between the decay and its conjugate, A, and the ratio of the sum compared to the favoured control mode $B^- \to D^0 h^-$, R.

The GLW method was proposed by Gronau, Wyler and London [9, 10]. It is a theoretically clean measurement of the angle γ from the rate and asymmetry measurement of $B^- \to D_{CP}K^-$ decays, where the D^0 meson decays to CP eigenstates: $D^0 \to K^+K^-$, $D^0 \to \pi^+\pi^-$. This method benefits from the interference between the dominant $b \to cu$ transition with the doubly CKM-suppressed $b \to uc$ transition. The asymmetry and ratio observables are defined by

$$R_{CP+} = 2\frac{\Gamma(B^- \to D_\pm K^-) + \Gamma(B^+ \to D_\pm K^+)}{\Gamma(B^- \to D^0K^-) + \Gamma(B^+ \to D^0K^+)} = 1 + r_B^2 \pm 2r_B \cos\delta_B \cos\gamma,$$

$$A_{CP+} = \frac{\Gamma(B^- \to D_\pm K^-) - \Gamma(B^+ \to D_\pm K^+)}{\Gamma(B^- \to D_\pm K^-) + \Gamma(B^+ \to D_\pm K^+)} = \pm 2r_B \sin\delta_B \sin\gamma / R_{CP+}$$

with the relative magnitude of suppressed amplitude $r_B = |A(b \to u)/A(b \to c)|$, the strong phase $\delta_B = \arg(A(b \to u)/A(b \to c)$ and the weak phase γ.

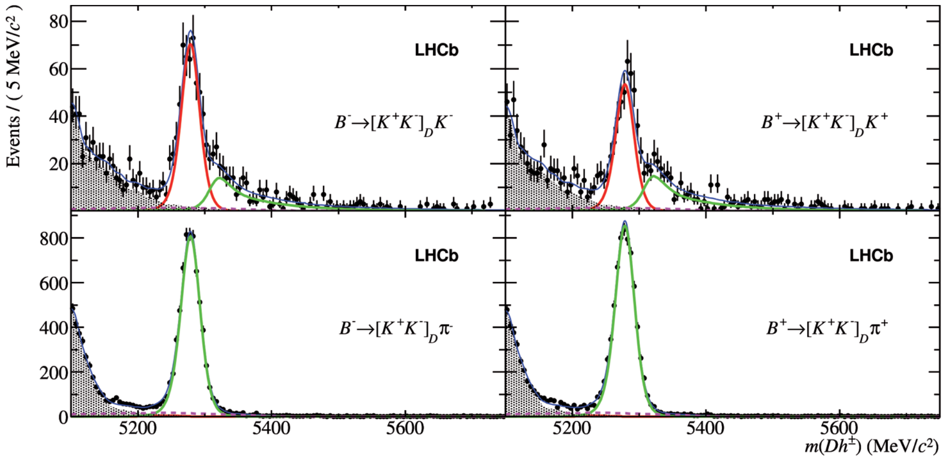

Fig. 2. – Invariant-mass distributions of selected $B^{\pm} \to [K^+K^-]_D h^{\pm}$ candidates [8]. The left plots are B^- candidates, B^+ are on the right. In the top plots, the bachelor track is assigned to be a kaon, although in the bottom plots it is a pion. The dark (red) curve represents the $B \to DK^{\pm}$ events, the light (green) curve is $B \to D\pi^{\pm}$. The shaded contribution are partially reconstructed events and the total PDF includes the combinatorial component. The contribution from $\Lambda_b \to \Lambda_c^{\pm} h^{\mp}$ decays is indicated by the dashed line.

The ADS method is a modification of the GLW approach, developed by Atwood, Dunietz and Soni [11]. In the $B^- \to D^0 K^-$ decays, the D^0 meson decays to flavour specific final states: $D^0 \to K\pi$. The favoured transition $b \to c$ is followed by the doubly CKM-suppressed D decay interfering with the supressed $b \to u$ transition followed by the CKM-favoured D decay. The asymmetry and ratio are given by

$$R_{ADS} = \frac{\Gamma(B^- \to D_{\pm}K^-) + \Gamma(B^+ \to D_{\mp}K^+)}{\Gamma(B^- \to D_{\mp}K^-) + \Gamma(B^+ \to D_{\pm}K^+)} = r_B^2 + r_D^2 + 2r_B r_D \cos(\delta_B + \delta_D)\cos\gamma,$$

$$A_{ADS} = \frac{\Gamma(B^- \to D_{\pm}K^-) - \Gamma(B^+ \to D_{\mp}K^+)}{\Gamma(B^- \to D_{\pm}K^-) + \Gamma(B^+ \to D_{\mp}K^+)} = \frac{2r_B r_D \sin(\delta_B + \delta_D)\sin\gamma}{R_{ADS}},$$

with r_B, δ_B, γ already defined for the GLW method, and r_D, δ_D the corresponding amplitude ratio and strong phase difference of the D meson decay amplitudes.

For this analysis, the strategy is to reconstruct every mass hypothesis combination, then to extract the ratios and asymmetries with a simultaneous fit. Figures 2 and 3 show, respectively, the invariant-mass distributions of $B^{\pm} \to D_{CP}\pi^{\pm}$ and $B^{\pm} \to D_{\pm}\pi^{\pm}$. In fig. 2, there is a clear asymmetry in $B^{\pm} \to [KK]_D K^{\pm}$, but no asymmetry in $B^{\pm} \to [KK]_D \pi^{\pm}$.

The measurements give

$$A_{CP+} = 0.15 \pm 0.03 \pm 0.01 \quad \text{and} \quad R_{CP+} = 1.01 \pm 0.04 \pm 0.01,$$

$$A_{ADS(K)} = -0.520 \pm 0.150 \pm 0.021 \quad \text{and} \quad R_{ADS(K)} = 0.0152 \pm 0.0020 \pm 0.0004,$$

$$A_{ADS(\pi)} = 0.143 \pm 0.062 \pm 0.011 \quad \text{and} \quad R_{ADS(\pi)} = 0.0041 \pm 0.0003 \pm 0.0001.$$

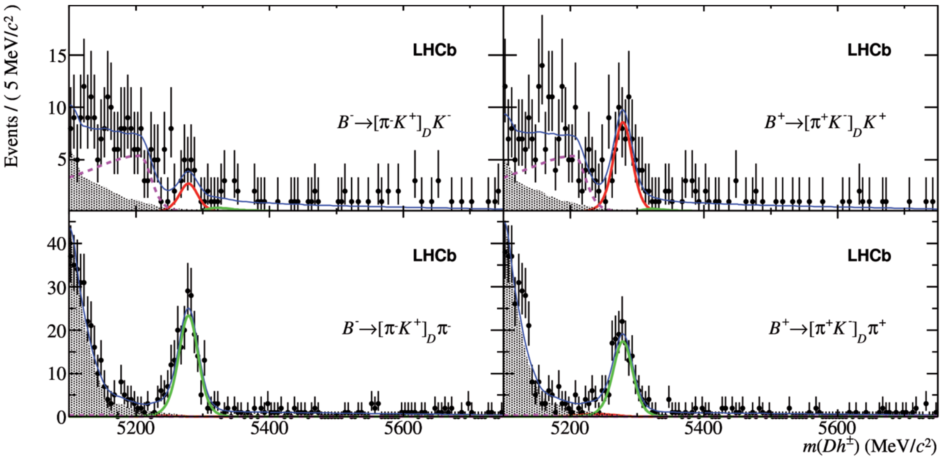

Fig. 3. – Invariant-mass distribution of selection $B^\pm \to [\pi^\pm K^\mp]_D h^\pm$ candidates [8]. See the caption of 2 for a full description. The dashed line here represents the partially reconstructed, but Cabbibo-favoured, $B_s \to \overline{D}^0 K^- \pi^+$ and $\overline{B}_s \to D^0 K^+ \pi^-$ decays where the pions are lost. The pollution from favoured mode cross feed is drawn, but is too small to be seen.

These measurements are an important contribution to a future extraction of the γ angle. They are the most precise measurement and in good agreement with the B factories [5].

4. – B_s^0 mixing phase ϕ_s

The interference between B_s^0 decays to $J/\psi\phi$ either directly or via B_s^0-$\overline{B}_s^0$ oscillation gives rise to a CP-violating phase ϕ_s. In the Standard Model, this phase is predicted to be $\simeq -2\beta_s$, where $\beta_s = \arg(-V_{ts}V_{tb}^*/V_{cs}V_{cb}^*)$. The indirect determination via global fits to experimental data gives $2\beta_s = (0.0364 \pm 0.0016)$ rad [6], within the Standard Model. ϕ_s is one of the CP observables with the smallest theoretical uncertainty in the Standard Model, neglecting the penguins contributions, and New Physics could significantly modify this prediction.

The decays $B_s^0 \to J/\psi\phi$ are pseudo-scalar to vector-vector transitions. Morever, the K^+K^- non-resonant state, the S-wave, is taken into account. Thus the final state is a mixture of CP odd and CP even states. It is described by a four time-dependent decay amplitudes corresponding to transitions in which the J/ψ and ϕ or K^+K^- have a relative orbital momentum L of 0, 1, or 2. In the transversity formalism [12], the initial amplitudes at time $t = 0$, $A_0(0)$ and $A_\parallel(0)$ describe the decays with $L = 0, 2$ while $A_\perp(0)$ and A_S describes the $L = 1$ final states. The arguments of these complex amplitudes are strong phases denoted δ_0, $\delta_\parallel$, $\delta_\perp$ and δ_S.

The measurement of ϕ_s phase requires a very good proper-time resolution to resolve the fast B_s^0 oscillations. It has been measured in $B_s^0 \to J/\psi\phi$ channel: $\sigma_t = 50$ fs. Another key step towards the ϕ_s measurement is the tagging of the initial B-flavour. The tagging algorithm exploits charged tracks originating from the b-hadron opposite to the signal B-meson (kaon, muon, electron and vertex charge) and also tracks close to the signal B-meson (same-side tagging). The opposite side algorithm is optimized using $B^0 \to D^{*-}\mu^+\nu_\mu$ and $B^+ \to J/\psi K^+$ events and calibrated using $B^+ \to J/\psi K^+$,

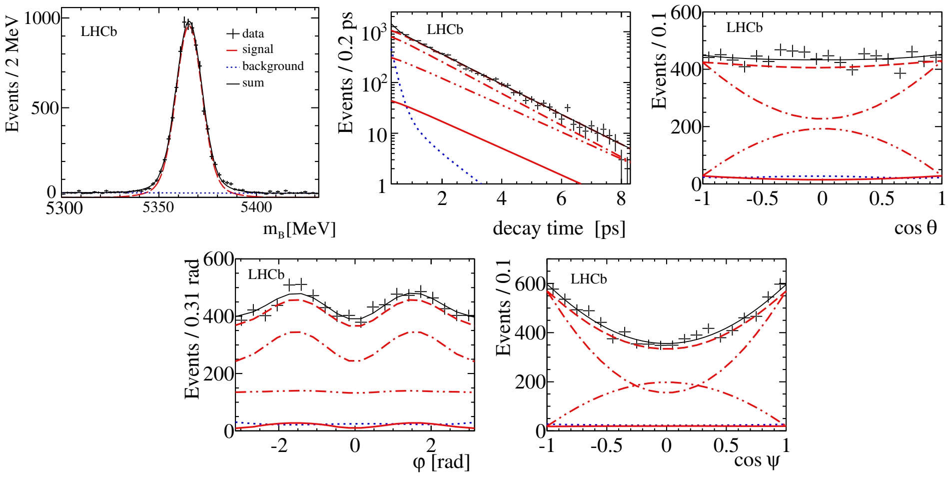

Fig. 4. – Data points overlaid with fit projections for the reconstructed invariant mass, decay time and transversity angle distributions of selected $B_s^0 \to J/\psi\phi$, candidates, in a mass range of $\pm 20\,\mathrm{MeV}/c^2$ around the reconstructed B_s^0 mass except for the invariant mass distribution [13]. The total fit result is represented by the black line. The signal components are represented by the red lines, and the background component by the blue line.

$B^0 \to J/\psi K^{*0}$ events [14]. An additional test is performed in [15], by measuring the B_s^0-$\overline{B}_s^0$ mixing frequency using $B_s^0 \to D_s^-(3)\pi^+$ events using $370\,\mathrm{pb}^{-1}$:

$$\Delta m_s = 17.725 \pm 0.041(\text{stat.}) \pm 0.026(\text{syst.})\,\mathrm{ps}^{-1},$$

which is compatible and competitive with the world best measurement [16].

The physical parameters are extracted from a maximum likelihood fit to the mass, proper time and angles distributions of the fully reconstructed candidates as shown in fig. 4. In $370\,\mathrm{pb}^{-1}$, $8\,276 \pm 94$ $B_s^0 \to J/\psi\phi$ signal events are extracted [13]. Two solutions are available in the plan $(\Delta\Gamma_s, \phi_s)$, due to the invariance of the differential decay rate under the transformation $(\phi_s, \Delta\Gamma_s, \delta_\parallel - \delta_0, \delta_\perp - \delta_0, \delta_s - \delta_0) \leftrightarrow (\pi - \phi_s, -\Delta\,\Gamma_s, \delta_0 - \delta_\parallel, \delta_0 - \delta_\perp, \delta_0 - \delta_s)$. LHCb has recently solved this ambiguity [17] by studying the interferences between the S-wave and the P-wave, following similar method as BaBar $\cos(2\beta)$ measurement [18]. In the $B_s^0 \to J/\psi\phi$ channel, we measure [13]:

$$\begin{aligned}
\phi_s &= 0.15 \pm 0.18 \pm 0.06\,\mathrm{rad},\\
\Gamma_s &= 0.656 \pm 0.009 \pm 0.008\,\mathrm{ps}^{-1},\\
\Delta\Gamma_s &= 0.123 \pm 0.029 \pm 0.011\,\mathrm{ps}^{-1},\\
|A_\perp(0)|^2 &= 0.237 \pm 0.015 \pm 0.012,\\
|A_0(0)|^2 &= 0.497 \pm 0.013 \pm 0.030,\\
|A_S|^2 &= 0.042 \pm 0.015 \pm 0.018,\\
\delta_\parallel &= 2.95 \pm 0.37 \pm 0.12,\\
\delta_S &= 2.98 \pm 0.36 \pm 0.12,
\end{aligned}$$

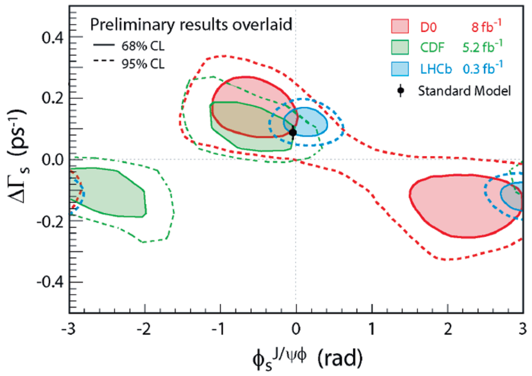

Fig. 5. – Artist's view of the $\Delta\Gamma_s$ and ϕ_s measurements at the end of 2011. CDF update is missing: $\phi_s \in [-\pi, -2.52] \cup [-0.60, 0.12] \cup [3.02, \pi]$ at 68% CL, with $9.6\,\mathrm{pb}^{-1}$ [19].

where the first error is the statistical error from the fit and the second error is the systematic uncertainty. It the first direct evidence of non-zero $\Delta\Gamma_s$.

The ϕ_s phase is extracted from the decay $B_s^0 \to J/\psi f_0$ too [20]. A simultaneous fit in these two channels with common ϕ_s, Γ_s, $\Delta\Gamma_s$ and Δm_s gives [21]:

$$\phi_s = 0.03 \pm 0.16(\mathrm{stat}) \pm 0.07(\mathrm{syst})\,\mathrm{rad}.$$

It is the most precise measurement of the ϕ_s phase, as illustrated by the artist's view in fig. 5. This value is compatible with the Standard Model, but there is still room for New Physics.

5. – Epilogue

While completing these proceedings, CDF has confirmed the ΔA_{CP} measurement from LHCb with: $\Delta A_{CP} = (-0.62 \pm 0.21 \pm 0.10)\%$ [22]. LHCb has released its results on ϕ_s [23] using $1\,\mathrm{fb}^{-1}$: $\phi_s = -0.001 \pm 0.101 \pm 0.027\,\mathrm{rad}$, still compatible with the Standard Model.

6. – Conclusions

2011 has been an excellent year for LHCb with many measurements related to CP violation. Among all these measurements, LHCb made the first evidence of CP violation at 3.5σ in charm. Important milestones have been achieved to measure the CKM angle γ with the determination of R_{CP}, A_{CP}, R_{ADS}, A_{ADS} using $1\,\mathrm{fb}^{-1}$. In the B_s^0, system, LHCb made the first direct evidence of a non-zero $\Delta\Gamma_s$, using $0.4\,\mathrm{fb}^{-1}$, and the CP-violating phase ϕ_s has been measured: $\phi_s = 0.03 \pm 0.16(\mathrm{stat}) \pm 0.07(\mathrm{syst})\,\mathrm{rad}$, consistent with the Standard Model.

* * *

I wish to thanks the organizers of the "Rencontres de Physique de la valle d'Aoste", for the nice atmosphere during the conference, and the LHCb collaboration for this beautiful opportunity.

REFERENCES

[1] Grossman Y., Kagan A. L. and Nir Y., *Phys. Rev. D*, **75** (2007) 036008.
[2] Bobrowski M., Lenz A., Riedl J. and Rohrwild J., *JHEP*, **03** (2010) 009.
[3] Bigi I. I., Blanke M., Buras A. J. and Recksiegel S., *JHEP*, **07** (2009) 097.
[4] The LHCb Collaboration, *Phys. Rev. Lett.*, **108** (2012) 111602.
[5] Asner D. *et al.* (Heavy Flavour Averaging Group), arXiv:1010.1589 [hep.ex].
[6] Charles J. *et al.* (CKMfitter group), *Eur. Phys. J. C*, **41** (2005) 1, hep-ph/0406184, updated results and plots available at `http://ckmfitter.in2p3.fr/`.
[7] See for example LHCb-CONF-2011-031, LHCb-CONF-2011-057, LHCb-CONF-2011-042, etc.
[8] The LHCb Collaboration, "Observation of CP violation in $B^{\pm} \to DK^{\pm}$ decays", LHCb-PAPER-2012-001.
[9] Gronau M. and London D., *Phys. Lett. B*, **253** (1991) 483.
[10] Gronau M. and Wyler D., *Phys. Lett. B*, **256** (1991) 172.
[11] Atwood D., Dunietz I. and Soni A., *Phys. D*, **63** (2001) 036005.
[12] The LHCb Collaboration, "Roadmap for selected key measurements of LHCb.", LHCB-PUB-2009-029, arXiv:0912.4179.
[13] The LHCb Collaboration, "Measurement of the CP-violating phase ϕ_s in the decay $B_s^0 \to J/\psi\phi$", LHCb-PAPER-2011-021.
[14] The LHCb Collaboration, "Opposite-side flavour tagging of the B mesons at the LHCb experiment", LHCb-PAPER-2011-027.
[15] The LHCb Collaboration, LHCb-CONF-2011-050.
[16] Abulencia A. *et al.* (CDF Collaboration), *Phys. Rev. Lett.*, **97** (2006) 242003.
[17] The LHCb Collaboration, "Determination of the sign of the decay width difference in the B_s^0 system", LHCb-PAPER-2011-028.
[18] BaBar Collaboration, *Phys. Rev. D*, **71** (2007) 032005.
[19] CDF Collaboration, Public Note 10778, 2012.
[20] The LHCb Collaboration, "Measurement of the CP-violating phase ϕ_s in $B_s^0 \to J/\psi f_0$", LHCb-PAPER-2011-031.
[21] The LHCb Collaboration, LHCb-CONF-2011-056.
[22] CDF Collaboration, Public Note 10784, 2012.
[23] The LHCb Collaboration, LHCb-CONF-2012-002.

IL NUOVO CIMENTO Vol. 35 C, N. 6 Novembre-Dicembre 2012
DOI 10.1393/ncc/i2012-11364-8

Colloquia: LaThuile12

Charm physics at CDF

A. Di Canto on behalf of the CDF Collaboration

Physikalisches Institut, Ruprecht-Karls-Universität - Heidelberg, Germany, and
INFN, Sezione di Pisa - Pisa, Italy

ricevuto il 7 Settembre 2012

Summary. — The study of the charm quark continues to have wide interest as a possible avenue for the discovery of physics beyond the Standard Model and can as well be used as a tool for understanding the non-perturbative aspects of the strong interactions. Owning to the large production cross-section available at the Tevatron collider and to the flexibility of a trigger for fully hadronic final states, the CDF experiment, in a decade of successful operations, collected millions of charmed mesons decays which can be used to investigate the details of the physics of the production and decay processes of the charm quark. Here we present a brief collection of new CDF results on this subject.

PACS 11.30.Er – Charge conjugation, parity, time reversal, and other discrete symmetries.
PACS 13.25.Ft – Decays of charmed mesons.
PACS 25.75.Dw – Particle and resonance production.

1. – Fragmentation of charm quarks

Heavy quark fragmentation is a non-perturbative process for which Monte Carlo event generators implement only phenomenological models that should be tuned to reproduce the observed properties of hadron production. CDF performs an analysis, described with further details in ref. [1], that probes the process of quark fragmentation more directly by studying kaons produced during the fragmentation of charm quarks to form a $D^{\pm}_{(s)}$ meson.

In a data sample corresponding to about $360\,\mathrm{pb}^{-1}$ of $p\overline{p}$ collisions, we reconstruct about 260000 D_s^+ and 140000 D^+ mesons decaying to the $\phi(\to K^+K^-)\pi^+$ final state (charge-conjugated decays are implied, unless otherwise stated). Promptly produced charmed mesons are statistically separated from products of b-hadron decays using the impact parameter distribution of the D candidate. Time-of-flight and ionization energy loss measurements are used to identify kaons and measure their fraction in the sample of

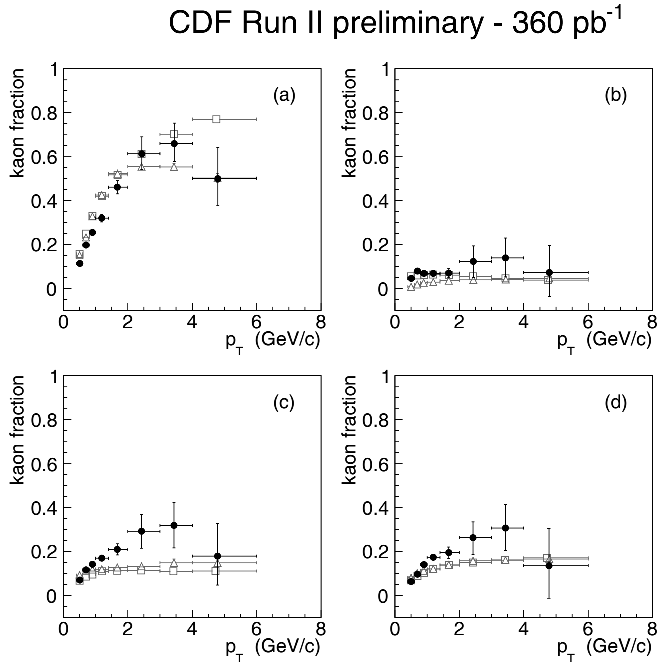

Fig. 1. – Transverse-momentum distribution of the measured kaon fraction (solid symbols) in the sample of charged tracks produced in association with D_s^+, (a) and (c), and D^+ mesons, (b) and (d), separately in the opposite-sign, (a) and (b), and same-sign, (c) and (d), combinations. Also shown are the kaon fractions calculated using PYTHIA (open squares) and HERWIG (open triangles).

maximum-p_T tracks produced in a $\Delta R = \sqrt{\Delta\varphi^2 + \Delta\eta^2} \leqslant 0.7$ cone around the $K^+K^-\pi^+$ candidate. The resulting kaon fractions, separately for same-sign and opposite-sign categories, are then compared to the predictions of both the string fragmentation model used in PYTHIA [2] and the cluster fragmentation model used in HERWIG [3], as a function of several observables: transverse momentum (p_T) of the track; invariant mass (m_{DK}) of the track (using the kaon mass hypothesis) and the D candidate; difference in rapidity along the fragmentation axis (Δy) between the track and the D meson. In the opposite-sign combination category, where the track in the cone and the D candidate are oppositely charged, we expect the kaon production to be enhanced around D_s^+ with respect to D^+ mesons since formation of a prompt D_s^+ requires conservation of strangeness in the first fragmentation branch. Conversely, in the same-sign combination we expect the kaon production to be similar around both D_s^+ and D^+ mesons since same sign kaons are likely to be produced in later branches of the fragmentation process.

The results of the comparative study show that the p_T distribution for early fragmentation kaons is in better qualitative agreement with predictions than for generic kaons produced in later fragmentation branches, for which the models underestimate the fraction of kaons, as shown in fig. 1. Conversely, the m_{DK} and Δy distributions indicate that the fragmentation models overestimate the fraction of kaons produced in early stages of the fragmentation process compared to the fraction of generic kaons that are produced in later branches, for which the data show good agreement with predictions.

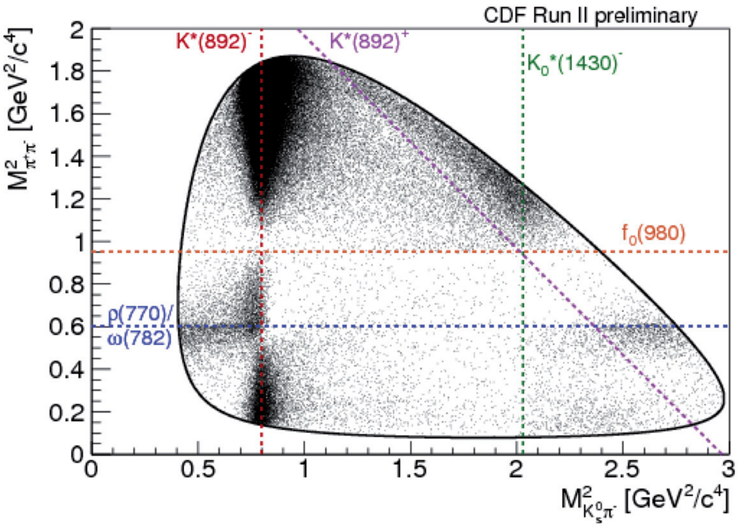

Fig. 2. – Dalitz plot of the reconstructed $D^0 \to K^0_S\pi^+\pi^-$ candidates, where some relevant intermediate resonances are indicated by colored dashed lines.

2. – Search for CP violation in neutral charmed mesons decays

While CP violation is well established for B and K mesons, this is not the case for charm mesons. First evidence for CP violation in two-body singly Cabibbo-suppressed D^0 decays has been recently reported by the LHCb Collaboration [4]. Whether this is a hint of possible new physics contributions to the decay amplitude or not is not yet clear. It is important to broaden our search for CP violation in further charmed-meson decays. Here we present two new searches for CP violation in neutral D mesons decays which are among the world's most sensitive to date.

2·1. *Time-integrated asymmetries in* $D^0 \to K^0_S\pi^+\pi^-$ *decays.* – In a data sample corresponding to an integrated luminosity of $6\,\mathrm{fb}^{-1}$, CDF searches for time-integrated CP asymmetries in the resonant substructure of the three-body $D^0 \to K^0_S\pi^+\pi^-$ decay. As the Standard Model expectation of these CP asymmetries is $\mathcal{O}(10^{-6})$, well below the experimental sensitivity, an observation of CP violation would be a clear hint of new physics.

We reconstruct approximately 350000 $D^0 \to K^0_S(\to \pi^+\pi^-)\pi^+\pi^-$ candidates with the D^0 originating from the strong $D^{*+} \to D^0\pi^+$ decay, in order to unambiguously determine the flavor of the charmed meson at production from the charge of the accompanying pion. Two complementary approaches are used: a full Dalitz fit and a model-independent bin-by-bin comparison of the D^0 and $\overline{D}^0$ Dalitz plots. We briefly present here only the result of the first approach, a more comprehensive description of the analysis can be found in ref. [5].

Figure 2 shows the Dalitz plot of the reconstructed $D^0 \to K^0_S\pi^+\pi^-$ candidates with the most relevant sub-resonant decay modes highlighted. For the first time at a hadron collider, a Dalitz amplitude analysis is applied for the description of the dynamics of the decay. We employ the isobar model and determine the asymmetries between the different

TABLE I. – *Comparison of the measured fit fraction asymmetries, $\mathcal{A}_{FF}$, for the considered intermediate resonances of the $D^0 \to K^0_S\pi^+\pi^-$ decay with the results from the CLEO experiment* [6]. *For the CDF results the first uncertainties are statistical and the second combined systematic. For the CLEO results the first uncertainties are statistical, the second experimental systematic, and the third modeling systematic.*

Resonance	$\mathcal{A}_{\mathrm{FF}}$ (CDF) [%]	$\mathcal{A}_{\mathrm{FF}}$ (CLEO) [%]
$K^*(892)^-$	$0.36 \pm 0.33 \pm 0.40$	$2.5 \pm 1.9^{+1.5}_{-0.7}{}^{+2.9}_{-0.3}$
$K^*_0(1430)^-$	$4.0 \pm 2.4 \pm 3.8$	$-0.2 \pm 11^{+9}_{-5}{}^{+2}_{-1}$
$K^*_2(1430)^-$	$2.9 \pm 4.0 \pm 4.1$	$-7 \pm 25^{+8}_{-26}{}^{+10}_{-1}$
$K^*(1410)^-$	$-2.3 \pm 5.7 \pm 6.4$	...
$\rho(770)$	$-0.05 \pm 0.50 \pm 0.08$	$3.1 \pm 3.8^{+2.7}_{-1.8}{}^{+0.4}_{-1.2}$
$\omega(782)$	$-12.6 \pm 6.0 \pm 2.6$	$-26 \pm 24^{+22}_{-2}{}^{+2}_{-4}$
$f_0(980)$	$-0.4 \pm 2.2 \pm 1.6$	$-4.7 \pm 11^{+25}_{-7}{}^{+0}_{-5}$
$f_2(1270)$	$-4.0 \pm 3.4 \pm 3.0$	$34 \pm 51^{+25}_{-71}{}^{+21}_{-34}$
$f_0(1370)$	$-0.5 \pm 4.6 \pm 7.7$	$18 \pm 10^{+2}_{-21}{}^{+13}_{-6}$
$\rho(1450)$	$-4.1 \pm 5.2 \pm 8.1$	...
$f_0(600)$	$-2.7 \pm 2.7 \pm 3.6$	...
σ_2	$-6.8 \pm 7.6 \pm 3.8$	...
$K^*(892)^+$	$1.0 \pm 5.7 \pm 2.1$	$-21 \pm 42^{+17}_{-28}{}^{+22}_{-4}$
$K^*_0(1430)^+$	$12 \pm 11 \pm 10$	...
$K^*_2(1430)^+$	$-10 \pm 14 \pm 29$	...
$K^*(1680)^-$	...	$-36 \pm 19^{+9}_{-35}{}^{+5}_{-1}$

D^0 and $\overline{D}^0$ sub-resonance fit fractions in order to be insensitive to any global instrumental asymmetry in the reconstruction and identification of the candidates of interest. Table I shows the results in comparison with the most recent measurements performed by the CLEO collaboration [6]. Our analysis represents a significant improvement in terms of precision, but still no hints of any CP-violating effects are found. The measured value for the overall integrated CP asymmetry is

$$\mathcal{A}_{CP}(D^0 \to K^0_S\pi^+\pi^-) = (-0.05 \pm 0.57\ (\mathrm{stat}) \pm 0.54\ (\mathrm{syst}))\,\%.$$

Following the procedure described in ref. [7] and assuming no direct CP violation in the $D^0 \to K^0_S\pi^+\pi^-$ decay ($\mathcal{A}^{\mathrm{dir}}_{CP} = 0$), we can derive a measurement of time-integrated CP violation in D^0 mixing ($\mathcal{A}^{\mathrm{ind}}_{CP}$) since the measured time-integrated asymmetry can be approximately expressed as

$$\mathcal{A}_{CP}(D^0 \to f) \approx \mathcal{A}_{CP}^{\mathrm{dir}}(D^0 \to f) + \frac{\langle t \rangle}{\tau}\, \mathcal{A}_{CP}^{\mathrm{ind}}, \tag{1}$$

where f indicates a generic final state and $\langle t \rangle/\tau \approx 2.28$ is the observed average D^0 decay time of the sample in units of D^0 lifetimes. We then find

$$\mathcal{A}_{CP}^{\mathrm{ind}} = (-0.02 \pm 0.25\ (\mathrm{stat}) \pm 0.24\ (\mathrm{syst}))\,\%,$$

in agreement with our previous determination of this quantity [7].

2˙2. *Difference of time-integrated asymmetries in $D^0 \to K^+K^-$ and $D^0 \to \pi^+\pi^-$ decays*. – Building upon the techniques developed for the previous measurement of individual asymmetries in $D^0 \to h^+h^-$ ($h = \pi$ or K) decays [7], CDF updated and optimized the analysis toward the measurement of the difference of asymmetries, $\Delta\mathcal{A}_{CP} = \mathcal{A}_{CP}(D^0 \to K^+K^-) - \mathcal{A}_{CP}(\pi^+\pi^-)$. The offline selection has been loosened with respect to the measurement of individual asymmetries, since their difference is much less sensitive to instrumental effects allowing for a more inclusive selection, and we now use the full CDF Run II data sample, which corresponds to $9.7\,\mathrm{fb}^{-1}$ of integrated luminosity. Requirements on the minimum number of hits for reconstructing tracks are loosened, the p_T threshold for D decay products is lowered from 2.2 to $2.0\,\mathrm{GeV}/c$ and $\sim 12\%$ fraction of charmed mesons produced in B decays, whose presence does not bias the difference of asymmetries, is now used in the analysis. As a result of the improved selection, the D^0 yield nearly doubles and the expected resolution on $\Delta\mathcal{A}_{CP}$ becomes competitive with LHCb's [4]. In the following we briefly present the result, more details can be found in ref. [8].

The production flavor of the neutral D meson is tagged by the charge of the pion from the $D^{*+} \to D^0\pi^+$ decay. The presence of such an additional "soft" (low-momentum) pion causes a bias in the measurement of the asymmetry, induced by a few percent difference in reconstruction efficiency between positive and negative pions at low momentum. However, provided that the relevant kinematic distributions are equalized in the two decay channels, this spurious asymmetry cancels to an excellent level of accuracy in $\Delta\mathcal{A}_{CP}$, leading to systematic uncertainties at the 0.1% level. Using the approximately $550000\,D^*$-tagged $D^0 \to \pi^+\pi^-$ and $1.21 \cdot 10^6\,D^*$-tagged $D^0 \to K^+K^-$ decays shown in fig. 3, we measure

$$\Delta\mathcal{A}_{CP} = (-0.62 \pm 0.21\ (\mathrm{stat}) \pm 0.10\ (\mathrm{syst}))\,\%,$$

which is 2.7σ different from zero and consistent with the LHCb result [4], suggesting that CDF data support CP violation in charm.

By means of eq. (1) and using the observed values of $\langle t \rangle/\tau \approx 2.4$ (2.65) for $D^0 \to \pi^+\pi^-$ ($D^0 \to K^+K^-$) candidates, the observed asymmetry can be combined with all other available measurements of CP violation in $D^0 \to h^+h^-$ decays to extract the values of $\mathcal{A}_{CP}^{\mathrm{ind}}$ and $\Delta\mathcal{A}_{CP}^{\mathrm{dir}} = \mathcal{A}_{CP}^{\mathrm{dir}}(D^0 \to K^+K^-) - \mathcal{A}_{CP}^{\mathrm{dir}}(D^0 \to \pi^+\pi^-)$. The combination, shown graphically in fig. 4, yields $\Delta\mathcal{A}_{CP}^{\mathrm{dir}} = (-0.67 \pm 0.16)\%$ and $\mathcal{A}_{CP}^{\mathrm{ind}} = (-0.02 \pm 0.22)\%$, which deviates by approximately 3.8σ from the no–CP-violation point.

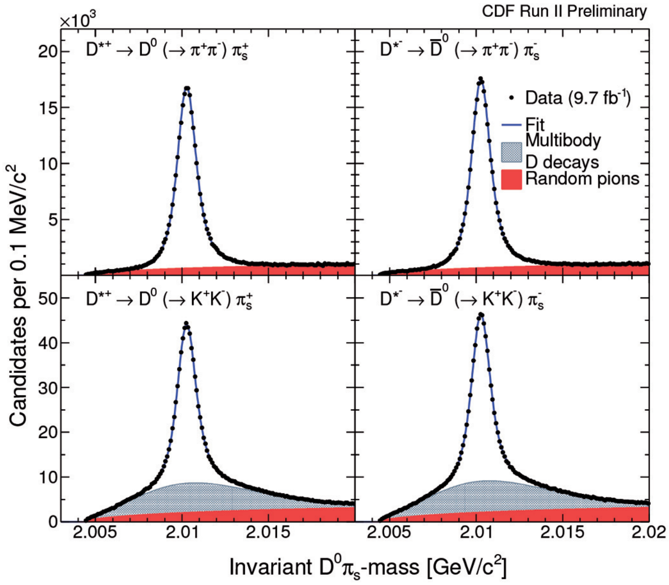

Fig. 3. – Invariant $D^0\pi_s$ mass distribution of D^*-tagged $D^0 \to \pi^+\pi^-$ (top) and $D^0 \to K^+K^-$ (bottom) decays with fit projections overlayed. $D^{*+} \to D^0\pi_s^+$ candidates are on the left, $D^{*-} \to \overline{D}^0\pi_s^-$ ones on the right.

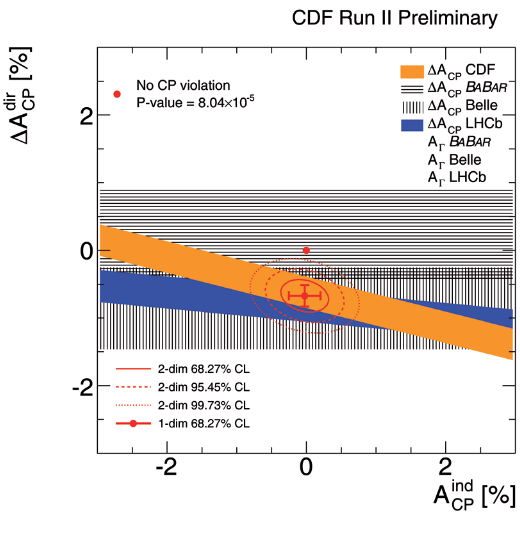

Fig. 4. – Representation of the current knowledge on CP violation in $D^0 \to h^+h^-$ decays in the plane $(\mathcal{A}_{CP}^{\rm ind}, \Delta\mathcal{A}_{CP}^{\rm dir})$. The combination of all results (listed in ref. [9]) assumes Gaussian, fully uncorrelated uncertainties.

REFERENCES

[1] Aaltonen T. *et al.* (CDF Collaboration), CDF Public Note 10704.
[2] Sjöstrand T., Mrenna S. and Skands P., arXiv:0710.3820 [hep-ph].
[3] Bahr M. *et al.*, *Eur. Phys. J. C*, **58** (2008) 639.
[4] Aaij R. *et al.* (LHCb Collaboration), *Phys. Rev. Lett.*, **108** (2012) 111602.
[5] Aaltonen T. *et al.* (CDF Collaboration), http://www-cdf.fnal.gov/physics/new/bottom/111013.blessed-D0KSpipi_ACP/.
[6] Asner D. M. *et al.* (CLEO Collaboration), *Phys. Rev. D*, **70** (2004) 091101(R).
[7] Aaltonen T. *et al.* (CDF Collaboration), *Phys. Rev. D*, **85** (2012) 012009.
[8] Aaltonen T. *et al.* (CDF Collaboration), CDF Public Note 10784.
[9] Asner D. *et al.* (HFAG), arXiv:1010.1589 [hep-ex] and online updates at http://www.slac.stanford.edu/xorg/hfag.

IL NUOVO CIMENTO Vol. 35 C, N. 6 Novembre-Dicembre 2012
DOI 10.1393/ncc/i2012-11365-7

Colloquia: LaThuile12

CP violation in the charm system

J. F. Kamenik(*)

J. Stefan Institute - Jamova 39, P.O. Box 3000, 1001 Ljubljana, Slovenia and
Department of Physics, University of Ljubljana - Jadranska 19, 1000 Ljubljana, Slovenia

ricevuto il 7 Settembre 2012

Summary. — I review the implications of recent measurements of CP violation in D meson decays. The results are discussed in the context of the standard model (SM), as well as its extensions. The observed size of CP violation is not easily explained within the SM, although the required non-perurbative enhancements of the relevant hadronic matrix elements cannot be ruled out from first principles. On the other hand, using effective theory methods, one can derive significant constraints on the possible non-standard contributions from measurements of D^0-$\bar{D}^0$ mixing and CP violation in kaon decays (ϵ'/ϵ). Due to an approximate universality of CP violation in new physics scenarios which only break the $SU(3)_Q$ flavor symmetry of the SM, such contributions are particularly constrained by ϵ'/ϵ. Explanations of the observed effect within several explicit well-motivated new physics frameworks are briefly discussed. Finally I comment on possible future experimental tests able to distinguish standard *vs.* non-standard explanations of the observed CP violation in the charm sector.

PACS `14.40.Lb` – Charmed mesons.
PACS `13.25.Ft` – Decays of charmed mesons.
PACS `11.30.Er` – Charge conjugation, parity, time reversal, and other discrete symmetries.

1. – Introduction

CP violation in charm provides a unique probe of New Physics (NP). Not only is it sensitive to NP in the up sector, in the Standard Model (SM) charm processes are dominated by two generation physics with no hard GIM breaking, and thus CP conserving to first approximation. Until very recently, the common lore was that "any signal for CP violation in charm would have to be due to NP". The argument was based on the fact the in the SM and in the heavy charm quark limit $m_c \gg \Lambda_{\mathrm{QCD}}$, CP violation in neutral D meson mixing enters at $\mathcal{O}(|\lambda_b/\lambda_s|) \sim 10^{-3}$ ($\lambda_q \equiv V_{cq}V_{uq}^*$), while CP-violating contributions to singly Cabibbo-suppressed D decays only appear at $\mathcal{O}(|\lambda_b/\lambda_s|\alpha_s(m_c)/\pi) \sim 10^{-4}$ [1].

(*) E-mail: `jernej.kamenik@ijs.si`

2. – CP violation in D^0-$\bar{D}^0$ mixing

Charm mixing arises from $|\Delta c| = 2$ interactions that generate off-diagonal terms in the mass matrix for D^0 and $\bar{D}^0$ mesons. The D^0-$\bar{D}^0$ transition amplitudes are defined as

$$\langle D^0|\mathcal{H}|\bar{D}^0\rangle = M_{12} - \frac{i}{2}\Gamma_{12}. \tag{1}$$

The three physical quantities related to the mixing can be defined as

$$y_{12} \equiv \frac{|\Gamma_{12}|}{\Gamma}, \qquad x_{12} \equiv 2\frac{|M_{12}|}{\Gamma}, \qquad \phi_{12} \equiv \arg\left(\frac{M_{12}}{\Gamma_{12}}\right), \tag{2}$$

where x_{12} and y_{12} are CP-conserving, while ϕ_{12} denotes the physical CP-violating mixing phase. HFAG has performed a fit to these theoretical quantities, (allowing also for CP violation in decays discussed below) using existing measurements, and obtained the following 95% CL regions [2]

$$\begin{aligned} &x_{12} \in [0.25,\, 0.99]\,\%, \qquad y_{12} \in [0.59,\, 0.99]\,\%, \\ &\phi_{12} \in [-7.1^\circ,\, 15.8^\circ]. \end{aligned} \tag{3}$$

The SM contributions to these quantities cannot be estimated reliably from first principles. On the other hand, short distance NP effects can be predicted and encoded in terms of an effective $|\Delta c| = 2$ Hamiltonian

$$\mathcal{H}^{\rm eff}_{|\Delta c|=2} = \frac{G_F}{\sqrt{2}}\sum_i C_i^{cu(\prime)} \mathcal{Q}_i^{cu(\prime)}, \tag{4}$$

where the definitions of the relevant operators $\mathcal{Q}_i^{cu(\prime)}$ can be found *i.e.* in [3]. Simply requiring such contributions to at most saturate the above experimental bounds on x_{12}, y_{12} and ϕ_{12} leads to very strong constraints on $C_i^{cu(\prime)}$ [4]. In particular, writing $\mathrm{Im}(C_i^{cu(\prime)}) = v_{\rm EW}^2/\Lambda_i^2$, constrains on CP-violating contributions to charm mixing in eq. (3) imply $\Lambda_i > 10^{3-4}$ TeV and are second in their strength only to the bounds on new contributions to ϵ_K.

3. – CP violation in D decays: Experiment *vs.* SM expectations

On the other hand, CP violation in neutral D meson decays to CP eigenstates f is probed with time-integrated CP asymmetries (a_f). These can arise from interferences between decay amplitudes with non-zero CP odd (ϕ_f) and even (δ_f) phase differences

$$a_f^{\rm dir} = -\frac{2r_f \sin\delta_f \sin\phi_f}{1 + 2r_f\cos\delta_f\cos\phi_f + r_f^2}, \tag{5}$$

where r_f is the absolute ratio of the two interfering amplitudes. Recently both the LHCb [5] and CDF [6] Collaborations reported evidence for a non-zero value of the

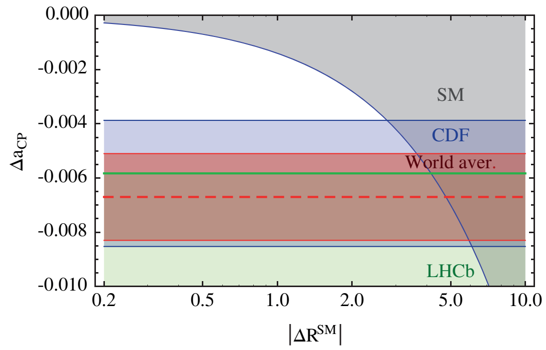

Fig. 1. – Comparison of the experimental Δa_{CP} values with the SM reach as a function of $|\Delta R^{\rm SM}|$. See text for details.

difference $\Delta a_{CP} \equiv a_{K^+K^-} - a_{\pi^+\pi^-}$. Combined with other measurements of these CP asymmetries [2], the present world average is

$$\Delta a_{CP} = -(0.67 \pm 0.16)\%. \tag{6}$$

This observation calls for a reexamination of theoretical expectations within the SM. The SM effective weak Hamiltonian relevant for hadronic singly Cabibbo-suppressed D decays, renormalized at a scale $m_c < \mu < m_b$ can be decomposed as [3]

$$\mathcal{H}^{\rm SM}_{|\Delta c|=1} = \frac{G_F}{\sqrt{2}} \sum_{q=s,d} \lambda_q \sum_{i=1,2} C^q_i \mathcal{Q}^q_i + \text{h.c.} + \dots, \tag{7}$$

where $\mathcal{Q}^q_{1,2} = [\bar{c}^\alpha \gamma_\mu (1-\gamma_5) q^{\alpha,\beta}][\bar{q}^\beta \gamma^\mu (1-\gamma_5) u^{\beta,\alpha}]$, α, β denote color indices, and the dots denote neglected penguin operators with tiny Wilson coefficients. Using CKM unitarity ($\sum_{q=d,s,b} \lambda_q = 0$), the corresponding $D^0 \to K^+K^-, \pi^+\pi^-$ decay amplitudes ($A_{K,\pi}$) can be written compactly as $A_{K,\pi} = \lambda_{s,d}(A^{s,d}_K - A^{d,s}_K) - \lambda_b A^{d,s}_K$. In the isospin limit the two different isospin amplitudes in the first term provide the necessary condition for non-zero $\delta_{K,\pi}$, while $\phi^{\rm SM}_{K,\pi} = \text{Arg}(\lambda_b/\lambda_{s,d}) \approx \pm 70°$. On the other hand $r_{K,\pi}$ are controlled by the CKM ratio $\xi = |\lambda_b/\lambda_s| \simeq |\lambda_b/\lambda_d| \approx 0.0007$. Parametrizing the remaining unknown hadronic amplitude ratios as $R^{\rm SM}_{K,\pi} \equiv -A^{d,s}_{K,\pi}/(A^{s,d}_{K,\pi} - A^{d,s}_{K,\pi})$, the SM contribution to Δa_{CP} can be written as

$$\Delta a_{CP} \approx (0.13\%)\, \text{Im}(\Delta R^{\rm SM}), \tag{8}$$

where $\Delta R^{\rm SM} = R^{\rm SM}_K + R^{\rm SM}_\pi$. Comparison of this estimate with current experimental results is shown in fig. 1. One observes that $|\,\text{Im}(\Delta R^{\rm SM})| = \mathcal{O}(2\text{–}5)$ is needed to reproduce the experimental results in eq. (6), in contrast to perturbative estimates in the heavy charm quark limit ($|R_{K,\pi}| \sim \alpha_s(m_c)/\pi \sim 0.1$) (see [1] and the more recent analyses in refs. [7]). However, ξ suppressed amplitudes in the numerator of R_i cannot be constrained by rate measurements alone, and it has been pointed out a long time ago that "$\Delta I = 1/2$ rule" type enhancements are possible [8] (see also [10]). Recently [9], an explicit estimate of potentially large $1/m_c$ suppressed contributions has been performed, yielding $\Delta a^{\rm SM}_{CP} \lesssim 0.4\%$. Although this is an order of magnitude above naïve expectations, the experimental value in eq. (6) cannot be reached.

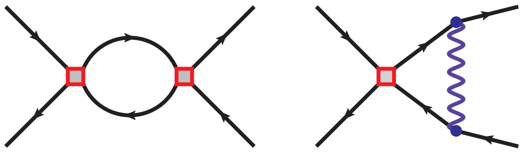

Fig. 2. – One-loop contributions of $\mathcal{H}^{\mathrm{eff-NP}}_{|\Delta c|=1}$ (red square) to $|\Delta c| = 2$ and $|\Delta s| = 1$ operators. Weak mixing effects via a W (blue wavy line) exchange (right-hand-side diagram) and UV sensitive contributions, quadratic in $\mathcal{H}^{\mathrm{eff-NP}}_{|\Delta c|=1}$ (left-hand-side diagram).

4. – Implications of Δa_{CP} for physics beyond SM

In the following we will therefore assume the SM does not saturate the experimental value, leaving room for potential NP contributions. These can again be parametrized in terms of an effective Hamiltonian valid below the W and top mass scales

$$\mathcal{H}^{\mathrm{eff-NP}}_{|\Delta c|=1} = \frac{G_F}{\sqrt{2}} \sum_i C_i^{\mathrm{NP}(\prime)} \mathcal{Q}_i^{(\prime)}, \tag{9}$$

where the relevant operators $\mathcal{Q}_i^{(\prime)}$ have been defined in [3]. Introducing also the NP hadronic amplitude ratios as $R^{\mathrm{NP},i}_{K,\pi} \equiv G_F \langle K^+K^-, \pi^+\pi^- | \mathcal{Q}_i^{(\prime)} | D^0 \rangle / \sqrt{2}(A^{s,d}_{K,\pi} - A^{d,s}_{K,\pi})$ and writing $C_i^{\mathrm{NP}} = v^2_{\mathrm{EW}}/\Lambda^2$, the relevant NP scale Λ is given by

$$\frac{(10\,\mathrm{TeV})^2}{\Lambda^2} = \frac{(0.61 \pm 0.17) - 0.12\,\mathrm{Im}(\Delta R^{\mathrm{SM}})}{\mathrm{Im}(\Delta R^{\mathrm{NP},i})}\,. \tag{10}$$

Comparing this estimate to the much higher effective scales probed by CP violating observables in D mixing and also in the kaon sector, one first needs to verify, if such large contributions can still be allowed by other flavor constraints. Within the effective theory approach, this can be estimated via so-called "weak mixing" of the effective operators (see fig. 2). In particular, time-ordered correlators of $\mathcal{H}^{\mathrm{eff-NP}}_{|\Delta c|=1}$ with the SM effective weak Hamiltonian can, at the one weak loop order, induce important contributions to CP violation in both D meson mixing and kaon decays (ϵ'/ϵ). On the other hand, analogue correlators, quadratic in $\mathcal{H}^{\mathrm{eff-NP}}_{|\Delta c|=1}$ turn out to be either chirally suppressed and thus negligible, or yield quadratically divergent contributions, which are thus highly sensitive to particular UV completions of the effective theory [3].

4·1. *Universality of CP violation in $\Delta F = 1$ processes.* – The strongest bounds can be derived for a particular class of operators, which transform non-trivially only under the $SU(3)_Q$ subgroup of the global SM quark flavor symmetry $\mathcal{G}_F = SU(3)_Q \times SU(3)_U \times SU(3)_D$, respected by the SM gauge interactions. In particular one can prove that their CP-violating contributions to $\Delta F = 1$ processes have to be approximately universal between the up and down sectors [11]. Within the SM one can identify two unique sources of $SU(3)_Q$ breaking given by $\mathcal{A}_u \equiv (Y_u Y_u^\dagger)_{\not{tr}}$ and $\mathcal{A}_d \equiv (Y_d Y_d^\dagger)_{\not{tr}}$, where $\not{tr}$ denotes the traceless part. Then in the two generation limit, one can construct a single source of CP violation, given by $J \equiv i[\mathcal{A}_u, \mathcal{A}_d]$ [12]. The crucial observation is that J is invariant under $SO(2)$ rotations between the $\mathcal{A}_u$ and $\mathcal{A}_d$ eigenbases. Introducing now $SU(2)_Q$ breaking NP effective operator contributions of the form $\mathcal{Q}_L = [(X_L)^{ij}\, \overline{Q}_i \gamma^\mu Q_j] L_\mu$, where L_μ

denotes a flavor singlet current, it follows that their CP-violating contributions have to be proportional to J and thus invariant under flavor rotations. The universality of CP violation induced by $\mathcal{Q}_L$ can be expressed explicitly as [11]

$$\mathrm{Im}(X_L^u)_{12} = \mathrm{Im}(X_L^d)_{12} \propto \mathrm{Tr}\,(X_L \cdot J)\,. \tag{11}$$

The above identity holds to a very good approximation even in the three-generation framework. In the SM, large values of $Y_{b,t}$ induce a $SU(3)/SU(2)$ flavor symmetry-breaking pattern [13] which allows to decompose X_L under the residual $SU(2)$ in a well-defined way. Finally, residual SM $SU(2)_Q$ breaking is necessarily suppressed by small mass ratios $m_{c,s}/m_{t,b}$, and small CKM mixing angles θ_{13} and θ_{23}.

The most relevant implication of eq. (11) is that it predicts a direct correspondence between $SU(3)_Q$-breaking NP contributions to Δa_{CP} and ϵ'/ϵ [11]. It follows immediately that stringent limits on possible NP contributions to the later, require $SU(3)_Q$-breaking contributions to the former to be below the per mile level (for $\Delta R^{\mathrm{NP},i} = \mathcal{O}(1)$).

As a corollary, one can show that within NP scenarios which only break $SU(3)_Q$, existing stringent experimental bounds on new contributions to CP-violating rare semileptonic kaon decays $K_L \to \pi^0(\nu\bar\nu, \ell^+\ell^-)$ put robust constraints on CP asymmetries of corresponding rare charm decays $D \to \pi(\nu\bar\nu, \ell^+\ell^-)$. In particular $|a_{\pi e^+e^-}^{\cancel{SU(3)_Q}}| \lesssim 2\%$ [11].

The viability of the remaining 4-quark operators in $\mathcal{H}^{\mathrm{eff-NP}}_{|\Delta c|=1}$ as explanations of the Δa_{CP} value in eq. (6), depends crucially on their flavor and chiral structure. In particular, operators involving purely right-handed quarks are unconstrained in the effective theory analysis but may be subject to severe constraints from their UV sensitive contributions to D mixing observables. On the other hand, QED and QCD dipole operators are at present only weakly constrained by nuclear EDMs and thus present the best candidates to address the Δa_{CP} puzzle [3].

5. – Explanations of Δa_{CP} within NP models

Since the announcement of the LHCb result, several prospective explanations of Δa_{CP} within various NP frameworks have appeared. In the following we briefly discuss Δa_{CP} within some of the well-motivated beyond SM contexts.

In the Minimal Supersymmetric SM (MSSM), the right size of the QCD dipole operator contributions can be generated with non-zero left-right up-type squark mixing contributions $(\delta^u_{12})_{LR}$ [1, 14] (see fig. 3). Para- metrically such effects in Δa_{CP} can be written as [14]

$$|\Delta a_{CP}^{\mathrm{SUSY}}| \approx 0.6\% \left(\frac{|\,\mathrm{Im}(\delta^u_{12})_{LR}|}{10^{-3}}\right)\left(\frac{\mathrm{TeV}}{\tilde m}\right), \tag{12}$$

where $\tilde m$ denotes a common squark and gluino mass scale. At the same time dangerous contributions to D mixing observables are chirally suppressed. It turns out however that even the apparently small $(\delta^u_{12})_{LR}$ value required implies a highly nontrivial flavor structure of the UV theory, in particular large trilinear (A) terms and sizable mixing among the first two generation squarks (θ_{12}) are required [14]

$$\mathrm{Im}(\delta^u_{12})_{LR} \approx \frac{\mathrm{Im}(A)\theta_{12} m_c}{\tilde m} \approx \left(\frac{\mathrm{Im}(A)}{3}\right)\left(\frac{\theta_{12}}{0.3}\right)\left(\frac{\mathrm{TeV}}{\tilde m}\right) 0.5\times 10^{-3}.$$

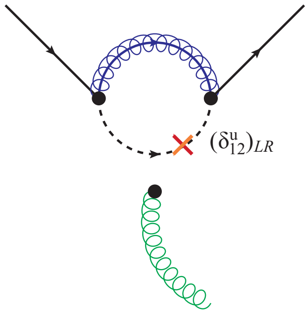

Fig. 3. – Sample one-loop squark (dashed black line)-gluino (combined straight and curly purple line) exchange diagram contributing to $|\Delta c| = 1$ QCD dipole operators in the MSSM. The (red) cross denotes an off-diagonal mass insertion ($(\delta^u_{12})_{LR}$). The gluon (curly green line) can be attached to any of the other (quark, squark, gluino) lines.

Similarly, warped extra dimensional models [15] that explain the quark spectrum through flavor anarchy [15, 16] can naturally give rise to QCD dipole contributions (see fig. 4) affecting Δa_{CP} as [17]

$$|\Delta a^{\rm RS}_{CP}| \approx 0.6\% \left(\frac{Y_5}{6}\right)^2 \left(\frac{3\,\text{TeV}}{m_{KK}}\right)^2 , \tag{13}$$

where m_{KK} is the KK scale and Y_5 is the 5D Yukawa coupling in appropriate units of the AdS curvature. Reproducing the experimental value of Δa_{CP} requires near-maximal 5D Yukawa coupling, close to its perturbative bound [18] of $4\pi/\sqrt{N_{KK}} \simeq 7$ for $N_{KK} = 3$ perturbative KK states. In term, this helps to suppress dangerous tree-level contributions to CP violation in D-$\bar{D}$ mixing [19]. This scenario can also be interpreted within the framework of partial compositeness in four dimensions, but generic composite models typically predict even larger contributions [20].

On the other hand, in the SM extension with a fourth family of chiral fermions Δa_{CP}

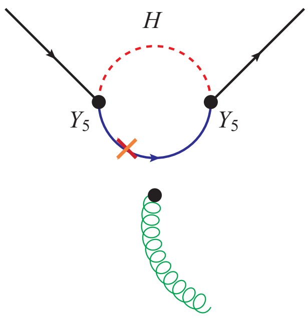

Fig. 4. – Sample one-loop Higgs (dashed red line)-(KK) quark (straight blue line) exchange diagram contributing to $|\Delta c| = 1$ QCD dipole operators in warped extra-dimensional (and similarly in partial compositeness) models. The (red) cross denotes a Dirac mass insertion. The gluon (curly green line) can be attached to any of the quark lines.

can be affected by 3×3 CKM nonunitarity and b' penguin operators

$$|\Delta a_{CP}^{\mathrm{4th\,gen}}| \propto \mathrm{Im}\left(\frac{\lambda_{b'}}{\lambda_d - \lambda_s}\right). \tag{14}$$

However, due to the existing stringent constraints on the new CP-violating phases entering $\lambda_{b'}$ [21], only moderate effects comparable to the SM estimates are allowed [22].

6. – Prospects

Continuous progress in Lattice QCD methods (*c.f.* [23]) gives hope that ultimately the role of SM long distance dynamics in Δa_{CP} could be studied from first principles. In the meantime it is important to identify possible experimental tests able to distinguish standard *vs.* non-standard explanations of the observed value.

Explanations of Δa_{CP} via NP contributions to the QCD dipole operators generically predict sizable effects in radiative charm decays [24]. First, in most explicit NP models the short-distance contributions to QCD and EM dipoles are expected to be similar. Moreover, even assuming that only a non-vanishing QCD dipole is generated at some high scale, the mixing of the two operators under the QCD renormalization group implies comparable size of the two contributions at the charm scale. Unfortunately, the resulting effects in the rates of radiative $D \to X\gamma$ decays are typically more than two orders of magnitude below the long-distance dominated SM effects [17]. This suppression can be partly lifted when considering CP asymmetries in exclusive $D^0 \to P^+P^-\gamma$ transitions, where $M_{PP} = \sqrt{(p_{P^+} + p_{P^-})^2}$ is close to the ρ, ω, ϕ masses [24].

An alternative strategy makes use of (sum rules of) CP asymmetries in various hadronic D decays (necessarily including neutral mesons). It is effective in isolating possible non-standard contributions to Δa_{CP} if they are generated by effective operators with a $\Delta I = 3/2$ isospin structure [25] (which unfortunately does not include the QCD dipoles).

We note in passing that even though potential NP contributions to Δa_{CP} at short distances may respect U-spin (like the QCD dipole operators), the measured $D \to \pi\pi, K\pi, KK$ decay rates imply sizable flavor $SU(3)$ breaking due to final state long distance rescattering effects [7, 10]. Thus $a_{\pi^+\pi^-} \simeq -a_{K^+K^-}$ cannot be expected neither if the measured Δa_{CP} value is due to enhanced SM long-distance dynamics, nor if it is due to short-distance NP contributions.

Finally, correlations of non-standard contributions to Δa_{CP} with other CP-violating observables like electric dipole moments, rare top decays or down-quark phenomenology are potentially quite constraining but very NP model dependent [14, 26].

* * *

The author would like to thank the organizers of *La Thuile 2012* for the invitation and warm hospitality during this exciting conference. This work is supported in part by the Slovenian Research Agency.

REFERENCES

[1] Grossman Y., Kagan A. L. and Nir Y., *Phys. Rev. D*, **75** (2007) 036008 [hep-ph/0609178].
[2] Asner D. *et al.* (Heavy Flavor Averaging Group), arXiv:1010.1589 [hep-ex]; and updates at `http://www.slac.stanford.edu/xorg/hfag/`.

[3] Isidori G., Kamenik J. F., Ligeti Z. and Perez G., [arXiv:1111.4987 [hep-ph]].
[4] Isidori G., Nir Y. and Perez G., *Annu. Rev. Nucl. Part. Sci.*, **60** (2010) 355 [arXiv:1002.0900 [hep-ph]].
[5] Mat Charles (LHCb Collaboration), talk presented at HCP2011 (Nov 14–18, 2011, Paris, France), `http://hcp2011.lpnhe.in2p3.fr/`; Aaij R. *et al.* (LHCb Collaboration), arXiv:1112.0938 [hep-ex].
[6] Di Canto A. (CDF Collaboration), talk presented at this conference; (CDF Collaboration), CDF Note 10784; see also Aaltonen T. *et al.* (CDF Collaboration), *Phys. Rev. D*, **85** (2012) 012009 [arXiv:1111.5023].
[7] Cheng H.-Y. and Chiang C.-W., *Phys. Rev. D*, **85** (2012) 034036 [arXiv:1201.0785]; Li H.-n., Lu C.-D. and Yu F.-S., arXiv:1203.3120; Franco E., Mishima S. and Silvestrini L., arXiv:1203.3131.
[8] Golden M. and Grinstein B., *Phys. Lett. B*, **222** (1989) 501.
[9] Brod J., Kagan A. L. and Zupan J., arXiv:1111.5000 [hep-ph].
[10] Pirtskhalava D. and Uttayarat P., arXiv:1112.5451; Bhattacharya B., Gronau M. and Rosner J. L., *Phys. Rev. D*, **85** (2012) 054014 [arXiv:1201.2351]; Feldmann T., Nandi S. and Soni A., arXiv:1202.3795; Brod J., Grossman Y., Kagan A. L. and Zupan J., arXiv:1203.6659.
[11] Gedalia O., Kamenik J. F., Ligeti Z. and Perez G., [arXiv:1202.5038 [hep-ph]].
[12] Gedalia O., Mannelli L. and Perez G., *Phys. Lett. B*, **693** (2010) 301 [arXiv:1002.0778 [hep-ph]]; Gedalia O., Mannelli L. and Perez G., *JHEP*, **10** (2010) 046 [arXiv:1003.3869 [hep-ph]].
[13] Kagan A. L., Perez G., Volansky T. and Zupan J., *Phys. Rev. D*, **80** (2009) 076002 [arXiv:0903.1794 [hep-ph]].
[14] Giudice G. F., Isidori G. and Paradisi P., *JHEP*, **04** (2012) 060 [arXiv:1201.6204 [hep-ph]].
[15] Randall L. and Sundrum R., *Phys. Rev. Lett.*, **83** (1999) 3370 [hep-ph/9905221];
[16] Goldberger W. D. and Wise M. B., *Phys. Rev. Lett.*, **83** (1999) 4922 [hep-ph/9907447]; Grossman Y. and Neubert M., *Phys. Lett. B*, **474** (2000) 361 [hep-ph/9912408]; Huber S. J. and Shafi Q., *Phys. Lett. B*, **498** (2001) 256 [arXiv:hep-ph/0010195]; Gherghetta T. and Pomarol A., *Nucl. Phys. B*, **586** (2000) 141 [arXiv:hep-ph/0003129].
[17] Delaunay C., Kamenik J. F., Perez G. and Randall L., arXiv:1207.0474.
[18] Agashe K., Azatov A. and Zhu L., *Phys. Rev. D*, **79** (2009) 056006 [arXiv:0810.1016 [hep-ph]]; Csaki C., Perez G., Surujon Z. 'e. and Weiler A., *Phys. Rev. D*, **81** (2010) 075025 [arXiv:0907.0474 [hep-ph]].
[19] Isidori G., Nir Y. and Perez G., *Annu. Rev. Nucl. Part. Sci.*, **60** (2010) 355 [arXiv:1002.0900 [hep-ph]]; Gedalia O., Grossman Y., Nir Y. and Perez G., *Phys. Rev. D*, **80** (2009) 055024 [arXiv:0906.1879 [hep-ph]].
[20] Keren-Zur B., Lodone P., Nardecchia M., Pappadopulo D., Rattazzi R. and Vecchi L., *Nucl. Phys. B*, **867** (2013) 429 [arXiv:1205.5803 [hep-ph]].
[21] Buras A. J., Duling B., Feldmann T., Heidsieck T., Promberger C. and Recksiegel S., *JHEP*, **09** (2010) 106 [arXiv:1002.2126 [hep-ph]]; Nandi S. and Soni A., *Phys. Rev. D*, **83** (2011) 114510 [arXiv:1011.6091 [hep-ph]].
[22] Feldmann T., Nandi S. and Soni A., arXiv:1202.3795 [hep-ph].
[23] Hansen M. T. and Sharpe S. R., arXiv:1204.0826 [hep-lat].
[24] Isidori G. and Kamenik J. F., arXiv:1205.3164 [hep-ph].
[25] Grossman Y., Kagan A. L. and Zupan J., arXiv:1204.3557 [hep-ph].
[26] Hochberg Y. and Nir Y., arXiv:1112.5268 [hep-ph]; Altmannshofer W., Primulando R., Yu C.-T. and Yu F., *JHEP*, **04** (2012) 049 [arXiv:1202.2866 [hep-ph]].

IL NUOVO CIMENTO Vol. 35 C, N. 6 Novembre-Dicembre 2012
DOI 10.1393/ncc/i2012-11366-6

Colloquia: LaThuile12

Heavy-flavor physics at the Tevatron

H. Miyake on behalf of the CDF and D0 Collaborations
High Energy Accelerator Research Organization - Tsukuba, Ibaraki, Japan

ricevuto il 7 Settembre 2012

Summary. — The CDF and D0 experiments at the Fermilab Tevatron proton-antiproton collider have been producing world's leading results on many interesting heavy-flavor physics topics. We report here three recent CDF results on B_s^0 meson dynamics. An updated search for ultra rare B_s^0 meson decays into dimuon final states and new bounds on the B_s^0 mixing phase and decay-width difference using $B_s^0 \to J/\psi\phi$ decays are summarized, both based on the whole Run II dataset corresponding to $10\,\text{fb}^{-1}$. A new measurement of the branching fractions of the $B_s^0 \to D_s^{(*)+} D_s^{(*)-}$ decays uses $6.8\,\text{fb}^{-1}$ of data is also reported.

PACS 11.30.Er – Charge conjugation, parity, time reversal, and other discrete symmetries.
PACS 13.20.He – Decays of bottom mesons.
PACS 13.25.Hw – Decays of bottom mesons.

1. – Introduction

Heavy-flavor physics enables probing the fundamental structure of matter and its interactions. Besides its significant contributions in establishing the standard model (SM), flavor physics plays a central role in the pursuit of new physics beyond the standard model (BSM). Decays of B_s^0 mesons are especially interesting since limited experimental information was available until recently, and a few tantalizing puzzles have emerged from data, *e.g.* the 3.9σ anomaly in the dimuon charge asymmetry [1].

In the last decade, the Tevatron $p\bar{p}$ collider at $\sqrt{s} = 1.96\,\text{TeV}$ has been providing the most promising opportunity to study B_s^0 physics. At the Tevatron, b quarks are pair-produced with a cross section [2] three orders of magnitude higher than at e^+e^- colliders, and with an energy sufficient to generate all sorts of b hadrons. This allowed study of ultra rare decays, such as those arising from flavor changing neutral current (FCNC) processes and to first access measurements of CP-violating parameter in B_s^0 meson mixing and decay.

The Tevatron ended its operations in late September 2011, and many analyses are now in progress at CDF and D0 that use the whole dataset, corresponding to about

$10\,\mathrm{fb}^{-1}$ or a large fraction of that. We report here three recent CDF results including an updated search for rare B_s^0 meson decays, new bounds on the B_s^0 mixing phase and on the B_s^0 mass-eigenstates decay-width difference using $B_s^0 \to J/\psi\phi$ decays, and the measurement of the branching fractions of the $B_s^0 \to D_s^{(*)+} D_s^{(*)-}$ decays.

2. – $B_{s,d} \to \mu\mu$

The $B_s^0(B^0) \to \mu^+\mu^-$ decays involve a flavor-changing neutral current (FCNC) process. The decay rates are further suppressed by the helicity factor, $(m_\mu/m_B)^2$. The B^0 decay is also suppressed with respect to the B_s^0 decay by the ratio of CKM elements, $|V_{td}/V_{ts}|^2$. The SM expectations for these branching fractions are $\mathcal{B}(B_s^0 \to \mu^+\mu^-) = (3.2 \pm 0.2) \times 10^{-9}$ and $\mathcal{B}(B^0 \to \mu^+\mu^-) = (1.0 \pm 0.1) \times 10^{-10}$ [3]. As many new physics models can enhance the rate significantly, these decays provide sensitive probes for new physics. Over the last decade, ever improving upper limits where set by the CDF and D0 collaborations, which strongly constrained the parameters space of such models.

Using $7\,\mathrm{fb}^{-1}$ of data, in 2011 CDF reported an intriguing excess of signal-like events over background in the $B_s^0 \to \mu^+\mu^-$ channel at a level of 2.5 standard deviations, which led to the first double-sided bounds on the rate of the $B_s^0 \to \mu^+\mu^-$ [4]. Despite the hint of an excess, the CDF result was compatible with the SM expectation and null searches with similar sensitivity by LHCb [5] and CMS [6] as well as with an older D0 result [7]. In early 2012, CDF updated the analysis to the whole dataset of nearly $10\,\mathrm{fb}^{-1}$ to further investigate such effect. No improvements were introduced in the analysis on purpose to keep it identical to the $7\,\mathrm{fb}^{-1}$ analysis and study the evolution of the effect in the most unbiased way.

CDF selects two oppositely-charged muon candidates within a dimuon mass $4.669 < m_{\mu^+\mu^-} < 5.969\,\mathrm{GeV}/c^2$. The muon candidates are required to have $p_T > 2.0\,\mathrm{GeV}/c$, and $\vec{p_T}^{\mu^+\mu^-} > 4\,\mathrm{GeV}/c$, where $\vec{p_T}^{\mu^+\mu^-}$ is the transverse component of the sum of the muon momentum vectors. Data are divided into two exclusive categories, "CC" (both muon in the central detector) and "CF" (one muon central the other muon forward). The event selection is optimized using an artificial neural network (NN) that uses 14 discriminating variables, such as the dimuon isolation and dimuon impact parameter. The NN discriminant is designed to have no dimuon mass dependence, and such a condition is verified by cross checks data. Figure 1 shows both the signal and background distribution represented by the simulated signal and the sideband data.

The dominant residual background comes from the smoothly distributed combinatorial component. Peaking backgrounds from $B \to hh$ decays where the hadrons fake muons also contribute. Their effect is determined from data and simulation to affect the B_d^0 search more than the B_s^0. The background estimation is tested in various control samples, *e.g.* opposite-sign muon pairs which have negative B lifetime or same-sign dimuons, showing good agreement with observed background yields.

Data from the $B^0 \to \mu^+\mu^-$ search are shown in fig. 2. The data are consistent with the background prediction, yielding an observed limit of $\mathcal{B}(B^0 \to \mu^+\mu^-) < 4.6(3.8) \times 10^{-9}$ at the 95% (90%) CL An ensemble of background-only pseudoexperiments is used to estimate the consistency of data with the background-only hypothesis as a p-value of 41%. In the B_s^0 search, the data show a mild excees over background prediction in bins with NN > 0.97 (fig. 3) The p-value for the background-only hypothesis is 0.94%, which becomes 7.1% if the hypothesis of a SM signal and background is tested. A likelihood fit determines $\mathcal{B}(B_s^0 \to \mu^+\mu^-) = (1.3^{+0.9}_{-0.7}) \times 10^{-8}$. Additionally, a bound at 90% (95%) CL

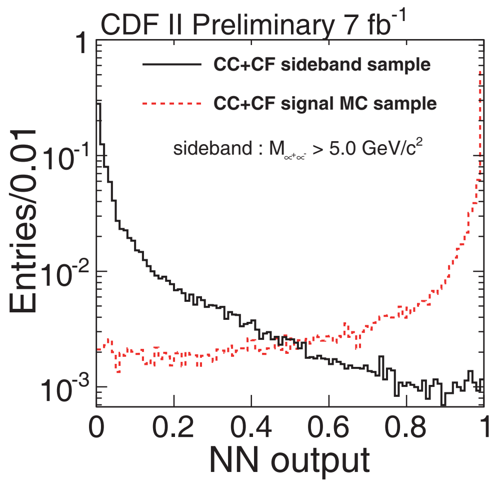

Fig. 1. – NN distributions of the simulated signal (dashed) and the sideband data (solid).

on the branching fraction of the $B_s^0 \to \mu^+\mu^-$ is set at $0.8 \times 10^{-9} < \mathcal{B}(B_s^0 \to \mu^+\mu^-) < 3.9 \times 10^{-8}$ ($2.2 \times 10^{-9} < \mathcal{B}(B_s^0 \to \mu^+\mu^-) < 3.0 \times 10^{-8}$). The mild excess observed in summer 2011 is not reinforced by the 30% additional data, but a larger than 2σ deviation from the background-only expectation remains. These results are consistent with previous CDF measurement [4], other experiments [7-9], and the SM.

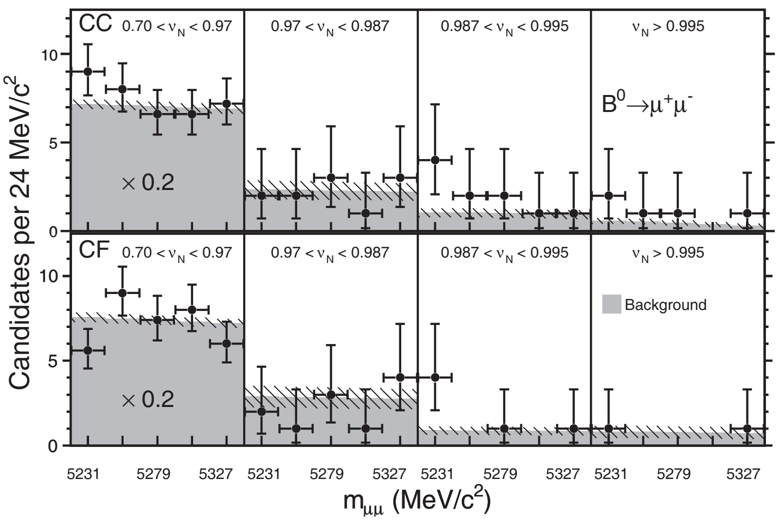

Fig. 2. – Dimuon mass distributions for the $B^0 \to \mu^+\mu^-$ measurements. The CC (top) and CF (bottom) categories are divided into 8 NN bins each, of which the lowest 5 NN bins are combined into one bin. The data points represent the observed number of events. The solid (hashed) areas show the background estimates (their systematic uncertainties).

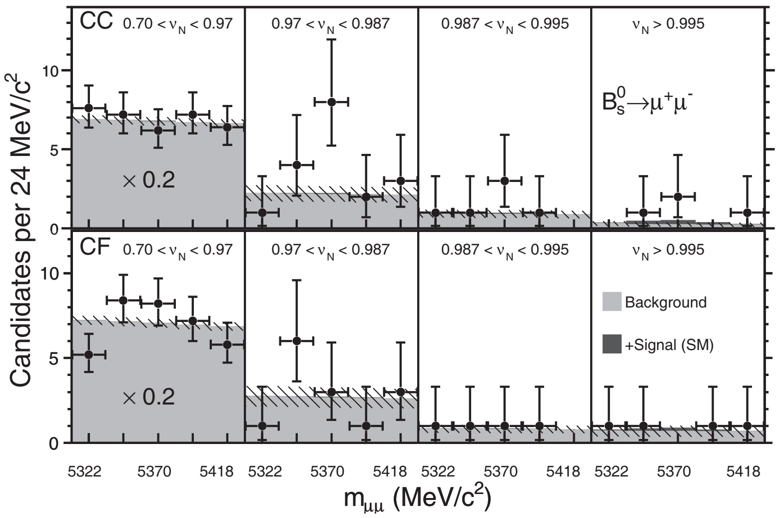

Fig. 3. – Dimuon mass distribution for the $B_s^0 \to \mu^+\mu^-$ measurements. The SM expectations are shown by the dark-gray areas, as in fig. 2.

3. – *CP* violation in the B_s^0 system

As in the neutral B^0 system, CP violation in the B_s^0 system may occur also through interference of decays with and without the B_s^0-$\overline{B}_s^0$ mixing. The B_s^0-$\overline{B}_s^0$ mixing occurs via second-order weak processes. It is described in the SM by Δm_s and $\Delta\Gamma_s$, the mass and decay width difference of the two mass eigenstates, ${B_s^0}_H$ and ${B_s^0}_L$. The quantity $\Delta\Gamma_s = \Gamma_{sL} - \Gamma_{sH} = 2|\Gamma_{12}|\cos(\phi_s)$ is sensitive to new physics effects that affect the phase $\phi_s = \arg(-M_{12}/\Gamma_{12})$, where Γ_{12} and M_{12} are the off-diagonal elements of the mass and decay matrices and $\Gamma_{sH}(\Gamma_{sL})$ is the decay width of ${B_s^0}_H$ (${B_s^0}_L$). In the SM, the B_s^0-$\overline{B}_s^0$ CP-violating phase ϕ_s^{SM} is predicted to be as small as 0.004 [10]. However a broad class of BSM models predict new sources of CP violation that can greatly enhance it. If such new physics has a different phase ϕ_s^{NP} from the SM, the ϕ_s could be dominated by ϕ_s^{NP}. The most promising probe of the phase is the study of the time-evolution of $B_s^0 \to J/\psi\phi$ decays, where the CP-violating phase $\beta_s^{J/\psi\phi}$ enters. This is defined as the phase between the direct $B_s^0 \to J/\psi\phi$ decay amplitude and mixing followed by decay amplitude. The phase β_s^{SM} is described by CKM matrix elements as $\arg(-V_{ts}V_{tb}^*/V_{cs}V_{cb}^*)$ and predicted to be small, 0.02 [10]. Since ϕ_s^{NP} contributes to both ϕ_s and β_s, large β_s would indicate the existence of a new physics contribution. CDF updates the β_s measurement using the whole dataset, collected with a low-p_T dimuon trigger corresponding to nearly $10\,\mathrm{fb}^{-1}$. Candidate $B_s^0 \to J/\psi\phi$ decays are reconstructed from $J/\psi \to \mu^+\mu^-$ and $\phi \to K^+K^-$ final states. About 11 000 signal events are selected with a neural network discriminator (fig. 4 (left)). To extract $\Delta\Gamma_s$ and β_s, an unbinned maximum-likelihood fit is performed on the time-evolution of signal candidates. Enhanced sensitivity to the desired observables is reached by using an angular analysis to statistically separate CP-even and -odd final states. Information about mixing is obtained from tagging the production flavor of the bottom-strange mesons. Two flavor tagging algorithms are employed, opposite-side tagging (OST) and same-side kaon

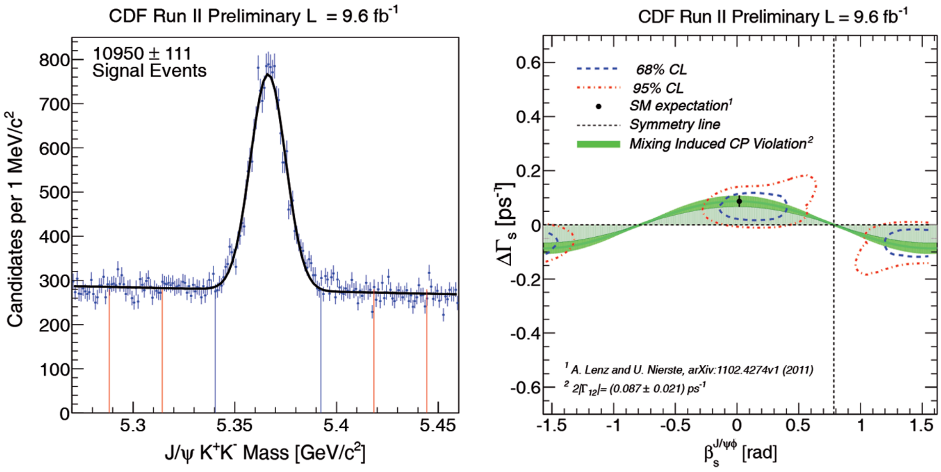

Fig. 4. – Left: $J/\psi K^+K^-$ mass distribution. Right: Two-dimensional 68% (95%) C.L. regions of $\beta_s^{J/\psi\phi}$ (horizontal) and $\Delta\Gamma_s$ (vertical) shown as enclosed by the dashed (dot-dashed) contours. The shaded band shows the allowed region if only mixing-induced CP violation occurs.

tagging (SSKT). The OST exploits the charge information of decay products coming from opposite side of the B_s^0 meson while the SSKT uses the charge of the kaon produced in association with the b or $\bar{b}$ quark in the fragmentation process. OST has been recalibrated using about 82 000 $B^\pm \to J/\psi K^\pm$ decays, achieving a tagging performance of $\varepsilon D^2 = (1.39 \pm 0.01)\%$. The SSKT algorithm has only been used in half of the data sample ($\varepsilon D^2 = (3.2 \pm 1.4)\%$), since calibration on the full sample has not been completed yet. This degrades the statistical resolution of the mixing phase measurement by no more than 15%. Assuming no CP violation, CDF finds

$$\begin{aligned}
\tau_s &= 1.528 \pm 0.019(\mathrm{stat}) \pm 0.009(\mathrm{syst})\,\mathrm{ps},\\
\Delta\Gamma_s &= 0.068 \pm 0.026(\mathrm{stat}) \pm 0.007(\mathrm{syst})\,\mathrm{ps}^{-1},\\
|A_0(0)|^2 &= 0.512 \pm 0.012(\mathrm{stat}) \pm 0.017(\mathrm{syst}),\\
|A_{||}(0)|^2 &= 0.229 \pm 0.010(\mathrm{stat}) \pm 0.014(\mathrm{syst}),\\
\delta_\perp &= 2.79 \pm 0.53(\mathrm{stat}) \pm 0.15(\mathrm{syst})\,\mathrm{rad}.
\end{aligned}$$

These quantities are consistent with previous measurements [11, 12] and amongst the world's most precise currently available. From a fit in which CP violation is allowed, CDF extracts confidence intervals using a profile-likelihood ratio statistics in which coverage has been verified against the effect of systematic uncertainties and irregularities of the likelihood, $\beta_s \in [-\pi/2, -1.51] \cup [-0.06, 0.30] \cup [1.26, \pi/2]$ at the 68% confidence level, and $\beta_s \in [-\pi/2, -1.36] \cup [-0.21, 0.53] \cup [1.04, \pi/2]$ at the 95% confidence level, in agreement with the SM prediction. CDF also reports 68% and 95% confidence regions in the β_s-$\Delta\Gamma_s$ plane including systematic uncertainties in fig. 4 (right). The measurements are compatible with the SM predictions of β_s and $\Delta\Gamma_s$ within less than one standard deviation, and also consistent with other recent determinations [12, 13].

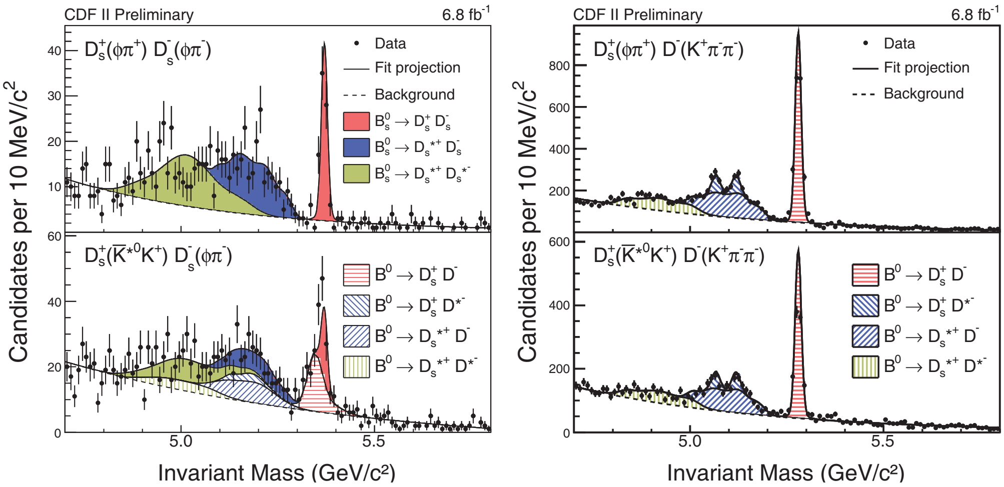

Fig. 5. – From top-left to bottom-right, $B^0_s \to D^+_s(\to \phi\pi^+)D^-_s(\to \phi\pi^-)$, $B^0 \to D^+_s(\to \phi\pi^+)D^-(\to K^+\pi^-\pi^-)$, $B^0_s \to D^+_s(\to \bar{K}^{*0}K^+)D^-_s(\to \phi\pi^-)$, $B^0 \to D^+_s(\to \bar{K}^{*0}K^+)D^-(\to K^+\pi^-\pi^-)$ invariant mass distributions, respectively. The points show data. The solid curves and dashed curve mean the fitted signals and background, respectively.

4. – $B^0_s \to D^{(*)+}_s D^{(*)-}_s$

A measurement of the decay rates of $B^0_s \to D^{(*)+}_s D^{(*)-}_s$ decays may provide useful information on the B^0_s width difference in the SM. Some authors suggest that $\Delta\Gamma_s/\Gamma_s$ can be inferred by a measurement of $\mathcal{B}(B^0_s \to D^{(*)+}_s D^{(*)-}_s)$ under certain theoretical assumptions on the decay model [14, 15], *i.e.*,

$$2\mathcal{B}(B^0_s \to D^{(*)+}_s D^{(*)-}_s) \sim \frac{\Delta\Gamma_s}{\Gamma_s + \Delta\Gamma_s/2}\,. \tag{1}$$

However, it has been pointed out recently that three-body decays may provide a significant contribution to $\Delta\Gamma_s$, thus invalidating the above relationship. The branching fractions have been measured by CDF [16], D0 [17], and Belle [18], but more data are necessary to reach a precision that can provide some constraint on $\Delta\Gamma_s$.

CDF updates the measurement of the decay modes using $6.8\,\mathrm{fb}^{-1}$ of data collected with a trigger on tracks displaced by the primary $p\bar{p}$ interaction. The decays are partially reconstructed as $B^0_s \to D^+_s D^-_s +$ anything, since the photon and the neutral pion from the $D^{*+}_s \to D^+_s\gamma$ and $D^{*+}_s \to D^+_s\pi^0$ decays are not reconstructed due to their low detection efficiency. The D_s meson is reconstructed from $D_s \to K^{*0}K$ or $D_s \to \phi(\to KK)\pi$ decays. The K^{*0} meson is selected with $0.837 < M(K^-\pi^+) < 0.947\,\mathrm{GeV}/c^2$ centered on the known K^{*0} mass and the ϕ meson is selected with $1.005 < M(K^+K^-) < 1.035\,\mathrm{GeV}/c^2$ centered on the known ϕ mass. As a normalization channel, $B^0 \to D^+(\to K\pi\pi)D^-_s$ is reconstructed to normalize the branching fractions. Pairs of $D^+_s \to \phi\pi^+$ or $D^+_s \to \bar{K}^{*0}K^+$ candidates and $D^-_s \to \phi\pi^-$ candidates are combined to form B^0_s candidates and fitted to a common vertex. Combinations of K^{*0} decay channels are not used since that final state has a large background compared to the signal. The event selection is further optimized using a neural network. A simultaneous fit to the reconstructed signal and normalization mass distribution yields B^0_s production rate times $B^0_s \to D^{(*)+}_s D^{(*)-}_s$

branching fractions relative to $B^0 \to D_s^+ D^-$:

$$f_X = \frac{f_s}{f_d} \frac{\mathcal{B}(B_s^0 \to X)}{\mathcal{B}(B^0 \to D_s^+ D^-)}\,, \tag{2}$$

for $X = D_s^+ D_s^-$, $D_s^{*\pm} D_s^{\mp}$, $D_s^{*+} D_s^{*-}$, and $D_s^{(*)+} D_s^{(*)-}$, where f_s/f_d is the relative production rate of B_s^0 to B^0 mesons. The simultaneous fit helps the determination of the yields of the four final states while properly accounting for the effect ofcross feeds. Figure 5 shows mass distributions with fit results overlaid. The D_s Dalitz structure is explicitly considered in the reconstruction for accurate acceptance determination and reduction of the relevant systematic uncertainty. The following absolute branching fractions are derived:

$$\begin{aligned}
\mathcal{B}(B_s^0 \to D_s^+ D_s^-) &= (0.49 \pm 0.06 \pm 0.05 \pm 0.08)\%,\\
\mathcal{B}(B_s^0 \to D_s^{*\pm} D_s^{\mp}) &= (1.13 \pm 0.12 \pm 0.19 \pm 0.09)\%,\\
\mathcal{B}(B_s^0 \to D_s^{*+} D_s^{*-}) &= (1.75 \pm 0.19 \pm 0.17 \pm 0.29)\%,\\
\mathcal{B}(B_s^0 \to D_s^{(*)+} D_s^{(*)-}) &= (3.38 \pm 0.25 \pm 0.30 \pm 0.56)\%.
\end{aligned}$$

The first, second, and third component of the uncertainty refers to the statistical, systematic, and normalization uncertainties, respectively. The above results are the most precise branching fractions for these modes from a single experiment.

REFERENCES

[1] Abazov V. M. *et al.* (D0 Collaboration), *Phys. Rev. D*, **84** (2011) 052007, arXiv: 1106.6308.
[2] Aaltonen T. *et al.* (CDF Collaboration), *Phys. Rev. D*, **79** (2009) 092003, arXiv: 0903.2403.
[3] Buras A. J. *et al.*, *JHEP*, **09** (2010) 106, arXiv:1002.2126.
[4] Aaltonen T. *et al.* (CDF Collaboration), *Phys. Rev. Lett.*, **107** (2011) 239903, arXiv: 1107.2304.
[5] Aaij R. *et al.* (LHCb Collaboration), *Phys. Lett. B*, **708** (2012) 55.
[6] Chatrchyan S. *et al.* (CMS Collaboration), *Phys. Rev. Lett.*, **107** (2011) 191802, arXiv:1107.5834.
[7] Abazov V. M. *et al.* (D0 Collaboration), *Phys. Lett. B*, **693** (2010) 539, arXiv: 1006.3469.
[8] Aaij R. *et al.* (LHCb Collaboration), arXiv:1203.4493 (2012).
[9] Chatrchyan S. *et al.* (CMS Collaboration), *JHEP*, **04** (2012) 033, arXiv:1203.3976.
[10] Lenz A. and Nierste U., *JHEP*, **06** (2007) 072, arXiv:hep-ph/0612167.
[11] Aaltonen T. *et al.* (CDF Collaboration), *Phys. Rev. D*, **85** (2012) 072002, arXiv: 1112.1726.
[12] Abazov V. M. *et al.* (D0 Collaboration), *Phys. Rev. D*, **85** (2012) 032006, arXiv: 1109.3166.
[13] LHCb Collaboration, LHCb-CONF-2012-002.
[14] Aleksan R., Le Yaouanc A., Oliver L., Pene O. and Raynal J., *Phys. Lett. B*, **316** (1993) 567.
[15] Dunietz I., Fleisher R. and Nierste U., *Phys. Rev. D*, **63** (2001) 114015, arXiv:hep-ph/0012219.
[16] Aaltonen T. *et al.* (CDF Collaboration), *Phys. Rev. Lett.*, **100** (2008) 021803.
[17] Abazov V. *et al.* (D0 Collaboration), *Phys. Rev. Lett.*, **102** (2009) 091801, arXiv: 0811.2173.
[18] Esen S., arXiv:1110.2099 (2011).

IL NUOVO CIMENTO Vol. 35 C, N. 6 Novembre-Dicembre 2012
DOI 10.1393/ncc/i2012-11367-5

Colloquia: LaThuile12

Latest B physics results from ATLAS

J. Kirk on behalf of the ATLAS Collaboration
Rutherford Appleton Laboratory - Chilton, Oxfordshire, UK

ricevuto il 7 Settembre 2012

Summary. — B physics results from the ATLAS detector at the LHC are presented using data collected during 2010 and 2011. Inclusive production cross-sections for quarkonia are measured and compared to theoretical predictions. Both the average B-hadron lifetime and the lifetime of exclusively reconstructed B_d^0 and B_s^0 mesons are presented. A first observation of the $\chi_b(3P)$ $b\bar{b}$ state is also reported.

PACS 13.20.Gd – Decays of J/Ψ, Υ, and other quarkonia.
PACS 14.40.Nd – Bottom mesons ($|B| > 0$).
PACS 14.40.Pq – Heavy quarkonia.

1. – Introduction

The ATLAS detector [1] at the Large Hadron Collider (LHC) is designed as a general-purpose detector with the main focus on high-momentum discovery physics. However, it also has a dedicated B physics programme, the latest results from which are presented here. The B physics programme concentrates on low momentum dimuon B signatures which can be efficiently triggered at an affordable event rate. This allows the study of quarkonia production (an important test of QCD), B-hadrons decaying to $J/\psi X$ (for mixing and CP violation studies) and the search for rare decays of B-hadrons into final states containing two muons.

The most important elements of the detector for B physics measurements are the Inner Detector tracker and the Muon Spectrometer. The Inner Detector consists of silicon pixel and microstrip detectors and a transition radiation tracker covering $|\eta| < 2.5$ and immersed in a 2 T magnetic field. The Muon Spectrometer covers $|\eta| < 2.7$, it consists of precision tracking chambers and detectors designed for triggering, both of which are within a toroidal magnetic field of 0.5 T. During 2010 and 2011 ATLAS has recorded $48\,\mathrm{pb}^{-1}$ and $5.6\,\mathrm{fb}^{-1}$ of data from p-p collisions at a centre-of-mass energy $\sqrt{s} = 7\,\mathrm{TeV}$.

During low luminosity data-taking in early 2010 B physics events could be triggered using low momentum single muons. With increasing luminosity these triggers were either prescaled or had increased thresholds applied which severely limits the acceptance for B physics events. For this reason, dedicated B physics triggers based on dimuons had been

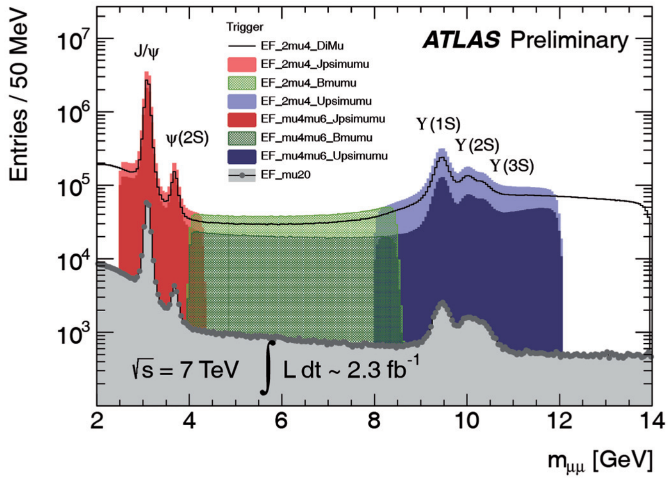

Fig. 1. – Invariant mass of oppositely charged muon candidate pairs selected by a variety of ATLAS triggers. The coloured histograms show those events selected by the dedicated Bphysics triggers compared to those triggered by the single muon trigger (grey). The different colours correspond to triggers with different mass ranges (red: 2.5–4.3 GeV ("Jpsimumu"), green: 4–8.5 GeV ("Bmumu"), blue: 8–12 GeV ("Upsimumu")).

developed. These require two low-momentum muons ($p_T > 4\,\mathrm{GeV}$) to be identified at the first (hardware) level of the trigger. Once the muons are confirmed in the High Level Trigger, a fit is performed to the combined vertex and mass constraints are applied.

Figure 1 shows the dimuon mass spectrum for events recorded during the first half of 2011 data taking. It was possible to run the lowest theshold ("2mu4") triggers unprescaled for the whole of the 2011 data-taking period. The coloured histograms show the significant data sample collected by the dedicated B physics triggers.

2. – Quarkonia production measurements

Quarkonia (J/ψ and Υ) production has been studied since the discovery of the particles in the 1970s but it is still not fully understood. In particular, there is no explanation of the production mechanism which can explain both cross-section and spin-alignment measurements from previous experiments. The LHC provides the opportunity to test existing models at a higher energy regime, higher transverse momentum scale and wider rapidity range than previously.

Using $2.2\,\mathrm{pb}^{-1}$ of data from 2010, ATLAS has measured the inclusive $J/\psi \to \mu^+\mu^-$ cross-section and the fraction of J/ψ which are produced non-promptly via decay of a B-hadron [2]. By combining these two measurements, separate cross-sections for the prompt and non-prompt J/ψ are also made.

The selected J/ψ events are corrected event-by-event for detector acceptance, reconstruction efficiency and trigger efficiency. An unbinned maximum-likelihood fit to the J/ψ mass spectrum is used to extract the cross-section in bins of rapidity and transverse momentum (p_T). Figure 2 shows the inclusive J/ψ cross-section for one rapidity bin. The largest source of systematic uncertainty on the measurement of the J/ψ cross-section is due to the spin alignment of the J/ψ which is unknown and affects the kinematic acceptance. Five extreme spin alignment scenarios are considered and maximum devia-

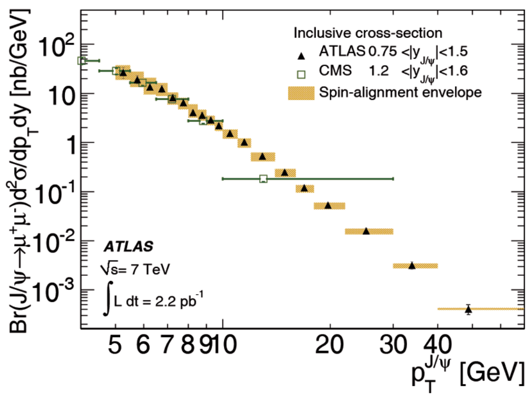

Fig. 2. – Inclusive J/ψ cross-section as a function of J/ψ transverse momentum for the rapidity bin $0.75 < |y| < 1.5$. The equivalent results from CMS are overlaid. The luminosity uncertainty (3.4%) is not shown.

tions of the acceptance correction are assigned as systematic effects. These uncertainties are regarded as theoretical rather than experimental and are shown in fig. 2.

At the LHC, J/ψ can be produced either promptly from the hard interaction or non-promptly via the decay of a B-hadron. It is possible to distinguish the J/ψ from b-decays from those produced promptly as the prompt decays occur at the primary vertex while the non-prompt J/ψ have a measurably displaced dimuon vertex due to the long lifetime of the parent B-hadron. The pseudo-proper time (τ) (using the mass and transverse momentum of the J/ψ rather than those of the B-hadron) is used as a discriminant:

$$\tau = \frac{L_{xy}\, m_{\mathrm{PDG}}^{J/\psi}}{p_T^{J/\psi}}\,. \tag{1}$$

where L_{xy} is the transverse decay length of the J/ψ vertex. The sample is divided into bins of p_T and rapidity of the J/ψ candidates. In each bin, a simultaneous unbinned maximum likelihood fit to the invariant mass and pseudo-proper time is performed to extract the fraction of J/ψ produced via B-decays. Figure 3 shows the pseudo-proper time distribution (left) and the non-prompt fraction (right) for one bin and the fraction results are compared to those from CDF and CMS. The non-prompt fraction increases rapidly with p_T and no significant rapidity dependence is observed. The results agree well with both the CMS and CDF results where they overlap. The agreement with CDF indicates that there is no dependence of the fraction on the collision energy.

By combining the information from the inclusive cross-section and the non-prompt B-fraction (F) it is possible to extract the non-prompt and prompt cross-sections separately; the prompt cross-section can be derived by multiplying the inclusive production cross-section by $(1 - F)$. Figure 4 shows the non-prompt (left) and prompt (right) J/ψ production cross-sections as a function of J/ψ transverse momentum compared to theoretical predictions. The measured non-prompt cross-section is in good agreement with Fixed-Order Next-to-Leading-Log theoretical predictions [3]. The prompt cross-section is compared to colour singlet (CSM) NLO and NNLO* pQCD predictions [4] and to the phenomenological Colour Evaporation Model (CEM) [5]. The CEM prediction is generally lower than the data and does not describe the shape of the distribution well. The

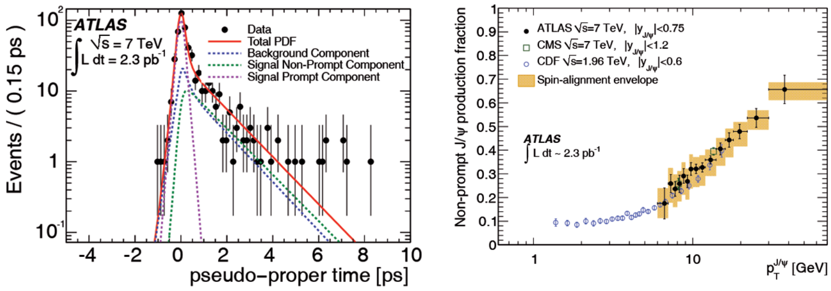

Fig. 3. – Left: Pseudo-proper time distribution of $J/\psi \to \mu^+\mu^-$ candidates for a selected p_T bin ($9.5 < p_T < 10.0\,\mathrm{GeV}$) in the $|y| < 0.75$ rapidity bin. The points are data, the solid line is the result of the unbinned maximum-likelihood fit. Right: J/ψ non-prompt fraction as a function of J/ψ transverse momentum. Overlaid is a band representing the variation of the result under various spin-alignment scenarios. Results from CMS and CDF are also shown.

CSM predictions describe the shape better and the NNLO* prediction shows a significant improvement in the normalisation over the NLO prediction.

Using $1.1\,\mathrm{pb}^{-1}$ of 2010 data, an unbinned maximum-likelihood fit to the $\Upsilon(1S)$ invariant mass spectrum is used to measure the cross-section in bins of rapidity and transverse momentum [6]. In this case the measurement is restricted to the fiducial region $p_T^\mu > 4\,\mathrm{GeV}$, $|\eta^\mu| < 2.5$ to remove the spin alignment uncertainty. An example of the unfolded differential cross-section in one rapidity bin is shown in fig. 5. The data are compared to the colour singlet NLO (CSM) prediction and significant disagreement is observed. However, the prediction does not include feed-down from higher mass states which was estimated to contribute a factor of two at the Tevatron. A comparison is also made to predictions from PYTHIA 8.135 using NRQCD, the shape of the data distribution is not well described although the overall nomalisation agrees within a factor 2.

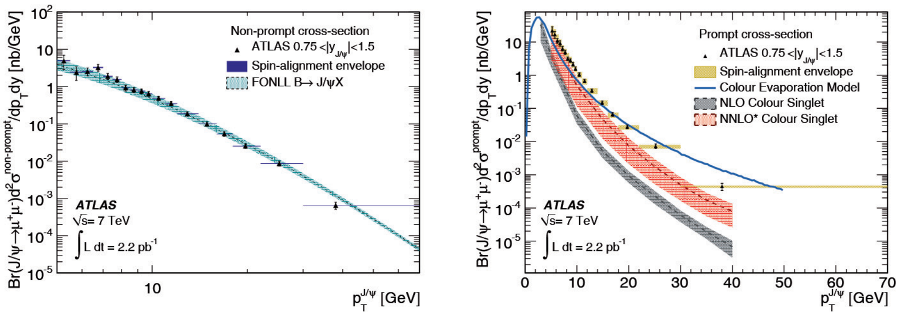

Fig. 4. – Non-prompt (left) and prompt (right) J/ψ production cross-sections as a function of J/ψ p_T. The non-prompt cross-section is compared to predictions from FONLL theory. The prompt cross-section is compared to predictions from NLO and NNLO* calculations, and the Colour Evaporation Model. Overlaid are bands representing the variation of the result under various spin-alignment scenarios representing a theoretical uncertainty on the non-prompt and prompt component.

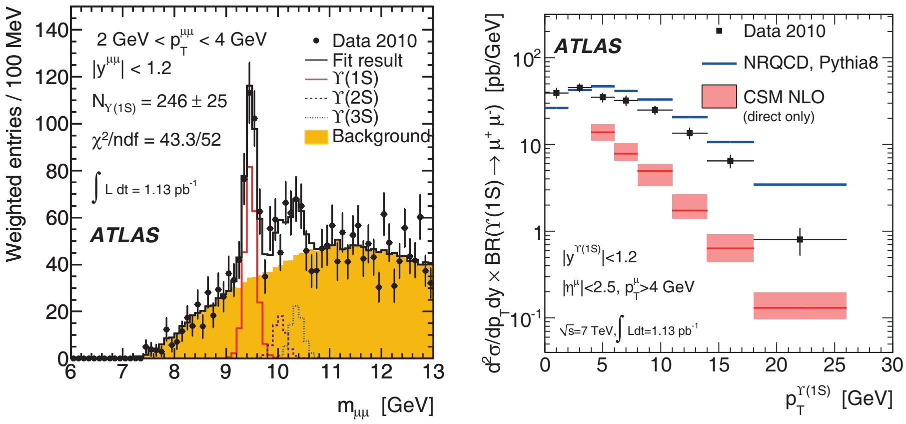

Fig. 5. – Left: Dimuon mass distribution for a representative bin in rapidity and p_T. The data (filled circles) are shown together with the result of the unbinned maximum-likelihood fit (histogram). Right: $\Upsilon(1S)$ cross-section for the $|y^{\Upsilon(1S)}| < 1.2$ rapidity bin as a function of $p_T^{\Upsilon(1S)}$, for $p_T^{\mu} > 4\,\mathrm{GeV}$ and $|\eta^{\mu}| < 2.5$ on both muons. Also shown is the CSM prediction and the NRQCD prediction as implemented in PYTHIA8 for a particular choice of parameters.

3. – B-hadron properties

In ATLAS, B-hadrons can be reconstructed exclusively from their decays to J/ψ, *i.e.* $B \to J/\psi(\mu^+\mu^-)X$. A number of B-hadrons have been observed in ATLAS through such decays [7]. Some of these are useful as reference channels for other measurements, *e.g.* $B^{\pm} \to J/\psi K^{\pm}$ is used as a reference in the search for the rare B-decay $B_s \to \mu^+\mu^-$. Other channels will be used in the future for important physics measurements, *e.g.* $B_s^0 \to J/\psi\phi$ for CP violation studies, $\Lambda_b \to J/\psi\Lambda$ for the measurement of the Λ_b polarisation. Two example invariant mass distributions are shown in fig. 6 for $\Lambda_b \to J/\psi\Lambda(p^+\pi^-)$ (left) and $B_d^0 \to J/\psi K_s^0(\pi\pi)$ (right). For all observed B-hadrons the measured masses are in good agreement with the PDG values.

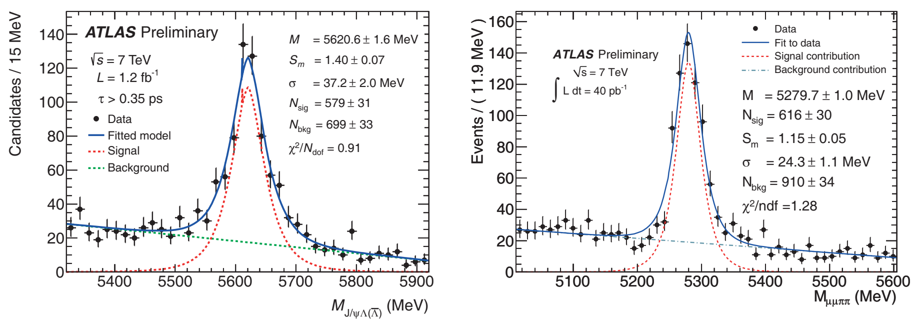

Fig. 6. – Left: Distribution of the invariant mass of $\Lambda_b \to J/\psi\Lambda(p^+\pi^-)$ and right: $B_d \to J/\psi K_s^0(\pi\pi)$ candidates reconstructed in data after a proper decay time cut of 0.35 ps.

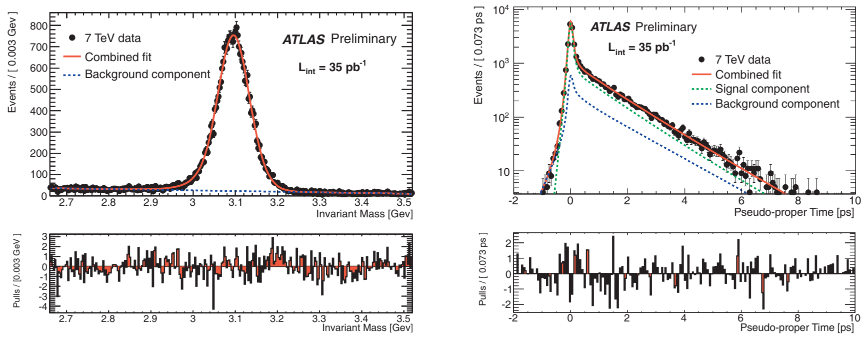

Fig. 7. – Invariant mass (left) and pseudo-proper time (right) projections (with respective pull distributions) of the simultaneous fit to these distributions in the average B-hadron lifetime measurement.

Precise measurement of B-hadron lifetimes allow tests of theoretical predictions. Lifetime ratios for different species of B-hadrons are predicted by theory at the per cent level. The lifetime difference of the two mass eigenstates of the B_s^0 system allows the measurement of the B_s^0 mixing phase which generates CP violation in the $B_s^0 \to J/\psi\phi$ channel.

Before making such measurements the performance of the track and secondary vertex reconstruction can be validated by measuring the lifetime of inclusive $B \to J/\psi(\mu^+\mu^-)X$ decays. This inclusive sample has orders of magnitude higher statistics that fully reconstructed exclusive B-hadrons. The average B-lifetime is extracted from the data by peforming an unbinned maximum-likelihood fit simultaneously to the J/ψ invariant mass and pseudo-proper decay time [8]. A correction factor is applied for the smearing introduced by the use of the pseudo-proper time to extract the real B-hadron lifetime. This factor is obtained from MC where the J/ψ momentum spectrum is re-weighted to match the BaBar data. Figure 7 shows the invariant mass and pseudo-proper time projections

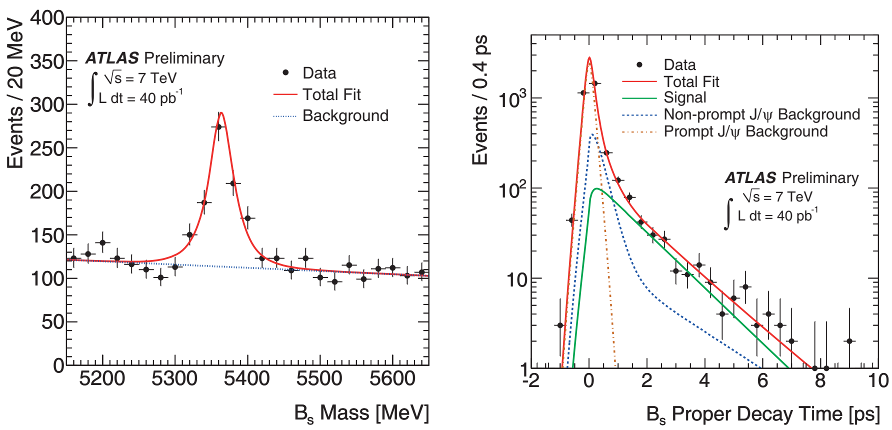

Fig. 8. – Invariant mass (left) and B_s^0 proper decay time (right) of reconstructed $B_s^0 \to J/\psi\phi$ decay candidates. The points with error bars are data. The solid line is the mass projection of the simultaneous mass and lifetime fit. Also shown are the fitted signal, prompt and non-prompt background distributions.

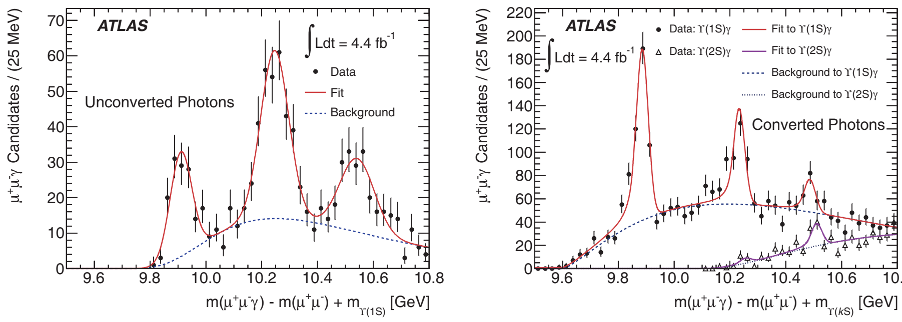

Fig. 9. – The mass distribution of $\chi_b \to \Upsilon(kS)\gamma$ $(k = 1, 2)$candidates for unconverted photons (left) and converted phtons (right). The data for decays of $\chi_b \to \Upsilon(1S)\gamma$ and $\chi_b \to \Upsilon(2S)\gamma$ are plotted using circles and triangles, respectively. Solid lines represent the total fit result for each mass window. The dashed lines represent the background components only.

from the fit. The measured average B-hadron lifetime is $1.1489 \pm 0.016 \pm 0.043$ ps. The main systematic uncertainty in this measurement is from the uncertainty in the radial alignment of the Inner Detector. The result is in agreement with the expected average lifetime computed using PDG lifetimes and production fractions from the different B-hadron species. Lifetimes of the B_d^0 and B_s^0 mesons are measured using the exclusive decay modes $B_d^0 \to J/\psi K^*$ and $B_s^0 \to J/\psi\phi$ [9]. Since in this case the B-hadron is fully reconstructed the proper decay time ($\tau = L_{xy} m^B / p_T^B$) can be used together with the mass in order to extract the yield, mass and lifetime in each channel. Figure 8 shows the mass and proper time disributions for the $B_s^0 \to J/\psi\phi$ candidates. These measurements use the full 2010 dataset and yield 2750 B_d^0 and 463 B_s^0 signal events. The lifetimes are measured to be

$$\tau_{B_d^0} = 1.51 \pm 0.04(\text{stat.}) \pm 0.04(\text{syst.})\,\text{ps}, \tag{2}$$

$$\tau_{B_s^0} = 1.41 \pm 0.08(\text{stat.}) \pm 0.05(\text{syst.})\,\text{ps}. \tag{3}$$

4. – Observation of $\chi_b(3P)$

The P-wave $b\bar{b}$ χ_b states can be reconstructed in ATLAS through the radiative decay to Υ. The $\chi_b(1P)$ and $\chi_b(2P)$ states have already been observed through this decay mode at other experiments. Using $4.4\,\text{fb}^{-1}$ of data from 2011, ATLAS has made the first observation of the $\chi_b(3P)$ state [10].

Pairs of oppositely charged muons are fit to a common vertex and required to have an invariant mass in the ranges $9.25 < m_{\mu\mu} < 9.65$ GeV and $9.80 < m_{\mu\mu} < 10.10$ GeV in order to select $\Upsilon(1S)$ and $\Upsilon(2S)$ candidates. Photons are reconstructed either directly in the calorimeter or through a conversion to e^+e^-. χ_b candidates are formed by combining a reconstructed $\Upsilon \to \mu^+\mu^-$ candidate with a reconstructed photon candidate. The invariant mass difference $\Delta m = m(\mu\mu\gamma) - m(\mu\mu)$ is calculated in order to minimise the effect of $\Upsilon \to \mu\mu$ mass resolution. In order to compare the Δm distributions for the $\Upsilon(1S)\gamma$ and the $\Upsilon(2S)\gamma$ the variable $\tilde{m}_k = \Delta m + m_{\Upsilon(kS)}$ is defined, where $m_{\Upsilon(kS)}$ are the world average masses [11] of the $\Upsilon(kS)$ states.

Figure 9 shows the distribution for unconverted photons (left) and converted photons (right). In addition to the expected peaks for $\chi_b(1P, 2P) \to \Upsilon(1S, 2S)\gamma$, structures are observed at an invariant mass of approximately 10.5 GeV. These additional structures are interpreted as the radiative decays of the previously unobserved $\chi_b(3P)$ states, $\chi_b(3P) \to \Upsilon(1S)\,\gamma$ and $\chi_b(3P) \to \Upsilon(2S)\,\gamma$. The higher threshold for unconverted photons (2.5 GeV *versus* 1 GeV for converted photons) prevents the reconstruction of the soft photons from $\chi_b(2P, 3P)$ decays into $\Upsilon(2S)$. An unbinned maximum likelihood fit is performed to the $\tilde{m}_k$ distributions, the mass for $\chi_b(3P)$ is found to be consistent in the unconverted and converted photon cases. Since the uncertainty on the conversion measurement is smaller this is used for the final mass determination of $10.539 \pm 0.005(\text{stat.}) \pm 0.009(\text{syst.})$ GeV.

5. – Summary and outlook

The ATLAS B-physics programme has made many interesting and important measurements of production cross-sections which are already providing important input for theoretical models. ATLAS has also observed many B-hadrons and made measurements of masses and lifetimes. These measurements are in agreement with PDG values and demonstrate the experimental techniques which will be needed for future measurements including searches for CP violation and rare B decays. The first observation of the $\chi_b(3P)$ state is reported. New results on CP violation measurements and rare decay searches using the 2011 dataset can be expected soon.

REFERENCES

[1] ATLAS Collaboration, *JINST*, **3** (2008) S08003.
[2] ATLAS Collaboration, *Nucl. Phys. B*, **850** (2011) 387.
[3] Cacciari M. *et al.*, *JHEP*, **05** (1998) 007; *JHEP*, **03** (2001) 006.
[4] Lansberg J. P., *Eur. Phys. J. C*, **61** (2009) 693.
[5] Ullrich t. *et al.*, *Phys. Rep.*, **462** (2008) 125.
[6] ATLAS Collaboration, *Phys. Lett. B*, **705** (2011) 9.
[7] ATLAS Collaboration, ATLAS-CONF-2010-098, ATLAS-CONF-2011-050, ATLAS-CONF-2011-105, ATLAS-CONF-2011-124, ATLAS-CONF-2011-136.
[8] ATLAS Collaboration, ATLAS-CONF-2011-145.
[9] ATLAS Collaboration, ATLAS-CONF-2011-092.
[10] ATLAS Collaboration, *Phys. Rev. Lett.*, **108** (2012) 152001.
[11] Nakamura K. *et al.* (Particle Data Group), *J. Phys. G*, **37** (2010) 075021.

IL NUOVO CIMENTO Vol. 35 C, N. 6 Novembre-Dicembre 2012
DOI 10.1393/ncc/i2012-11368-4

Colloquia: LaThuile12

Heavy-flavor physics results from CMS

M. Galanti for the CMS Collaboration(*)
Department of Physics, University of Cyprus - P.O. Box 20537, 1678 Nicosia, Cyprus

ricevuto il 7 Settembre 2012

Summary. — In this article, we summarize some recent heavy-flavor measurements performed by the CMS experiment. The inclusive b production cross-section, the study of $\Lambda_b \to J/\psi\Lambda$ and of other exclusive B-hadron decays, and the analysis of prompt and non-prompt J/ψ and $\psi(2s)$ are reviewed.

PACS `13.85.Qk` – Inclusive production with identified leptons, photons, or other nonhadronic particles.
PACS `14.20.Mr` – Bottom baryons ($|B| > 0$).
PACS `14.40.Nd` – Bottom mesons ($|B| > 0$).
PACS `14.40.Pq` – Heavy quarkonia.

1. – Introduction

The analyses presented here were all performed with data collected by the CMS experiment at LHC [1] during 2010 and 2011. In these two years, LHC has delivered proton-proton collisions with a center-of-mass energy $\sqrt{s} = 7\,\mathrm{TeV}$, and the luminosity collected by CMS has been $\sim 40\,\mathrm{pb}^{-1}$ in 2010 and $\sim 5\,\mathrm{fb}^{-1}$ in 2011.

The heavy-flavor program of CMS relies mainly on specialized di-muon triggers, and takes advantage of the excellent tracking and vertexing capabilities of the CMS detector. The di-muon triggers make use of the very flexible high-level-trigger (HLT) framework of CMS, which allows to apply selections on such observables as invariant mass, decay length, transverse momentum, and rapidity, already at the trigger level. This is needed in order to keep a high trigger efficiency, coping at the same time with the strict bandwidth limitations at the HLT.

The offline selections further refine the quality of the objects used in the analyses. In particular, for the muons, the analyses described below use a set of "tight" selections, having a rate of hadrons misidentified as muons of $O(0.1\%)$ and an efficiency $> 80\%$.

(*) Present address: Dipartimento di Fisica e Astronomia "Galileo Galilei", Università di Padova and INFN, Sezione di Padova - via Marzolo, 8 - 35131 Padova, Italy.

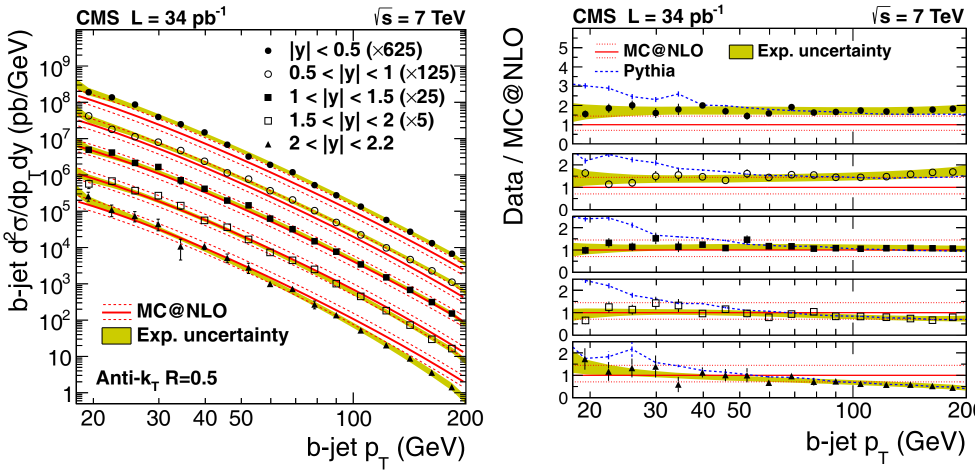

Fig. 1. – The inclusive b-jet cross-section as a function of the b-jet p_T for several rapidity ranges, measured with the jet-based analysis in [2], compared with the predictions of MC@NLO (left), and the ratio between data and NLO prepdictions (right).

This article is structured as follows: in sect. **2** we present the inclusive measurements of b hadron properties, in sect. **3** we show some recent results on the reconstruction of exclusive B-hadron final states, and in sect. **4** we review the measurements of charmonium properties.

2. – Inclusive b and b$\bar{\text{b}}$ production

2·1. *Inclusive b cross-section measurements.* – The cross-section for the inclusive production of b-jets has been measured in 2010 data with two different methods: a jet-based analysis, which uses a sample corresponding to an integrated luminosity of 34 pb^{-1}, and a muon-based analysis, which uses a sample of 3 pb^{-1} of integrated luminosity [2]. The jet data were collected using a combination of minimum-bias and single-jet triggers, while the events used in the muon analysis were required to pass a single-muon trigger, with $p_T^\mu > 9$ GeV and $|\eta^\mu| < 2.4$.

For both analyses, the b-tagging technique based on the presence of a secondary vertex is used to enhance the b fraction of the sample. In the jet analysis, the b-tagging purity is estimated with a template fit on the distribution of the secondary vertex mass, and for the muon-based one, a fit on the muon momentum transverse to the direction of the jet, $p_T^{\rm rel}$, is used to discriminate between the b events and the background.

For both analyses, the main sources of systematic uncertainties are the jet energy corrections (JEC), the determination of the b-tagging efficiency and purity, and the integrated luminosity measurement.

In the left panel of fig. 1, the measured b-jet cross-section is shown as a function of the jet p_T for different rapidity bins. The theoretical prediction from MC@NLO [3, 4] is also shown in the figure by the solid lines. In the right panel of fig. 1, the ratio between the measured cross-section and the theoretical predictions is shown. The MC@NLO predictions are below data in the central region, and tend to be above data in the forward region.

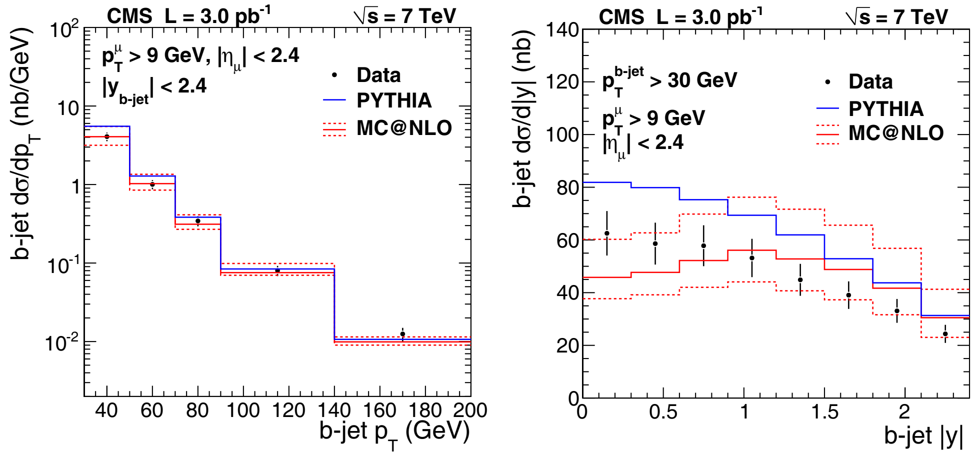

Fig. 2. – The inclusive b-jet cross-section as a function of the b-jet p_{T} (left) and $|y|$ (right), measured with the muon-based analysis in [2], compared with the predictions of PYTHIA and MC@NLO.

The results of the muon-based analysis are shown in fig. 2 as a function of the b-jet p_{T} (left) and $|y|$ (right), compared with the predictions from PYTHIA [5] and MC@NLO. The differential cross-section as a function of p_{T} is in good agreement with MC@NLO, while PYTHIA predicts higher values at low transverse momentum. The shape of the rapidity dependence measured in data is in agreement with the PYTHIA prediction, while a significant difference is observed with respect to MC@NLO.

The ratio between the b-jet and the inclusive jet cross-sections is shown in the left panel of fig. 3. The fraction of b-jets increases with p_{T} by a factor of 2, especially in the central region.

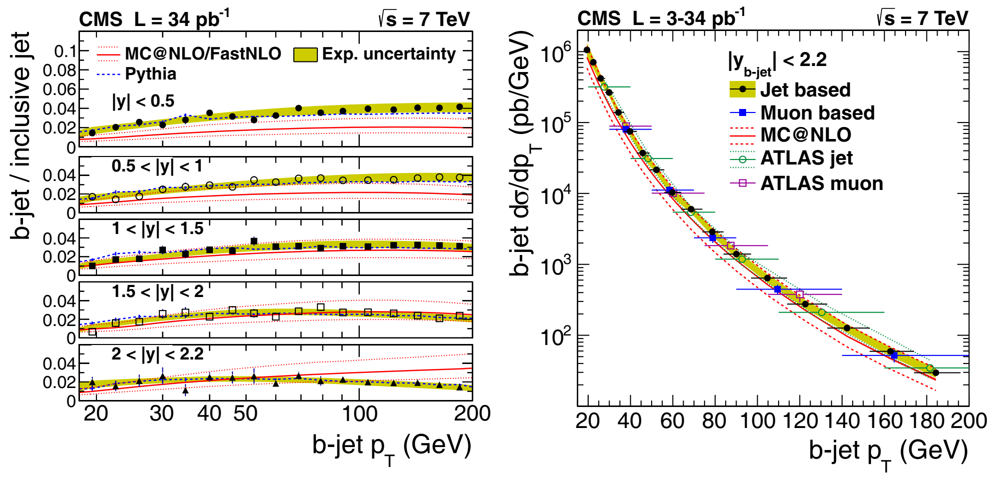

Fig. 3. – The ratio between b-jet and and the inclusive jet cross-sections (left), and the comparison between the b-jet p_{T} spectrum for several CMS and ATLAS measurements (right) [2].

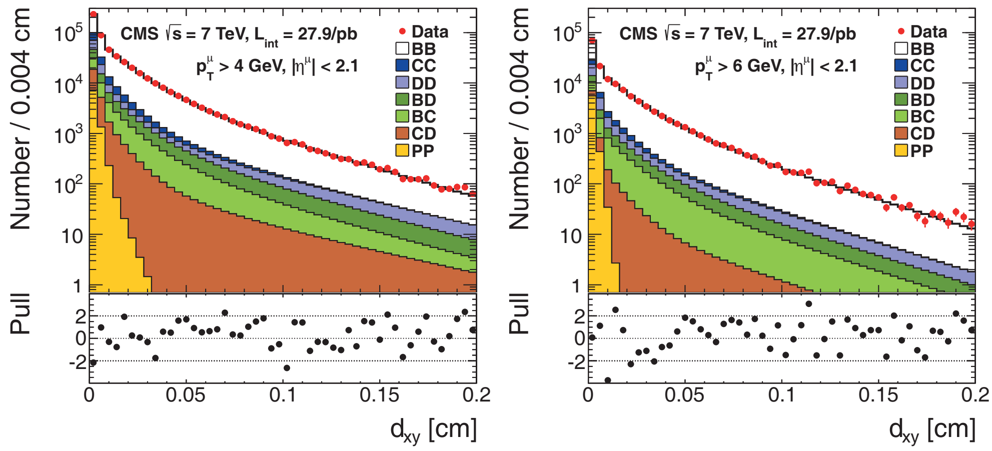

Fig. 4. – Projections of the two-dimensional template fits used to measure the cross-section of the process $pp \to b\bar{b}X \to \mu\mu X'$, for $p_T > 4\,\text{GeV}$ (left) and $p_T > 6\,\text{GeV}$ (right) [7].

The right panel of fig. 3 shows the results for the muon-based and the jet-based analyses of CMS, compared with two sets of measurements from the ATLAS Collaboration [6]. The CMS and ATLAS results are compatible with each other, within the experimental uncertainties.

2·2. *Inclusive* $b\bar{b}$ *cross-section with muon pairs*. – The cross-section for the inclusive production of $b\bar{b}$ pairs, both decaying into muons, has also been measured with $27.9\,\text{pb}^{-1}$ of data collected by CMS in 2010 [7].

The process $pp \to b\bar{b}X \to \mu\mu X'$ has been studied by looking at events containing pairs of muons, each with transverse momentum $p_T > 4\,\text{GeV}$ ($6\,\text{GeV}$) and pseudorapidity $|\eta| < 2.1$. The sample composition has been determined by using a two-dimensional template fit on the transverse impact parameters d_{xy} of the two muons. Templates for muons coming from b-hadron decays (B), c-hadron decays (C), and in-flight decays of pions and kaons (D) have been determined from the simulation, while the template for the prompt muon production (P) has been found from $\Upsilon \to \mu\mu$ decays in data.

Projections of the two-dimensional fits are shown in fig. 4 for the two p_T thresholds studied. The fraction of events with both muons coming from B decays is $66.8 \pm 0.3\%$ for $p_T > 4\,\text{GeV}$ and $70.2 \pm 0.3\%$ for $p_T > 6\,\text{GeV}$, where the errors are statistical only.

The main systematic uncertainties of the measurement come from the efficiency determination, from the models used to build the templates, and from the impact parameter resolution.

The measured cross-sections are

$$\sigma\left(pp \to b\bar{b}X \to \mu\mu X', p_T > 4\,\text{GeV}\right) = 26.4 \pm 0.1(\text{stat.}) \pm 2.4(\text{syst.}) \pm 1.1(\text{lumi.})\,\text{nb},$$

and

$$\sigma\left(pp \to b\bar{b}X \to \mu\mu X', p_T > 6\,\text{GeV}\right) = 5.12 \pm 0.03(\text{stat.}) \pm 0.48(\text{syst.}) \pm 0.20(\text{lumi.})\,\text{nb}.$$

These values can be compared with the NLO predictions from MC@NLO, that are

$$\sigma_{\text{MC@NLO}}\left(\mathrm{pp} \to \mathrm{b\bar{b}X} \to \mu\mu\mathrm{X}', p_{\mathrm{T}} > 4\,\mathrm{GeV}\right) = 19.7 \pm 0.3(\text{stat.})^{+6.5}_{-4.1}(\text{syst.})\,\mathrm{nb},$$

and

$$\sigma_{\text{MC@NLO}}\left(\mathrm{pp} \to \mathrm{b\bar{b}X} \to \mu\mu\mathrm{X}', p_{\mathrm{T}} > 6\,\mathrm{GeV}\right) = 4.40 \pm 0.14(\text{stat.})^{+1.10}_{-0.84}(\text{syst.})\,\mathrm{nb}.$$

Both predictions are lower than the measurements, but compatible with them within the experimental and the theoretical uncertainties.

3. – Exclusive B decays

3·1. $\Lambda_{\mathrm{b}} \to \mathrm{J}/\psi\Lambda$ *cross-section.* – The production cross-section of the Λ_{b} baryon has been studied at CMS as a function of the transverse momentum and rapidity, using a data sample collected in 2011 and corresponding to an integrated luminosity of $1.9\,\mathrm{fb}^{-1}$. The decay $\Lambda_{\mathrm{b}} \to \mathrm{J}/\psi\Lambda$, followed by $\mathrm{J}/\psi \to \mu^+\mu^-$ and $\Lambda \to \mathrm{p}\pi$ has been used [8].

Events are triggered by the presence of a pair of muons compatible with the decay of a J/ψ displaced by at least three standard deviations from the average position of the main proton-proton collision. Muons are selected offline by requiring them to be fully reconstructed in the tracker and in the muon stations, with “tight” quality selections.

The Λ candidates are formed from tracks with opposite charge which come from a common vertex. Candidate pairs of tracks are retained for the analysis only if they have an invariant mass compatible with the world-average Λ mass. Λ_{b} candidates are built by combining a J/ψ candidate and a Λ candidate coming from a common vertex, using a fit having the masses of the two particles constrained to their world-average values.

The overall efficiency to reconstruct the Λ_{b} decay chain is factorized as the product of several terms, including the efficiencies to trigger and reconstruct the single muons, and to combine them into the Λ_{b} candidate. The single-muon terms are taken from the data, using the Tag&Probe technique, while the simulation truth is used to estimate the effect of the di-muon correlation and to find the acceptance.

The measured differential cross-sections times the branching fraction, calculated in bins of p_{T} and y of the Λ_{b}, is shown in fig. 5 compared with the NLO predictions of POWHEG [9, 10] and with the results of PYTHIA. The slope of transverse momentum spectrum is steeper than the theoretical predictions, while the shape of the rapidity spectrum is in agreement with them, within the uncertainties.

The total cross-section for $p_{\mathrm{T}}^{\Lambda_{\mathrm{b}}} > 10\,\mathrm{GeV}$ and $|y^{\Lambda_{\mathrm{b}}}| < 2.0$, obtained as the sum of all bins, is

$$\sigma\left(\mathrm{pp} \to \Lambda_{\mathrm{b}}\mathrm{X}\right) \times \mathcal{B}\left(\Lambda_{\mathrm{b}} \to \mathrm{J}/\psi\Lambda\right) = 1.16 \pm 0.06 \pm 0.12\,\mathrm{nb}.$$

This is in good agreement with PYTHIA, which predicts a cross-section of $1.19 \pm 0.64\,\mathrm{nb}$, and higher than POWHEG, which predicts $0.63^{+0.41}_{-0.37}\,\mathrm{nb}$, with uncertainties dominated by the one on $\mathcal{B}(\Lambda_{\mathrm{b}} \to \mathrm{J}/\psi\Lambda)$.

The analysis also found the ratio $\sigma(\overline{\Lambda}_{\mathrm{b}})/\sigma(\Lambda_{\mathrm{b}})$ in bins of $p_{\mathrm{T}}^{\Lambda_{\mathrm{b}}}$ and $|y^{\Lambda_{\mathrm{b}}}|$, to be consistent with unity within the experimental precision, conferming the theoretical predictions.

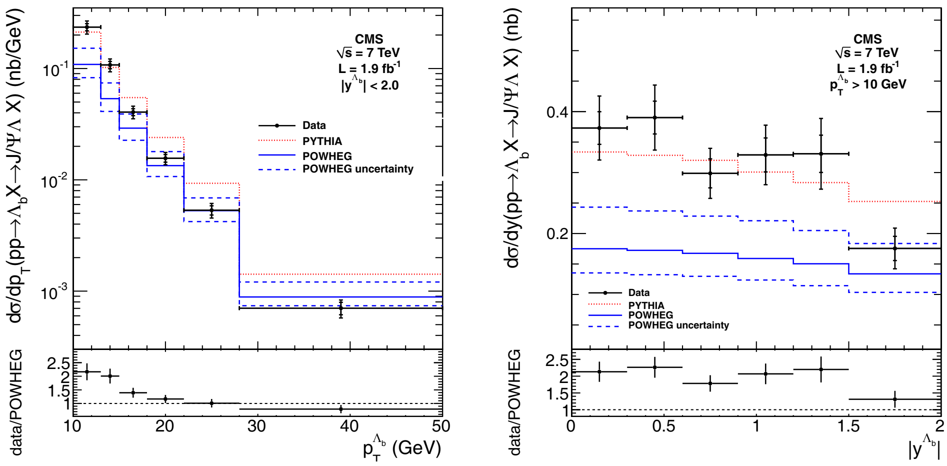

Fig. 5. – The differential cross-section for the process pp $\rightarrow \Lambda_b \rightarrow J/\psi\Lambda$ as a function of the transverse momentum p_T (left) and of the rapidity y (right) of the Λ_b [8].

3·2. *Summary of cross-section measurements with exclusive* B *decays*. – The result for Λ_b can be compared to the previous CMS measurements of the production cross-section of B^+ [11], B^0 [12], and B_s [13]. Figure 6 shows the differential cross-sections *vs.* p_T for the four particles, fitted to the Tsallis function [14]. The fit indicates a more steeply falling p_T spectrum for Λ_b than for the mesons, hinting to a change of the production rate of Λ_b relative to mesons with p_T. The observed behavior is compatible with previous measurements performed at the Tevatron [15], and with a recent result released by the LHCb Collaboration [16].

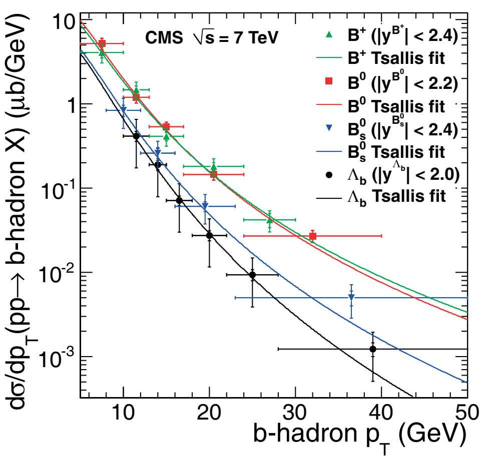

Fig. 6. – The differential cross-sections as a function of the transverse momentum p_T for the four B hadrons studied at CMS [8].

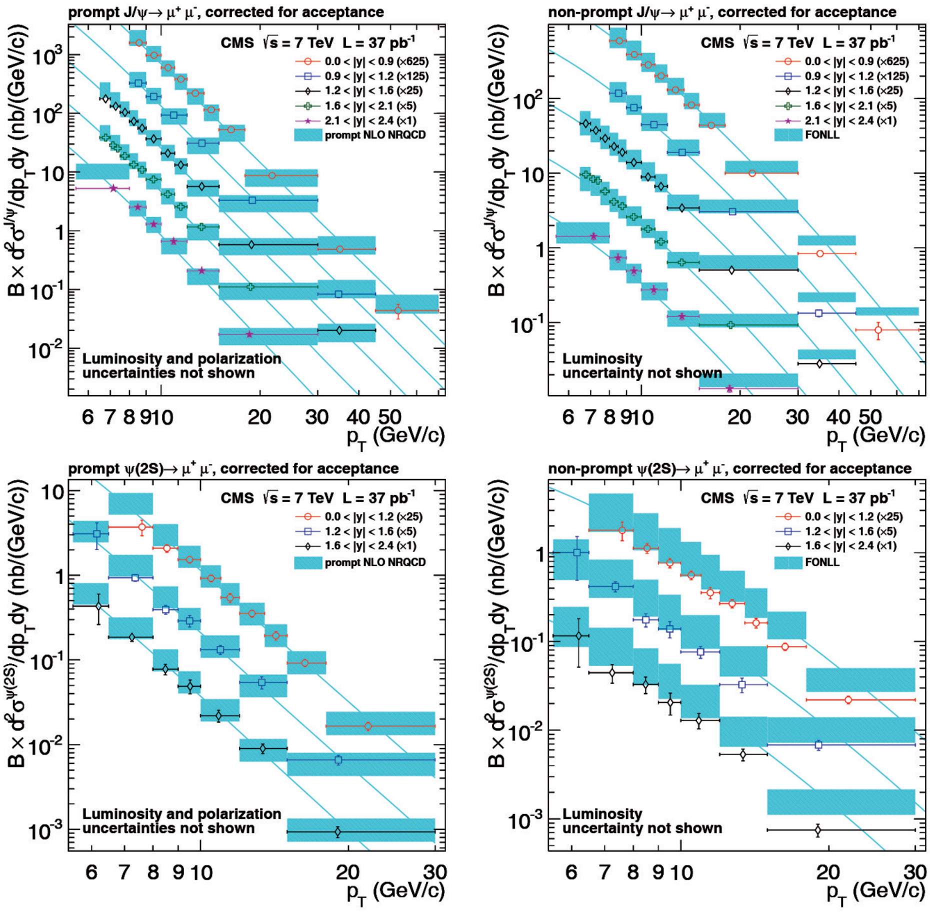

Fig. 7. – Differential cross-sections for the production of J/ψ (top) and $\psi(2s)$ (bottom) as a function of the transverse momentum p_{T} in different rapidity ranges. Prompt production is shown in the left plots, and non-prompt in the right ones [17].

4. – Measurement of charmonium properties

The production of prompt and non-prompt J/ψ and $\psi(2s)$ has been studied on a data sample collected in 2010 by CMS and corresponding to $37\,\mathrm{pb}^{-1}$ of integrated luminosity [17]. The decays of J/ψ and $\psi(2s)$ into $\mu^+\mu^-$ are reconstructed by looking at events triggered by the presence of two muons, and selecting pairs of muons with opposite charge which pass the "tight" quality selections and whose inner tracks come from a common vertex.

The data has been divided into bins of rapidity and transverse momentum of the J/ψ and $\psi(2s)$, and for each bin the yield of prompt and non prompt production has been found with a 2D unbinned maximum-likelihood fit on the invariant mass and the *pseudo-proper decay length* ℓ of the two mesons, defined as the most probable value of the transverse distance between the di-muon vertex and the primary vertex, corrected for the Lorentz boost. The cross-section in each bin is extracted from the result of the fit, corrected for the loss in efficiency and for the acceptance. The main sources of uncertainties are the statistical error of the likelihood fits, the correlations of the muon efficiencies, the vertex assignment, the models used in the fits, and the luminosity measurement.

The results for the measured cross-sections are shown in fig. 7, compared with the theoretical predictions from FONLL [18,19]. The differential cross-sections for the prompt production are in good agreement with the theory for both particles. For the non-prompt production, the cross-section of the J/ψ is in agreement with the theory only for $p_{\mathrm{T}} < 30\,\mathrm{GeV}$ and is below it for larger transverse momenta, and the one of the $\psi(2s)$ is systematically lower than the prediction.

From the ratio of the non-prompt J/ψ and $\psi(2s)$ cross-sections it is possible to extract the branching fraction for the processes $\mathrm{B} \to \psi(2s) + \mathrm{X}$. This is found to be

$$\mathrm{BF}\,[\mathrm{B} \to \psi(2s) + \mathrm{X}] = [3.08 \pm 0.12(\mathrm{stat}-\mathrm{syst}) \pm 0.13(\mathrm{theor}) \pm 0.42(\mathrm{BF}_{\mathrm{PDG}})] \cdot 10^{-3}.$$

This value is about three times more accurate than the previous world average [20].

5. – Conclusions

In the past two years, the CMS experiment has carried out a rich program of heavy-flavor physics. The inclusive cross-sections for b quark production and for the production of $\mathrm{b\bar{b}}$ pairs decaying into muons have been measured using a variety of techniques ranging from the b-tagging to the use of template fits based on $p_{\mathrm{T}}^{\mathrm{rel}}$ and impact parameter. The cross-section of the process $\Lambda_{\mathrm{b}} \to \mathrm{J}/\psi\Lambda$ has also been measured, and compared with the results previously obtained for B^0, B^+, and $\mathrm{B_s}$, finding differences in the p_{T} behavior that hint to a dependence of the b fragmentation on the transverse momentum. Lastly, the cross-section for the prompt and non-prompt production of J/ψ and $\psi(2s)$ have been measured, and from the latter, the most accurate measurement done so far of the branching ratio of $\mathrm{B} \to \psi(2s) + \mathrm{X}$ has been extracted.

REFERENCES

[1] CMS Collaboration, *JINST*, **3** (2008) S08004.
[2] CMS Collaboration, *JHEP*, **04** (2012) 084.
[3] Frixione S. and Webber B. R., *JHEP*, **06** (2002) 029.
[4] Frixione S., Nason P. and Webber B. R., *JHEP*, **08** (2003) 007.
[5] Sjöstrand T., Mrenna S. and Skands P., *JHEP*, **05** (2006) 026.
[6] ATLAS Collaboration, *Eur. Phys. J. C*, **71** (2011) 1846.
[7] CMS Collaboration, *JHEP*, **06** (2012) 110.
[8] CMS Collaboration, *Phys. Lett. B*, **714** (2012) 136.
[9] Alioli S., Nason P., Oleari C. *et al.*, *JHEP*, **06** (2010) 043.
[10] Frixione S., Nason P. and Ridolfi G., *JHEP*, **09** (2007) 126.
[11] CMS Collaboration, *Phys. Rev. Lett.*, **106** (2011) 112001.
[12] CMS Collaboration, *Phys. Rev. Lett.*, **106** (2011) 252001.
[13] CMS Collaboration, *Phys. Rev. D*, **84** (2011) 052008.
[14] Tsallis C., *J. Stat. Phys.*, **52** (1988) 479.
[15] CDF Collaboration, *Phys. Rev. D*, **77** (2008) 072003.
[16] LHCb Collaboration, *Phys. Rev. D*, **85** (2012) 032008.
[17] CMS Collaboration, *JHEP*, **02** (2012) 011.
[18] Cacciari M., Greco M. and Nason P., *JHEP*, **05** (1998) 007.
[19] Cacciari M., Frixione S. and Nason P., *JHEP*, **03** (2001) 006.
[20] Particle Data Group Collaboration, *J. Phys. G*, **37** (2010) 075021.

IL NUOVO CIMENTO Vol. 35 C, N. 6 Novembre-Dicembre 2012
DOI 10.1393/ncc/i2012-11369-3

Colloquia: LaThuile12

Heavy-flavour spectroscopy (X, Y, Z, B_c, B^{**})

Wenbin Qian on behalf of the LHCb Collaboration
Syracuse University - New York, NY, USA

ricevuto il 7 Settembre 2012

Summary. — The LHCb measurements in the area of heavy-flavour spectroscopy (X, Y, Z, B_c, B^{**}) with part of the data collected in 2010 and 2011 are described in this paper. We first summarise the recent results for $X(3872)$ mass and production and searches for $X(4140)$. We then show the results of the search for orbitally excited mesons ($B^{**}_{(s)}$) and their mass measurements. We also measure the mass and production of B_c^+ meson and report the first observation of $B_c^+ \to J/\psi\pi^+\pi^+\pi^-$ decay channel.

PACS `14.40.Nd` – Bottom mesons ($|B| > 0$).
PACS `14.40.Rt` – Exotic mesons.

1. – The LHCb Experiment

The LHCb experiment [1], one of the four large detector experiments at the LHC, is optimized for heavy-quark physics with the unique coverage in the forward region. It collected around $0.04\,\mathrm{fb}^{-1}$ data in 2010 and $1\,\mathrm{fb}^{-1}$ data in 2011 with proton-proton collisions at a centre-of-mass energy of $7\,\mathrm{TeV}$. With the large amount of b events in its acceptance ($O(10^{11})$/fb), LHCb is shedding new light in the field of heavy flavour spectroscopy.

2. – X, Y, Z states

Recently, discoveries or evidences of new resonance structures have been made in the charmonium or bottomonium systems which can not be included in the quark model. The new resonance structures are denoted as "X, Y, Z" to indicate their unknown nature. Many models [2] are discussed to explain these resonance structures such as tetraquark models [3], molecular states [4] or charmonium hybrids with an excited degree of freedom [5]. LHCb has a program to understand the nature of these states. The current results for the $X(3872)$ and $X(4140)$ states are described here.

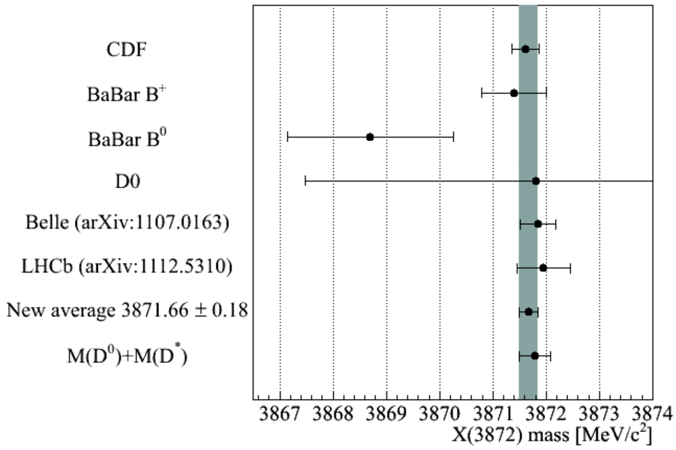

Fig. 1. – Published measurements of the $X(3872)$ mass in the $J/\psi\pi^+\pi^-$ mode, by the Belle [6], D0 [8], BaBar [13] and CDF [14] collaborations, and their comparision with the current LHCb measurement. The average including the LHCb measurement is performed according to the prescription given in ref. [15]. The sum of the D^0 and D^{*0} masses [15] is also shown.

2·1. $X(3872)$. – The $X(3872)$ meson was discovered in 2003 by the Belle Collaboration with $B^\pm \to X(3872)K^\pm$ and $X(3872) \to J/\psi\pi^+\pi^-$ [6]. It was quickly confirmed by other collaborations [7-9]. Some properties of $X(3872)$ have been measured: for example, the dipion mass spectrum by CDF [10], the quantum numbers constrained to either $J^{PC} = 2^{-+}$ or 1^{++} [11], but its nature remains unknown. One possibility is that the $X(3872)$ state is a loosely bounded $D^{*0}\bar{D}^0$ molecular [12] motivated by the proximity of its mass to the $D^{*0}\bar{D}^0$ threshold. In this case the $X(3872)$ mass should be smaller than the $D^{*0}\bar{D}^0$ threshold to have a negative binding energy. It is thus important to measure $X(3872)$ mass precisely to test it. The first measurement of the $X(3872)$ mass in LHCb is done with $37\,\mathrm{pb}^{-1}$ data collected in 2010 and yields:

$$M_{X(3872)} = 3871.96 \pm 0.46_{\mathrm{stat}} \pm 0.10_{\mathrm{syst}}\,\mathrm{MeV}/c^2. \tag{1}$$

We summarise the current experiment measurements of the mass of $X(3872)$ in fig. 1. The LHCb measurement is in good agreement with the published results [6,8,13,14]. Adding our and the recent Belle [6] results, the world average of the mass of $X(3872)$ is improved from $3871.57 \pm 0.25\,\mathrm{MeV}/c^2$ [15] to $3871.66 \pm 0.18\,\mathrm{MeV}/c^2$. It is still indistinguishable from the sum of the D^0 and D^{*0} masses obtained from the results of the global PDG fit [15]. More precise measurements are needed to solve the puzzle. The current LHCb result is dominated by the statistical error. With the collected 2011 data and coming 2012 data, our precision will be significantly improved.

Besides the measurement of the mass of $X(3872)$, the inclusive production cross-section is also studied in the phase space region $p_T \in [5, 20]\,\mathrm{GeV}/c$ and $\eta \in [2.5, 4.5]$ where p_T and η are the transverse momentum and rapidity of the $X(3872)$. The measurement gives

$$\sigma(pp \to X(3872) + X) \times \mathcal{B}(X(3872) \to J/\psi\pi^+\pi^-) = 4.7 \pm 1.1_{\mathrm{stat}} \pm 0.7_{\mathrm{syst}}\,\mathrm{nb}. \tag{2}$$

The result is compared with the current available calculation for LHC using a non-relativistic QCD model assuming that the cross-section is dominated by the production of charm quark paris with negligible relative momentum [16]. The calculated results are summed in our measured region and yield 13.0 ± 2.7 nb, which exceeds our measurement by 2.8σ.

2·2. $X(4140)$. – The observation of the $X(4140)$ state (also referred to as $Y(4140)$) is claimed by the CDF Collaboration with 3.8σ evidence [17] using $p\bar{p}$ collision data collected at the Tevatron at a centre-of-mass energy of 1.96 TeV. A preliminary update with $6.0\,\mathrm{fb}^{-1}$ data increases the significance to more than 5σ with 115 ± 12 reconstructed $B^+ \to J/\psi\phi K^+$ events and 19 ± 6 $X(4140)$ candidates. The measured mass and width are $4143.4^{+2.9}_{-3.0} \pm 0.6\,\mathrm{MeV}/c^2$ and $15.3^{+10.4}_{-6.1} \pm 2.5\,\mathrm{MeV}/c^2$ respectively. The relative branching fraction was measured to be $\mathcal{B}(B^+ \to X(4140)K^+) \times \mathcal{B}(X(4140) \to J/\psi\phi)/\mathcal{B}(B^+ \to J/\psi\phi K^+) = 0.149 \pm 0.039_{\mathrm{stat}} \pm 0.024_{\mathrm{syst}}$. There is also a claim of a 3.1σ evidence of a second resonance state ($X(4274)$) in higher mass region with mass and width to be $4274.4^{+8.4}_{-6.7} \pm 1.9\,\mathrm{MeV}/c^2$ and $32.3^{+21.9}_{-15.3} \pm 7.6\,\mathrm{MeV}/c^2$, respectively. The observation of the two resonance states near threshold has triggered widespread interest as charmonium states above the open charm threshold are generally broad [18].

Using $0.37\,\mathrm{fb}^{-1}$ data collected in 2011, LHCb performed a similar search with 346 ± 20 reconstructed $B^+ \to J/\psi\phi K^+$ events. The invariant mass difference ($M(J/\psi\phi) - M(J/\psi)$) distribution for the $B^+ \to J/\psi\phi K^+$ in the B^+ ($\pm 2.5\sigma$) and ϕ ($\pm 15\,\mathrm{MeV}/c^2$) mass window is shown in fig. 2. To ease the comparison with CDF, we employ the same fit model using a spin-zero relativistic Breit-Wigner shape for signal distribution together with a three-body phase-space function for background distribution. Both are convolved with the detector resolution ($1.5\pm0.1\,\mathrm{MeV}/c^2$). The efficiency is obtained from full simulation and coped into the distribution. Using the central value of the mass and width from CDF, a binned maximum likelihood yields 6.4 ± 4.9 $X(4140)$ candidates while the expected number from CDF gives $35 \pm 9 \pm 6$. The fitted distribution and expected distribution are shown on the top plot of fig. 2. An alternative background model is also tried using a quadratic function multiplied by the three-body phase space factor, the fit results are shown on the bottom plot of fig. 2. It gives a fit yield of 0.6 events with a positive error of 7.1 events. Taking into account statistical and systematic errors of both experiments, we conclude a 2.4σ (2.7σ with the alternative background modelling) disagreement with the CDF result. We do not confirm the exsitence of $X(4140)$. An upper limit on the branching fraction at 90% confidence level is set to be

$$\frac{\mathcal{B}(B^+ \to X(4140)K^+) \times \mathcal{B}(X(4140) \to J/\psi\phi)}{\mathcal{B}(B^+ \to J/\psi\phi)} < 0.07. \tag{3}$$

Similar results are obtained for $X(4274)$, we expect 53 ± 19 $X(4274)$ events using the measurements from CDF while the fit results give $3.4^{+6.5}_{-3.4}$ and 0^{+10}_{-0} respectively using two different background modellings. This yields an upper limit of

$$\frac{\mathcal{B}(B^+ \to X(4274)K^+) \times \mathcal{B}(X(4274) \to J/\psi\phi)}{\mathcal{B}(B^+ \to J/\psi\phi)} < 0.08, \tag{4}$$

at 90% confidence level.

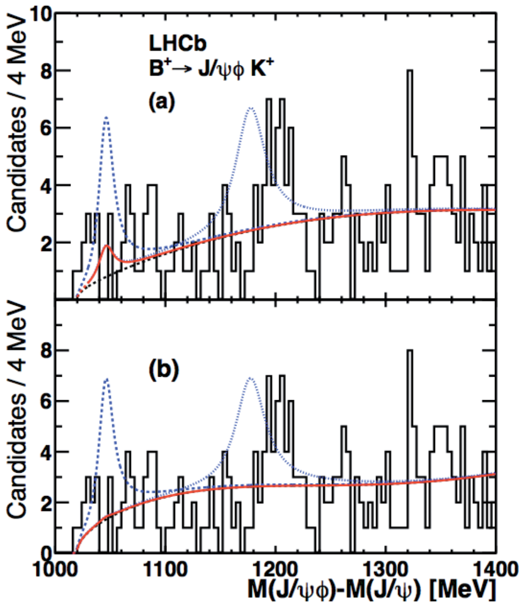

Fig. 2. – Invariant-mass difference $M(J/\psi\phi) - M(J/\psi)$ distribution for the $B^+ \to J/\psi\phi K^+$ in the B^+ ($\pm 2.5\sigma$) and ϕ ($\pm 15\,\mathrm{MeV}/c^2$) mass window. The dashed black line on top shows the background distribution using the same model as in CDF (three-body phase space) and the dashed black line on bottom shows the background distribution using a quadratic function multiplied by the three-body phase space. The dotted blue lines shows the expected distribution using the central value from CDF while the red solid line gives our fit results. Both fit functions on top and bottom are corrected with efficiencies obtained from simulation.

3. – Orbitally excited $B_{(s)}$ mesons

Properties of excited $B_{(s)}$ mesons containing a light quark (B_s^0, B^0, B^+) have been well predicted by heavy quark effective theory [19-21]. The system is described by three quantum numbers: the orbital angular momentum L, the angular momentum of the light quark $j_q = |L \pm 1/2|$ and the total angular momentum $J = |j_q \pm 1/2|$. In the heavy-quark limit, an essential idea is that the heavy-quark spin and j_q are conserved separately. For $j_q = 1/2 = L \pm 1/2$, the ground-state pesudo-scalar and vector mesons are with $L = 0$ while the orbital excited states ($L = 1$) are labelled as $B_{(s)}^{**}$. There are two more $L = 1$ orbital excitations with $j_q = 3/2$, they are all parity-even excited states.

Among the $B_{(s)}^{**}$ states, $B_1(5721)^0$ and $B_2^*(5747)^0$ have been observed by both CDF [22] and D0 [23]; $B_{s1}(5830)^0$ has been seen by CDF [24] and $B_{s2}^*(5840)^0$ has been seen by both CDF [24] and D0 [25]. The isospin partners of $B_1(5721)^0$ and $B_2^*(5747)^0$ are expected but not observed previously. In both experiments, the $B_{(s)}^{**}$ are reconstructed using $B + h$ ($h = \pi, K$). The soft photon from $B^* \to B + \gamma$ is ignored during the reconstruction if $B_{(s)}^{**}$ decays to B^*. The reconstructed mass in this case is shifted by $45.78 \pm 0.35\,\mathrm{MeV}/c^2$ ($M(B^*) - M(B)$).

The LHCb search is performed with $0.34\,\mathrm{fb}^{-1}$ data collected in 2011 and we search for B_s^{**} with decay channel $B^{(*)-} + K^+$, B^{**0} with decay channel $B^{(*)-} + \pi^+$ and B^{**+} with decay channel $B^{(*)0} + \pi^+$. The invariant-mass distribution $Q(h) = M(Bh^+) - M(B) - M(h^+)$ for the three processes are shown in fig. 3 and 4, respectively. In fig. 3,

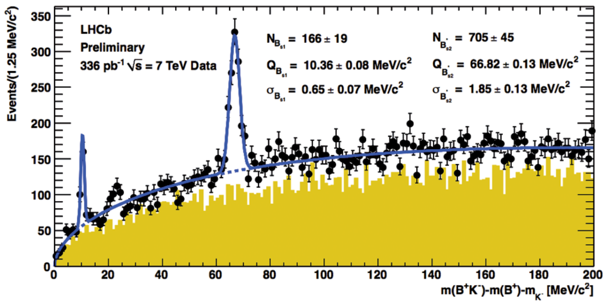

Fig. 3. – Invariant-mass distribution of $M(B^+K^-) - M(B^+) - M(K^-)$. The data distribution is labelled with black points. The yellow hist is the wrong sign combination. The solid blue line shows the fitted distribution.

two narrow peaks which corresponds to $B_{s1}(5830)^0$ and $B^*_{s2}(5840)^0$ could be clearly seen. The widths of the peaks are around $1\,\mathrm{MeV}/c^2$, mainly due to detector resolution and we model the signal distributions using Gaussian functions. As there is no visible sign of the $B^{*0}_{s2} \to B^{*-} + K^+$ mass peak, we do not include it in our analysis. The measured masses and significances are summarised in table I.

Due to the large width of B^{**0} and B^{**+} mesons, decays from different excited states overlap as shown in fig. 4 and we use a Breit-Wigner function to fit signal distributions. The three Breit-Wigner distributions shown at the bottom of each plot correspond to $B_1^{0(+)} \to B^{*-(0)}\pi^+$, $B_2^{0(+)} \to B^{*-(0)}\pi^+$ and $B_2^{0(+)} \to B^{-(0)}\pi^+$ from left to right. During the fit, the mass difference between two B_2^* decay channels are fixed to be $45.78\,\mathrm{MeV}/c^2$ and the widths of the resonance are fixed to be the same. The relative yields of the two decay channels are fixed to be 0.93 ± 0.18 based on the theoretical predictions [26]. The ratio of the widths of the two excited states are fixed to be 0.9 ± 0.2 [27]. The left plot of fig. 4 gives the invariant-mass difference distribution for $B^{*-} + \pi^+$ with fitted function superimposed. The fitted masses and significances for B^{**0} mesons are also summarised in table I. The measured masses agree with previous measurements [22, 23]. The invariant-mass difference distribution for the isospin partner of B^{**0} is shown in

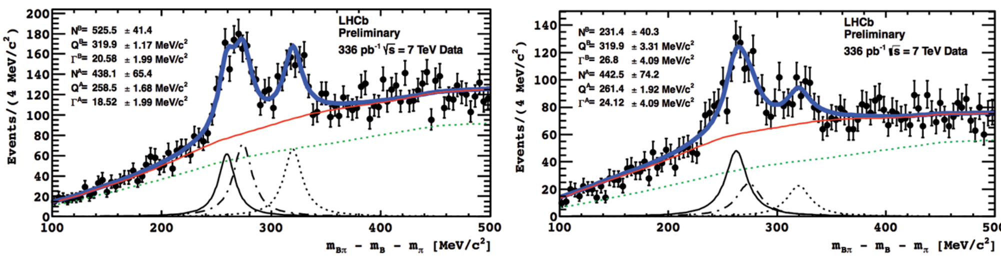

Fig. 4. – Invariant-mass distribution of $M(B^-\pi^+) - M(B^-) - M(\pi^+)$ (left) and $M(B^0\pi^+) - M(B^0) - M(\pi^+)$ (right). The black points show the data distribution. The green dotted curve gives wrong sign combination. The solid blue line shows the fitted distribution with the solid red curve as background distribution including combinatorial background and associated production. The three breit-wigner distributions at the bottom of each plot correspond to $B_1^{0(+)} \to B^{*-(0)}\pi^+$, $B_2^{0(+)} \to B^{*-(0)}\pi^+$ and $B_2^{0(+)} \to B^{-(0)}\pi^+$ from left to right.

TABLE I. – *Measured masses and significances of orbital excited $B_{(s)}$ mesons.*

Decay channels	Mass (MeV/c^2)	Significance
$B^0_{s1} \to B^{*+} + K^-$	$5828.99 \pm 0.08_{\rm stat} \pm 0.13_{\rm syst} \pm 0.45^{B{\rm mass}}_{\rm syst}$	12.5σ
$B^{*0}_{s2} \to B^+ + K^-$	$5839.67 \pm 0.13_{\rm stat} \pm 0.17_{\rm syst} \pm 0.5^{B{\rm mass}}_{\rm syst}$	22σ
$B^0_1 \to B^{*+} + \pi^-$	$5724.1 \pm 1.7_{\rm stat} \pm 2.0_{\rm syst} \pm 0.45^{B{\rm mass}}_{\rm syst}$	13.5σ
$B^0_2 \to B^{(*)+} + \pi^-$	$5738.6 \pm 1.2_{\rm stat} \pm 1.2_{\rm syst} \pm 0.3^{B{\rm mass}}_{\rm syst}$	$8.0(2.6)\sigma$
$B^+_1 \to B^{*0} + \pi^-$	$5726.3 \pm 1.9_{\rm stat} \pm 3.0_{\rm syst} \pm 0.5^{B{\rm mass}}_{\rm syst}$	9.9σ
$B^+_2 \to B^{(*)0} + \pi^-$	$5739.0 \pm 3.3_{\rm stat} \pm 1.6_{\rm syst} \pm 0.3^{B{\rm mass}}_{\rm syst}$	$4.0(0.0)\sigma$

the right plot of fig. 4. Two new B^{**+} excited states are observed with 9.9 $(4.0)\sigma$, respectively with their masses and significances in table I using similar fit procedure as for B^{**0}.

4. – B_c^+ meson

The B_c mesons are the unique double heavy-flavoured mesons in the standard model. Precise calculations could be done in the B_c system due to large b and c quark masses. It is thus very interesting to measure its properties and compare them with theoretical predictions. The LHCb has a program to measure B_c properties such as the B_c^+ mass and lifetime, B_c^+ production and decay modes etc. Current results on B_c^+ mass, B_c^+ production and a new observed decay channel $B_c^+ \to J/\psi\pi^+\pi^-\pi^+$ are shown here.

Using $35\,{\rm pb}^{-1}$ data, 28 ± 7 $B_c^+ \to J/\psi\pi^+$ events are reconstructed and the measured

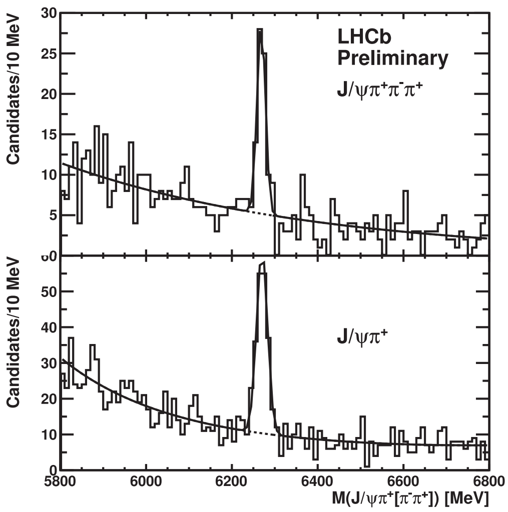

Fig. 5. – Invariant-mass distribution of $J/\psi\pi^+\pi^-\pi^+$ (top) and $J/\psi\pi^+$ (bottom) with fit function superimposed.

mass is found to be

$$M(B_c^+) = 6268.0 \pm 4.0_{\rm stat} \pm 0.6_{\rm syst}\,{\rm MeV}/c^2. \tag{5}$$

The measured mass agrees with previous measurement from CDF [28] and D0 [29]. The B_c^+ production is measured with the same dataset in the range $p_T > 4\,{\rm GeV}/c$ and $\eta \in [2.5, 4.5]$. The relative branching fraction gives

$$\frac{\sigma(B_c^\pm)\mathcal{B}(B_c^\pm \to J/\psi\pi^\pm)}{\sigma(B^\pm)\mathcal{B}(B^\pm \to J/\psi\pi^\pm)} = 2.2 \pm 0.8_{\rm stat} \pm 0.2_{\rm syst}\%. \tag{6}$$

With more dataset collected in 2011 ($0.3\,{\rm fb}^{-1}$), the LHCb is able to discover more "rare" decays, *i.e.* $B_c^+ \to J/\psi\pi^-\pi^+\pi^+$. In fact, its branching fraction is predicted to be $1.5 \sim 2.3$ times larger than $B_c^+ \to J/\psi\pi^+$, but due to lower detection efficiency (~ 10 times less), more data is needed to observe it than $B_c^+ \to J/\psi\pi^+$. The invariant mass distribution for $B_c^+ \to J/\psi\pi^+\pi^+\pi^-$ and $B_c^+ \to J/\psi\pi^+$ are shown in fig. 5. The observed number of $B_c^+ \to J/\psi\pi^+\pi^+\pi^-$ ($B_c^+ \to J/\psi\pi^+$) is 58.2 ± 9.6 (163.1 ± 15.7) corresponding to 6.8 (11)σ significance. Together with the relative efficiencies between the two decay channels (0.119 ± 0.006), we determine the branching fraction ratio to be $3.0 \pm 0.6_{\rm stat} \pm 0.4_{\rm syst}$. Our result favours the prediction of the ratio to be 2.3 [30]. Further look of the invariant mass distributions of $\pi^+\pi^-$ and $\pi^+\pi^+\pi^-$ shows that the dominated contribution of this channel comes from $B_c^+ \to J/\psi a_1^+(1260)$ with $a_1^+(1260) \to \rho^0\pi^+$.

5. – Conclusion

The LHCb experiment has a rich program on the search of heavy-quark spectrum. First studies of $X(3872)$ and $X(4140)$ demonstrate its potential to explore exotic meson sector. Future results with larger dataset will be built on this. It has also access to the poorly explored $B_{(s)}^{**}$ and B_c sectors, and will significantly improve the knowledge of their properties and decays.

REFERENCES

[1] Alves jr A. A. *et al.* (LHCb Collaboration), *JINST*, **3** (2008) S08005.
[2] Brambilla N. *et al.*, *Eur. Phys. J. C*, **71** (2011) 1534; arXiv:hep-ph/1010.5827.
[3] Maiani L., Piccinini F., Polosa A. D. and Riquer V., *Phys. Rev. D*, **71** (2005) 014028; arXiv:hep-ph/0412098.
[4] Tornqvist N. A., *Phys. Rev. Lett.*, **67** (1991) 556.
[5] Horn D. and Mandula J., *Phys. Rev. D*, **17** (1978) 898.
[6] Choi S. K. *et al.* (Belle Collaboration), *Phys. Rev. Lett.*, **91** (2003) 262001; arXiv:hep-ex/0309032.
[7] Acosta D. *et al.* (CDF Collaboration), *Phys. Rev. Lett.*, **93** (2004) 072001; arXiv:hep-ex/0312021.
[8] Abazov V. M. *et al.* (D0 Collaboration), *Phys. Rev. Lett.*, **93** (2004) 162002; arXiv:hep-ex/0405004.
[9] Aubert B. *et al.* (Babar Collaboration), *Phys. Rev. D*, **71** (2005) 071103; arXiv:hep-ex/0406022.
[10] Abulencia A. *et al.* (CDF Collaboration), *Phys. Rev. Lett.*, **96** (2006) 102002; arXiv:hep-ex/0512074.

[11] Abulencia A. *et al.* (CDF Collaboration), *Phys. Rev. Lett.*, **98** (2007) 132002; arXiv:hep-ex/0612053.
[12] Swanson E., *Phys. Rep.*, **429** (2006) 243; arXiv:hep-ex/0601110.
[13] Aubert B. *et al.* (Babar Collaboration), *Phys. Rev. D*, **77** (2008) 111101; arXiv:hep-ex/0803.2838.
[14] Aaltonen T. *et al.* (CDF Collaboration), *Phys. Rev. Lett.*, **103** (2009) 152001; arXiv:hep-ex/0906.5218.
[15] Nakamura K. *et al.* (Particle Data Group), *J. Phys. G*, **37** (2010) 075021.
[16] Artoisenet P. and Braaten E., *Phys. Rev. D*, **81** (2010) 114018.
[17] Aaltonen T. *et al.* (CDF Collaboration), *Phys. Rev. Lett.*, **102** (2009) 242002; arXiv:hep-ex/0903.2229.
[18] Brambilla N. *et al.*, *Eur. Phys. J. C*, **71** (2011) 1534; arXiv:hep-ph/1010.5827.
[19] Di Pierro M. and Eichten E., *Phys. Rev. D*, **64** (2001) 114004; arXiv:hep-ph/0104208.
[20] Echiten E. J., Hill C. T. and Quigg C., *Phys. Rev. Lett.*, **71** (1993) 4116; arXiv:hep-ph/9308337.
[21] Falk A. F. and Mehen T., *Phys. Rev. D*, **53** (1996) 231; arXiv:hep-ph/9507311.
[22] Aaltonen T. *et al.* (CDF Collaboration), *Phys. Rev. Lett.*, **102** (2009) 102003; arXiv:hep-ex/0809.5007.
[23] Abazov V. M. *et al.* (D0 Collaboration), *Phys. Rev. Lett.*, **99** (2007) 172001; arXiv:hep-ex/0705.3229.
[24] Aaltonen T. *et al.* (CDF Collaboration), *Phys. Rev. Lett.*, **100** (2008) 082001; arXiv:hep-ex/0710.4199.
[25] Abazov V. M. *et al.* (D0 Collaboration), *Phys. Rev. Lett.*, **100** (2008) 082002; arXiv:hep-ex/0711.0319.
[26] Di Pierror M. and Eichten E., *Phys. Rev. D*, **64** (2001) 114004.
[27] Falk A. F. and Mehen T., *Phys. Rev. D*, **53** (1996) 231.
[28] Aaltonen T. *et al.* (CDF Collaboration), *Phys. Rev. Lett.*, **100** (2008) 182002.
[29] Abazov V. M. *et al.* (D0 Collaboration), *Phys. Rev. Lett.*, **101** (2008) 012001.
[30] Likhoded A. K. and Luchinsky A. V., *Phys. Rev. D*, **81** (2010) 014015.

IL NUOVO CIMENTO Vol. 35 C, N. 6 Novembre-Dicembre 2012
DOI 10.1393/ncc/i2012-11370-x

Colloquia: LaThuile12

Bottomonium states

P. Krokovny for the Belle Collaboration
Budker Institute of Nuclear Physics SB RAS - Novosibirsk, Russia

ricevuto il 7 Settembre 2012

Summary. — Recent results on studies of bottomonium states at Belle are reported. The results are obtained with a $121.4\,\mathrm{fb}^{-1}$ data sample collected with the Belle detector in the vicinity of the $\Upsilon(5S)$ resonance at the KEKB asymmetric-energy e^+e^- collider.

PACS `14.40.-n` – Mesons.

1. – Introduction

Bottomonium is the bound system of $b\bar{b}$ quarks and is considered an excellent laboratory to study Quantum Chromodynamics (QCD) at low energies. The system is approximately non-relativistic due to the large b quark mass, and therefore the quark-antiquark QCD potential can be investigated via $b\bar{b}$ spectroscopy.

The spin-singlet states $h_b(mP)$ and $\eta_b(nS)$ alone provide information concerning the spin-spin (or hyperfine) interaction in bottomonium. Measurements of the $h_b(mP)$ masses provide unique access to the P-wave hyperfine splitting, the difference between the spin-weighted average mass of the P-wave triplet states ($\chi_{bJ}(nP)$ or n^3P_J) and that of the corresponding $h_b(mP)$, or n^1P_1. These splittings are predicted to be close to zero [1], and recent measurements of the $h_c(1P)$ mass validates this expectation for charmonium.

Recently, the CLEO Collaboration observed the process $e^+e^- \to h_c(1P)\pi^+\pi^-$ at a rate comparable to that for $e^+e^- \to J/\psi\pi^+\pi^-$ in data taken above open charm threshold [2]. Such a large rate was unexpected because the production of $h_c(1P)$ requires a c-quark spin-flip, while production of J/ψ does not. Similarly, the Belle Collaboration observed anomalously high rates for $e^+e^- \to \Upsilon(nS)\pi^+\pi^-$ ($n = 1, 2, 3$) at energies near the $\Upsilon(5S)$ mass [3]. Together, these observations motivated a more detailed study of bottomonium production at the $\Upsilon(5S)$ resonance.

We use a $121.4\,\mathrm{fb}^{-1}$data sample collected on or near the peak of the $\Upsilon(5S)$ resonance ($\sqrt{s} \sim 10.865\,\mathrm{GeV}$) with the Belle detector [4] at the KEKB asymmetric energy e^+e^- collider [5].

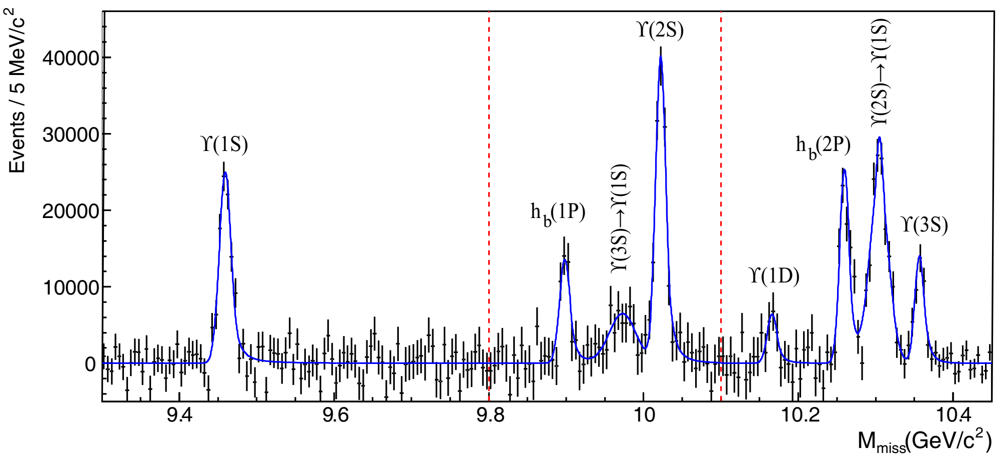

Fig. 1. – The inclusive $M_{\text{miss}}(\pi^+\pi^-)$ spectrum with the combinatorial background and K_S^0 contribution subtracted (points with errors) and signal component of the fit function overlaid (smooth curve). The vertical lines indicate boundaries of the fit regions.

2. – Observation of $h_b(mP)$

Our hadronic event selection requires a reconstructed primary vertex consistent with the run-averaged interaction point, at least three high-quality charged tracks. The $\pi^+\pi^-$ candidates are pairs of well reconstructed, oppositely charged tracks that are identified as pions and are not consistent with being electrons. Continuum $e^+e^- \to q\bar{q}$ $(q = u, d, s, c)$ background is suppressed by requiring the ratio of the second to zeroth Fox-Wolfram moments to satisfy $R_2 < 0.3$. More details can be found in ref. [6].

For all the $\pi^+\pi^-$ combinations we calculate missing mass defined as $M_{\text{miss}}(\pi^+\pi^-) \equiv \sqrt{(P_{\Upsilon(5S)} - P_{\pi^+\pi^-})^2}$, where $P_{\Upsilon(5S)}$ is the 4-momentum of the $\Upsilon(5S)$ determined from the beam momenta and $P_{\pi^+\pi^-}$ is the 4-momentum of the $\pi^+\pi^-$ system. The $M_{\text{miss}}(\pi^+\pi^-)$ spectrum is divided into three adjacent regions with boundaries at $M_{\text{miss}}(\pi^+\pi^-) = 9.3$, 9.8, 10.1 and 10.45 GeV/c^2 and fitted separately in each region. In the third region, prior to fitting, we perform bin-by-bin subtraction of the background associated with the $K_S^0 \to \pi^+\pi^-$ production. To fit the combinatorial background we use a 6th-7th order Chebyshev polynomial function for the first two (third) regions. The signal component of the fit includes all signals observed in the $\mu^+\mu^-\pi^+\pi^-$ data as well as those arising from $\pi^+\pi^-$ transitions to $h_b(mP)$ and $\Upsilon(1D)$. The peak positions of all signals are floated, except that for $\Upsilon(3S) \to \Upsilon(1S)\pi^+\pi^-$, which is poorly constrained by the fit. The $M_{\text{miss}}(\pi^+\pi^-)$ spectrum, after subtraction of all the background contributions along with the signal component of the fit function overlaid is shown in fig. 1, where clear signals of both $h_b(1P)$ and $h_b(2P)$ are visible. The signal parameters are listed in table I. Statistical significance of all signals except that for the $\Upsilon(1D)$ exceeds 5σ.

The measured masses of $h_b(1P)$ and $h_b(2P)$ are $M = (9898.3 \pm 1.1^{+1.0}_{-1.1})\,\text{MeV}/c^2$ and $M = (10259.8 \pm 0.6^{+1.4}_{-1.0})\,\text{MeV}/c^2$, respectively. Using the world average masses of the $\chi_{bJ}(nP)$ states, we determine the hyperfine splittings to be $\Delta M_{\text{HF}} = (+1.6 \pm 1.5)\,\text{MeV}/c^2$ and $(+0.5^{+1.6}_{-1.2})\,\text{MeV}/c^2$, respectively, where statistical and systematic uncertainties are combined in quadrature.

Table I. – *The yield and mass determined from the fits to the $M_{\mathrm{miss}}(\pi^+\pi^-)$ distributions.*

	Yield, 10^3	Mass, MeV/c^2
$\Upsilon(1S)$	$105.2 \pm 5.8 \pm 3.0$	$9459.4 \pm 0.5 \pm 1.0$
$h_b(1P)$	$50.4 \pm 7.8^{+4.5}_{-9.1}$	$9898.3 \pm 1.1^{+1.0}_{-1.1}$
$3S \to 1S$	56 ± 19	9973.01
$\Upsilon(2S)$	$143.5 \pm 8.7 \pm 6.8$	$10022.3 \pm 0.4 \pm 1.0$
$\Upsilon(1D)$	22.0 ± 7.8	10166.2 ± 2.6
$h_b(2P)$	$84.4 \pm 6.8^{+23.}_{-10.}$	$10259.8 \pm 0.6^{+1.4}_{-1.0}$
$2S \to 1S$	$151.7 \pm 9.7^{+9.0}_{-20.}$	$10304.6 \pm 0.6 \pm 1.0$
$\Upsilon(3S)$	$45.6 \pm 5.2 \pm 5.1$	$10356.7 \pm 0.9 \pm 1.1$

We also measure the ratio of cross sections $R \equiv \frac{\sigma(h_b(mP)\pi^+\pi^-)}{\sigma(\Upsilon(2S)\pi^+\pi^-)}$. To determine the reconstruction efficiency we use the results of resonant structure studies reported below. We determine the ratio of cross sections to be $R = 0.46 \pm 0.08^{+0.07}_{-0.12}$ for the $h_b(1P)$ and $R = 0.77 \pm 0.08^{+0.22}_{-0.17}$ for the $h_b(2P)$. Hence $\Upsilon(5S) \to h_b(mP)\pi^+\pi^-$ and $\Upsilon(5S) \to \Upsilon(2S)\pi^+\pi^-$ proceed at similar rates, despite the fact that the production of $h_b(mP)$ requires a spin-flip of a b-quark.

3. – Observation of $Z_b(10610)$ and $Z_b(10650)$

As it was mentioned above, the processes $\Upsilon(5S) \to h_b(mP)\pi^+\pi^-$, which require a heavy-quark spin flip, are found to have rates that are comparable to those for the heavy-quark spin conserving transitions $\Upsilon(5S) \to \Upsilon(nS)\pi^+\pi^-$, where $n = 1, 2, 3$. These observations differ from *a priori* theoretical expectations and strongly suggest that some exotic mechanisms are contributing to $\Upsilon(5S)$ decays.

First we perform an amplitude analysis of three-body $\Upsilon(5S) \to \Upsilon(nS)\pi^+\pi^-$ decays. To reconstruct $\Upsilon(5S) \to \Upsilon(nS)\pi^+\pi^-$, $\Upsilon(nS) \to \mu^+\mu^-$ candidates we select events with four charged tracks with zero net charge that are consistent with coming from the interaction point. Charged pion and muon candidates are required to be positively identified. Exclusively reconstructed events are selected by the requirement $|M_{\mathrm{miss}}(\pi^+\pi^-) - M(\mu^+\mu^-)| < 0.2\,\mathrm{GeV}/c^2$. Candidate $\Upsilon(5S) \to \Upsilon(nS)\pi^+\pi^-$ events are selected by requiring $|M_{\mathrm{miss}}(\pi^+\pi^-) - m_{\Upsilon(nS)}| < 0.05\,\mathrm{GeV}/c^2$, where $m_{\Upsilon(nS)}$ is the mass of an $\Upsilon(nS)$ state [8]. Sideband regions are defined as $0.05\,\mathrm{GeV}/c^2 < |M_{\mathrm{miss}}(\pi^+\pi^-) - m_{\Upsilon(nS)}| < 0.10\,\mathrm{GeV}/c^2$. To remove background due to photon conversions in the innermost parts of the Belle detector we require $M^2(\pi^+\pi^-) > 0.20/0.14/0.10\,\mathrm{GeV}/c^2$ for a final state with an $\Upsilon(1S), \Upsilon(2S), \Upsilon(3S)$, respectively. More details can be found in ref. [7].

Amplitude analyses are performed by means of unbinned maximum-likelihood fits to two-dimensional $M^2[\Upsilon(nS)\pi^+]$ *vs.* $M^2[\Upsilon(nS)\pi^-]$ Dalitz distributions. The fractions of signal events in the signal region are determined from fits to the $M_{\mathrm{miss}}(\pi^+\pi^-)$ spectrum and are found to be $0.937 \pm 0.015(\mathrm{stat.})$, $0.940 \pm 0.007(\mathrm{stat.})$, $0.918 \pm 0.010(\mathrm{stat.})$ for final states with $\Upsilon(1S)$, $\Upsilon(2S)$, $\Upsilon(3S)$, respectively. The variation of reconstruction efficiency across the Dalitz plot is determined from a GEANT-based MC simulation. The distribution of background events is determined using sideband events and found to be uniform across the Dalitz plot.

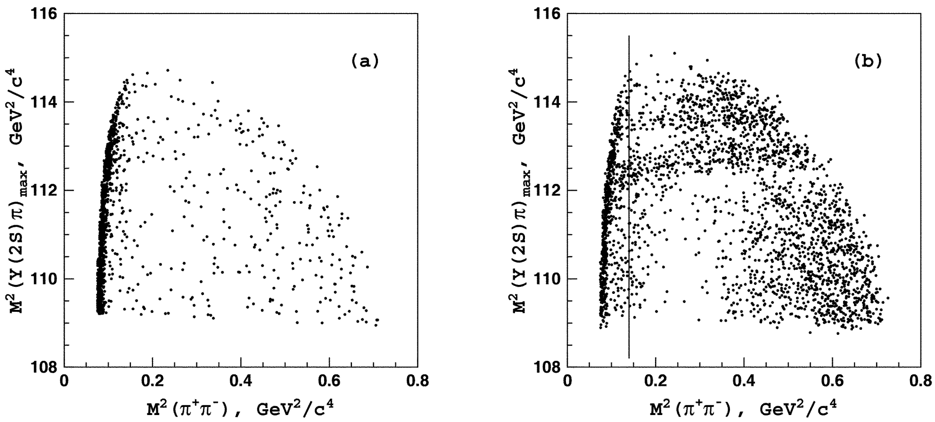

Fig. 2. – Dalitz plots for $\Upsilon(2S)\pi^+\pi^-$ events in the (a) $\Upsilon(2S)$ sidebands; (b) $\Upsilon(2S)$ signal region. Events to the left of the vertical line are excluded.

Dalitz distributions of events in the $\Upsilon(2S)$ sidebands and signal regions are shown in figs. 2(a) and 2(b), respectively, where $M(\Upsilon(nS)\pi)_{\max}$ is the maximum invariant mass of the two $\Upsilon(nS)\pi$ combinations. Two horizontal bands are evident in the $\Upsilon(2S)\pi$ system near $112.6\,\mathrm{GeV}^2/c^4$ and $113.3\,\mathrm{GeV}^2/c^4$, where the distortion from straight lines is due to interference with other intermediate states, as demonstrated below. One-dimensional invariant-mass projections for events in the $\Upsilon(nS)$ signal regions are shown in fig. 3, where two peaks are observed in the $\Upsilon(nS)\pi$ system near $10.61\,\mathrm{GeV}/c^2$ and $10.65\,\mathrm{GeV}/c^2$. In the following we refer to these structures as $Z_b(10610)$ and $Z_b(10650)$, respectively.

We parametrize the $\Upsilon(5S) \to \Upsilon(nS)\pi^+\pi^-$ three-body decay amplitude by

$$M = A_{Z_1} + A_{Z_2} + A_{f_0} + A_{f_2} + A_{\mathrm{nr}}, \tag{1}$$

where A_{Z_1} and A_{Z_2} are amplitudes to account for contributions from the $Z_b(10610)$ and $Z_b(10650)$, respectively. Here we assume that the dominant contributions come from amplitudes that preserve the orientation of the spin of the heavy quarkonium state and, thus, both pions in the cascade decay $\Upsilon(5S) \to Z_b\pi \to \Upsilon(nS)\pi^+\pi^-$ are emitted in an S-wave with respect to the heavy quarkonium system. An angular analysis support this assumption [9]. Consequently, we parametrize the observed $Z_b(10610)$ and $Z_b(10650)$ peaks with an S-wave Breit-Wigner function $BW(s, M, \Gamma) = \frac{\sqrt{M\Gamma}}{M^2 - s - iM\Gamma}$, where we do not consider possible s-dependence of the resonance width. To account for the possibility of $\Upsilon(5S)$ decay to both $Z_b^+\pi^-$ and $Z_b^-\pi^+$, the amplitudes A_{Z_1} and A_{Z_2} are symmetrized with respect to π^+ and π^- transposition. Using isospin symmetry, the resulting amplitude is written as

$$A_{Z_k} = a_{Z_k} e^{i\delta_{Z_k}} (BW(s_1, M_k, \Gamma_k) + BW(s_2, M_k, \Gamma_k)), \tag{2}$$

where $s_1 = M^2[\Upsilon(nS)\pi^+]$, $s_2 = M^2[\Upsilon(nS)\pi^-]$. The relative amplitudes a_{Z_k}, phases δ_{Z_k}, masses M_k and widths Γ_k ($k = 1, 2$) are free parameters. We also include the A_{f_0} and A_{f_2} amplitudes to account for possible contributions in the $\pi^+\pi^-$ channel from the $f_0(980)$ scalar and $f_2(1270)$ tensor states, respectively. We use a Breit-Wigner function

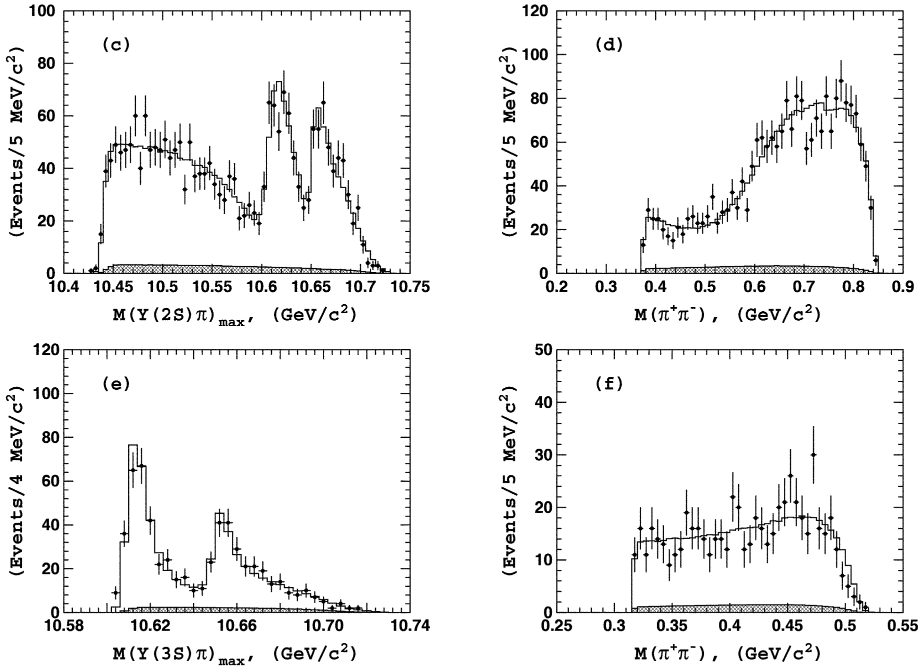

Fig. 3. – Comparison of fit results (open histogram) with experimental data (points with error bars) for events in the $\Upsilon(2S)$ (top) and $\Upsilon(3S)$ (bottom) signal regions. The hatched histogram shows the background component.

to parametrize the $f_2(1270)$ and a coupled-channel Breit-Wigner function for the $f_0(980)$. The mass and width of the $f_2(1270)$ state are fixed at their world average values [8]; the mass and the coupling constants of the $f_0(980)$ state are fixed at values determined from the analysis of $B^+ \to K^+\pi^+\pi^-$: $M[f_0(980)] = 950\,\mathrm{MeV}/c^2$, $g_{\pi\pi} = 0.23$, $g_{KK} = 0.73$ [10].

Following suggestions in ref. [11], the non-resonant amplitude A_{nr} is parametrized as $A_{\mathrm{nr}} = a_1^{\mathrm{nr}}\, e^{i\delta_1^{\mathrm{nr}}} + a_2^{\mathrm{nr}}\, e^{i\delta_2^{\mathrm{nr}}}\, s_3$, where $s_3 = M^2(\pi^+\pi^-)$ (s_3 is not an independent variable and can be expressed via s_1 and s_2 but we use it here for clarity), a_1^{nr}, a_2^{nr}, δ_1^{nr} and δ_2^{nr} are free parameters of the fit.

The logarithmic likelihood function $\mathcal{L}$ is then constructed as

$$\mathcal{L} = -2\sum \log(f_{\mathrm{sig}} S(s_1, s_2) + (1 - f_{\mathrm{sig}}) B(s_1, s_2)), \tag{3}$$

where $S(s_1, s_2)$ is the density of signal events $|M(s_1, s_2)|^2$ convolved with the detector resolution function, $B(s_1, s_2)$ describes the combinatorial background that is considered to be constant and f_{sig} is the fraction of signal events in the data sample. Both $S(s_1, s_2)$ and $B(s_1, s_2)$ are efficiency corrected.

Results of the fits to $\Upsilon(5S) \to \Upsilon(nS)\pi^+\pi^-$ signal events are shown in fig. 3, where one-dimensional projections of the data and fits are compared. The combined statistical significance of the two peaks exceeds $10\,\sigma$ for all tested models and for all $\Upsilon(nS)\pi^+\pi^-$ channels.

To study the resonant substructure of the $\Upsilon(5S) \to h_b(mP)\pi^+\pi^-$ ($m = 1, 2$) three-body decays we measure their yield as a function of the $h_b(1P)\pi^\pm$ invariant mass. The

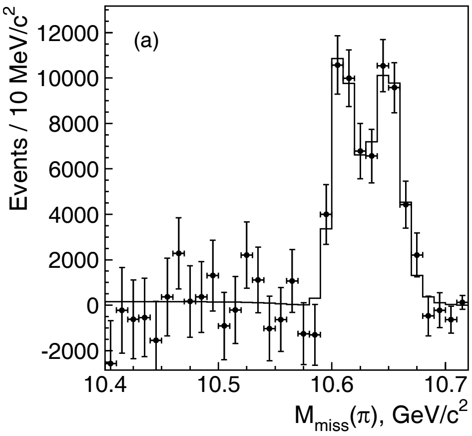

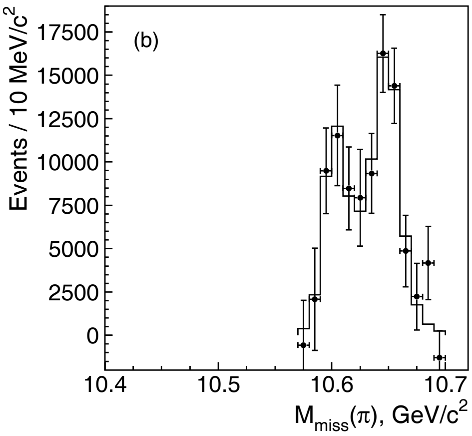

Fig. 4. – The (a) $h_b(1P)$ and (b) $h_b(2P)$ yields as a function of $M_{\rm miss}(\pi)$ (points with error bars) and results of the fit (histogram).

decays are reconstructed inclusively using missing mass of the $\pi^+\pi^-$ pair, $M_{\rm miss}(\pi^+\pi^-)$. We fit the $M_{\rm miss}(\pi^+\pi^-)$ spectra in bins of $h_b(1P)\pi^\pm$ invariant mass, defined as the missing mass of the opposite sign pion, $M_{\rm miss}(\pi^\mp)$. We combine the $M_{\rm miss}(\pi^+\pi^-)$ spectra for the corresponding $M_{\rm miss}(\pi^+)$ and $M_{\rm miss}(\pi^-)$ bins and we use half of the available $M_{\rm miss}(\pi)$ range to avoid double counting.

The fit function is a sum of peaking components due to dipion transitions and combinatorial background as described sect. **2**. The positions of all peaking components are fixed to the values measured from the fit to the overall $M(\pi^+\pi^-)$ spectrum (see table I).

Since the $\Upsilon(3S) \to \Upsilon(1S)$ reflection is not well constrained by the fits, we determine its normalization relative to the $\Upsilon(5S) \to \Upsilon(2S)$ signal from the exclusive $\mu^+\mu^-\pi^+\pi^-$ data for every $M_{\rm miss}(\pi)$ bin. In case of the $h_b(2P)$ we use the range of $M_{\rm miss}(\pi^+\pi^-) < 10.34\,{\rm GeV}/c^2$, to exclude the region of the $K_S^0 \to \pi^+\pi^-$ reflection. The peaking components include the $\Upsilon(5S) \to h_b(2P)$ signal and a $\Upsilon(2S) \to \Upsilon(1S)$ reflection.

The results for the yield of $\Upsilon(5S) \to h_b(mP)\pi^+\pi^-$ $(m = 1, 2)$ decays as a function of the $M_{\rm miss}(\pi)$ are shown in fig. 4. The distribution for the $h_b(1P)$ exhibits a clear two-peak structure without a significant non-resonant contribution. The distribution for the $h_b(2P)$ is consistent with the above picture, though the available phase-space is much smaller. We associate the two peaks with the production of the $Z_b(10610)$ and $Z_b(10650)$. To fit the $M_{\rm miss}(\pi)$ spectrum we use the following combination:

$$|BW_1(s, M_1, \Gamma_1) + ae^{i\phi}BW_1(s, M_2, \Gamma_2) + be^{i\psi}|^2 \frac{qp}{\sqrt{s}}. \tag{4}$$

Here $\sqrt{s} \equiv M_{\rm miss}(\pi)$; the variables M_k, Γ_k $(k = 1, 2)$, a, ϕ, b and ψ are free parameters; $\frac{qp}{\sqrt{s}}$ is a phase-space factor, where p (q) is the momentum of the pion originating from the $\Upsilon(5S)$ (Z_b) decay measured in the rest frame of the corresponding mother particle. The P-wave Breit-Wigner amplitude is expressed as $BW_1(s, M, \Gamma) = \frac{\sqrt{M\,\Gamma}\,F\,(q/q_0)}{M^2 - s - iM\,\Gamma}$. Here F is the P-wave Blatt-Weisskopf form factor $F = \sqrt{\frac{1+(q_0R)^2}{1+(qR)^2}}$, q_0 is a daughter momentum calculated with pole mass of its mother, $R = 1.6\,{\rm GeV}^{-1}$. The function (eq. (4)) is convolved with the detector resolution function, integrated over the histogram bin and corrected for the reconstruction efficiency. The fit results are shown as solid histograms in fig. 4. We find that the non-resonant contribution is consistent with zero in accord with the expectation that it is suppressed due to heavy quark spin-flip. In case of the $h_b(2P)$ we fix the non-resonant amplitude at zero.

4. – Conclusion

In summary, we have observed the P-wave spin-singlet bottomonium states $h_b(1P)$ and $h_b(2P)$ in the reaction $e^+e^- \to \Upsilon(5S) \to h_b(mP)\pi^+\pi^-$. The measured hyperfine splittings are consistent with zero as expected. A detailed analysis revealed that $h_b(mP)$ states in $\Upsilon(5S)$ decays are dominantly produced via intermediate charged bottomonium-like resonances $Z_b(10610)$ and $Z_b(10650)$. Resonances $Z_b(10610)$ and $Z_b(10650)$ have also been observed in decays $\Upsilon(5S) \to \Upsilon(nS)\pi^+\pi^-$. Weighted averages over all five channels give $M = 10607.2 \pm 2.0\,\mathrm{MeV}/c^2$, $\Gamma = 18.4 \pm 2.4\,\mathrm{MeV}$ for the $Z_b(10610)$ and $M = 10652.2 \pm 1.5\,\mathrm{MeV}/c^2$, $\Gamma = 11.5 \pm 2.2\,\mathrm{MeV}$ for the $Z_b(10650)$, where statistical and systematic errors are added in quadrature. The $Z_b(10610)$ production rate is similar to that of the $Z_b(10650)$ for each of the five decay channels. Their relative phase is consistent with zero for the final states with the $\Upsilon(nS)$ and consistent with 180 degrees for the final states with $h_b(mP)$. Analysis of charged pion angular distributions [9] favor the $J^P = 1^+$ spin-parity assignment for both the $Z_b(10610)$ and $Z_b(10650)$. Since the $\Upsilon(5S)$ has negative G-parity, the Z_b states have positive G-parity due to the emission of the pion.

The minimal quark content of the $Z_b(10610)$ and $Z_b(10650)$ is a four quark combination. The measured masses of these new states are a few MeV/c^2 above the thresholds for the open beauty channels $B^*\overline{B}$ ($10604.6\,\mathrm{MeV}/c^2$) and $B^*\overline{B}^*$ ($10650.2\,\mathrm{MeV}/c^2$). This suggests a "molecular" nature of these new states, which might explain most of their observed properties [12].

REFERENCES

[1] Godfrey S. and Rosner J. L., *Phys. Rev. D*, **66** (2002) 014012.
[2] Pedlar T. K. *et al.* (CLEO Collaboration), *Phys. Rev. Lett*, **107** (2011) 041803.
[3] Chen K.-F. *et al.* (Belle Collaboration), *Phys. Rev. Lett.*, **100** (2008) 112001.
[4] Abashian A. *et al.* (Belle Collaboration), *Nucl. Instrum. Methods Phys. Res. A*, **479** (2002) 117.
[5] Kurokawa S. and Kikutani E., *Nucl. Instrum. Methods Phys. Res. A*, **499** (2003) 1, and other papers included in these Proceedings.
[6] Adachi I. *et al.* (Belle Collaboration), *Phys. Rev. Lett.*, **108** (2012) 032001.
[7] Bondar A., Garmash A., Mizuk R., Santel D., Kinoshita K. *et al.* (Belle Collaboration), *Phys. Rev. Lett.*, **108** (2012) 122001.
[8] Nakamura K. *et al.* (Particle Data Group), *J. Phys. G*, **37** (2010) 075021.
[9] Adachi I. *et al.* (Belle Collaboration), arXiv:1105.4583 [hep-ex].
[10] Garmash A. *et al.* (Belle Collaboration), *Phys. Rev. Lett.*, **96** (2006) 251803.
[11] Voloshin M. B., *Prog. Part. Nucl. Phys.*, **61** (2008) 455; Voloshin M. B., *Phys. Rev. D*, **74** (2006) 054022 and references therein.
[12] Bondar A. E., Garmash A., Milstein A. I., Mizuk R. and Voloshin M. B., *Phys. Rev. D*, **84** (2011) 054010.

IL NUOVO CIMENTO Vol. 35 C, N. 6 Novembre-Dicembre 2012
DOI 10.1393/ncc/i2012-11371-9

Colloquia: LaThuile12

Searching for New Physics with flavor-violating observables

W. Altmannshofer

Fermi National Accelerator Laboratory - P.O. Box 500, Batavia, IL 60510, USA

ricevuto il 7 Settembre 2012

Summary. — In this paper, I review the status and prospects of several low-energy flavor observables that are highly sensitive to New Physics effects. In particular I discuss the implications for possible New Physics in $b \to s$ transitions coming from the recent experimental results on the B_s mixing phase, the branching ratio of the rare decay $B_s \to \mu^+\mu^-$, and angular observables in the $B \to K^*\mu^+\mu^-$ decay. Also the recent evidence for direct CP violation in singly Cabibbo-suppressed charm decays and its interpretation in the context of New Physics models is briefly discussed.

PACS 12.60.-i – Models beyond the standard model.
PACS 13.20.-v – Leptonic, semileptonic, and radiative decays of mesons.
PACS 13.25.Ft – Decays of charmed mesons.

1. – Introduction

In the Standard Model (SM), flavor-changing neutral current (FCNC) processes are absent at the tree level. They only appear at the loop level and are further strongly suppressed by small CKM mixing angles. Consequently, FCNCs are highly sensitive probes of any new physics (NP) that is not flavor blind. Remarkably, up to now all experimental results on flavor observables are consistent with SM expectations and lead to strong indirect constraints on NP models even at energy scales far beyond the direct reach of colliders. Indeed if new degrees of freedom exist that couple to quarks at tree level with generic flavor and CP-violating interactions, flavor constraints, in particular constraints from neutral Kaon mixing, require the corresponding NP scale to be above $\Lambda \gtrsim 10^4\,\text{TeV}$. If NP does exist at the TeV scale, as naturalness arguments indicate, then current flavor constraints already imply that its flavor structure has to be highly non-generic.

In this paper I describe the impact that the recent experimental progress on B and charm physics observables has on models of NP. After reviewing the status of the tension between $B \to \tau\nu$ and $\sin 2\beta$ in sect. **2**, I discuss in sect. **3** the current constraints on CP violation in B_s mixing. In sects. **4** and **5** the implications of the recent experimental results on $B_s \to \mu^+\mu^-$ and $B \to K^*\mu^+\mu^-$ for NP models are analyzed. Finally, in sect. **6** I discuss the recent evidence for direct CP violation in singly Cabibbo-suppressed charm decays and its interpretation in the context of NP models.

2. – $B \to \tau\nu$ and $\sin 2\beta$

Combining BaBar and Belle results of the $B \to \tau\nu$ decay leads to the following average for its branching ratio [1]

$$\mathcal{B}(B \to \tau\nu)_{\text{exp}} = (1.64 \pm 0.34)10^{-4}. \tag{1}$$

In the SM, the charged current $B \to \tau\nu$ decay proceeds through tree level exchange of a W boson and is helicity suppressed by the τ mass. The SM prediction of the branching ratio depends sensitively on the value of the CKM element $|V_{ub}|$. Using an average, obtained from direct measurements in inclusive and exclusive semi-leptonic B decays, $|V_{ub}| = (3.89 \pm 0.44)10^{-3}$ [2] as well as the precise lattice determination of the B meson decay constant $f_B = (190 \pm 4)\,\text{MeV}$ [3], one obtains

$$\mathcal{B}(B \to \tau\nu)_{\text{SM}} = (0.97 \pm 0.22)10^{-4}. \tag{2}$$

Within 2σ, this is compatible with the experimental value.

If one instead uses an indirect determination of $|V_{ub}|$ from the measurements of $\sin 2\beta$ as well as $\Delta M_d/\Delta M_s$ one finds

$$\mathcal{B}(B \to \tau\nu)_{\text{SM}} = (0.75 \pm 0.10)10^{-4}, \tag{3}$$

which is more than a factor of two and almost 3σ below the experimental value. Interpreted as a hint for NP, this tension between $\mathcal{B}(B \to \tau\nu)$ and $\sin 2\beta$ can be addressed either by a sizable negative NP phase in B_d mixing or by $O(1)$ NP effects in $B \to \tau\nu$. A well known example is tree level charged Higgs exchange that can lead to large modifications of $B \to \tau\nu$. While in two Higgs doublet models of type II, the charged Higgs contribution necessarily interferes destructively with the SM, the more general framework of two Higgs doublet models with minimal flavor violation (MFV) allows also for constructive interference and an explanation of the tension [4].

3. – CP violation in B_s mixing

CP violation in B_s mixing is strongly suppressed in the SM and therefore an excellent probe of NP. Assuming NP only in the dispersive part of the B_s mixing amplitude M_{12}, a possible NP phase ϕ_s^{NP} enters in a correlated way the semi-leptonic asymmetry in the decay of B mesons to "wrong sign" leptons

$$a^s_{\text{SL}} = \frac{\Gamma(\bar{B}_s \to X\ell^+\nu) - \Gamma(B_s \to X\ell^-\nu)}{\Gamma(\bar{B}_s \to X\ell^+\nu) + \Gamma(B_s \to X\ell^-\nu)} = \left|\frac{\Gamma^s_{12}}{M^s_{12}}\right| \sin(\phi_s^{\text{SM}} + \phi_s^{\text{NP}}) \tag{4}$$

and the time dependent CP asymmetries in decays to CP eigenstates f

$$S_f \sin(\Delta M_s t) = \frac{\Gamma(\bar{B}_s(t) \to f) - \Gamma(B_s(t) \to f)}{\Gamma(\bar{B}_s(t) \to f) + \Gamma(B_s(t) \to f)}, \qquad S_f = \sin(2|\beta_s| - \phi_s^{\text{NP}}). \tag{5}$$

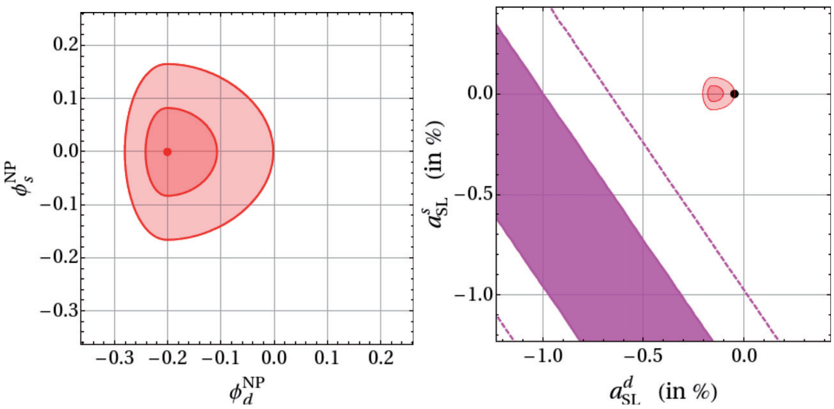

Fig. 1. – Left: Constraints on NP phases in B_d and B_s mixing from measurements of time-dependent CP asymmetries in $B_d \to \psi K_s$, $B_s \to \psi\phi$ and $B_s \to \psi\pi\pi$. Right: Corresponding region in the $a^d_{\rm SL}$-$a^s_{\rm SL}$ plane. The black point shows the SM prediction, the diagonal band shows the measurement of $A^b_{\rm SL}$ from D0. (Update from [7]).

The small SM phases are $\phi_s^{\rm SM} \simeq 0.2°$ and $\beta_s \simeq 1°$. A related observable is the like-sign dimuon charge asymmetry $A^b_{\rm SL}$ at D0. Assuming that it is caused by CP violation in B mixing, $A^b_{\rm SL}$ is a combination of the semileptonic asymmetries in the B_s and B_d system [5]

$$A^b_{\rm SL} \simeq 0.41 a^s_{\rm SL} + 0.59 a^d_{\rm SL}. \tag{6}$$

The large value of $A^b_{\rm SL} = (-0.787 \pm 0.172 \pm 0.093)\%$ measured by D0 [5] is almost 4σ above the tiny SM prediction.

On the other hand, the latest experimental results on time dependent CP asymmetries, in particular the recent results from LHCb [6], are all compatible with SM expectations. The left plot of fig. 1 shows the allowed ranges for NP phases in B meson mixing taking into account the most recent data on the time dependent CP asymmetry in $B_d \to \psi K_s$ from the B factories, the time dependent CP asymmetry in $B_s \to \psi\phi$ from CDF and D0 as well as the time dependent CP asymmetries in $B_s \to \psi\phi$ and $B_s \to \psi\pi\pi$ from LHCb. While the B_s mixing phase is perfectly consistent with the SM expectation, the tensions in the Unitarity Triangle slightly prefer a small negative NP phase in B_d mixing, $\phi_d^{\rm NP} = -0.2 \pm 0.1$.

The right plot of fig. 1 shows the possible values for the semileptonic asymmetries $a^d_{\rm SL}$ and $a^s_{\rm SL}$, given the constraints on the NP phases. It is evident that the large like-sign dimuon charge asymmetry observed by D0 cannot be explained by NP in the dispersive part of the B mixing amplitude alone [8, 7, 9].

The small preference for a negative NP phase in B_d mixing on the other hand can be addressed for example in two Higgs doublet models with MFV through tree level exchange of flavor changing neutral Higgs bosons. If the quartic couplings in the Higgs potential are MSSM-like, these models predict a much larger NP phase in B_s mixing than in B_d mixing [10], which is clearly excluded by the current data. With more general Higgs potentials however, one generically finds $\phi_d^{\rm NP} \simeq \phi_s^{\rm NP}$ [11] and a small $\phi_d^{\rm NP}$ can still be accommodated. In the context of supersymmetric models with MFV, this is possible if the Higgs sector is extended by physics beyond the MSSM [12, 7]. These models will be challenged soon with improved measurements of the time-dependent CP asymmetries in $B_s \to \psi\phi$ and $B_s \to \psi\pi\pi$ by LHCb.

4. – $B_s \to \mu^+\mu^-$ and $B_d \to \mu^+\mu^-$

In the SM, the rare leptonic decays $B_s \to \mu^+\mu^-$ and $B_d \to \mu^+\mu^-$ are strongly helicity suppressed by the muon mass and their branching ratios are tiny—at the level of 10^{-9} and 10^{-10}, respectively. Due to the remarkably precise determinations of the B meson decay constants on the lattice [3], the SM predictions for both decays have reached theory uncertainties of less than 10%. Taking into account the correction to $\mathcal{B}(B_s \to \mu^+\mu^-)$ coming from the large width difference in the B_s meson system recently pointed out in [13, 14], one gets

$$\begin{aligned} \mathcal{B}(B_s \to \mu^+\mu^-)_{\rm SM} &= (3.32 \pm 0.17)10^{-9}, \\ \mathcal{B}(B_d \to \mu^+\mu^-)_{\rm SM} &= (1.0 \pm 0.1)10^{-10}. \end{aligned} \tag{7}$$

In extensions of the SM where NP contributions to these decays arise from scalar operators, *e.g.* through neutral Higgs exchange in the MSSM with large $\tan\beta$, the helicity suppression is lifted and order of magnitude enhancements of the branching ratios are possible. On the other hand, if the NP induces operators with a helicity structure analogous to the SM, *e.g.* through Z or Z' exchange, it has been shown that constraints from the semileptonic decays $B \to X_s\ell^+\ell^-$ and $B \to K^*\mu^+\mu^-$ only allow an enhancement of $\mathcal{B}(B_s \to \mu^+\mu^-)$ up to 5.6×10^{-9} [15].

On the experimental side, D0 [16], Atlas [17], CMS [18] and LHCb [19] give upper bounds on the branching ratio. CDF reported an excess in $B_s \to \mu^+\mu^-$ candidates leading to a two sided limit on $\mathcal{B}(B_s \to \mu^+\mu^-)$ at 95% C.L. [20] that, at the 2σ level, is consistent with the upper bounds. For $B_d \to \mu^+\mu^-$, upper bounds are reported by CDF [20], CMS [18] and LHCb [19]. Performing a naive combination of the available results one finds

$$\mathcal{B}(B_s \to \mu^+\mu^-)_{\rm exp} = (2.4 \pm 1.6)10^{-9}, \qquad \mathcal{B}(B_d \to \mu^+\mu^-)_{\rm exp} < 8.6 \times 10^{-10}. \tag{8}$$

While in $B_d \to \mu^+\mu^-$ there is still room for almost an order of magnitude enhancement, the recent results on $B_s \to \mu^+\mu^-$ only allow for moderate deviations from the SM prediction. On the one hand this leads to very strong constraints on models with scalar operators, on the other hand, models without scalar operators are starting to be probed by $B_s \to \mu^+\mu^-$ only now.

An important observable in the future will be the ratio of the B_s and B_d branching ratios. In models with minimal flavor violation there exists a strong correlation

$$\frac{\mathcal{B}(B_s \to \mu^+\mu^-)}{\mathcal{B}(B_d \to \mu^+\mu^-)} \simeq \frac{f_{B_s}^2}{f_{B_d}^2}\frac{\tau_{B_s}}{\tau_{B_d}}\frac{|V_{ts}|^2}{|V_{td}|^2} \simeq 35. \tag{9}$$

Given the existing bounds on $\mathcal{B}(B_s \to \mu^+\mu^-)$, an enhancement of $\mathcal{B}(B_d \to \mu^+\mu^-)$ by more than a factor of 2 would not only be a clear indication of NP, but also of new sources of flavor violation beyond the CKM matrix.

5. – Angular observables in $B \to K^* \mu^+\mu^-$

The semileptonic exclusive $B \to K^*(\to K^+\pi^-)\mu^+\mu^-$ decay and its conjugated mode $\bar{B} \to \bar{K}^*(\to K^-\pi^+)\mu^+\mu^-$ are described by 4-fold differential decay distributions $\mathrm{d}\Gamma$ and $\mathrm{d}\bar{\Gamma}$ in terms of the dimuon invariant mass q^2, and three angles θ_{K^*}, θ_ℓ and ϕ (see, *e.g.*, [21] for details), offering a multitude of observables that can be used to search for NP.

One-dimensional angular distributions give access to the well-known observables F_L, the K^* longitudinal polarization fraction, and A_{FB}, the forward-backward asymmetry. Also the transversal asymmetry S_3 and the T-odd CP asymmetry A_9 can be obtained from a one-dimensional angular analysis

$$\frac{\mathrm{d}(\Gamma+\bar{\Gamma})}{\mathrm{d}q^2\mathrm{d}\cos\theta_{K^*}} \propto 2F_L\cos^2\theta_{K^*} + (1-F_L)\sin^2\theta_{K^*}, \tag{10}$$

$$\frac{\mathrm{d}(\Gamma-\bar{\Gamma})}{\mathrm{d}q^2\mathrm{d}\cos\theta_{\ell}} \propto A_{\mathrm{FB}}\cos\theta_\ell + \frac{3}{4}F_L\sin^2\theta_\ell + \frac{3}{8}(1-F_L)(1+\cos^2\theta_\ell), \tag{11}$$

$$\frac{\mathrm{d}(\Gamma+\bar{\Gamma})}{\mathrm{d}q^2\mathrm{d}\phi} \propto 1 + S_3\cos 2\phi + A_9\sin 2\phi. \tag{12}$$

Additional observables, like the T-odd CP asymmetries A_7 and A_8 require two- or three-dimensional angular analyses [22].

Measurements of angular observables exist from BaBar [23], Belle [24], CDF [25] and LHCb [26] and all show reasonable agreement with the SM predictions so far. The various observables each depend in a characteristic way on the Wilson coefficients of the dimension six $\Delta F = 1$ operators contributing to $B \to K^*\mu^+\mu^-$. Particularly interesting are the observables S_3 and A_9 as they are easily accessible, very small in the SM, and highly sensitive to CP-conserving and CP-violating right-handed currents that are predicted in various NP models.

Analyses that put constraints on the Wilson coefficients and therefore determine in a model independent way the room left for NP in $B \to K^*\mu^+\mu^-$ have been performed, *e.g.*, for the magnetic penguin operators [27], the SM operator basis [28, 29] and for the very general case of the SM operators as well as their chirality flipped counterparts [15, 30]. In [30] we include all the available experimental results on the $B \to K^*\mu^+\mu^-$ observables as well as all relevant observables in the $B \to K\mu^+\mu^-$, $B \to X_s\ell^+\ell^-$, $B \to X_s\gamma$, $B \to K^*\gamma$ and $B_s \to \mu^+\mu^-$ decays. Results for the Wilson coefficients $C_{7,9,10}$ are shown in fig. 2. Analogous results for the right-handed coefficients $C'_{7,9,10}$ can be found in [30].

The strongest bounds currently come from branching ratios and CP-averaged angular coefficients, and therefore the imaginary parts of $C_{7,9,10}$ are much less constrained than the real parts. Future improved measurements of CP asymmetries in $B \to K^*\mu^+\mu^-$ that are directly sensitive to new CP-violating phases will be essential to probe the imaginary parts of the Wilson coefficients.

6. – Direct CP Violation in $D \to K^+K^-$ and $D \to \pi^+\pi^-$

CP Violation in the charm sector is highly Cabibbo suppressed in the SM and therefore very sensitive to possible NP effects. Current bounds on CP-violating parameters in D^0-$\bar{D}^0$ mixing are at the level of 10%–20% [1] and still far above the naive SM expectation of $O(|V_{ub}V^*_{cn}|/|V_{us}V^*_{cs}|) \simeq 10^{-3}$. Naive SM estimates for direct CP violation in singly Cabibbo suppressed D decays such as $D \to K^+K^-$ and $D \to \pi^+\pi^-$ are even smaller, $O(|V_{ub}V^*_{cb}|/|V_{us}V^*_{cs}|\alpha_s/\pi) \simeq 10^{-4}$.

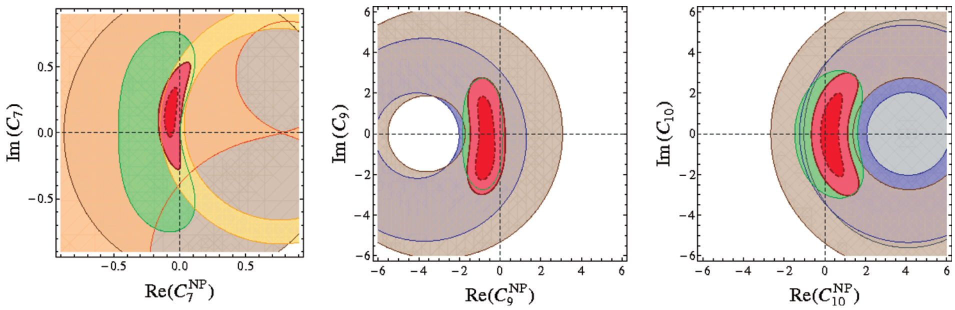

Fig. 2. – Allowed regions in the complex planes of the Wilson coefficients $C_{7,9,10}$ at 1 and 2σ (red). Shown are also the individual 2σ constraints from $\mathcal{B}(B_s \to \mu^+\mu^-)$ (gray), $\mathcal{B}(B \to X_s\ell^+\ell^-)$ (brown), $\mathcal{B}(B \to K\mu^+\mu^-)$ (blue), $B \to K^*\mu^+\mu^-$ (green), $\mathcal{B}(B \to X_s\gamma)$ (yellow) and $A_{\rm CP}(B \to X_s\gamma)$ (orange). (From [30].)

Remarkably, the LHCb collaboration recently found first evidence for charm CP violation [31]. The reported value for $\Delta A_{\rm CP}$, the difference in the time integrated CP asymmetries in $D \to K^+K^-$ and $D \to \pi^+\pi^-$, is non-zero at 3.5σ. This result has been confirmed by CDF [32] and a combination that includes also previous results from BaBar and Belle leads to [1]

$$\Delta A_{\rm CP} = -(0.656 \pm 0.154)\%, \tag{13}$$

which is approximately 4σ away from 0. To a very good approximation, $\Delta A_{\rm CP}$ corresponds to the difference in the direct CP asymmetries in $D \to K^+K^-$ and $D \to \pi^+\pi^-$ and is therefore expected to be at least one order of magnitude smaller in the SM, unless the hadronic matrix elements entering the SM prediction are strongly enhanced with respect to naive estimates [33]. While the required strong enhancement is not expected to be natural in the SM [34,35], it cannot be excluded presently [36-39]. Nonetheless, the interpretation of the experimental results as a signal of NP is interesting and motivated. Possible NP explanations typically will predict non-standard signals also in other low energy flavor observables or characteristic signatures at colliders that can be searched for and that can be used to test the NP hypothesis.

Both model independent analyses [40], and studies of concrete NP scenarios (see *e.g.* [41-46]) show that NP explanations of large direct CP violation in singly Cabibbo suppressed D^0 decays are often highly constrained by other flavor observables, in particular D^0-$\bar{D}^0$ mixing and ϵ'/ϵ, *i.e.* direct CP violation in neutral kaon decays. Among the numerous NP possibilities, the one that generically avoids both these constraints are loop induced chromomagnetic dipole operators

$$O_8 = \frac{g_s}{16\pi^2} m_c\, \bar{u}(\sigma G) P_R c, \qquad O_8 = \frac{g_s}{16\pi^2} m_c\, \bar{u}(\sigma G) P_L c, \tag{14}$$

that can lead to chirally enhanced contributions to the direct CP asymmetries. Studies of CP asymmetries in radiative $D \to V\gamma$ decays could help to probe the possible dipole origin of $\Delta A_{\rm CP}$ [47].

Among NP models that contribute significantly to $\Delta A_{\rm CP}$ through tree-level induced four fermion operators, only few are viable. Known examples include models where the NP contribution is mediated by scalars with masses at the electro-weak scale and flavor changing couplings [42, 44]. If these models induce $\Delta I = 3/2$ operators, they can be tested using isospin sum rules for CP asymmetries [48]. The necessarily light scalars can be searched for at the LHC.

Finally, depending on the exact flavor structure of the tree-level models, $\Delta A_{\rm CP}$ can originate from either $A_{\rm CP}^{K^+K^-}$ or $A_{\rm CP}^{\pi^+\pi^-}$ or from both. This is in contrast to the dipole operator explanation where one (naively) expects $A_{\rm CP}^{K^+K^-} \simeq -A_{\rm CP}^{\pi^+\pi^-}$. Correspondingly, the separate measurement of the direct CP asymmetries in $D \to K^+K^-$ and $D \to \pi^+\pi^-$ would add valuable information to pin down the possible origin of direct CP violation in charm decays.

7. – Summary

In the absence of any direct evidence for new physics at the LHC, flavor physics continues to stay at the forefront of the search for new phenomena at the TeV scale. While the current experimental results on rare decays like $B_s \to \mu^+\mu^-$ and $B \to K^*\mu^+\mu^-$ are in reasonable agreement with SM predictions, they still allow for sizable new physics effects, that can be uncovered with improved precision in the near future. Moreover, anomalies in the current flavor data, like the tension between $B \to \tau\nu$ and $\sin 2\beta$, the large dimuon charge asymmetry or the recent evidence for direct CP violation in charm decays might already be the first indirect signs of physics beyond the Standard Model.

Improved experimental results on all these observables will be most exciting and certainly improve our understanding of possible new physics at the TeV scale and beyond.

* * *

I would like to thank the organizers for the invitation to this wonderful conference. Fermilab is operated by Fermi Research Alliance, LLC under Contract No. De-AC02-07CH11359 with the United States Department of Energy.

REFERENCES

[1] Asner D. *et al.*, Heavy Flavor Averaging Group, arXiv:1010.1589 and online update at `http://www.slac.stanford.edu/xorg/hfag`.
[2] Nakamura K. *et al.*, *J. Phys. G*, **37** (2010) 075021.
[3] Davies C., arXiv:1203.3862 [hep-lat].
[4] Blankenburg G. and Isidori G., arXiv:1107.1216 [hep-ph].
[5] Abazov V. M. *et al.*, *Phys. Rev. D*, **84** (2011) 052007.
[6] LHCb Collaboration, conference note LHCb-CONF-2012-002.
[7] Altmannshofer W. and Carena M., *Phys. Rev. D*, **85** (2012) 075006.
[8] Bobeth C. and Haisch U., arXiv:1109.1826 [hep-ph].
[9] Lenz A. *et al.*, arXiv:1203.0238 [hep-ph].
[10] Buras A. J., Carlucci M. V., Gori S. and Isidori G., *JHEP*, **10** (2010) 009.
[11] Buras A. J., Isidori G. and Paradisi P., *Phys. Lett. B*, **694** (2011) 402.
[12] Altmannshofer W., Carena M., Gori S. and de la Puente A., *Phys. Rev. D*, **84** (2011) 095027.
[13] de Bruyn K. *et al.*, arXiv:1204.1735 [hep-ph].
[14] de Bruyn K. *et al.*, arXiv:1204.1737 [hep-ph].
[15] Altmannshofer W., Paradisi P. and Straub D. M., *JHEP*, **04** (2012) 008.
[16] Abazov V. M. *et al.*, *Phys. Lett. B*, **693** (2010) 539.
[17] Aad G. *et al.*, arXiv:1204.0735 [hep-ex].
[18] Chatrchyan S. *et al.*, arXiv:1203.3976 [hep-ex].

[19] Aaij R. *et al.*, arXiv:1203.4493 [hep-ex].
[20] Aaltonen T. *et al.*, *Phys. Rev. Lett.*, **107** (2011) 239903, update with the full data sample at `http://www.cdf.fnal.gov/physics/new/bottom/bottom.html`.
[21] Altmannshofer W. *et al.*, *JHEP*, **01** (2009) 019.
[22] Bobeth C., Hiller G. and Piranishvili G., *JHEP*, **07** (2008) 106.
[23] Akar S., talk given at "Lake Louise Winter Institute 2012".
[24] Wei J.-T. *et al.*, *Phys. Rev. Lett.*, **103** (2009) 171801.
[25] Aaltonen T. *et al.*, *Phys. Rev. Lett.*, **108** (2012) 081807.
[26] LHCb Collaboration, conference note LHCb-CONF-2012-008.
[27] Descotes-Genon S., Ghosh D., Matias J. and Ramon M., *JHEP*, **06** (2011) 099.
[28] Bobeth C., Hiller G., van Dyk D. and Wacker C., *JHEP*, **01** (2012) 107.
[29] Beaujean F., Bobeth C., van Dyk D. and Wacker C., arXiv:1205.1838 [hep-ph].
[30] Altmannshofer W. and Straub D. M., arXiv:1206.0273 [hep-ph].
[31] Aaij R. *et al.*, *Phys. Rev. Lett.*, **108** (2012) 111602.
[32] CDF Collaboration, public Note 10784.
[33] Golden M. and Grinstein B., *Phys. Lett. B*, **222** (1989) 501.
[34] Cheng H.-Y. and Chiang C.-W., *Phys. Rev. D*, **85** (2012) 034036.
[35] Franco E., Mishima S. and Silvestrini L., arXiv:1203.3131 [hep-ph].
[36] Brod J., Kagan A. L. and Zupan J., arXiv:1111.5000 [hep-ph].
[37] Bhattacharya B., Gronau M. and Rosner J. L., *Phys. Rev. D*, **85** (2012) 054014.
[38] Feldmann T., Nandi S. and Soni A., arXiv:1202.3795 [hep-ph].
[39] Brod J., Grossman Y., Kagan A. L. and Zupan J., arXiv:1203.6659 [hep-ph].
[40] Isidori G., Kamenik J. F., Ligeti Z. and Perez G., *Phys. Lett. B*, **711** (2012) 46.
[41] Grossman Y., Kagan A. L. and Nir Y., *Phys. Rev. D*, **75** (2007) 036008.
[42] Hochberg Y. and Nir Y., arXiv:1112.5268 [hep-ph].
[43] Giudice G. F., Isidori G. and Paradisi P., *JHEP*, **04** (2012) 060.
[44] Altmannshofer W., Primulando R., Yu C.-T. and Yu F., *JHEP*, **04** (2012) 049.
[45] Hiller G., Hochberg Y. and Nir Y., arXiv:1204.1046 [hep-ph].
[46] Keren-Zur B., Lodone P., Nardecchia M., Pappadopulo D., Rattazzi R. *et al.*, arXiv:1205.5803 [hep-ph].
[47] Isidori G. and Kamenik J. F., arXiv:1205.3164 [hep-ph].
[48] Grossman Y., Kagan A. L. and Zupan J., arXiv:1204.3557 [hep-ph].

SESSION V - ELECTROWEAK AND TOP PHYSICS

IL NUOVO CIMENTO Vol. 35 C, N. 6 Novembre-Dicembre 2012
DOI 10.1393/ncc/i2012-11375-5

Colloquia: LaThuile12

Electroweak physics at the Tevatron

V. Cavaliere on behalf of the CDF and DØ Collaborations
University of Illinois - Urbana - Champaign, IL, USA

ricevuto il 7 Settembre 2012

Summary. — We present a review of the recent Tevatron diboson measurements in leptonic and semileptonic decay modes. The most stringent limits on anomalous triple gauge couplings are reported for each final state.

PACS 14.70.Fm – W bosons.
PACS 14.70.Hp – Z bosons.
PACS 13.38.Be – Decays of W bosons.
PACS 13.38.Dg – Decays of Z bosons.

1. – Introduction

Following the ending of the Tevatron collider program, we can review the significant progress that has been made in the diboson sector over the ten years of Run 2. The availability of theoretical tools such as MCFM [1] and MC@NLO [2] has allowed the standard model to be tested in the diboson sector. Measuring diboson production is a fundamental as it is an important electroweak process and a major background to Higgs searches. Furthermore, measuring diboson production allows access to triple gauge couplings, which could provide indications of new physics.

2. – $W\gamma$ and $Z\gamma$

The most up to date measurement of $W\gamma$ and $Z\gamma$ production comes from the DØ Collaboration that analyzed $4.2\,\mathrm{fb}^{-1}$ and $6.2\,\mathrm{fb}^{-1}$ of data, respectively [3].

The event selection for $W\gamma$ starts by requiring an electron or muon, a photon, and missing transverse energy. The analysis uses a neural network for photon identification to improve sensitivity to $WW\gamma$ coupling. Backgrounds are at the 20–25% level, overwhelmingly W+jets, and are estimated from data. An important property of the standard model prediction at leading order is that interference between the s- and t-channel amplitudes produces a zero in the total $W\gamma$ yield at a specific angle $\theta*$ between the W boson and the incoming quark in the $W\gamma$ rest frame. Although it is difficult to measure the angle directly, this so-called radiation amplitude zero is also visible in the charge-signed

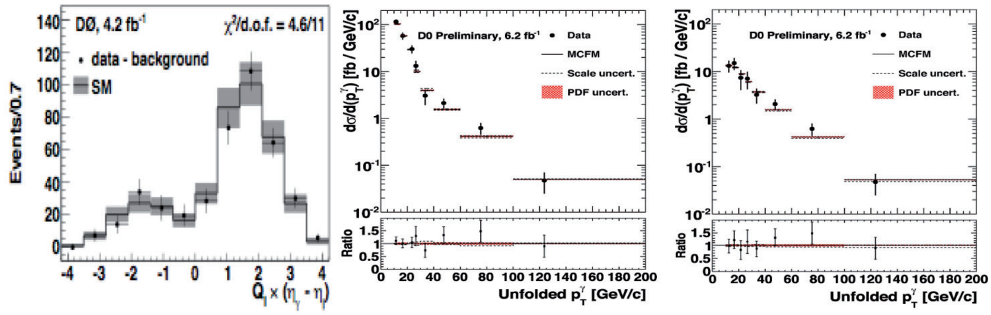

Fig. 1. – Left: charge-signed photon-lepton rapidity difference. The radiation zero amplitude can be seen as a dip at $-1/3$. Center and right: the differential cross-section $\mathrm{d}\sigma/\mathrm{d}p_T(\gamma)$ for all $M(\ell\ell\gamma)$, and for the ISR-dominated sample $M(\ell\ell\gamma) > 110\,\mathrm{GeV}/c^2$.

photon-lepton rapidity difference as a dip at around $-1/3$. Figure 1 shows the dip, compared with the signal prediction. The measured cross-section for the kinematic region $E_T(\gamma) > 15\,\mathrm{GeV}$ and $\Delta R(\ell\gamma) >$ is $7.6\pm0.4(\mathrm{stat})\pm0.6(\mathrm{sys})$ pb, in good agreement with the standard model prediction of 7.6 ± 0.2 pb. If there were anomalous triple gauge couplings, the photon E_T spectrum would be modified and more high-E_T photons observed. The photon E_T spectrum may therefore be used to derive limits on anomalous $WW\gamma$ couplings. A binned likelihood fit to data is used, and the 1-d limits 95% CL limits obtained are $-0.4 < \Delta\kappa\gamma < 0.4$ and $-0.08 < \lambda_\gamma < 0.07$ for a new physics scale $\Lambda = 2\,\mathrm{TeV}$.

Also the $Z\gamma$ analysis uses a neural network technique to provide a robust differentiation between photons and jets. Background is at the 5 10% level and is dominated by Z+jets. The $Z\gamma$ system has the property that initial state photon radiation (ISR) may be selected preferentially over final state photon radiation by requiring the three-body invariant mass $M(\ell\ell\gamma)$ to be above the Z boson mass. With $M(\ell\ell\gamma) > 110\,\mathrm{GeV}/c^2$, around 300 events are observed in each of the final states. The differential cross-section $\mathrm{d}\sigma/\mathrm{d}p_T(\gamma)$ is measured, using matrix inversion to unfold the experimental distribution, and is shown in fig. 1 both for all $M(\ell\ell\gamma)$, and for the ISR-dominated sample $M(\ell\ell\gamma) > 110\,\mathrm{GeV}/c^2$. The data are compared with the NLO prediction from MCFM, and are seen to be consistent. Total cross-sections are also quoted: for the kinematic region $|\eta(\gamma)| < 1$, $E_T(\gamma) > 10\,\mathrm{GeV}$, $\Delta R(\ell\gamma) > 0.7$ and $M(\ell\ell\gamma) > 60\,\mathrm{GeV}/c^2$ the result is $1.09 \pm 0.04(\mathrm{stat}) \pm 0.07(\mathrm{sys})$ pb, to be compared with the standard model prediction of 1.10 ± 0.03 pb; and for $M(\ell\ell\gamma) > 110\,\mathrm{GeV}/c^2$ the result is $0.29\pm0.02(\mathrm{stat})\pm0.01(\mathrm{sys})$ pb, to be compared with the standard model prediction 0.29 ± 0.01 pb.

3. – Heavy diboson production

3·1. *Leptonic decay channels: WZ and ZZ.* – These final states are characterized by low branching ratio and clean yields. All the analysis use improved lepton definitions to increase the acceptance.

The WZ production in $\ell\ell\ell\nu$ final state had been studies by CDF using $7.1\,\mathrm{fb}^{-1}$ of integrated luminosity [4]. The analysis incorporates improvements in lepton selection and uses a neural network to separate the signal from the background (ZZ contribution is the biggest). The measured cross-section is found to be $\sigma(p\bar{p} \to WZ) = (3.9^{+0.6}_{0.5}(\mathrm{stat})^{+0.6}_{0.4}(\mathrm{syst}))$ pb in good agreement with the SM prediction of 3.46 ± 0.21 pb.

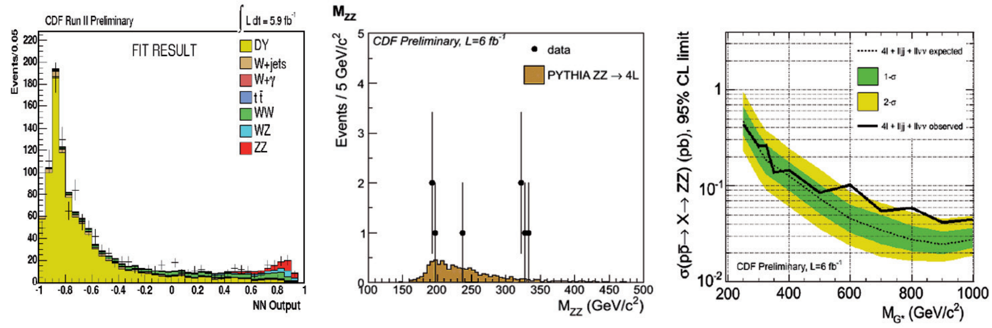

Fig. 2. – Left: NN output for ZZ to four lepton analysis. Center: M_{ZZ} distribution shows the clustering of events around $325\,\mathrm{GeV}/c^2$. Right: Limits on the presence of a Randall-Sundrum (RS) graviton decaying to two Z bosons.

Triple gauge couplings limits are extracted from the Zp_T distribution for a new physics scale of 1.5 and 2.0 TeV. The DØ Collaboration has also performed an measurement of the WZ cross-section in this final state and of ZZ production in four leptons [5]. The peculiarity of these analyses is that they do not restrict the offline event selection to events satisfying specific trigger conditions but analyse all recorded data in order to maximise the event yields. For the WZ cross-section a likelihood fit to the M_T is performed, while for the ZZ a neural network output is used as a discriminator. The systematic uncertainties are reduced by taking the ratio to the measured $Z \to \ell\ell$ cross-section and then multiplying for the theoretical calculation of the Z boson production cross-section. The results are $\sigma(p\bar{p} \to WZ) = 4.50 \pm 0.61(\mathrm{stat.})^{+0.16}_{-0.25}(\mathrm{syst.})$ pb and $\sigma(p\bar{p} \to ZZ) = 1.64 \pm 0.44(\mathrm{stat.})^{+0.13}_{-0.15}(\mathrm{syst.})$ pb, in agreement with the SM prediction.

CDF has also new measurement of the ZZ production cross-section in the four-lepton final state and $\ell\ell\nu\nu$ using $6\,\mathrm{fb}^{-1}$ of integrated luminosity [6]. The four lepton analysis uses a counting experiment, while for $ZZ \to \ell\ell\nu\nu$ that is afflicted by a large Drell-Yan background contribution a NN is used to extract the cross-section (see fig. 2a). The combination of the two analysis leads to $\sigma(p\bar{p} \to ZZ) = 1.64^{+0.44}_{-0.38}$ pb. These final states together with the semileptonic ones are used to search for ZZ resonances [7]. A clustering of events at high mass is observed (see fig. 2). However, analysis of the other ZZ final states $ZZ \to \ell\ell\nu\nu$ and $ZZ \to \ell\ell jj$ showed them to be more sensitive to a resonance of mass around $325\,\mathrm{GeV}/c^2$ decaying to ZZ, and the data in those channels are in agreement with standard model predictions (limits are set using a Randall-Sundrum (RS) graviton decaying to two Z bosons see fig. 2). The four-lepton events therefore appear to arise from standard model sources.

3˙2. *Semileptonic decay channels*. – Given their similarity to key Higgs boson signatures, there have been ongoing efforts to observe diboson production in final states with jets.

Two CDF analyses observed WW and WZ production in the $\ell\nu jj$ final state in 2010. This final state is very similar to that expected from WH associated production. W+jets is the overwhelming background. In the first analysis the signal was extracted from a χ^2 fit to the dijet mass distribution as shown in fig. 3, giving an extracted cross-section $\sigma(WW + WZ) = (18.1 \pm 3.3(\mathrm{stat}) \pm 2.5(\mathrm{sys}))$ pb with 5.2σ significance [8]. The second analysis used a matrix element technique, for which the final event probability

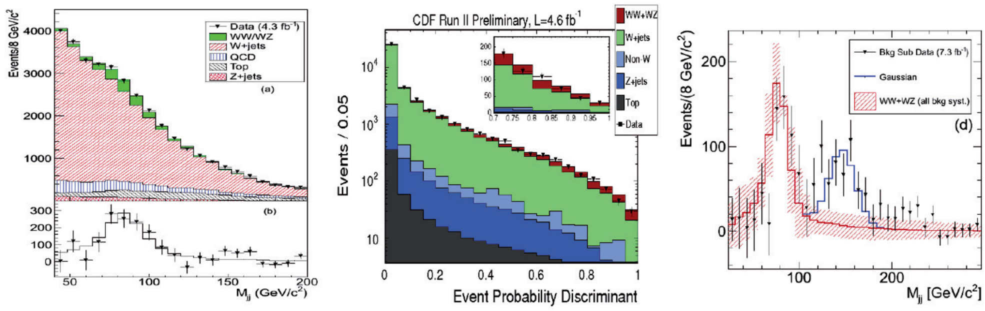

Fig. 3. – Left: Dijet mass spectrum in WW/WZ analysis showing the diboson contribution. Center: Matrix Element Discriminator for WW/WZ analysis. Right: Dijet mass spectrum for W+2jet event with harder cuts showing the excess around $150\,\mathrm{GeV}/c^2$.

discriminant is shown in fig. 3. Here, the extracted cross-section was $\sigma(WW + WZ) = (16.5^{+3.3}_{-3.0})$ pb, with 5.4σ significance [8]. The first analysis was also used to look for higher mass resonances. A 4.1σ excess is observed in dijet mass spectrum of W+2jet sample [9], as shown in fig. 3c. Studies are still in progress to understand the cause of the excess. The DØ Collaboration tried to replicate the analysis and found no significant discrepancy with the respect to the background model.

DØ also updated their measurement in the $\ell\nu jj$ final state, using $4.3\,\mathrm{fb}^{-1}$ of integrated luminosity [10]. A random forest multivariate discriminant is used to separate signal from background, and since Z bosons can decay to b-quark pairs but W bosons cannot, b-tagging is employed both to improve the significance of the observation, and to separate the WW and WZ components. Both the random forest discriminant output, and the dijet invariant mass for the no b-tag data sample, are shown in fig. 4. A cross-section $\sigma(WW + WZ) = 19.6^{+3.1}_{-3.0}$ pb is measured, with 8σ significance, and contours of the separated WW and WZ cross-sections are given in fig. 4.

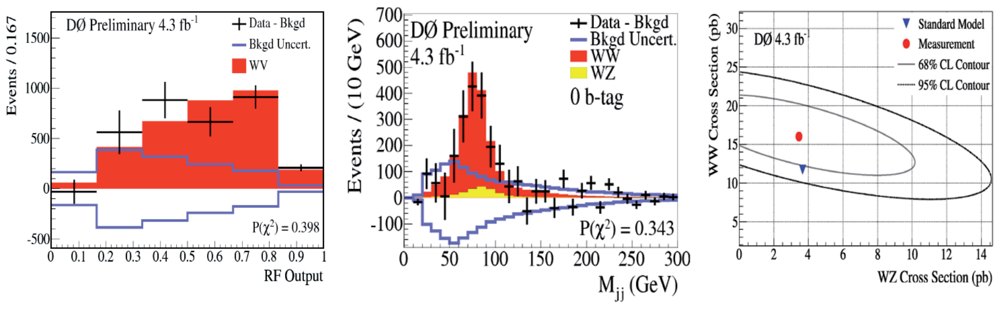

Fig. 4. – Results from DØs WW/WZ analysis in the $\ell\nu jj$ final state: (left) random forest multivariate discriminant output; (centre) background-subtracted dijet mass; (right) contours of WW and WZ production cross-section.

4. – Conclusion

A rich programme of Tevatron diboson physics has made huge advances over the ten years of Run 2, testing the standard model, probing for new physics, and underpinning electroweak symmetry-breaking searches. Both experiments have a final dataset of around $10\,\mathrm{fb}^{-1}$, so as well as being combined, these analyses should be updated once more for legacy measurements.

REFERENCES

[1] Campbell J. M. and Ellis R. K., *Phys. Rev. D*, **60** (1999) 113006.
[2] Frixione S. and Webber B. R., *JHEP*, **06** (2002) 029.
[3] Abazov *et al.* (DØ Collaboration), *Phys. Rev. Lett.*, **107** (2011) 241803.
[4] Aaltonen T. *et al.* (CDF Collaboration), arXiv:1202.6629.
[5] Abazov V. M. *et al.* (DØ Collaboration), arXiv:1201.5652v1.
[6] Aaltonen T. *et al.* (CDF Collaboration), *Phys. Rev. Lett.*, **108** (2012) 101801.
[7] Aaltonen T. *et al.* (CDF Collaboration), *Phys. Rev. D*, **85** (2012) 012008.
[8] Aaltonen T. *et al.* (CDF Collaboration), *Phys. Rev. Lett.*, **104** (2010) 101801.
[9] Aaltonen T. *et al.* (CDF Collaboration), *Phys. Rev. Lett.*, **106** (2011) 171801.
[10] Abazov V. M. *et al.* (DØ Collaboration), *Phys. Rev. D*, **80** (2009) 053012.

IL NUOVO CIMENTO Vol. 35 C, N. 6 Novembre-Dicembre 2012
DOI 10.1393/ncc/i2012-11376-4

Colloquia: LaThuile12

Recent results on top-quark physics from the Tevatron

A. Grohsjean
Deutsches Elektronen-Synchrotron - Hamburg, Germany

ricevuto il 7 Settembre 2012

Summary. — Seventeen years after the discovery of the top quark at the Fermilab Tevatron collider, many aspects of the top-quark sector are now well known. Besides the measurement of basics properties, such as the production cross section, the top-quark mass, width and charge, many new aspects, such as spin correlation in top-quark decays, have been explored for the first time. Due to their well-understood and clean signatures, top-quark events have also been applied to investigate important properties of quantum chromodynamics (QCD) such as the color flow between partons. This review summarizes the latest results from the Tevatron.

PACS 14.65.Ha – Top quarks.
PACS 12.38.Qk – Experimental tests.
PACS 13.85.Qk – Inclusive production with identified leptons, photons, or other nonhadronic particles.

1. – Top quarks in a nutshell

With a mass of $173.2 \pm 0.9\,\mathrm{GeV}$ [1], the top quark is the heaviest of all known elementary particles. From a theoretical point of view, top quarks are of special interest, as their coupling to the Higgs boson is close to unity, suggesting that the top quark may play a special role in electroweak symmetry breaking. From an experimental point of view, its short lifetime of about $10^{-25}\,\mathrm{s}$ is of particular interest as top quarks decay before hadronization and thereby provide an opportunity for studying bare quarks. At the Tevatron $p\bar{p}$ collider, with a center-of-mass energy of $1.96\,\mathrm{TeV}$, 85% of the $t\bar{t}$ pairs are produced through quark-antiquark annihilation and 15% originate from gluon-gluon fusion. In next-to-next-to leading order in pertubative QCD, the rate of pair production is predicted to be $7.46\,\mathrm{pb}$ [2], which is a factor of about 2 larger than the electroweak production cross section of single top quarks [3]. In the standard model (SM), top quarks decay almost exclusively to a W boson and a bottom quark, such that $t\bar{t}$ events can be classified into all $-$ jets, $\ell +$ jets and dilepton events, depending on the modes of the two W decays. The $\ell +$ jets channel is characterized by four jets, one isolated, energetic charged lepton, and an imbalance in transverse momentum. The irreducible background comes mainly from W+jets events. Instrumental background arises from events in which a jet is misidentified as a lepton, and from events with heavy quarks that decay into leptons that pass isolation requirements. The topology of the dilepton channel is defined by two jets, two isolated, energetic charged leptons, and a significant imbalance in transverse momentum from the undetected neutrinos. Here, the main background processes are from Z+jets and diboson events (WW, WZ and ZZ with associated jets), as well as the kind of instrumental background characterized above.

2. – Probing top-quark production at $\sqrt{s} = 1.96\,\mathbf{TeV}$

One of the basic analyses involves the measurement of the $t\bar{t}$ production cross section. This requires a well-modeled background as well as a clean and large signal fraction. A good separation between signal and background can be achieved either through b-jet identification or by using multivariate statistical techniques or both, to achieve greater precision. To reduce the main systematic uncertainty from the integrated luminosity, the CDF experiment explored the possibility of using the ratio of the measured $t\bar{t}$ to $Z \to \ell\ell$ cross sections and multiplying this by the theoretical cross section for $Z \to \ell\ell$ production. Such analyses [4, 5] yield:

$$\text{CDF in } 4.6\,\text{fb}^{-1} \text{ of } \ell + \text{jets data}: \sigma_{t\bar{t}} = 7.82 \pm 0.55 \text{ (stat + syst) pb},$$
$$\text{DØ in } 5.3\,\text{fb}^{-1} \text{ of } \ell + \text{jets data}: \sigma_{t\bar{t}} = 7.78^{+0.77}_{-0.64} \text{ (stat + syst) pb}.$$

Both measurements are limited by systematic uncertainties, specifically, in the modeling of $t\bar{t}$ production at CDF, and on the luminosity at DØ. The total uncertainties are comparable to the theoretical uncertainties. As new physics may affect different final states in different ways, and to probe different parts of the phase space as well as the effect of different backgrounds, $t\bar{t}$ production is measured in many different channels, such as dilepton [6, 7], hadronically decaying τ+lepton [8] and τ+jets [9, 10], as well as all $-$ jets [11, 12] final states. So far, all results are consistent among channels and theoretical predictions. A future combination based on the full data of the CDF and DØ experiments, will achieve a precision of better than 5%, and go beyond the theoretical uncertainty, which is dominated by the uncertainty on parton distribution functions (PDF).

The measurement of the production cross section $\sigma_{t\bar{t}}$ can be extended to a measurement of the ratio R of events in which the top quark decays to Wb divided by the number of events with top quarks decaying to Wq, where q can be any down-type quark. In the SM, this ratio is predicted to be one. Smaller values would provide a direct indication for physics beyond the SM, such as the existence of a 4th generation of quarks. In the ℓ + jets channel, the DØ experiment splits events into three categories: i) events with no identified b jet, ii) one b jet and iii) two b jets. The dilepton final state relies on the continuous output of the b-jet-identification algorithm. Based on $5.4\,\text{fb}^{-1}$, the DØ experiment obtains $R = 0.90 \pm 0.04$ (stat + syst) [13] combining both channels. The main systematic uncertainty is from b-jet identification.

The first measurement of the $t\bar{t} + \gamma$ production cross section was performed by the CDF Collaboration. This is particularly challenging, as the production rate is one order of magnitude smaller than that for $t\bar{t}$ production. In addition, the $t\bar{t}+\gamma$ analysis requires a well-developed photon identification and excellent modeling of the background. Based on $6.0\,\text{fb}^{-1}$ of data, CDF observes 26.9 ± 3.4 candidate events where 30 are expected. The measured cross section of $\sigma_{t\bar{t}+\gamma} = 0.18 \pm 0.08$ pb [14] is consistent with the predicted value of 0.17 ± 0.03 pb [15]. This represents first evidence for $t\bar{t} + \gamma$ production with a significance of 3.0 standard deviations (SD).

After the observation of the top quark in the $t\bar{t}$ final state, it took another 14 years to observe single top-quark production. The production rate of single top quarks probes directly the electroweak Wtb interaction. Sophisticated, multivariate analysis techniques are needed to extract the small signal from an overwhelming background, mainly from $W+$ jets. Both CDF [16] and DØ [17] extracted the cross section for the combined contribution of s and t channel processes, yielding:

$$\begin{aligned} \text{CDF in } 3.2\,\text{fb}^{-1} \text{ of data} : \sigma_{s+t} &= 2.3 \pm 0.6 \ (\text{stat} + \text{syst})\,\text{pb}, \\ \text{DØ in } 5.4\,\text{fb}^{-1} \text{ of data} : \sigma_{s+t} &= 3.4 \pm 0.7 \ (\text{stat} + \text{syst})\,\text{pb}. \end{aligned}$$

Assuming that the production of single top quarks in the s and t channel is directly proportional to $|V_{tb}|^2$, and that $|V_{ts}|^2 + |V_{td}|^2 \ll |V_{tb}|^2$, the above measurements can be translated into a measurement of $|V_{tb}|$, yielding

$$\begin{aligned} |V_{tb}| &= 0.91 \pm 0.13 \ (\text{stat} + \text{syst}), \\ |V_{tb}| &= 1.02 \pm 0.11 \ (\text{stat} + \text{syst}), \end{aligned}$$

for CDF and DØ, respectively. As the production of single top quarks in the t and s channel is sensitive to different physics beyond the SM, CDF [18] and DØ [19] measured not only their sum, but both of the processes in a simultaneous fit to the data using separate multivariate techniques for each of the channels. For the t channel the results give

$$\begin{aligned} \text{CDF in } 3.2\,\text{fb}^{-1} \text{ of data} : \sigma_{t} &= 0.8 \pm 0.4 \ (\text{stat} + \text{syst})\,\text{pb}, \\ \text{DØ in } 5.4\,\text{fb}^{-1} \text{ of data} : \sigma_{t} &= 2.9 \pm 0.6 \ (\text{stat} + \text{syst})\,\text{pb}. \end{aligned}$$

DØ claims first observation of this process with a significance of 5.5 SD. The main systematic uncertainty comes from the modeling of background. The analysis of the s channel is not yet sensitive enough to claim evidence for s channel production. This will only be reached using the full set of data. However, this channel is especially important, as it is the only production mode that is not very enhanced at the LHC, while the contamination from background is significantly larger than at the Tevatron.

3. – Measuring the mass of the top quark

There are two fundamentally different approaches to measure the mass of the top quark. One is based on mass-dependent distributions of templates, *e.g.*, the mass of the top quark, m_t, reconstructed from the decay products, or the degree of consistency $w_{\nu,\not{p}_T}$ of the reconstructed neutrino momenta and the measured imbalance in transverse momentum. Monte Carlo (MC) simulated events for different top-quark masses are used to form mass-dependent templates. The top-quark mass is extracted through a comparison of templates to data. All measurements are calibrated using pseudo-experiments, making sure that the measurement is bias-free and that the statistical uncertainty is properly estimated. To reduce the main systematic uncertainty from the jet energy, a global jet energy scale (JES) correction is extracted simultaneously with the mass of the top quark. This correction relies on the fact that the mass of the W boson, m_W, is well measured, and can therefore be used to constrain the energies of the jets. In dilepton events, however, this procedure is not possible, and the JES correction from ℓ+jets events is transferred directly to the jets in the dilepton channels. Any remaining difference is accounted for as a systematic uncertainty.

TABLE I. – *Latest results from Tevatron on the mass of the top quark.*

Experiment	L (fb^{-1})	Final state	Method	m_t (GeV)	stat (GeV)	syst (GeV)
CDF	8.7	$\ell +$ jets	m_t, m_{jj}	172.8	0.7	0.8
CDF	5.8	all $-$ jets	m_t, m_W	172.5	1.7	1.1
CDF	5.6	dilepton	m_t	170.3	2.0	3.1
DØ	5.4	dilepton	$w_{\nu,\not{p}_T}$	174.0	2.4	1.4
DØ	5.4	dilepton	ME	174.0	1.8	2.4
DØ	3.6	$\ell +$ jets	ME	174.9	1.1	1.0
CDF	3.6	$\ell +$ jets	ME	172.4	1.4	1.3

The most precise measurements of m_t, are obtained using the Matrix-Element (ME) method, where for each final state y, the probability to originate from $q\bar{q} \to t\bar{t}$ is calculated as a function of m_t:

$$P_{t\bar{t}}(x; m_t) = \frac{1}{\sigma_{\text{obs}}(m_t)} \int \mathrm{d}\epsilon_1 \mathrm{d}\epsilon_2 f_{\text{PDF}}(\epsilon_1) f_{\text{PDF}}(\epsilon_2) \, \frac{(2\pi)^4 |M(y)|^2}{\epsilon_1 \epsilon_2 s} \, \mathrm{d}\Phi_6 \, W(x,y), \tag{1}$$

where ϵ_1, ϵ_2 denote the energy fraction of the incoming quarks from the protons and antiprotons, f_{PDF} represent the parton distribution function, s is the square of the energy in the $p\bar{p}$ center of mass, $M(y)$ is the leading-order (LO) matrix element for $t\bar{t}$ production and decay [20] and $\mathrm{d}\Phi_6$ is an element of the 6-body phase space. The resolution of the detector is taken into account through a transfer function $W(x,y)$ that describes the probability of a partonic final state y to be measured as x in the detector. The signal probability is normalized by the observable cross section σ_{obs} for the specific ME.

An overview of the latest results from template and ME methods is given in table I. For template based results, the variables used to construct the templates are given in the appropriate row under "Method". All results are consistent with each other. Almost all results are limited by systematic uncertainties, where the remaining jet uncertainties and the modeling of $t\bar{t}$, *i.e.*, hadronization and the underlying event, NLO effects, initial and final-state radiation, as well as color reconnection, dominate. The latest combination of all measurements yields an average value of $m_t = 173.2 \pm 0.6$ (stat) $\pm\, 0.8$ (syst) GeV, with a total uncertainty of less than 1 GeV.

Besides systematic effects, another particular challenge in mass measurements is the theoretical interpretation, *i.e.* the question of how close the measured mass, which relies on MC simulation, is to the pole mass of the top quark. To bypass this problem, DØ pioneered a different approach [21], where the measured $t\bar{t}$ cross section is compared to higher order QCD predictions performed using either the pole mass or the $\overline{\text{MS}}$ mass definition. Based on 5.3 fb^{-1} of $\ell +$ jets events, the pole mass is extracted to be $m_t^{\text{pole}} = 167.5^{+5.2}_{-4.7}$ GeV, while the mass for the $\overline{\text{MS}}$ scheme is $m_t^{\overline{\text{MS}}} = 160.0^{+4.8}_{-4.3}$ GeV. Both results are smaller than the direct measurements, but the pole mass agrees better within its uncertainties with the combination of the direct measurements.

4. – Unique top-quark properties at the Tevatron

Due to the fact that at the Tevatron about 85% of the $t\bar{t}$ production arises from quark-antiquark annihilation, while at the LHC 90% is from gluon-gluon fusion, some features of production differ between the two colliders. One of these is the correlation expected for the spins of the two top quarks. Although the t and $\bar{t}$ are not produced polarized, their spins are correlated if angular momentum is conserved in the process. At the Tevatron, near the production threshold, all top-quark spins are expected to point in the same direction at LO for $q\bar{q}$ induced processes only. This fraction is reduced to 78% [22] taking account of effects from NLO corrections and gluon-gluon fusion using the beam momentum vector as quantization axis. Due to the short lifetime of the top quark, the top-quark spin does not flip, and its orientation is reflected in the angular distribution of the decay products: The spin-correlation coefficient C can therefore be measured by studying, *e.g.*, the doubly differential cross section:

$$\frac{\mathrm{d}^2\sigma_{t\bar{t}}}{\mathrm{d}\cos\theta_1 \mathrm{d}\cos\theta_2} = \frac{\sigma_{t\bar{t}}}{4}(1 - C\cos\theta_1\cos\theta_2), \tag{2}$$

where θ_1 and θ_2 denote the angle between the spin-quantization axis and the direction of flight of the down-type fermion from W-boson decay in the respective parent t or $\bar{t}$ rest frame. At both CDF and DØ, the spin correlation has been measured using templates in angular distributions. The DØ experiment uses the product of the lepton angles [23], while the CDF experiment considers two two-dimensional templates, one based on lepton angles, and one on the angles of the b quarks [24]. In the $\ell+\text{jets}$ channel, the CDF Collaboration uses the product of the cosines of the leptons and of the down-type quarks as well as the product of the cosines of the leptons and the b quarks [25]. A particular challenge in the $\ell+\text{jets}$ final state is the identification of the down-type quark from W-boson decay. The small efficiency of slightly more than 60% leads to a large dilution of the measurement. Based on about $5\,\mathrm{fb}^{-1}$, the template based measurements yield the following correlation coefficients in the beam frame:

$$\begin{aligned}\text{CDF in } 5.3\,\mathrm{fb}^{-1} \text{ of } \ell+\text{jets data} : C_{\mathrm{beam}} &= 0.72 \pm 0.69 \text{ (stat + syst)},\\ \text{CDF in } 5.1\,\mathrm{fb}^{-1} \text{ of dilepton data} : C_{\mathrm{beam}} &= 0.04 \pm 0.56 \text{ (stat + syst)},\\ \text{DØ in } 5.4\,\mathrm{fb}^{-1} \text{ of dilepton data} : C_{\mathrm{beam}} &= 0.10 \pm 0.45 \text{ (stat + syst)}.\end{aligned}$$

All these measurements are consistent with the SM expectation of $C_{\mathrm{beam}} = 0.78 \pm 0.04$ at NLO QCD. However, none of these is sensitive enough to distinguish between the case of SM spin correlation and no spin correlation. A significant improvement, can be achieved making use of matrix-element information [27].

The event probability for $q\bar{q} \to t\bar{t}$ production can also be written as a function of spin correlation. Two hypotheses H are considered in the analysis: spins correlated according to the SM ($H = c$) and uncorrelated spins ($H = u$). Using the above notation, the probabilities can be written as

$$P_{t\bar{t}}(x; H) \propto \int \mathrm{d}\epsilon_1 \mathrm{d}\epsilon_2 f_{PDF}(\epsilon_1) f_{PDF}(\epsilon_2) \frac{|M(y; H)|^2}{\epsilon_1 \epsilon_2 s} W(x, y) \mathrm{d}\Phi_6. \tag{3}$$

Based on these probabilities, a powerful variable R can be defined,

$$R = \frac{P_{t\bar{t}}(H = c)}{P_{t\bar{t}}(H = c) + P_{t\bar{t}}(H = u)}, \tag{4}$$

that discriminates between $t\bar{t}$ events with (c) and without (u) SM spin correlation [26]. Using $5.4\,\mathrm{fb}^{-1}$ of dilepton $t\bar{t}$ events, DØ obtained $C_{\mathrm{beam}} = 0.57 \pm 0.31$ (stat + syst). Compared to the measurements based on angular templates, this improves the sensitivity by about 30%. The largest systematic uncertainty of ± 0.07 is from limited statistics of forming the MC templates.

This approach is also applied to $5.3\,\mathrm{fb}^{-1}$ of $\ell+$jets events [28]. Requiring at least two jets to be identified as coming from b quarks, the signal purity is increased to about 90%. To increase the sensitivity, and to reduce the dilution from initial and final state radiation, events are split into four subsamples by dividing the data into two groups of events, one with four jets and the other with more than four jets. To reduce the contamination from events in which a b jet is mistakenly taken to emerge from W boson decay, these two groups are again separated according to whether the invariant mass of the two light-flavor jets is within 25 GeV of the accepted mass of the W boson. From a total of 729 $t\bar{t}$ candidate events, C_{beam} is extracted to be $C_{\mathrm{beam}} = 0.89 \pm 0.33$ (stat + syst). Combining results from the dilepton and $\ell+$jets channel yields

$$C_{\mathrm{beam}} = 0.66 \pm 0.23 \text{ (stat + syst)},$$
$$C_{\mathrm{beam}} > 0.04 \text{ at } 99.7\% \text{ CL},$$

providing first evidence for a non-vanishing spin correlation in $t\bar{t}$ events.

Another important property of top-quark production that is different between LHC and the Tevatron, is the angular asymmetry in the t and $\bar{t}$ production, *i.e.*, the question whether top (antitop) quarks are produced more often in the direction of the proton (antiproton) at the Tevatron. At LO, $t\bar{t}$ production is supposed to be symmetric in the collision center of mass, however, at NLO interferences from contributions symmetric and asymmetric under $t\bar{t}$ exchange yield asymmetries. Thus, the SM predicts an enhanced production of t ($\bar{t}$) quarks in the direction of the proton (antiproton) of 5%. Extension of the SM with Z' bosons or warped extra dimensions, increase the expected asymmetry, while *e.g.*, axi-gluons would decrease it. Depending on the quantization axis and the objects considered, this asymmetry can be defined and checked in multiple ways. One possibility is the direction of the reconstructed t and $\bar{t}$ in the laboratory frame. Based on their rapidity $y = \frac{1}{2}\ln(\frac{E+p}{E-p})$, one can define the forward/backward (FB) asymmetry:

$$A_{\mathrm{FB}}^{t\bar{t}} = \frac{N(\Delta y_{t\bar{t}} > 0) - N(\Delta y_{t\bar{t}} < 0)}{N(\Delta y_{t\bar{t}} > 0) + N(\Delta y_{t\bar{t}} < 0)}\,. \tag{5}$$

However, due the relatively large energy resolution of jets and the challenge of reconstructing the neutrinos, an improved definition makes use of the lepton direction, which can be very well measured. It is given by

$$A_{\mathrm{FB}}^{\ell} = \frac{N(q_\ell y_\ell > 0) - N(q_\ell y_\ell < 0)}{N(q_\ell y_\ell > 0) + N(q_\ell y_\ell < 0)}\,, \tag{6}$$

where y_ℓ is the rapidity and q_ℓ the charge of the lepton.

To calculate the asymmetry defined in eq. (5), the full $t\bar{t}$ event must be reconstructed. This is done using kinematic fitters, that reconstruct the event under the $t\bar{t}$ hypothesis using mass and resolution constraints [29-31]. The background contribution is subtracted from the data and the result is unfolded correcting for the biases of reconstruction and acceptance. CDF uses a matrix-inversion method, while DØ applies a regularized unfolding procedure. These results can be compared directly to asymmetries from MC generators or theoretical calculations. For MC@NLO [32], the asymmetry is predicted to be 5%, Ahrens *et al.* calculate an asymmetry of 7% at NLO+NNLL [33] and Holik *et* *al.* find 9% at NLO that includes corrections from quantum electrodynamics (QED) [34]. The experimental results for eq. (5) are

$$\begin{aligned}
\text{CDF in } 5.1\,\text{fb}^{-1} \text{ of dilepton data} : A_{\text{FB}}^{t\bar{t}} &= (42.0 \pm 15.0\ (\text{stat}) \pm 5.0\ (\text{syst}))\%,\\
\text{CDF in } 5.1\,\text{fb}^{-1} \text{ of } \ell + \text{jets data} : A_{\text{FB}}^{t\bar{t}} &= (15.8 \pm 7.2\ (\text{stat}) \pm 1.7\ (\text{syst}))\%,\\
\text{DØ in } 5.4\,\text{fb}^{-1} \text{ of } \ell + \text{jets data} : A_{\text{FB}}^{t\bar{t}} &= (19.6 \pm 6.0\ (\text{stat})^{+1.8}_{-2.6}\ (\text{syst}))\%.
\end{aligned}$$

Similarly, the leptonic asymmetry defined in eq. (6) is measured by the DØ Collaboration in the ℓ+jets channel using $5.4\,\text{fb}^{-1}$ of data, with the extracted value of A_{FB}^{ℓ} being $(15.2 \pm 4.0)\%$, which exceeds the predicted value of $A_{\text{FB}}^{\ell} = (2.1 \pm 0.1)\%$ from MC@NLO. As new physics could lead to a different mass dependence, both experiments also studied the dependence of the asymmetry on the mass of the $t\bar{t}$ system and the rapidity difference in t and $\bar{t}$. The largest deviation of more than 3 SD was observed by the CDF Collaboration in the mass bin above 450 GeV. However, to get a full understanding of the observed discrepancies, it is not only sufficient to reduce the statistical uncertainty on these results, but one also has to address remaining questions such as the modeling of the transverse momentum of the $t\bar{t}$ system. To rule out models that try to accommodate the observed asymmetries, it is also desirable to examine any polarization of top quarks, as certain models may lead to polarized top quarks [35].

The well-understood and clean environment of $t\bar{t}$ events makes this channel important also for exploring effects of soft QCD and developing new tools, such as the color flow. The color connection between particles depends on the nature of the decaying particle. For color singlets, such as the W or Higgs bosons, the color string connects the decay particles, while for octets, such as gluons, it connects the decay particles to the beam remnants. Color flow can be used to discriminate *e.g.*, $ZH \to Zbb$ from $Z +$ jets. The so-called jet-pull variable can be used to describe color flow [36]. This variable is defined by the vectorial sum of all calorimeter cells within a given jet, *i.e.*

$$\vec{p} = \sum_{i}^{cells} \frac{E_T^i |r_i|}{E_T^{\text{jet}}} \vec{r}_i, \tag{7}$$

where E_T^i is the transverse energy deposited in cell i with respect to the nominal center of the detector, $\vec{r}_i$, the location of the cell and E_T^{jet}, the transverse energy of the jet. For jets from color singlets, the jet pulls point towards each other, while for color octets, they have opposite directions. As a first test, DØ used this variable to measure the fraction of events in $t\bar{t}$ in which the $W \to q\bar{q}$ decay is identified as a color singlet. Based on $5.3\,\text{fb}^{-1}$ of $\ell +$ jets data, the fraction is extracted to be $f_{\text{Singlet}} = 0.56 \pm 0.42$ (stat + syst). Based on MC pseudo-experiments, the hypothesis that the W boson is a color octet can be excluded at the 99% CL, however, in data, this hypothesis can only be ruled out at 95% CL [37].

5. – Conclusion and prospects

Seventeen years after the observation of top quarks at the Tevatron collider, many aspects of this massive quark have been measured precisely. By now, the top-quark mass is known to less than 1 GeV. In addition, the well understood detectors at the Tevatron pioneered studies of many new aspects of the top quark, such as spin correlation in $t\bar{t}$ decays, and applications of the so-called jet-pull variable to study color flow in top-quark events. So far, all measurements are consistent with the SM predictions. Nevertheless, discrepancies between data and theory are observed in the forward-backward asymmetry. However, as the statistical uncertainties are still large, more data are needed to learn whether these differences are due to an underestimated effect in modeling $t\bar{t}$ and background or whether this is caused by new physics beyond the SM. Thus far, most analyses make use of half of the total data. Hence, the Tevatron legacy on this and other issues still needs to be resolved. Many aspects of the physics differ between the LHC top factory and the Tevatron—the discovery machine of the top quark. Additional interesting results can still be expected from the full data sample at the Tevatron.

REFERENCES

[1] The Tevatron electroweak working group, arXiv:1107.5255v3.
[2] Moch S. and Uwer P., *Phys. Rev. D*, **78** (2008) 034003.
[3] Kidonakis N., *Phys. Rev. D*, **74** (2006) 114012.
[4] Abazov V. M. *et al.* (DØ Collaboration), *Phys. Rev. D*, **84** (2011) 012008.
[5] Aaltonen T. *et al.* (CDF Collaboration), *Phys. Rev. Lett.*, **105** (2009) 012001.
[6] Aaltonen T. *et al.* (CDF Collaboration), CDF Note 10163 (2010).
[7] Abazov V. M. *et al.* (DØ Collaboration), *Phys. Lett. B*, **704** (2011) 403.
[8] Abazov V. M. *et al.* (DØ Collaboration), DØ Note 5607 (2008).
[9] Aaltonen T. *et al.* (CDF Collaboration), CDF Note 10562 (2011).
[10] Abazov V. M. *et al.* (DØ Collaboration), *Phys. Rev. D*, **82** (2010) 071102.
[11] Aaltonen T. *et al.* (CDF Collaboration), *Phys. Rev. D*, **81** (2010) 052011.
[12] Abazov V. M. *et al.* (DØ Collaboration), *Phys. Rev. D*, **82** (2010) 032002.
[13] Abazov V. M. *et al.* (DØ Collaboration), *Phys. Rev. Lett.*, **107** (2011) 121802.
[14] Aaltonen T. *et al.* (CDF Collaboration), *Phys. Rev. D*, **84** (2011) 031104.
[15] Peng-Fei D., arXiv:0907.1324v2.
[16] Aaltonen T. *et al.* (CDF Collaboration), *Phys. Rev. Lett.*, **103** (2009) 092002.
[17] Abazov V. M. *et al.* (DØ Collaboration), *Phys. Rev. D*, **84** (2011) 112001.
[18] Aaltonen T. *et al.* (CDF Collaboration), *Phys. Rev. D*, **82** (2009) 112005.
[19] Abazov V. M. *et al.* (DØ Collaboration), *Phys. Lett. B*, **705** (2011) 313.
[20] Mahlon G. and Parke S., *Phys. Rev. D*, **53** (1996) 4886, *Phys. Lett. B*, **411** (1997) 173.
[21] Abazov V. M. *et al.* (DØ Collaboration), *Phys. Lett. B*, **703** (2011) 422.
[22] Bernreuther W. *et al.*, *Nucl. Phys. B*, **690** (2004) 81.
[23] Abazov V. M. *et al.* (DØ Collaboration), *Phys. Lett. B*, **702** (2011) 16.
[24] Aaltonen T. *et al.* (CDF Collaboration), CDF Note 10719 (2011).
[25] Aaltonen T. *et al.* (CDF Collaboration), CDF Note 10211 (2010).
[26] Melnikov K. and Schulze M., *Phys. Lett. B*, **700** (2011) 17.
[27] Abazov V. M. *et al.* (DØ Collaboration), *Phys. Rev. Lett.*, **107** (2011) 032001.
[28] Abazov V. M. *et al.* (DØ Collaboration), *Phys. Rev. Lett.*, **108** (2012) 032004.
[29] Aaltonen T. *et al.* (CDF Collaboration), CDF Note 10436 (2011).
[30] Aaltonen T. *et al.* (CDF Collaboration), *Phys. Rev. D*, **83** (2011) 112003.
[31] Abazov V. M. *et al.* (DØ Collaboration), *Phys. Rev. D*, **84** (2011) 112055.
[32] Frixione S. and Webber B. R., *JHEP*, **06** (2002) 029.
[33] Ahrens V. *et al.*, arXiv:1106.6051v1.
[34] Holik W. and Pagani D., arXiv:1107.2606v1.
[35] Bernreuther W. and Si Z. G., *Nucl. Phys. B*, **837** (2010) 90.
[36] Gallicchio J. and Schwartz M., *Phys. Rev. Lett.*, **105** (2010) 022001.
[37] Abazov V. M. *et al.* (DØ Collaboration), *Phys. Rev. D*, **83** (2011) 092002.

IL NUOVO CIMENTO Vol. 35 C, N. 6 Novembre-Dicembre 2012
DOI 10.1393/ncc/i2012-11377-3

Colloquia: LaThuile12

Electroweak physics results from CMS

I. Kravchenko for the CMS Collaboration
University of Nebraska-Lincoln - Lincoln, NE, USA

ricevuto il 7 Settembre 2012

Summary. — We present results of the most recent CMS electroweak measurements performed at the LHC with the data collected in proton-proton collisions at 7 TeV. Production of W and Z bosons is discussed at length, including differential cross sections and asymmetries with respect to several kinematic variables, the weak mixing angle measurement, and production of W and Z in association with light and heavy (b, c) quarks.

PACS `14.70.-e` – Gauge bosons.
PACS `12.38.-t` – Quantum chromodynamics.
PACS `12.15.-y` – Electroweak interactions.

1. – Introduction

In this report, we present the most prominent recent results on electroweak physics from the CMS experiment at the LHC. The LHC has concluded its 7 TeV proton-proton running and delivered $5.7\,\text{fb}^{-1}$ to the CMS experiment. The measurements discussed in this paper are based on up to $2.1\,\text{fb}^{-1}$, and the remaining data are presently being analyzed. These data have been collected with the CMS detector over the years 2010 and 2011.

Throughout the year 2011, the instantaneous luminosity of the LHC has been increasing, and with the luminosity the number of multiple interactions per bunch crossing, the so-called pile-up, has increased as well. By the end of 2011, a typical pile-up level per bunch crossing at CMS was 15 interactions, which posed a challenge to all measurements reported here as it made more difficult to distinguish isolated leptons critical for any measurement involving W and Z bosons, as well as to correctly calculate the jets energy.

2. – Reconstruction of W and Z bosons

All measurements discussed in this paper involve W and Z bosons. They are reconstructed in the leptonic channels, typically electron or muon, as these channels offer the cleanest samples. The transverse energy and momentum of both electrons and muons is required to be above 20–25 GeV. Only isolated leptons are selected with a limited amount

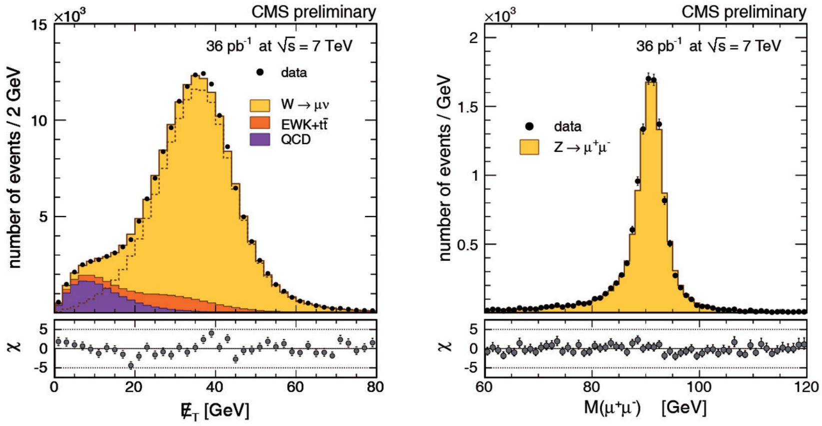

Fig. 1. – The W and Z samples in the muon channel observed in the 2010 CMS data.

of energy seen in the detector in the cone $\Delta R \equiv \sqrt{\Delta\eta^2 + \Delta\phi^2}$ of 0.3 or 0.4 around the lepton direction. For W decays, missing transverse momentum is required in the event, and for Z reconstruction, the dilepton mass has to be consistent with the Z mass.

In nearly all measurements reported, the background prediction is derived from the data. The reconstruction efficiencies and resolutions are estimated from the data as well. Corrections for pile-up–related effects are applied on an event-by-event basis by subtracting the average pile-up activity in the lepton isolation and jet energy.

3. – Inclusive W and Z production cross sections

The measurements of the inclusive W and Z cross sections in the electron and muon channels are most straightforward and are based on $36\,\mathrm{fb}^{-1}$ of the 2010 data. These results have already been published in [1], and are systematics limited, thus they will not be updated with a larger dataset. The distributions shown in fig. 1 demonstrate the quality of the W signal in the event missing transverse energy distribution and of the Z signal in the dimuon mass distribution. All the measured inclusive cross sections are in agreement with theory, the complete list of numerical values is found in [1]. The full 7 TeV dataset of CMS contains roughly 100 times large sample of W and Z bosons. At present, W and Z reconstruction at CMS is very well understood, and clean W/Z samples are used widely for a variety of calibrations for more complex measurements.

Somewhat more challenging are measurements of the inclusive W and Z cross section in the tau channels. The measurements are also based on the 2010 CMS dataset. While these cross sections have relatively large errors, the measurements in tau channels allow one to calibrate and understand tau reconstruction which is critical for Higgs and new physics searches. The measurement of the $Z \to \tau\tau$ production [2] combines several possible tau decays. The considered cases are tau decays to electrons, muons, and hadronic tau decays to one or three charged particles with neutrals allowed. In fig. 2, a clean Z peak is seen in one of the decay modes. The production cross section in graphical form is found in fig. 3. The measurement of the W production with W decaying through its tau channel is performed as well [3]. The hadronic decays of tau lepton are employed, as for the Z case, with one or three charged hadrons with some neutral hadrons used in

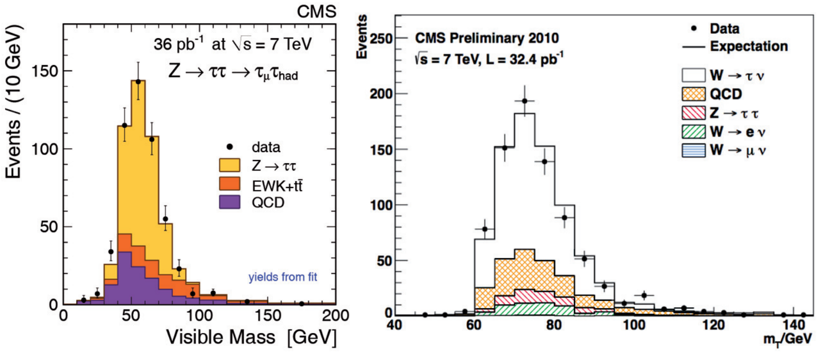

Fig. 2. – The visible mass distribution of the $Z \to \tau\tau$ candidates (left); the transverse mass distribution of the $W \to \tau\nu_\tau$ candidates (right).

reconstruction. The W peak in the transverse mass distribution is found in fig. 2, and the numerical values for the cross section, including separate results for W^+ and W^-, are quoted in the table in fig. 3.

4. – Differential cross sections and asymmetries for W and Z

With a larger dataset collected in 2011, CMS has made several detailed measurements of W and Z production. The differential cross sections of Z production with respect to Z invariant mass and rapidity have been performed in the electron and muon Z decay channels [4,5], and are useful for constraining proton PDFs. The measured behaviour of the invariant mass spectrum above the Z peak is especially important as this is where signs of new physics could be found. The measured $\mathrm{d}\sigma/\mathrm{d}M$ and $\mathrm{d}\sigma/\mathrm{d}y$, the latter is for the candidates in the mass range 60–120 GeV, are presented in fig. 4. The results are in a good agreement with theory predictions. At present, the measurement of the double differential cross section $\mathrm{d}^2\sigma/\mathrm{d}M\mathrm{d}y$ is in progress in CMS.

The dependence of Z production cross section on the transverse momentum of the Z has been measured with 36 pb^{-1} of 2010 data [5] for the mass range 60–120 GeV. A more precise measurement with a much larger dataset is in progress. In fig. 5, the measured momentum dependence of the cross section is shown separately for the different momentum ranges. For lower momenta, non-perturbative QCD is in effect and the data

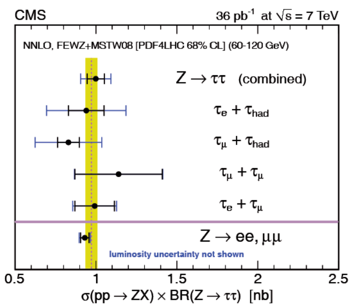

Channel	$\sigma(pp \to WX) \times \mathcal{B}$ (nb)	NNLO (nb)
$W \to \tau\nu$	$8.96 \pm 0.51(\text{stat.})^{+2.32}_{-2.26}(\text{syst.}) \pm 0.36(\text{lumi.})$	10.44 ± 0.52
$W^+ \to \tau^+\nu$	$5.26 \pm 0.39(\text{stat.})^{+1.36}_{-1.29}(\text{syst.}) \pm 0.21(\text{lumi.})$	6.15 ± 0.29
$W^- \to \tau^-\nu$	$3.40 \pm 0.33(\text{stat.})^{+0.92}_{-0.93}(\text{syst.}) \pm 0.14(\text{lumi.})$	4.29 ± 0.23

Fig. 3. – The production cross section results for the Z and W decaying to tau lepton(s).

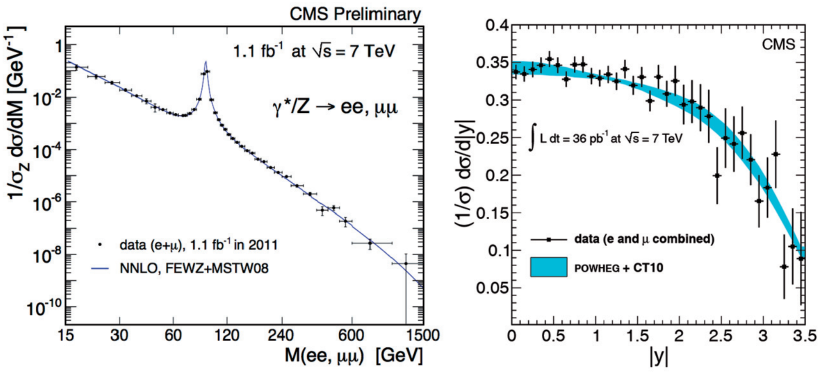

Fig. 4. – Differential cross sections of the Z boson production with respect to the mass (left) and rapidity (right) of the Z.

are best described by Pythia with several free parameters. It is found that the Z2 and ProQ20 Pythia tunes work rather well. The distribution for the high-p_T region (above 25 GeV) is well predicted by perturbative calculations.

At LHC in proton-proton collisions, in order to produce a W$^+$, most commonly a valence u quark is combined with a sea $\bar{d}$ quark, and for W$^-$ it is a valence d quark combined and a sea $\bar{u}$ quark. Due to a larger number of u valence quarks in comparison to d valence quarks, there is an overall excess of W$^+$ *vs.* W$^-$. The overall ratio of W$^+$/W$^-$ measured by CMS in the past is in a good agreement with SM predictions. Taking it one step further, one can measure this asymmetry as a function of W rapidity, the quantity very sensitive to proton PDFs. In the CMS measurement of this asymmetry [6], the muon decay channel of W is employed. Experimentally, the accessible quantity is the

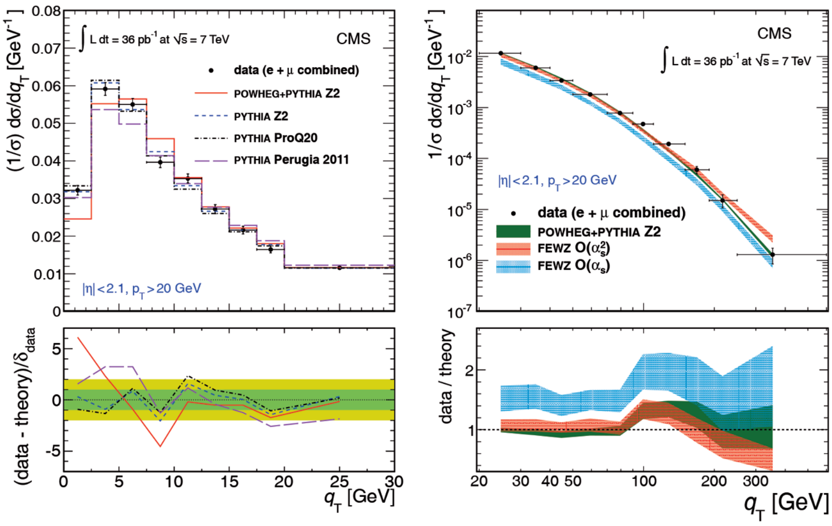

Fig. 5. – Differential cross section of the Z boson production with respect to the p_T of the Z for the lower (left) and higher (right) p_T regions.

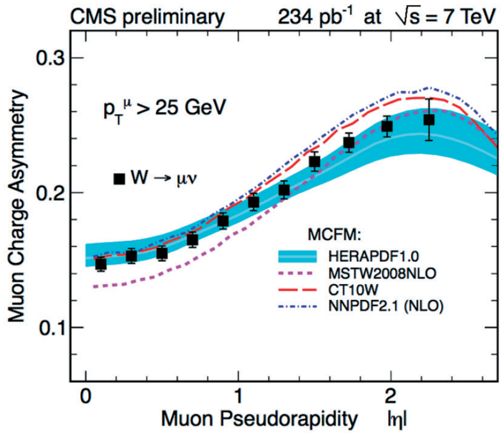

Fig. 6. – Muon charge asymmetry as a function of pseudorapidity for $\mathrm{W} \to \mu\nu_\mu$ candidates.

muon charge asymmetry as a function of the muon pseudo-rapidity:

$$A = \frac{\mathrm{d}\sigma(\mathrm{W}^+)/\mathrm{d}y - \mathrm{d}\sigma(\mathrm{W}^-)/\mathrm{d}y}{\mathrm{d}\sigma(\mathrm{W}^+)/\mathrm{d}y + \mathrm{d}\sigma(\mathrm{W}^-)/\mathrm{d}y} \to \frac{\mathrm{d}N(\ell^+)/\mathrm{d}\eta - \mathrm{d}N(\ell^-)/\mathrm{d}\eta}{\mathrm{d}N(\ell^+)/\mathrm{d}\eta + \mathrm{d}N(\ell^-)/\mathrm{d}\eta}\,.$$

The observed asymmetry is plotted in fig. 6. In this measurement, the selected candidates are required to have the transverse momentum of at least 25 GeV. A good agreement with HERAPDF is observed. However, the measured distributions is more flat than the predictions produced using MSTW, CT10, and NNPDF.

5. – Measurement of the weak mixing angle

The weak mixing angle is one of the fundamental parameters of the standard model and is presently known to better than 0.1%. The previous measurements performed at Tevatron experiments achieved the accuracy of about 1%. In this paper, a CMS measurement of the weak mixing angle that is of similar accuracy is reported [7]. At LHC, measuring the weak mixing angle is more difficult than at the Tevatron. This measurement is made by analyzing the process $q\bar{q} \to \ell^+\ell^-$. At the Tevatron, in proton-antiproton collisions the forward-backward asymmetry of the ℓ^+ and ℓ^- production can be exploited. At LHC in *pp* collisions, this is not possible as the valence quark can come either of the colliding protons, while the sea anti-quark will come from the other, and no asymmetry is seen in ℓ^+ and ℓ^- production. Instead, in the CMS measurement of the weak mixing angle, a simultaneous fit of the three observables of the $q\bar{q} \to \mu^+\mu^-$ process is performed: of dimuon rapidity, their invariant mass, and the decay angle (see fig. 7). The shapes of the distributions of these observables have sensitivity to the value of the effective weak mixing angle, which is found to be

$$\sin^2\theta_{eff} = 0.2287 \pm 0.0020(\mathrm{stat}) \pm 0.0025(\mathrm{syst}).$$

6. – W and Z production with accompanying jets

Measurements of W and Z production along with one or more jets provides a stringent test of perturbative QCD. Moreover, vector bosons accompanied by several jets produced

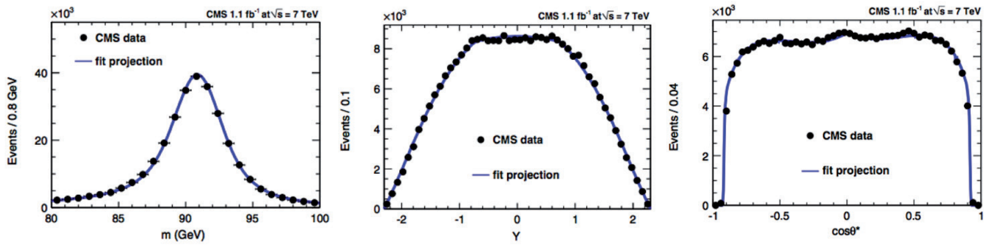

Fig. 7. – The distributions of the three observables (invariant mass, rapidity, and the decay angle) of dilepton pairs entering the multivariate analysis that yields the weak mixing angle measurement.

via standard model processes is a background to searches for new physics, Higgs searches, and top quark measurements. Several characteristics of W and Z production at 7 TeV were measured by CMS. This report contains results based on 2010 dataset of $36\,\mathrm{pb}^{-1}$. In this measurement, W and Z are identified through their decays into both electron and muon channels. Jets are reconstructed with the anti-k_T algorithm with the cone size 0.5 in ΔR, and their energy is corrected for pile-up. The measured dependencies include the production rates of W and Z plus n jets to inclusive of the corresponding vector boson production, as well as the ratio of the above mentioned ratios between W and Z. Several of these results are shown in fig. 8, while the complete set is found in [8]. The observed ratios are found to be in a good agreement with prediction from simulations based on the Madgraph generator.

7. – W and Z plus heavy-quark production

The production of W accompanied by a c quark which hadronizes into a jet is sensitive to the strange content of proton PDF. This process at LHC proceeds primarily as hard scattering of an s or $\bar{s}$ and a gluon. More than 10% of W+jets events with jet $p_T > 20\,\mathrm{GeV}$ contain a charm quark. Recently, CMS measured the ratio $R_c^{\pm} \equiv \sigma(\mathrm{W}^+c)/\sigma(\mathrm{W}^-c)$. This

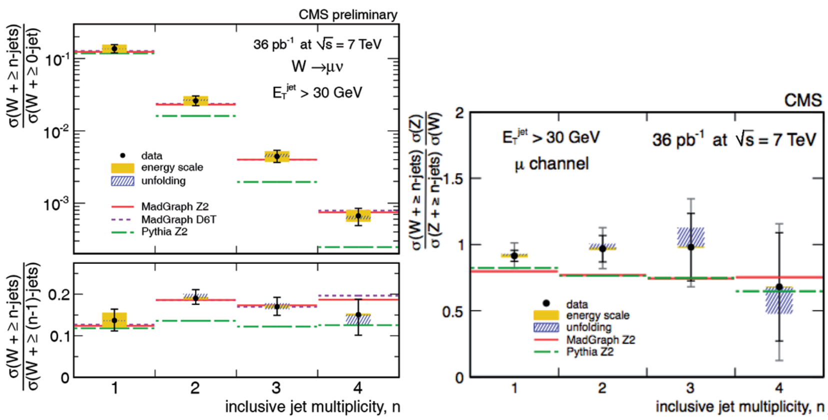

Fig. 8. – Multiplicities of jets produced in association with W and Z and normalized to the inclusive W and Z production.

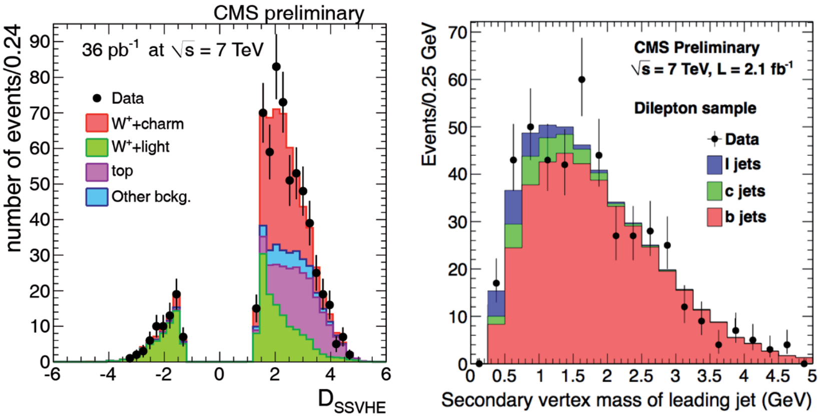

Fig. 9. – The distribution of the discriminant based on the significance of the secondary vertex displacement for W+charm candidates (left); the distribution of the leading jet secondary vertex mass for $\mathrm{Z}+b(b)$ candidates (right).

ratio is expected to be close to 1.0 as the s and $\bar{s}$ quarks have approximately the same PDF. The result [9] is consistent with the expectations:

$$R_c^{\pm} = 0.92 \pm 0.19(\mathrm{stat}) \pm 0.04(\mathrm{syst}).$$

Additionally, the fraction of the charm in W+jets events is of interest, and is reflected in the observable $R_c \equiv \sigma(\mathrm{W}^{\pm}+c)/\sigma(\mathrm{W}^{\pm}+\mathrm{jets})$. CMS measures this fraction to be [9]

$$R_c = 0.143 \pm 0.015(\mathrm{stat}) \pm 0.024(\mathrm{syst}),$$

which agrees with NLO predictions.

In measuring both R_c and $R_c^{\pm}$, W candidates are reconstructed in the muon channel. Jet reconstruction is the same as described in sect. **6**. Jets containing the charm quark are found by requiring a displaced secondary vertex. Figure 9 depicts the discriminant based on the 3D decay length significance which is used to measure the number of W events with charm in the sample. The signal W+charm is quite clean.

The production of Z along with a b quark is sensitive to the b component of proton PDFs. Moreover, it is both a benchmark and a background to Higgs searches with decays involving b quarks. CMS measures the production cross section of the Z boson accompanied by one or two b quarks [10]. The Z bosons are reconstructed in both electron and muon channels, and jets are found as in sect. **6**. The b jets are selected by

Table I. – *Production cross section of the* $\mathrm{Z}+b(b)$ *measured at CMS.*

Multiplicity bin	ee	$\mu\mu$
$\sigma_{hadron}(\mathrm{Z}+1b, \mathrm{Z}\to\ell\ell)(pb)$	$3.25 \pm 0.08 \pm 0.29 \pm 0.06$	$3.47 \pm 0.06 \pm 0.27 \pm 0.11$
$\sigma_{hadron}(\mathrm{Z}+2b, \mathrm{Z}\to\ell\ell)(pb)$	$0.39 \pm 0.04 \pm 0.07 \pm 0.02$	$0.36 \pm 0.03 \pm 0.07 \pm 0.03$
$\sigma_{hadron}(\mathrm{Z}+b, \mathrm{Z}\to\ell\ell)(pb)$	$3.64 \pm 0.09 \pm 0.35 \pm 0.08$	$3.83 \pm 0.07 \pm 0.31 \pm 0.14$

requiring the presence of a secondary vertex in the jet. The cross section is measured in acceptance, where both leptons have $p_T > 20\,\text{GeV}$ and $|\eta| < 2.5$, dilepton mass is in the interval 76–106 GeV, and the b jets are required to have $p_T > 25\,\text{GeV}$, $|\eta| < 2.1$, and be separated from the leptons by ΔR of at least 0.5. The quality of the selected sample is illustrated on the figure of the invariant mass of the particles in the secondary vertex found in b jet candidates (see fig. 9). The total production cross section of Zbb is found to be

$$\sigma(\text{Z}bb) = 0.37 \pm 0.02(\text{stat}) \pm 0.07(\text{syst}) \pm 0.02(\text{theory})\,\text{pb}.$$

This value agrees well with the expectation, obtained using Madgraph, of $0.33 \pm 0.01\,\text{pb}$. A breakdown by channel and results for different b quark multiplicities are found in table I.

8. – Conclusions

In this report, we present a number of detailed measurements of W and Z production and V+jets production including heavy quarks based on partial 7 TeV proton-proton data collected by the CMS experiment at LHC. All presented results are consistent with theory predictions. Most of these measurements are expected to be updated by CMS once the full analysis of the 2010-2011 7 TeV dataset is completed.

* * *

We congratulate our colleagues in the CERN accelerator departments for the excellent performance of the LHC machine. We thank the technical and administrative staff at CERN and other CMS institutes, and acknowledge support from: FMSR (Austria); FNRS and FWO (Belgium); CNPq, CAPES, FAPERJ, and FAPESP (Brazil); MES (Bulgaria); CERN; CAS, MoST, and NSFC (China); COLCIENCIAS (Colombia); MSES (Croatia); RPF (Cyprus); MoER, SF0690030s09 and ERDF (Estonia); Academy of Finland, MEC, and HIP (Finland); CEA and CNRS/IN2P3 (France); BMBF, DFG, and HGF (Germany); GSRT (Greece); OTKA and NKTH (Hungary); DAE and DST (India); IPM (Iran); SFI (Ireland); INFN (Italy); NRF and WCU (Korea); LAS (Lithuania); CINVESTAV, CONACYT, SEP, and UASLP-FAI (Mexico); MSI (New Zealand); PAEC (Pakistan); MSHE and NSC (Poland); FCT (Portugal); JINR (Armenia, Belarus, Georgia, Ukraine, Uzbekistan); MON, RosAtom, RAS and RFBR (Russia); MSTD (Serbia); SEIDI and CPAN (Spain); Swiss Funding Agencies (Switzerland); NSC (Taipei); TUBITAK and TAEK (Turkey); STFC (United Kingdom); DOE and NSF (USA).

REFERENCES

[1] Chatrchyan S. *et al.* (The CMS Collaboration), *JHEP*, **10** (2011) 132.
[2] Chatrchyan S. *et al.* (The CMS Collaboration), *JHEP*, **08** (2011) 117.
[3] The CMS Collaboration, CMS Physics Analysis Summary CMS-PAS-EWK-11-019.
[4] The CMS Collaboration, CMS Physics Analysis Summary CMS-PAS-EWK-11-020.
[5] Chatrchyan S. *et al.* (The CMS Collaboration), *Phys. Rev. D*, **85** (2012) 032002.
[6] The CMS Collaboration, CMS Physics Analysis Summary CMS-PAS-EWK-11-005.
[7] Chatrchyan S. *et al.* (The CMS Collaboration), *Phys. Rev. D*, **84** (2011) 112002.
[8] Chatrchyan S. *et al.* (The CMS Collaboration), *JHEP*, **01** (2012) 010.
[9] The CMS Collaboration, CMS Physics Analysis Summary CMS-PAS-EWK-11-013.
[10] The CMS Collaboration, CMS Physics Analysis Summary CMS-PAS-EWK-12-003.

IL NUOVO CIMENTO Vol. 35 C, N. 6 Novembre-Dicembre 2012
DOI 10.1393/ncc/i2012-11378-2

Colloquia: LaThuile12

Electroweak results from ATLAS

S. Glazov on behalf of the ATLAS Collaboration
DESY - Notkestrasse 85, 22607, Hamburg, Germany

ricevuto il 7 Settembre 2012

Summary. — Measurements of single W and Z as well as diboson WW, WZ and ZZ production at the LHC performed by the ATLAS Collaboration in 2010 and 2011 are presented. The data provide accurate tests of the theory in a wide kinematic range. A QCD analysis of the W and Z boson differential distributions reveals a novel sensitivity to the strange-quark density which is found to be large compared to previous expectations. Studies of $W + b$ and $Z + b$ jet production and W polarisation test NLO QCD calculations and proton PDFs. The diboson cross section measurements are used to determine limits on the anomalous couplings. No deviation from the Standard Model is observed.

PACS 12.38.Qk – Experimental tests.
PACS 13.38.Be – Decays of W bosons.
PACS 13.38.Dg – Decays of Z bosons.
PACS 14.70.Hp – Z bosons.

1. – Introduction

Successful start and continuous delivery of the luminosity enabled rediscovery of the Standard Model processes at the LHC. The processes with the highest cross section, such as production of single W and Z bosons, were accurately measured already using the data collected during the first year of the operation, in 2010. Further increase of the integrated luminosity in 2011 allowed the ATLAS Collaboration to extend the reach to rarer processes, in particular production of diboson states.

The measurements reported by the LHC Collaborations have an unprecedented accuracy for the detectors which are at the beginning of their operation cycle. In particular, the ATLAS detector shows very good performance. For example, the lepton (e, μ) identification efficiency is understood typically to better than 1%, the calorimeter energy scale is known to better than 1% [1], and the jet energy scale is calibrated with up to 2.5% accuracy for the central jets at medium transverse momenta (p_T) [2]. Last but not least ingredient enabling success of the Standard Model physics analyses at the LHC is the accurate determination of the luminosity which is measured to 3.4% precision [3].

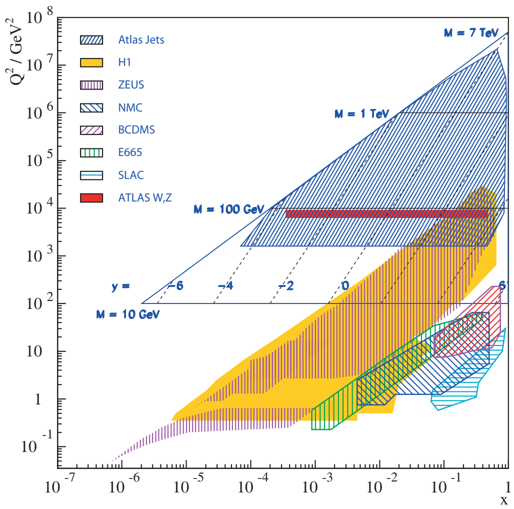

Fig. 1. – Kinematic reach of the measurements at fixed target and collider ep experiments and at the LHC.

Standard Model predictions at the LHC require higher-order QCD calculations and knowledge of the proton structure. The parton distribution functions (PDFs) are measured primarily using deep-inelastic lepton-proton scattering data. The PDFs are parameterised as a function of Bjorken-x variable, their values at different four momentum transfers Q^2 are related using evolution equations. The pp scattering processes at the LHC are predicted using these universal PDFs and coefficient functions, calculated perturbatively. Large center of mass energy $S = 4E_p^2$ of the LHC leads to a kinematic coverage extending to high Q^2 and low x, see fig. 1. Comparison of the data with the predictions thus provides tests of perturbative QCD and shed additional light on the proton structure.

2. – Measurements based on production of W and Z bosons

The production of W, Z vector bosons at the LHC is the standard candle process which can be used to calibrate and monitor performance of the detectors and to validate the Standard Model predictions. Accurate measurements of the W and Z boson production are performed by the ATLAS Collaboration in the electron and muon channels [4] using the data collected in 2010. The Standard Model predicts that W and Z bosons couple identically to the leptons from different generations and thus production rates should be the same up to effects proportional to the lepton masses ("lepton universality"). Figure 2 shows that the ATLAS measurements expressed in term of the ratios of $Z \to e^+e^-$ to $Z \to \mu^+\mu^-$ and $W^\pm \to e\nu$ to $W^\pm \to \mu\nu$ production cross sections are consistent with the lepton universality at a few percent level of accuracy. For the W boson, the precision of the result is comparable with the PDG world average [5].

The measurements of the total cross section in e and μ channels are combined and compared to the predictions in fig. 3 which shows experimental results obtained at pp and $p\bar{p}$ colliders and at different center of mass energies. For $p\bar{p}$ colliders, W^+ and W^- production has identical cross section while for pp colliders W^+ production cross section is larger since the u-quark has larger density that the d-quark. Overall, there is a very

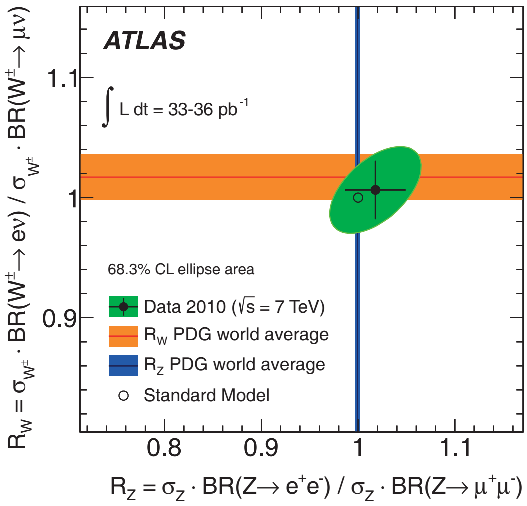

Fig. 2. – ATLAS results for the ratio of cross section measurements in e and μ channel for Z and W production compared to the PDG and Standard Model expectations [4]. The ellipse shows the 68% CL for the correlated measurement of the ratios while the error bars correspond to the one-dimensional uncertainties.

good agreement between the data and expectations. There is also a very good agreement observed between ATLAS and CMS total cross section measurements.

Additional information on the proton structure can be obtained by performing differential cross section measurements, in particular by using the boson rapidity y. At leading order, y is given by x_1 and x_2 values of the colliding quarks as $x_{1,2} = M/\sqrt{S}\exp(\pm y)$ where $M = M_W$ or $M = M_Z$. Since for the W bosons it is impossible to reconstruct y due to the missing neutrino, the pseudorapidity of the reconstructed lepton η_ℓ is used instead.

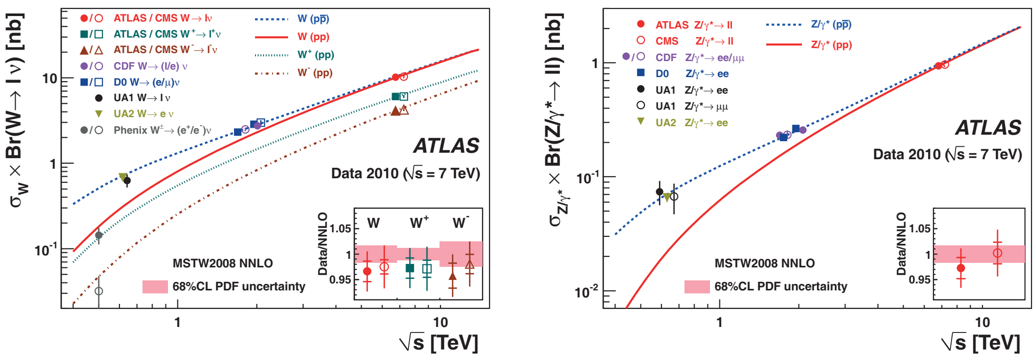

Fig. 3. – Total $W^\pm$ and Z cross section measured at pp and $p\bar{p}$ colliders at different $\sqrt{s}$ [6]. The inserts show the results at $\sqrt{S} = 7\,\text{TeV}$ from the ATLAS and CMS Collaborations as ratios to NNLO predictions.

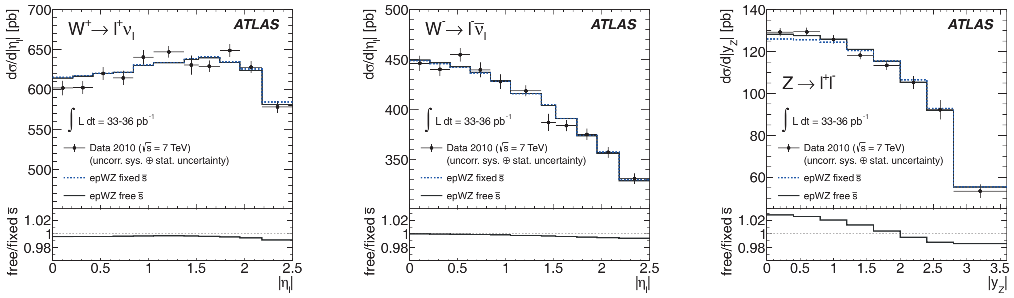

Fig. 4. – Differential $\mathrm{d}\sigma/\mathrm{d}\eta_\ell$ (left, middle) cross section measurement for $W \to \ell\nu$ and $\mathrm{d}\sigma/\mathrm{d}_Z$ (right) cross section measurement for $Z \to \ell\ell$ [7]. The error bars represent statistical and uncorrelated systematic uncertainties added in quadrature while the theory predictions are adjusted for the correlated systematic error shifts. The fits with free and fixed strangeness are shown, and their ratios are given in the lower panels.

The combined differential cross sections $\mathrm{d}\sigma/\mathrm{d}\eta_\ell$ and $\mathrm{d}\sigma/\mathrm{d}y_Z$ were included in a QCD fit [7] using a HERAFitter program [8]. The analysis uses full correlation information among the measurements. Two fits were performed, using different levels of the strange-sea quark density, they are shown in fig. 4. The fit in which ratio of strange-to-down quark density $r_s = 0.5(\bar{s}+s)/\bar{d}$ is let free shows significantly improved agreement with the data compared to the fit with fixed $r_s = 0.5$.

The ATLAS measures $r_s = 1.00^{+0.09}_{-0.10}$ at $x = 0.013$, corresponding to $y_Z = 0$, and $Q^2 = M_Z^2$. The measurement is compared in fig. 5 with predictions from different PDF groups. The ATLAS data are above all expectations, they are consistent with the prediction of CT10 [9], while the other groups show lower values. The large strangeness fraction results in a better description of the ratio of the W to Z total cross sections, calculated in fiducial volume of the measurement, as it is also shown in the fig. 5.

The flavour decomposition of PDFs can be also studied using boson production with jets where the jets are flavour tagged using displaced vertex information or B meson decays. The $W+b$ jet production is, however, mostly sensitive to the b quark production from the QCD radiation. The ATLAS results [11] are shown in fig. 6, they are somewhat exceeding the expectations for larger jet multiplicities, however the data and theory are

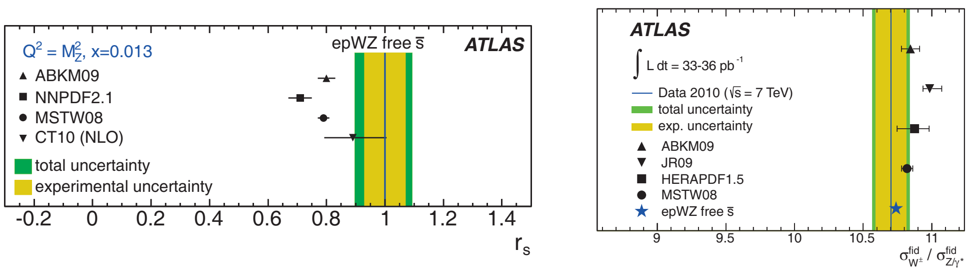

Fig. 5. – Predictions obtained for the ratio r_s at $Q^2 = M_Z$ and $x = 0.013$ (left). Ratio of fiducial cross sections, $(W^+ + W^-)/Z$ (right) [10]. Points show predictions from different PDF groups, bands represent the ATLAS result with inner band showing experimental and outer band total uncertainty. The blue star "epWZ free $\bar{s}$" is the result of the ATLAS fit.

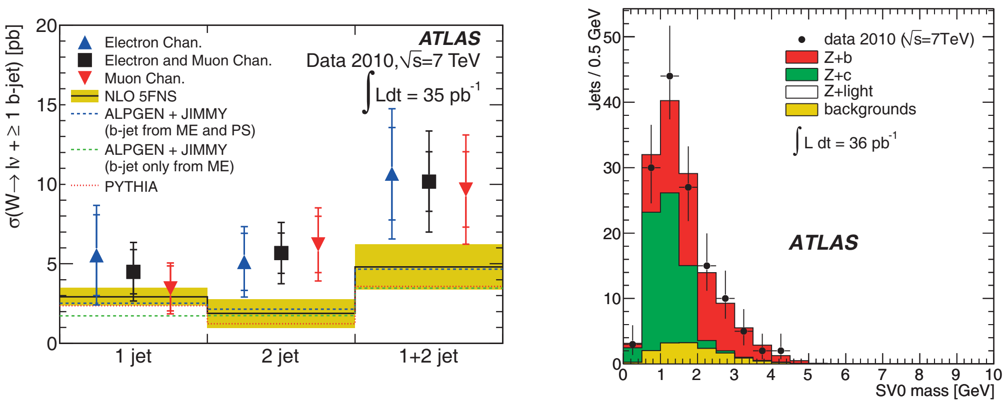

Fig. 6. – Measured fiducial cross section for W and b-jet production in electron, muon and combined electron plus muon channel (left) [11]. The cross section is given in 1, 2, and $1 + 2$ exclusive bins. The measurements are compared with NLO predictions with total uncertainties, estimated as a sum in quadrature of the renormalisation and factorisation scale variation, PDF and non-perturbative correction uncertainties. Secondary vertex mass distribution for jets in Z and b-tagged jet events (right) [12]. The fitted contributions from b, light, and c jets are displayed together with other backgrounds.

consistent within the uncertainties. The production of b-tagged jets associated with the Z boson provides a check of the b quark PDF. Larger coupling to the Z boson for the b compared to c quark can lead to improved sensitivity with respect to the measurements of the b-PDF at HERA. Figure 6 shows the secondary vertex mass distribution which indicates the high purity of $Z + b$ jet events for high masses. The ATLAS result for the $Z+b$ jet production cross section [12] is consistent with the expectations. At leading order QCD, W bosons are produced left- (f_L) or right-handed (f_R) and for large rapidities they are predominantly left-handed since on average the valence quarks carry larger momenta compared to the sea antiquarks. A comparison of left- *vs.* right-handed W bosons thus gives a handle on the valence - sea quark separation. In addition, at NLO, for production at significant transverse momentum p_T^W, the longitudinal polarisation (f_0) arises from the gluon density. The polarisation fractions obey $f_L + f_R + f_0 = 1$ relation leaving two of them independent. ATLAS measurements [13] are shown in fig. 7 in terms of f_0 as a function of $f_L - f_R$ for different ranges in p_T^W. The ATLAS result establishes $f_L > f_R$ as expected from the valence quark dominance. The longitudinal polarisation fraction f_0 is consistent with the expectations and is above zero at 1–2σ level.

3. – Measurements of diboson production

At the LHC, the main diagrams for the W^+W^- production are the t-channel quark exchange and the s-channel diagram containing the triple gauge coupling (TGC) vertex. The gluon-gluon fusion box diagram contributes less that 10% at $\sqrt{S} = 7\,\text{TeV}$. For the ZZ and WZ pair production, the TGC vertex vanishes in the Standard Model. Accurate measurements of the diboson production cross sections provide thus stringent tests of the Standard Model and may show indications of physics beyond it. All ATLAS results presented here are based on $1.02\,\text{fb}^{-1}$ of data collected in 2011.

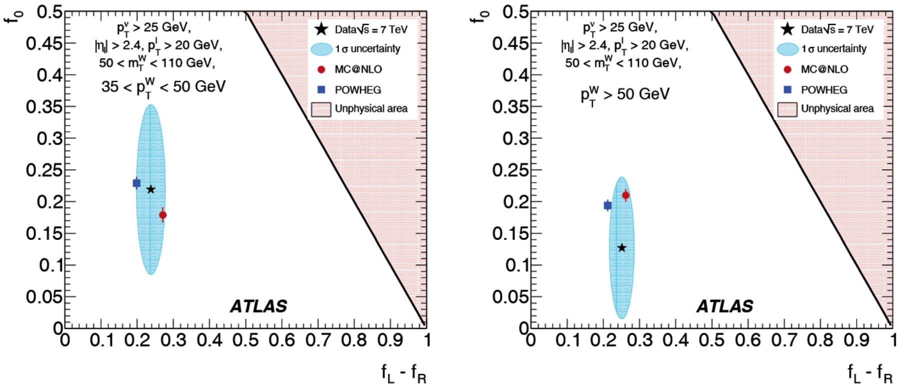

Fig. 7. – Measured values of f_0 and $f_L - f_R$, after corrections, with acceptance cuts for $35 < p_T^W < 50\,\text{GeV}$ (left) and for $p_T^W > 50\,\text{GeV}$ (right) compared with the predictions from NLO simulations [13]. The ellipses around the data points correspond to one standard deviation, summing quadratically the statistical and systematic uncertainties.

For the processes involving massive gauge bosons in the final state, W^+W^- production has the highest cross section. The final state is however not fully reconstructed and there are sizable background contributions even after all selection criteria are applied, providing additional challenges for the analysis. The ATLAS Collaboration measured the W^+W^- production cross section using $\mu^+\mu^-$, e^+e^- and $e^\pm\mu^\mp$ final states with missing transverse energy [14]. The ATLAS measurement, $\sigma(pp \to WW) = 54 \pm 4.0_{\text{stat}} \pm 3.9_{\text{syst}} \pm 2.0_{\text{lumi}}\,\text{pb}$, is found to be consistent with the Standard Model prediction of $44.4 \pm 2.8\,\text{pb}$. Figure 8 shows comparisons of the data with the sum of the signal and background predictions for the invariant mass of the charged leptons. Background contribution from the Drell-Yan process around the Z boson mass is clearly visible in this plot. No significant deviation from the expectation is observed.

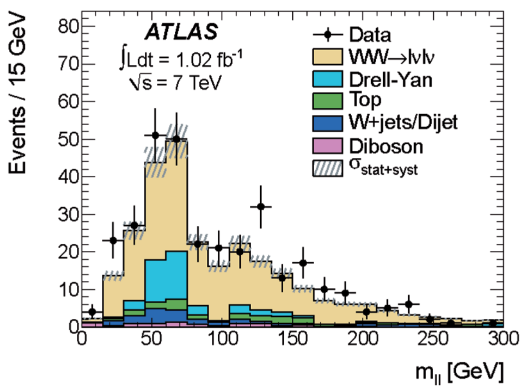

Fig. 8. – The distribution of the invariant mass of the charged leptons after the final selection for WW candidates from combined ee, $\mu\mu$ and $e\mu$ channels [14]. The data (dots) are compared to the expectation from WW and the background contributions.

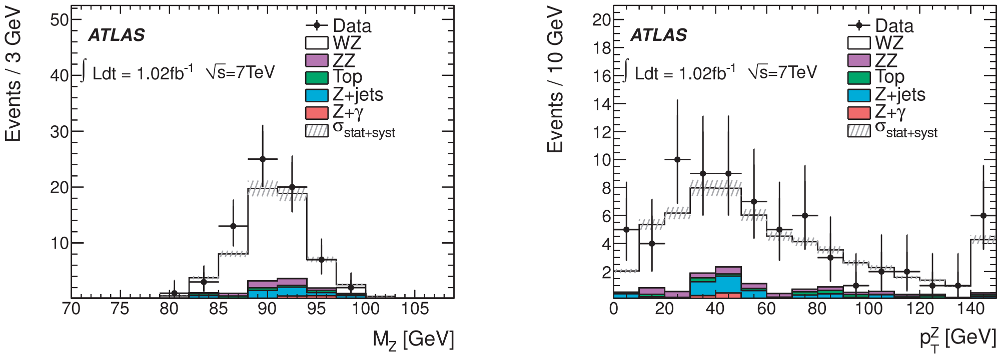

Fig. 9. – For WZ candidates after the full selection, the invariant mass of the lepton pair attributed to the Z boson (left) and the transverse momentum of the Z boson (right) [15]. The stacked histograms represent the predictions from simulation or data-driven estimates, including the uncertainties shown by shaded bands. The last bin of the right panel includes the overflow.

Compared to WW production, requirement of a presence of a fully reconstructed Z boson suppresses the background processes for the WZ production. The invariant mass of the lepton pair for the Z boson candidates in shown in fig. 9 where only small contamination of the background is observed. The total cross section measured by ATLAS [15], $\sigma(pp \to WZ) = 20.5^{+3.1}_{-2.8}{}_{\rm stat}{}^{+1.4}_{-1.3}{}_{\rm syst}{}^{+0.9}_{-0.8}{}_{\rm lumi}$ pb, is consistent with the Standard Model prediction $17.3^{+1.3}_{-0.8}$ pb. There is also good agreement observed between the measured transverse momentum distribution of the Z boson and the expectations, up to highest p_T^Z values, see fig. 9.

The ATLAS measurement of ZZ production in $2\mu2\mu$, $2e2e$ and $2\mu2e$ channels [16] is based on observed 12 events with a background expectation of $0.3 \pm 0.3_{\rm stat}{}^{+0.4}_{-0.3}{}_{\rm syst}$ events. The correlation of the invariant masses of the dilepton pairs for the leading

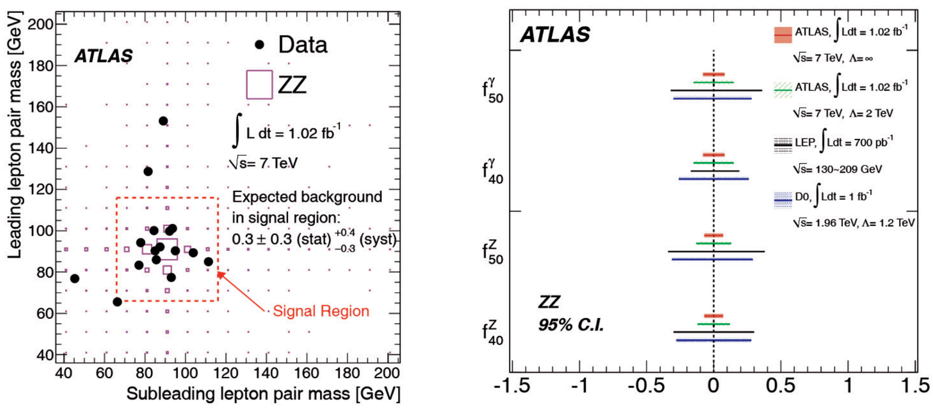

Fig. 10. – The mass of the leading lepton pair *versus* the mass of the subleading lepton pair for the ZZ candidate events (left) [16]. The events observed in the data are shown as solid circles and the ZZ signal prediction from the simulation as boxes. Anomalous TGC 95% confidence intervals from various experiments (right).

and sub-leading in p_T Z boson candidates is shown in fig. 10. Based on these data, the ATLAS Collaboration measured the production cross section of $\sigma(pp \to ZZ) = 8.5^{+2.7}_{-2.3}{}_{\text{stat}}{}^{+0.4}_{-0.3}{}_{\text{syst}} \pm 0.3_{\text{lumi}}$ pb which is consistent with the Standard Model expectation of $6.5^{+0.3}_{-0.2}$ pb.

From the measurement of the WW, WZ and ZZ diboson production the ATLAS Collaboration has derived limits on the anomalous TGC. An example result is shown for the forbidden $Z(\gamma) \to ZZ$ coupling in fig. 10. The limits are comparable to those obtained by the other experiments.

4. – Summary

The ATLAS measurements of the Standard Model processes show remarkable agreement between the data and expectations. The data are precise enough to impose constraints on the proton structure. An accurate measurement of the W and Z production cross sections provides a check of the lepton universality. The differential measurements are used as a stringent test of the proton PDFs; a QCD analysis of the data reveals a novel constraint on the strange-sea quark density which is found to be unsuppressed compared to the down-sea. Studies of $W + b$ and $Z + b$ jet production are used to investigate higher-order QCD effects and the b quark density. The valence and gluon densities are probed using the measurement of the W-polarisation, consistency is observed between the data and NLO QCD calculations.

The data collected in 2011 were used to measure the rare WW, WZ and ZZ diboson production processes. For all of them, the data are found to be consistent with the Standard Model expectations. Limits are derived on the anomalous couplings which are competitive with the other experiments.

REFERENCES

[1] ATLAS Collaboration, *Eur. Phys. J. C*, **72** (2012) 1909.
[2] ATLAS Collaboration, arXiv:1203.1302 [hep-ex] (2012) accepted by EPJC.
[3] ATLAS Collaboration, *Eur. Phys. J. C*, **71** (2011) 1630; ATLAS Collaboration, ATLAS-CONF-2011-011, `http://cdsweb.cern.ch/record/1334563`.
[4] ATLAS Collaboration, *Phys. Rev. D*, **85** (2012) 072004.
[5] Nakamura K. *et al.*, *J. Phys. G*, **37** (2010) 075021.
[6] ATLAS Collaboration, `http://atlas.web.cern.ch/Atlas/GROUPS/PHYSICS/PAPERS/STDM-2011-06`.
[7] ATLAS Collaboration, arXiv:1203.4051 [hep-ph] (2012) accepted by PRL.
[8] HERAFitter, `http://projects.hepforge.org/herafitter`.
[9] Lai H.-L. *et al.*, *Phys. Rev. D*, **82** (2010) 074024.
[10] ATLAS Collaboration, `http://atlas.web.cern.ch/Atlas/GROUPS/PHYSICS/PAPERS/STDM-2011-43`.
[11] ATLAS Collaboration, *Phys. Lett. B*, **707** (2012) 418.
[12] ATLAS Collaboration, *Phys. Lett. B*, **706** (2012) 295.
[13] ATLAS Collaboration, *Eur. Phys. J. C*, **72** (2012) 2001.
[14] ATLAS Collaboration, *Phys. Lett. B*, **712** (2012) 289.
[15] ATLAS Collaboration, *Phys. Lett. B*, **709** (2012) 341.
[16] ATLAS Collaboration, *Phys. Rev. Lett.*, **108** (2012) 041804.

IL NUOVO CIMENTO Vol. 35 C, N. 6 Novembre-Dicembre 2012
DOI 10.1393/ncc/i2012-11379-1

Colloquia: LaThuile12

Latest top physics results at ATLAS

L. Mijović(*) on behalf of the ATLAS Collaboration
CEA-Saclay, IRFU/SPP - bât. 141, 91191 Gif sur Yvette Cedex, France

ricevuto il 7 Settembre 2012

Summary. — Recent top-physics results obtained at ATLAS using the LHC data collected during 2011 are reviewed. For the top and antitop pair production process, measurements of the cross section and the top quark mass are summarized and the measurements yielding the most precise results are discussed. Results of other recent measurements of top quark properties in top and antitop pair production production events are summarized. Then the searches for the new physics predicting top quark production mechanisms other than Standard Model ones or final-state signatures similar to the top production processes signatures are reviewed. Finally measurements in the single-top production processes are reviewed.

PACS 14.65.Ha – Top quarks.

1. – Introduction

In 2011, the LHC delivered an integrated luminosity of $\mathcal{L}_{\text{int}} = 5.6\,\text{fb}^{-1}$ of pp collisions at 7 TeV centre-of-mass energy to the ATLAS [1] experiment. The data fulfilling all quality requirements of top quark production analyses corresponds to the integrated luminosity of $\mathcal{L}_{\text{int}} = 4.7\,\text{fb}^{-1}$. The top physics results obtained to date with the 2011 data are presented in this contribution(1). At the LHC top quarks are predominantly produced via the strong-interaction processes resulting in pair production of top and antitop ($t\bar{t}$ production). The pair production cross section is approximately twice as large as the total cross section of the weak-interaction production leading to single-top-quark final states. The latter include the exchange of a virtual W boson in the t-channel or in the s-channel, and the associated production of a top quark and an on-shell W boson (Wt-channel production). The top quark is expected to decay to a W boson and a b quark with a branching ratio B_r close to 1. For the $t\bar{t}$ production the decay channels are classified depending on the W boson decays as follows: in dileptonic, single lepton and fully hadronic decay channel both, one and none of the W bosons decays to leptons.

The top quark production event selection consists of event cleaning, trigger requirements, requirements on the multiplicities of the final-state object and event properties requirements that are expected to enhance the signal (S) over background (B) ratio. The event cleaning includes the detector and data quality requirements, the presence of at

(*) E-mail: liza.mijovic@cern.ch
(1) All public ATLAS top quark physics results are available at [2].

least one good primary vertex candidate [3] and the absence of jets failing quality criteria [4] as well as requirements aimed at cosmic background rejection. The trigger, object and event properties requirements are analysis specific and are detailed *e.g.* in refs. [5-7] for dileptonic, single lepton and fully hadronic $t\bar{t}$ decay channel analyses and in refs. [8-10] for single top t-, Wt- and s- production channel analyses. Typical kinematic requirements used for e (μ, jet) are ($|\eta| < 2.5$) and $E_{\mathrm{T}} > 25\,\mathrm{GeV}$ ($p_{\mathrm{T}} > 20\,\mathrm{GeV}$) or higher, where η, E_{T} and p_{T} denote the pseudorapidity(²), transverse energy and momentum, respectively. Jets are reconstructed using the anti-k_t algorithm [11] with a radius parameter of 0.4. Clusters of adjacent calorimeter cells [12] are used as clustering inputs. The missing transverse momentum ($E_{\mathrm{T}}^{\mathrm{miss}}$) is calculated using clusters of adjacent calorimeter cells and corrected for the presence of e, μ and jets [13]. The identification of jets originating from b quarks is performed using a discriminant obtained from one or combination of more b tagging algorithms. The taggers rely on impact parameters of the track within the jet (IP3D), properties of the vertices reconstructed within the jet (SV1) or topology of b and c hadron decays (JetFitter) [14]. The tagger working points are typically chosen such that the tagging efficiency of $\sim 60\%$–70% and the light jet rejection of ~ 500 are achieved.

For each of the top quark production processes a number of Monte Carlo (MC) generators and setups is used for the baseline MC prediction and to assess the modeling systematics. For the $t\bar{t}$ and s- and Wt-channel single-top events the baseline samples are generated using MC@NLO [15] generator interfaced to Herwig [16] and Jimmy [17]. For t-channel the AcerMC generator [18] interfaced to Pythia (v6) [19] is used. Supervising generators parameters are set according to tunes including ATLAS data [20, 21]. Samples generated with POWHEG-hvq [22], interfaced with Pythia as well as Herwig and Jimmy, ALPGEN [23], interfaced with Herwig and Jimmy, and Sherpa [24] generators are used for modeling systematics. Apart from generator to generator comparisons the modeling systematics is also addressed by using dedicated samples with Pythia generator parameter variations. The bulk of background samples is generated with ALPGEN interfaced to Herwig and Jimmy generators. Generated events are processed through the simulation of the ATLAS detector that relies on GEANT4 simulation toolkit [25]. The reconstruction of simulated samples is performed using the same software release as for the data. Pile-up is simulated using minimum bias events generated with Pythia (v6) generator. Signal Monte Carlo samples are normalized such that inclusive cross sections correspond to the recent theoretical predictions. For analyses discussed in this contribution the $t\bar{t}$ cross section is normalized to the approximate next-to-next-to-leading–order prediction value of $164.6 + 11.5 - 15.8\,\mathrm{pb}$, obtained using the HATHOR tool [26] and CTEQ6.6 NLO parton distribution functions (PDF) set [27]. Single top production cross sections are normalized to the approximate next-to-next-to-leading–order prediction values of $64.6 + 2.7 - 2.0\,\mathrm{pb}$, $4.6 \pm 0.2\,\mathrm{pb}$ and $15.7 \pm 1.1\,\mathrm{pb}$ for the t, s and Wt production channels, respectively [28]. Reference single-top cross section values are obtained using MSTW2008 NNLO PDF set [29]. For both $t\bar{t}$ and single top production the uncertainties are obtained by linear addition of PDF and scale uncertainties. The cross sections are evaluated at the top quark mass of $m_t = 172.5\,\mathrm{GeV}$ that is used for simulated samples.

(²) ATLAS uses a right-handed coordinate system with its origin at the nominal interaction point (IP) in the centre of the detector and the z-axis along the beam pipe. The x-axis points from the IP to the centre of the LHC ring, and the y axis points upward. Cylindrical coordinates (r, ϕ) are used in the transverse plane, ϕ being the azimuthal angle around the beam pipe. The pseudorapidity is defined in terms of the polar angle θ as $\eta = -\ln\tan(\theta/2)$.

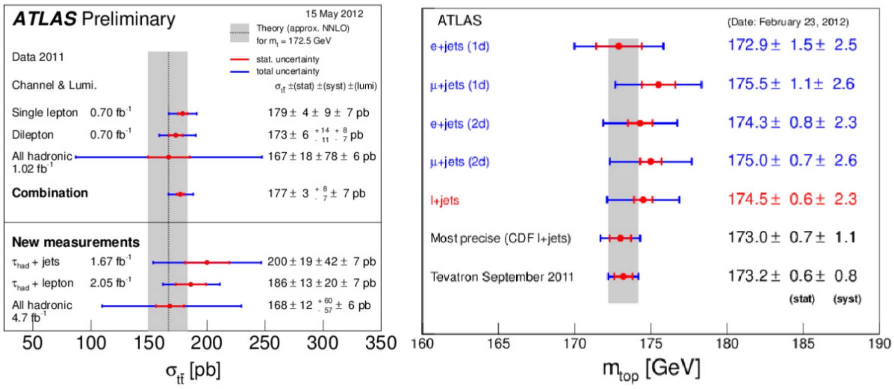

Fig. 1. – Left: summary of ATLAS measurements of the $t\bar{t}$ production cross section compared to the theoretical expectation [2]. Right: measurements on the top quark mass from the individual ATLAS analyses and the combined result from the 2d analysis described in the text. The results are compared to the results of the Tevatron experiments [30].

2. – $t\bar{t}$ production measurements

Measurements in $t\bar{t}$ production processes obtained to date with the data collected in 2011 are summarized in the following.

Measurements of $t\bar{t}$ production cross section enable precision tests of perturbative QCD predictions. Cross section measurements are also of importance for new physics searches, since many new physics models predict the existence of additional production mechanisms that result in enhancements of the $t\bar{t}$ production cross section with respect to the Standard Model prediction. The knowledge of $t\bar{t}$ production rates in various kinematic regimes is needed for many new physics searches for which $t\bar{t}$ production represents an important background. The cross section measurements at ATLAS with the data collected in 2011 are summarized and compared to the theoretical expectation in fig. 1 (left). The total uncertainty of the combined result is comparably small to the state of the art theory calculations (sect. **1**) and the systematics uncertainty exceeds the statistical uncertainty.

The ATLAS single most precise cross section measurement is obtained in the single-lepton (e or μ) decay channel [6] using $\mathcal{L}_{\mathrm{int}} = 0.7\,\mathrm{fb}^{-1}$ of collected data. Apart from the lepton requirement, events are requested to contain large $E_{\mathrm{T}}^{\mathrm{miss}}$ and at least three high p_{T} jets. The method for signal and background separation exploits differences in distributions of the following kinematic variables: lepton η, leading jet p_{T} and event shape variables aplanarity and $H_{\mathrm{T,3p}}$(3). These observables are used as inputs to a likelihood discriminant. The analysis is performed in six channels corresponding to different lepton flavor (e or μ) and jet multiplicity (3, 4 and ≥ 5 jets). Signal and background templates are constructed for each of the channels and the $t\bar{t}$ cross section is extracted from a simultaneous fit of the templates to the the data:

$$\sigma_{t\bar{t}} = 179.0 \pm 4(\mathrm{stat.}) \pm 9(\mathrm{syst.}) \pm 7(\mathrm{lumi.})\,\mathrm{pb}. \tag{1}$$

(3) $H_{\mathrm{T,3p}}$ corresponds to the transverse momentum of all but the two leading jets, normalized to the sum of absolute values of all longitudinal momenta in the event.

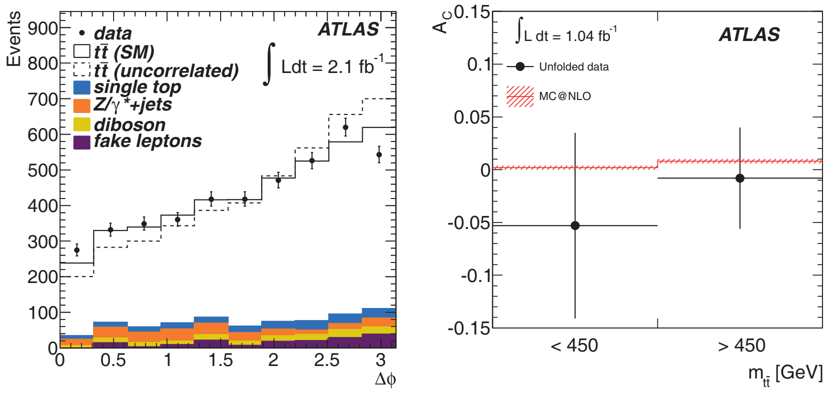

Fig. 2. – Left: lepton $\Delta\varphi$ distribution used for the measurement of the spin correlation in $t\bar{t}$ production [31]. Right: $t\bar{t}$ charge asymmetry values in two $t\bar{t}$ invariant-mass bins, unfolded and compared to the theoretical SM prediction [32].

Dominant sources of systematic uncertainty are the choice of the signal MC generator, followed by the jet energy scale and initial and final state radiation modeling uncertainties.

The top quark mass m_t is a fundamental parameter of the Standard Model (SM). It can be used to derive constraints on the masses of the Higgs boson and of heavy particles predicted by SM extensions. Measurements of m_t performed at ATLAS with the data collected in 2011 are summarized and compared to Tevatron experiments results in fig. 1 (right). The most precise measurement is obtained in the single-lepton (e or μ) $t\bar{t}$ channel [30] using data corresponding to the integrated luminosity of $\mathcal{L}_{\text{int}} = 1.04\,\text{fb}^{-1}$. The m_t is extracted using a two-dimensional template method (2d analysis). The two fitted quantities are the m_t and a global (averaged over η and p_{T}) jet energy scale factor (JSF). The main observables from which the m_t and JSF are extracted are the selected jet pair and jet triplet invariant masses. These serve as estimators of the reconstructed W boson and reconstructed m_t. The combined value of e and μ channel results is,

$$m_t = 174.5 \pm 0.6(\text{stat.}) \pm 2.3(\text{syst.})\,\text{GeV}. \tag{2}$$

While the statistical uncertainty of the ATLAS and Tevatron measurements are comparable, a reduction of the systematics uncertainty claimed by ATLAS is needed in order to reach the Tevatron measurements precision. The largest sources of systematics are the relative b-jet to light jet energy scale, followed by the light quark jet energy scale and the modeling of the initial and final state radiation. These sources account for $\sim 85\%$ of the systematic uncertainty.

Spin correlation in $t\bar{t}$ production has been measured with the data corresponding to $\mathcal{L}_{\text{int}} = 2.05\,\text{fb}^{-1}$ in dileptonic (e or μ) decay channel [31]. Due to its short life-time the top quark is expected to decay before hadronising. The spin correlation of t and $\bar{t}$ is transferred to decay products and can be inferred from their respective angular distributions. The lepton $\Delta\varphi$ distribution shown in fig. 2 (left) is found to be a sensitive observable. The distribution measured in the data is compared to the theoretical predictions obtained in the cases of t and $\bar{t}$ spin correlations as predicted by the SM and the uncorrelated t and $\bar{t}$ spin hypothesis. Using templates produced from samples with and without spin correlations a fraction of SM-like events is extracted and found to be consistent with 1.0. The hypothesis of zero spin correlation is excluded at 5.1 standard deviations.

TABLE I. – *Summary of* 95% *confidence level (CL) limits obtained in searches for the pair-produced heavy quarks, same-sign top production and resonances decaying to top quarks at ATLAS with the data collected in* 2011.

Process	Channel	$\mathcal{L}_{\text{int}}$ [fb^{-1}]	Excl. limits	Ref.
		pair-produced heavy quarks $Q\overline{Q}$		
$Q\overline{Q} \to W^+qW^-\overline{q}$ ($q = u, d, c, s, b$)	dilepton	1.04	$m_Q < 350\,\text{GeV}$	[39]
$Q\overline{Q} \to W^+bW^-\overline{b}$	single lepton	1.04	$m_Q < 404\,\text{GeV}$	[40]
$Q\overline{Q} \to W^+tW^-\overline{t}$	single lepton	1.04	$m_Q < 480\,\text{GeV}$	[42]
$Q\overline{Q} \to W^+tW^-\overline{t}$	dilepton	1.04	$m_Q < 450\,\text{GeV}$	[41]
$Q\overline{Q} \to t\bar{t} + E_{\text{T}}^{\text{miss}}$	single lepton	1.04	$m_Q < 420\,\text{GeV}$, $m_{A_0} < 140\,\text{GeV}$	[43]
		Resonances decaying to top final states		
tt	$\mu^+\mu^+, \mu^-\mu^-$	1.6	$\sigma'_Z = 3.7 - 2.2\,\text{pb}$ for $m_{Z'} = 0.1\text{–} \gg 1\,\text{TeV}$	[44]
tt	$l^+l^+, l^-l^-, l = e, \mu$	1.04	$\sigma'_Z = 2.0 - 1.4\,\text{pb}$ for $m_{Z'} = 0.1 - 0.2\,\text{TeV}$	[41]
$t\bar{t}$	di- & single lept.	2.05	$500 < m_{Z'} < 880\,\text{GeV}$, $500 < m_{gKK} < 1130\,\text{GeV}$	[45]
tb	$l\nu bb$	1.04	$m_{W'_R} < 1.13\,\text{TeV}$	[46]

The charge asymmetry A_c measurement has been performed with $\mathcal{L}_{\text{int}} = 1.04\,\text{fb}^{-1}$ in the single-lepton (e or μ) channel [32]. LHC A_c measurement are particularly interesting due to the deviations from the SM predictions recently reported for forward-backward asymmetry by the Tevatron experiments [33]. Results of the measurements done at ATLAS to date yield results consistent with SM predictions, as shown in fig. 2 (right).

Further top quark property measurements in $t\bar{t}$ events include the measurement of W polarization [34], top quark charge [35] and searches for flavor-changing neutral-current (FCNC) decays of the top quark [36]. In all cases the results are consistent with the SM expectations. The measurements of the $t\bar{t}$ production in association with jets [37] and photons [38] have also been performed.

3. – New particle searches in top(-like) production

A number of new particle searches have been performed in top(-like) production with the data collected in 2011. These include searches for pair-produced heavy quarks, same-sign top production and resonances decaying to top quarks. In these processes final-state signatures are similar to top quark production processes or top quarks are produced. The results are summarized in table I([4]). In all cases no excess over SM expectations has

([4]) The following labels are used in the table: A_0 denotes a stable, neutral weakly interacting particle, Z' denotes a narrow resonance, g_{KK} denotes a Kaluza-Klein gluon excitation in the Randall-Sundrum model and W'_R denotes a right-handed charged heavy gauge boson.

TABLE II. – *Summary of single-top cross section measurements at ATLAS.*

Channel	$\mathcal{L}_{\rm int}$ [fb^{-1}]	Cross section [pb]	SM prediction [pb]	Ref.
t	1.04	83 ± 4(stat.) $+ 20 - 19$(syst.)	64.57 +2.7 -2.0	[8]
Wt	2.05	16.8 ± 2.9(stat.) ± 4.9(syst.)	15.7 ± 1.1	[9]
s	0.70	$< 26.5(20.5)$ obs.(exp.) @ 95% CL	4.6 ± 0.2	[10]

been observed, which enables setting limits on new particle properties and new physics processes. Searches for pair-produced heavy quarks ($Q\overline{Q}$) are a direct tests of the fourth-generation quark existence. In the scenarios summarized in the table the heavy-quark mass m_Q exceeds the mass of the top quark and the $t\bar{t}$ production is the main background process. The limits quoted for refs. [39,40] apply to heavy up- and down-type quark pair production as well as exotic quark pair production decaying to the final state used in the analysis. Many of new physics models predict the existence of resonances decaying to top quarks. The searches for same sign top production, $t\bar{t}$ and tb resonances summarized in the table enable setting more stringent limits on the resonance masses than the existing limits from Tevatron experiments. In ref. [41] the limits are also placed on models that could explain the larger than expected forward-backward asymmetry in $t\bar{t}$ production observed at Tevatron.

4. – Single-top production results

The single-top-quark production proceeds via the weak interactions. With respect to the $t\bar{t}$ production it provides additional means to probe tWb vertex. Single-top production is a sensitive probe of a number of new physics models [47]. It can also be used for direct measurements of the CKM matrix element $|V_{tb}|$. Hence, despite lower production rates and more challenging signal to background separation with respect to the $t\bar{t}$ production, a number of single-top production measurements have been performed ATLAS in 2011. The cross section measurements have been performed in the t, Wt and s channels. The measured values and their associated statistical and systematic (stat., syst.) uncertainties or upper observed and expected (obs.(exp.)) 95% CL limits are reported in table II.

In the t-channel measurement [8] the final states with one lepton (e, μ), $E_{\rm T}^{\rm miss}$, and two or three jets, exactly one of them identified as originating from a b quark, are selected. The multijet background and the normalization of the background coming from the W production in association with jets are derived from the data. Theoretical predictions are used for the $t\bar{t}$ backgrounds and other smaller background contribution processes. The cross section is measured by fitting the distribution of a multivariate discriminant constructed with a neural network (NN). The estimator of the invariant top mass, obtained from the b tagged jet, the charged lepton, and the neutrino is the NN input variable with the highest discrimination power. The NN output is shown in fig. 3 (left). The extracted cross section reported in table II is in good agreement with the SM prediction. Dominant sources of systematic uncertainty are the b-tagging efficiency and the ISR/FSR modeling systematics that account for approximately 80% of the total systematic uncertainty. The NN analysis result is cross-checked with the cut-based method, using additional cuts in order to increase the expected significance of the

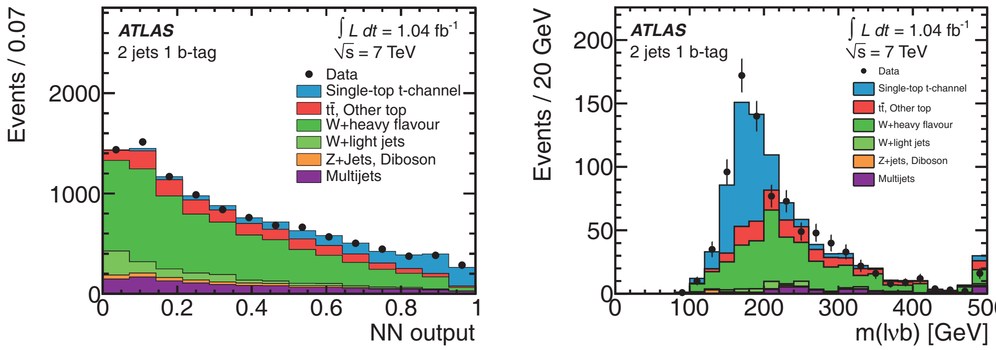

Fig. 3. – Left: the NN output distribution used for extracting the t-channel single top cross section. Right: estimator of the invariant top mass after cut-based method requirements. The signal is normalized to NN fit result (left) and to the observed cross section (right). Source: [8].

t-channel single-top-quark signal. The distribution of the invariant top mass estimator obtained in cut-based method is shown in fig. 3 (right). The CKM matrix element $|V_{tb}|$ is measured to be $|V_{tb}| = 1.13 +0.14 -0.13$ and $|V_{tb}| = 1.03 +0.16 -0.19$ in t- and Wt-channel analyses.

A search for the FCNC has also been performed for the single top production with $\mathcal{L}_{\text{int}} = 2.05\,\text{fb}^{-1}$ [48]. The search results are consistent with the SM hypothesis and the following 95% CL limits are set: $\sigma(qg \to t) \cdot B(t \to Wb) < 3.9\,\text{pb}$ and $B(t \to ug) < 5.7 \cdot 10^{-5}$, $B(t \to cg) < 2.7 \cdot 10^{-4}$.

5. – Summary

The knowledge of top-physics is extended by new and more precise results obtained at ATLAS with the data collected in 2011 at 7 TeV centre-of-mass energy. The results obtained to date are consistent with the SM predictions. It is expected that more data than in 2011 will be collected at 8 TeV center of mass collisions during 2012, hence statistical uncertainty of top quark measurements will be reduced. The systematics uncertainty due to the jet energy scale and generator modeling which are dominant uncertainty sources in many measurements will also be reduced. The latter is expected to decrease notably due to generator tuning and comparisons to the LHC data (*e.g.* [49]). ATLAS will therefore continue to play a key role in top physics efforts.

REFERENCES

[1] ATLAS Collaboration, *JINST*, **3** (2008) S08003.
[2] ATLAS Collaboration, top group public results webpage: `https://twiki.cern.ch/twiki/bin/view/AtlasPublic/TopPublicResults`.
[3] ATLAS Collaboration, ATLAS-CONF-2012-042, `https://cdsweb.cern.ch/record/1435196`.
[4] ATLAS Collaboration, ATLAS-CONF-2010-038, `https://cdsweb.cern.ch/record/1277678`.
[5] ATLAS Collaboration, *JHEP*, **05** (2012) 059.

[6] ATLAS Collaboration, ATLAS-CONF-2011-121, `http://cdsweb.cern.ch/record/1376413`.
[7] ATLAS Collaboration, ATLAS-CONF-2011-140, `http://cdsweb.cern.ch/record/1385033`.
[8] ATLAS Collaboration, *Phys. Lett. B*, **717** (2012) 330.
[9] ATLAS Collaboration, *Phys. Lett. B*, **716** (2012) 142.
[10] ATLAS Collaboration, ATLAS-CONF-2011-118, `http://cdsweb.cern.ch/record/1376410`.
[11] Cacciari M. *et al.*, *JHEP*, **07** (2003) 001.
[12] ATLAS Collaboration, *Eur. Phys. J. C*, **71** (2011) 1512.
[13] ATLAS Collaboration, *Eur. Phys. J. C*, **72** (2012) 1844.
[14] ATLAS Collaboration, ATLAS-CONF-2011-102, `https://cdsweb.cern.ch/record/1369219`.
[15] Frixione S. *et al.*, *JHEP*, **06** (2002) 029.
[16] Corcella G. *et al.*, *JHEP*, **01** (2001) 010.
[17] Butterworth J. M. *et al.*, *Z. Phys. C*, **72** (1996) 637.
[18] Kerševan B. P. *et al.*, arXiv:hep-ph/0405247.
[19] Sjostrand T. *et al.*, *JHEP*, **05** (2006) 026.
[20] ATLAS Collaboration, ATL-PHYS-PUB-2010-014, `https://cdsweb.cern.ch/record/1303025`.
[21] ATLAS Collaboration, ATLAS-CONF-2010-031, `https://cdsweb.cern.ch/record/1277665`.
[22] Frixione S. *et al.*, *JHEP*, **11** (2007) 070.
[23] Mangano M. L. *et al.*, *JHEP*, **07** (2003) 001.
[24] Gleisberg T. *et al.*, *JHEP*, **02** (2009) 007.
[25] Agostinelli S. *et al.*, *Nucl. Instrum. Methods A*, **506** (2003) 250.
[26] Aliev M. *et al.*, *Comput. Phys. Commun.*, **182** (2011) 1034.
[27] Nadolsky P. M. *et al.*, *Phys. Rev. D*, **78** (2008) 013004.
[28] Kidonakis N., *Phys. Rev. D*, **83** (2011) 091503; **81** (2010) 054028; **82** (2010) 054018.
[29] Martin A. D. *et al.*, *Eur. Phys. J. C*, **63** (2009) 189.
[30] ATLAS Collaboration, *Eur. Phys. J. C*, **72** (2012) 2046.
[31] ATLAS Collaboration, *Phys. Rev. Lett.*, **108** (2012) 212001.
[32] ATLAS Collaboration, *Eur. Phys. J. C*, **72** (2012) 2039.
[33] D0 Collaboration, *Phys. Rev. Lett.*, **100** (2008) 142002; *Phys. Rev. D*, **84** (2011) 112005; CDF Collaboration, *Rev. Lett.*, **101** (2008) 202001; *Phys. Rev. D*, **83** (2011) 112003.
[34] ATLAS Collaboration, *JHEP*, **06** (2012) 088.
[35] ATLAS Collaboration, ATLAS-CONF-2011-141, `http://cdsweb.cern.ch/record/1385517`.
[36] ATLAS Collaboration, ATLAS-CONF-2011-154, `http://cdsweb.cern.ch/record/1398198`.
[37] ATLAS Collaboration, ATLAS-CONF-2011-142, `http://cdsweb.cern.ch/record/1385518`.
[38] ATLAS Collaboration, ATLAS-CONF-2011-153, `http://cdsweb.cern.ch/record/1398197`.
[39] ATLAS Collaboration, *Phys. Rev. D*, **86** (2012) 012007.
[40] ATLAS Collaboration, *Phys. Rev. Lett.*, **108** (2012) 261802.
[41] ATLAS Collaboration, *JHEP*, **04** (2012) 069.
[42] ATLAS Collaboration, *Phys. Rev. Lett.*, **109** (2012) 032001.
[43] ATLAS Collaboration, *Phys. Rev. Lett.*, **108** (2012) 041805.
[44] ATLAS Collaboration, *Phys. Rev. D*, **88** (2012) 032004.
[45] ATLAS Collaboration, *Eur. Phys. J. C*, **72** (2012) 2093.
[46] ATLAS Collaboration, *Phys. Rev. Lett.*, **109** (2012) 081801.
[47] Tait T. M. P. and Yuan C. P., *Phys. Rev. D*, **63** (2000) 014018.
[48] ATLAS Collaboration, *Phys. Lett. B*, **712** (2012) 351.
[49] ATLAS Collaboration, *Eur. Phys. J. C*, **72** (2012) 2043.

IL NUOVO CIMENTO Vol. 35 C, N. 6 Novembre-Dicembre 2012
DOI 10.1393/ncc/i2012-11380-8

Colloquia: LaThuile12

Precision measurement of the W boson mass at CDF

B. Jayatilaka on behalf of the CDF Collaboration
Duke University - Durham, NC, USA

ricevuto il 7 Settembre 2012

Summary. — A measurement of the mass of the W boson, M_W, is presented using $2.2\,\text{fb}^{-1}$ of the data from $p\bar{p}$ collisions at $\sqrt{s} = 1.96\,\text{TeV}$ collected with the CDF II detector at the Fermilab Tevatron. The mass is determined by fitting simulated signal and background distributions to 470126 W candidates decaying to $e\nu_e$ and 624708 decaying to $\mu\nu_\mu$. The result is $M_W = 80387 \pm 19\,\text{MeV}$ and is the most precise determination of the mass to date.

PACS 14.70.Fm – W bosons.
PACS 12.15.Ji – Applications of electroweak models to specific processes.
PACS 13.38.Be – Decays of W bosons.

1. – Introduction

The mass of the W boson (M_W) is an important parameter of the standard model (SM). Precise measurements of M_W and of the top quark mass (m_t) significantly constrain the mass of the, as yet, unobserved Higgs boson. Prior to the measurement presented here, the world average of $M_W = 80.399 \pm 0.023\,\text{GeV}$(1) and $m_t = 173.2 \pm 0.9\,\text{GeV}$, yielded a limit on the SM Higgs boson mass of $M_H < 161\,\text{GeV}$ at 95% confidence level (CL).

The previous measurement of M_W by the CDF Collaboration was determined to be $M_W = 80.413 \pm 0.048\,\text{GeV}$ [1] from $200\,\text{pb}^{-1}$ of data while a recent measurement by the DØ Collaboration from $1\,\text{fb}^{-1}$ of data gave $M_W = 80.401 \pm 0.043\,\text{GeV}$ [2]. Presented here is the most recent measurement made by CDF, utilizing data corresponding to $2.2\,\text{fb}^{-1}$ of integrated luminosity.

2. – Analysis strategy

At the Tevatron, W bosons are primarily produced in $q\bar{q}$ annihilation, $q\bar{q} \to W + X$, where X can include QCD radiation that results in measurable hadronic recoil in events.

(1) We use units where $c = 1$ throughout.

$W \to l\nu_l$ decays, where $l = e$ or μ, are selected with high purity by the CDF detector and used to measure M_W. As the longitudinal momentum of the neutrino is not measured, we use transverse(2) components of charged lepton momentum (p_T^l), neutrino momentum (p_T^ν) and the transverse mass,

$$m_T = \sqrt{2p_T(l)p_T(\nu)[1 - \cos(\phi_l - \phi_\nu)]}, \tag{1}$$

which depend only on measurable quantities of the W decay, to measure M_W. A Monte Carlo simulation is used to predict the shape of these distributions as a function of M_W. A binned maximum-likelihood fit of these predictions to the data is used to determine the W boson mass.

These line-shape predictions depend on the kinematic distributions of the W decay products and detector effects, which are constrained from control samples and theoretical calculations. The kinematic distributions are determined by several effects including internal QED radiation, the intrinsic W boson transverse momentum, and the proton parton distribution functions (PDFs). Detector effects include external bremsstrahlung and ionisation energy loss in the detector material, tracker momentum scale, calorimeter energy scale, resolutions of the tracker and calorimeter, and the detector acceptance. A sophisticated, fast simulation has been developed that enables a study of these effects at a level below 1 part in 10^4.

3. – Event generation and simulation

W boson events are generated with the RESBOS Monte Carlo [3], which captures the relevant QCD physics and models the W p_T spectrum. QED processes, including final-state photon radiation, are simulated using PHOTOS [4], and are cross-checked against HORACE [5].

Non-perturbative physics, which are described by parameters that must be determined from experimental data, affect the shape of the W boson p_T. We determine these parameters from a fit to the dilepton spectra of $Z \to ee$ and $Z \to \mu\mu$ candidate events.

Parton distribution functions (PDFs) affect the W boson mass measurement through their effects on the kinematics of the decay charged lepton and because the measurement only uses charged leptons in a restricted rapidity range. The uncertainty arising from the PDFs is evaluated using the 68% CL MSTW2008 [6] error set. This is cross-checked by comparing the 90% CL CTEQ6.6 [7] error set with the 90% CL MSTW2008 error set.

The tracker and calorimeter response and the electron and muon acceptance are simulated using a parameterized fast detector simulation. Tracks in the CDF drift chamber associated with electrons and muons are simulated at the hit level. Electrons and muons are propagated along a helical trajectory from the production point, stepping through the layers of passive material, whose effects are simulated. The most relevant processes are ionisation energy loss for muons, bremsstrahlung ($e \to e\gamma$) for electrons, and conversion ($\gamma \to e^+e^-$) for photons. Multiple Coulomb scattering is simulated in order to incorporate its effect on track resolution.

(2) CDF uses a cylindrical coordinate system with the z axis along the proton beam axis. Pseudorapidity is $\eta \equiv -\ln(\tan(\theta/2))$, where θ is the polar angle, and ϕ is the azimuthal angle relative to the proton beam direction, while $p_T = |p|\sin(\theta)$, $E_T = E\sin(\theta)$.

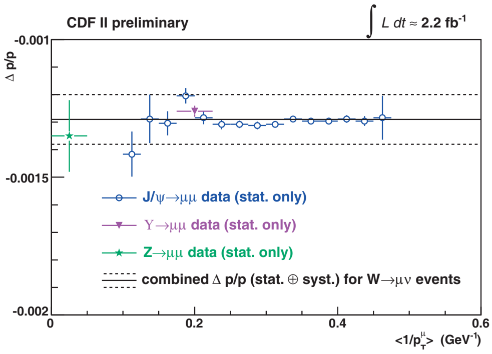

Fig. 1. – The fractional momentum correction for data as a function of the mean inverse momentum of muons from J/ψ, $\Upsilon(1S)$, and Z boson data.

The deposition of electromagnetic energy in the calorimeter for leptons and photons is simulated using parameterizations for the energy scale and resolution; energy loss in the solenoidal coil and due to longitudinal leakage; and non-linear response. The parameters for the scale and resolution, and the non-linearity, are fit from the data.

4. – Event selection

The event selection criteria for the W boson mass measurement are optimized to produce a sample with low background and which can be accurately modeled. W and Z boson candidates are selected by requiring the charged leptons have p_T greater than 30 GeV. Muon candidates are required to have hits in the muon detectors and electron candidates must have an E/p value of less than 1.6. Additionally two leptons of the same flavor and opposite charge as well as the mass of the dilepton system to be in the range $66 < m_{ll} < 116$ GeV are required for Z candidates. For W boson candidates, the recoil energy in the calorimeter is required to be less than 15 GeV, $\not{E}_T > 30$ GeV and $60 < m_T < 100$ GeV. These selection criteria are applied to data collected between February 2002 and September 2007. The data correspond to an integrated luminosity of 2.2 fb^{-1}. The selection criteria yield 470126 $W \to e\nu$ candidates and 624708 $W \to \mu\nu$ candidates.

5. – Momentum scale calibration

The high-statistics $J/\psi \to \mu\mu$ and $\Upsilon(1S) \to \mu\mu$ quarkonia decays, along with the $Z \to \mu\mu$ sample, are used to set the momentum scale. The momentum scale is extracted from a binned maximum-likelihood fit of the data to simulated invariant-mass templates generated using the world average values.

The J/ψ sample has the advantage that its cross section is sufficiently large to enable a study of the momentum scale as a function of other variables. The $\Upsilon(1S)$ resonance has an invariant mass three times larger than the J/ψ, and supplies an intermediate reference point to study the momentum dependence of the momentum scale. The Υ hadrons also have the advantage that they are all produced promptly, allowing a study of the momentum scale using tracks that are beam-constrained in the same way as the tracks in the W and Z samples. The consistency of the momentum correction obtained

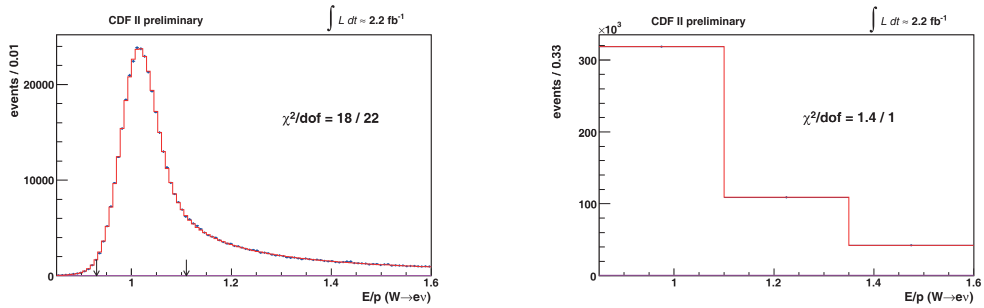

Fig. 2. – The E/p distribution of the $W \to e\nu$ data (points) used to determine the calorimeter energy scale (left) and to scale the radiative material in the simulation (right). The arrows indicate the fitting range used for the electron energy calibration.

from fits to J/ψ and Υ data can be seen in fig. 1. The combined momentum scale obtained from the J/ψ and Υ samples is applied to the W and Z samples.

The $Z \to \mu\mu$ mass fit is shown in fig. 3 (left), along with the statistical uncertainty and fit χ^2. A value of $m_Z = 91180 \pm 12_{\text{stat}} \pm 10_{\text{syst}}$ MeV is obtained, consistent with the world average value of $m_Z = 91188 \pm 2$ MeV [8]. The final momentum scale applied to the W boson data is obtained from combining the J/ψ, Υ, and Z measurements.

The tracking resolution is parameterized in the simulation by the tracking chamber hit resolution $\sigma_h = 150 \pm 3\,\mu$m and the beamspot size $\sigma_b = 35 \pm 3\,\mu$m, which affects track resolution through the beam-constraint in the track fit. We fix σ_h with the non-beam-constrained $\Upsilon(1S)$ mass distribution and σ_b with the beam-constrained Z mass distribution.

6. – Energy scale calibration

The electron cluster is simulated by merging energies of the primary electron and proximate bremsstrahlung photons and conversion electrons. The distribution of electron and photon energy loss in the solenoid coil and leakage into the hadronic calorimeter are determined using GEANT.

The electromagnetic calorimeter energy scale is set using the peak of the E/p electron distribution from $W \to e\nu$ events (fig. 2, left) and $Z \to ee$ events. The electromagnetic calorimeter non-linearity is determined from E/p fits as a function of transverse energy from the $W \to e\nu$ and $Z \to ee$ samples. The tail of the E/p distribution is used to tune the absolute number of radiation lengths in the tracker material, as shown in fig. 2 (right).

The electromagnetic calorimeter resolution is parameterized as

$$\sigma_E/E = 12.6\%/\sqrt{E_T} \oplus \kappa, \tag{2}$$

where κ is the non-stochastic term in the resolution. Two κs are defined. The first, κ_e, defines the smearing of the primary high-E_T electron and is tuned from the peak region of the E/p distribution. The second, κ_γ, smears the energy contribution of each of the secondary electromagnetic particles: the bremsstrahlung photons and the conversion electrons. κ_γ is tuned on the width of the $Z \to ee$ distribution selected using high E/p ($E/p > 1.06$) electrons.

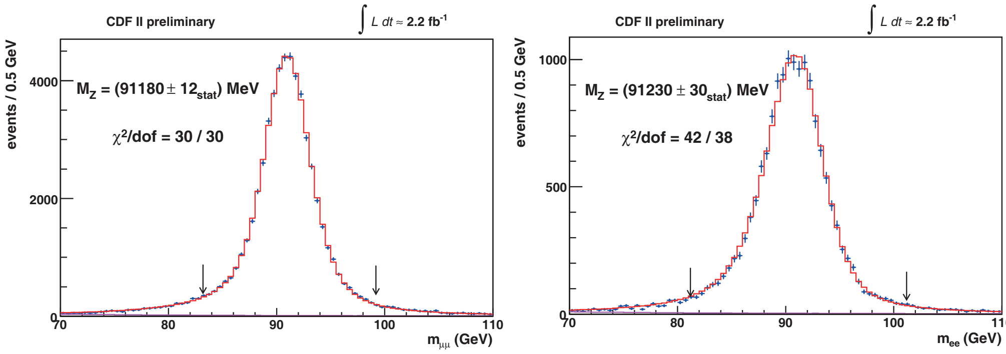

Fig. 3. – The maximum-likelihood fit to the $Z \to \mu\mu$ (left) and $Z \to ee$ (right) mass peaks, with the fitted mass values. The data (points) are shown along with the best-fit simulation template (histogram). The arrows indicate the fitting range.

The $Z \to ee$ mass is fitted to cross-check the energy scale and the non-linearity (fig. 3, right). A value of $m_Z = 91230 \pm 30_{\text{stat}} \pm 14_{\text{syst}}$ MeV is obtained, consistent with the world average. Thus, the measurements from E/p and the $Z \to ee$ mass are combined to obtain the final energy scale, applied to $W \to e\nu$ data.

7. – Recoil calibration

All particles recoiling against the W or Z boson are collectively referred to as the recoil. The recoil vector $\mathbf{u}$ is defined as the vector sum of transverse energy over all electromagnetic and hadronic calorimeter towers in the detector range $|\eta| < 2.4$. The calorimeter towers associated with the leptons are explicitly removed from the recoil calculation. A combination of minimum bias data and $Z \to ll$ data is used to model the behavior of the hadronic recoil, and $W \to l\nu$ data is used to cross-check the data corrections and the simulation.

The response of the calorimeter to the hadronic recoil is described by a response function, R, which scales the true recoil magnitude to simulate the measured magnitude.

The recoil resolution is assumed to have two components, which are summed vectorially: a "sampling" term representing the calorimeter "jet" resolution, and an underlying event component from the spectator and additional $p\bar{p}$ interactions.

$Z \to \mu\mu$ and $Z \to ee$ events are used to tune the recoil response and resolution parameters. The η axis is defined to be the geometric bisector of the two leptons and the ξ axis to be perpendicular to η. We project the vector p_T-balance onto the η and ξ axes and compare the data distribution to the simulation. Figure 4 shows the mean (left) and RMS (right) of the p_T-balancing in $Z \to ee$ events as a function of Z boson p_T.

8. – Backgrounds

Backgrounds passing the event selection cuts have different kinematic distributions from the W signal, and are therefore included in the template fits. The backgrounds to the $W \to \mu\nu$ and $W \to e\nu$ samples come from hadronic jet production, decays in flight, Z production, $W \to \tau\nu$ decays, and cosmic rays. The background rates and kinematics are determined using a combination of Monte-Carlo–based and data-based

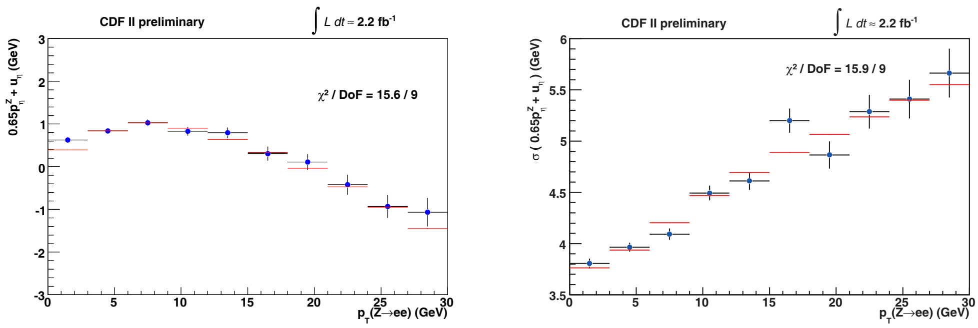

Fig. 4. – Mean value (left) and RMS (right) of the scaled p_T-balance projected onto the η axis as a function of $p_T(ll)$ for $Z \to ee$.

methods. Background fractions for the muon (electron) datasets are evaluated to be 7.35% (0.14%) from Z decays, 0.88% (0.93%) from $W \to \tau\nu$ decays, 0.04% (0.39%) from hadronic jets, 0.24% from DIF, and 0.02% from cosmic rays.

9. – Results and conclusions

The W boson mass is measured by performing a binned maximum-likelihood fit to the lepton p_T, neutrino p_T, and m_T distributions for each lepton channel. 1600 signal templates for M_W are generated between 80 GeV and 81 GeV and background templates are added with the shapes and normalisations described in sect. **8**. The final fit values were hidden during analysis by adding an unknown offset in the range [−75,75] MeV. The results of the fits to the m_T (fig. 5), p^l_T, and p^ν_T kinematic distributions for both the electron and muon channels are summarized in table I.

Fits of simulated data to Monte Carlo templates have been performed to measure the statistical correlation between the fits to the m_T, p^l_T and p^ν_T distributions. The final results are combined, taking these correlations into account, using the BLUE [9] method.

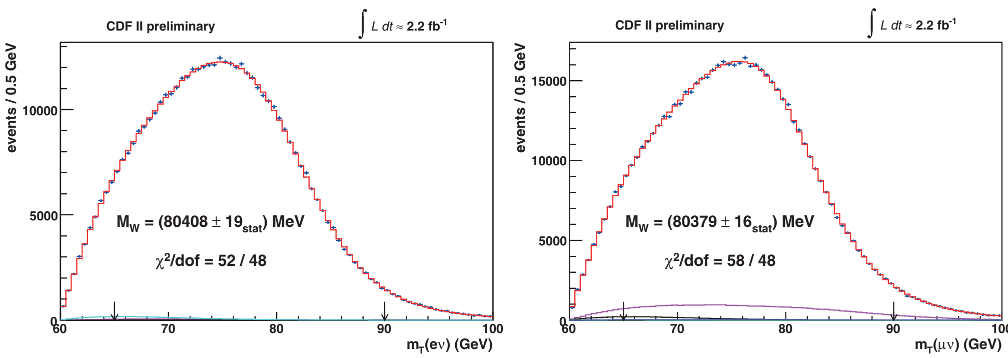

Fig. 5. – The W transverse mass fits for the electron (left) and muon (right) channels. The data (points) are shown along with the best-fit simulation template (red histogram). The background contributions to the template, including $Z \to ll$ (magenta histogram) and hadronic jets (cyan histogram), are overlaid. The arrows indicate the fitting range.

TABLE I. – *Fit results and uncertainties for M_W. The fit windows are* 65–90 GeV *for the m_T fit and* 32–48 GeV *for the p_T^ℓ and p_T^ν fits. The χ^2 of the fit is computed using the expected statistical errors on the data points.*

Distribution	W-boson mass (MeV)	χ^2/dof
$m_T(e,\nu)$	$80\ 408 \pm 19_{\mathrm{stat}} \pm 18_{\mathrm{syst}}$	52/48
$p_T^\ell(e)$	$80\ 393 \pm 21_{\mathrm{stat}} \pm 19_{\mathrm{syst}}$	60/62
$p_T^\nu(e)$	$80\ 431 \pm 25_{\mathrm{stat}} \pm 22_{\mathrm{syst}}$	71/62
$m_T(\mu,\nu)$	$80\ 379 \pm 16_{\mathrm{stat}} \pm 16_{\mathrm{syst}}$	58/48
$p_T^\ell(\mu)$	$80\ 348 \pm 18_{\mathrm{stat}} \pm 18_{\mathrm{syst}}$	54/62
$p_T^\nu(\mu)$	$80\ 406 \pm 22_{\mathrm{stat}} \pm 20_{\mathrm{syst}}$	79/62

TABLE II. – *Uncertainties for the final combined result on M_W.*

Source	Uncertainty (MeV)
Lepton energy scale and resolution	7
Recoil energy scale and resolution	6
Lepton removal	2
Backgrounds	3
$p_T(W)$ model	5
Parton distributions	10
QED radiation	4
W boson statistics	12
Total	19

Combining all six fits, we obtain a result of

$$M_W = 80\,387 \pm 12_{\mathrm{stat}} \pm 15_{\mathrm{syst}}\,\mathrm{MeV}, \tag{3}$$

or $M_W = 80\,387 \pm 19\,\mathrm{MeV}$. The systematic uncertainties for the combined result are shown in table II. In combination with previous measurements from LEP and the Tevatron, the updated world-average W boson mass is $M_W = 80\,390 \pm 16\,\mathrm{MeV}$. This updated world average impacts the global electroweak fits resulting in a revised upper bound on the Higgs boson mass of $M_H < 145\,\mathrm{GeV}$ at 95% CL.

* * *

The author would like to thank the organizers of La Thuile 2012 for the invitation to speak at a scientifically rewarding and well-organized conference. The author would also like to thank the dedicated team at the CDF Collaboration for the result presented, as well as the many funding agencies worldwide that make the Tevatron research program possible.

REFERENCES

[1] Aaltonen T. *et al.*, *Phys. Rev. Lett.*, **99** (2007) 151801.
[2] Abazov V. *et al.*, *Phys. Rev. Lett.*, **103** (2009) 141801.
[3] Balazs C. and Yuan C.-P., *Phys. Rev. D*, **56** (1997) 5558.
[4] Golonka P. and Was Z., *Eur. J. Phys. C*, **45** (2006) 97.
[5] Carloni Calame C. M. *et al.*, *JHEP*, **10** (2007) 109.
[6] Martin A. D., Stirling W. J., Thorne R. S. and Watt G., *Eur. Phys. J. C*, **63** (2009) 189.
[7] Pumplin J., Stump D., Huston J., Lai H.-L., Nadolsky P. and Tung W.-K., *JHEP*, **07** (2002) 012.
[8] The ALEPH, DELPHI, L3, OPAL, SLD Collaborations, *Phys. Rep.*, **427** (2006) 257.
[9] Lyons L., Gibaut D. and Clifford P., *Nucl. Instrum. Methods A*, **270** (1988) 110.

SESSION VI - HIGGS SEARCHES

IL NUOVO CIMENTO Vol. 35 C, N. 6 Novembre-Dicembre 2012
DOI 10.1393/ncc/i2012-11383-5

Colloquia: LaThuile12

Low-mass Higgs searches at the Tevatron

S. Desai on behalf of the D0 and CDF Collaborations
Fermi National Accelerator Laboratory - Batavia, IL, USA

ricevuto il 7 Settembre 2012

Summary. — We report on recent searches for a low-mass Higgs boson at the Tevatron $p\bar{p}$ collider. Sensitivity to a Higgs boson with a mass less than $\sim 135\,\text{GeV}$ arises dominantly from the production of a Higgs boson decaying to $b\bar{b}$, in association with a W or Z boson decaying leptonically. However additional sensitivity is gained by searching in other final states such as diphotons, or final states with τ leptons. Both the CDF and D0 collaborations have conducted searches in up to $10\,\text{fb}^{-1}$ of $p\bar{p}$ collisions collected at $\sqrt{s} = 1.96\,\text{TeV}$. The results from the two experiments are combined to set 95% confidence level limits on the Higgs production cross section. At a Higgs mass of 115 GeV, the observed (expected) limit is 1.17 (1.16) times the standard model cross section.

PACS 14.80.Bn – Standard-model Higgs bosons.
PACS 13.85.Rm – Limits on production of particles.

1. – Introduction

One of the most important unresolved problems in particle physics is the nature of electroweak symmetry breaking. The standard model (SM) addresses this problem through the Higgs mechanism. In addition to generating masses for the W and Z boson, this mechanism produces a heavy spin-0 particle: the Higgs boson (H).

Precision electroweak data, including the latest W boson mass measurements from CDF [1] and D0 [2], constrain the mass of a SM Higgs boson to $M_H < 152\,\text{GeV}$ [3] at 95% CL. Searches at the CERN LEP e^+e^- collider have excluded a SM Higgs boson with $M_H < 114\,\text{GeV}$ [4]. Previous searches at the Fermilab Tevatron $p\bar{p}$ collider [5] and by the CMS and ATLAS collaborations at the LHC using pp collisions have restricted the allowed range of M_H to 117–127 GeV [6, 7].

For $M_H \lesssim 135\,\text{GeV}$, the decay $H \to b\bar{b}$ dominates, and observation of this decay mode will be critical to the interpretation of any potential signal. At the Tevatron, Higgs bosons are produced primarily by gluon fusion through a top-quark loop: $gg \to H$. The large multijet background makes searches for $gg \to H \to b\bar{b}$ impractical. Instead, searches for $H \to b\bar{b}$ are focused on the associated production modes, in which the Higgs boson is produced with a W or Z boson that decays leptonically. The sensitivity of the Tevatron $p\bar{p}$ collider to the $H \to b\bar{b}$ mode complements searches at the LHC pp collider, where the sensitivity to a Higgs boson is driven by the $\gamma\gamma$, ZZ and WW decay modes.

Although the Tevatron reach is driven by the associated production modes, we adopt a strategy of searching for a Higgs signal in many different final states. Here, we also discuss searches for $gg \to H \to \gamma\gamma$; and for final states involving τ leptons that are sensitive to gluon fusion production, associated production, and vector boson fusion production: $q\bar{q} \to W(Z)qW(Z)\bar{q} \to Hq\bar{q}$. Moreover, searches that are traditionally used for $M_H \gtrsim 135\,\text{GeV}$ also contribute significant sensitivity in the low mass region, and are discussed elsewhere in these proceedings [8].

2. – Searches for $H \to b\bar{b}$

In the narrow range of M_H that has not yet been excluded, sensitivity to a Higgs boson at the Tevatron is dominated by the searches for WH and ZH production in which the Higgs boson decays to $b\bar{b}$, and the W or Z decays leptonically. Both CDF and D0 have conducted searches in the resulting $\nu\nu b\bar{b}$ [9,10], $\ell\nu b\bar{b}$ [11,12], and $\ell\ell b\bar{b}$ [13,14] final states, using integrated luminosities from 7.5–8.6 fb^{-1}.

2˙1. *Event selection.* – Both experiments select events with two electrons or two muons; exactly one electron or muon; or no charged leptons. Neutrinos are inferred through the presence of an imbalance of the total transverse momentum in the event ($\not{E}_{\text{T}}$). Events are also required to contain a Higgs boson candidate, consisting of two high-energy jets.

The backgrounds to these searches include the production of W or Z boson with jets, and $t\bar{t}$ and diboson (WW, WZ and ZZ) production. These backgrounds are estimated with Monte Carlo (MC) simulations. There is also a contribution from multijet events with non-prompt muons, or with jets that are misidentified as electrons. Such events can have a large apparent $\not{E}_{\text{T}}$ from the mismeasurement of jet energies. This background is estimated from control samples in the data. In the $\nu\nu b\bar{b}$ searches, multivariate discriminants provide a powerful tool to reduce the initially overwhelming multijet background.

At least one of the jets in the selected events must be identified as likely to originate from a b-quark (b-tagged). CDF uses two algorithms, one based on the reconstruction of displaced decay vertices within the jet, and one that uses high impact parameter tracks associated with the jet. D0 combines this information into a single neural network discriminant. The b-tagging efficiency for b-jets is typically 50–70%, whereas the the misidentfication rate for light jets is 0.5–5%, depending on the precise criterion applied. To maximize sensitivity, both experiments consider events with exactly one tagged jet, or with at least two tagged jets in independent samples.

2˙2. *Statistical analysis.* – After the final event selection, both experiments employ multivariate discriminants, based on neural networks or boosted decision trees, to separate the Higgs signal from the remaining backgrounds. Example distributions of the final discriminants from the D0 $\nu\nu b\bar{b}$ and CDF $\ell\nu b\bar{b}$ searches are shown in fig. 1. We obtain limits on the Higgs production cross section using a Bayesian technique [15].

The calculation compares the predicted background-only and signal-plus-background distributions of the multivariate discriminants to the corresponding distributions in the data. This is accomplished through the construction of a Poisson likelihood function in which the signal prediction is multiplied by an arbitrary scale factor, R; and both the signal and background predictions are functions of nuisance parameters with Gaussian

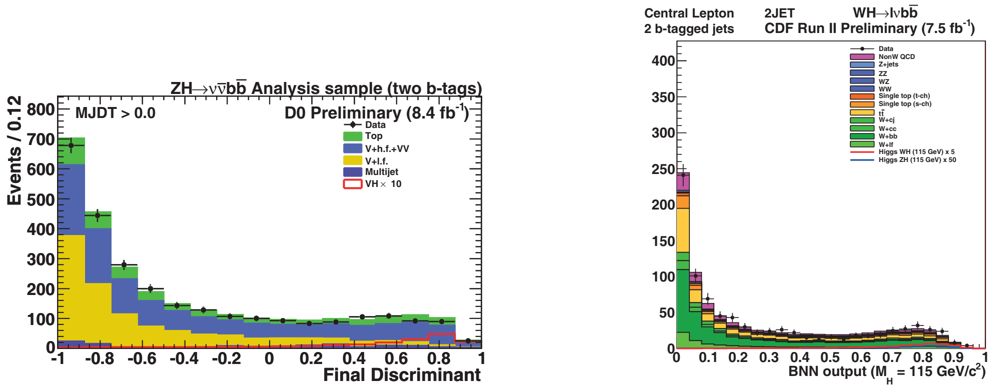

(a) (b)

Fig. 1. – Distributions of the final discriminants in events with two b-tagged jets from (a) the D0 $ZH \to \nu\nu b\bar{b}$ analysis, and (b) the CDF $WH \to \ell\nu b\bar{b}$ analysis.

distributions that account for systematic uncertainties. We integrate the likelihood function over the nuisance parameters, resulting in a one-dimensional function of R. The value of R that corresponds to 95% of the area of this distribution is the 95% CL upper limit on R. We check this calculation with a modified frequentist technique (CL_S) [16,17] that is found to yield consistent results.

2·3. *Results.* – Figure 2 shows the limits for WH/ZH production, with $H \to b\bar{b}$ as a ratio to the predicted SM rate. These searches exclude a SM Higgs boson with $100 < M_H < 108\,\text{GeV}$. For $M_H = 115\,\text{GeV}$, the observed (expected) limit is a factor of 1.18 (1.26) greater than the SM prediction. To validate the analysis techniques, we have also searched for diboson production in which one weak boson decays leptonically, and one hadronically, yielding cross section times branching ratio measurements that are in agreement with the SM. This test is discussed elsewhere in these proceedings [18].

3. – Searches in final states with τ leptons

Searches in final states with τ leptons are sensitive to $gg \to H$ as well as the associated and vector boson fusion production mechanisms. In the associated production mechanism, the τ lepton can originate from either the Higgs boson decay or from the decay of a W or Z boson. Because of the diversity of signal production modes, searches in this final state offer a sensitivity that depends only weakly on the mass of the Higgs boson.

D0 has conducted a search using a data set of $7.0\,\text{fb}^{-1}$ in a final state with a muon and two hadronically decaying τ leptons [20]. This result is reported here for the first time. Because of the presence of a third lepton, this analysis is primarily sensitive to the associated production mechanisms. Selected events are categorized according to the number of jets present in the event, to take advantage of the different signal-to-background ratios for different jet multiplicities. The final discriminant used to extract results is H_T, the scalar sum of the $\not{E}_T$ and the transverse momenta of the leptons and jets, shown for zero-jet events in fig. 3a. For $M_H = 115\,\text{GeV}$, the limit on the cross section is 11 times the SM prediction, with an expected limit equal to 14 times the SM prediction.

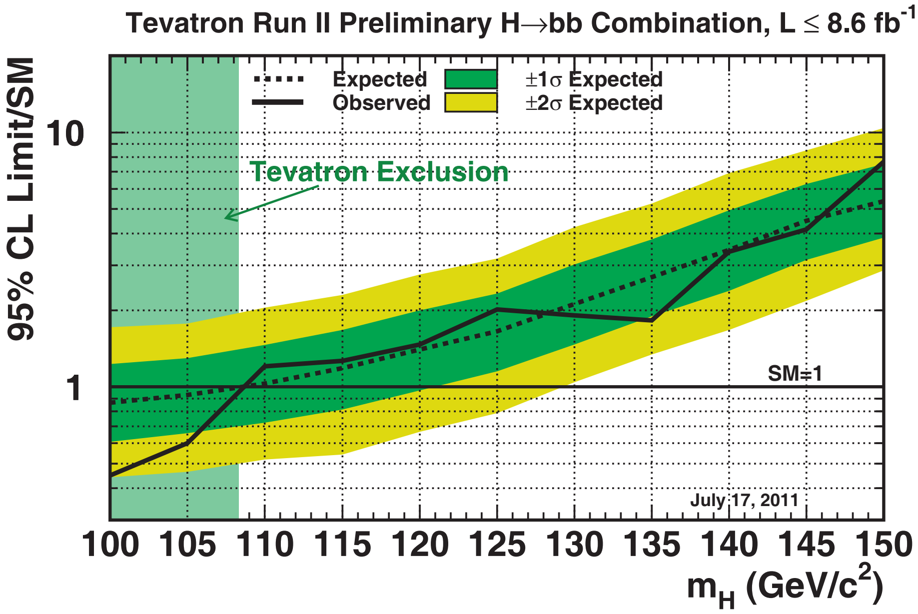

Fig. 2. – Expected and observed 95% CL cross section upper limits, from the combination of all Tevatron searches for WH/ZH production, with $H \to b\bar{b}$. Limits are expressed as a ratio to the SM production rate. Also shown are the one (green) and two (yellow) standard deviation variations about the expected limits.

The CDF $\tau\tau$+jets analysis [21] is divided into two independent samples: the $e\mu$ sample which contains events with one electron and one muon; and the $e/\mu + \tau$ sample, which contains events with one electron or muon and a hadronically decaying τ. Selected events in each sample must also contain at least one jet, and are further categorized according to jet mutliplicity.

Support vector machines (SVMs) are used as final discriminants to search for a signal. An independently trained SVM is used for each subsample. Figure 3b displays the resulting distribution for the $e/\mu + 2$ jet sample. For $M_H = 115\,\text{GeV}$, CDF observes a limit of 12 times the predicted SM rate, and expects a limit of 13 times the SM rate.

4. – Searches for $H \to \gamma\gamma$ production

Both D0 [22] and CDF [23] search for a Higgs boson decaying to the diphoton final state. Both have been updated to use the full Tevatron dataset since the most recent Tevatron combined Higgs search [19], and have achieved improvements in sensitivity of 15–25% beyond the expectation from the additional data.

The D0 search uses a Monte Carlo simulation to estimate the background from $Z/\gamma^* \to e^+e^-$, in which electrons are misidentified as photons. Other backgrounds include direct production of diphoton events as well as photon plus jet and dijet events, in which one or more jets is misidentified as a photon. These backgrounds are estimated from control samples in the data. D0 then uses boosted decision trees (BDTs) to search for the presence of a Higgs boson. The BDT distribution for $M_H = 120\,\text{GeV}$ is shown in fig. 4a. The observed upper limit on the cross section times branching ratio

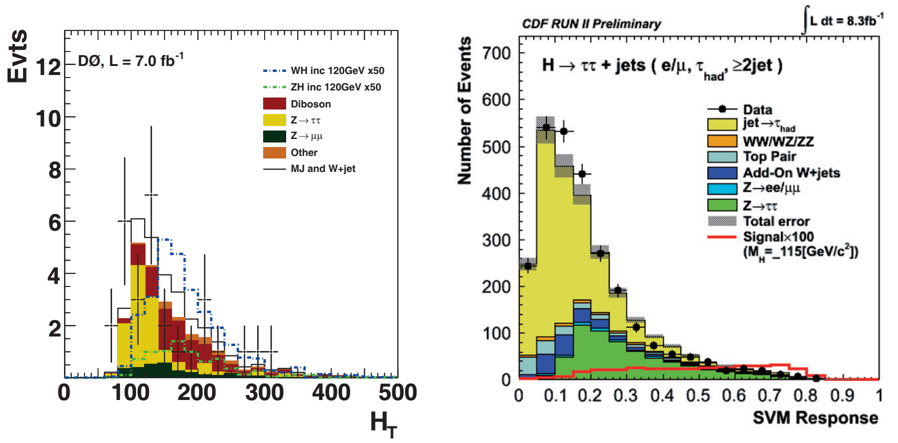

(a) (b)

Fig. 3. – Distributions of the final discriminants (a) in D0 $\tau\tau\mu$ search in events with no jets, and (b) in the CDF $\tau\tau$+jets search in events with one electron or muon, one hadronically decaying τ and at least two jets.

at $M_H = 115\,\text{GeV}$ is a factor of 8.4 larger than the SM prediction, with an expected sensitivity of 12 times the SM prediction.

The CDF analysis extends the selection of two photons to include events in the forward calorimeter. A specialized reconstruction is used to identify photons that have converted to e^+e^- pairs. The diphoton mass spectrum, shown in fig. 4b is used as the final discriminant. The background is estimated using a sideband fit. For $M_H = 115\,\text{GeV}$, the observed upper limit on the cross section times branching ratio is a factor of 11 larger than the SM prediction, with an expected sensitivity of 13 times the SM prediction.

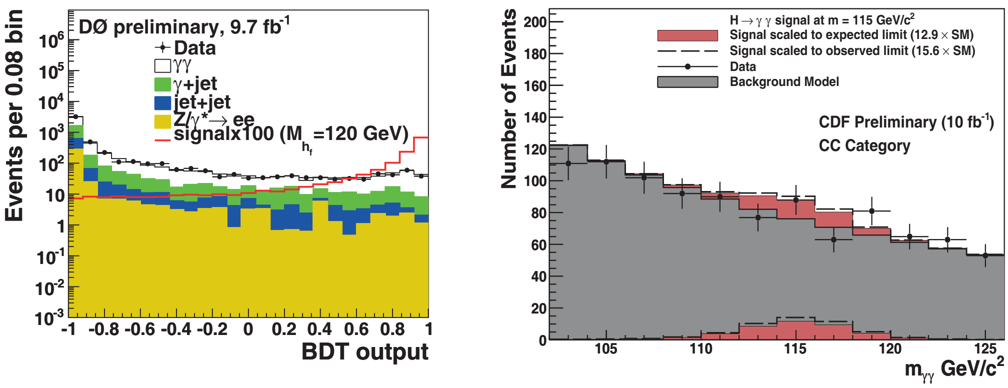

(a) (b)

Fig. 4. – Distributions of (a) the BDT trained to identify SM Higgs with $M_H = 120\,\text{GeV}$ in diphoton events from D0, and (b) the diphoton mass spectrum from CDF in events with two central photons.

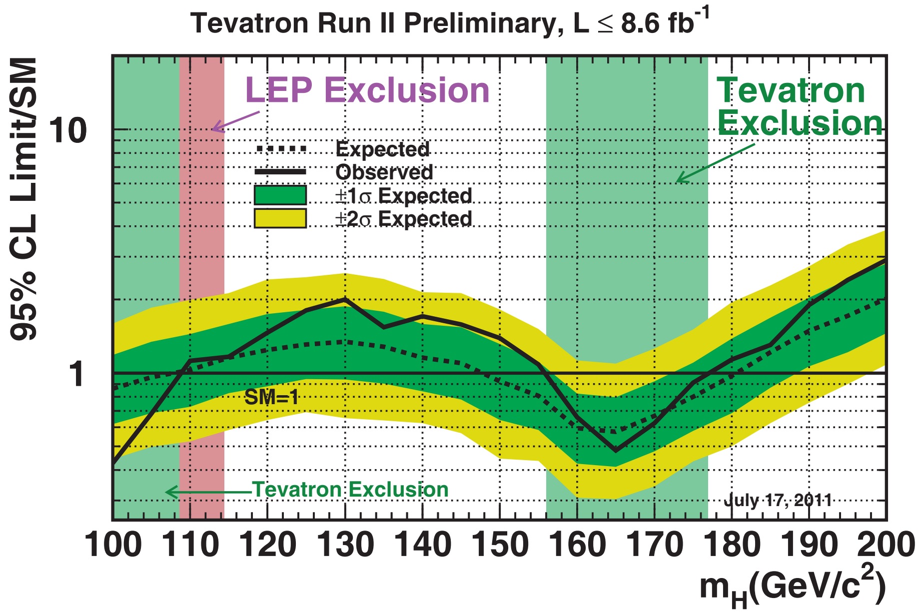

Fig. 5. – Expected and observed 95% CL cross section upper limits, from the combination of all Tevatron searches. Limits are expressed as a ratio to the SM production rate. Also shown are the one (green) and two (yellow) standard deviation variations about the expected limits.

5. – Combined Higgs search results

For a wide range of M_H there is no single search channel that is sensitive to the presence of a SM Higgs boson. Therefore the CDF and D0 collaborations have combined the results of all SM Higgs searches conducted at the Tevatron [19], although several of the searches presented here were not included in this combination. Figure 5 shows the expected and observed limits as a function of M_H, expressed as ratio to the rate predicted by the SM. For $M_H = 115\,\text{GeV}$, the observed (expected) limit is 1.17 (1.16) times the SM rate.

6. – Summary

In the summer of 2011, the CDF and D0 collaborations released a combined search for the Higgs boson that approaches sensitivity to the SM prediction across the entire range of allowed masses. At $M_H = 115\,\text{GeV}$, the observed (expected) limit is a factor of 1.17 (1.16) larger than the SM expectation. The combination of the Tevatron $H \to b\bar{b}$ searches results in an observed (expected) limit on Higgs boson production is a factor of 1.18 (1.26) larger than the SM prediction. The Tevatron sensitivity in this primary decay mode complements the LHC sensitivity in other decay modes, and will provide important insights into the nature of electroweak symmetry breaking.

* * *

The author would like to thank the organizers for a stimulating conference with many interesting presentations.

REFERENCES

[1] Aaltonen T. *et al.* (CDF Collaboration), *Phys. Rev. Lett.*, **108** (2012) 151803.
[2] Abazov V. M. *et al.* (D0 Collaboration), *Phys. Rev. Lett.*, **108** (2012) 151804.
[3] The LEP Electroweak Working Group, "Status as of March 2012", `http://lepewwg.web.cern.ch/LEPEWWG`.
[4] The LEP Higgs Working Group, *Phys. Lett. B*, **565** (2003) 61.
[5] The Tevatron New Phenomena and Higgs Working Group, arXiv:1007.4587 [hep-ex] (2010).
[6] The CMS Collaboration, CMS-PAS-HIG-11-032 (2011).
[7] The ATLAS Collaboration, *Phys. Lett. B*, **710** (2012) 49.
[8] Denis R. St., these proceedings.
[9] The D0 Collaboration, D0 Note 6223-CONF (2011).
[10] The CDF Collaboration, CDF Conference Note 10583 (2011).
[11] The D0 Collaboration, D0 Note 6220-CONF (2011).
[12] The CDF Collaboration, CDF Conference Note 10596 (2011), The CDF Collaboration, CDF Conference Note 10217 (2010).
[13] The D0 Collaboration, D0 Note 6256-CONF (2011).
[14] The CDF Collaboration, CDF Conference Note 10593 (2011), The CDF Collaboration, CDF Conference Note 10572 (2011).
[15] The CDF Collaboration, CDF Conference Note 10609 (2011).
[16] Junk T., *Nucl. Instrum. Methods Phys. Res. A*, **434** (1999) 435; Read A., *J. Phys. G*, **28** (2002) 2693.
[17] Fisher W., FERMILAB-TM-2386-E (2007).
[18] Enari Y., talk presented at this conference.
[19] The Tevatron New Phenomena and Higgs Working Group, arXiv:1107.5518 [hep-ex] (2011).
[20] The D0 Collaboration, D0 Note 6286-CONF (2012).
[21] The CDF Collaboration, CDF Conference Note 10625 (2011).
[22] The D0 Collaboration, D0 Note 6297-CONF (2012).
[23] The CDF Collaboration, CDF Conference Note 10737 (2012).

IL NUOVO CIMENTO Vol. 35 C, N. 6 Novembre-Dicembre 2012
DOI 10.1393/ncc/i2012-11384-4

Colloquia: LaThuile12

Tevatron results on the Standard Model Higgs search in the high-mass region

R. St. Denis on behalf of the CDF and D0 Collaborations

Department of Physics and Astronomy, University of Glasgow - Glasgow G12 8QQ, UK

ricevuto il 7 Settembre 2012

Summary. — Results for the Tevatron search for the Higgs boson decaying to W boson pairs in proton antiproton collisions at $\sqrt{s} = 1960\,\mathrm{GeV}/c^2$ are presented. The CDF results are based on the entire Tevatron Run II dataset having an integrated luminosity of $9.7\,\mathrm{fb}^{-1}$. The CDF results exclude a Standard Model Higgs at 95% confidence level for a Higgs mass M_H in the range $148 \leq M_H \leq 173\,\mathrm{GeV}/c^2$ with an expected sensitivity of $153 \leq M_H \leq 177\,\mathrm{GeV}/c^2$, comparable to the previous Tevatron combined sample from July 2011.

PACS 14.80.Bn – Standard-model Higgs bosons.

1. – Introduction

The Tevatron experiments have enjoyed an annual doubling of the integrated luminosity delivered and recorded until the programme ended on September 30, 2011 after nearly 26 years of operation. This has led to an avalanche of new results in the area of electroweak symmetry breaking and in particular in direct searches for the source of electroweak symmetry breaking in the standard model [1], the Higgs Boson [2]. The physics reach of the Tevatron is built on a mountain of measurements that confirm the ability of the Tevatron collaborations to use the detectors to find new particles. Each measurement is of itself a significant result. Measurements begin with the largest cross section processes, those of B physics, but move on to processes with small branching ratios and backgrounds that are hard to distinguish from the signal. The measurement of B_s oscillations [3] demonstrates the performance of the silicon tracking and vertexing. Discovery of single-top production [4], WZ production [5], and evidence for the ZZ production [6] in leptonic, neutrino hadronic modes [7] provide the final base camp from which the Higgs summit is in sight. Multivariate techniques in the Higgs analysis are at the heart of what is required to reach sensitivity to the Higgs. Processes such as single top and ZZ act as important messengers heralding the impending arrival of the Higgs. This journey through lower and lower cross section processes represents our approach to provide convincing evidence of these processes, first as discovery then as measurements that constrain the Standard Model.

2. – Direct searches for the Standard Model Higgs

The Higgs searches at the Tevatron are separated into "high"- and "low"-mass channels. The high-mass channel is characterized by the decay mode $H^0 \to W^+W^-$ whereas the low-mass channels focus on decays to b quark-antiquark pairs or tau pairs.

There are four main production mechanisms for the Standard Model Higgs at the Tevatron: gluon fusion, $gg \to H^0$, associated production or "Higgsstrahlung", $q\bar{q} \to (W^\pm/Z^0)H^0$, and vector boson fusion (VBF), $q\bar{q} \to W(Z)q'W(Z)\bar{q}' \to H^0 q'\bar{q}'$. In all cases the high-mass Higgs search uses the decay modes into charged leptons and neutrinos: $H^0 \to W^+W^- \to \ell^+\ell^-\bar{\nu}_{\ell+}\nu_{\ell-}$. The charged leptons ℓ may be electrons, muons or taus. In the case of taus current searches include the τ decay channels $\tau^- \to e^-\bar{\nu_e}$ or $\tau^- \to \mu^-\bar{\nu_\mu}$ and charge conjugate channels. Hadronic decays of the τ from one W where the other W decays to an electron or muon are also studied and new results on trilepton analysis where two of the leptons are electrons or muons and the third is a tau is reported here for the first time. Channels with four leptons include the "golden channel" of $H^0 \to Z^0Z^0 \to \ell^+\ell^-\ell^+\ell^-$ as well as $Z^0H^0 \to W^+W^- \to \ell^+\ell^-\ell^+\ell^-\bar{\nu}_{\ell+}\nu_{\ell-}$.

The search for the decay of Higgs to W boson pairs which decay to leptons has sensitivity that is comparable to any of the low mass modes down to a Higgs mass of about $M_h = 120$ to $130\,\mathrm{GeV}/c^2$ and reach above $170\,\mathrm{GeV}/c^2$ with the best sensitivity around $M_h = 2M_w$, where M_w is the W boson mass. The high-mass mode is characterized by two high-transverse-momentum oppositely charged leptons which have a spin correlation that leads to angular correlations between the charged leptons that distinguish it from other Standard Model modes of charged-dilepton production. Requiring that the charged leptons be isolated removes the large number of charged dileptons from B decays as evidenced by the fact that the kinematics of the remaining dilepton events are well described by the Drell-Yan predictions. Drell-Yan production is the dominant source of oppositely charged lepton pairs at the Tevatron. These leptons tend to have an azimuthal separation of 180 degrees and these events are easily distinguished from Higgs events because they have no missing transverse energy. Once a transverse energy cut is applied, the background composition depends on the number of jets and the invariant mass of the leptons, $M_{\ell\ell}$. A majority of events are examined with the requirement that $M_{\ell\ell} > 16(15)\,\mathrm{GeV}/c^2$ CDF (D0). Events with 0 jets are dominated by WW background while those with 1 jet have a background consisting of a mixture of Drell Yan and WW. Events with two more jets sample are dominated by top quarks. The analysis is divided into distinct samples by the number of jets. D0 also divides the samples further by dilepton type: e^+e^-, $\mu^+\mu^-$ and $\tau^+\tau^-$. CDF also does an analysis of $M_{\ell\ell} < 16\,\mathrm{GeV}/c^2$ where the dominant background is $W\gamma$ production. The charged leptons in the WW background tend not to have the strong azimuthal correlation offered by the Higgs decay. In CDF care was taken in defining the lepton isolation such that a second lepton candidate within the lepton isolation cone was removed in determining the isolation energy. Other differences in kinematic variables between the background and signal are exploited by using the multivariate techniques described in the next section. Results for the high mass Higgs are shown for the D0 analysis in fig. 1 for $H^0 \to W^+W^- \to \mu^-e^+\bar{\nu}_\mu\nu_e$ and complex conjugate modes.

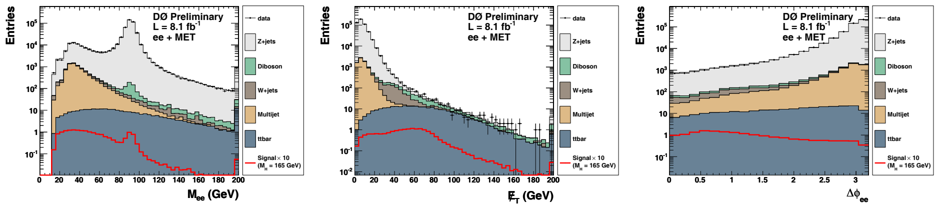

Fig. 1. – The invariant mass of isolated dileptons (left), the $\not{E}_{\mathrm{T}}$ spectrum of isolated leptons (center) and the cosine of the angle between dileptons after cuts for input to the discriminant analysis for the D0 experiment.

3. – Multivariate techniques

The major multivariate techniques in use are the Boosted Decision Trees (BDT) (used by D0 and CDF) and the Matrix Element (ME) and the Neural Net (NN) used by CDF. These are compared and contrasted here.

In CDF the ME method employs leading-order computations of the matrix elements for the signals and backgrounds. The inputs are the measured four-vectors of the leptons and jets and the x- and y-components of the missing transverse energy. The probability that these values represent each physics process is computed by integrating over the matrix element while convoluting the matrix element quantities with a *transfer function* that converts them to values that are observable. This transfer function represents the detector resolution and may include initial state radiation effects. A likelihood discriminator is formed by taking the ratio of the probability that the observed quantities represent the signal, divided by the total probability that the event is signal plus the probabilities that the event is background. The background probabilities are weighted according to their relative abundances. The computation of these probabilities is carried out on a set of simulated background and signal events. The distribution of the ME computation for each background and the signal is used to form a *template*.

At this point the analysis proceeds as for any cut analysis, with the likelihood ratio being used in place of a kinematic quantity such as the angular separation of the charged leptons. The data distribution is computed and the data are fitted to the templates with the signal normalization allowed to vary freely and the background normalizations constrained within the estimated systematic uncertainties. The probability that the background represents the data compared to the probability that the background plus the signal represents the data is evaluated by performing a number of pseudoexperiments on the background alone to represent the statistical accuracy of the data in the absence of a signal, and the distribution of the cross sections is formed. This distribution is compared to the fit result for the actual data and the probability that the data are consistent with background is computed by determining the number of pseudoexperiments that have a value less than or equal to that observed. If the data lie within 95% of the experiments performed, a limit is set. If the data exceed expectations then a cross section can be determined.

The NN approach contains similar elements to that of the ME. First there is a matrix element computation performed in both followed by a conversion of values from the ideal four vectors to the observed quantities. These values are sampled over some region of phase space. In the case of the ME, the phase space is spanned using a program that performs a numerical integral over that space whereas in the NN, simulated events that are meant to span a sufficient portion of the phase space are generated and the minimization of the NN determines the overall response. Each has limitations in numerical methods of the integration and in the representation of the response of the detector.

The two approaches also contain complementary characteristics. While the four vectors that are input to the ME are easy to identify, the functional form that characterizes the physics is not obvious. This becomes important in understanding how to determine the systematic uncertainties. For example, the Higgs to WW decay mode must depend on the angle of the leptons and hence it is important to determine how well the detector measures these angles. For the NN it is less obvious what values to choose and one must make a guess at what will be the important variables. Simply giving the same four vectors that were input to the ME may fail to work well if the statistics for populating the phase space is poor and variables that are not helpful in discriminating are examined by the NN. However, the most sensitive variables can be determined and the systematic uncertainties are evaluated by a straightforward variation of the most important discriminator and examination of the change of the output distribution.

The differences in the approaches can be exploited to help determine the quantities that are important in the ME computation while at the same time providing evidence that the quantities needed in the NN computation have been included. This is accomplished by including the ME computation as input to the NN. If this shows significant improvement, then important values have been missed in the NN inputs. If there is little change, then values can be removed from the input list of the NN until a change is noticed, or conversely, they can be added one at a time. This shows which quantities are most important in the ME.

D0 uses two separate BDT trainings. The BDT operates by optimizing a set of cuts and determining the best to be used. One of the D0 BDTs is used to eliminate the Drell-Yan (DY) background and the second is used on the remaining sample to separate the surviving background from the Higgs.

3˙1. *Control regions*. – Control regions play an important role in the quantitative computation of backgrounds and their systematic uncertainties and in determining that the lepton identification is properly done. For example in the $H^0 \to W^+W^- \to (e)\mu^-\tau^+\bar{\nu}_{(e)\mu}\nu_\tau$ where the τ decays hadronically, requiring the invariant mass of the τ and (e)μ to be larger than $20\,\mathrm{GeV}/c^2$, $\not{E}_\mathrm{T} < 20\,\mathrm{GeV}/c^2$ and the azimuthal separation of the (e)μ and the missing transverse energy to be less than 0.5 leads to a very pure sample of $Z \to \tau^+\tau^-$ decays in which the tau properties may be examined and systematic uncertainties in the difference between the simulation and data can be determined. Another important example is in the CDF analysis using $M_{\ell\ell} < 16\,\mathrm{GeV}/c^2$. Here two control regions are defined to determine the main background, $W\gamma$ and the Drell-Yan production. The $W\gamma$ events arise from a lepton from the W and a conversion electron from the γ. By choosing a sample of events selected identically to those for the Higgs analysis except for requiring the signs of the leptons to be the same. MadGraph [8] is used and it is found to agree with the data within statistics. The other control region is a sideband region in $\not{E}_\mathrm{T}$ with $15 < \not{E}_\mathrm{T} < 25\,\mathrm{GeV}$.

3˙2. *Channels with smaller contributions*. – Associated production with $H^0 \to W^+W^-$ leads to events with two charged leptons having the same sign, or to trilepton events. While the yields of these are much lower than of gluon fusion, the background compositions are very different: there is very little background. These channels are important to study because if an excess begins to emerge in one of the channels with larger

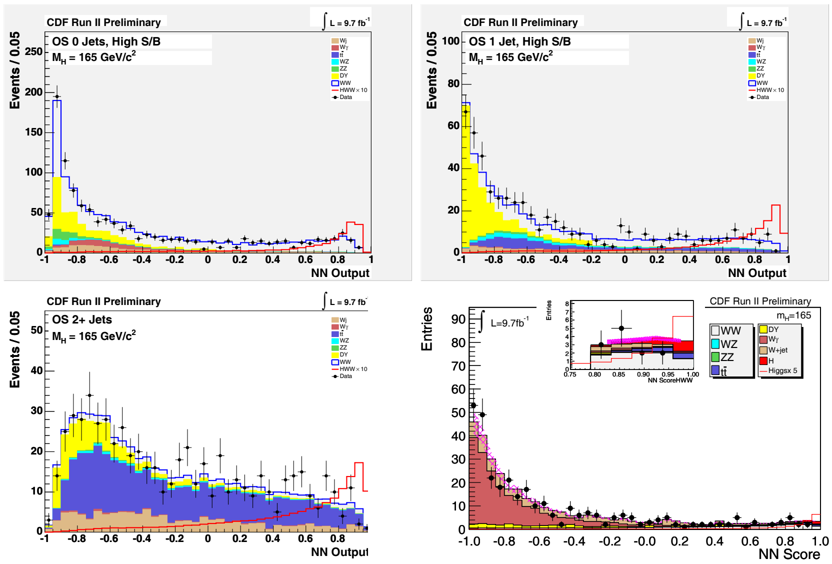

Fig. 2. – The Neural Net score distribution for opposite-sign dileptons in the 0, 1 and 2 jet for $M_{\ell\ell} > 16\,\text{GeV}/c^2$ and $M_{\ell\ell} < 16\,\text{GeV}/c^2$ channels.

signal but also more background, these channels confirm the observation with a small number of events where very little background is expected and since the main background to these analyses is WZ production, it is a different background.

3˙3. *Results.* – Representative results for the neural net analysis are shown in fig. 2 before the fit is performed. The data having low neural net score values provide a strong control over the background and its dynamics as reflected in the neural net. The contribution of a Higgs signal is fit simultaneously with variation of the backgrounds within their uncertainties but as constrained by the NN distribution. It is also noteworthy that for $M_H = 165\,\text{GeV}/c^2$ CDF expect of order 70 Standard Model Higgs events in the full data sample. Results for the trilepton searches are illustrated in fig. 3 for ZH, $Z \to l^+l^-$, $H \to W^+W^- \to l^\pm q\bar{q}'$ and in WH, where one of the leptons may be a tau decaying hadronically.

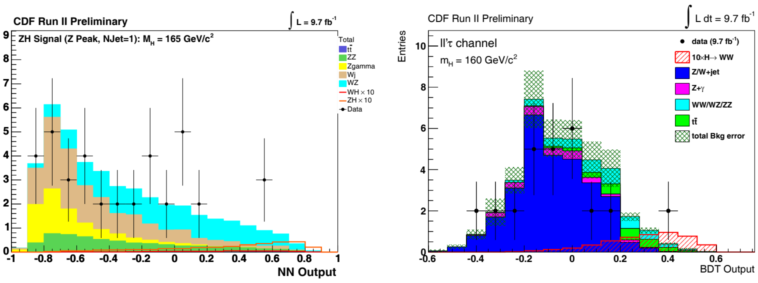

Fig. 3. – Neural net score distribution for for trileptons where opposite-sign pair invariant masses are in a 10 GeV window around the Z mass (left) and BDT distribution for the case where one of the trileptons is a hadronic tau (right).

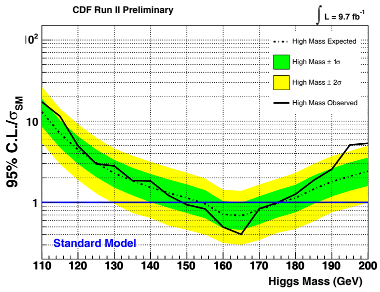

Fig. 4. – 95% confidence limits on the Standard Model Higgs boson for various masses for CDF for the $9.7\,\mathrm{fb}^{-1}$ analysis.

3˙4. *Limits*. – As described in sect. **3** a fit to the cross section for a particle having the dynamics of a Standard Model Higgs is performed on the NN or BDT distributions. The CDF results using $9.7\,\mathrm{fb}^{-1}$ of integrated luminosity are shown in fig. 4, the D0 results and the Tevatron combination from July 2011 may be found in [9]. The sensitivity to the Standard Model Higgs cross section covers the range $153 \leq M_H \leq 177\,\mathrm{GeV}/c^2$ with an observed 95% exclusion probability in the range $148 \leq M_H \leq 173\,\mathrm{GeV}/c^2$.

4. – Conclusions

This conference is held at a remarkable moment in the understanding of electroweak symmetry breaking. Rapid changes in data collection and more sophisticated experimental technique are leading to a constantly changing picture. The Tevatron has delivered more than $8\,\mathrm{fb}^{-1}$ and has recently improved its luminosity by another 20%. Evidence and discovery of channels in WZ, ZZ and single top, the messengers of the Higgs, have now been observed. Of particular note is the observation of the hadronic modes of the W/Z in the WW and ZZ production. The strategy of "no channel too small" has been successful, lending additional sensitivity and a different background composition. The CDF results based on the full Tevatron dataset has sensitivity to the Standard Model Higgs Boson in the range $153 \leq M_H \leq 177\,\mathrm{GeV}/c^2$ with an observed 95% exclusion probability in the range $148 \leq M_H \leq 173\,\mathrm{GeV}/c^2$.

* * *

The author would like to thank the organizers for this invitation to speak and the wonderful atmosphere of the conference.

REFERENCES

[1] Glashow S. L., *Nucl. Phys.*, **22** (1961) 579; Weinberg S., *Phys. Rev. Lett.*, **19** (1967) 1264; Salam A., "*Proceedings of the 8th Nobel Symposium*", 367 (1969).

[2] Englert F. and Brout R., *Phys. Rev. Lett.*, **13** (1964) 321; Higgs Peter W., *Phys. Rev. Lett.*, **13** (1964) 508; Higgs Peter W., *Phys. Lett.*, **12** (1964) 132.

[3] Abulencia A. *et al.*, *Phys. Rev. Lett.*, **97** (2006) 242003.

[4] Abazovy V. M. *et al.* (The D0 Collaboration), *Phys. Rev. Lett.*, **98** (2007) 181802, Aaltonen T. *et al.* (The CDF Collaboration), *Phys. Rev. Lett.*, **103** (2009) 092002.

[5] Abazov V. M. *et al.* (The D0 Collaboration), *Phys. Rev. Lett.*, **95** (2005) 141802, Abazov V. M. *et al.* (The D0 Collaboration), *Phys. Rev. D*, **76** (2007) 111104, Abulencia A. *et al.* (The CDF Collaboration), *Phys. Rev. Lett.*, **98** (2007) 161801.
[6] Abulencia A. *et al.* (The CDF Collaboration), *Phys. Rev. Lett.*, **100** (2008) 201801, Abazov V. M. *et al.* (The D0 Collaboration), *Phys. Rev. Lett.*, **101** (2008) 171803.
[7] Abazov V. M. *et al.* (The D0 Collaboration), *Phys. Rev. Lett.*, **102** (2009) 161801, Aaltonen T. *et al.* (The CDF Collaboration), *Phys. Rev. D*, **82** (2010) 112001.
[8] Alwall J. *et al.*, *JHEP*, **06** (2011) 128.
[9] Proceedings of Science: `http://pos.sissa.it/cgi-bin/reader/conf.cgi?confid=134`.

IL NUOVO CIMENTO Vol. 35 C, N. 6 Novembre-Dicembre 2012
DOI 10.1393/ncc/i2012-11385-3

Colloquia: LaThuile12

Search for the Standard Model Higgs boson at ATLAS

J. Tanaka on behalf of the ATLAS Collaboration

International Center for Elementary Particle Physics and Department of Physics
The University of Tokyo - Tokyo, Japan

ricevuto il 7 Settembre 2012

Summary. — A search for the Standard Model Higgs boson has been performed with the ATLAS experiment at the LHC using data corresponding to integrated luminosities from $1.04\,\mathrm{fb}^{-1}$ to $4.9\,\mathrm{fb}^{-1}$ of pp collisions collected at $\sqrt{s} = 7\,\mathrm{TeV}$ in 2011. The Higgs boson mass ranges 112.9–115.5 GeV, 131–238 GeV and 251–466 GeV are excluded at the 95% confidence level, while the range 124–519 GeV is expected to be excluded in the absence of a signal. An excess of events is observed around the mass of 126 GeV with a local significance of 3.5 standard deviations. The global probability for the background to produce such a fluctuation anywhere in the explored Higgs boson mass range 110–600 GeV is estimated to be $\sim 1.4\%$, or 2.2 standard deviations from the background-only hypothesis.

PACS 14.80.Bn – Standard-model Higgs bosons.

1. – Introduction

The discovery of the Standard Model (SM) Higgs boson [1-3] is one of the primary goals of the ATLAS experiment [4] at the Large Hadron Collider (LHC) [5], to understand the mechanism of electroweak symmetry breaking and the origin of mass of elementary particles. Direct searches at the CERN LEP e^+e^- collider excluded the production of a SM Higgs boson with mass below 114.4 GeV at the 95% confidence level (CL) [6]. Searches at the Fermilab Tevatron $p\bar{p}$ collider have excluded the production of a Higgs boson with mass between 156 GeV and 177 GeV at the 95% CL [7].

In 2011, the ATLAS experiment collected and analysed data with an integrated luminosity up to $4.9\,\mathrm{fb}^{-1}$ fulfilling all the data quality requirements to search for the SM Higgs boson. In this paper, the analysis and results of three different channels, $H \to \gamma\gamma$ [8], $H \to ZZ^{(*)} \to \ell^+\ell^-\ell'^+\ell'^-$ [9], and $H \to WW^{(*)} \to \ell^+\nu\ell'^-\bar{\nu}$ [10] are briefly summarized. A combined search [11] is presented which includes also $H \to ZZ \to \ell^+\ell^-\nu\bar{\nu}$ [12], $H \to ZZ \to \ell^+\ell^-q\bar{q}$ [13] and $H \to WW \to \ell\nu q\bar{q}'$ [14] channels, covering a mass range of 110–600 GeV.

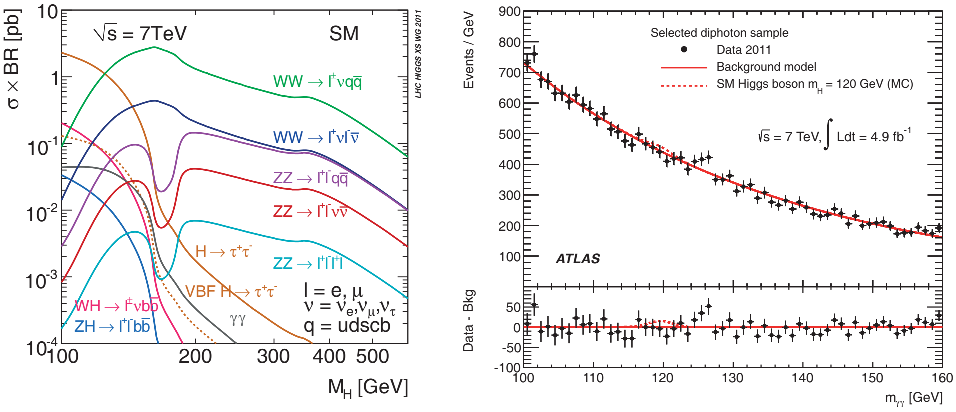

Fig. 1. – Left: SM Higgs boson production cross section times branching ratio [15] for several SM Higgs boson decay channels as a function of Higgs boson mass. Right: Invariant-mass distribution [8] for the inclusive data sample, overlaid with the sum of the background-only fits in different categories and the signal expectation for a mass hypothesis of 120 GeV corresponding the the SM cross section. The figure below displays the residual of the data with respect to the background-only fit sum.

2. – Analysis and results of specific channels

The products of production cross sections and decay branching ratios for several SM Higgs channels are shown in fig. 1 (left). $H \to \gamma\gamma$ is important in a low Higgs mass range ($m_H < 150$ GeV). Five other channels contribute to the entire mass range considered. However due to the difficulty of suppressing the the main backgrounds, only $H \to ZZ^{(*)} \to \ell^+\ell^-\ell'^+\ell'^-$ and $H \to WW^{(*)} \to \ell^+\nu\ell'^-\bar{\nu}$ are analysed down to a Higgs mass of 110 GeV.

2˙1. $H \to \gamma\gamma$ *channel*. – The search for $H \to \gamma\gamma$ [8] is performed for Higgs boson masses between 110 and 150 GeV using 4.9 fb^{-1}. The event selection requires two isolated, high transverse momentum (p_T) photons with $p_T > 40$ GeV and 25 GeV. Selected events are separated into nine independent categories. This categorisation is based on the direction of each photon and whether it was reconstructed as a converted or unconverted photon, together with the momentum component of the diphoton system transverse to the thrust axis defined by the diphoton system. The diphoton invariant mass $m_{\gamma\gamma}$ is used as a discriminating variable to separate signal from background, to take advantage of the good mass resolution of approximately 1.4% for $m_H \sim 120$ GeV. The distribution of $m_{\gamma\gamma}$ in the data is fitted to an exponential function to estimate the background. The inclusive invariant mass distribution of the observed candidates, summing over all the categories, is shown in fig. 1 (right).

The observed and expected local p_0 values and 95% CL upper limits on the Higgs boson production cross section divided by the SM prediction are shown in fig. 2. (The statistical methods used are described in sect. **3**.) The largest excess with respect to the background-only hypothesis in the mass range of 110–150 GeV is observed at 126.5 GeV with a local significance of 2.9 standard deviations. When the uncertainties on photon energy scale and also the look-elsewhere effect in the mass range of 110–150 GeV are taken into account, this excess becomes 1.5 standard deviations. The median expected

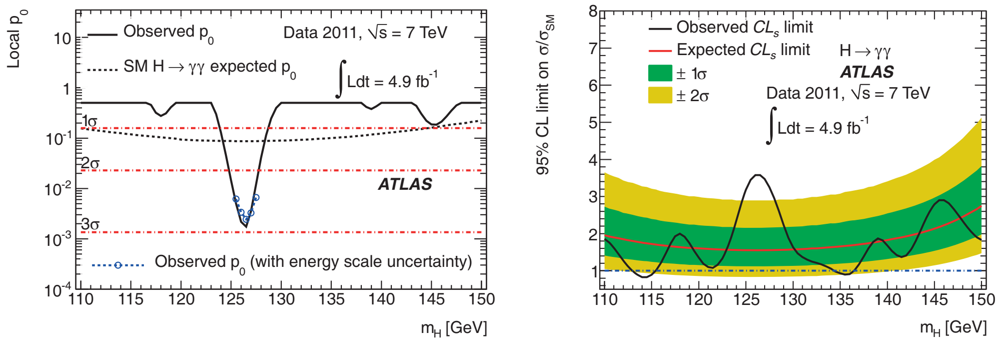

Fig. 2. – Left: The expected and observed local p_0 [8]. The open points indicate the observed local p_0 value when energy scale uncertainties are taken into account. Right: The expected and observed 95% CL upper limits [8] on the SM Higgs boson production normalized to the predicted cross section as a function of m_H.

upper limits of the cross section at the 95% CL vary between 1.6 and 2.7 in the mass range of 110–150 GeV while the observed limit varies between 0.83 and 3.6. A SM Higgs boson is excluded at the 95% CL in the mass ranges of 113–115 GeV and 134.5–136 GeV.

2·2. *$H \to ZZ^{(*)} \to \ell^+\ell^-\ell'^+\ell'^-$ channel.* – The search for $H \to ZZ^{(*)} \to \ell^+\ell^-\ell'^+\ell'^-$ [9] is carried out for Higgs boson masses between 110 GeV and 600 GeV using 4.8 fb^{-1}. Three different categories based on lepton flavor are introduced; $e^+e^-e^+e^-$, $e^+e^-\mu^+\mu^-$ and $\mu^+\mu^-\mu^+\mu^-$. Higgs boson candidates are selected by requiring two same-flavour, opposite-sign isolated lepton pairs in an event. These four leptons are required to have $p_T > 20$, 20, 7 and 7 GeV. The invariant mass of the lepton pair closest to Z boson mass is required to be within 15 GeV of the known Z mass, while that of another lepton pair is required to be smaller than 115 GeV and larger than 15–60 GeV depending on the four-lepton invariant mass ($m_{4\ell}$). The dominant irreducible $ZZ^{(*)}$ background is estimated using Monte Carlo simulation. The reducible Z+jets background, which becomes important in the low mass range, is estimated from control regions in the data. The top-quark background normalisation is validated in a control sample. The mass resolutions are approximately 1.5% in the four-muon channel and 2% in the four-electron channel for $m_H \sim 130$ GeV. The four-lepton invariant mass is used as a discriminating variable as shown in fig. 3 (left) for the low mass range and fig. 3 (right) for the full mass range.

Figure 4 (left) shows the observed and expected 95% CL cross section upper limits as a function of m_H. A SM Higgs boson is excluded at 95% CL in the mass ranges 134–156 GeV, 182–233 GeV, 256–265 GeV and 268–415 GeV. The expected exclusion ranges are 136–157 GeV and 184–400 GeV. Figure 4 (right) shows the local p_0 as a function of m_H. The most significant upward deviations from the background-only hypothesis are observed for $m_H = 125$ GeV with a local p_0 of 1.6% (2.1σ), $m_H = 244$ GV with a local p_0 of 1.3% (2.2σ), and $m_H = 500$ GV with a local p_0 of 1.8% (2.1σ). When the look-elsewhere effect is taken into account, the global p_0 for each excess becomes $O(50\%)$.

2·3. *$H \to WW^{(*)} \to \ell^+\nu\ell'^-\bar{\nu}$ channel.* – The search for $H \to WW^{(*)} \to \ell^+\nu\ell'^-\bar{\nu}$ [10] is performed as an event counting analysis for Higgs boson masses between 110 GeV and

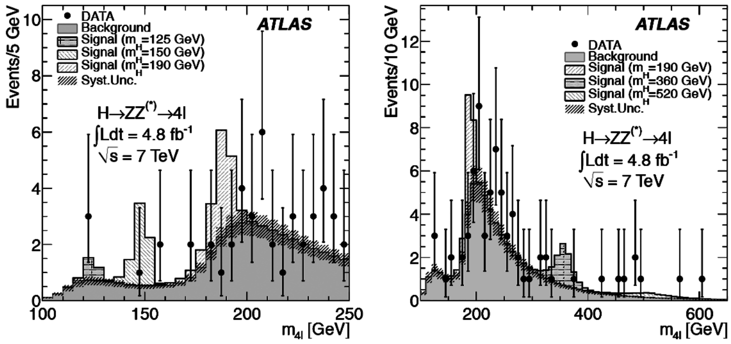

Fig. 3. – $m_{4\ell}$ distribution [9] of the selected candidates, compared to the background expectation for the 100–250 GeV mass range (left) and the full mass range of the analysis (right). The signal expectation for several m_H hypothesis is also shown.

300 GeV using 2.05 fb^{-1}. Events are required to have two opposite-sign isolated leptons with $p_T > 20$ GeV for electron and 15 GeV for muon. The leading lepton p_T must be larger than 25 GeV to match a trigger requirement. Because of the presence of two neutrinos from W boson decay, a large missing transverse momentum ($E_{\mathrm{T}}^{\mathrm{miss}}$) is required. Figure 5 (left) shows the distribution of the quantity $E_{\mathrm{T,rel}}^{\mathrm{miss}}$, which is defined as $E_{\mathrm{T}}^{\mathrm{miss}}$ if the angle $\Delta\phi$ between the missing transverse mass and the transverse momentum of the nearest lepton or jet is greater than $\pi/2$, or $E_{\mathrm{T}}^{\mathrm{miss}} \sin(\Delta\phi)$ otherwise. Good agreement between real data and Monte Carlo simulation is observed. In addition, since the direction of two leptons from W boson decay are preferentially close, due to the spin quantum numbers of Higgs and W bosons, a small angle between the two leptons, as well as a low invariant mass of two leptons ($m_{\ell\ell^{(\prime)}}$) are required. The selected events are separated into 0-jet and 1-jet categories as well as according to lepton flavour. Figure 5 (right) shows the jets multiplicity distribution. Non-resonant WW is dominant in the 0-jet category, and top-quark production is dominant in the 1-jet category. The non-resonant WW production is estimated from the data using control regions based on $m_{\ell\ell^{(\prime)}}$. In the

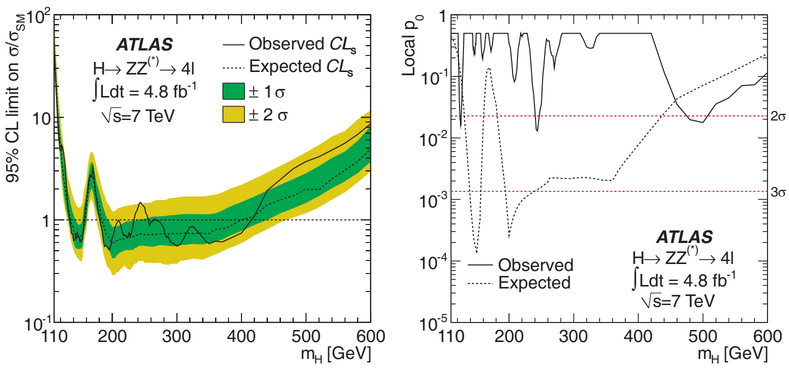

Fig. 4. – The expected and observed 95% CL upper limits (left) [9] and local p_0 (right) [9] as a function of m_H.

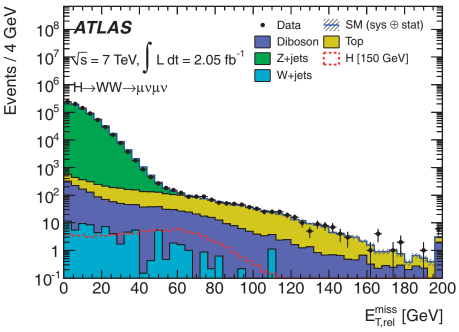

Fig. 5. – Left: The $E_{\mathrm{T,rel}}^{\mathrm{miss}}$ distribution [16] of the $H \to WW^{(*)} \to \mu^+\nu\mu'^-\bar{\nu}$ channel after the requirement of lepton p_T and $m_{\ell\ell}$. Right: Multiplicity of jets [16] with $p_T > 25\,\mathrm{GeV}$ after the cut on $E_{\mathrm{T,rel}}^{\mathrm{miss}}$.

1-jet category, a b-jet veto is applied to reject events from top-quark production. The transverse mass distribution of events for both jet categories is shown in fig. 6.

Figure 7 (left) shows the expected and observed limits. The mass range of 145–206 GeV is excluded at 95% CL while the median expected limit excludes the mass range of 134–200 GeV. Figure 7 (right) shows the local p_0 and no significance deviation from background is observed.

3. – Combination

Figure 8 show results from six different channels, which are combined [11] by using the profile likelihood ratio. The signal strength, μ, is defined as $\mu = \sigma/\sigma_{\mathrm{SM}}$, where σ is the Higgs boson production cross section being tested and σ_{SM} its SM value. The signal strength is extracted from the full likelihood including all the parameters describing the systematic uncertainties and their correlations. The details of this procedure are found in refs. [17, 18]. Exclusion limits are based on the CL_S method [19] and a value of μ is regarded as excluded at the 95% CL when CL_S takes on the corresponding value.

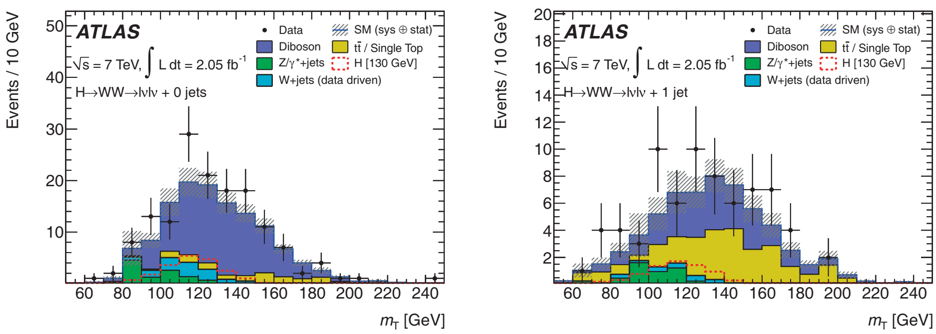

Fig. 6. – The transverse mass distribution [16] of events for the 0-jet (left) and 1-jet (right) categories. The expected signal is also shown for $m_H = 130\,\mathrm{GeV}$.

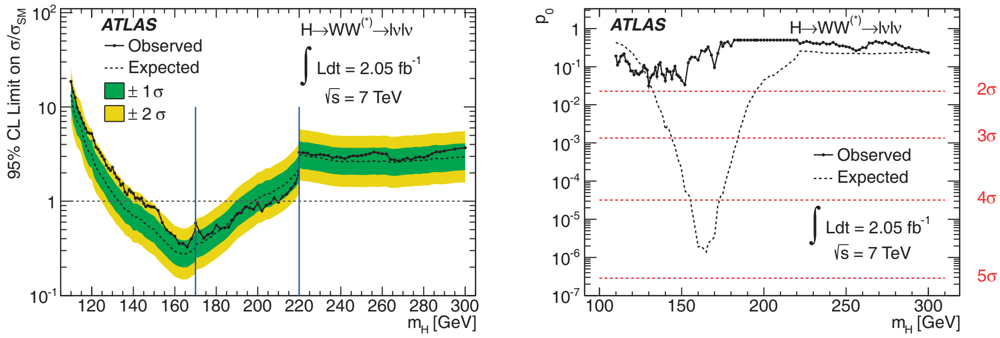

Fig. 7. – The expected and observed 95% CL upper limits (left) [10] and local p_0 (right) [16] as a function of m_H.

The combined 95% CL exclusion limits on μ are shown in fig. 9 (left) for the full mass range and fig. 9 (right) for the low mass range. These results are based on the asymptotic approximation described in [20]. The Higgs boson mass ranges 112.9–115.5 GeV, 131–238 GeV and 251–466 GeV are excluded at the 95% CL, while the range 124–519 GeV is expected to be excluded in the absence of a signal.

In fig. 9 (right), an excess of events is observed at $m_H \sim 126\,\text{GeV}$. Such an excess can be tested by the probability (p_0) that a background-only experiment fluctuates to be more signal-like than what is observed. The equivalent formulation in terms of number of standard deviations is referred to as the significance. The profile likelihood ratio test statistic is defined such that p_0 cannot exceed 50%. The local p_0 probability and significance are defined for a fixed m_H hypothesis and then the global p_0 probability and significance are evaluated by taking the look-elsewhere effect [17, 21] into account. Figure 10 (left) shows the local p_0 as a function of m_H. The largest local significance in the combination is found at $m_H = 126\,\text{GeV}$, where it reaches 3.6σ with an expected value of 2.5σ for a SM Higgs boson signal. The observed (expected) local significance for $m_H = 126\,\text{GeV}$ is 2.8σ (1.4σ) in the $H \to \gamma\gamma$ channel, 2.1σ (1.4σ) in the $H \to ZZ^{(*)} \to \ell^+\ell^-\ell'^+\ell'^-$ channel, and 1.4σ (1.4σ) in the $H \to WW^{(*)} \to \ell^+\nu\ell'^-\bar{\nu}$ channel. By taking

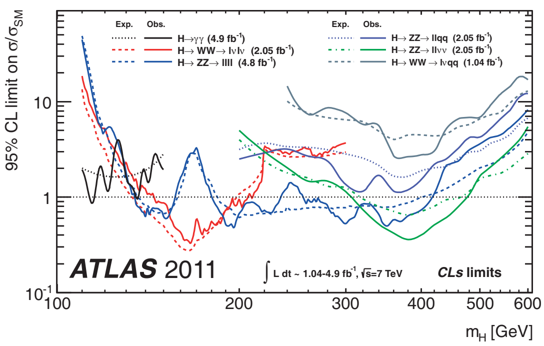

Fig. 8. – The expected and observed cross section limits for the individual search channels [22].

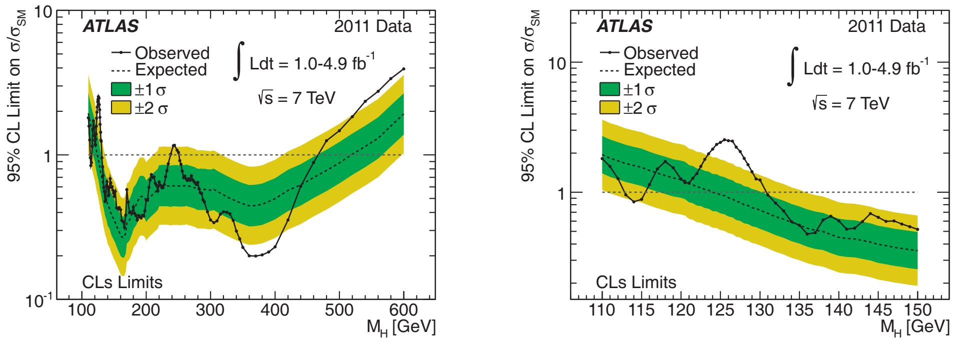

Fig. 9. – The expected and observed 95% CL upper limits [22] on the SM Higgs boson production normalized to the predicted cross section for the full (left) and the low-mass (right) range.

into account the systematic uncertainties on energy scale, this excess slightly reduces from 3.6σ to 3.5σ. The global p_0 for this combined 3.5σ excess to be found anywhere in the mass range 110–600 GeV is 1.4% (2.2σ).

Figure 10 (right) shows the best-fit signal strength μ as a function of m_H for the low-mass range. The μ value indicates by what factor the SM Higgs boson cross section would have to be scaled to match to the observed data and the excess observed at $m_H = 126\,\mathrm{GeV}$ corresponds to a value of μ of approximately $1.5^{+0.5}_{-0.6}$, which is consistent with the signal expected from a SM Higgs boson at that mass.

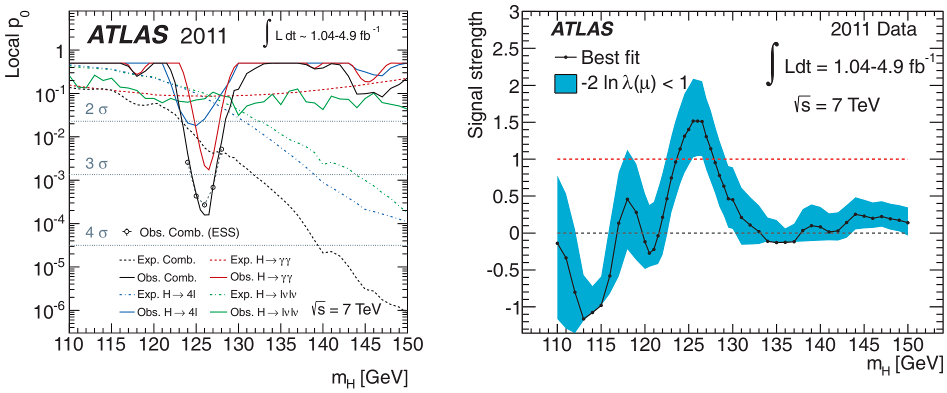

Fig. 10. – Left: The expected and observed local p_0 as a function of m_H [11]. The solid curves give the individual and combined observed p_0, estimated using the asymptotic approximation. The dashed curves show the median expected value for the hypothesis of a SM Higgs boson signal at that mass. The points indicate the observed local p_0 estimated using ensemble tests and taking into account energy scale systematic uncertainties. Right: The best-fit signal strength μ as a function of m_H for the low mass range [22].

4. – Conclusion

A search for the Standard Model Higgs boson has been performed with the ATLAS experiment at the LHC using data corresponding to integrated luminosities from $1.04\,\mathrm{fb}^{-1}$ to $4.9\,\mathrm{fb}^{-1}$ of pp collisions collected at $\sqrt{s} = 7\,\mathrm{TeV}$ in 2011. The Higgs boson mass ranges 112.9–115.5 GeV, 131–238 GeV and 251–466 GeV are excluded at the 95% CL, while the range 124–519 GeV is expected to be excluded in the absence of a signal. An excess of events is observed around the mass of 126 GeV with a local significance of 3.5σ. The local significance of $H \to \gamma\gamma$, $H \to ZZ^{(*)} \to \ell^+\ell^-\ell'^+\ell'^-$, $H \to WW^{(*)} \to \ell^+\nu\ell'^-\bar{\nu}$, the three most sensitive channels in this mass range, are 2.8σ, 2.1σ and 1.4σ, respectively. The global probability for the background to produce such a fluctuation anywhere in the explored Higgs boson mass range 110–600 GeV is estimated to be $\sim 1.4\%$.

Finally, an integrated luminosity of $15\,\mathrm{fb}^{-1}$ is expected at $\sqrt{s} = 8\,\mathrm{TeV}$ in 2012. With this data, it might be possible either to discover the SM Higgs boson of mass around 120–131 GeV or to exclude the mass range of 115.5–131 GeV.

REFERENCES

[1] Englert F. and Brout R., *Phys. Rev. Lett.*, **13** (1964) 321.
[2] Higgs P., *Phys. Rev. Lett.*, **12** (1964) 132; **13** (1964) 508.
[3] Guralnik G. S., Hagen C. R. and Kibble T. W. B., *Phys. Rev. Lett.*, **13** (1964) 585.
[4] ATLAS Collaboration, *JINST*, **3** (2008) S08003.
[5] Evans L. and Bryant P., *JINST*, **3** (2008) S08001.
[6] ALEPH, DELPHI, L3 and OPAL Collaborations and the LEP Working Group for Higgs boson searches, *Phys. Lett. B*, **565** (2003) 61.
[7] TEVNPH (Tevatron New Phenomena and Higgs Working Group), arXiv:1107:5518.
[8] ATLAS Collaboration, *Phys. Rev. Lett.*, **108** (2012) 111803.
[9] ATLAS Collaboration, *Phys. Lett. B*, **710** (2012) 383.
[10] ATLAS Collaboration, *Phys. Rev. Lett.*, **108** (2012) 111802.
[11] ATLAS Collaboration, *Phys. Lett. B*, **710** (2012) 49.
[12] ATLAS Collaboration, ATLAS-CONF-2011-148 (`https://cdsweb.cern.ch/record/1392668`).
[13] ATLAS Collaboration, *Phys. Lett. B*, **707** (2012) 27.
[14] ATLAS Collaboration, *Phys. Rev. Lett.*, **107** (2011) 231801.
[15] LHC Higgs Cross Section Working Group, CERN-2011-002, arXiv:1101:0593.
[16] ATLAS Collaboration, `https://atlas.web.cern.ch/Atlas/GROUPS/PHYSICS/PAPERS/HIGG-2011-08/`.
[17] ATLAS and CMS Collaborations, LHC Higgs Combination Working Group Report, ATL-PHYS-PUB-2011-011 (`https://cdsweb.cern.ch/record/1375842`) CMS-NOTE-2011-005 (`https://cdsweb.cern.ch/record/1379837`).
[18] ATLAS Collaboration, *Eur. Phys. J. C*, **71** (2010) 1782.
[19] Read A. L., *J. Phys. G*, **28** (2002) 2693.
[20] Cowan G., Crammer K., Gross E. and Vitells O., *Eur. Phys. J. C*, **71** (2010) 1554.
[21] Gross E. and Vitells O., *Eur. Phys. J. C*, **70** (2010) 525.
[22] ATLAS Collaboration, `https://atlas.web.cern.ch/Atlas/GROUPS/PHYSICS/PAPERS/HIGG-2012-03/`.

SESSION VII - SEARCHING FOR NEW PHYSICS

Adam Falkowski	Interpreting the 125 GeV Higgs
Markus Warsinsky	Searches for beyond the Standard Model Higgs Bosons at ATLAS
Marakus Stoye	SUSY searches at CMS
Renaud Brunelière	Searches for Supersymmetry at ATLAS
Simonetta Gentile	Phenomenology of new heavy neutral gauge bosons in an extended MSSM
Ilja Doršner	Colored scalars as flavor messengers in grand unified theories

IL NUOVO CIMENTO Vol. 35 C, N. 6 Novembre-Dicembre 2012
DOI 10.1393/ncc/i2012-11386-2

Colloquia: LaThuile12

Interpreting the 125 GeV Higgs

D. Carmi([1]), A. Falkowski([2]), E. Kuflik([1]) and T. Volansky([1])

([1]) *Raymond and Beverly Sackler School of Physics and Astronomy, Tel-Aviv University Tel-Aviv 69978, Israel*
([2]) *Laboratoire de Physique Théorique d'Orsay, UMR8627–CNRS Université Paris–Sud - Orsay, France*

ricevuto il 7 Settembre 2012

Summary. — The LHC and Tevatron Higgs data are interpreted as constraints on an effective theory of a Higgs boson with the mass $m_h \simeq 125\,\mathrm{GeV}$. We focus on the $h \to \gamma\gamma$, $h \to ZZ^* \to 4l$, and $h \to WW^* \to 2l2\nu$ channels at the LHC, and the $b\bar{b}$ channel at the Tevatron, which are currently the most sensitive probes of a Higgs with such a mass. Combining the available data in these channels, we derive the favored regions of the parameter space of the effective theory. We further provide the relevant mapping between the effective theory and the relevant rates, allowing for a more precise extraction of the favored region to be derived by the ATLAS and CMS collaborations.

PACS 14.80.Bn – Higgs boson.
PACS 01.50.Wg – Physics of toys.

1. – Introduction

Discovering the Higgs boson and measuring its properties is currently the key objective of the high-energy physics program. Within the Standard Model (SM), the coupling to the Higgs boson is completely fixed by the particle mass. This is no longer the case in many scenarios beyond the SM, where the Higgs couplings to the SM gauge bosons and fermions may display sizable departures from the SM predictions. Indeed, precision studies of the Higgs couplings may be the shortest route to new physics.

Recently, ATLAS [1] and CMS [2] have reported the results of Higgs searches based on $5\,\mathrm{fb}^{-1}$ of LHC data while CDF and D0 presented Higgs searches based on $10\,\mathrm{fb}^{-1}$ of Tevatron data [3]. The results suggest the existence of a Higgs boson with $m_h \approx 125\,\mathrm{GeV}$ manifesting itself in the diphoton and 4-lepton final states at the LHC, and in the $b\bar{b}$ final state at the Tevatron. Assuming these signals are in indeed due to a Higgs boson, it is natural to ask the following questions:

– Are the experimental data consistent with the predictions of the SM Higgs?

– Do the data favor or disfavor any particular scenarios beyond the SM?

– What are the implications of Higgs data for new physics models addressing the naturalness problem of the SM?

To address these questions, we combine the LHC and Tevatron Higgs results in 5 search channels that are currently most sensitive to the signal of a 125 GeV Higgs:

– The inclusive diphoton channels in ATLAS [4] and CMS [5].

– The dijet tag exclusive diphoton channel in CMS [5].

– The inclusive $ZZ \to 4l$ channels in ATLAS [6] and CMS [7].

– The inclusive $WW \to 2l2\nu$ channel in ATLAS [8].

– The W/Z associated Higgs production in the $b\bar{b}$ channel at the Tevatron [3].

We use these channels to identify the best-fit regions of an effective theory describing general interactions of a 125 GeV Higgs boson. This proceedings is based, on ref. [9] updated with Higgs search results that subsequently appeared in refs. [3, 8]. One of the goals of this note is to collect the corresponding formulae that are needed in order to map the Higgs effective theory to rates measured at colliders, hoping it will help the experimental collaborations to present similar fits once additional data becomes available. A number of partly overlapping papers have recently investigated the 125 GeV Higgs-like excess, see [10]. In addition to the the channels discussed here, one may consider other available Higgs measurements (*e.g.*, the $b\bar{b}$ and $\tau^+\tau^-$ channel at the LHC, the W^+W^- and the diphoton channel at the Tevatron, etc.). Those, however, are currently less sensitive to a 125 GeV Higgs, and including them does not alter the fits significantly [11].

2. – Formalism

We first lay out in some detail the formalism we employ to describe interactions of the Higgs boson with matter.

2·1. *Lagrangian.* – We introduce the effective Lagrangian defined at the scale of $\mu = m_h$ (assuming the Higgs is lighter than the top), describing the interactions of a scalar Higgs boson with matter,

$$\begin{aligned}(1)\quad \mathcal{L}_{eff} = {} & c_V \frac{2m_W^2}{v} h\, W_\mu^+ W_\mu^- + c_V \frac{m_Z^2}{v} h\, Z_\mu Z_\mu - c_b \frac{m_b}{v} h\, \bar{b}b - c_\tau \frac{m_\tau}{v} h\, \bar{\tau}\tau - c_c \frac{m_c}{v} h\, \bar{c}c \\ & + c_g \frac{\alpha_s}{12\pi v} h\, G_{\mu\nu}^a G_{\mu\nu}^a + c_\gamma \frac{\alpha}{\pi v} h\, A_{\mu\nu} A_{\mu\nu} - c_{inv} h\, \bar{\chi}\chi.\end{aligned}$$

The couplings of the Higgs boson are allowed to take arbitrary values, parametrized by c_i. To be even more general, we also allow for a coupling to weakly interacting stable particles χ, leading to an invisible Higgs partial width. This effective approach harbors very few theoretical assumptions. One is that of custodial symmetry, $c_W = c_Z \equiv c_V$, so as to satisfy the experimental bounds on the T-parameter (see however ref. [12]). Another theoretical assumption is that the Higgs width is dominated by decays into up to 2 SM particles; more sophisticated BSM scenarios may predict cascade decays into multiple SM particles which would require a more general treatment. Finally, we assummed that the Higgs is a positive-parity scalar; more generally, one could allow for pseudoscalar interactions.

The top quark has been integrated out in eq. (1) and its effects are included in the effective dimension-5 Higgs couplings parametrized by c_g and c_γ. However these 2 couplings may well receive additional contributions from integrating out new physics, and therefore are also kept as free parameters. This effective Lagrangian provides a good description processes where the Higgs boson is dominantly produced near threshold([1]).

In the SM, the terms in the first line of eq. (1) arise at tree-level:

$$c_{V,\mathrm{SM}} = c_{t,\mathrm{SM}} = c_{b,\mathrm{SM}} = c_{\tau,\mathrm{SM}} = 1. \tag{2}$$

The following 2 terms arise at 1 loop and are dominated by the contribution of the top quark,

$$c_{g,\mathrm{SM}} \simeq 1, \qquad c_{\gamma,\mathrm{SM}} \simeq \frac{2}{9}\,. \tag{3}$$

Finally, $c_{inv,\mathrm{SM}} = 0$([2]).

2·2. *Decay*. – With the help of the effective theory parameters c_i we can easily write down the partial Higgs decay widths relative to the SM value. Starting with the decays mediated by the lower-dimenensional interactions in the first line of eq. (1) we have,

$$\Gamma_{bb} \simeq |c_b|^2\Gamma_{bb}^{\mathrm{SM}}, \quad \Gamma_{\tau\tau} \simeq |c_\tau|^2\Gamma_{\tau\tau}^{\mathrm{SM}}, \quad \Gamma_{WW} = |c_V|^2\Gamma_{WW}^{\mathrm{SM}}, \quad \Gamma_{ZZ} = |c_V|^2\Gamma_{ZZ}^{\mathrm{SM}}, \tag{4}$$

where the SM widths for $m_h = 125\,\mathrm{GeV}$, are given by [13]

$$\Gamma_{bb}^{\mathrm{SM}} = 2.3\,\mathrm{MeV}, \quad \Gamma_{\tau\tau}^{\mathrm{SM}} = 0.25\,\mathrm{MeV}, \quad \Gamma_{WW}^{\mathrm{SM}} = 0.86\,\mathrm{MeV}, \quad \Gamma_{ZZ}^{\mathrm{SM}} = 0.1\,\mathrm{MeV}. \tag{5}$$

Strictly speaking, eq. (4) is valid at leading order. However, higher-order diagrams which involve one c_i insertion leave these relations intact. Thus, eq. (4) remains true when higher order QCD corrections are included. The decays to gluons and photons are slightly more complicated because, apart from the dimension-5 effective coupling proportional to c_g, c_γ, they receive contribution from the loop of the particles present in eq. (1). One finds

$$\Gamma_{gg} = \frac{|\hat{c}_g|^2}{|\hat{c}_{g,\mathrm{SM}}|^2}\Gamma_{gg}^{\mathrm{SM}}, \qquad \Gamma_{\gamma\gamma} = \frac{|\hat{c}_\gamma|^2}{|\hat{c}_{\gamma,\mathrm{SM}}|^2}\Gamma_{\gamma\gamma}^{\mathrm{SM}}, \tag{6}$$

where, keeping the leading 1-loop contribution in each case one finds,

$$\hat{c}_g = c_g + c_b A_f(\tau_b) + c_c A_f(\tau_c), \tag{7}$$

$$\hat{c}_\gamma = c_\gamma + c_V A_v(\tau_W) + \frac{1}{18}c_b A_f(\tau_b) + \frac{2}{9}c_c A_f(\tau_c) + \frac{1}{6}c_\tau A_f(\tau_\tau). \tag{8}$$

([1]) Obviously, this formalism is not suitable for describing the $t\bar{t}$ associated Higgs production process, which may be observable in the 14 TeV LHC run. Moreover, it may yield quantitatively incorrect results for exclusive processes requiring Higgs produced with a much larger boost, $p_{T,h} \gg m_h$.

([2]) But note that even in the SM there is a small invisible width via the tree-level $h \to ZZ^* \to 4\nu$ and the 1-loop $h \to 2\nu$ decay modes.

Above we introduced the customary functions describing the 1-loop contribution of fermion and vector particles to the triangle decay diagram,

$$A_f(\tau) \equiv \frac{3}{2\tau^2}\left[(\tau-1)f(\tau)+\tau\right],$$
$$A_v(\tau) \equiv \frac{-1}{8\tau^2}\left[3(2\tau-1)f(\tau)+3\tau+2\tau^2\right],$$
$$f(\tau) \equiv \begin{cases} \arcsin^2\sqrt{\tau}, & \tau \le 1, \\ -\frac{1}{4}\left[\log\frac{1+\sqrt{1-\tau^{-1}}}{1-\sqrt{1-\tau^{-1}}} - i\pi\right]^2, & \tau > 1, \end{cases} \tag{9}$$

and $\tau_i = m_h^2/4m_i^2$. Numerically, for $m_h \simeq 125\,\mathrm{GeV}$, $A_v(\tau_W) \simeq -1.04$, $A_f(\tau_b) \simeq -0.06 + 0.09i$. so that $\hat{c}_g \simeq c_g - 0.06c_b$ and $\hat{c}_\gamma \simeq c_\gamma - c_V$. In the SM c_g and c_γ arise from integrating out the top quark, thus $c_{g,\mathrm{SM}} = A_f(\tau_t) \approx 1.03$, and $c_{\gamma,\mathrm{SM}} = (2/9)c_{g,\mathrm{SM}}$. The SM witdhs are $\Gamma_{gg}^{\mathrm{SM}} \simeq 0.34\,\mathrm{MeV}$ and $\Gamma_{\gamma\gamma}^{\mathrm{SM}} \simeq 0.008\,\mathrm{MeV}$.

In order to compute the branching fractions in a given channel we need to divide the corresponding partial width by the total width,

$$\mathrm{Br}(h \to ii) = \frac{\Gamma_{ii}}{\Gamma_{tot}}\,. \tag{10}$$

The latter includes the sum of the width in the visible channels, and the invisible width, which once again, for $m_h = 125\,\mathrm{GeV}$ is, $\Gamma_{inv} \simeq 1.2\times 10^3 c_{inv}^2 \Gamma_{tot}^{\mathrm{SM}}$. We can write it as

$$\Gamma_{tot} = |C_{tot}|^2 \Gamma_{tot}^{\mathrm{SM}}\,, \tag{11}$$

where $\Gamma_{tot}^{\mathrm{SM}} \simeq 4.0\,\mathrm{MeV}$, and

$$\begin{aligned} |C_{tot}|^2 \simeq{}& |c_b|^2\Gamma_{bb}^{\mathrm{SM}} + |c_V|^2\left(\Gamma_{WW}^{\mathrm{SM}} + \Gamma_{ZZ}^{\mathrm{SM}}\right) + \frac{|c_g|^2}{\left|c_g^{\mathrm{SM}}\right|^2}\Gamma_{gg}^{\mathrm{SM}} + |c_\tau|^2\Gamma_{\tau\tau}^{\mathrm{SM}} \\ &+ |c_c|^2\Gamma_{cc}^{\mathrm{SM}} + \frac{\Gamma_{inv}}{\Gamma_{tot}^{\mathrm{SM}}}\,. \\ \simeq{}& 0.58|c_b|^2 + 0.24|c_V|^2 + 0.09|c_g|^2 + 0.06|c_\tau|^2 + 0.03|c_c|^2 + \frac{\Gamma_{inv}}{\Gamma_{tot}^{\mathrm{SM}}}\,. \end{aligned} \tag{12}$$

Typically, the total width is dominated by the decay to b-quarks and $\Gamma_{tot} \simeq c_b^2$, however this scaling may not be valid be in models which couple only weakly to bottoms ($c_b < 1$) or gauge fields ($c_V > 1$), or that have a significant invisible width ($c_{inv} \gtrsim 0.03$).

2.3. *Production.* – Similarly, one can express the relative cross sections for the Higgs production processes in terms of the parameters c_i. For the LHC and the Tevatron the currently relevant partonic processes are

– Gluon fusion (ggF), $gg \to h + \mathrm{jets}$,

– Vector boson fusion (VBF), $qq \to hqq + \mathrm{jets}$,

– Vector boson associate production (VH), $q\bar{q} \to hV + \mathrm{jets}$.

The relative cross sections in these channels can be approximated at tree-level by,

$$\frac{\sigma_{ggF}}{\sigma_{ggF}^{\rm SM}} \simeq \frac{|\hat{c}_g|^2}{|\hat{c}_{g,\rm SM}|^2} \simeq |c_g|^2, \qquad \frac{\sigma_{VBF}}{\sigma_{VBF}^{\rm SM}} \simeq |c_V|^2, \qquad \frac{\sigma_{VH}}{\sigma_{VH}^{\rm SM}} \simeq |c_V|^2. \tag{13}$$

For $m_h = 125\,\text{GeV}$ with the SM, the 7 TeV proton-proton cross sections are: $\sigma_{ggF}^{\rm SM} = 15.3\,\text{pb}$, $\sigma_{VBF}^{\rm SM} = 1.2\,\text{pb}$ and $\sigma_{VH}^{\rm SM} = 0.9\,\text{pb}$ [13]. Using eq. (13), we find the total inclusive $pp \to h$ cross section σ_{tot},

$$\frac{\sigma_{tot}}{\sigma_{tot}^{\rm SM}} \simeq \frac{|\hat{c}_g|^2 \sigma_{ggF}^{\rm SM}/|\hat{c}_{g,\rm SM}|^2 + |c_V|^2 \sigma_{VBF}^{\rm SM} + |c_V|^2 \sigma_{VH}^{\rm SM}}{\sigma_{ggF}^{\rm SM} + \sigma_{VBF}^{\rm SM} + \sigma_{VH}^{\rm SM}}, \tag{14}$$

is typically dominated by the gluon fusion process, and therefore it scales as $\sigma_{tot} \sim c_g^2$.

2·4. *Rates.* – The event count in experiments depends on the product of the Higgs branching fractions and the production cross section in a given channel. Typically, the results are presented as constraints on R defined as the event rates relative to the rate predicted by the SM (sometimes denoted as $\hat{\mu}$). These rates can be easily expressed in terms of the parameters of our effective Lagrangian in eq. (1). First, the ATLAS and CMS searches in the $\gamma\gamma$, ZZ^* and WW^* channels probe, to a good approximation, the inclusive Higgs cross section. Thus, we have

$$\begin{aligned} R_{VV^*}^{\rm inc} &\equiv \frac{\sigma_{tot}}{\sigma_{tot}^{SM}} \frac{{\rm Br}(h \to VV^*)}{{\rm Br}_{SM}(h \to VV^*)} \simeq \left| \frac{\hat{c}_g c_V}{\hat{c}_{g,\rm SM} C_{tot}} \right|^2, \\ R_{\gamma\gamma}^{\rm inc} &\equiv \frac{\sigma_{tot}}{\sigma_{tot}^{SM}} \frac{{\rm Br}(h \to \gamma\gamma)}{{\rm Br}_{SM}(h \to \gamma\gamma)} \simeq \left| \frac{\hat{c}_g \hat{c}_\gamma}{\hat{c}_{g,SM} \hat{c}_{\gamma,SM} C_{tot}} \right|^2. \end{aligned} \tag{15}$$

The approximation holds assuming the Higgs production remains dominated by the gluon fusion subprocess. The more precise relations (which we use in our fits) can be easily extracted by substituting eqs. (4), (6), (11), (12) and (14) into the above. ATLAS and CMS also made a number of exclusive studies where kinematic cuts were employed to enhance the VBF contribution. In that case, it is important to take into account the corresponding cut efficiencies ϵ_i for the different production channels. For example for exclusive diphoton searches we have,

$$\begin{aligned} &R_{\gamma\gamma}^{\rm exc} = \\ &\frac{\epsilon_{ggF} |\hat{c}_g|^2 \sigma_{ggF}^{\rm SM}/|\hat{c}_{g,\rm SM}|^2 + |c_V|^2 \epsilon_{VBF} \sigma_{VBF}^{\rm SM} + |c_V|^2 \epsilon_{VH} \sigma_{VH}^{\rm SM}}{\epsilon_{ggF} \sigma_{ggF}^{\rm SM} + \epsilon_{VBF} \sigma_{VBF}^{\rm SM} + \epsilon_{VH} \sigma_{VH}} \frac{{\rm Br}(h \to \gamma\gamma)}{{\rm Br}_{SM}(h \to \gamma\gamma)}. \end{aligned} \tag{16}$$

The most prominent example is the dijet class of the CMS diphoton channel [5], where 2 forward jets with a large rapidity gap are required. In that case Monte Carlo simulations suggest $\epsilon_{ggF}/\epsilon_{VBF} \sim 0.03$, and $\epsilon_{VH}/\epsilon_{VBF} \sim 0$. Large systematic uncertainties are expected however. Another example is the ATLAS fermiophobic Higgs search [14], where $\epsilon_{ggF}/\epsilon_{VBF} \sim 0.3$. Thus, the ATLAS fermiophobic selection (much like the inclusive selection in the CMS fermiophobic search [15], but unlike the CMS dijet tag class) is typically dominated by the ordinary ggF production mode, unless $c_g/c_V \ll 1$.

At the Tevatron the channel most sensitive to a light Higgs signal is the $h \to b\bar{b}$ final state produced in association with a W/Z boson. In this case the relevant rate is

$$R_{bb}^{\rm Tev} \equiv \frac{\sigma(p\bar{p} \to Vh)}{\sigma_{\rm SM}(p\bar{p} \to Vh)} \frac{{\rm Br}(h \to b\bar{b})}{{\rm Br}_{SM}(h \to b\bar{b})} \simeq \left| \frac{c_V c_b}{C_{tot}} \right|^2 . \tag{17}$$

Finally, it is interesting to consider the invisible Higgs rates at the LHC defined as

$$R_{inv}^{ggF} \equiv \frac{\sigma_{ggF}\,{\rm Br}(h \to \chi\bar{\chi})}{\sigma_{ggF}^{\rm SM}} , \qquad R_{inv}^{VBF} \equiv \frac{\sigma_{VBF}\,{\rm Br}(h \to \chi\bar{\chi})}{\sigma_{VBF}^{\rm SM}} . \tag{18}$$

Currently, there is no official LHC limits on invisible Higgs rate. Recasting the results of the LHC monojets searches one can arrive at the limits $R_{inv}^{ggF} < 1.9$, $R_{inv}^{VBF} < 4.3$ at 95% CL [16]. Combining ggF and VBF (assuming they come in the same proportions as in the SM), a somewhat stronger limit $R_{inv} < 1.3$ can be obtained. In any case, the currently available data can place a non-trivial direct constraint on the invisible Higgs branching fraction only in models where the Higgs production cross section is enhanced, for example in models with the 4th generation of chiral fermions where Higgs decays into 4th-generation neutrinos [17]. Alternatively, in a more model-dependent fashion, one can constrain the invisible Higgs width indirectly from the fact of observing the *visible* Higgs decays. Assuming other Higgs couplings take the SM value, ref. [11] argues that ${\rm Br}(h \to \chi\bar{\chi}) > 40\%$ is disfavored.

3. – Fits

We are ready to place constraints on the parameters of the effective theory. With enough data from the LHC one could in principle perform a full seven-parameter fit, however for the time being we pursue a simpler approach. Throughout we assume $c_c = c_\tau = c_b$, and $c_{inv} = 0$, and study the LHC and Tevatron constraints on $\delta c_g = c_g - c_{g,{\rm SM}}$, $\delta c_\gamma = c_\gamma - c_\gamma^{\rm SM}$, c_b, and c_V. We allow two of these parameter to vary freely while fixing the other two. Sample results are displayed in fig. 1. In each plot the "Combined" region corresponds to $\Delta\chi^2 < 4.61$, which can be interpreted as the 90% CL favored region in new physics models where only the two parameters on the axes are varied.

The top left plot characterizes models in which loops containing beyond the SM fields contribute to the effective $h\, G_{\mu\nu}^a G_{\mu\nu}^a$ and $h\, A_{\mu\nu} A_{\mu\nu}$ operators, while leaving the lower-dimension Higgs couplings in eq. (1) unchanged relative to the SM prediction. Note that in these plots the Tevatron band are absent. That's because the Tevatron $b\bar{b}$ rate depends mostly on the parameters c_b and c_V, and very weakly on c_g and c_γ. Interestingly, in this section of the parameter space the Tevatron result is always outside the 1σ band. In the remaining plots we fix $\delta c_\gamma = (2/9)\delta c_g$, which is the case in top partner models where only scalars and fermions with the same charge and color as the top quark contribute to these effective five-dimensional operators. The results are shown for three different sets of assumptions about the lower-dimension Higgs couplings that can be realized in concrete models addressing the Higgs naturalness problem. In particular, the assumptions in the top-right plot are inspired by composite Higgs models [18], where the couplings to the electroweak gauge bosons and the couplings all the SM fermions are scaled by common factors, c_V and c_b, respectively. The coupling to the top quark c_t in the UV completion is also assumed to be rescaled by c_b, producing the corresponding shift of c_g and c_γ in our effective theory. The interesting feature of this plot is the presence of two disconnected

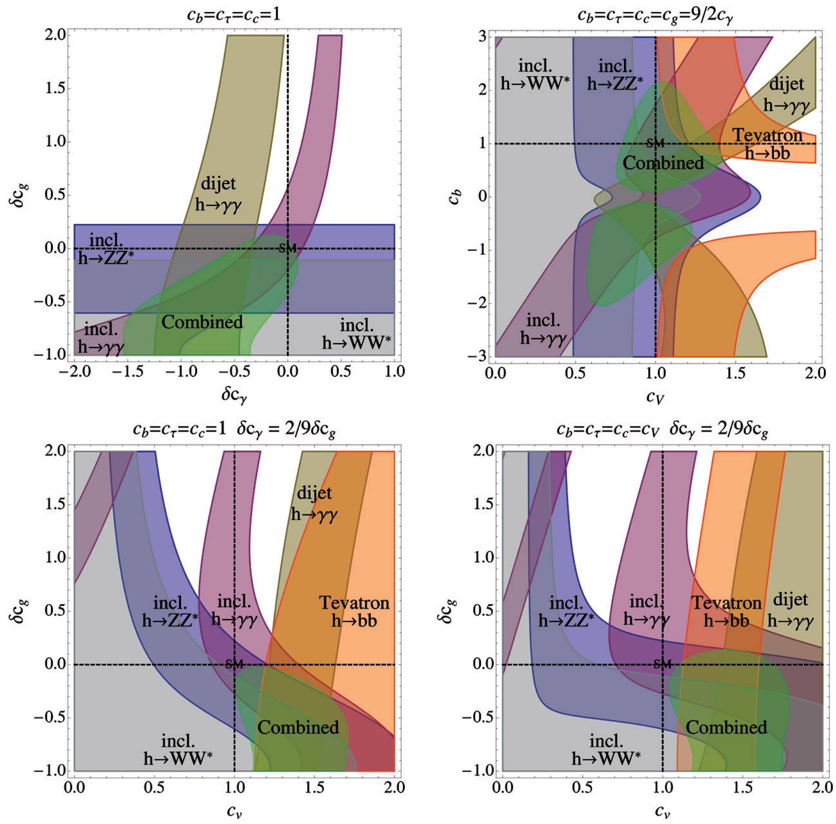

Fig. 1. – The allowed parameter space of the effective theory given in eq. (1) derived from the ATLAS, CMS and Tevatron constraints for $m_h = 125\,\text{GeV}$. We display the 1σ regions allowed by the LHC inclusive $h \to \gamma\gamma$ channel (mauve), the LHC inclusive $h \to ZZ^* \to 4l$ channel (indigo), the CMS dijet class of the $h \to \gamma\gamma$ channel (beige), the ATLAS inclusive $h \to WW^* \to 2l2\nu$ channel (light grey), and the Tevatron $h \to b\bar{b}$ W/Z boson associated channel (peach), The green region is the one favored at 95% CL from the combination of these channels. The dashed lines show the SM values.

best-fit regions. This reflects the degeneracy of the relevant Higgs rates in the VV^* and $b\bar{b}$ channels under the reflection $c_b \to -c_b$, which is broken only in the $\gamma\gamma$. Amusingly, a slightly better fit is obtained in the $c_b < 0$ region, although it may be difficult to construct a microscopic model where such a possibility is realized naturally. It is worth noting that the fermiophobic Higgs scenario, corresponding to $c_b = 0$ and $c_V = 1$, is disfavored by the data (more generally, the fermiophobic line $c_b = 0$ is disfavored for any c_V). The two bottom plots demonstrate that the current data show a preference for a slightly enhanced Higgs coupling to the electroweak gauge bosons, $c_V > 1$ and a slightly suppressed effective couplings to the gluons, $c_g < 1$. This result is driven by the somewhat low event rate (with respect to the SM) observed in the WW^* and, to a lesser extent in the ZZ^* channels (sensitive to the gluon fusion production), while data in the diphoton channel and in the Tevatron $b\bar{b}$ channel (sensitive to the Higgs coupling to W/Z), are well above the SM expectations. Several well-studied models such as the

MSSM or the minimal composite Higgs (and more generally, models with only $SU(2)$ singlets and doublets in the Higgs sector), predict $c_V \leq 1$. If $c_V > 1$ is confirmed in the 8 TeV LHC run, it would point to a very specific direction for electroweak symmetry breaking [19].

To conclude, the LHC and Tevatron Higgs data appear to be a very promising tool to test the consistency of the SM. With the limited statistics available, any conclusion about the Higgs couplings should be taken with a grain of salt. Nonetheless, the analysis presented here demonstrates the strength of constraining the effective Higgs Lagrangian as a mean to place bounds on new physics. With more data we will soon learn whether the intriguing patterns currently visible shall disappear or rather they are the first signs of new physics.

* * *

AF thanks the organizers of the XXVI Rencontres de Physique de la Vallée d'Aoste for the invitation and the view.

REFERENCES

[1] ATLAS Collaboration, arXiv:1202.1408 [hep-ex].
[2] CMS Collaboration, arXiv:1202.1488 [hep-ex].
[3] TEVNPHWG, CDF and D0 Collaborations, arXiv:1203.3774 [hep-ex].
[4] ATLAS Collaboration, arXiv:1202.1414 [hep-ex].
[5] CMS Collaboration, arXiv:1202.1487 [hep-ex] CMS PAS HIG-12-001.
[6] ATLAS Collaboration, arXiv:1202.1415 [hep-ex].
[7] CMS Collaboration, arXiv:1202.1997 [hep-ex].
[8] ATLAS-CONF-2012-012.
[9] Carmi D., Falkowski A., Kuflik E. and Volansky T., arXiv:1202.3144 [hep-ph].
[10] Azatov A., Contino R. and Galloway J., arXiv:1202.3415 [hep-ph]; Espinosa J. R., Grojean C., Muhlleitner M. and Trott M., arXiv:1202.3697 [hep-ph]; Rauch M., arXiv:1203.6826 [hep-ph]; Ellis J. and You T., arXiv:1204.0464 [hep-ph]; Klute M., Lafaye R., Plehn T., Rauch M. and Zerwas D., arXiv:1205.2699 [hep-ph].
[11] Giardino P. P., Kannike K., Raidal M. and Strumia A., arXiv:1203.4254 [hep-ph].
[12] Farina M., Grojean C. and Salvioni E., arXiv:1205.0011 [hep-ph].
[13] Dittmaier S. *et al.* (LHC Higgs Cross Section Working Group Collaboration), arXiv:1101.0593 [hep-ph].
[14] ATLAS Collaboration, arXiv:1205.0701 [hep-ex].
[15] CMS-PAS-HIG-12-008.
[16] Djouadi A., Falkowski A., Mambrini Y. and Quevillon J., arXiv:1205.3169 [hep-ph].
[17] Kuflik E., Nir Y. and Volansky T., arXiv:1204.1975 [hep-ph]. Djouadi A. and Lenz A., arXiv:1204.1252 [hep-ph].
[18] Giudice G. F., Grojean C., Pomarol A. and Rattazzi R., *JHEP*, **06** (2007) 045 [hep-ph/0703164]; Contino R., arXiv:1005.4269 [hep-ph].
[19] Falkowski A., Rychkov S. and Urbano A., *JHEP*, **04** (2012) 073 [arXiv:1202.1532 [hep-ph]].

IL NUOVO CIMENTO Vol. 35 C, N. 6 Novembre-Dicembre 2012
DOI 10.1393/ncc/i2012-11387-1

Colloquia: LaThuile12

Searches for beyond the Standard Model Higgs Bosons at ATLAS

M. Warsinsky on behalf of the ATLAS Collaboration

Albert-Ludwigs-Universität Freiburg, Physikalisches Institut - Hermann-Herder-Str. 3
D-79104 Freiburg, Germany

ricevuto il 7 Settembre 2012

Summary. — Searches for beyond the Standard Model Higgs bosons with the ATLAS detector at the Large Hadron Collider are presented. The individual results are based on datasets with integrated luminosities between 35 pb^{-1} and 1.6 fb^{-1} of proton-proton collisions at a centre-of-mass energy of 7 TeV. No significant deviation from Standard Model predictions without a Higgs boson are observed. Exclusion limits are set on production cross-sections as a function of the Higgs boson mass and in the parameter space of supersymmetric models.

PACS `14.80.Da` – Supersymmetric Higgs bosons.
PACS `14.80.Fd` – Other charged Higgs bosons.
PACS `12.60.Fr` – Extensions of electroweak Higgs sector.

1. – Introduction

One of the primary goals of the ATLAS experiment [1] at the Large Hadron Collider (LHC) is to probe the mechanism responsible for electroweak symmetry breaking and the origin of mass of elementary particles. In the Standard Model (SM) [2] electroweak symmetry breaking is accomplished by adding an additional complex $SU(2)$ doublet field which acquires a vacuum expectation value [3]. A direct prediction of this mechanism is the existence of one additional massive scalar particle, the Higgs boson [3], which couples to both fermions and bosons with coupling strengths that are directly predicted by the theory, with the only unknown quantity being the mass of the Higgs boson. Results from the ATLAS experiment on searches for a SM-like Higgs boson can be found in [4].

Extensions of the Standard Model can significantly alter the phenomenology of the Higgs sector, thus requiring additional search strategies in order to ensure a discovery. Among the possible extensions of the SM, one of the most popular ones is the Minimal Supersymmetric Standard Model (MSSM) [5], where an additional Higgs doublet field of opposite hypercharge is required. This results in five observable Higgs bosons, three of them being electrically neutral (the CP-even h, H, the CP-odd A), and two being charged ($H^{\pm}$). In addition the coupling strengths to fermions and bosons of the neutral

Higgs bosons can be very different from the SM case. Further extensions of the SM gauge sector, such as left-right-symmetric models [6], Higgs triplet models [7], and little Higgs models [8] predict the existence of doubly charged Higgs bosons. Models like the next-to-minimal supersymmetric standard model (NMSSM) [9] can lead to an even more complex Higgs sector. Finally, fermiophobic models [10] can cause the Higgs boson to not couple to some or all of the SM fermions.

In these proceedings, ATLAS results from searches for Higgs bosons in scenarios beyond the Standard Model are reported.

2. – Neutral MSSM $h/H/A \to \tau\tau$

In the MSSM the coupling strength of the neutral Higgs bosons to fermions and gauge bosons is significantly altered. For large values of $\tan\beta$ one of the two CP-even Higgs bosons is always predicted to have about the same mass as the A boson and these two mass degenerate states will have increased couplings to down-type fermions, while the couplings to gauge bosons will be suppressed or even completely absent in the case of the A boson. The other CP-even Higgs boson has couplings similar to the SM case.

The two mass degenerate Higgs bosons are produced predominantly in gluon-gluon-fusion and in association with b quarks. Decay to down-type fermions are favoured, with branching fractions of about 90% into $b\bar{b}$ and about 10% into $\tau^+\tau^-$. The latter decay mode is one of the most promising channels. However, it is difficult to reconstruct the Higgs boson mass due to the presence of neutrinos in the tau lepton decays, and the large jet background to hadronic tau lepton decays (τ_h) has to be suppressed.

In ATLAS the search for neutral Higgs bosons of the MSSM has been performed in a jet-inclusive way based on the decay of the Higgs bosons into tau leptons using $1.06\,\text{fb}^{-1}$ of data [11]. Four different final states according to decays of tau leptons have been considered, with τ_h denoting a tau lepton decay involving hadrons, $e\mu 4\nu$, $e\tau_h 3\nu$, $\mu\tau_h 3\nu$, $\tau_h\tau_h 2\nu$, corresponding to branching fractions of 6%, 23%, 23% and 42% respectively(1). Various estimates for the invariant mass of the Higgs boson candidate have been used: In the $\tau_h\tau_h$ channel the invariant (also called visible) mass of the two hadronic systems has been used. For the $e\mu$ channel, the missing momentum was added to the visible tau decay products to produce an effective mass. For the channels with one leptonic and one hadronic tau lepton decay the missing mass calculator (MMC) technique as introduced in [12] has been used.

For channels with leptons in the final state the dominant background $Z \to \tau\tau$ has been estimated from data with a technique where $Z \to \mu\mu$ events are selected in data. The muons are removed from the event and their momenta used as momenta of fictitious tau leptons. The tau lepton decays are simulated along with the detector response and the simulated energy deposits are re-merged with the data event before re-reconstruction. In this way the additional hadronic activity in the event is taken from data.

For the $\tau_h\tau_h$ channel the dominant background is multi-jet production, which has been estimated from data. Details on the analysis can be found in [11].

Figure 1 shows the resulting mass spectra of the three different channels. Data are compatible with background expectations for all channels and exclusion limits at the 95% CL are set on the production cross-section times branching fraction of a generic scalar resonance ϕ as a function of its mass as shown in fig. 2 (left). The cross-section

---

(1) In the following the $e\tau_h$ and $\mu\tau_h$ channels will be summarized as one $\ell\tau_h$ channel.

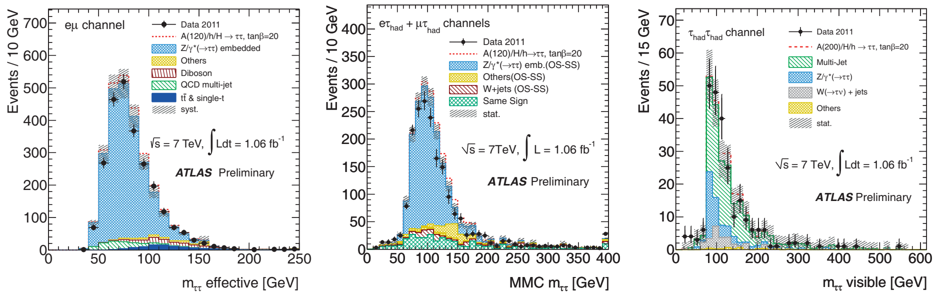

Fig. 1. – Reconstructed masses in the search for $h/H/A \to \tau\tau$ using $1.06\,\mathrm{fb}^{-1}$ [11]. From left to right: Effective mass in the $e\mu$ channel, MMC mass in the $\ell\tau_h$ channels, visible mass in the $\tau_h\tau_h$ channel.

limit is produced separately for two different production mechanisms, $gg \to \phi$ and b quark associated production. The interpretation of the search results within the MSSM is shown in fig. 2 (right), where the exclusion limits are set on $\tan\beta$ as a function of the mass of the CP-odd Higgs boson A. Here the MHMAX [13] scenario has been assumed.

3. – Searches for charged Higgs bosons

Charged Higgs bosons occur in all extensions of the SM Higgs sector with more than one Higgs doublet field, such as the MSSM. In all analysis presented in these proceedings, a charged Higgs boson mass smaller than the top quark mass is assumed and the charged Higgs boson is searched for in decays of top quark pairs ($t\bar{t} \to H^+ bW^-\bar{b}$ + c.c.).

3˙1. *Charged* $H^+ \to \tau^+\nu_\tau$. – The decay of the charged Higgs boson into tau leptons is important in the MSSM especially for large values of $\tan\beta$. The search for this decay channel has been performed in three different final states using $1.03\,\mathrm{fb}^{-1}$ of data. Details

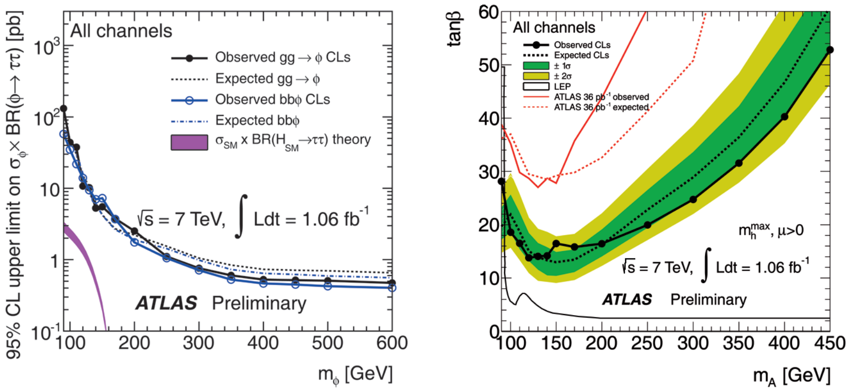

Fig. 2. – Expected and observed exclusion limits at the 95% CL from the combination of the analyses in the $e\mu$, $\ell\tau_h$ and $\tau_h\tau_h$ channels [11]. Left: Limits on production cross-section times branching fraction of a single scalar resonance decaying into $\tau\tau$. Right: Limits in the m_A-$\tan\beta$ plane of the MSSM in the MHMAX scenario.

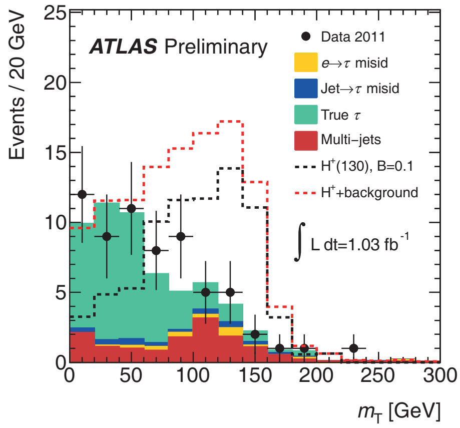

Fig. 3. – Transverse mass of the hadronic tau candidate and the missing transverse energy in the search for $H^+ \to \tau\nu$ for the analysis using hadronic tau lepton decays [14] using $1.03\,\mathrm{fb}^{-1}$.

of the analysis for the case where both the tau lepton and the W boson from the second top quark decaying hadronically can be found in [14]. In [15] the analysis where either only the tau lepton decays leptonically or in addition also the W boson from the second top quark decays leptonically can be found.

In the hadronic channel, dominant backgrounds are top quark pairs and W+jets with real tau leptons, which are estimated using a data-driven technique where events are selected with a similar event topology as in the analysis, but requiring a reconstructed muon instead of a tau candidate. The reconstructed muon is removed from the event and replaced by a simulated tau lepton decaying hadronically, where the tau momentum is taken from the reconstructed muon. Fake tau lepton contributions are estimated by applying measured fake rates to simulation. The multi-jet background is estimated using control regions defined by inverting tau identification and b-tagging requirements.

The transverse mass of the tau candidate and the missing momentum is used as a final discriminant [14] and is shown in fig. 3. The observation is consistent with background expectations and upper limits are set on $BR(t \to H^+b) \cdot BR(H^+ \to \tau\nu)$, as shown in fig. 4 (left). This result can also be interpreted in the MSSM using the MHMAX [13] scenario as limits on the $\tan\beta$ in dependence of the mass of the charged Higgs boson, as shown in fig. 4 (right).

In the channels involving electrons or muons, the signal is enhanced by cutting on the invariant mass of the b-quark and the electron or muon coming from the same top quark decay. The final discriminating variables used are transverse masses obtained by maximizing the invariant mass over all possible values of neutrino momenta in each event, as described in [16]. Also in these two channels the observation is consistent with background expectations [15]. Limits are set on $BR(t \to H^+b)$ assuming $BR(H^+ \to \tau\nu) = 1$ and on $\tan\beta$ in dependence of the charged Higgs boson mass in the MHMAX scenario [13] of the MSSM. The combined limit of the leptonic channels is shown in fig. 5.

Although the presence of leptons suppresses the backgrounds significantly, the higher statistics of hadronic tau decays leads to stronger limits from the hadronic channel than from the leptonic ones.

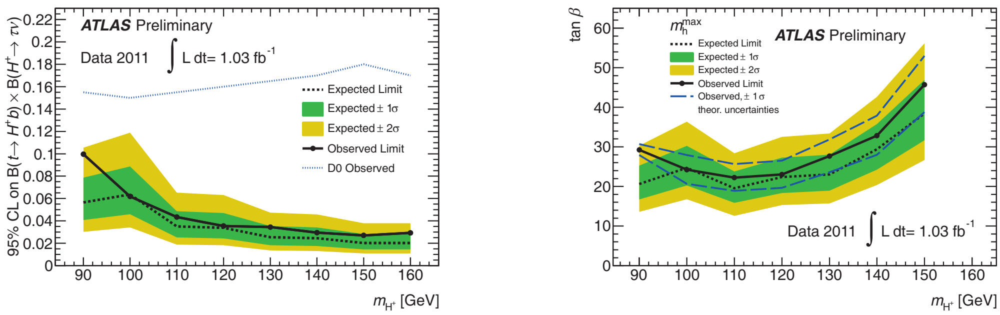

Fig. 4. – Expected and observed exclusion limits on the production of a charged Higgs boson in top quark decays in the hadronic channel [14] in dependence of the charged Higgs boson mass. Left: Limit on the braching fractions, right: limit on $\tan\beta$ using the MHMAX scenario of the MSSM.

3˙2. *Charged* $H^+ \to c\bar{s}$. – A search for charged Higgs bosons in the $H^+ \to c\bar{s}$ using $35\,\mathrm{pb}^{-1}$ of data taken in 2010 is documented in detail in [17]. This decay mode is important for low values of $\tan\beta < 1$. The analysis makes use of an electron or muon from the decay of the W-boson emanating from the second top quark decay. The signal characteristic is similar to semi-leptonic $t\bar{t}$ events, with the exception of the invariant mass of the two jets from the H^+ decay, which peaks at m_{H^+} instead of m_W. A kinematic fit is performed to select the two jets originating from the H^+ candidate. Both the overall number of events and the shape of the di-jet mass distribution are found to be consistent with SM expectations. Limits are set on the branching fraction $BR(t \to H^+ b)$, assuming $BR(H^+ \to c\bar{s}) = 1$, see fig. 6.

4. – Search for a fermiophobic Higgs boson

Fermiophobic extensions of the Standard Model [10] can lead to suppressed or even absent couplings of the Higgs field to some or all fermion generations. In this way, both production and decay of the Higgs boson are altered significantly. In the ATLAS analysis reported in [18] the fermiophobic benchmark scenario [10] is assumed, where all Higgs

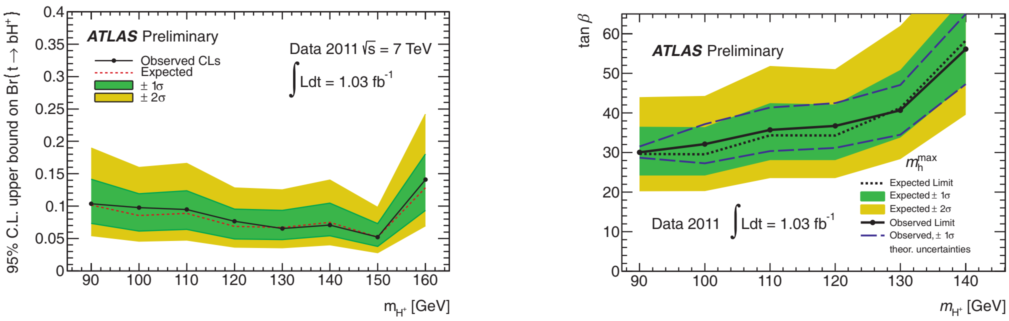

Fig. 5. – Expected and observed exclusion limits on the prodcution of a charged Higgs boson in top quark decays in the leptonic channels [15] in dependence of the charged Higgs boson mass. Left: Limit on the braching fraction, right: limit on $\tan\beta$ using the MHMAX scenario of the MSSM.

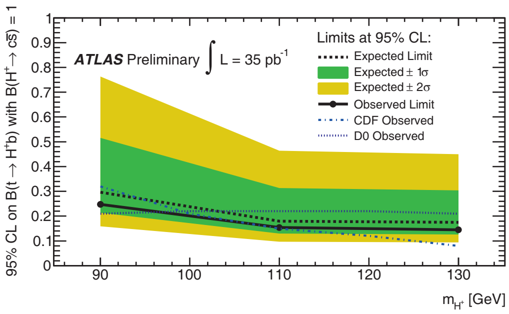

Fig. 6. – Expected and observed upper limit on the branching fraction $t \to H^+ b$ assuming only decays $H^+ \to c\bar{s}$ using a dataset of $35\,\mathrm{pb}^{-1}$ [17].

boson couplings to fermions are set to zero, but the couplings to gauge bosons are left at the Standard Model values. In this model the decay $H \to \gamma\gamma$ is strongly enhanced compared to the SM case, especially for low Higgs boson masses. The analysis follows the ATLAS Standard Model search for $H \to \gamma\gamma$ [4], using an integrated luminosity of $1.08\,\mathrm{fb}^{-1}$. Two energetic isolated photons with transverse momenta of at least 40 GeV and 25 GeV are required. The background consists primarily of di-photon production and misidentified photon-jet events. As in comparison to the SM case the Higgs boson is produced only in vector-boson fusion and Higgsstrahlung production, it has on average a higher transverse momentum. This particular topology is employed to increase the sensitivity of the analysis by considering the di-photon invariant mass spectrum in three ranges of the transverse momentum of the fermion pair. The three resulting mass spectra are fitted simultanously for Higgs boson mass hypotheses between 110 GeV and 130 GeV. No significant excess is observed, and the resulting exclusion limits are shown in fig. 7. The mass ranges 110–111 GeV and 113.5–117.5 GeV are excluded at the 95% CL.

5. – Search for doubly charged Higgs bosons

Doubly charged Higgs bosons are predicted by a number of extensions of the Standard Model, such as left-right symmetric models [6], Higgs triplet models [7] or little Higgs

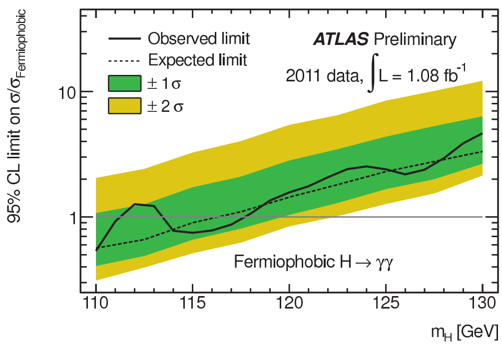

Fig. 7. – Exclusion limits at the 95% CL on the production rate of a fermiophobic Higgs boson normalized to the prediction of the fermiophobic benchmark scenario as a function of the Higgs boson mass hypothesis [18] using an integrated luminosity of $1.08\,\mathrm{fb}^{-1}$.

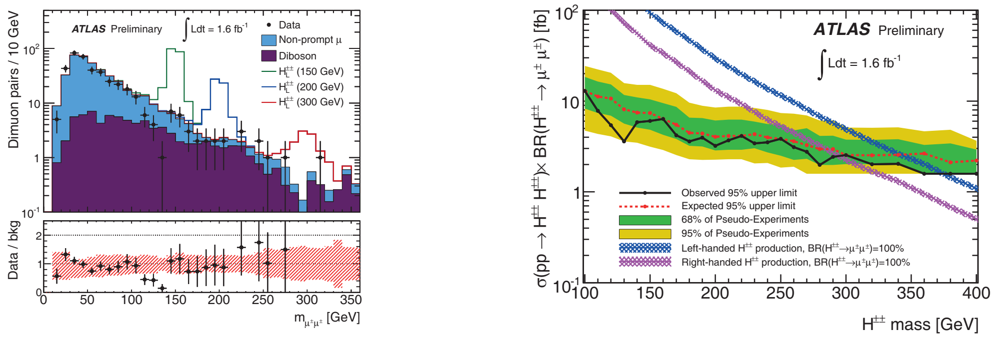

Fig. 8. – Results of the search for doubly charged Higgs bosons using 1.6 fb^{-1} of data [19]. Left: Invariant di-muon mass spectrum after selection cuts. Right: Upper limit at the 95% CL on the cross-section times branching fraction for pair production of doubly charged Higgs bosons decaying into muons.

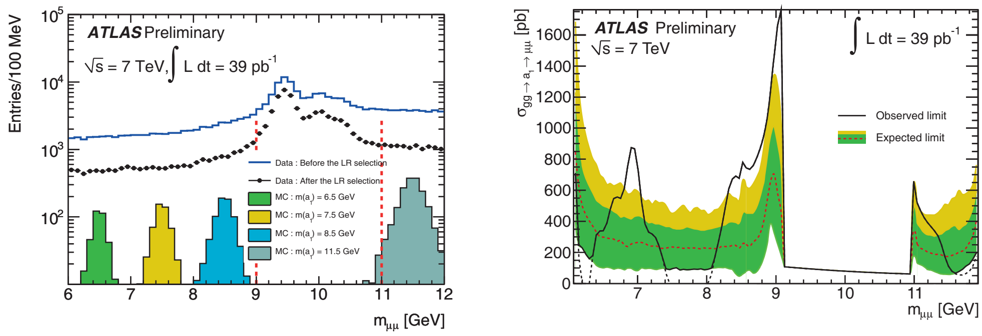

Fig. 9. – Left: Invariant di-muon mass spectrum for the search for $a_1 \to \mu\mu$ using a dataset of 39 pb^{-1} [21]. Right: Expected and observed exclusion limits on cross-section times branching fraction for $gg \to a_1 \to \mu\mu$ in dependence of the di-muon invariant mass [21].

models [8]. In proton-proton collisions, doubly charged Higgs bosons are dominantly produced in pairs via the Drell-Yann process $pp \to H^{++}H^{--}$. In a dataset with an integrated luminosity of 1.6 fb^{-1}, events with two muons with same electric charge are selected [19]. To ensure a short lifetime ($c\tau < 10\,\mu$m) and a relative natural width of the doubly charged Higgs boson of less than 1%, only coupling values of the H^{++} to muons between 10^{-5} and 0.5 are considered. The resulting di-muon invariant mass spectrum as shown in fig. 8 (left) is in good agreement with background predictions. The main background at low masses arises from non-prompt muons from heavy flavour decays or decays in flight of pions or kaons. For high invariant masses di-boson production gives an additional contribution. Limits are set on the production cross-section of doubly charged Higgs bosons as shown in fig. 8 (right). Assuming a branching fraction of the doubly charged Higgs boson into muons of one, limits are set on the H^{++} mass of 295 GeV (375 GeV) for right-handed (left-handed) production(2).

(2) The production cross-section for left-handed production is a factor of two larger than for right-handed production.

6. – Search for NMSSM $a_1 \to \mu^+\mu^-$

The Next-to-MSSM (NMSSM) introduces an additional complex singlet scalar field to solve the so-called μ-problem [9]. As a consequence, the Higgs sector expands to three CP-even scalars ($h_1 h_2 h_3$), two CP-odd scalars (a_1, a_2) and two charged scalars ($H^{\pm}$). The light CP-odd scalar a_1 can be rather light, *i.e.* below the threshold to produce B-hadron pairs ($m_{a_1} < 2m_B$). As in [20] the direct production of the a_1 in gluon-gluon fusion and the decay into muons has been considered in the ATLAS analysis presented in [21]. The signal over background ratio is enhanced by cutting on a Likelihood ratio (LR) based on the dimuon vertex fit and on muon isolation variables. The obtained invariant mass spectrum is shown in fig. 9 (left). The region around the Υ resonances is excluded from the search. Exclusion limits on the production cross-section are shown in fig. 9 (right). Deviations of the observed limit from its expected value are consistent with statistical fluctiations without an additional resonance after taking into account look-elsewhere effects [22].

7. – Summary

The ATLAS experiment has probed a wide variety of possible extensions of the SM Higgs sector. Neutral and charged Higgs bosons within the MSSM, fermiophobic models in $H \to \gamma\gamma$, doubly charged Higgs bosons and also light Higgs bosons within the NMSSM have been probed. In all analyses presented, using data between $35\,\text{pb}^{-1}$ and $1.6\,\text{fb}^{-1}$, the observations are compatible with background-only expectations. Stringent limits on production cross-sections and/or branching fractions have been set, and in part also been interpreted within the MSSM.

* * *

We acknowledge the support of the Initiative and Networking Fund of the Helmholtz Association, contract HA-101 (Physics at the Terascale).

REFERENCES

[1] ATLAS Collaboration, *JINST*, **3** (2008) S08003.
[2] Glashow S. L., *Nucl. Phys.*, **22** (1961) 579; Weinberg S., *Phys. Rev. Lett.*, **19** (1967) 1264; Salam A., *Conf. Proc. C*, **680519** (1968) 367.
[3] Higgs P. W., *Phys. Lett.*, **12** (1964) 132; *Phys. Rev. Lett.*, **13** (1964) 508; *Phys. Rev.*, **145** (1966) 1156; Englert F. and Brout R., *Phys. Rev. Lett.*, **13** (1964) 321; Guralnik G. S., Hagen C. R. and Kibble T. W. B., *Phys. Rev. Lett.*, **13** (1964) 585.
[4] ATLAS Collaboration, *Phys. Lett. B*, **710** (2012) 49.
[5] Nilles H. P., *Phys. Rep.*, **110** (1984) 1; Haber H. E. and Kane G. L., *Phys. Rep.*, **117** (1985) 75.
[6] Senjanovic G. and Mohapatra R. N., *Phys. Rev. D*, **12** (1975) 1502.
[7] Georgi H. and Machacek M., *Nucl. Phys. B*, **262** (1985) 463; Gunion J. F., Vega R. and Wudka J., *Phys. Rev. D*, **42** (1990) 1673.
[8] Arkani-Hamed N. *et al.*, *JHEP*, **08** (2002) 021.
[9] Maniatis M., *Int. J. Mod. Phys. A*, **25** (2010) 3505.
[10] LEP Higgs WG and ALEPH, DELPHI, L3 and OPAL Collaborations, hep-ex/0107035.
[11] ATLAS Collaboration, ATLAS-CONF-2011-132, `https://cdsweb.cern.ch/record/1383835`.

[12] Elagin A., Murat P., Pranko A. and Safonov A., *Nucl. Instrum. Methods A*, **654** (2011) 481.
[13] Carena M. S., Heinemeyer S., Wagner C. E. M. and Weiglein G., hep-ph/9912223.
[14] ATLAS Collaboration, ATLAS-CONF-2011-138, `https://cdsweb.cern.ch/record/1383841`.
[15] ATLAS Collaboration, ATLAS-CONF-2011-151, `https://cdsweb.cern.ch/record/1398187`.
[16] Gross E. and Vitells O., *Phys. Rev. D*, **81** (2010) 055010.
[17] ATLAS Collaboration, ATLAS-CONF-2011-094, `https://cdsweb.cern.ch/record/1367737`.
[18] ATLAS Collaboration, ATLAS-CONF-2011-149, `https://cdsweb.cern.ch/record/1397815`.
[19] ATLAS Collaboration, ATLAS-CONF-2011-127, `https://cdsweb.cern.ch/record/1383792`.
[20] Gunion J. F., *JHEP*, **08** (2009) 032.
[21] ATLAS Collaboration, ATLAS-CONF-2011-020, `https://cdsweb.cern.ch/record/1336749`.
[22] Lyons L., *Ann. Appl. Stat.* 2008, Vol. 2, No. 3, 887-915; Demortier L., *Proceedings of PHYSTAT-LHC Workshop 2007*, CERN-2008-001; Gross E. and Vitells O., *Eur. Phys. J. C*, **70** (2010) 525.

IL NUOVO CIMENTO Vol. 35 C, N. 6 Novembre-Dicembre 2012
DOI 10.1393/ncc/i2012-11388-0

Colloquia: LaThuile12

SUSY searches at CMS

M. Stoye on behalf of the CMS Collaboration
CERN - Geneva, Switzerland

ricevuto il 7 Settembre 2012

Summary. — This article summarizes searches for supersymmetry at the CMS detector performed in 2011 at the LHC with *pp* collisions energies of 7 TeV. For several leptonic and photonic supersymmetry searches results are presented with an integrated luminosity of approximately $5\,\text{fb}^{-1}$ that are shown for the first time in public at this conference. In none of the searches a potential supersymmetry signal has been observed and within the CMSSM gluiono masses below ~ 750 and first generation squarks masses below $\sim 1250\,\text{GeV}$ have been excluded. Finally an outlook on the focus of supersymmetry related activities at the CMS detector in the near future is given.

PACS 11.30.Pb – Supersymmetry.

1. – Introduction

Supersymmetry is one of the most favored extensions to the standard model. Supersymmetry can provide an explanation for the fine-tuning problem of the Higgs mass [1,2], dark matter WIMP particle candidates [3,4], and has further advantages. This proceeding reports on searches for events with supersymmetric topologies in proton-proton collisions at a center-of-mass energy of 7 TeV with a data sample that was collected by the Compact Muon Solenoid (CMS [5]) experiment during 2011 at the Large Hadron Collider (LHC). The integrated luminosity of the presented results ranges from approximately 1 to $5\,\text{fb}^{-1}$.

2. – Supersymmetry searches at CMS

A typical decay of two gluinos (supersymmetric partner of the gluon) is illustrated in fig. 1 for the R-parity-conserving case. For R parity conservation the two lightest stable particles (LSP) of supersymmetry leave the detector undetected. A large mass difference between the initially produced sparticles (super partners of particles) and the stable final state (s)particles leads to high transverse energy in the experiment. The typically large momenta of the LSPs in the sparticle decays of supersymmetry models lead to large

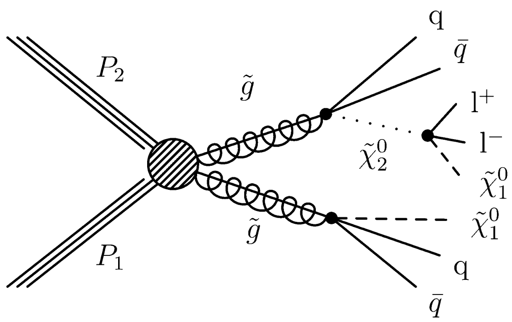

Fig. 1. – Typical supersymmetric decay chain.

missing transverse energy ($\not\!\!E_{\mathrm{T}}$) in the detector. The standard model particles of the decay lead to large visible transverse energy, which is often quantified by the scalar sum of the transverse energy of the jets (H_{T}) in an event. The observables $\not\!\!E_{\mathrm{T}}$ and H_{T} build the basis for many of the searches for superymmetry. Also a variety of kinematic variables are used in CMS. These variables include more information on angular distributions and individual energies of the visible decay products than H_{T}. Several kinematic variables used by CMS are described in the following:

α_T: This variable represents the balance of QCD topology events and is extremely robust against detector effects. The tails of the α_T distribution are effectively QCD free, but do contain significant fractions of events with supersymmetric topologies [6].

M_R,R^2: M_R approximates under certain assumptions [7] the mass-difference between the initially produced sparticles and the final state sparticles. R^2 is a ratio of two different approximation of the mass difference, which should only be correlated for supersymmetric events. Both variables separate potential supersymmetric events (or other pair produced particles that produce $\not\!\!E_{\mathrm{T}}$ in their decay) and standard model events.

M_{T2}: This variable is a generalization of the transverse mass, as *e.g.* used for W-bosons, to the case of two invisible particles. At large values of M_{T2} supersymmetric events would be expected to occur. Also information about the spectra of supersymmetry could be revealed in case of discovery [8].

L_P: (one leptonic search) This variable reflects the polarization behavior [9] for boosted W-bosons in standard model events and for supersymmetric events it would reveal the level of decorrelation between the $\not\!\!E_{\mathrm{T}}$ and the charged lepton due to the multiple particles contributing to $\not\!\!E_{\mathrm{T}}$. Again it separates well supersymmetry like events and standard model events.

Apart from the different variables used naturally many final states of sparticles decays are probed at CMS. These decays can be fully hadronic, *i.e.* without charged leptons in the final state. The fully hadronic searches have the best sensitivity in the constrained minimal supersymmetric model (CMSSM [10, 11]). The leptonic searches add to the sensitivity and also open the door to look for electroweak production of supersymmetric particles, especially in low background multi-lepton searches. The final states with photons are especially interesting for gauge mediated (GM [12]) supersymmetry, in which often χ^0s decay to a vector bosons, *i.e.* often photons, and a gravitino. Tags of b-jets

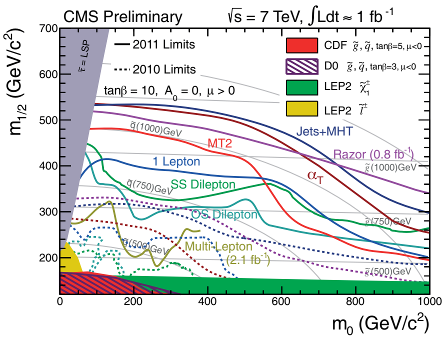

Fig. 2. – Limits of different analyses in the CMSSM for $\tan\beta = 10$ and $A_0 = 0$ with the 2011 CMS data for an integrated luminosity of approximately $1\,\mathrm{fb}^{-1}$.

are also used, *e.g.* especially to enhance sensitivity to the supersymmetric partner of top or bottom quarks. b-jets as well as τs play also an important role in supersymmetric Higgs searches, which are not covered here, but in the general report on Higgs searches at CMS.

Individual searches are published for each final state and in the most promising final states several analysis with different background estimation methods and different variables are available. At the time of the conference more than 30 results on SUSY searches have been made public. The limits in the CMSSM for several analysis done with $\sim 1\,\mathrm{fb}^{-1}$ of integrated luminosity is are shown in fig. 2. All CMS searches have in common that the background prediction is done using experimental data and not by directly comparing the simulation to the experimental data.

3. – First results with full 2011 dataset

This section describes first new results of the CMS searches with the dataset of the complete 2011 run, which has an integrated luminosity of approximately $5\,\mathrm{fb}^{-1}$.

3·1. *One leptonic search.* – The main background in one leptonic searches [13] are boosted W-bosons from W+jet or $t\bar{t}$ decays. Two alternative methods have been used to predict this background, both of which utilize the knowledge of the W-boson polarizations in the standard model. Recently, progress was made in theoretical prediction for the polarization of boosted W bosons in W+jets events at pp colliders [14]. Experimentally, the prediction were confirmed [9]. The polarization in $t\bar{t}$ is theoretically well known [15] and was also recently measured at the LHC [16, 17].

The relation between charged and neutral leptons in the decay of boosted W-bosons is governed by the polarization of the W boson. The relation of the spectra of neutrino and charged leptons are very different for the individual charges. The dominant polarization for boosted W-bosons in W + jets events at the LHC is lefthanded, thus most of the W-boson transverse momentum is given to the lefthanded lepton, which is the neutrino in the W^+ and the charged lepton in the W^- case. After the combination of the charges and the application of acceptance correction the charged and neutrino momentum spectra are roughly similar and most importantly; their relation is well understood. For $t\bar{t}$ events the dominant longitudinal polarization leads to charge and handedness symmetric lepton distribution. The lefthanded (right-handed) component of the $W^{+(-)}$ boson prefers giving its momentum to the neutrino. The dominant ($\sim 70\%$) longitudinlly po-

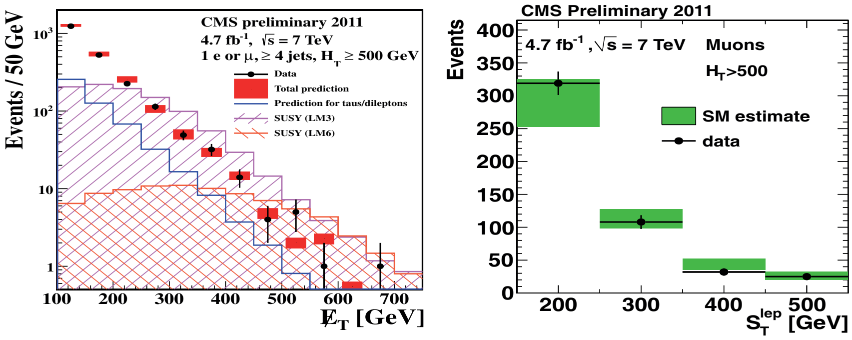

Fig. 3. – Left: Prediction of $\not{E}_{\mathrm{T}}$ with the LS method, right: S_T^{lep} predictions with the L_P method in the μ channel.

larized W-bosons distribute their transverse momentum equally to all charges. Again, after the acceptance cuts, charged lepton spectra and neutrino spectra are similar. For typical supersymmetric decays however $\not{E}_{\mathrm{T}}$ is expected to be significantly higher than the transverse momentum of the charged leptons, given that $\not{E}_{\mathrm{T}}$ is composed of the two LSPs and a neutrino compared to the single lepton. While charged lepton and $\not{E}_{\mathrm{T}}$ are typically aligned in the standard model, since both originate from the boosted W-boson decay, supersymmetric events show much looser angular correlations between the two.

One search selects exclusively one isolated lepton (μ or e) and greater or equal to four jets. The signal is enhanced by using several $\not{E}_{\mathrm{T}}$ bins and different H_{T} thresholds. The background prediction is done via the lepton spectrum method (LS method). In this method the charged lepton transverse-momentum distribution is used to predict the neutrino distribution. Contributions from fully leptonic $t\bar{t}$ events are estimated separately as well as resolution effects.

The other search in the exclusive one lepton channel (L_P method) selects events with greater than two jets. The events are also required to have L_P smaller than 0.15, where L_P is the projection of the transverse momentum of the charged lepton to the direction of the W-boson transverse momentum and normalized to the W-boson transverse momentum: $L_P = P_T(l^{\pm})\cos((l^{\pm}, W)/P_T(W))$. For the selected events the charged lepton is thus either not aligned with $\not{E}_{\mathrm{T}}$ ($\sim$boosted W-boson direction in standard model) or the transverse momentum of the charged lepton is much smaller than $\not{E}_{\mathrm{T}}$. Both ingredients separate supersymmetry and standard model. Thresholds on H_{T} and bins in $S_T^{lep}(= \not{E}_{\mathrm{T}} + P_T(l^{\pm}))$ are used to further reduce the background. The main control sample used for the background prediction are the events with $L_P > 0.3$, *i.e.* events in which $\not{E}_{\mathrm{T}}$ and charged lepton are aligned in ϕ and have similar amplitude.

Figure 3 shows the prediction of $\not{E}_{\mathrm{T}}$ using the LS method as well as prediction of S_T^{lep} bins using the L_P method. No excess had been observed for any H_{T} threshold. The interpretation of the result in context of the CMSSM for the $H_{\mathrm{T}} > 750\,\mathrm{GeV}$ and the $H_{\mathrm{T}} > 1\,\mathrm{TeV}$ thresholds are presented in fig. 4.

3·2. *Opposite-sign leptonic search.* – The searches requires two leptons with opposite charge. The leptons can be of any flavor (e, μ, τ). One search uses the variables $\not{E}_{\mathrm{T}}$ and H_{T}, one uses a mass edge technique [18, 19] and one an artificial neural network with several input variables [20]. The first is discussed here in more detail. The dominant background to the $\not{E}_{\mathrm{T}}$ search is $t\bar{t}$. The same principle as in the single lepton searches is applied for the main background, namely that the relation between charged leptons

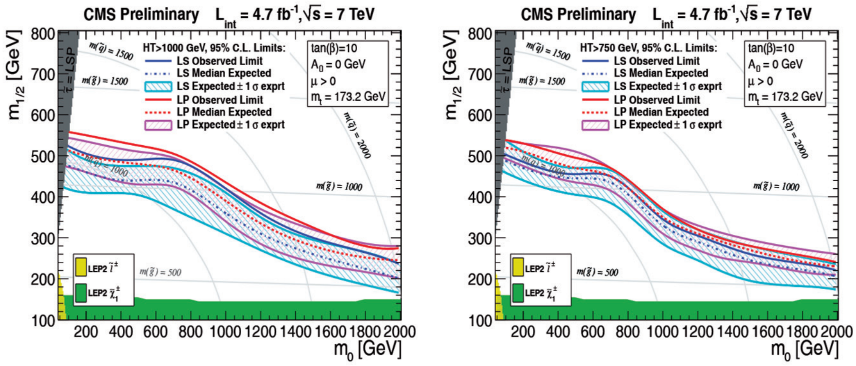

Fig. 4. – Left: limits in CMSSM for a H_{T} threshold of 750 GeV, right: limits in CMSSM for a H_{T} threshold of 1 TeV.

and neutrinos is well known. The transverse momentum of the vector sum the transverse momenta of the charged leptons ($P_T(ll)$) is used for the prediction $\not{E}_{\mathrm{T}}$. $P_T(ll)$ is scaled according to the known ratio of $P_T(ll)$ over $P_T(\nu\nu)$ and smeared according to a $\not{E}_{\mathrm{T}}$ resolution that has been determined in data as for the LS method. Figure 5 shows the prediction and the observed events for various H_{T} and $\not{E}_{\mathrm{T}}$ thresholds. No excess over the expected number of standard model events has been observed. Figure 5 shows the interpretation of the result in the context of the CMSSM.

3·3. *Same-signs leptonic search.* – In this search two isolated leptons of any flavor, but of same charge are required. The small backgrounds allow relatively relaxed $\not{E}_{\mathrm{T}}$ and H_{T} thresholds, if none of the leptons is a hadronic τ. To reduce more background in the τ channels $\not{E}_{\mathrm{T}}$ and H_{T} thresholds are increased. The dominant background stems from "fake" isolated leptons, *e.g.* lepton from heavy flavor jets, photon conversions and other sources. In most cases only one of the leptons is fake, as can happen, *e.g.*, in semileptonic $t\bar{t}$ decays, where one b-quark produces a "fake" isolated lepton. This background is estimated via a "Tight-Loose" ratio. The ratio of "fake" leptons in a loose

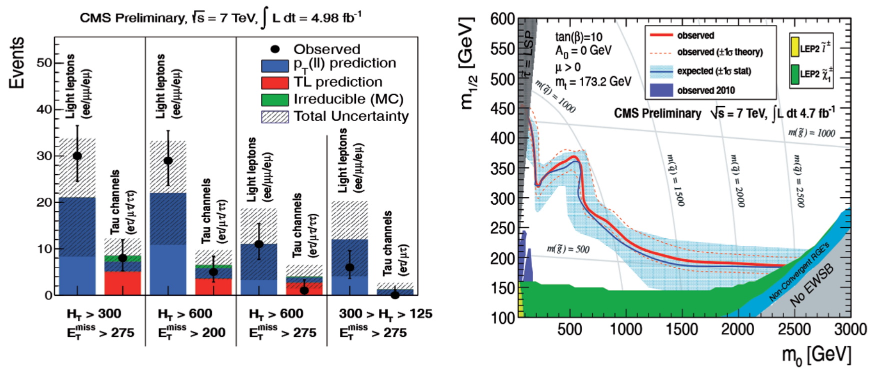

Fig. 5. – Left: prediction for different kinematic regions for the opposite-sign lepton search, right: limit of opposite lepton search in the CMSSM for $\tan\beta = 10$ with the 2011 CMS data (updates results of [18, 19] to full 2011 dataset with approximately $5\,\mathrm{fb}^{-1}$).

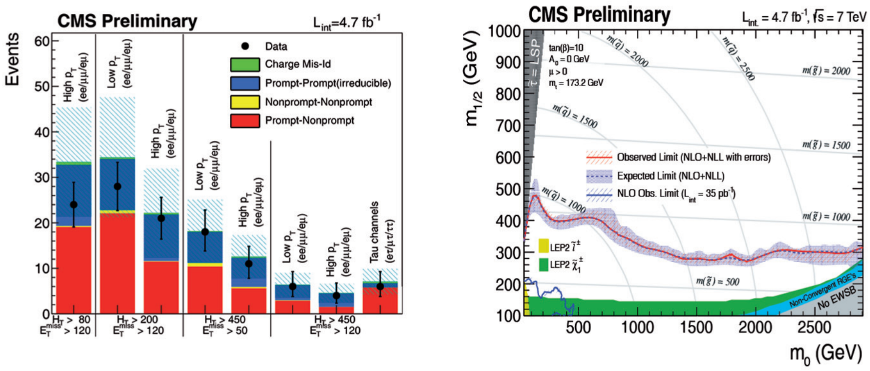

Fig. 6. – Left: prediction for different kinematic regions for the same sign leptons search, right: limit of same-sign lepton search in the CMSSM for $\tan\beta = 10$ with the 2011 CMS data (updates results of [21, 22] to full 2011 dataset with approximately $5\,\mathrm{fb}^{-1}$).

lepton identification to a tight identification used in the search is measured in data in a multijet sample. This ratio is than applied to an control sample done with the loose electron selection (but else the final selection) to estimate the "fake" lepton events for the tight selection. Details and further background estimations can be found in [21, 22]. The irreducible background from WW and WZ is estimated from simulation and a 50% uncertainty on these numbers has been derived.

The prediction for the different backgrounds and the data signal yield is presented in fig. 6. No excess is observed and the interpretation of the result in the context of the CMSSM is shown in fig. 6. The search is especially sensitive at large m_0. In this region electroweak production enhances (multi) leptonic channels.

3·4. *One and two photon searches*. – Photon searches for supersymmetry [23] are especially interesting in the context of GM supersymmetry. If the gravitino is the LSP, than the next lightest sparticle is typically a neutralino or chargino. The neutralinos decay to gravitino and photon or Z-boson. Neutralinos are an admixture of wino and bino, if the neutralino is more bino like, than the photon decay is preferred, else the Z-boson channel is enhanced (fig. 7). The search does not veto on leptons in order to keep events in which a chargino decays to gravitino and a W-boson, that can decay leptonically.

The search for signal is done in $\not{E}_{\mathrm{T}}$ bins. The two-photon search requires only at least one jet and two rather loose photons. Due to trigger constraints, the single photon search requires H_{T} greater than 450 GeV and a single high P_T (> 80 GeV) photon. In both

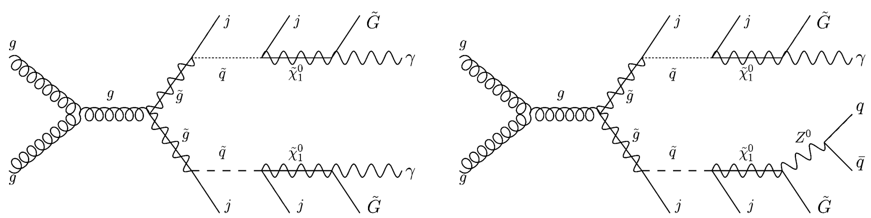

Fig. 7. – Left: typical decay chain for bino-like χ_1^0, right: typical decay for wino-like χ_1^0.

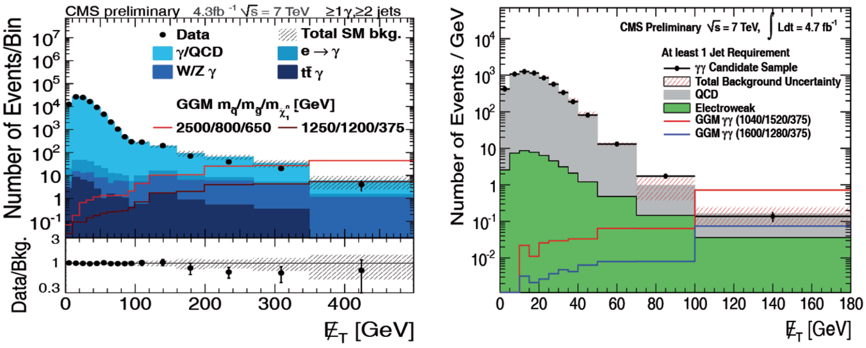

Fig. 8. – Left [23]: predicted and observed $\not{E}_{\mathrm{T}}$ distribution for single γ channel, right [23]: predicted and observed $\not{E}_{\mathrm{T}}$ distribution for two-γ channel.

selections the main backgrounds are events with $\not{E}_{\mathrm{T}}$ that does not stem from a single isolated neutrino, but rather detector effects and heavy flavor jets. The photons for this background are either jets mimicking photons from pure QCD events or prompt photons produced in conjunction with jets. The main background estimation is done via a control sample in which the photon identification criteria are relaxed, but do not include the final photons. To model the shape of the $\not{E}_{\mathrm{T}}$ distribution for the final selection the events of the control sample are weighted according to their transverse momentum to reproduce the transverse momentum of the photon of the tight selection. The $\not{E}_{\mathrm{T}}$ distribution of the weighted control sample is than normalized to the $\not{E}_{\mathrm{T}}$ distribution of the final selection in a signal free region of $\not{E}_{\mathrm{T}}$, which is, *e.g.*, $\not{E}_{\mathrm{T}} < 20\,\mathrm{GeV}$ for the $\gamma\gamma$ case. The renormalized $\not{E}_{\mathrm{T}}$ distribution is used as estimation of the background in the high $\not{E}_{\mathrm{T}}$ search region. The second largest background are events where an electron is misidentified as photon in W-boson decays, *i.e.* events with true $\not{E}_{\mathrm{T}}$ from neutrinos. The probability of electrons to "fake" photons has been determined in data. To estimate the background from electron mislabeled as photon, this "fake" probability is applied to a control sample in which, instead of photons, electrons have been selected. The background prediction and the observed events for the different $\not{E}_{\mathrm{T}}$ bins are presented in fig. 8. No excess has been observed and the interpretation of the result in the context of supersymmetry is shown in fig. 9.

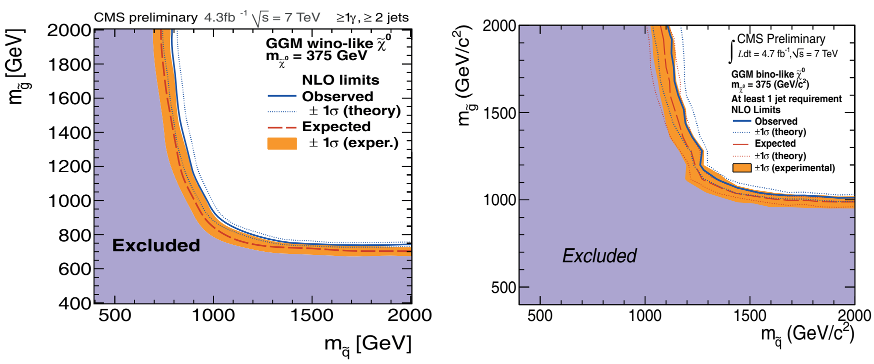

Fig. 9. – Left [23]: exclusion limit from γ+jets for wino-like χ^0, right [23]: exclusion limit from $\gamma\gamma$+jets for bino-like χ^0.

4. – Outlook and future activities

Currently much effort is directed towards the search for third generation squarks in CMS. To solve the hierarchy problem without any tuning of supersymmetry a light squark ($\mathcal{O}$(few 100 GeV)) is needed. The third generation is likely to be the lightest generation of squarks. See the report of A. Falkowski in this conference for details on this topic. At the time of the conference no new constrains on third generation squark were available, however the year 2012 will presumably yield enough data to constrain the third generation significantly, if no hint of any signal is found.

Other new searches with respect to last year have been introduced, among them several more exclusive searches with many final state particles. *E.g.* a search in the WZ will probe the electroweak production of supersymmetry. Further, more sophisticated analysis methods are started to be deployed. The first neural-net based analysis [20] has recently been presented.

5. – Conclusion

New results with the full 2011 dataset from CMS have been presented. They did not show any excess of data with respect to the standard model. In the context of CMSSM, CMS constrains first generation squarks to masses above ~ 1.25 TeV and gluinos above ~ 750 GeV. The year 2012 will be very interesting for supersymmetry and results for searches for the third generation squarks will be presented.

REFERENCES

[1] Witten E., *Nucl. Phys. B*, **188** (1981) 513.
[2] Dimopoulos S. and Georgi H., *Nucl. Phys. B*, **193** (1981) 150.
[3] Zwicky F., *Helv. Physica Acta*, **6** (1933) 110.
[4] Jungman G. and Kamionkowski M., *Phys. Rep.*, **267** (1996) 195.
[5] CMS Collaboration, *JINST*, **03** (2008) S08004.
[6] CMS Collaboration, *Phys. Lett. B*, **698** (2011) 196218.
[7] CMS Collaboration, *Phys. Rev. D*, **85** (2012) 012004.
[8] CMS Collaboration, CMS-PAS-SUS-12-002.
[9] CMS Collaboration, *Phys. Rev. Lett.*, **107** (2011) 021802.
[10] Kane G. *et al.*, *Phys. Rev. D*, **49** (1994) 6173.
[11] Chamseddine A. H. *et al.*, *Phys. Rev. Lett.*, **49** (1982) 970.
[12] Meade P. *et al.*, *JHEP*, **03** (2009) 016.
[13] CMS Collaboration, CMS-PAS-SUS-12-010.
[14] Bern Z. *et al.*, *Phys. Rev. D*, **84** (2011) 034008.
[15] Fischer M. *et al.*, *Phys. Rev. D*, **63** (2001) 031501.
[16] ATALS Collaboration, arXiv:1205.2484v1.
[17] CMS Collaboration, CMS-PAS-TOP-11-020.
[18] CMS Collaboration, *JHEP*, **06** (2011) 026.
[19] CMS Collaboration, CMS-PAS-SUS-11-010.
[20] CMS Collaboration, CMS-PAS-SUS-11-018.
[21] CMS Collaboration, *JHEP*, **06** (2011) 077.
[22] CMS Collaboration, CMS-PAS-SUS-11-010.
[23] CMS Collaboration, CMS-PAS-SUS-12-001.

IL NUOVO CIMENTO Vol. 35 C, N. 6 Novembre-Dicembre 2012
DOI 10.1393/ncc/i2012-11389-y

Colloquia: LaThuile12

Searches for Supersymmetry at ATLAS

R. Brunelière on behalf of the ATLAS Collaboration
Fakultät für Mathematik und Physik, Albert-Ludwigs-Universität - Freiburg i.Br., Germany

ricevuto il 7 Settembre 2012

Summary. — Recent results of searches for supersymmetry by the ATLAS Collaboration in up to $4.7\,\mathrm{fb}^{-1}$ of $\sqrt{s} = 7\,\mathrm{TeV}$ pp collisions recorded with the LHC in 2011 are reported. Emphasis is placed on the different classes of supersymmetric particles being sought and limits are set within the context of a wide variety of models.

PACS 12.60.Jv – Supersymmetric models.

1. – Introduction

With its centre-of-mass energy of 7 TeV, the Large Hadron Collider (LHC) provides a unique facility to test models beyond the Standard Model (SM) of particle physics. Supersymmetry (SUSY) [1] is one of the most promising theories extending the Standard Model as it could solve the gauge hierarchy problem. In its simplest form, the Minimal Supersymmetric Standard Model (MSSM), a supersymmetric partner differing by a half-of-unit of spin is associated to every Standard Model particle. After the symmetry is broken, if solving the hierarchy problem, some of the superpartners should have masses not far from the TeV scale and thus could be observed in pp collisions at the LHC. Depending on the mass spectrum and properties of the new supersymmetric particles, different search strategies are used. In R-parity–conserving models, supersymmetric particles are always produced in pairs and the lightest supersymmetric particle (LSP) is stable, escaping the detector and thus providing a possible dark-matter candidate. In addition, if the superpartners of the quarks, the squarks, or the gluon, the gluino, can be directly produced in pp collisions, then their production dominates the cross section leading to final states with multiple jets, large missing transverse momentum and possibly leptons. This class of signature is treated in sect. **2**. However, if SUSY solves naturally the gauge hierarchy problem, *i.e.* without extensive fine-tuning of the parameters, only the third generation squarks contributing mainly to the Higgs radiative corrections are required to be light. Depending on the mass spectrum, it could be that only third-generation squarks or third-generation squarks plus the gluino can be produced at the LHC leading to more specific final states enhanced in heavy flavor quarks. Those important specific cases are discussed in sect. **3**. Finally, sect. **4** deals with more exotic final states involving a resonance such as can occur if R-parity is not conserved, or long-lived particles obtained when the mass splitting between the lightest and the next-to-lightest supersymmetric particles is sufficiently small that the particle becomes quasi-stable.

2. – Generic strong production signatures

The ATLAS Collaboration is carrying out a set of analyses dedicated to the search of supersymmetric particles produced via strong interaction and leading to the following signatures:

– 0 leptons plus 2-6 jets and large missing transverse momentum [2, 3],

– 0 leptons plus 6-8 jets and moderate missing transverse momentum [4, 5],

– 1 lepton plus 2-4 jets and large missing transverse momentum [6, 7],

– 2 same-sign leptons plus 4 jets and large missing transverse momentum [8],

where a lepton means an isolated electron or muon. Although SUSY particles are produced via strong processes, leptons could appear during the cascade decays when gauginos or sleptons are produced. Since no excess has been observed, all results were interpreted in a number of models and exclusion limits were set. The most common approach is to interpret the results in the MSUGRA/CMSSM model [9] which is modeled via 5 free parameters. The limits are set in a plane spanned by a common scalar mass parameter at the GUT scale m_0 and a common gaugino mass parameter at the GUT scale $m_{1/2}$. The three remaining free parameters are defined to a constant value; $A_0 = 0$ for the common trilinear coupling parameter, $\mu > 0$ for the Higgs missing parameter, and $\tan(\beta) = 10$ for the ratio of the vacuum expectation values of the two Higgs doublets. Figure 1 shows on its left the limits obtained for the different channels studied by ATLAS.

Another common approach is to consider the MSSM keeping only a subset of SUSY particles and possible decays within reach. The right part of fig. 1 shows results obtained with an example of such a model where only the gluino, one common first or second generation squark and the lightest neutralino are considered. Limits are set as a function of the gluino and squark masses when the LSP is massless. For all models and analyses, the $\mathrm{CL_s}$ prescription [10] is used to derive 95% Confidence Level (CL) exclusion regions. Signal cross sections are calculated to next-to-leading order in the strong coupling constant (NLO) [11] including the resummation of soft gluon emission at next-to-leading-logarithmic accuracy (NLL) [12]. In the simplified model with light neutralinos the limit on the gluino mass is approximately 940 GeV, and on the squark mass is 1380 GeV. In the CMSSM/MSUGRA case, equal mass squarks and gluinos are excluded below 1400 GeV.

3. – Signatures involving third-generation supersymmetric particles

As has been mentioned in the introduction, one of the most important motivations for TeV-scale supersymmetry is the fact that SUSY might provide a "natural" way to solve the gauge hierarchy problem, limiting sensitivity of the Higgs boson mass to radiative corrections. To stabilize the Higgs mass naturally, the necessary ingredients should be a relatively light top quark partner, the stop, an associated sbottom quark not much heavier, and a gluino of mass not much larger than approximately 1.5 TeV. The masses

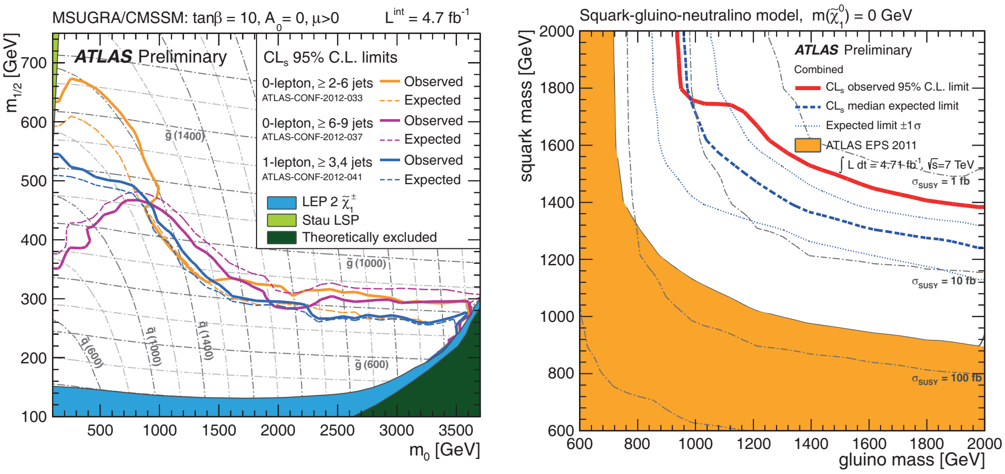

Fig. 1. – Left: Exclusion contours in the MSUGRA/CMSSM m_0-$m_{1/2}$ plane for $A_0 = 0$, $\tan(\beta) = 10$ and $\mu > 0$ [7]. Results are shown for three different analyses with 0 leptons plus 2–6 jets plus missing momentum, 0 leptons plus 6–8 jets plus missing momentum, and 1 lepton plus 2–4 jets plus missing momentum. Right: 95% $\mathrm{CL_s}$ exclusion limits obtained in a simplified MSSM scenario with only strong production of gluinos and first- and second-generation squarks, and direct decays to jets and neutralinos [3].

of other SUSY particles are not significantly constrained by the Higgs mass and can be set to much heavier masses. This model leads, depending on the mass hierarchy of the different remaining particles, to the characteristic signatures:

– If the gluino is sufficiently light, pair production of gluinos decaying subsequently into bottom and top quarks via on-shell or off-shell sbottoms and stops. A large number of b-tagged jets, large missing transverse momentum and possibly leptons (when top quarks decay leptonically) are expected in the final state leading to striking signatures.

– If the gluino is too heavy, the only remaining production process is the direct production of a pair of sbottoms or stops. The former case leads possibly to a final state with exactly two bottom quarks and large missing transverse momentum. The latter case is more complicated to constrain due to its similarity with top quark pair production and the large number of possible decay processes.

Whichever is the decay process, results are interpreted in term of simplified models where only the relevant SUSY particles are considered. Gluino-mediated sbottom pair production is tested in channels with no lepton, at least three jets, large missing transverse momentum and at least one or two b-tagged jets [13]. Figure 2 on the left shows the exclusion limits obtained in a MSSM model where the gluino decays exclusively into the lightest sbottom and a bottom quark, and the sbottom decays into a bottom and a neutralino. The neutralino mass is set to 60 GeV. Gluino masses below 920 GeV are excluded for sbottom masses up to about 800 GeV. In order to constrain the gluino-mediated stop pair production, two channels are used, either with one lepton, at least four jets, large missing transverse momentum and one b-tagged jet, or with two same-sign leptons, at least four jets, and large missing transverse momentum. Results are

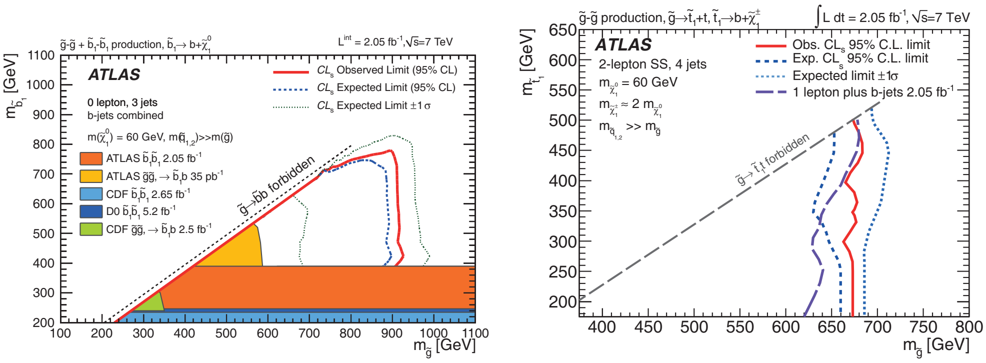

Fig. 2. – Left: 95% $\mathrm{CL_s}$ exclusion limits obtained in the context of a MSSM model in the $m_{\tilde{g}}$-$m_{\tilde{b}_1}$ plane [13]. Right: 95% $\mathrm{CL_s}$ exclusion limits obtained in the context of a MSSM model in the $m_{\tilde{g}}$-$m_{\tilde{t}_1}$ plane [8].

interpreted in a MSSM model with each gluino decaying into a stop and a top, a stop decaying into a bottom quark and a chargino, and a chargino decaying to the neutralino plus a W. Figure 2 on the right shows the exclusion limits in the $m_{\tilde{g}}$-$m_{\tilde{t}_1}$ plane with the chargino and neutralino masses set to $m(\tilde{\chi}_1^{\pm}) = 2 \cdot m(\tilde{\chi}_1^0)$ and $m(\tilde{\chi}_1^0) = 60\,\mathrm{GeV}$, respectively. Gluino masses below 660 GeV are excluded for stop masses up to about 460 GeV. The search for sbottom pair production has been performed when assuming that the sbottom fully decays into a bottom quark and the lightest neutralino leading to a characteristic signature with exactly two b-tagged jets and large missing transverse momentum [14]. Results are interpreted in the plane $m(\tilde{b}_1) - m(\tilde{\chi}_1^0)$ and shown in fig. 3 (left). Sbottom masses up to 390 GeV are excluded for neutralino masses below 60 GeV.

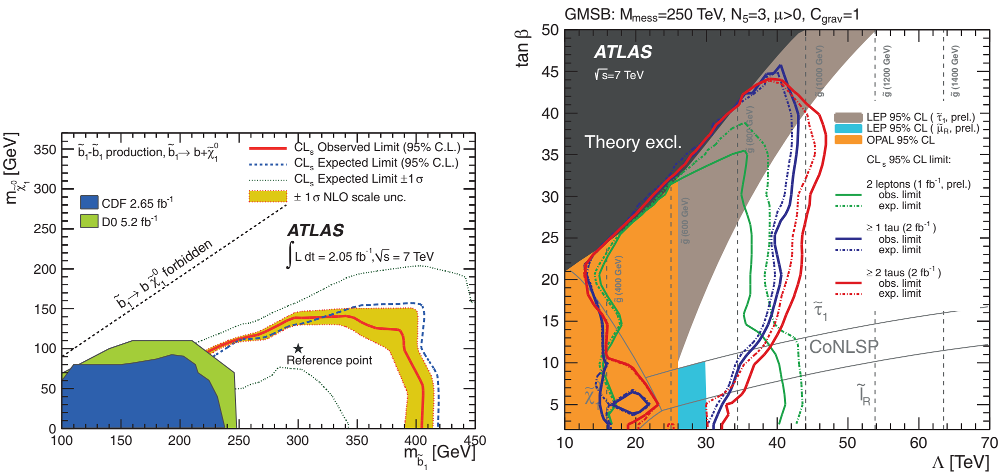

Fig. 3. – Left: 95% $\mathrm{CL_s}$ exclusion limits in the $m(\tilde{b}_1)$-$m(\tilde{\chi}_1^0)$ plane for a model assuming 100% decay of the lightest sbottom into a bottom quark and the lightest neutralino [14]. Right: 95% $\mathrm{CL_s}$ exclusion limits obtained for the minimal GMSB model in the Λ-$\tan(\beta)$ plane [18]. The CoNLSP region means that both the $\tilde{\tau}_1$ and the $\tilde{l}_R$ are the NLSP.

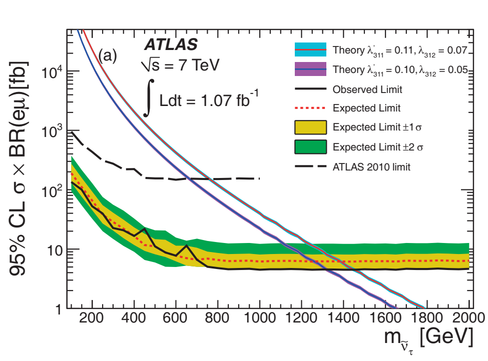

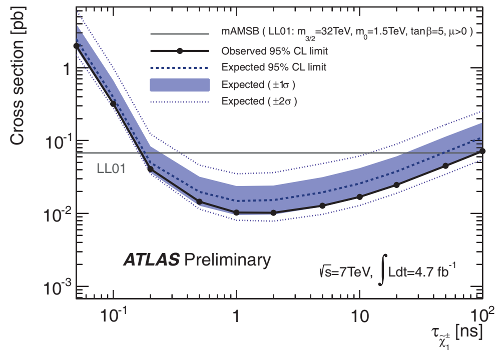

Fig. 4. – Left: 95% CL upper limits on $\sigma(pp \to \tilde{\nu}_\tau) \times BR(\tilde{\nu}_\tau \to e\mu)$ as a function of $m(\tilde{\nu}_\tau)$ [19]. Right: 95% CL upper limits on the signal cross section as a function of chargino lifetime for $m(\tilde{\chi}_1^\pm) = 90.2\,\text{GeV}$ [23].

For a given flavor, third generation SUSY particles are generally lighter than the first and second generation sparticles because of the mixing between the left-handed and the right-handed states which is proportional to the Standard Model particle mass. In particular, in Gauge Mediated Supersymmetry Breaking (GMSB) models [15], the SUSY partner of the tau lepton, the stau, could be the next-to-lightest SUSY particle leading to final states with a substantial number of tau leptons. In order to search for such a possible scenario, channels with one or two hadronic tau candidates, multiple jets and high missing transverse momentum have been designed [16, 17]. Since no excess was found, results have been interpreted in the minimal GMSB model which is formalized as a function of 6 free parameters: the SUSY breaking mass scale felt by the low-energy sector Λ, the messenger mass M_{mess}, the number of $SU(5)$ messengers N_5, the ratio of the vacuum expectation values $\tan(\beta)$, the Higgs sector mixing parameter μ, and the scale factor for the gravitino mass C_{grav}. Assuming $M_{mess} = 250\,\text{TeV}$, $N_5 = 3$, $\mu > 0$, and $C_{grav} = 1$, exlusion limits are set in the Λ-$\tan(\beta)$ plane and shown on fig. 3(right).

4. – Exotic signatures with resonances or long-lived particles

While most signatures studied in sects. **2** and **3** incorporate requirements for significant missing transverse momentum, this constraint can be evaded in some supersymmetric scenarios and require specific search studies. This is the case when R-parity is violated and the SUSY particle promptly decays to Standard Model particles. There are many possible R-parity violating couplings, which can lead to numerous possible final states. As an example, lepton and baryon violating couplings although constrained by precision electroweak data could exist and lead to the direct production of $e\mu$ pairs either via exchange of an s-channel tau neutrino SUSY partner $\tilde{\nu}_\tau$ exchange [19] or via exchange of a t-channel top quark SUSY partner $\tilde{t}_1$ [20]. The s-channel $\tilde{\nu}_\tau$ exchange leads to a final state with an $e\mu$ resonance, while the t-channel $\tilde{t}_1$ exchange results in an $e\mu$ continuum excess. Figure 4 (left) shows the upper limit obtained on $\sigma(pp \to \tilde{\nu}_\tau) \times BR(\tilde{\nu}_\tau \to e\mu)$ as a function of $m(\tilde{\nu}_\tau)$. Assuming coupling values $\lambda_{311} = 0.10$ and $\lambda_{312} = 0.05$, tau sneutrinos with a mass below 1.32 TeV are excluded.

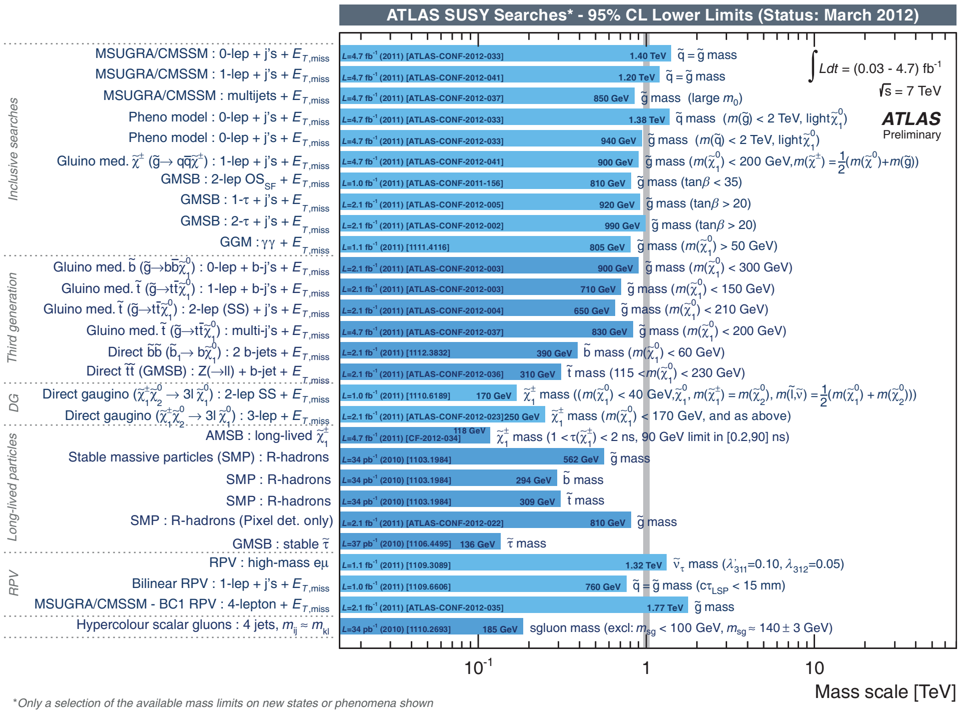

Fig. 5. – Mass reach of ATLAS searches for Supersymmetry [28]. Only a representative selection of the available results is shown.

Another SUSY search strategy involves seeking long-lived SUSY particles inside the ATLAS detector. Depending on the lifetime and the nature of the SUSY particle, the ATLAS Collaboration has been searching for displaced vertices [21], for kinked or disappearing tracks [22, 23], and for stable massive particles [24-26]. Kinked or disappearing tracks could exist in Anomaly Mediated Supersymmetry-Breaking (AMSB) models [27] when the lightest chargino $\tilde{\chi}_1^{\pm}$ and the lightest neutralino $\tilde{\chi}_1^0$ are almost degenerate. Results are interpreted as a function of the chargino mass and lifetime and upper limits are set on the cross-section as a function of these parameters as shown in fig. 4 (right). Other parameters from the minimal AMSB model are set to $m_{3/2} = 32\,\text{TeV}$ for the gravitino mass, $m_0 = 1.5\,\text{TeV}$ for the universal scalar mass, $\tan(\beta) = 10$ for the ratio of Higgs vacuum expectation values, and $\mu > 0$ for the sign of the higgsino mass term.

5. – Conclusion

Key figures from ATLAS supersymmetry searches are summarized in fig. 5 [28]. No evidence for supersymmetry has been found but new data with increased centre-of-mass energies and the study of new channels will bring new opportunities for the discovery of a potential excess.

REFERENCES

[1] See the review of Martin S. P., *A Supersymmetry primer*, hep-ph/9709356v6.
[2] Atlas Collaboration, *Phys. Lett. B*, **710** (2012) 67 arXiv:1109.6572 [hep-ex].
[3] ATLAS Collaboration, ATLAS-CONF-2012-033, `https://cdsweb.cern.ch/record/1432199`.
[4] Atlas Collaboration, *JHEP*, **11** (2011) 099 arXiv:1110.2299 [hep-ex].
[5] ATLAS Collaboration, ATLAS-CONF-2012-037, `https://cdsweb.cern.ch/record/1432204`.
[6] Atlas Collaboration, *Phys. Rev. D*, **85** (2012) 012006 arXiv:1109.6606 [hep-ex].
[7] ATLAS Collaboration, ATLAS-CONF-2012-041, `https://cdsweb.cern.ch/record/1435195`.
[8] Atlas Collaboration, *Phys. Rev. Lett.*, **1008** (2012) 241802 arXiv:1203.5763 [hep-ex].
[9] Chamseddine A. H., Arnowitt R. L. and Nath P., *Phys. Rev. Lett.*, **49** (1982) 970; Barbieri R., Ferrara S. and Savoy C. A., *Phys. Lett. B*, **119** (1982) 343; Ibanez L. E., *Phys. Lett. B*, **118** (1982) 73.
[10] Read A. L., *J. Phys. G*, **28** (2002) 2693.
[11] Beenakker W., Hopker R. and Spira M., hep-ph/9611232.
[12] Beenakker W., Brensing S., Kramer M., Kulesza A., Laenen E., Motyka L. and Niessen I., *Int. J. Mod. Phys. A*, **26** (2011) 2637 arXiv:1105.1110 [hep-ph].
[13] Atlas Collaboration, *Phys. Rev. D*, **85** (2012) 112006 arXiv:1203.6193 [hep-ex].
[14] Atlas Collaboration, *Phys. Rev. Lett.*, **108** (2012) 181802 arXiv:1112.3832 [hep-ex].
[15] Dine M. and Fischler W., *Phys. Lett. B*, **110** (1982) 227; Alvarez-Gaume L., Claudson M. and Wise M. B., *Nucl. Phys. B*, **207** (1982) 96; Nappi C. R. and Ovrut B. A., *Phys. Lett. B*, **113** (1982) 175; Dine M. and Nelson A. E., *Phys. Rev. D*, **48** (1993) 1277 hep-ph/9303230; Dine M., Nelson A. E. and Shirman Y., *Phys. Rev. D*, **51** (1995) 1362 hep-ph/9408384; Dine M., Nelson A. E., Nir Y. and Shirman Y., *Phys. Rev. D*, **53** (1996) 2658 hep-ph/9507378.
[16] Atlas Collaboration, arXiv:1204.3852 [hep-ex].
[17] Atlas Collaboration, arXiv:1203.6580 [hep-ex].
[18] Atlas Collaboration, public material from `https://atlas.web.cern.ch/Atlas/GROUPS/PHYSICS/PAPERS/SUSY-2011-16/`.
[19] Atlas Collaboration, *Eur. Phys. J. C*, **71** (2011) 1809 arXiv:1109.3089 [hep-ex].
[20] Atlas Collaboration, arXiv:1205.0725 [hep-ex].
[21] Atlas Collaboration, *Phys. Lett. B*, **707** (2012) 478 arXiv:1109.2242 [hep-ex].
[22] Atlas Collaboration, *Eur. Phys. J. C*, **72** (2012) 1993 arXiv:1202.4847 [hep-ex].
[23] ATLAS Collaboration, ATLAS-CONF-2012-034, `https://cdsweb.cern.ch/record/1432200`.
[24] Atlas Collaboration, *Phys. Lett. B*, **701** (2011) 1 arXiv:1103.1984 [hep-ex].
[25] ATLAS Collaboration, ATLAS-CONF-2012-022, `http://cdsweb.cern.ch/record/1430731`.
[26] Atlas Collaboration, *Eur. Phys. J. C*, **72** (1965) 2012 arXiv:1201.5595 [hep-ex].
[27] Giudice G. F., Luty M. A., Murayama H. and Rattazzi R., *JHEP*, **12** (1998) 027 hep-ph/9810442; Randall L. and Sundrum R., *Nucl. Phys. B*, **557** (1999) 79 hep-th/9810155.
[28] Atlas Collaboration, public material from `https://twiki.cern.ch/twiki/bin/view/AtlasPublic/CombinedSummaryPlots`.

IL NUOVO CIMENTO Vol. 35 C, N. 6 Novembre-Dicembre 2012
DOI 10.1393/ncc/i2012-11390-6

Colloquia: LaThuile12

Phenomenology of new heavy neutral gauge bosons in an extended MSSM

S. Gentile

Dipartimento di Fisica, Università di Roma "La Sapienza" and
INFN, Sezione di Roma Piazzale A. Moro 2, I-00185, Roma, Italy

ricevuto il 7 Settembre 2012

Summary. — An extension of the Standard Model based on $U(1)'$ gauge symmetry, predicting a new heavy boson Z', in the TeV mass range, is discussed in this paper. Particular attention is devoted to the Z' decays into supersymmetric channels in addition to the Standard Model modes, so far investigated. The D-term contribution, due to the breaking of $U(1)'$, is taken into account for slepton and squark masses and its effect is investigated on Z' decays into sfermions. The Z' production cross section at the Large-Hadron Collider at center of mass energies of 8 and 14 TeV is calculated and the corresponding expected number of events containing a Z' decaying into supersymmetric particles for some integrated luminosity are predicted.

PACS 14.70.Pw – Other gauge bosons.
PACS 12.60.Jv – Supersymmetric models.
PACS 13.85.-t – Hadron-induced high- and super-high-energy interactions (energy > 10 GeV).

1. – Introduction

The validity of the Standard Model (SM) of the strong and electroweak interactions has been so far experimentally tested with success using LEP, Tevatron, LHC (Large-Hadron-Collider) data. Nevertheless, many extensions of the SM have been proposed, involving a gauge group of larger rank, the introduction of one extra string-inspired $U(1)'$ factor, which leads to the prediction of a new neutral gauge boson Z' (see, *e.g.*, [1]). Moreover, the Sequential Standard Model ($Z'_{\rm SSM}$), *i.e.* a heavy gauge boson with the same couplings to fermions and gauge bosons as the Z of the SM, has been, as well, investigated. The experimental limits on the new boson reached are in the range approximately 1.5 TeV for the string-inspired scenario and 1.8 TeV for the SM-like case [2-5]. All these bounds on the Z' mass, $m_{Z'}$, rely on the assumption that the Z' decays into Standard Model particles, with branching ratios depending on its mass and, in the string-like case, on the parameters characterizing the specific $U(1)'$ model. But, there is no actual reason to exclude Z' decays into channels beyond the SM, such as its supersymmetric extension, the Minimal Supersymmetric Standard Model (MSSM). This new physics contributions to the Z' width significantly decreases the branching ratios into SM particles, and therefore the mass limits quoted by the experiments may have to be revisited.

The aim of this paper is the investigation of the phenomenology of Z' bosons at the LHC, assuming that they can decay into both SM and supersymmetric particles, as in the MSSM [6]. The Z' decays into supersymmetric particles, if existing, represent an excellent tool to investigate the electroweak sector at the LHC in a phase-space corner that cannot be explored by employing the usual techniques. Through this work, particular care will be taken about the decay of the Z' into leptonic final state. Here, only the main points are summarized referring to the original paper for a more extensive description [7].

2. – Z' production and decay

In this section the extensions of the Standard Model leading to Z' bosons, allowing the decays into both standard and supersymmetric particles (MSSM) and its properties are summarized.

2·1. $U(1)'$ *models*. – There are several possible extensions of the SM that can be achieved by adding an extra $U(1)'$ gauge group, typical of string-inspired theories, each model is characterized by the coupling constants, possibly of the same order as the electroweak scale, the breaking scale of $U(1)'$ and scalar particle responsible for its breaking, the quantum numbers of fermions and bosons according to $U(1)'$. The most experimentally investigated models are characterized by an angle θ and a Z' boson which can be expressed as

$$Z'(\theta) = Z'_\psi \cos\theta - Z'_\chi \sin\theta. \tag{1}$$

Each value of the mixing angle θ corresponds to a $U(1)'$ group and leads to a different Z' phenomenology. The most widely used models, with their corresponding mixing angle, are: $Z'_\eta\,(\arccos\sqrt{5/8})$, $Z'_\psi\,(0)$, $Z'_{\mathrm{N}}\,(\arctan\sqrt{15}-\pi/2)$, $Z'_{\mathrm{I}}\,(\arccos\sqrt{5/8}-\pi/2)$, $Z'_{\mathrm{S}}\,(\arctan(\sqrt{15}/9)-\pi/2)$, $Z'_\chi\,(-\pi/2)$.

The charge of a field Φ is expressed through the same mixing angle θ as: $Q'(\Phi) = Q_\psi(\Phi)\cos\theta - Q_\chi(\Phi)\sin\theta$. with Q_ψ and Q_χ charge values for standard and supersymmetric particles quoted in [6].

Another model which is experimentally investigated is the so-called Sequential Standard Model (SSM), with the new boson Z'_{SSM} heavier than the Z boson, but with the same couplings to fermions and gauge bosons as in the SM.

In the following, in addition to the SM groups coupling constants g_1, g_2 ($g_1 = g_2\tan\theta_W$, θ_W being the Weinberg angle), is considered that to the $U(1)'$ group, $g' = \sqrt{\frac{5}{3}}g_1$ [6].

The Z and Z' are assumed to correspond, within a very good approximation, to the mass eigenstates.

2·2. *Particle content of the Minimal Supersymmetric Standard Model*. – The MSSM contains the supersymmetric partners of the SM particles: sfermions, as sleptons $\tilde{\ell}$ and $\tilde{\nu}_\ell$ ($\ell = e, \mu, \tau$), squarks $\tilde{q}$ and gauginos $\tilde{g}$, $\tilde{W}^\pm$, $\tilde{Z}$ and $\tilde{\gamma}$. It requires two Higgs doublets, which, after giving mass to W and Z bosons, lead to five scalar degrees of freedom, usually parametrized in terms of two CP-even neutral scalars, the lighter h and H, one CP-odd neutral pseudoscalar A and a pair of charged Higgs bosons $H^{\pm}$. Each Higgs will have a supersymmetric fermionic partner, named higgsino.

The weak gauginos mix with the higgsinos to form the corresponding mass eigenstates: two pairs of charginos ($\tilde{\chi}_1^{\pm}$ and $\tilde{\chi}_2^{\pm}$) and four neutralinos ($\tilde{\chi}_1^0$, $\tilde{\chi}_2^0$, $\tilde{\chi}_3^0$ and $\tilde{\chi}_4^0$), where $\tilde{\chi}_1^0$ is the lightest and $\tilde{\chi}_4^0$ the heaviest. The lightest neutralino, *i.e.* $\tilde{\chi}_1^0$, is often assumed to be the stable Lightest Supersymmetric Particle (LSP).

3. – Extending the MSSM with the extra $U(1)'$

In this section, few relevant points are summarized important for our discussion, referring to the work in [6] for more details.

3˙1. *Higgs bosons in the MSSM and* $U(1)'$ *model.* – As debated above, the MSSM itself predicts two Higgs doublets, whereas a third Higgs boson is required to break the $U(1)'$ gauge symmetry and give mass to the Z' boson. Then, the scalar components of the three Higgs bosons are two weak-isospin doublets Φ_1, Φ_2 and one singlet, Φ_3. The vacuum expectation values of the neutral Higgs bosons will be given by $\langle\phi_i^0\rangle = v_i/\sqrt{2}$, with $v_1 < v_2 < v_3$.

The superpotential, which in the MSSM contains a Higgs coupling term giving rise to the μ parameter, because of the extra Higgs field Φ_3 presents an additional contribution $W = \lambda\Phi_1\Phi_2\Phi_3$, leading to a trilinear scalar potential for the neutral Higgs bosons $V_\lambda = \lambda A\phi_1^0\phi_2^0\phi_3^0$. The parameter λ is related to the usual μ term by means a relation, $\mu = \frac{\lambda v_3}{\sqrt{2}}$, involving the vacuum expectation value of the third Higgs [6].

After the symmetry breaking and giving mass to W, Z and Z' bosons,in the model, there are: two charged ($H^{\pm}$), and four neutral Higgs bosons, one pseudoscalar A and three scalars h, H and H'. The mass of the heaviest H' is typically about the Z' mass, and therefore the Z' will not be able to decay into channels containing H'. Moreover, the introduction of the extra Higgs field Φ_3 singlet has impact also on the the other Higgs masses.

3˙2. *Neutralinos and charginos.* – Besides the four neutralinos of the MSSM, $\tilde{\chi}_1^0, \ldots,$ $\tilde{\chi}_4^0$, two extra neutralinos are required, namely $\tilde{\chi}_5^0$ and $\tilde{\chi}_6^0$, associated with the Z' and with the extra neutral Higgs breaking $U(1)'$. Their mass eigenstates are obtained diagonalizing a 6×6 matrix, depending on the Higgs vacuum expectation values, on the gaugino masses M_1, M_2 and M', and on the Higgs $U(1)'$ charges. As the extra Z' and Higgs are neutral, the chargino sector of the MSSM remains unchanged even after adding the extra $U(1)'$ group.

3˙3. *Sfermion masses.* – In many models for supersymmetry breaking, one typically expresses the sfermion squared mass as the sum of a soft term, m_0^2, often set to the same value for both squark and sleptons at a given scale, and a correction, called D-term, which, for the purposes of our study, consists of two contributions. A first term is a correction due to the hyperfine splitting driven by the electroweak symmetry breaking and is already present in the MSSM [7]. A second contribution to the D-term is present once one has extensions of the MSSM, such as our $U(1)'$ group, and is due to the Higgs bosons, which are necessary to break the new symmetry: $\Delta\tilde{m}_a'^2 = \frac{g'^2}{2}(Q_1'v_1^2+Q_2'v_2^2+Q_3'v_3^2)$, where Q_a' is the charge of the fermion a under $U(1)'$ and Q_1', Q_2' and Q_3' are the $U(1)'$ charges of the three neutral Higgs bosons. In the Sequential Standard Model, only the first contribution to the D-term will be evaluated.

Left- and right-handed sfermions in general mix, and therefore, in order to obtain the mass eigenstates, the squared mass matrix has to be diagonalized. As in ref. [6], it is assumed a common soft mass at the Z' scale and the D-term contribution it is added to it. As an example, the expression for the matrix elements in the case of an up-type squark is

$$\left(M^{\tilde{u}}_{\mathrm{LL}}\right)^2 = \left(m^0_{\tilde{u}_{\mathrm{L}}}\right)^2 + m_u^2 + \left(\frac{1}{2} - \frac{2}{3}x_w\right) m_Z^2 \ \cos 2\beta + Q'_{\tilde{u}_{\mathrm{L}}}\Delta\tilde{m}'^2_{\tilde{u}_L} \tag{2}$$

$$\left(M^{\tilde{u}}_{\mathrm{RR}}\right)^2 = \left(m^0_{\tilde{u}_R}\right)^2 + m_u^2 + \left(\frac{1}{2} - \frac{2}{3}x_w\right) m_Z^2 \ \cos 2\beta + Q'_{\tilde{u}_R}\Delta\tilde{m}'^2_{\tilde{u}_R} \tag{3}$$

$$\left(M^{\tilde{u}}_{\mathrm{LR}}\right)^2 = m_u(A_u - \mu\cot\beta). \tag{4}$$

where $x_w = \sin^2\theta_W$, $m^0_{\tilde{u}_{\mathrm{L,R}}}$ is the $\tilde{u}_{\mathrm{L,R}}$ mass at the Z' energy scale and $A_f = m_u A_u$ is the coupling constant entering in the Higgs-sfermion interaction term. The dependence on $m_{Z'}$ and the mixing angle θ is embedded in the $\Delta\tilde{m}_{D'}$ term. Analogous expressions hold for down squarks and sleptons [6]; after diagonalizing the corresponding mass matrix, the up-squark mass eigenstates are named as $\tilde{u}_1$ and $\tilde{u}_2$ and their masses as $m_{\tilde{u}_1}$ and $m_{\tilde{u}_2}$. As the mass of light quarks and leptons is very small, the mixing term, eq. (4), is negligible and the mass matrix of sleptons and light squarks is roughly diagonal.Instead the mixing term M_{LR} for top squarks is relevant, and therefore the stop mass eigenstates $\tilde{t}_{1,2}$ are in general different from the weak states $\tilde{t}_{\mathrm{L,R}}$. In the other cases is $\tilde{t}_{1,2} \approx \tilde{t}_{\mathrm{L,R}}$.

In conclusion, the $U(1)'$ group addition implies an additional heavy Higgs, H', two extra neutralinos are required and as for the sfermions, an extra contribution, the so-called D-term, to squark and slepton masses, depending on the $U(1)'$ sfermion charges and Higgs vacuum expectation values. This D-terms has a crucial impact on sfermion masses and, whenever large and negative, they may even lead to discarding some MSSM/$U(1)'$ scenarios.

4. – Representative point

The analysis on Z' production and decays into SM and MSSM particles depends on $U(1)'$, MSSM several parameters, among them the Z' or MSSM masses; the experimental searches for physics beyond the Standard Model set exclusion limits on such quantities.

In the following, it is considered a specific configuration of the parameter space, the so-called "Representative Point", to study the Z' phenomenology with non-zero branching ratios in the more relevant SM and MSSM decay channels. Then, each parameter is varied individually, fixing the others to the following values:

$$\begin{aligned} & m_{Z'} = 3\,\mathrm{TeV}, \qquad \theta = \arccos\sqrt{\frac{5}{8}} - \frac{\pi}{2}, \qquad \mu = 200, \qquad \tan\beta = 20, \\ & A_q = A_\ell = A_f = 500\,\mathrm{GeV}, \\ & m^0_{\tilde{q}_L} = m^0_{\tilde{q}_R} = m^0_{\tilde{\ell}_L} = m^0_{\tilde{\ell}_R} = m^0_{\tilde{\nu}_L} = m^0_{\tilde{\nu}_R} = 2.5\,\mathrm{TeV}, \\ & M_1 = 100\,\mathrm{GeV}, \qquad M' = 1\,\mathrm{TeV}. \end{aligned} \tag{5}$$

where by q and ℓ denote any possible quark and lepton flavor, respectively. The gaugino masses M_1 and M_2 satisfy, within very good accuracy, the GUT-inspired relation: $\frac{M_1}{M_2} = \frac{5}{3}\tan^2\theta_W$,then $M_2 = 200\,\mathrm{GeV}$. The Beyond-Standard-Model (BSM) particle

TABLE I. – *Masses in* GeV *of non-Standard Model particle masses in the MSSM/$U(1)'$ scenarios, at Reference Point eq.* (5).

$m_{\tilde{u}_1}$	$m_{\tilde{u}_2}$	$m_{\tilde{d}_1}$	$m_{\tilde{d}_2}$	$m_{\tilde{\ell}_1}$	$m_{\tilde{\ell}_2}$	$m_{\tilde{\nu}_1}$	$m_{\tilde{\nu}_2}$
2499.4	2499.7	2500.7	1323.1	3279.0	2500.4	3278.1	3279.1
$m_{\tilde{\chi}_1^0}$	$m_{\tilde{\chi}_2^0}$	$m_{\tilde{\chi}_3^0}$	$m_{\tilde{\chi}_4^0}$	$m_{\tilde{\chi}_5^0}$	$m_{\tilde{\chi}_6^0}$	$m_{\tilde{\chi}_1^\pm}$	$m_{\tilde{\chi}_2^\pm}$
94.6	156.5	212.2	260.9	2541.4	3541.4	154.8	262.1
m_h	m_A	m_H	$m_{H'}$	$m_{H^\pm}$			
90.7	1190.7	1190.7	3000.0	1193.4			

masses with eq. (5) setting are summarized in table I and some parameter dependence is discussed in the following. A complete study is in ref. [7].

4·1. *Sfermion masses.* – The sfermion masses are given by the sum of a common mass, set to the same values for all squarks and sleptons at the Z' scale, as in eq. (5), and the D-term. In fact, the D-term, and then the sfermion squared masses, is expected to depend strongly on the $U(1)'$ and MSSM parameters, and can even become negative, then leading to an unphysical (imaginary) sfermion mass.

Figure 1, left, shows the remarkable dependence of all slepton masses on θ, $U(1)'$ mixing angle. The regions of small and large θ have been discarded in the plots, since they would correspond to a negative, and thus unphysical, squared mass. The squark ($\tilde{u}$ and $\tilde{d}$, $\tilde{t}$) masses dependence on θ mixing angle is also important [7]. In this particular point of parameter space (eq. (5)), the mixing term is negligible and therefore the $\tilde{t}_{1,2}$ masses are roughly equal to the masses of the other up-type squarks. The D-term correction and then sfermion masses, is also function of Z' mass, this dependence is shown in fig. 1, right.

The sfermion masses are monotonically increasing function on the $m^0_{\tilde{q},\tilde{\ell}}$ mass, as expected. being the D-term negligible for $\tilde{u}_1$, $\tilde{u}_2$, $\tilde{d}_1$ and ℓ_2.

4·2. *Neutralino and chargino masses.* – The neutralino masses, unlike the sfermion masses, depend also on M_1, M_2 and M'. The Z' decays into $\tilde{\chi}_5^0$ and $\tilde{\chi}_6^0$ are prevent for

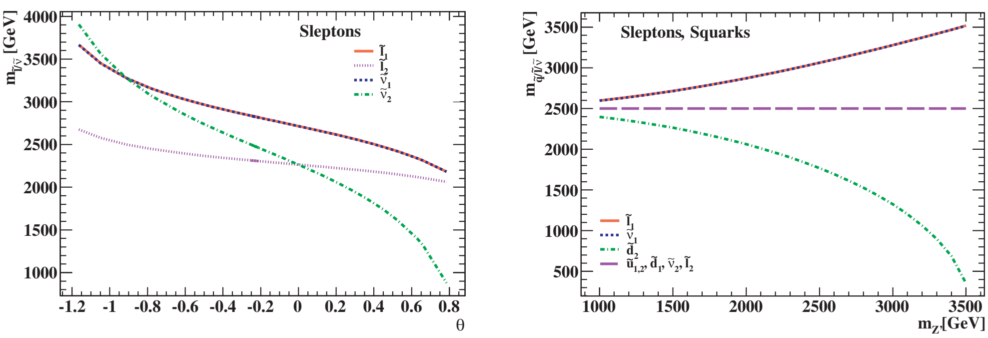

Fig. 1. – Dependence on the $U(1)'$ mixing angle θ of slepton masses (left) and sfermion masses on the Z' mass (right).

their masses, unlike those into the lighter, table I, then will be not considered in the following.

The dependence of the neutralino masses on the mixing angle θ is negligible, whereas the actual value of the $m_{Z'}$ and M' affects significantly only $\tilde{\chi}_5^0$ and $\tilde{\chi}_6^0$. The masses of $\tilde{\chi}_5^0$ and $\tilde{\chi}_6^0$ are linearly increasing functions of $m_{Z'}$, whereas they exhibit opposite behavior with respect to M', as $m_{\tilde{\chi}_5^0}$ increases and $m_{\tilde{\chi}_6^0}$ decreases.

The variation of the other four neutralino masses with respect to M_1, or equivalently M_2, exhibits a step-like behavior.

As discussed before, the chargino sector stays unchanged even after the introduction of the neutral boson Z', therefore their masses don't depend on θ, $m_{Z'}$, M'.

4·3. *Higgs masses.* – An additional Higgs, H', $U(1)'$-inherited is present respect to MSSM framework. The Z' decays into it are prevent, due to is mass about 3 TeV, approximately equal to $m_{Z'}$ in all $\tan\beta$ range. The other decay channels containing Higgs are kinematically accessible, table I.

The mass of the lightest scalar Higgs (m_h) is roughly independent of both $\tan\beta$ and μ, being of the order of m_Z and the others H, A and $H^{\pm}$ have a common mass of about 1190.0 GeV. The heavier MSSM Higgs H mass is physical, *i.e.* its mass squared positive only for positive values of μ. Then, in the following we only the positive space ($\mu > 0$) is discussed.

4·4. *Branching ratios in the Representative Point.* – From sect. **4·1** it is possible to conclude that all up-type, including the stop, and down-type squark masses are degenerate; therefore are denoted in the following as $m_{\tilde{u}_i}$ and $m_{\tilde{d}_i}$, regardless of the flavor.

At this point, it is possible calculate the Z' widths into the kinematically allowed decay channels.

The SM Z' decays are the same of Z boson, quark or lepton pairs, but in addition, due to its higher mass the WW decay is permitted.

Furthermore, the extended MSSM allows Z' decays into sfermions, *i.e.* $\tilde{f}_i\tilde{f}_j^*$ ($f = u, d, \ell, \nu$), neutralino ($\tilde{\chi}_{1,2,3,4}^0$), chargino ($\tilde{\chi}^+\tilde{\chi}^-$), or Higgs ($hh$, HH, hH, hA, HA, $H'A$, H^+H^-) pairs, as well as into states with Higgs bosons associated with W/Z, such as Zh, ZH and $H^{\pm}W^{\mp}$. Summing up all partial rates, one can thus obtain the Z' total width and the branching ratios into all allowed decay channels. Several decay channels are forbidden for phase space limitations.

The Z' kinematically not accessible decay states (from table I) as into up-type squarks and sleptons, the heaviest neutralinos and $U(1)'$-inherited Higgs H' have a null branching fraction. The only allowed decay into sfermion pairs is the one into down-type squarks $\tilde{d}_2\tilde{d}_2^*$. Despite is kinematically permitted, the branching ratios into up-type is null because the partial widths [6] are weighted by a null coefficient in the Z'_{I} model.

Since, at a scale of 3 TeV, one does not distinguish the quark or lepton flavor, the branching ratios summed over all possible flavors, in brackets, are: $u\bar{u}$ (0.0%), $d\bar{d}$ (40.67%), $\ell^+\ell^-$ (13.56%) and $\nu\bar{\nu}$ (27.11%). Likewise, $\tilde{u}\tilde{u}^*$ (0.0%), $\tilde{d}\tilde{d}^*$ (9.58%), $\tilde{\ell}\tilde{\ell}^*$ (0.0%) and $\tilde{\nu}\tilde{\nu}^*$ (0.0%) are their MSSM counterparts.

The most significant branching ratios into neutralinos are $\tilde{\chi}_2^0\tilde{\chi}_3^0$ (2.13), $\tilde{\chi}_3^0\tilde{\chi}_3^0$ (1.75), $\tilde{\chi}_3^0\tilde{\chi}_4^0$ (1.34), into chargino $\tilde{\chi}_1^{\pm}\tilde{\chi}_1^{\mp}$ (1.76) and $\tilde{\chi}_1^{\pm}\tilde{\chi}_2^{\mp}$ (1.95) The $\tilde{\chi}_1^0\tilde{\chi}_1^0$ has a small rate and is experimentally invisible.

Summarizing, at the Representative Point, the SM decays account for about the 77% of the total Z' width, and the BSM ones the remaining 23%. These are splitted into down quark decays ($\sim 9\%$) into charginos(4.2%) and neutralinos (8.4%). The Z' decays

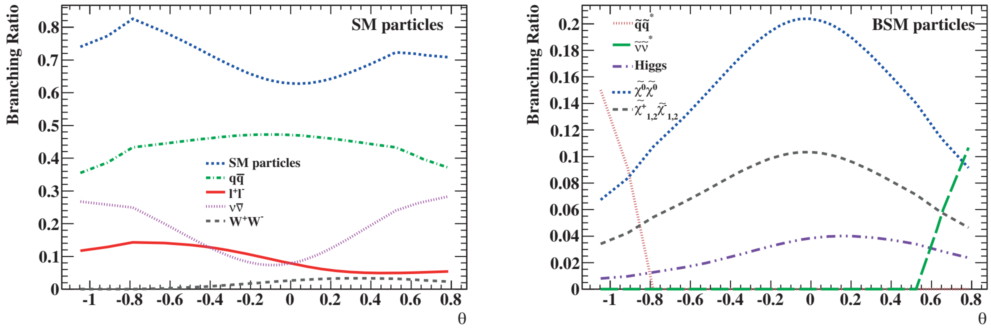

Fig. 2. – Dependence of the Z' decay rates on the $U(1)'$ mixing angle θ (left) SM modes; BSM channels (right).

into Higgs are characterized from negligible branching fractions: H^+H^- and HA are about 0.5%, $H^\pm W^\mp$ only 0.1% and even more modest rate($\mathcal{O}(10^{-7})$) is due to Higgs gauge boson decays, hZ, ZH, hA.

The validity of these considerations, obtained in a particular configuration (Reference Point, eq. (5)) can be extended in a more general context. On these basis, it is possible conclude that the Z' BSM branching fractions are not negligible and consequently have to be accounted in the search for new physics.

At this point, it is interesting to investigate the dependence of the branching fractions into standard model and supersymmetric particles on the $U(1)'$ and MSSM parameters, at Reference Point (eq. (5)), varying individually one parameter at time. In fig. 2, the dependence of the branching ratios on the parameter θ, the model parameter, are presented for SM (left) and BSM (right) decays.

5. – Z' decays into final states with leptons

Leptonic final states are typically the golden channels for the LHC experimental searches. Therefore, the decays of the Z' into supersymmetric particles, leading to final states with charged leptons and missing energy, due to the presence of neutralinos or neutrinos are investigated.

The two charged lepton final state may originate from primary decays $Z' \to \tilde{\ell}^+\tilde{\ell}^-$ followed by $\tilde{\ell}^\pm \to \ell^\pm\tilde{\chi}_1^0$ or from chargino chain decays $Z' \to \tilde{\chi}_2^\pm\tilde{\chi}_2^\mp$ with a subsequently decay of $\tilde{\chi}_2^\pm \to \ell^\pm\tilde{\chi}_1^0$.

The four charged lepton final state is originated from sneutrino, $\tilde{\nu}$, decays or $Z' \to \tilde{\nu}_2\tilde{\nu}_2^*$ with a subsequent decay chain $\tilde{\nu}_2 \to \tilde{\chi}_2^0\nu$, and $\tilde{\chi}_2^0 \to \tilde{\ell}^+\tilde{\ell}^-\tilde{\chi}_1^\pm$ and finally $\tilde{\ell}^\pm \to \ell^\pm\tilde{\chi}_1^0$. At same four lepton final is contributing as well the Z' decays into neutralino. The SUSY decay chain is $Z' \to \tilde{\chi}_2^0\tilde{\chi}_2^0$ with subsequent $\tilde{\chi}_2^0 \to \tilde{\ell}^\pm\tilde{\ell}^\mp$ and $\tilde{\ell}^\pm \to \ell^\pm\tilde{\chi}_1^0$ processes. In the following, it is performed the study of Z' decays into leptonic final states for a given set of the MSSM and $U(1)'$ parameters, in the various models of sect. **2**·2, varying $m_{\tilde{\ell}}^0$, the initial common slepton mass, at various $m_{Z'}$ values. The same set of parameters as eq. (5) but $m_{\tilde{q}} = 5\,\text{TeV}$ and $M_1 = 150\,\text{TeV}$ are used.

– *Reference Point: Model* Z'_η. The Z' boson cannot decay into charged slepton because of phase space limitations, but the Z' decays into charginos and neutralinos are accessible, with a branching ratios about 5–6% and up to 10–12%, respectively. Decays

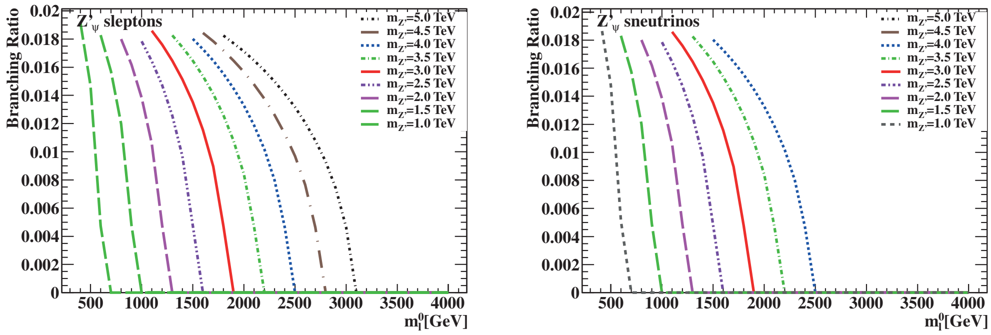

Fig. 3. – Branching ratio of the Z'_ψ boson into charged slepton (left) sneutrino (right) pairs as a function of the initial condition for the slepton mass, $m^0_{\tilde{\ell}}$, and for several values of $m_{Z'}$.

into WW pairs, or Higgs bosons associated with Z's are also permitted, with rates about 3%. The sneutrinos branching fraction decreases at higher $m^0_{\tilde{\ell}}$ results in an enhancement of the SM branching ratios into $q\bar{q}$ and $\nu\bar{\nu}$ pairs. Summing up the contributions from sneutrinos, charginos and neutralinos, the branching ratio into non-standard model particles, $\mathrm{BR_{BSM}}$, runs from 24 to 33%, confirming the relevance of these decays in any analysis accounting for Z' production in a supersymmetric scenario.

– *Reference Point:* Z'_ψ. In this case, the supersymmetric decays into charged slepton and neutral slepton pairs have the same branching fractions ($\sim 2\%$). Furthermore, even the decays into gauginos are relevant, with the branching fractions into $\tilde{\chi}^+\tilde{\chi}^-$ and $\tilde{\chi}^0\tilde{\chi}^0$ being about 10 and 20%, respectively. The rates into boson pairs, *i.e.* Zh and WW, are also non-negligible and account for about 3% of the total decay probability.

As a whole, the Z'_ψ modeling, above depicted, yields branching ratios about 35–40% into BSM particle, and therefore it may look like being a promising scenario to investigate Z' production within the MSSM. Figure 3 finally displays the branching ratios into sneutrinos and charged sleptons as a function of $m^0_{\tilde{\ell}}$ and for several values of $m_{Z'}$.

– *Reference Point:* Z'_N. Both decays into pairs $\tilde{\ell}_2\tilde{\ell}_2^*$ and $\tilde{\nu}_2\tilde{\nu}_2^*$ are kinematically allowed, whereas $\tilde{\ell}_1$ and $\tilde{\nu}_1$ are too heavy to be produced in Z' decays. The D-term addition to the initial condition for slepton mass, $m^0_{\tilde{\ell}}$, has an opposite effect on the two lepton mass eigenstates; increases the $\tilde{\ell}_1$, $\tilde{\nu}_1$ values and decreases $\tilde{\ell}_2$. Its impact on $\tilde{\nu}_2$ is neglegible, consequently it is possible assume $m_{\tilde{\nu}_2} \simeq m^0_{\tilde{\ell}}$. Although, the $Z' \to \tilde{\nu}_2\tilde{\nu}_2^*$ is kinematically allowed, the coupling Z' to sneutrinos is zero, as the corresponding branching fractions. As for the other supersymmetric decay channels, the rates into charginos and neutralinos are quite significant and amount to about 9% and 18%, respectively. The decays into WW and Zh states account approximately 1–2%, whereas the branching ratio into charged slepton pairs just about 1%, even in the most favorable case. As a whole, the rates into BSM final states run from 28 to about 35%, thus displaying a quite relevant contribution to the total Z' cross section.

– *Reference Point:* Z'_I. This model has been extensively discussed as Representative Point, in sect. **4**. It exhibits the property that the initial slepton mass $m^0_{\tilde{\ell}}$ can decreases as low few GeV, still preserving a physical scenario for the sfermion masses. D-term correction to the slepton mass is quite relevant for $\tilde{\ell}_1$, $\tilde{\nu}_1$ and $\tilde{\nu}_2$, especially for small values of $m^0_{\tilde{\ell}}$, whereas it is quite irrelevant for the $\tilde{\ell}_2$ case. As the D-term turns out to be positive and quite large, this has the result that the only kinematically permitted decay would $Z' \to \tilde{\ell}_2\tilde{\ell}^*_2$. Unfortunately, with the same arguments discussed for $Z'_{\rm N}$ model, the coupling of the Z' to $\tilde{\ell}_2$ is null, preventing the slepton production in Z' decays, as this scenario is concerned.

In conclusion, Z' can decay neither in neutral neither in charged slepton. Therefore, the dependence on $m^0_{\tilde{\ell}}$ is uninteresting. The total $\mathrm{BR_{BSM}}$ ratio lies between 12 and 17% and is mostly due to decays into chargino ($\sim 4\%$) and neutralino (~ 8–9%) pairs. Decays involving supersymmetric Higgses as H^+H^-, WH, HA are possible, but with a negligible branching ratio at lower Z' masses, reaching at most $\sim 3\%$ for $m_{Z'} > 4\,\mathrm{TeV}$.

– *Reference Point:* $Z'_{\rm S}$. As in $Z'_{\rm I}$ model, the initial slepton mass $m^0_{\tilde{\ell}}$ can reach few GeV, still having a meaningful supersymmetric spectrum. Consequently, the $m^0_{\tilde{\ell}}$ low limit is chosen at 200 GeV, on basis of direct limit set by experimental searches. The $Z'_{\rm S}$ decay rates are roughly independent of initial slepton mass. The D-term impact on slepton masses is always positive, having an important effect on $m_{\tilde{\ell}_1}$, $m_{\tilde{\nu}_1}$, $m_{\tilde{\nu}_2}$, but limited on $m_{\tilde{\ell}_2}$. Then, $Z' \to \tilde{\ell}_2\tilde{\ell}^*_2$ is the only decay kinematically allowed. in the leptonic sector. However, the branching ratio into charged sleptons is very small, about 0.1%, even for low $m^0_{\tilde{\ell}}$ values.

As for the other BSM decay modes, the most relevant are the chargino ($\sim 3\%$) and neutralino (~ 6–7%) pairs, being the others quite negigible. For $m_{Z'} = 5\,\mathrm{TeV}$ branching ratio into squark pairs is important, roughly 8%. The D-term for $\tilde{d}_2$-type squarks is negative, and at large values of the Z' mass, as 5 TeV, became important and allowing the decays into $\tilde{d}_2\tilde{d}^*_2$. The slepton branching ratios are small for any $m_{Z'}$ and independent of the slepton mass.

As a whole, one can say that, in this case, for $m_{Z'} < 5\,\mathrm{TeV}$ the non-standard model decay rate is about 10–12%, becaming higher at larger Z' masses, even above 20%, due to the opening of the decay into squark pairs. The experimental signature of squark production is jets final state, difficult to separate from the QCD SM backgrounds. Therefore, this scenario seems, therefore, not very promising for a possible discovery of supersymmetry via Z' decays.

– *Reference Point:* Z'_χ. The $U(1)'$ group, Z'_χ does not lead to a meaningful sfermion scenario within our parametrization, as the sfermion masses are unphysical after the addition of the D-term. For any $m_{Z'}$, the rates into quark and neutrino pairs are the dominant (~ 40–45%), whereas the branching ratio into lepton states is approximately 12% and the other modes (WW, Zh, HA and $H^\pm H^\mp$) accounting for the remaining 1–3%. As a whole, the Z'_χ model is not adequate for possible supersymmetry analysis.

– *Reference Point:* $Z'_{\rm SSM}$. This model is considered as benchmark, since the production cross section just depends only on the Z' mass, neither on the mixing angle θ, neither on possible new physics parameters, as MSSM. As for the supersymmetric sector, the sfermion masses get the D-term part originated from the hyperfine splitting contribution, and not that from MSSM further extensions. Moreover, the Z' coupling constant to the sfermions can be simply written as $g_{\rm SSM} = g_2/(2\cos\theta_W)$. As the hyperfine-splitting D-term is not too large, the sfermion spectrum is physical, even at very small $m^0_{\tilde{\ell}}$ values.

At $m^0_{\tilde{\ell}} = 100\,\mathrm{GeV}$, including the D-term, $m_{\tilde{\nu}_1}$ decreases by about 25%; $m_{\tilde{\ell}_1}$, $m_{\tilde{\ell}_2}$ undergo to slightly positive variation; $m_{\tilde{\nu}_2}$ is roughly unchanged. At larger $m^0_{\tilde{\ell}}$ values, D-term effect on all slepton masses is negligible and are approximatly equal to initial slepton mass, $m^0_{\tilde{\ell}}$.

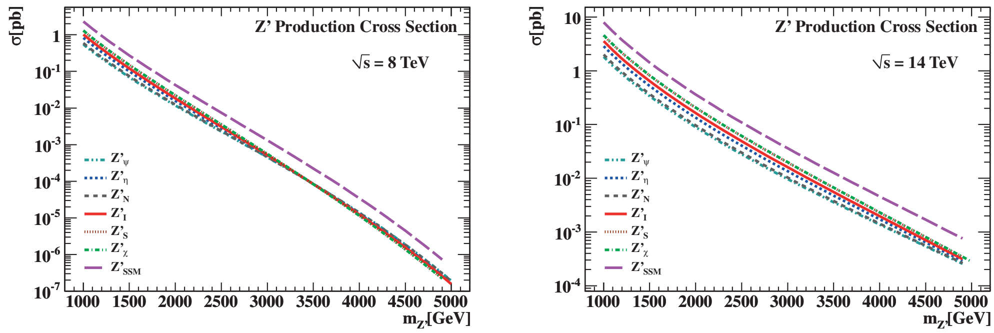

Fig. 4. – Cross section (logarithmic scale) of Z' production in pp collisions at the center-of-mass energy $\sqrt{s} = 8\,\text{TeV}$ (left) and $\sqrt{s} = 14\,\text{TeV}$ (right), for various models (see text).

The decays into non-standard model particles, B_{BSM}, exhibit rates, about 60–65%, BR_{SM} higher than the standard model ones, 35–40%. The B_{BSM} is composed mostly from decays into neutralinos ($\sim 30\%$) and charginos ($\sim$ 16–18%), with a more limited contribution into sneutrinos ($\sim 4\%$) and charged sleptons (1–2%). Other channels involving Higgs and gauge boson are contributing as WW (4–5%), H^+H^- (3%) for $m_{Z'} > 2.5\,\text{TeV}$, Zh and hA (1–4%) $m_{Z'} > 1.5\,\text{TeV}$.

6. – Cross sections and event rates at the LHC

In this section, the Z' total production cross section at the LHC is presented according to the several models discussed through this paper (sect. **2**˙2), including the Sequential Standard Model. The pp collisions at two center-of-mass energies: $\sqrt{s} = 8\,\text{TeV}$ (2012 run) and $\sqrt{s} = 14\,\text{TeV}$, the ultimate project energy, are considered. For these two values, the cross sections are calculated and the expected number of events with Z' decaying into supersymmetric particles, with few integrated luminosities, $\int \mathcal{L}\,\mathrm{d}t$ are estimated.

6˙1. *Leading-order Z' production cross section.* – The cross sections is calculated at leading order (LO) with, for consistency, the LO parton distribution functions CTEQ6L. Different LO PDFs have a negligible impact on the cross section results. In the calculations, the factorization is set equal to the Z' mass.

As far as the total cross section is concerned, the parton-level process is analogous to Z production, *i.e.* it is the purely SM quark-antiquark annihilation $q\bar{q} \to Z'$.

Since the coupling of the Z' to the quarks depends on the specific $U(1)'$ scenario, the production rate is a function of the mixing angle θ, and of the Z' mass, but not of the MSSM parameters.

Figure 4 presents in logarithmic the total cross section for the different models, including the SSM, as a function of $m_{Z'}$ at $\sqrt{s} = 8\,\text{TeV}$ (fig. 4, left) and 14 TeV (fig. 4, right). The highest production cross section corresponds to SSM model, whereas the lowest to Z'_ψ model. The others model cross sections are lying between those and are indistinguishable at large $m_{Z'}$ value.

The cross section varies according $m_{Z'}$, center-of-mass energy and model.

The model choice has a more limited impact on the absolute value of cross section, but there are important differences as function of $\sqrt{s}$. The change by several order of magnitudes is present as function of Z' mass.

TABLE II. – *Number of supersymmetric particles (N_{casc} and N_{slep}) at the LHC, for Z' production in different $U(1)'$ models as well as in the Sequential Standard Model as function of $m_{Z'}$ in* TeV*, at $\sqrt{s} = 8\,\text{TeV}$, $\int \mathcal{L}\,\text{d}t = 20\,\text{fb}^{-1}$ and at $\sqrt{s} = 14\,\text{TeV}$, $\int \mathcal{L}\,\text{d}t = 100\,\text{fb}^{-1}$.*

Model	$m_{Z'}$	$N_{\text{casc}}^{\sqrt{s}=8\,\text{TeV}}$	$N_{\text{slep}}^{\sqrt{s}=8\,\text{TeV}}$	$N_{\text{casc}}^{\sqrt{s}=14\,\text{TeV}}$	$N_{\text{slep}}^{\sqrt{s}=14\,\text{TeV}}$
Z'_η	1.5	523	–	13650	–
Z'_η	2	55	–	2344	–
Z'_ψ	1.5	599	36	10241	622
Z'_ψ	2	73	4	2784	162
Z'_{N}	1.5	400	17	9979	414
Z'_{N}	2	70	3	2705	104
Z'_{I}	1.5	317	–	8507	–
Z'_{I}	2	50	–	2230	–
Z'_{S}	1.5	30	–	8242	65
Z'_{S}	2	46	–	2146	16
Z'_{SSM}	1.5	2968	95	775715	24774
Z'_{SSM}	2	462	14	19570	606

6·2. *Event rates with sparticle production in Z' decays at the LHC*. – In the following, the domain where the supersymetric Z' decays would be detectable is investigated. For this purpose, two scenarios are considered: $\sqrt{s} = 8\,\text{TeV}$ with an expected integrated luminosity, $\int \mathcal{L}\,\text{d}t = 20\,\text{fb}^{-1}$, as expected in 2012 LHC data taking and a future scenario $\sqrt{s} = 14\,\text{TeV}$ with $\int \mathcal{L}\,\text{d}t = 100\,\text{fb}^{-1}$.

The number of expected events in this two scenarios is summarized in table II for $m_{Z'} = 1.5$ and $2\,\text{TeV}$. As discussed in sect. **6**, the leptonic final state can be yielded by direct slepton decays or by a SUSY cascade originated from primary decays into sneutrinos, charginos and neutralino pairs, ($N_{\text{casc}} = N_{\tilde{\nu}\tilde{\nu}^*} + N_{\tilde{\chi}^+\tilde{\chi}^-} + N_{\tilde{\chi}^0\tilde{\chi}^0}$). Likewise, N_{slep} is the number of events with a Z' decaying to charged-slepton pairs.

In both luminosity (energy) regimes, due to a large cross sections, the Sequential Standard Model is the one yielding the highest number of events with production of supersymmetric particles in Z' decays, up to $\mathcal{O}(10^5\text{–}10^4)$ at $\sqrt{s} = 14\,\text{TeV}$ with $\int \mathcal{L}\,\text{d}t = 100\,\text{fb}^{-1}$ and a Z' mass $m_{Z'} = 1.5\,\text{TeV}$.

As already discussed (sect. **6**) in the Z'_η and Z'_{I} models the Z' direct slepton decays are prevented, as reflected in table II and the only supersymmetric decays are into sneutrino, neutralino and chargino pairs. The direct slepton decays can be produced in Z'_{N} model and a few hundreds of them are expected in the high luminosity phase. In the Z'_{S} scenario, Z' boson leads to many cascade particles in the high luminosity regime, according to the Z' mass and a few tenths of direct leptons.

Before concluding this subsection, it has to be pointed out that, although the numbers in table II encourage optimistic prediction on the discovery of Z' decays into sparticles specially in the high-luminosity phase, however, before drawing a conclusive statement on this issue, it is necessary to carry out a study taking into account detector acceptance and resolution, trigger, and analysis cuts on jets and leptons. Then, the result presented through this paper should be seen as a first step towards a more through investigation, which requires, above all, the implementation of the models herein discussed into a Monte Carlo event generator.

7. – Conclusions

In this paper, the production and decays of new neutral Z' boson, according to new physics models based on a $U(1)'$ gauge group and to the Sequential Standard Model is discussed. Decays in standard model and non-standard model particles are included. In this perspective, all quoted experimental limits have to be revisited.

The extension of the Minimal Supersymmetric Standard Model with $U(1)'$ group implies new features as an extra Higgs boson, two novel neutralinos and a modification of the sfermion mass by a D-term, where the new features are embedded. All these aspects have been studied as a function of various $U(1)'$/MSSM parameters, *e.g.* $U(1)'$ mixing angle θ, the Z' boson mass, M_1, M_2, M', the soft masses for the gaugino etc. Only scenarios with all physical sfermion masses are considered.

A study, as a function of slepton and Z' masses, has been performed on the partial widths and branching ratios of the Z', with attention to final states with charged leptons and missing energy. These configurations are favorable to experimental detection in hadronic events and can be yielded by intermediate charged sleptons or a SUSY cascade through neutralinos, chargino, sneutrinos.

Then, the LO production cross sections in all investigated models has been evaluated and an estimate of expected events at few centre-of-mass energy and integrated luminosity has been provided. The result of this study is that for some models and parametrization, one can even have 10^4–10^5 events with sparticle production in Z' decays.

As additional remarks, the $Z' \to \tilde{\ell}^+\tilde{\ell}^-$ decay present two interesting issues. One for the determination of slepton masses having the additional constraint of the Z' mass. The second is to explore the corner of the high region of slepton masses unreachable with other productions.

In summary, this can be considered a useful starting point to study Z' production and decay beyond the Standard Model, as well as within supersymmetric theories, drawing a guideline for future experimental analysis.

REFERENCES

[1] Langacker P., *Rev. Mod. Phys.*, **81** (2009) 1199.
[2] Aaltonen T. (CDF Collaboration), *Phys. Rev. Lett.*, **102** (2009) 121801.
[3] Abazov V. M. (D0 Collaboration), *Phys. Lett. B*, **695** (2011) 88.
[4] Aad G. (ATLAS Collaboration), *Phys. Lett. B*, **700** (2011) 163.
[5] Chatrchyan S. (CMS Collaboration), *JHEP*, **05** (2011) 093.
[6] Gherghetta T., Kaeding T. A. and Kane G. L., *Phys. Rev. D*, **57** (1998) 3178.
[7] Corcella G. and Gentile S., *Nucl. Phys. B*, **866** (2013) 293.

IL NUOVO CIMENTO Vol. 35 C, N. 6 Novembre-Dicembre 2012
DOI 10.1393/ncc/i2012-11391-5

Colloquia: LaThuile12

Colored scalars as flavor messengers in grand unified theories

I. Doršner

Department of Physics, University of Sarajevo - Zmaja od Bosne 33-35, 71000 Sarajevo, Bosnia and Herzegovina

ricevuto il 7 Settembre 2012

Summary. — We critically review the proton decay due to the scalar leptoquark exchanges within $SU(5)$ and flipped $SU(5)$ frameworks to address the issue of the model dependence of the relevant tree level operators. We quantify if, and when, it is necessary to have the leptoquark mass close to a grand unification scale. We summarize novel results regarding a possibility to have a collider accessible leptoquark without a rapid proton decay. The relevant state could be observed indirectly through its influence on physical processes such as the forward-backward asymmetry in $t\bar{t}$ production due to an antisymmetric set of couplings to a pair of up-quarks. The same leptoquark could affect the muon anomalous magnetic moment through the interaction of a lepton-quark nature. We accordingly investigate whether both sets of couplings can be simultaneously sizable without any conflict with matter stability.

PACS 13.30.-a – Decays of baryons.
PACS 12.10.Dm – Unified theories and models of strong and electroweak interactions.

1. – Introduction

Scalar leptoquarks represent theoretically well-motivated source of new physics. Simply put, the leptoquark states take a quark into a lepton and vice versa. They are thus ubiquitous in any framework that unifies elementary fermions of the Standard Model (SM). We accordingly study these states in two different unification frameworks that correspond to the $SU(5)$ [1] and the flipped $SU(5)$ [2-4], *i.e.*, $SU(5) \times U(1)$, embeddings of the matter fields. These two scenarios are general enough to cover other possible (non)unifying schemes. Our aim is to present an excerpt from a comprehensive classification of scalar leptoquarks that simultaneously violate baryon (B) and lepton (L) numbers where a role these have in proton decay processes is addressed [5].

The leptoquark states that simultaneously violate B and L tend to mediate proton decay at tree level and are therefore taken to be very massive. However, it is possible to have a viable $SU(5)$ setup [6] with a very light leptoquark [7] that is in accord with the experimental limits on proton stability. The color triplet weak singlet scalar in question could then contribute to $t\bar{t}$ production [8] and explain the observed increase of the forward-backward asymmetry [9, 10]. It could also have an impact on the muon anomalous magnetic moment [11] that could reconcile experimental [12] and theoretical results [13]. It might, however, (re)generate proton decay through the higher-order loop diagrams that yield an effective $d = 6$ set of operators and a class of tree-level $d = 9$ operators. A question then is whether one can simultaneously address the $t\bar{t}$ asymmetry and the muon anomalous magnetic moment by using the very same leptoquark [5].

This contribution is organized as follows. In sects. **2** and **3** we list all scalar leptoquarks associated with proton decay in $SU(5)$ and flipped $SU(5)$ and give examples of the Yukawa couplings to the SM fermions for leptoquarks from one representation. In sect. **4** we introduce the effective dimension-six operators for proton decay and calculate associated effective coefficients for certain leptoquark states. There we also present current experimental lower bounds on the color triplet leptoquark mass within phenomenologically realistic $SU(5)$ and flipped $SU(5)$ scenarios. In sect. **5** we study leptoquarks that do not contribute to proton decay at leading order. We conclude in sect. **6**.

2. – Leptoquarks in $SU(5)$

The scalars that couple to matter at tree-level in $SU(5)$ reside in 5-, 10-, 15-, 45- and 50-dimensional representations because the SM matter fields comprise $\mathbf{10}_i$ and $\overline{\mathbf{5}}_j$, where $i, j = 1, 2, 3$ represent family indices. Namely, $\mathbf{10}_i = (\mathbf{1}, \mathbf{1}, 1)_i \oplus (\overline{\mathbf{3}}, \mathbf{1}, -2/3)_i \oplus (\mathbf{3}, \mathbf{2}, 1/6)_i = (e^C_i, u^C_i, Q_i)$ and $\overline{\mathbf{5}}_j = (\mathbf{1}, \mathbf{2}, -1/2)_j \oplus (\overline{\mathbf{3}}, \mathbf{1}, 1/3)_j = (L_j, d^C_j)$, where $Q_i = (u_i \quad d_i)^T$ and $L_j = (\nu_j \quad e_j)^T$ [1]. Possible contractions of the matter field representations hence read $\mathbf{10} \otimes \mathbf{10} = \overline{\mathbf{5}} \oplus \overline{\mathbf{45}} \oplus \overline{\mathbf{50}}$, $\mathbf{10} \otimes \overline{\mathbf{5}} = \mathbf{5} \oplus \mathbf{45}$ and $\overline{\mathbf{5}} \otimes \overline{\mathbf{5}} = \overline{\mathbf{10}} \oplus \overline{\mathbf{15}}$.

The scalar leptoquark states that violate both B and L are $(\mathbf{3}, \mathbf{1}, -1/3)$, $(\mathbf{3}, \mathbf{3}, -1/3)$ and $(\overline{\mathbf{3}}, \mathbf{1}, 4/3)$, if one *assumes* neutrinos to be Majorana particles. These states reside in **5**, **45** and **50**. However, if one allows for the possibility that neutrinos are Dirac particles there is another leptoquark—$(\overline{\mathbf{3}}, \mathbf{1}, -2/3)$—that is found in **10** of $SU(5)$ that violates both B and L and could thus also destabilize proton. Altogether, there are eighteen (fifteen) scalar leptoquarks that could mediate proton decay in case neutrinos are Dirac (Majorana) particles. Note that contributions to the up-quark, down-quark and charged lepton masses can come from both **5** and **45** whereas Majorana (Dirac) masses for neutrinos can be generated through **15** (**5**). Table I summarizes couplings to the matter of relevant states that reside in 45-dimensional representations. The couplings of the color triplets in 50-, 10- and 5-dimensional representations are spelled out in ref. [5].

Note that the $(\overline{\mathbf{3}}, \mathbf{1}, 4/3)$ state always couples to the up-quark pair in an antisymmetric manner. Hence the absence of the tree-level proton decay. Moreover, if the Yukawa matrices are symmetric the $(\overline{\mathbf{3}}, \mathbf{1}, 4/3)$ state would not destabilize matter whatsoever.

3. – Leptoquarks in flipped $SU(5)$

Another possibility to unify the SM matter into an $SU(5)$-based framework leads to the so-called flipped $SU(5)$ scenario [2-4]. The generator of electric charge in flipped $SU(5)$ is given as a linear combination of a $U(1)$ generator that resides in $SU(5)$ and an extra $U(1)$ generator as if both of these originate from an $SO(10) \to SU(5) \times U(1)$ decomposition. This guarantees anomaly cancelation at the price of introducing one extra state per family, *i.e.*, the right-handed neutrino ν^C. The transition between the $SU(5)$ and flipped $SU(5)$ embeddings is provided by the following set of transformations: $d^C \leftrightarrow u^C$, $e^C \leftrightarrow \nu^C$, $u \leftrightarrow d$ and $\nu \leftrightarrow e$.

Table I. – *Yukawa couplings of B and L violating scalars in 45-dimensional representation of $SU(5)$. $a, b, c(i, j) = 1, 2, 3$ are color (flavor) indices. Y^{10}_{ij} and $Y^{\overline{5}}_{ij}$ are Yukawa matrix elements.*

$SU(5)$	$Y^{10}_{ij}\mathbf{10}_i\mathbf{10}_j\mathbf{45}$	$Y^{\overline{5}}_{ij}\mathbf{10}_i\overline{\mathbf{5}}_j\mathbf{45}^*$
$(\mathbf{3},\mathbf{1},-1/3)$ $\equiv$ Δ	$2^{1/2}[Y^{10}_{ij}-Y^{10}_{ji}]e^{C\,T}_i C u^C_{a\,j}\Delta_a$	$2^{-1}Y^{\overline{5}}_{ij}\epsilon_{abc}u^{C\,T}_{a\,i}Cd^C_{b\,j}\Delta^*_c$ $-2^{-1}Y^{\overline{5}}_{ij}u^T_{a\,i}Ce_j\Delta^*_a$ $2^{-1}Y^{\overline{5}}_{ij}d^T_{a\,i}C\nu_j\Delta^*_a$
$(\mathbf{3},\mathbf{3},-1/3)$ $\equiv$ $(\Delta^1,\Delta^2,\Delta^3)$	$2^{1/2}\epsilon_{abc}[Y^{10}_{ij}-Y^{10}_{ji}]d^T_{a\,i}Cd_{b\,j}\Delta^1_c$ $-2\epsilon_{abc}[Y^{10}_{ij}-Y^{10}_{ji}]d^T_{a\,i}Cu_{b\,j}\Delta^2_c$ $-2^{1/2}\epsilon_{abc}[Y^{10}_{ij}-Y^{10}_{ji}]u^T_{a\,i}Cu_{b\,j}\Delta^3_c$	$Y^{\overline{5}}_{ij}u^T_{a\,i}C\nu_j\Delta^{1*}_a$ $2^{-1/2}Y^{\overline{5}}_{ij}u^T_{a\,i}Ce_j\Delta^{2*}_a$ $2^{-1/2}Y^{\overline{5}}_{ij}d^T_{a\,i}C\nu_j\Delta^{2*}_a$ $-Y^{\overline{5}}_{ij}d^T_{a\,i}Ce_j\Delta^{3*}_a$
$(\overline{\mathbf{3}},\mathbf{1},4/3)$ $\equiv$ Δ	$2^{1/2}[Y^{10}_{ij}-Y^{10}_{ji}]\epsilon_{abc}u^{C\,T}_{i\,a}Cu^C_{b\,j}\Delta_c$	$-Y^{\overline{5}}_{ij}e^{C\,T}_i Cd^C_{a\,j}\Delta^*_a$

The matter in flipped $SU(5)$ comprises $\mathbf{10}^{+1}_i$, $\overline{\mathbf{5}}^{-3}_i$ and $\mathbf{1}^{+5}_i$, where the superscripts correspond to the extra $U(1)$ charge. The SM hypercharge Y is defined through $Y = (Y(U(1)) - Y(U(1)_{SU(5)}))/5$, where $Y(U(1))$ and $Y(U(1)_{SU(5)})$ represent the quantum numbers of the extra $U(1)$ and the $U(1)$ in $SU(5)(\rightarrow SU(3)\times SU(2)\times U(1))$, respectively.

The scalar sector that can couple to matter directly is made out of $\mathbf{50}^{-2}$, $\mathbf{45}^{-2}$, $\mathbf{15}^{+6}$, $\mathbf{10}^{+6}$, $\mathbf{5}^{-2}$ and $\mathbf{1}^{-10}$. Representations that can generate contributions to the charged fermion masses and Dirac neutrino masses are $\mathbf{45}^{-2}$ and $\mathbf{5}^{-2}$, whereas Majorana mass for neutrinos can originate from interactions with $\mathbf{15}^{+6}$. Leptoquarks that violate B and L reside in $\mathbf{50}^{-2}$, $\mathbf{45}^{-2}$, $\mathbf{10}^{+6}$ and $\mathbf{5}^{-2}$. The relevant couplings to matter for $\mathbf{45}^{-2}$ are given in table II. All other color triplet couplings can be found in ref. [5].

4. – Proton decay

The dimension-six operators due to scalar exchange that violate B and L are

$$O_H(d_\alpha, e_\beta) = a(d_\alpha, e_\beta)\ u^T\ L\ C^{-1}\ d_\alpha\ u^T\ L\ C^{-1} e_\beta, \tag{1}$$

$$O_H(d_\alpha, e^C_\beta) = a(d_\alpha, e^C_\beta)\ u^T\ L\ C^{-1}\ d_\alpha\ e^{C\dagger}_\beta\ L\ C^{-1} u^{C*}, \tag{2}$$

$$O_H(d^C_\alpha, e_\beta) = a(d^C_\alpha, e_\beta)\ d^{C\dagger}_\alpha\ L\ C^{-1}\ u^{C*}\ u^T\ L\ C^{-1} e_\beta, \tag{3}$$

$$O_H(d^C_\alpha, e^C_\beta) = a(d^C_\alpha, e^C_\beta)\ d^{C\dagger}_\alpha\ L\ C^{-1}\ u^{C*}\ e^{C\dagger}_\beta\ L\ C^{-1} u^{C*}, \tag{4}$$

$$O_H(d_\alpha, d_\beta, \nu_i) = a(d_\alpha, d_\beta, \nu_i)\ u^T\ L\ C^{-1}\ d_\alpha\ d^T_\beta\ L\ C^{-1}\ \nu_i, \tag{5}$$

$$O_H(d_\alpha, d^C_\beta, \nu_i) = a(d_\alpha, d^C_\beta, \nu_i)\ d^{C\dagger}_\beta\ L\ C^{-1}\ u^{C*}\ d^T_\alpha\ L\ C^{-1}\ \nu_i, \tag{6}$$

$$O_H(d_\alpha, d^C_\beta, \nu^C_i) = a(d_\alpha, d^C_\beta, \nu^C_i)\ u^T\ L\ C^{-1}\ d_\alpha\ \nu^{C\dagger}_i\ L\ C^{-1}\ d^{C*}_\beta, \tag{7}$$

$$O_H(d^C_\alpha, d^C_\beta, \nu^C_i) = a(d^C_\alpha, d^C_\beta, \nu^C_i)\ d^{C\dagger}_\beta\ L\ C^{-1}\ u^{C*}\ \nu^{C\dagger}_i\ L\ C^{-1}\ d^{C*}_\alpha. \tag{8}$$

TABLE II. – *Yukawa couplings of B- and L-violating scalars in* 45*-dimensional representation of flipped $SU(5)$. $a,b,c(i,j)=1,2,3$ are color (flavor) indices. Y^{10} and $Y^{\overline{5}}$ are Yukawa matrices.*

$SU(5)\times U(1)$	$Y^{10}_{ij}\mathbf{10}^{+1}_i\mathbf{10}^{+1}_j\mathbf{45}^{-2}$	$Y^{\overline{5}}_{ij}\mathbf{10}_i\overline{\mathbf{5}}^{-3}_j\mathbf{45}^{*\,+2}$
$(\mathbf{3},\mathbf{1},-1/3)^{-2}$		$2^{-1}Y^{\overline{5}}_{ij}\epsilon_{abc}d^{C\,T}_{a\,i}Cu^C_{b\,j}\Delta^*_c$
$\equiv$	$2^{1/2}[Y^{10}_{ij}-Y^{10}_{ji}]\nu^{C\,T}_iCd^C_{a\,j}\Delta_a$	$-2^{-1}Y^{\overline{5}}_{ij}d^T_{a\,i}C\nu_j\Delta^*_a$
Δ		$2^{-1}Y^{\overline{5}}_{ij}u^T_{a\,i}Ce_j\Delta^*_a$
$(\mathbf{3},\mathbf{3},-1/3)^{-2}$	$2^{1/2}\epsilon_{abc}[Y^{10}_{ij}-Y^{10}_{ji}]u^T_{a\,i}Cu_{b\,j}\Delta^3_c$	$Y^{\overline{5}}_{ij}d^T_{a\,i}Ce_j\Delta^{3*}_a$
$\equiv$	$-2\epsilon_{abc}[Y^{10}_{ij}-Y^{10}_{ji}]u^T_{a\,i}Cd_{b\,j}\Delta^2_c$	$2^{-1/2}Y^{\overline{5}}_{ij}d^T_{a\,i}C\nu_j\Delta^{2*}_a$
		$2^{-1/2}Y^{\overline{5}}_{ij}u^T_{a\,i}Ce_j\Delta^{2*}_a$
$(\Delta^1,\Delta^2,\Delta^3)$	$-2^{1/2}\epsilon_{abc}[Y^{10}_{ij}-Y^{10}_{ji}]d^T_{a\,i}Cd_{b\,j}\Delta^1_c$	$-Y^{\overline{5}}_{ij}u^T_{a\,i}C\nu_j\Delta^{1*}_a$
$(\overline{\mathbf{3}},\mathbf{1},4/3)^{-2}$		
$\equiv$	$2^{1/2}[Y^{10}_{ij}-Y^{10}_{ji}]\epsilon_{abc}d^{C\,T}_{i\,a}Cd^C_{b\,j}\Delta_c$	$-Y^{\overline{5}}_{ij}\nu^{C\,T}_iCu^C_{a\,j}\Delta^*_a$
Δ		

Here, $i(=1,2,3)$ and $\alpha,\beta(=1,2)$ are generation indices, where all operators that involve a neutrino are bound to have $\alpha+\beta<4$ due to kinematical constraints. $L(=(1-\gamma_5)/2)$ is the left projection operator. The $SU(3)$ color indices are not shown due to a common $\epsilon_{abc}q_aq_bq_c$ contraction. This notation has already been introduced in ref. [14].

These operators allow us to extract relevant coefficients due to a particular leptoquark exchange [14]. Our convention for the charged fermion field redefinitions that yield the mass matrices in physical basis reads: $U^T_CM_UU=M^{\rm diag}_U$, $D^T_CM_DD=M^{\rm diag}_D$ and $E^T_CM_EE=M^{\rm diag}_E$. We introduce $U^\dagger D\equiv V_{UD}=K_1V_{CKM}K_2$, where K_1 (K_2) is a diagonal matrix containing three (two) phases. In the neutrino sector we have $N^T_CM_NN=M^{\rm diag}_N$ ($N^TM_NN=M^{\rm diag}_N$) with $E^\dagger N\equiv V_{EN}=K_3V_{PMNS}K_4$ ($V_{EN}=K_3V_{PMNS}$) in the Dirac (Majorana) neutrino case. K_3 (K_4) is a diagonal matrix containing three (two) phases. V_{CKM} (V_{PMNS}) is the Cabibbo-Kobayashi-Maskawa (Pontecorvo-Maki-Nakagawa-Sakata) mixing matrix.

For example, the relevant coefficients for $\Delta\equiv(\mathbf{3},\mathbf{1},-1/3)$ from $\mathbf{45}$ are

$$a(d^C_\alpha,e_\beta)=\frac{1}{4m^2_\Delta}\,(D^\dagger_CY^{\overline{5}\,\dagger}U^*_C)_{\alpha1}\,(U^TY^{\overline{5}}E)_{1\beta},\tag{9}$$

$$a(d^C_\alpha,e^C_\beta)=\frac{1}{\sqrt{2}m^2_\Delta}\,(D^\dagger_CY^{\overline{5}\,\dagger}U^*_C)_{\alpha1}\,(E^\dagger_C(Y^{10}-Y^{10\,T})^\dagger U^*_C)_{\beta1},\tag{10}$$

$$a(d_\alpha,d^C_\beta,\nu_i)=\frac{1}{4m^2_\Delta}\,(D^\dagger_CY^{\overline{5}\,\dagger}U^*_C)_{\beta1}\,(D^TY^{\overline{5}}N)_{\alpha i}.\tag{11}$$

TABLE III. – *Experimental bounds on selected partial proton decay lifetimes at* 90% *CL.*

Process	τ_p (10^{33} years)
$p \to \pi^0 e^+$	13.0 [15]
$p \to \pi^0 \mu^+$	11.0 [15]
$p \to K^0 e^+$	1.0 [16]
$p \to K^0 \mu^+$	1.3 [16]
$p \to \eta e^+$	4.2 [17]
$p \to \eta \mu^+$	1.3 [17]
$p \to \pi^+ \bar{\nu}$	0.025 [18]
$p \to K^+ \bar{\nu}$	4.0 [15]

The relevant coefficients for $\Delta \equiv (\mathbf{3}, \mathbf{1}, -1/3)^{-2}$ from $\mathbf{45}^{-2}$ in flipped $SU(5)$ are

$$a(d^C_\alpha, e_\beta) = \frac{1}{4m^2_\Delta} \; (D^\dagger_C Y^{\overline{5}\,*} U^*_C)_{\alpha 1} \; (U^T Y^{\overline{5}} E)_{1\beta}, \tag{12}$$

$$a(d_\alpha, d^C_\beta, \nu_i) = -\frac{1}{4m^2_\Delta} \; (D^\dagger_C Y^{\overline{5}\,*} U^*_C)_{\beta 1} \; (D^T Y^{\overline{5}} N)_{\alpha i}, \tag{13}$$

$$a(d^C_\alpha, d^C_\beta, \nu^C_i) = \frac{1}{\sqrt{2} m^2_\Delta} (D^*_C Y^{\overline{5}\,*} U^*_C)_{\beta 1} \; (N^\dagger_C (Y^{10} - Y^{10\,T})^\dagger D^*_C)_{i\alpha}. \tag{14}$$

The current experimental bounds on the partial proton lifetimes these operators contribute to are given in table III. We account for all these decay modes in our analysis.

4˙1. *Leading-order contributions in* $SU(5)$. – Let us present predictions of the simplest of all possible renormalizable models based on the $SU(5)$ gauge symmetry. We demand that both **5** and **45** of Higgs contribute to the down-quark and charged lepton masses [19] to generate phenomenologically viable masses and mixing parameters. We take all mass matrices to be symmetric, *i.e.*, $M_{U,D,E} = M^T_{U,D,E}$. Note that the symmetric mass matrix assumption eliminates contributions to proton decay of all other color triplets besides the $(\mathbf{3}, \mathbf{1}, -1/3)$ from 5- and 45-dimensional representations.

For example, to find widths for the charged anti-leptons in the final state when the triplet state from 5-dimensional representation dominates we need to determine $a(d_\alpha, e_\beta)$, $a(d_\alpha, e^C_\beta)$, $a(d^C_\alpha, e_\beta)$ and $a(d^C_\alpha, e^C_\beta)$. If the Yukawa couplings are symmetric the relevant input for these coefficients reads

$$(U^T (Y^{10} + Y^{10\,T}) D)_{1\alpha} = -\frac{1}{\sqrt{2} v_5} \; (M^{\text{diag}}_U V_{UD})_{1\alpha}, \tag{15}$$

$$(U^T Y^{\overline{5}} E)_{1\beta} = -\frac{1}{2v_5} \; (3 V^*_{UD} M^{\text{diag}}_D V^\dagger_{UD} U^*_2 + U_2 M^{\text{diag}}_E)_{1\beta}, \tag{16}$$

$$(D^\dagger Y^{\overline{5}\,\dagger} U^*)_{\alpha 1} = -\frac{1}{2v_5} \; (3 M^{\text{diag}}_D V^T_{UD} + V^\dagger_{UD} U^*_2 M^{\text{diag}}_E U^\dagger_2)_{\alpha 1}, \tag{17}$$

$$(E^\dagger (Y^{10} + Y^{10\,T})^\dagger U^*)_{\beta 1} = -\frac{1}{\sqrt{2} v_5} \; (U^T_2 M^{\text{diag}}_U)_{\beta 1}, \tag{18}$$

where $U_2 = U^T E^*$ and v_5 represents a vacuum expectation value (VEV) of 5-dimensional representation. Our normalization is such that $|v_5|^2/2 + 12|v_{45}|^2 = v^2$, where v ($= 246\,\mathrm{GeV}$) stands for the electroweak VEV. v_{45} is the VEV in 45-dimensional representation. A connection between Yukawa couplings and charged fermion mass matrices is spelled out elsewhere [11]. For the $p \to e_\delta^+ \pi^0$ channels we finally find

$$\Gamma(p \to e_\delta^+ \pi^0) =$$
$$\frac{(m_p^2 - m_{\pi^0}^2)^2}{64\pi f_\pi^2 m_p^3} \frac{\alpha^2}{v_5^4 m_\Delta^4} \left| (V_{UD})_{11} \left[m_u + \frac{3}{4} m_d \right] + \frac{1}{4} \left(V_{UD}^\dagger U_2^* M_E^{\mathrm{diag}} U_2^\dagger \right)_{11} \right|^2$$
$$\times \left(\left| \frac{3}{2} \left(V_{UD}^* M_D^{\mathrm{diag}} V_{UD}^\dagger U_2^* \right)_{1\delta} + \frac{1}{2} \left(U_2 M_E^{\mathrm{diag}} \right)_{1\delta} \right|^2 + 4|m_u (U_2)_{1\delta}|^2 \right) (1 + D + F)^2,$$

where α and β are the so-called nucleon matrix elements. $F+D$ and $F-D$ combinations are extracted from the nucleon axial charge and form factors in semileptonic hyperon decays, respectively [20, 21]. We take in what follows $f_\pi = 130\,\mathrm{MeV}$, $m_p = 938.3\,\mathrm{MeV}$, $D = 0.80(1)$, $F = 0.47(1)$ and $\alpha = -\beta = -0.0112(25)\,\mathrm{GeV}^3$ [21].

In the previous example we assume that contributions to proton decay of the triplet in 5-dimensional representation dominate over contributions of triplets in 45-dimensional representation. We actually find that the 5-dimensional triplet dominates over the 45-dimensional triplet for moderate values of v_{45} [5]. The suppression factor for the partial lifetimes approximately reads $10^2 (v_{45}/v_5)^4$.

In order to incorporate $p \to \pi^+ \bar\nu$ and $p \to K^+ \bar\nu$ decay modes in our study we note that one is free to sum over the neutrino flavors in the final state. The relevant coefficients that enter widths for these decays are $a(d_\alpha, d_\beta, \nu_i)$ and $a(d_\alpha, d_\beta^C, \nu_i)$ when the exchanged state is the triplet in 5-dimensional representation. The upshot of our results is that widths for decays with neutral anti-lepton in the final state again depend only on U_2 as far as the mixing parameters are concerned. We again find that the contribution of the triplet in 5-dimensional representation towards $p \to K^+ \bar\nu$ and $p \to \pi^+ \bar\nu$ dominates over the 45-dimensional triplet contributions for moderate values of v_{45}.

We numerically analyze all the decay modes given in table III to find the current bounds on the triplet mass in $SU(5)$ with symmetric Yukawa couplings. We take values of quark and lepton masses at M_Z, as given in [22]. The CKM angles are taken from ref. [18]. We randomly generate one million sets of values for nine parameters of U_2 and five phases of V_{UD}. As it turns out, it is $p \to K^+ \bar\nu$ that dominates in all instances. The most and least conservative bounds for this channel read

$$m_\Delta > 1.2 \times 10^{13} \left(\frac{\alpha}{0.0112\,\mathrm{GeV}^3} \right)^{1/2} \left(\frac{100\,\mathrm{GeV}}{v_5} \right) \mathrm{GeV}, \tag{19}$$

$$m_\Delta > 1.5 \times 10^{11} \left(\frac{\alpha}{0.0112\,\mathrm{GeV}^3} \right)^{1/2} \left(\frac{100\,\mathrm{GeV}}{v_5} \right) \mathrm{GeV}. \tag{20}$$

To summarize, if one is to maximize contributions from the triplets in 5- and 45-dimensional representations towards proton decay within renormalizable $SU(5)$ framework with symmetric mass matrices the current bounds on the triplet mass scale are given in eqs. (19) and (20) if the color triplet in **5** of Higgs dominates in the most and least conservative scenario, respectively. Any $SU(5)$ scenario where the triplet scalar mass exceeds the most conservative bound of eq. (19) is certainly safe with regard to the proton decay constraints on the scalar mediated proton decay. If the triplet mass is below the least conservative bound of eq. (20) the $SU(5)$ scenario is not viable.

4·2. *Leading-order contributions in flipped* $SU(5)$. – In the minimal flipped $SU(5)$ scenario it is sufficient to have only one 5-dimensional scalar representation present to generate realistic charged fermion masses. We accordingly present predictions of a flipped $SU(5)$ scenario with a single color triplet state. To be able to compare the flipped $SU(5)$ results with the case of ordinary $SU(5)$ we again take $M_{U,D,E} = M^T_{U,D,E}$.

We find that the decays with anti-neutrinos in the final state always dominate. To find corresponding decay widths for $p \to \pi^+\bar{\nu}$ and $p \to K^+\bar{\nu}$ we need to determine $a(d_\alpha, d_\beta, \nu_i)$ and $a(d_\alpha, d^C_\beta, \nu_i)$. In the minimal model with symmetric mass matrices the relevant input reads

$$(U^T(Y^{10} + Y^{10\,T})D)_{1\alpha} = -\frac{1}{\sqrt{2}v_5}\left(V^*_{UD}M^{\rm diag}_D\right)_{1\alpha}, \tag{21}$$

$$(D^T Y^{\bar{5}} N)_{\beta i} = -\frac{2}{v_5}\left(V^T_{UD}M^{\rm diag}_U U^*_2 V_{EN}\right)_{\beta i}, \tag{22}$$

$$(D^\dagger Y^{\bar{5}\,*} U^*)_{\beta 1} = -\frac{2}{v_5}\left(V^\dagger_{UD}M^{\rm diag}_U\right)_{\beta 1}. \tag{23}$$

The sum over neutrino flavors in the final state eliminates dependence on any unknown rotations in the quark and lepton sectors leaving us with decay widths that depend only on known masses and mixing parameters. This makes minimal flipped $SU(5)$ with symmetric mass matrices very special. We find the following limit on the triplet mass that originates from experimental constraints on $p \to K^+\bar{\nu}$ channel

$$m_\Delta > 1.0 \times 10^{12}\left(\frac{\alpha}{0.0112\,{\rm GeV}^3}\right)^{1/2}\ {\rm GeV}. \tag{24}$$

The fact that $p \to \pi^+\bar{\nu}$ is also a clean channel means that the minimal flipped $SU(5)$ predicts ratio between $\Gamma(p \to \pi^+\bar{\nu})$ and $\Gamma(p \to K^+\bar{\nu})$. We find it to be

$$\Gamma(p \to \pi^+\bar{\nu})/\Gamma(p \to K^+\bar{\nu}) = 9.0. \tag{25}$$

This result represents firm prediction within the framework of the minimal flipped $SU(5)$.

5. – Higher-order contributions

The $(\bar{\mathbf{3}}, \mathbf{1}, 4/3)$ state violates B and L but does not contribute to $d = 6$ proton decay operators at tree-level. We note that despite the absence of the tree-level contribution to proton decay of the $(\bar{\mathbf{3}}, \mathbf{1}, 4/3)$ state, weak corrections lead to proton destabilizing $d = 6$ and $d = 9$ operators [5]. The effect of the $d = 9$ operators can be rendered adequately small even in the case of simultaneously large leptoquark *and* diquark couplings, a situation that is favored by observables in $t\bar{t}$ production and value of $(g-2)_\mu$. This is achieved by finely-tuned cancellation of two amplitudes. To the contrary, similar cancellation is impossible in the case of $d = 6$ operator for $p \to \pi^0\mu^+$ decay and we are required to suppress either all leptoquark couplings involving μ or all diquark couplings. We conclude that the proton decay lifetime constraint allows to fully address either $A^{t\bar{t}}_{FB}$ or $(g - 2)_\mu$ observable with the $(\bar{\mathbf{3}}, \mathbf{1}, 4/3)$ state, but not both.

6. – Conclusions

We classify the scalar leptoquarks present in $SU(5)$ and flipped $SU(5)$ grand unification frameworks that mediate proton decay. In both frameworks the considered leptoquark states reside in scalar representations of $SU(5)$ of dimension 5, 10, 45, and 50. We integrate out the above states at tree-level and parameterize their contributions in terms of effective coefficients of a complete set of $d = 6$ operators. The mass constraint on the color triplet state contained in 5- and 45-dimensional representations is then derived. The precise lower bound in $SU(5)$ depends on the value of the VEV of these representation. For the VEV of 100 GeV the least (most) conservative lower bound on the triplet mass that originates from the $p \to K^+\bar{\nu}$ channel is approximately 10^{11} GeV (10^{13} GeV). The corresponding bound is derived within the flipped $SU(5)$ framework to read 10^{12} GeV and proves to be both mixing and VEV independent. Moreover, flipped $SU(5)$ theory with symmetric mass matrices predicts $\Gamma(p \to \pi^+\bar{\nu})/\Gamma(p \to K^+\bar{\nu}) = 9$.

The two leptoquark states that do not contribute to proton decay at tree-level are $(\bar{\mathbf{3}}, \mathbf{1}, 4/3)$ and $(\bar{\mathbf{3}}, \mathbf{1}, -2/3)^{+6}$ in the standard and flipped $SU(5)$ frameworks, respectively. We have estimated their contribution to dimension-six operators via box diagram and the tree-level contribution to dimension-nine operators. For the $(\bar{\mathbf{3}}, \mathbf{1}, 4/3)$ state it has been found that if it is to explain both the anomalous magnetic moment of the muon and the $t\bar{t}$ forward-backward asymmetry, then the contribution of the dimension-six operator would destabilize the proton in $p \to \mu^+\pi^0$ channel. Therefore only one of the two puzzles can be addressed with this leptoquark state.

* * *

I. Doršner acknowledges support by SNSF through the SCOPES project IZ74Z0_137346.

REFERENCES

[1] Georgi H. and Glashow S. L., *Phys. Rev. Lett.*, **32** (1974) 438.
[2] De Rujula A., Georgi H. and Glashow S. L., *Phys. Rev. Lett.*, **45** (1980) 413.
[3] Georgi H., Glashow S. L. and Machacek M., *Phys. Rev. D*, **23** (1981) 783.
[4] Barr S. M., *Phys. Lett. B*, **112** (1982) 219.
[5] Dorsner I., Fajfer S. and Kosnik N., *Phys. Rev. D*, **86** (2012) 015013 (arXiv:1204.0674 [hep-ph]).
[6] Fileviez Perez P., *Phys. Lett. B*, **654** (2007) 189 (hep-ph/0702287).
[7] Dorsner I., Fajfer S., Kamenik J. F. and Kosnik N., *Phys. Lett. B*, **682** (2009) 67 (arXiv:0906.5585 [hep-ph]).
[8] Dorsner I., Fajfer S., Kamenik J. F. and Kosnik N., *Phys. Rev. D*, **81** (2010) 055009 (arXiv:0912.0972 [hep-ph]).
[9] Aaltonen T. *et al.* (CDF Collaboration), *Phys. Rev. D*, **83** (2011) 112003 (arXiv: 1101.0034 [hep-ex]).
[10] Abazov V. M. *et al.* (D0 Collaboration), *Phys. Rev. D*, **84** (2011) 112005 (arXiv: 1107.4995 [hep-ex]).
[11] Dorsner I., Drobnak J., Fajfer S., Kamenik J. F. and Kosnik N., *JHEP*, **11** (2011) 002 (arXiv:1107.5393 [hep-ph]).
[12] Bennett G. W. *et al.* (Muon g-2 Collaboration), *Phys. Rev. Lett.*, **92** (2004) 161802 (hep-ex/0401008).
[13] Jegerlehner F., *Acta Phys. Polon. B*, **38** (2007) 3021 (hep-ph/0703125).
[14] Nath P. and Fileviez Perez P., *Phys. Rep.*, **441** (2007) 191 (hep-ph/0601023).
[15] Miura M., *PoS ICHEP*, **2010** (2010) 408.

[16] Kobayashi K. *et al.* (Super-Kamiokande Collaboration), *Phys. Rev. D*, **72** (2005) 052007 (hep-ex/0502026).
[17] Nishino H. *et al.* (Super-Kamiokande Collaboration), *Phys. Rev. D*, **85** (2012) 112001 (arXiv:1203.4030 [hep-ex]).
[18] Nakamura K. *et al.* (Particle Data Group Collaboration), *J. Phys. G*, **37** (2010) 075021.
[19] Georgi H. and Jarlskog C., *Phys. Lett. B*, **86** (1979) 297.
[20] Claudson M., Wise M. B. and Hall L. J., *Nucl. Phys. B*, **195** (1982) 297.
[21] Aoki Y. *et al.* (RBC-UKQCD Collaboration), *Phys. Rev. D*, **78** (2008) 054505 (arXiv:0806.1031 [hep-lat]).
[22] Dorsner I., Fileviez Perez P. and Rodrigo G., *Phys. Rev. D*, **75** (2007) 125007 (hep-ph/0607208).

SESSION VIII - YOUNG SCIENTIST FORUM

Felicitas Thorne	Results of $\mathrm{B_s^0} \to CP$ eigenstates at Belle
Ricardo Magana-Villalba	Studies of CP violation in the decay $B_s \to J/\psi\phi$ at DØ
Gianluca Inguglia	The time-dependent CP violation in charm
Louise Suter	BSM Higgs searches in tau final states at DØ
Caterina Vernieri	Finding a $\mathrm{Z} \to 2$ jets signal in $\mathrm{W} + 3$ jets events at CDF

IL NUOVO CIMENTO Vol. 35 C, N. 6 Novembre-Dicembre 2012
DOI 10.1393/ncc/i2012-11372-8

Colloquia: LaThuile12

Results of $\mathrm{B_s^0} \to CP$ eigenstates at Belle

F. Thorne and C. Schwanda for the Belle Collaboration
Institute of High Energy Physics, Austrian Academy of Science - Vienna, Austria

ricevuto il 7 Settembre 2012

Summary. — We report the measurement of the absolute branching fraction for $\mathrm{B_s^0} \to \mathrm{J}/\psi\,\phi$, for $\mathrm{B_s^0} \to \mathrm{J}/\psi\,\mathrm{K^+K^-}$ and a determination of the s-wave contribution in the ϕ mass range as well as a first observation of $\mathrm{B_s^0} \to \mathrm{J}/\psi\,\eta$ and $\mathrm{B_s^0} \to \mathrm{J}/\psi\,\eta'$. These results are based on a $121\,\mathrm{fb}^{-1}$ data sample collected with the Belle detector at the KEK-B asymmetric $\mathrm{e^+e^-}$ collider near the $\Upsilon(5S)$ resonance.

PACS 13.25.Hw – Decays of bottom mesons.

1. – Introduction

During its operation, the Belle experiment collected over $700\,\mathrm{fb}^{-1}$ of data near the $\Upsilon(4S)$ resonance and $121\,\mathrm{fb}^{-1}$ near the $\Upsilon(5S)$ resonance. This second data sample is unique at B factories and provides the opportunity to study decays of $\mathrm{B_s^0}$ mesons.

To extract the $\mathrm{B_s^0}$ signal, two nearly independant kinematic variables, ΔE and M_{bc}, are used:

$$\Delta E = E^*_{\mathrm{B}} - E^*_{\mathrm{beam}} \qquad \text{and} \qquad M_{\mathrm{bc}} = \sqrt{E^2_{\mathrm{beam}} - (p^*_{\mathrm{B}})^2}, \tag{1}$$

where E^*_{beam} is the beam energy in the center-of-mass frame and E^*_{B} and p^*_{B} denote the energy and the momentum of the reconstructed $\mathrm{B_s^0}$ meson, respectively, given in the center-of-mass system.

In the analyses presented below, the $\mathrm{B_s^0}$ meson is fully reconstructed. However, the photon from a possible $\mathrm{B_s^*} \to \mathrm{B_s^0}\gamma$ decay is not included. As the energy information from the photon from the $\mathrm{B_s^*}$ decay is lost, the signal region plotted in the M_{bc}-ΔE plane splits up into three areas, depending on the number of $\mathrm{B_s^*}$ mesons in the initial state. As these areas are not overlapping in M_{bc}, they can easily be separated during the analysis by a cut on M_{bc} (fig. 1(b)).

The Belle detector (fig. 1(a)), located at the asymmetric $\mathrm{e^+e^-}$ collider KEK-B in Tsukuba Japan, is a large-solid-angle magnetic spectrometer that consists of a silicon vertex detector (SVD), a 50-layer central drift chamber (CDC), an array of aerogel threshold

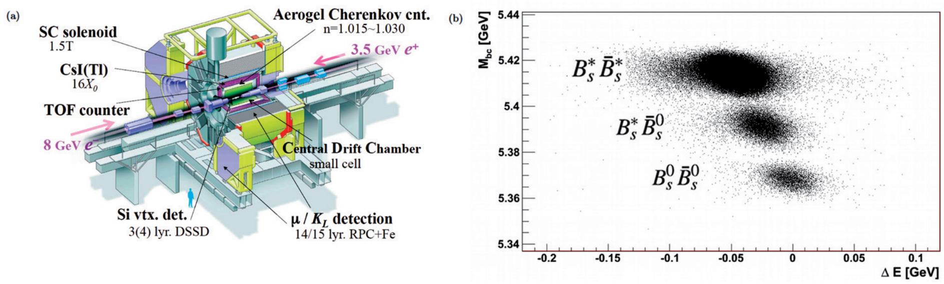

Fig. 1. – (a) Schematic view of the Belle detector. (b) Signal regions shown as a scatter plot in the $M_{\rm bc}$-ΔE plane.

Cherenkov counters (ACC), a barrel-like arrangement of time-of-flight scintillation counters (TOF), and an electromagnetic calorimeter (ECL) comprised of CsI(Tl) crystals located inside a superconducting solenoid coil that provides a 1.5 T magnetic field. An iron flux-return located outside of the coil is instrumented to detect $\mathrm{K_L^0}$ mesons and to identify muons (KLM). The detector is described in details elsewhere [1].

2. – Precise measurement of $\mathcal{B}(\mathrm{B_s^0} \to \mathrm{J}/\psi\,\phi)$ and $\mathcal{B}(\mathrm{B_s^0} \to \mathrm{J}/\psi\,\mathrm{K^+K^-})$

The decay $\mathrm{B_s^0} \to \mathrm{J}/\Psi\,\phi$ is an important mode for measuring the CP-violating phase $\beta_{\rm s}$ in the $\mathrm{B_s\overline{B}_s}$ mixing, which is of particular interest as it is expected to be sensitive to physics beyond the Standard Model [2]. Therefore, regarding the current PDG value of $\mathcal{B}(\mathrm{B_s^0} \to \mathrm{J}/\psi\,\phi) = (1.4 \pm 0.5)10^{-3}$ [3] measured by the CDF experiment [4], which provides a relative error of 35.7%, a precise measurement of this branching fraction is essential.

Furthermore, in this analysis the branching fraction of the decay $\mathrm{B_s^0} \to \mathrm{J}/\psi\,\mathrm{K^+K^-}$, which has not been measured so far, is determined together with the branching ratio of $\mathrm{B_s^0} \to \mathrm{J}/\psi\,\phi$. The study of this nonresonant mode is crucial, as it is the main background for the investigation of the decay $\mathrm{B_s^0} \to \mathrm{J}/\psi\,\phi$. By separating these two final states, it is also possible to calculate the s-wave contribution within the ϕ mass region.

In both final states, the same particles have to be identified: Two oppositely charged leptons and two oppositely charged kaons. To reconstruct the J/ψ meson, the invariant mass of the leptons and a possible bremstrahlung gamma is required to lie within $2.946\,\mathrm{GeV} \le m(\ell\ell)_{\mathrm{e^+e^-}(\gamma)} \le 3.133\,\mathrm{GeV}$ and $3.036\,\mathrm{GeV} \le m(\ell\ell)_{\mu^+\mu^-} \le 3.133\,\mathrm{GeV}$, respectively.

In case of the invariant kaon mass, only a lower cut of $m(\mathrm{K^+K^-}) \ge 0.95\,\mathrm{GeV}$ is applied, so that the full $m(\mathrm{K^+K^-})$ distribution can be investigated.

Finally, to extract the $\mathrm{B_s^0}$ meson, signal requirements on the kinematic parameters ΔE and $M_{\rm bc}$ are performed. In this analysis a region with $M_{\rm bc} > 5.4\,\mathrm{GeV}$ is used, which means only the dominant $\mathrm{B_s^*\overline{B}_s^*}$ signal region is investigated as this provides the best signal to background ratio.

To determine the branching ratios for $\mathrm{B_s^0} \to \mathrm{J}/\psi\,\phi$ and $\mathrm{B_s^0} \to \mathrm{J}/\psi\,\mathrm{K^+K^-}$ a two-dimensional unbinned likelihood fit in ΔE and $m(\mathrm{K^+K^-})$ is performed.

For these two channels, the probability density functions (pdfs) for the ΔE distribution are adjusted using a real data control sample. For this purpose the decay $\mathrm{B^0} \to \mathrm{J}/\psi\,\mathrm{K}^*(892)$ was chosen, as its final state is very similar to the final state of $\mathrm{B_s^0} \to \mathrm{J}/\psi\,\phi$ and $\mathrm{B_s^0} \to \mathrm{J}/\psi\,\mathrm{K^+K^-}$, except that one kaon is replaced by a pion.

TABLE I. – *Fit results for the* $\mu^+\mu^-$ *and the* e^+e^- *channel on* $121\,\mathrm{fb}^{-1}$.

Channel	$J/\psi\,\phi$	$J/\psi\,K^+K^-$	Combinatorial background
$\mu^+\mu^-$	158 ± 13	89 ± 13	304 ± 20
e^+e^-	168 ± 14	110 ± 16	239 ± 20

As for the K^+K^- invariant mass, the pdfs for $B_s^0 \to J/\psi\,\phi$ and $B_s^0 \to J/\psi\,K^+K^-$ are determined from generic Monte Carlo (MC) data. The simulation of this data basically includes all known contributions that can be found in the PDG. Investigating the $m(K^+K^-)$ distribution, the peak of the ϕ meson can be clearly identified at the low energy part of the spectrum, while the nonresonant decay $B_s^0 \to J/\psi\,K^+K^-$ provides a flat distribution up to the high-energy part of the $m(K^+K^-)$ spectrum which can be modeled by an Argus function. As a consequence, the two decay modes are distinguishable via the distribution of the invariant kaon mass, rather than by performing an angular analysis.

The fit results obtained from the full $121\,\mathrm{fb}^{-1}$ Belle data sample are presented in table I. The description of the ΔE and the $m(K^+K^-)$ distribution with the applied pdf model is in good agreement with the data for the muon channel (fig. 2) as well as for the electron channel (fig. 3).

With 158 ± 13 (168 ± 14) events for $B_s^0 \to J/\psi\,\phi$ in the muon (electron) channel the corresponding branching fraction can be calculated to be

$$\mathcal{B}(B_s^0 \to J/\psi_{\mu^+\mu^-}\,\phi) = (1.19 \pm 0.10_{\rm stat} \pm 0.19_{\rm sys})10^{-3}, \tag{2}$$

$$\mathcal{B}(B_s^0 \to J/\psi_{e^+e^-}\,\phi) = (1.33 \pm 0.11_{\rm stat} \pm 0.22_{\rm sys})10^{-3} \tag{3}$$

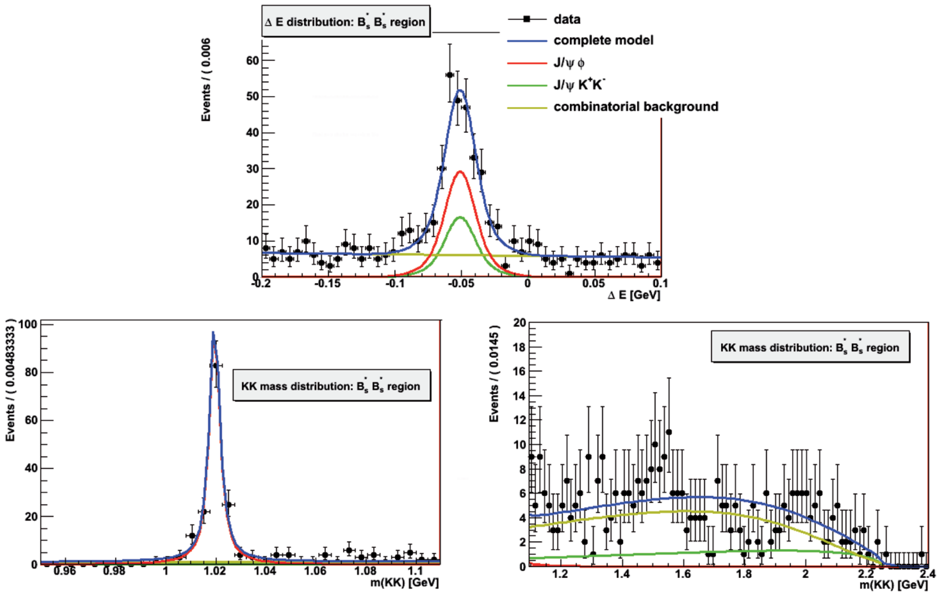

Fig. 2. – Fitted ΔE and $m(K^+K^-)$ distribution for the $\mu^+\mu^-$ channel on $121.061\,\mathrm{fb}^{-1}$.

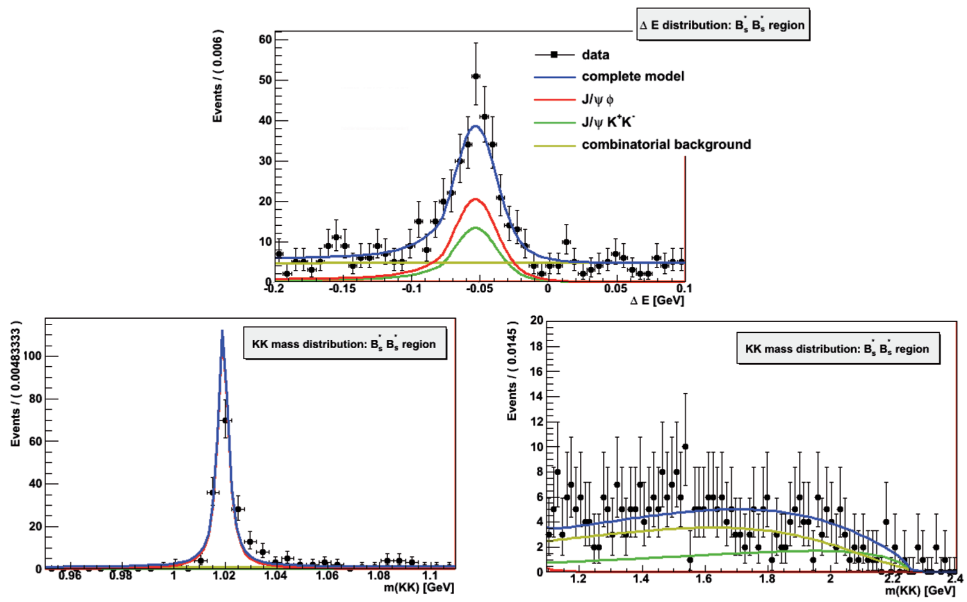

Fig. 3. – Fitted ΔE and $m(\mathrm{K}^+\mathrm{K}^-)$ distribution for the $\mathrm{e}^+\mathrm{e}^-$ channel on $121.061\,\mathrm{fb}^{-1}$.

with the weighted mean value of

$$\mathcal{B}(\mathrm{B}_\mathrm{s}^0 \to \mathrm{J}/\psi\,\phi) = (1.25 \pm 0.07_\mathrm{stat} \pm 0.20_\mathrm{sys})10^{-3}. \tag{4}$$

The obtained results for the branching fractions for the muon and the electron channel are comparable with each other within their statistical errors and are in good agreement with the current PDG value.

Summarizing all contributions to the systematic error that are presented in table II, the total systematic error is determined to be 16.3%. The dominant contribution to the systematic error is the uncertainty in f_s, the ratio of $\mathrm{B}_\mathrm{s}^*\overline{\mathrm{B}}_\mathrm{s}^*$ events within all produced $\mathrm{b}\overline{\mathrm{b}}$ pairs, which is therefore limiting the accuracy of the analysis at the present time.

The fit result for the nonresonant component $\mathrm{B}_\mathrm{s}^0 \to \mathrm{J}/\psi\,\mathrm{K}^+\mathrm{K}^-$ is 89 ± 13 (110 ± 16) events in the muon (electron) channel, which leads to

$$\mathcal{B}(\mathrm{B}_\mathrm{s}^0 \to \mathrm{J}/\psi_{\mu^+\mu^-}\mathrm{K}^+\mathrm{K}^-) = (0.33 \pm 0.05_\mathrm{stat}{}^{+0.06}_{-0.07\mathrm{sys}})10^{-3} \tag{5}$$

$$\mathcal{B}(\mathrm{B}_\mathrm{s}^0 \to \mathrm{J}/\psi_{\mathrm{e}^+\mathrm{e}^-}\mathrm{K}^+\mathrm{K}^-) = (0.43 \pm 0.06_\mathrm{stat}{}^{+0.10}_{-0.11\mathrm{sys}})10^{-3} \tag{6}$$

with the weighted mean value

$$\mathcal{B}(\mathrm{B}_\mathrm{s}^0 \to \mathrm{J}/\psi\,\mathrm{K}^+\mathrm{K}^-) = (0.36 \pm 0.04_\mathrm{stat} \pm 0.08_\mathrm{sys})10^{-3} \tag{7}$$

This measurement has a significance of 5.3σ. The sources of the systematic error are the same as for the measurement of $\mathrm{B}_\mathrm{s}^0 \to \mathrm{J}/\psi\,\phi$.

Another result that can be obtained from this analysis is the s-wave contribution in the mass region of the ϕ meson. For this purpose, the following assumptions are made:

– The p-wave contribution originates from the decay $\mathrm{B}_\mathrm{s}^0 \to \mathrm{J}/\psi\,\phi$.

– The s-wave contribution originates from the decay $\mathrm{B}_\mathrm{s}^0 \to \mathrm{J}/\psi\,\mathrm{K}^+\mathrm{K}^-$.

TABLE II. – *Values and systematic errors for the parameters used to calculate $\mathcal{B}(B_s^0 \to J/\psi\,\phi)$.*

Parameter	Value	Error	%
Luminosity	$121.061\,\mathrm{fb}^{-1}$	$0.847\,\mathrm{fb}^{-1}$	0.7
$\sigma_{b\bar{b}}^{\Upsilon(5S)}$ [5]	0.302 nb	0.014 nb	4.6
f_s [6]	0.193	0.029	15.0
$\mathcal{B}(\phi \to K^+K^-)$ [3]	0.489	0.005	1.0
$\mathcal{B}(J/\psi \to \mu^+\mu^-)$ [3]	0.0593	0.0006	1.0
$\mathcal{B}(J/\psi \to e^+e^-)$ [3]	0.0594	0.0006	1.0
$\epsilon_{\text{MC statistic}}$ $(\mu^+\mu^-)$	0.325	0.001	0.2
$\epsilon_{\text{MC statistic}}$ (e^+e^-)	0.307	0.001	0.3
$\epsilon_{\text{Polarisation}}$ $(\mu^+\mu^-)$	0.325	0.005	1.5
$\epsilon_{\text{Polarisation}}$ (e^+e^-)	0.307	0.004	1.3
tracking	–	–	1.4
Lepton and kaon ID	–	–	2.0
PDF shape $(\mu^+\mu^-)$	158 events	3.7 events	2.3
PDF shape (e^+e^-)	168 events	4.6 events	2.7
Sum $(\mu^+\mu^-)$	–	$0.19 \cdot 10^{-3}$	16.0
Sum (e^+e^-)	–	$0.22 \cdot 10^{-3}$	16.5

The two states are distinguishable via the $m(\mathrm{KK})$ distribution and the s-wave contribution (S) is calculated as the rate of the fitted number of events of the nonresonant decay compared to the total number of fitted events of the resonant and nonresonant decay within a specific mass range:

$$S = \frac{\alpha \cdot N(J/\psi\,K^+K^-)}{\alpha \cdot N(J/\psi\,K^+K^-) + \beta \cdot N(J/\psi\,\phi)}\,. \tag{8}$$

In eq. (8), $N(J/\psi\,K^+K^-)$ and $N(J/\psi\,\phi)$ are the fitted number of events for the $B_s^0 \to J/\psi\,K^+K^-$ and the $B_s^0 \to J/\psi\,\phi$ channel, respectively. The parameters α and β denote the percentage of the two components within the considered mass range.

The mass ranges that are investigated are the same as used by CDF and LHCb (see table III) and the obtained results are in agreement with the contributions calculated by these experiments. The statistical error originates from the statistical uncertainty of the fit results for $N(J/\psi\,K^+K^-)$ and $N(J/\psi\,\phi)$, while the systematic error is given by the uncertainty of the parameters α and β due to the uncertainty in the pdf shape.

3. – First observation of $B_s^0 \to J/\psi\,\eta$ and $B_s^0 \to J/\psi\,\eta'$

The measurement of the decays $B_s^0 \to J/\psi\,\eta$ and $B_s^0 \to J/\psi\,\eta'$ provide the possibility to investigate new CP-even eigenstates. Furthermore, the $SU(3)$ flavor symmetry

TABLE III. – *Results for the s-wave contribution in different mass regions around the ϕ peak. The numbers are in agreement with the results from CDF and LHCb.*

	CDF [7]	LHCb [8]
Mass range	1.009 GeV–1.028 GeV	1.007 GeV–1.031 GeV
Hadron collider results	$< 6.0\%$ at 95% CL	$4.2 \pm 1.5 \pm 1.8\%$
Belle result	$0.61 \pm 0.07_{\text{stat}} \pm 0.06_{\text{sys}}\%$	$0.75 \pm 0.09_{\text{stat}} \pm 0.09_{\text{sys}}\%$

predicts the ratio of these two branching fractions to be close to one and therefore, a measurement of these decay channels would allow to test the $SU(3)$ symmetry as well as the η-η' mixing (for more detail, see *e.g.* [9-12]).

However, these decays have not been observed so far. The L3 experiment published an upper limit of $\mathcal{B}(\mathrm{B_s^0} \to \mathrm{J}/\psi\,\eta) < 3.8 \cdot 10^{-3}$ at a 90% confidence level [13].

To determine the branching fractions of $\mathrm{B_s^0} \to \mathrm{J}/\psi\,\eta$ and $\mathrm{B_s^0} \to \mathrm{J}/\psi\,\eta'$ the $\mathrm{B_s^0}$ meson is reconstructed in five different final states. While the J/ψ meson is identified via two oppositely charged leptons, the η meson is reconstructed from a $\gamma\gamma$ or $\pi^+\pi^-\pi^0$ state and the η' meson is expected to decay into a $\rho^0\gamma$ or a $\eta\pi^+\pi^-$ final state. For more detailed information on the reconstruction and the fitting method in this analysis see [14].

The fit is performed as a two-dimensional unbinned, extended maximum-likelihood fit in ΔE and M_{bc}, simultaneously for all five final states. The fit results are presented in fig. 4 where the applied pdf model shows a good agreement with the data in all subchannels. With 141 ± 14 (86 ± 14) events found for $\mathrm{B_s^0} \to \mathrm{J}/\psi\,\eta$ ($\mathrm{B_s^0} \to \mathrm{J}/\psi\,\eta'$), the corresponding branching fractions are calculated to

$$\mathcal{B}(\mathrm{B_s} \to \mathrm{J}/\psi\,\eta) = \left(5.10 \pm 0.50_{\text{stat}} \pm 0.25_{\text{sys}}{}^{+1.14}_{-0.79}(N_{\mathrm{B_s^{(*)}}\overline{\mathrm{B}}_\mathrm{s}^{(*)}})\right) \cdot 10^{-4} \tag{9}$$

$$\mathcal{B}(\mathrm{B_s} \to \mathrm{J}/\psi\,\eta') = \left(3.71 \pm 0.61_{\text{stat}} \pm 0.18_{\text{sys}}{}^{+0.83}_{-0.57}(N_{\mathrm{B_s^{(*)}}\overline{\mathrm{B}}_\mathrm{s}^{(*)}})\right) \cdot 10^{-4} \tag{10}$$

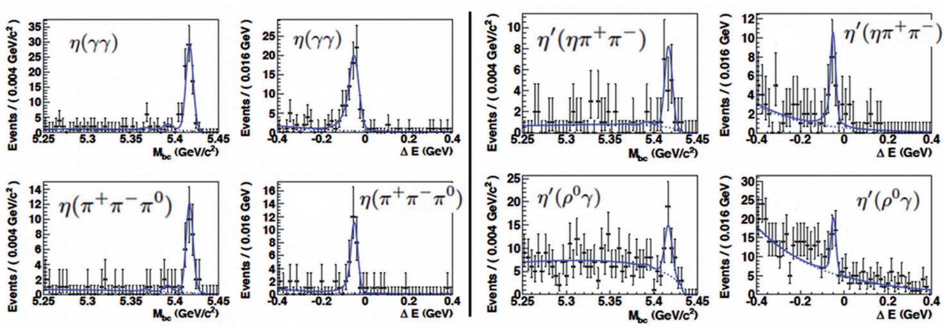

Fig. 4. – Fitted M_{bc} and ΔE distributions for $\mathrm{B_s^0} \to \mathrm{J}/\psi\,\eta$ (left) and $\mathrm{B_s^0} \to \mathrm{J}/\psi\,\eta'$ (right). The solid lines present the projection of the fit results, while the dotted curves illustrate the background component.

and their ratio is

$$\frac{\mathcal{B}(B_s \to J/\psi\eta')}{\mathcal{B}(B_s \to J/\psi\,\eta)} = 0.73 \pm 0.14_{\text{stat}} \pm 0.02_{\text{sys}}. \tag{11}$$

While the result for $B_s^0 \to J/\psi\,\eta$ is in agreement with the upper limit obtained from the L3 experiment, the determined ratio shows a deviation at a 2.1σ level with respect to the prediction.

4. – Summary

We presented the measurement of the absolute branching fraction for $B_s^0 \to J/\psi\,\phi$, for $B_s^0 \to J/\psi\,K^+K^-$ and a determination of the s-wave contribution in the ϕ mass range. The results concerning the branching fraction of $B_s^0 \to J/\psi\,\phi$ and the s-wave contribution are in good agreement with previous measurements from other experiments. The branching fraction of $B_s^0 \to J/\psi\,K^+K^-$ was determined for the first time with a significance of 5.3σ.

Furthermore, we presented the first observation of $B_s^0 \to J/\psi\,\eta$ and $B_s^0 \to J/\psi\,\eta'$. While the result for the branching fraction of $B_s^0 \to J/\psi\,\eta$ is in agreement with the upper limit of a former measurement, the ratio of the two branching fractions shows a deviation of 2.1 σ level with regard to the prediction.

* * *

This work is supported by the Austrian Science Fonds (FWF), under grant number P22742-N16. We thank the KEKB group for the excellent operation of the accelerator, the KEK cryogenics group for the efficient operation of the solenoid, and the KEK computer group and the National Institute of Informatics for valuable computing and SINET3 network support. We acknowledge support from the Ministry of Education, Culture, Sports, Science, and Technology of Japan and the Japan Society for the Promotion of Science; the Australian Research Council and the Australian Department of Education, Science and Training; the National Natural Science Foundation of China under contract No. 10575109 and 10775142; the Department of Science and Technology of India; the BK21 program of the Ministry of Education of Korea, the CHEP SRC program and Basic Research program (grant No. R01-2005-000-10089-0) of the Korea Science and Engineering Foundation, and the Pure Basic Research Group program of the Korea Research Foundation; the Polish State Committee for Scientific Research; the Ministry of Education and Science of the Russian Federation and the Russian Federal Agency for Atomic Energy; the Slovenian Research Agency; the Swiss National Science Foundation; the National Science Council and the Ministry of Education of Taiwan; and the US Department of Energy.

REFERENCES

[1] Abashian A. *et al.* (Belle Collaboration), *Nucl. Instrum. Methods A* , **479** (2002) 117.
[2] Anikeev K. *et al.*, *FERMILAB Report*, No. 01-197 (2001) and references therein.
[3] Nakamura K. *et al.* (Particle Data Group), *Review on particle physics*, *J. Phys. G*, **37** (2010) 075021.
[4] Abe F. *et al.* (CDF Collaboration), *Phys. Rev. D*, **54** (1996) 6596.

[5] Drutskoy A., *Phys. Rev. Lett.*, **98** (2007) 052001.
[6] Louvot R. *et al.* (Belle Collaboration), *Phys. Rev. Lett.*, **102** (2009) 021801.
[7] Aaltonen T. *et al.* (CDF Collaboration), arXiv:1112.1726v1 [hep-ex] (2011).
[8] LHCb Collaboration, arXiv:1202.4717v2 [hep-ex] (2012).
[9] Skands P. Z., *JHEP*, **01** (2001) 008.
[10] Datta A., Lipkin H. J. and O'Donnell P. J., *Phys. Lett. B*, **529** (2002) 93.
[11] Thomas C. E., *JHEP*, **10** (2007) 026.
[12] Fleischer R., Knegjens R. and Ricciardi G., *Eur. Phys. J. C*, **71** (2011) 1798.
[13] Acciarri M. *et al.* (L3 Collaboration), *Phys. Lett. B*, **391** (1997) 481.
[14] Li J. *et al.* (Belle Collaboration), *Phys. Rev. Lett.*, **108** (2012) 181808.

IL NUOVO CIMENTO Vol. 35 C, N. 6 Novembre-Dicembre 2012
DOI 10.1393/ncc/i2012-11373-7

Colloquia: LaThuile12

Studies of CP violation in the decay $B_s \to J/\psi\phi$ at DØ

R. Magana-Villalba

Centro de Investigación y Estudios Avanzados del IPN - México D.F., Mexico

ricevuto il 7 Settembre 2012

Summary. — We report a measurement of the lifetime, decay rate difference and CP-violating phase for B_s^0 mesons obtained from a flavour-tagged, time-dependent, angular analysis in a sample of 5598 ± 113 $B_s^0 \to J/\psi\phi$ decays selected in a $8\,\text{fb}^{-1}$ data sample of $p\overline{p}$ collisions at $\sqrt{s} = 1.96\,\text{TeV}$ recorded with the DØ experiment at Fermilab.

PACS 13.25.Hw – Decays of bottom mesons.
PACS 11.30.Er – Charge conjugation, parity, time reversal, and other discrete symmetries.

1. – Introduction

In the standard model (SM), the light (L) and heavy (H) mass eigenstates of the mixed B_s^0 system are expected to have sizeable mass and decay width differences: $\Delta M_s \equiv M_H - M_L$ and $\Delta\Gamma_s \equiv \Gamma_L - \Gamma_H$. The two mass eigenstates are expected to be almost pure CP eigenstates. The CP-violating phase that appears in $b \to c\overline{c}s$ decays, due to the interference of the decay with and without mixing, is predicted [1] to be $\phi_s^{J/\psi\phi} = -2\beta_s = 2\arg[-V_{tb}V_{ts}^*/V_{cb}V_{cs}^*] = -0.038 \pm 0.002$, where V_{ij} are elements of the Cabibbo-Kobayashi-Maskawa quark-mixing matrix [2]. New phenomena may alter the observed phase [3] to $\phi_s^{J/\psi\phi} \equiv -2\beta_s + \phi_s^{\Delta}$.

Here we present new results from the time-dependent amplitude analysis of the decay $B_s^0 \to J/\psi\phi$ using a data sample corresponding to an integrated luminosity of $8.0\,\text{fb}^{-1}$ collected with the D0 detector [4] at the Fermilab Tevatron Collider. We measure $\Delta\Gamma_s$; the average lifetime of the B_s^0 system, $\overline{\tau}_s = 1/\overline{\Gamma}_s$, where $\overline{\Gamma}_s \equiv (\Gamma_H + \Gamma_L)/2$; and the CP-violating phase $\phi_s^{J/\psi\phi}$.

2. – Data sample and event reconstruction

The analysis presented here is based on data accumulated between February 2002 and June 2010 and corresponds to $8\,\text{fb}^{-1}$ of integrated luminosity.

We reconstruct the decay chain $B_s^0 \to J/\psi\phi$, $J/\psi \to \mu^+\mu^-$, $\phi \to K^+K^-$ from candidate $(J/\psi, \phi)$ pairs consistent with coming from a common vertex and having an invariant mass in the range $5.37 \pm 0.20\,\mathrm{GeV}$. Events are collected with a mixture of single and dimuon triggers.

B_s^0 candidate events are required to include two opposite-sign muons accompanied by two opposite-sign tracks. The invariant mass range for muon pairs is $3.096 \pm 0.350\,\mathrm{GeV}$, consistent with J/ψ decay. J/ψ candidates are combined with pairs of oppositely charged tracks (assigned the kaon mass) consistent with production at a common vertex, and with an invariant mass in the range $1.019 \pm 0.030\,\mathrm{GeV}$. Each of the four final-state tracks is required to have at least one SMT hit.

A kinematic fit under the B_s^0 decay hypothesis constrains the dimuon invariant mass to the world-average J/ψ mass [5] and constrains the four-track system to a common vertex.

The primary vertex (PV) is reconstructed using tracks that do not originate from the candidate B_s^0 decay, and apply a constraint to the average beam-spot position in the transverse plane. We define the signed decay length of a B_s^0 meson, L_{xy}^B, as the vector pointing from the PV to the decay vertex, projected on the B_s^0 transverse momentum p_T. The proper decay time of a B_s^0 candidate is given by $t = M_{B_s}\vec{L}_{xy}^B \cdot \vec{p}/(p_T^2)$ where M_{B_s} is the world-average B_s^0 mass [5], and $\vec{p}$ is the particle momentum. Approximately 5 million events are accepted after the selection described in this section.

3. – Background suppression

The selection criteria are designed to optimize the measurement of $\phi_s^{J/\psi\phi}$ and $\Delta\Gamma_s$. Most of the background is due to directly produced J/ψ mesons accompanied by tracks arising from hadronization. This "prompt" background is distinguished from the "non-prompt", or "inclusive $B \to J/\psi + X$" background, where the J/ψ meson is a product of a b-hadron decay while the tracks forming the ϕ candidate emanate from a multi-body decay of a b hadron or from hadronization. Two different event selection approaches are used, one based on a multi-variate technique, and one based on simple limits on kinematic and event quality parameters.

Three Monte Carlo (MC) samples are used to study background suppression: signal, prompt background, and non-prompt background. All three are generated with PYTHIA [6]. Hadronization is also done in PYTHIA, but all hadrons carrying heavy flavors are passed on to EvtGen [7] to model their decays. The prompt background MC sample consists of $J/\psi \to \mu^+\mu^-$ decays produced in $gg \to J/\psi g$, $gg \to J/\psi\gamma$, and $g\gamma \to J/\psi g$ processes. The signal and non-prompt background samples are generated from primary $b\bar{b}$ pair production with all b hadrons being produced inclusively. For the signal sample, events with a $B_s^0 \to J/\psi\phi$ are selected. There are approximately 10^6 events in each background and the signal MC samples. All events are passed through a full standard chain of GEANT-based [8] detector software of DØ simulation.

4. – Multivariate event selection

To discriminate the signal from background events, we use the TMVA package [9]. In preliminary studies using MC simulation, the Boosted Decision Tree (BDT) algorithm was found to demonstrate the best performance. Since prompt and non-prompt backgrounds have different kinematic behavior, we train two discriminants, one for each type of background. We use a set of 33 variables for the prompt background and 35 variables for the non-prompt background.

To choose the best set of criteria for the two BDT discriminants, we start with 14 data samples with signal yields ranging from 4000 to 7000 events. For each sample we choose the pair of BDT cuts which gives the highest significance $S/\sqrt{S+B}$, where S (B) is the number of signal (background) events in the data sample. As the BDT criteria are loosened, the total number of events increases by a factor of ten, while the number of signal events increases by about 50%.

The choice of the final cut on the BDT output is based on an ensemble study. We perform a maximum-likelihood fit to the event distribution in the 2-dimensional (2D) space of B_s^0 candidate mass and proper time. This 2D fit provides a parametrization of the background mass and proper time distribution. We then generate pseudo-experiments in the 5D space of B_s^0 candidate mass, proper time, and three independent angles of decay products, using as input the parameters as obtained in a preliminary study, and the background from the 2D fit. We perform a 5D maximum likelihood fit on the ensembles and compare the distributions of the statistical uncertainties of $\phi_s^{J/\psi\phi}$ ($\sigma(\phi_s^{J/\psi\phi})$) and $\Delta\Gamma_s$ ($\sigma(\Delta\Gamma_s)$) for the different sets of criteria.

The mean statistical uncertainties of both $\phi_s^{J/\psi\phi}$ and $\Delta\Gamma_s$ systematically decrease with increasing signal, favoring looser cuts. The gain in the parameter resolution is slower for the three loosest criteria, while the total number of events doubles from about 0.25×10^6 to 0.5×10^6. Based on these results, we choose the sample that contains about 6500 signal events.

We select a second event sample by applying criteria on event quality and kinematic quantities. We use the consistency of the results obtained for the BDT and for this sample as a measure of systematic effects related to imperfect modeling of the detector acceptance and of the selection requirements. The criteria are the same as in ref. [10]. We refer to this second sample as the "Square-cuts" sample.

5. – Flavor tagging

At the Tevatron, b quarks are mostly produced in $b\bar{b}$ pairs. The flavor of the initial state of the B_s^0 candidate is determined by exploiting properties of particles produced by the other b hadron ("opposite-side tagging", or OST). The OST-discriminating variables are based primarily on the presence of a muon or an electron from the semi-leptonic decay of the other b hadron produced in the $p\bar{p}$ interaction.

The OST algorithm assigns to each event a value of the predicted tagging parameter d, in the range $[-1,1]$, with $d>0$ tagged as an initial b quark and $d<0$ tagged as an initial $\bar{b}$ quark. Larger $|d|$ values correspond to higher tagging confidence. The OST-discriminating variables and algorithm are described in detail in ref. [11].

The tagging dilution $\mathcal{D}$ is defined as $\mathcal{D} = N_{\rm cor} - N_{\rm wr}/(N_{\rm cor}+N_{\rm wr})$ where $N_{\rm cor}$ ($N_{\rm wr}$) is the number of events with correctly (wrongly) identified initial B-meson flavor.

The dependence of the tagging dilution on the tagging parameter d is calibrated with data for which the flavor (B or $\overline{B}$) is known. The dilution calibration is based on independent $B_d^0 \to \mu\nu D^{*\pm}$ data samples. We perform an analysis of the B_d^0-$\overline{B}_d^0$ oscillations described in ref. [12]. We divide the samples into five ranges of the tagging parameter $|d|$, and for each range we obtain a mean value of the dilution $|\mathcal{D}|$. The mixing frequency ΔM_d is fitted simultaneously and is found to be stable and consistent with the world average value. The measured values of the tagging dilution $|\mathcal{D}|$ for the running

TABLE I. – *Definition of nine real measurables for the decay $B_s^0 \to J/\psi\phi$ used in the maximum-likelihood fitting.*

Parameter	Definition
$\|A_0\|^2$	$\mathcal{P}$-wave longitudinal amplitude squared, at $t = 0$
$A1$	$\|A_\parallel\|^2/(1 - \|A_0\|^2)$
$\overline{\tau}_s$ (ps)	B_s^0 mean lifetime
$\Delta\Gamma_s$ (ps^{-1})	Heavy-light decay width difference
F_S	K^+K^- $\mathcal{S}$-wave fraction
β_s	CP-violating phase ($\equiv -\phi_s^{J/\psi\phi}/2$)
$\delta_\parallel$	$\arg(A_\parallel/A_0)$
$\delta_\perp$	$\arg(A_\perp/A_0)$
δ_s	$\arg(A_s/A_0)$

period of time is parametrized by function

$$|\mathcal{D}| = \frac{p_0}{(1 + \exp((p_1 - |d|)/p_2))} - \frac{p_0}{(1 + \exp(p_1/p_2))} \tag{1}$$

and the function is fitted to the data.

6. – Maximum-likelihood fit

We perform a six-dimensional (6D) unbinned maximum-likelihood fit to the proper decay time and its uncertainty, three decay angles characterizing the final state, and the mass of the B_s^0 candidate. We use events for which the invariant mass of the K^+K^- pair is within the range 1.01–1.03 GeV. There are 104,683 events in the BDT-based sample and 66455 events in the Square-cuts sample. We adopt the formulae and notation of ref. [13]. The normalized functional form of the differential decay rate includes an $\mathcal{S}$-wave KK contribution in addition to the dominant $\mathcal{P}$-wave $\phi \to K^+K^-$ decay.

6·1. *Signal model.* – The angular distribution of the signal is expressed in the transversity basis.

The P wave is decomposed into three independent components corresponding to linear polarization states of the vector mesons J/ψ and ϕ, which are either longitudinal (0) or transverse to their direction of motion, and parallel ($\|$) or perpendicular ($\perp$) to each other, The time evolution of the angular distribution of the decay products, expressed in terms of the magnitudes $|A_0|$, $|A_\parallel|$, and $|A_\perp|$, and two phases, $\delta_{||}$ and $\delta_\perp$. By convention, the phase of A_0 is set to zero.

The contribution from the decay to $J/\psi K^+K^-$ with the kaons in the S wave is expressed in terms of the S-wave fraction F_S and a phase δ_s. The squared sum of the P and S waves is integrated over the KK mass. For the P wave, we assume the nonrelativistic Breit-Wigner model with the ϕ meson mass 1.019 GeV and width 4.26 MeV. For the $\mathcal{S}$-wave component, we assume a uniform distribution in the range $1.01 < M(KK) < 1.03$ GeV. In the case of the BDT selection, it is modified by a KK-mass dependent factor corresponding to the BDT selection efficiency. We constrain the oscillation frequency to $\Delta M_s = 17.77 \pm 0.12\,\text{ps}^{-1}$, as measured in ref. [14]. Table I lists all physics parameters used in the fit.

For the signal mass distribution we use a Gaussian function with a free mean value, width, and normalization. The function describing the signal rate in the 6D space is invariant under the combined transformation $\beta_s \to \pi/2 - \beta_s$, $\Delta\Gamma_s \to -\Delta\Gamma_s$, $\delta_\parallel \to 2\pi - \delta_\parallel$, $\delta_\perp \to \pi - \delta_\perp$, and $\delta_s \to \pi - \delta_s$. In addition, with a limited flavor-tagging power, there is an approximate symmetry around $\beta_s = 0$ for a given sign of $\Delta\Gamma_s$.

We correct the signal decay rate by a detector acceptance factor $\epsilon(\psi, \theta, \varphi)$ parametrized by coefficients of expansion in Legendre polynomials $P_k(\psi)$ and real harmonics $Y_{lm}(\theta, \varphi)$. The coefficients are obtained from Monte Carlo simulation.

6˙2. *Background model.* – The proper decay time distribution of the background is described by a sum of a prompt component, modeled as a Gaussian function centered at zero, and a non-prompt component. The non-prompt component is modeled as a superposition of one exponential decay for $t < 0$ and two exponential decays for $t > 0$, with free slopes and normalizations. The lifetime resolution is modeled by an exponential convoluted with a Gaussian function, with two separate parameters for prompt and non-prompt background.

The mass distributions of the two components of background are parametrized by low-order polynomials: a linear function for the prompt background and a quadratic function for the non-prompt background. The angular distribution of background is parametrized by Legendre and real harmonics expansion coefficients. A separate set of expansion coefficients c^k_{lm} and c^k_{lm}, with $k = 0$ or 2 and $l = 0, 1, 2$, is used for the prompt and non-prompt background. A preliminary fit is first performed with all 17×2 parameters allowed to vary. In subsequent fits those that converge at values within two standard deviations of zero are set to zero. All background parameters described above are varied simultaneously with physics parameters. In total, there are 36 parameters used in the fit.

6˙3. *Systematic uncertainties.* – There are several possible sources of systematic uncertainty in the measurements. These uncertainties are estimated for:

– *Flavor tagging*: The nominal calibration of the flavor tagging dilution is determined as a weighted average of four samples separated by the running period. As an alternative we alter the nominal parameters by their uncertainties.

– *Proper decay time resolution*: To assess the effect, we have used two alternative parameterizations obtained by random sampling of the resolution function.

– *Detector acceptance*: The effects of imperfect modeling of the detector acceptance and of the selection requirements are estimated by investigating the consistency of the fit results for the sample based on the BDT selection and on the Square-cuts selection.

– $M(KK)$ *resolution*: The limited $M(KK)$ resolution may affect the results of the analysis, especially the phases and the $\mathcal{S}$-wave fraction F_S, through the dependence of the $\mathcal{S}$-$\mathcal{P}$ interference term on the $\mathcal{P}$-wave mass model. We repeat the fits using this altered $\phi(1020)$ propagator as a measure of the sensitivity to the $M(KK)$ resolution.

The differences between the best-fit values and the alternative fit values provide a measure of systematic effects. For the best estimate of the CL ranges for all the measured physics quantities, we conduct Markov Chain Monte Carlo (MCMC).

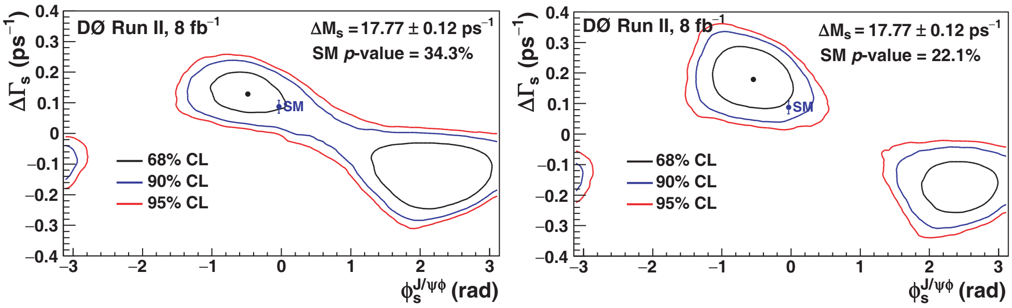

Fig. 1. – Two-dimensional 68%, 90% and 95% CL contour for BDT and square cuts selection. The standard model expectation is indicated as a point with an error.

7. – Confidence intervals

In addition to the free parameters determined in the fit, the model depends on a number of external constants whose inherent uncertainties are not taken into account in a given fit. Ideally, effects of uncertainties of external constants, such as time resolution parameters, flavor tagging dilution calibration, or detector acceptance, should be included in the model by introducing the appropriate parametrized probability density functions and allowing the parameters to vary. Such a procedure of proper integrating over the external parameter space would greatly increase the number of free parameters and would be prohibitive. Therefore, as a trade-off, we apply a random sampling of external parameter values within their uncertainties, we perform the analysis for thus created "alternative universes", and we average the results. To do the averaging in the multidimensional space, taking into account non-Gaussian parameter distributions and correlations, we use the MCMC technique.

While we do not use any external numerical constraints on the polarization amplitudes, we note that the best-fit values of their magnitudes and phases are consistent with those measured in the $U(3)$-flavor related decay $B_d^0 \to J/\psi K^*$ [5], up to the sign ambiguities. Reference [15] predicts that the phases of the polarization amplitudes in the two decay processes should agree within approximately 0.17 radians. For $\delta_\perp$, our measurement gives equivalent solutions near π and near zero, with only the former being in agreement with the value of 2.91 ± 0.06 measured for $B_d^0 \to J/\psi K^*$ by B factories. Therefore, in the following we limit the range of $\delta_\perp$ to $\cos\delta_\perp < 0$.

7˙1. *Results.* – The fit assigns 5598 ± 113 (5050 ± 105) events to the signal for the BDT (Square-cuts) sample.

Figure 1 shows 68%, 90% and 95% CL contours in the ($\phi_s^{J/\psi\phi}$,$\Delta\Gamma_s$) plane for the BDT-based and for the Square-cuts samples. The point estimates of physics parameters are obtained from one-dimensional projections. The minimal range containing 68% of the area of the probability density function defines the one standard deviation CL interval for each parameter, while the most probable value defines the central value.

The one-dimensional estimates of physics parameters for the BDT-cuts and Square-cuts sample are shown in table II.

To obtain the final CL ranges for physics parameters, we combine all eight MCMC chains, effectively averaging the probability density functions of the results of the fits to the BDT- and Square-cuts samples. Figure 2 shows 68%, 90% and 95% CL

TABLE II. – *The one-dimensional estimates of physics parameters for the BDT-cuts sample, Square-cuts sample and final result values with systematic error.*

Parameter	BDT-cut sample	Square-cut sample	Final result
$\overline{\tau}_s$ (ps)	$1.426^{+0.035}_{-0.032}$	$1.444^{+0.041}_{-0.033}$	$1.443^{+0.038}_{-0.035}$
$\Delta\Gamma_s$ (ps^{-1})	$0.129^{+0.076}_{-0.053}$	$0.179^{+0.059}_{-0.060}$	$0.163^{+0.065}_{-0.064}$
$\phi_s^{J/\psi\phi}$	$-0.49^{+0.48}_{-0.40}$	$-0.56^{+0.36}_{-0.32}$	$-0.55^{+0.38}_{-0.36}$
$\lvert A_0\rvert^2$	$0.552^{+0.016}_{-0.017}$	0.565 ± 0.017	$0.558^{+0.017}_{-0.019}$
$\lvert A_\parallel\rvert^2$	$0.219^{+0.020}_{-0.021}$	$0.249^{+0.021}_{-0.022}$	$0.231^{+0.024}_{-0.030}$
$\delta_\parallel$	3.15 ± 0.27	3.15 ± 0.19	3.15 ± 0.22
$\cos(\delta_\perp - \delta_s)$	-0.06 ± 0.24	$-0.20^{+0.26}_{-0.27}$	$-0.11^{+0.27}_{-0.25}$
F_S	0.146 ± 0.035	0.173 ± 0.036	0.173 ± 0.036

contours in the ($\phi_s^{J/\psi\phi}$,$\Delta\Gamma_s$) plane. The p-value for the SM point [16] $(\phi_s^{J/\psi\phi}, \Delta\Gamma_s) = (-0.038, 0.087\,\text{ps}^{-1})$ is 29.8%.

8. – Summary and discussion

We have presented a time-dependent angular analysis of the decay process $B_s^0 \to J/\psi\phi$. We measure B_s^0 mixing parameters, average lifetime, and decay amplitudes. In addition, we measure the amplitudes and phases of the polarization amplitudes. We also measure the level of the KK $\mathcal{S}$-wave contamination in the mass range 1.01–1.03 GeV, F_S. The final result values for the 68% CL intervals, including systematic uncertainties, with the oscillation frequency constrained to $\Delta M_s = 17.77 \pm 0.12\,\text{ps}^{-1}$, are shown in the last column of table II. The p-value for the SM point $(\phi_s^{J/\psi\phi}, \Delta\Gamma_s) = (-0.038, 0.087\,\text{ps}^{-1})$ is 29.8%.

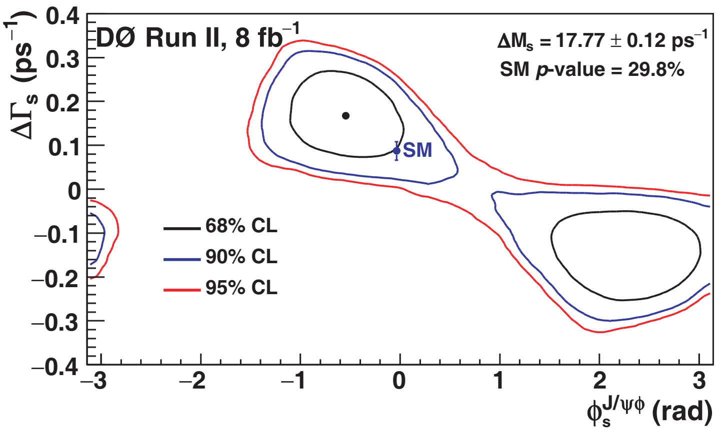

Fig. 2. – Two-dimensional 68%, 90% and 95% CL contours including systematic uncertainties. The standard model expectation is indicated as a point with an error.

* * *

We thank the staffs at Fermilab and collaborating institutions, and acknowledge support from the DOE and NSF (USA); CEA and CNRS/IN2P3 (France); FASI, Rosatom and RFBR (Russia); CNPq, FAPERJ, FAPESP and FUNDUNESP (Brazil); DAE and DST (India); Colciencias (Colombia); CONACyT (Mexico); KRF and KOSEF (Korea); CONICET and UBACyT (Argentina); FOM (The Netherlands); STFC and the Royal Society (United Kingdom); MSMT and GACR (Czech Republic); CRC Program and NSERC (Canada); BMBF and DFG (Germany); SFI (Ireland); The Swedish Research Council (Sweden); and CAS and CNSF (China).

REFERENCES

[1] Bona M. *et al.*, *JHEP*, **10** (2006) 081.
[2] Kobayashi M. and Maskawa T., *Prog. Theor. Phys.*, **49** (1973) 652.
[3] Bona M. *et al.*, *JHEP*, **10** (2006) 081.
[4] Abazov V. M. *et al.* (D0 Collaboration), *Nucl. Instrum. Methods Phys. Res. A*, **565** (2006) 463.
[5] Nakamura K. *et al.* (Particle Data Group), *J. Phys. G*, **37** (2010) 075021.
[6] Bengtsson H. U. and Sjöstrand T., *JHEP*, **05** (2006) 026.
[7] Lange D. J., *Nucl. Instrum. Methods A*, **462** (2001) 152.
[8] Brun R. and Carminati F., CERN Program Library Long Writeup No. W5013, 1993 (unpublished).
[9] `http://root.cern.ch`.
[10] Abazov V. M. *et al.* (D0 Collaboration), *Phys. Rev. Lett.*, **101** (2008) 241801.
[11] Abazov V. M. *et al.* (D0 Collaboration), *Phys. Rev. D*, **74** (2006) 112002.
[12] Abazov V. M. *et al.* (D0 Collaboration), *Phys. Rev. Lett.*, **97** (2006) 021802.
[13] Azfar F. *et al.*, *JHEP*, **11** (2010) 158.
[14] Abulencia A. *et al.* (CDF Collaboration), *Phys. Rev. Lett.*, **97** (2006) 242003.
[15] Gronau M. and Rosner J. L., *Phys. Lett. B*, **669** (2008) 321.
[16] Lenz A. and Nierste U., arXiv:1102.4274 [hep-ph].

IL NUOVO CIMENTO Vol. 35 C, N. 6 Novembre-Dicembre 2012
DOI 10.1393/ncc/i2012-11374-6

Colloquia: LaThuile12

The time-dependent CP violation in charm

G. Inguglia
Queen Mary, University of London - Mile End Road, E1 4NS, London, UK

ricevuto il 7 Settembre 2012

Summary. — A model which describes the time-dependent CP formalism in D^0 decays has recently been proposed. There it has been highlighted a possible measurement of the angle β_c, in the charm unitarity triangle, using the decays $D^0 \to K^+K^-$ and $D^0 \to \pi^+\pi^-$, and a measurement of the mixing phase ϕ_{MIX}. The same method can be used to measure the value of the parameter x, one of the two parameters defining charm mixing. We numerically evaluate the impact of a time-dependent analysis in terms of the possible outcomes from present and future experiments. We consider the scenarios of correlated D^0 mesons production at the center-of-mass energy of the $\Psi(3770)$ at Super$B$, uncorrelated production at the center-of-mass energy of the $\Upsilon(4S)$ at Super$B$ and Belle II, and LHCb. Recently a hint of direct CP violation in charm decays was reported by the LHCb Collaboration, we estimate the rate of time-dependent asymmetry that could be achieved using their available data, and we generalise the result for the full LHCb program. We conclude that LHCb is already able to perform a first measurement of $\beta_{c,eff}$, and slightly improve the present constraints on the parameters x and ϕ_{MIX}. A more precise determination of $\beta_{c,eff}$, ϕ_{MIX} and x will require a larger data sample, and most probably the cleaner environment of the new high-luminosities B-factories (both Super$B$ and Belle II) will be needed. We show that Super$B$ will be able to measure $\beta_{c,eff}$ and ϕ_{MIX} with a precision of 1.3° and improve the precision on x by a factor of two.

PACS 13.25.Hw – Decays of bottom mesons.
PACS 12.15.Hh – Determination of Cabibbo-Kobayashi & Maskawa (CKM) matrix elements.
PACS 11.30.Er – Charge conjugation, parity, time reversal, and other discrete symmetries.

1. – Introduction

Since the discovery in 1964 of CP violation in the kaon system [1], CP violation has been observed also in the B meson system [2,3]. In the charm sector, CP violation has long been expected to be too small to be observed at precision available until recently when, the LHCb Collaboration has reported a difference in direct CP asymmetries in $D^0 \to K^+K^-$ and $D^0 \to \pi^+\pi^-$ that is 3.5σ from the CP-conserving hypothesis [4]. In [5] the standard model (SM) description of these decays using the same CKM paradigm that provides a rather satisfactory description of such decays of B^0 mesons is considered. Since the LHCb result, a broader view of this paradigm that might accomodate the large asymmetry is examined in [6]. It is clear that, in order to understand the nature of CPV in D^0 decays, measurements of weak phases in these decays are essential. In [5], it is proposed that, as with B^0 decays, time-dependent CP asymmetries in D^0 decays may provide the most direct way to measure these phases. In this paper, we further examine the precision that might be anticipated in four experimental scenarios that are likely to be available over the coming decade to evaluate the rate of time-dependent CP asymmetries in $D^0 \to K^+K^-$ and $D^0 \to \pi^+\pi^-$ in the three proposed environments (Super$B$, LHCb, Belle II).

2. – Time-dependent *CP* violation in the charm sector

In the standard model (SM), CP violation is described in terms of the complex phase appearing in Cabibbo-Kobayashi-Maskawa (CKM) matrix [7,8]. The matrix is a unitary 3×3 matrix which provides a description of quark mixing in terms of the coupling strengths for up-to-down quark type transitions, and it may be written as

$$V_{CKM} = \begin{pmatrix} V_{ud} & V_{us} & V_{ub} \\ V_{cd} & V_{cs} & V_{cb} \\ V_{td} & V_{ts} & V_{tb} \end{pmatrix}. \tag{1}$$

Within this framework the probability to observe a transition between a quark q to a quark q' is proportional to $|V_{qq'}|^2$.

2·1. *Buras parametrisations of the CKM matrix.* – In ref. [5] the CKM matrix has been written using the "*Buras*" parametrisation [9]:

$$V_{CKM} = \begin{pmatrix} 1-\lambda^2/2-\lambda^4/8 & \lambda & A\lambda^3(\bar\rho-i\bar\eta)+A\lambda^5(\bar\rho-i\bar\eta)/2 \\ -\lambda+A^2\lambda^5[1-2(\bar\rho+i\bar\eta)]/2 & 1-\lambda^2/2-\lambda^4(1+4A^2)/8 & A\lambda^2 \\ A\lambda^3[1-(\bar\rho+i\bar\eta)] & -A\lambda^2+A\lambda^4[1-2(\bar\rho+i\bar\eta)]/2 & 1-A^2\lambda^4/2 \end{pmatrix} +\mathcal{O}(\lambda^6). \tag{2}$$

We adopt the convention of writing the CKM matrix in terms of $\overline{\rho}$ and $\overline{\eta}$ because these represent the coordinates of the apex of the well known bd unitarity triangle. Since unitarity triangles are mathematically exact, it is very important to measure their angles and sides to verify unitarity. One of the six unitarity relationships of the CKM matrix may be written as

$$V^*_{ud}V_{cd} + V^*_{us}V_{cs} + V^*_{ub}V_{cb} = 0, \tag{3}$$

which represents the cu triangle that we will call the *charm* unitarity triangle or simply *charm* triangle. The internal angles of this triangle are given by

$$\alpha_c = \arg\left[-V^*_{ub}V_{cb}/V^*_{us}V_{cs}\right], \tag{4}$$

$$\beta_c = \arg\left[-V^*_{ud}V_{cd}/V^*_{us}V_{cs}\right], \tag{5}$$

$$\gamma_c = \arg\left[-V^*_{ub}V_{cb}/V^*_{ud}V_{cd}\right]. \tag{6}$$

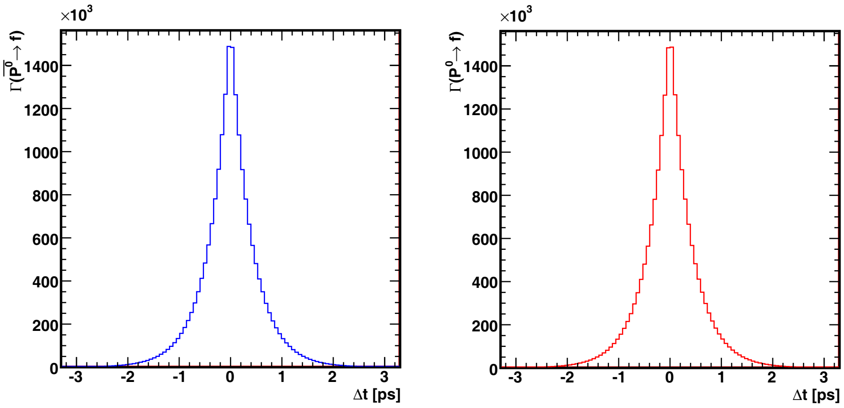

Fig. 1. – Generated distributions according to our formulas for $\overline{D^0} \to f$(left) and for $D^0 \to f$(right) produced at the center-of-mass energy of the $\Psi(3770)$.

In ref. [5] we proposed the measurement of $\beta_{c,eff}$ using time-dependent CP asymmetries in charm decays and using the results of Global CKM fits, predicted that

$$\beta_c = (0.0350 \pm 0.0001)^\circ. \tag{7}$$

On comparing eq. (5) with eq. (2), one can see that $V_{cd} = V_{cd}e^{i(\beta_c - \pi)}$ in this convention.

2˙2. *Time-dependent formalism.* – We consider two different cases of D^0 meson production: uncorrelated and correlated D^0 production. Uncorrelated D^0's are produced from the decays of B mesons in electron-positron colliders when particles are collided at a center-of-mass energy corresponding to the $\Upsilon(4S)$ resonance, from $c\bar{c}$ continuum, or in hadrons collider. The correlated D^0 mesons are produced in an electron-positron machine running at a center-of-mass energy corresponding to the $\Psi(3770)$ resonance. The time evolution for both situations, shown in fig. 1, is given by [5]

uncorrelated case

$$\begin{aligned}\Gamma_\pm \propto e^{-\Gamma_1 t}\Bigg[&\frac{(1+e^{\Delta\Gamma t})}{2} + \frac{\mathrm{Re}(\lambda_f)}{1+|\lambda_f|^2}\left(1-e^{\Delta\Gamma t}\right)\\ &\pm e^{\Delta\Gamma t/2}\left(\frac{1-|\lambda_f|^2}{1+|\lambda_f|^2}\cos\Delta M t - \frac{2\mathrm{Im}(\lambda_f)}{1+|\lambda_f|^2}\sin\Delta M t\right)\Bigg],\end{aligned} \tag{8}$$

correlated case

$$\begin{aligned}\Gamma_\pm \propto e^{-\Gamma_1|\Delta t|}\Bigg[&\frac{h_+}{2} + \frac{\mathrm{Re}(\lambda_f)}{1+|\lambda_f|^2}h_-\\ &\pm e^{\Delta\Gamma\Delta t/2}\left(\frac{1-|\lambda_f|^2}{1+|\lambda_f|^2}\cos\Delta M\Delta t - \frac{2\mathrm{Im}(\lambda_f)}{1+|\lambda_f|^2}\sin\Delta M\Delta t\right)\Bigg],\end{aligned} \tag{9}$$

where Γ_+ refers to $D^0(q_c = +2/3)$ decays and Γ_- to $\overline{D^0}(q_c = -2/3)$ decays, $h_\pm = 1 \pm e^{\Delta\Gamma\Delta t}$ and $\lambda_f = \frac{q}{p}\frac{\overline{A}}{A}$. Here q and p are the parameters defining the mixing and A ($\overline{A}$)

is the amplitude for the D ($\overline{D}$) decay to a final state f. If $|A|^2 \neq |\overline{A}|^2$ there is direct CP violation (in the decay) and $|q/p| \neq 1$ would signify CP violation in mixing. The study of λ_f (which should not be confused with the term λ appearing in the CKM matrix) is able to probe the combination of CP violation due to mixing and decay, and this form of CP violation is referred to as CP violation in the interference between mixing and decay. Considering eqs. (8) and (9) the time-dependent asymmetries associated with the time evolution of the D^0 mesons can be written in terms of the physical decay rate including the mistag probability, $\omega(\bar{\omega})$, for incorrect tagging of the D^0 ($\overline{D}^0$) flavour as follows:

$$\Gamma^{Phys}(t) = (1-\omega)\Gamma_+(t) + \overline{\omega}\,\Gamma_-(t), \tag{10}$$

$$\overline{\Gamma}^{Phys}(t) = \omega\Gamma_+(t) + (1-\overline{\omega})\Gamma_-(t), \tag{11}$$

where $\Gamma_+(t)$ and $\Gamma_-(t)$ are from eqs. (8) and (9) and ω ($\overline{\omega}$) represents the mistag probability for the particle (antiparticle) apparent decay rates for D^0 and $\overline{D}^0$, respectively. Hence for uncorrelated mesons the time dependent CP asymmetry accounting for mistag probability is

$$\begin{aligned} \mathcal{A}^{Phys}(t) &= \frac{\overline{\Gamma}^{Phys}(t) - \Gamma^{Phys}(t)}{\overline{\Gamma}^{Phys}(t) + \Gamma^{Phys}(t)} \\ &= \Delta\omega + \frac{(D-\Delta\omega)e^{\Delta\Gamma t/2}[(|\lambda_f|^2-1)\cos\Delta M t + 2\mathrm{Im}\lambda_f \sin\Delta M t]}{h_+(1+|\lambda_f|)^2/2 + \mathrm{Re}(\lambda_f)h_-}, \end{aligned} \tag{12}$$

where $\Delta\omega = \omega - \overline{\omega}$ and $D = 1 - 2\omega$.

Similarly the asymmetry for correlated mesons is

$$\begin{aligned} \mathcal{A}^{Phys}(\Delta t) &= \frac{\overline{\Gamma}^{Phys}(\Delta t) - \Gamma^{Phys}(\Delta t)}{\overline{\Gamma}^{Phys}(\Delta t) + \Gamma^{Phys}(\Delta t)} \\ &= -\Delta\omega + \frac{(D+\Delta\omega)e^{\Delta\Gamma\Delta t/2}[(|\lambda_f|^2-1)\cos\Delta M\Delta t + 2\mathrm{Im}\lambda_f \sin\Delta M\Delta t]}{h_+(1+|\lambda_f|)^2/2 + \mathrm{Re}(\lambda_f)h_-}. \end{aligned} \tag{13}$$

The above equations may be written in terms of x and y allowing for the measurement of the mixing phase. We report here the time-dependent asymmetry equation for correlated mesons (similar results may be obtained in the uncorrelated case):

$$\mathcal{A}^{Phys}_{x,y}(\Delta t) = -\Delta\omega + \frac{(D+\Delta\omega)e^{y\Gamma\Delta t}[(|\lambda_f|^2-1)\cos x\Gamma\Delta t + 2\mathrm{Im}\lambda_f \sin x\Gamma\Delta t]}{h_+(1+|\lambda_f|)^2/2 + \mathrm{Re}(\lambda_f)h_-}. \tag{14}$$

3. – MC test of time-dependent numerical analysis

One of the issues raised in [5] is the possibility to use different decay channels of the D^0 mesons to constrain the value of the angle β_c of the *charm* triangle. The decay $D^0 \to K^+K^-$ will be used to measure the mixing phase, the decay $D^0 \to \pi^+\pi^-$ will be used to measure $\phi_{MIX} - 2\beta_c$ and the difference between the two channels will provide a first measurement of the angle β_c. In this framework, long distance contributions to decay are not considered. The latter together with the different contribution to decay $D^0 \to \pi^+\pi^-$ from *penguin* topologies will introduce theoretical uncertainties, and for

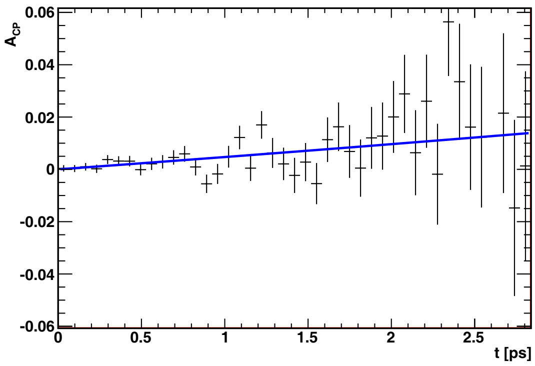

Fig. 2. – The time-dependent CP asymmetry expected for $D^0 \to \pi^+\pi^-$ decays in a $75\,\mathrm{ab}^{-1}$ sample of data at the $\Upsilon(4S)$.

this reason we refer to the angle β_c as $\beta_{c,eff}$ where *effective* indicates that there are theoretical uncertainties that need to be evaluated. To evaluate the asymmetry, and estimate the precision on $\beta_{c,eff}$ that one might achieve in the different experimental environments described in the previous section, we generate a set of one hundred Monte Carlo data samples. Each one based on the expected number of tagged D^0 decays in the corresponding experimental setup, and we generate data according to the distributions given in eqs. (8) and (9), where the parameters involved are evaluated as in ref. [10]. We evaluate the asymmetry given in eqs. (12) and (13) including the expected mistag probabilities, and perform a binned fit to the simulated data. The distributions that we are considering here have been expressed as functions of $|\lambda_f|$ and $\arg(\lambda_f) \equiv \phi = \phi_{MIX} - 2\phi_{CP}$, and the fit is performed keeping $|\lambda_f| = 1$ and allowing $\arg(\lambda_f)$ to vary. The same results are obtained when also $|\lambda_f|$ is also allowed to vary in the fit. It is important to mention that a measurement of $\lambda_f \neq 1$ in an experiment would be a signature of direct CP violation [5].

3˙1. *SuperB at the* $\Upsilon(4S)$. – The Super$B$ Collaboration is expected to start taking data in 2017 [11-14], and the integrated luminosity which will be achieved with the full program is expected to be $75\,\mathrm{ab}^{-1}$. With this luminosity one would expect to reconstruct 6.6×10^6 tagged $D^0 \to \pi^+\pi^-$ events in a data sample of $75\,\mathrm{ab}^{-1}$ with a purity of 98% [5]. The results of the numerical analysis are shown in fig. 2.

The asymmetry parameters determined here have a precision of $\sigma_{arg(\lambda_{\pi\pi})} = \sigma_{\phi_{\pi\pi}} = 2.2°$. The same procedure when applied to the $D^0 \to K^+K^-$ channel to measure $\sigma_{arg(\lambda_{KK})} = \sigma_{\phi_{KK}}$, for which one would expect to reconstruct 1.8×10^7 events, leads to precision of $\sigma_{\phi_{KK}} = 1.6°$. When the results from $D^0 \to K^+K^-$ and $D^0 \to \pi^+\pi^-$ are combined one obtains a precision in $\beta_{c,eff}$ of $\sigma_{\beta_{c,eff}} = 1.4°$.

3˙2. *SuperB at the* $\Psi(3770)$. – The Super$B$ Collaboration is planning to have a dedicated run at the center-of-mass energy of the $\Psi(3770)$ resonance, to collect an integrated luminosity of $1.0\,\mathrm{ab}^{-1}$. With this luminosity one would expect to record 979000 $D^0 \to \pi^+\pi^-$ reconstructed events, when the full set of semi-leptonic decays $K^{(*)}\ell\nu_\ell$ $\ell = e,\mu$ is used to tag the flavor of D^0 mesons (with negligible mistag probability). The results of the numerical analysis are shown in fig. 3.

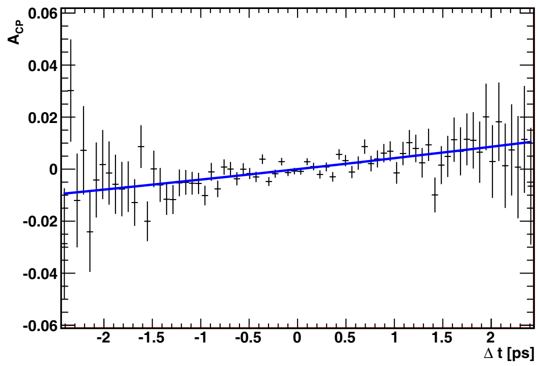

Fig. 3. – The time-dependent CP asymmetry expected for $D^0 \to \pi^+\pi^-$ decays in $1\,\mathrm{ab}^{-1}$ sample of data at the $\Psi(3770)$.

The phase $\phi_{\pi\pi}$ could be measured with a precision of $\sigma_{\phi_{\pi\pi}} = 5.7°$. One may also consider using hadronically tagged events, for example, $D^0 \to K^-X$ (K^+X), where X is anything, which corresponds to 54% (3%) of all D^0 meson decays from which one would expect $\omega \simeq 0.03$, and that the asymmetry in particle identification of K^+ and K^- in the detector will naturally lead to a small, but non-zero value of $\Delta\omega$. We expect that there would be approximately 4.8 million kaon tagged $D^0 \to \pi^+\pi^-$ events in $1.0\,\mathrm{ab}^{-1}$ at charm threshold. Using these data alone, one would be able to measure $\phi_{\pi\pi}$ to a precision of 2.7°. Hence if one combines the results from semi-leptonic and kaon tagged events, a precision of $\sigma_{\phi_{\pi\pi}} \sim 2.4°$ is achievable.

3˙3. *LHCb*. – Another possible scenario is that of measuring time-dependent asymmetries from uncorrelated D mesons in a hadronic environment, in particular the LHCb experiment. Here dilution and background effects will be larger than those at an e^+e^- machine, but the data are already available and it would be interesting to perform the time-dependent analysis, especially after the recent results on time integrated CP violation in ref. [4]. As already mentioned a measurement of $|\lambda_f| \neq 1$ will signify direct CP violation. Given that the measurement of λ_f is likely expected to be dominated by uncertainties, especially in ω and $\Delta\omega$, it is not clear what the ultimate precision obtained from LHCb will be. The best way to ascertain this would be to perform the measurement on the existing data set. We have estimated that LHCb will collect 4.9×10^6 D^* tagged $D^0 \to \pi^+\pi^-$ decays in $5\,\mathrm{fb}^{-1}$ of data, based on the $0.62\,\mathrm{fb}^{-1}$ of data shown in [4], and we consider also the outcome of a measurement for $1.1\,\mathrm{fb}^{-1}$ (equivalent to 0.7×10^6 D^* tagged $D^0 \to \pi^+\pi^-$ decays) already available after the 2011 LHC run. In [5] we estimate a purity of $\simeq 90\%$ and $\omega \simeq 6\%$ which results in the asymmetry obtained in fig. 4 for $5\,\mathrm{fb}^{-1}$ of data.

This fit is translated into a potential measurement of the phase $\phi_{\pi\pi}$ with a precision of 3.0°. With $1.1\,\mathrm{fb}^{-1}$ of data we estimate that LHCb may be able to reach a precision of 8° on $\phi_{\pi\pi}$.

3˙4. *Belle II*. – The last scenario considered here is that of Belle II with $50\,\mathrm{ab}^{-1}$ of data collected at the center-of-mass energy of the $\Upsilon(4S)$ [15]. We have considered the same efficiency and mistag probability as for Super$B$ and we expect that 4.4×10^6 D^* tagged $D^0 \to \pi^+\pi^-$ will be collected. The resulting asymmetry is shown in fig. 5. The precision on $\phi_{\pi\pi}$ obtained for this scenario is estimated to be 2.8°.

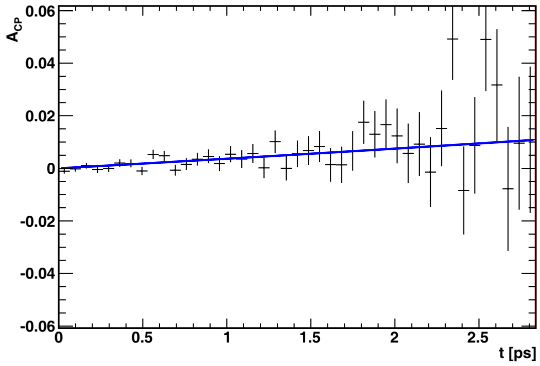

Fig. 4. – The time-dependent CP asymmetry expected for $D^0 \to \pi^+\pi^-$ decays in a $5\,\mathrm{fb}^{-1}$ sample of data at LCHb.

4. – Time-dependent sensitivity studies

4$\cdot$1. *Sensitivity to x.* – We consider the same data sample discussed in the previous sections for $D^0 \to \pi^+\pi^-$ and $D^0 \to K^+K^-$. While we find that results from the time-dependent analysis are not sensitive to the parameter y, and that with $1.0\,\mathrm{ab}^{-1}$ of data collected at charm threshold at Super$B$ it will be possible to improve the currently known precision on x by a factor of two with respect to the most recent HFAG values [16]. The precision that could be reached is shown in table I.

4$\cdot$2. *Sensitivity to $\beta_{c,eff}$, ϕ_{MIX} and ϕ_{CP}.* – We show in table II a summary of the possible sensitivities that the different experiments could achieve when measuring the mixing and the weak phase.

At first order the decay $D^0 \to K^+K^-$ measure the mixing phase, therefore one can consider $\phi_{KK} = \arg(\lambda_{KK}) = \phi_{MIX}$ and use the time dependent analysis to measure it to a precision of $\approx 1.4°$–$1.6°$.

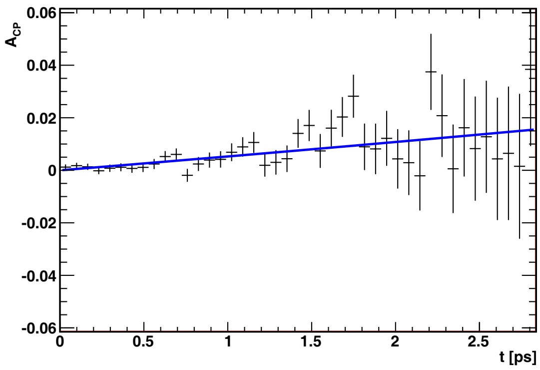

Fig. 5. – The time-dependent CP asymmetry expected for $D^0 \to \pi^+\pi^-$ decays in a $50\,\mathrm{ab}^{-1}$ sample of data at the $\Upsilon(4S)$ at Belle II.

TABLE I. – *Estimates of the sensitivity on x for all the experimental scenarios and their projected luminosities for the decays $D^0 \to \pi^+\pi^-$ and $D^0 \to K^+K^-$ and $\phi = \phi_{MIX} - 2\beta_{c,eff}$.*

Experiment/HFAG	$\sigma_x(\phi = \pm 10°)$	$\sigma_x(\phi = \pm 20°)$
Super$B$ [$\Upsilon(4S)$]		
$D^0 \to \pi^+\pi^-$	0.12%	0.06%
$D^0 \to K^+K^-$	0.08%	0.04%
Super$B$ [$\Psi(3770)$]		
$D^0 \to \pi^+\pi^-(SL)$	0.30%	0.15%
$D^0 \to \pi^+\pi^-(SL+K)$	0.13%	0.06%
$D^0 \to K^+K^-(SL)$	0.19%	0.10%
$D^0 \to K^+K^-(SL+K)$	0.08%	0.04%
LHCb		
$D^0 \to \pi^+\pi^-$ ($1.1\,\mathrm{fb}^{-1}$)	0.40%	0.20%
$D^0 \to K^+K^-$ ($1.1\,\mathrm{fb}^{-1}$)	0.22%	0.11%
$D^0 \to \pi^+\pi^-$ ($5.0\,\mathrm{fb}^{-1}$)	0.15%	0.08%
$D^0 \to K^+K^-$ ($5.0\,\mathrm{fb}^{-1}$)	0.09%	0.04%
Belle II		
$D^0 \to \pi^+\pi^-$	0.14%	0.07%
$D^0 \to K^+K^-$	0.10%	0.04%
HFAG	0.20%	

4·3. *Systematic uncertainties*. – The knowledge of the parameters x and y which define the mixing is limited by their relative uncertainties. Since our analysis is not sensitive to the parameter y, we considered the most recent results from the HFAG [16] and we evaluated the effect of varying the parameter $\Delta\Gamma = 2y\Gamma$ considering plus-and-minus one standard deviation. This is the systematic uncertainty due to the limited precision in y.

TABLE II. – *Summary of expected uncertainties from $1\,\mathrm{ab}^{-1}$ of data at charm threshold, $75\,\mathrm{ab}^{-1}$ of data at the $\Upsilon(4S)$, $5\,\mathrm{fb}^{-1}$ of data from LHCb, and $50\,\mathrm{ab}^{-1}$ of data at the $\Upsilon(4S)$ at Belle II for $D^0 \to \pi^+\pi^-$ decays. The column marked SL corresponds to semi-leptonic tagged events, and the column SL+K corresponds to semi-leptonic and kaon tagged events at charm threshold. The last row shows the precision in $\beta_{c,eff}$ expected from a simultaneous fit to $\pi\pi$ and KK where we assume that, for KK, the decay is dominated by a tree amplitude.*

Parameter		Super$B$		LHCb	Belle II
	$\Psi(3770)$ SL	$\Psi(3770)$ SL+K	$\Upsilon(4S)$ $\pi_s^\pm$	$\pi_s^\pm$	$\pi_s^\pm$
$\sigma_{\phi_{\pi\pi}} = \sigma_{arg(\lambda_{\pi\pi})}$	5.7°	2.4°	2.2°	3.0°	2.8°
$\sigma_{\phi_{KK}} = \sigma_{arg(\lambda_{KK})}$	3.5°	1.4°	1.6°	1.8°	1.8°
$\sigma_{\beta_{c,eff}}$	3.3°	1.4°	1.4°	1.9°	1.7°

TABLE III. – *Summary of expected systematic uncertainties due to the limited knowledge of the parameter y from* $1\,\mathrm{ab}^{-1}$ *of data at charm threshold and* $75\,\mathrm{ab}^{-1}$ *of data at the* $\Upsilon(4S)$. *The column marked SL corresponds to semi-leptonic tagged events, and the column SL+K corresponds to semi-leptonic and kaon tagged events at charm threshold while* $\pi_s^{\pm}$ *refers to the slow pion tag at the* $\Upsilon(4S)$.

Parameter	$\Psi(3770)$ SL	$\Psi(3770)$ SL+K	$\Upsilon(4S)$ $\pi_s^{\pm}$
$\sigma_{\phi_{\pi\pi}}$(sys.)	0.5°	0.2°	0.05°
$\sigma_{\phi_{KK}}$(sys.)	0.2°	0.1°	0.02°
$\sigma_{\beta_{c,eff}}$(sys.)	0.27°	0.11°	0.03°

The value of the uncertainty in the parameter y is 0.013% and it is given in [16]. The results are shown in table III.

4˙4. *Combined results for SuperB.* – We evaluated the combination of the results obtained for the different centre-of-mass energy at Super$B$. The final results are made on the assumption that $\phi = \phi_{MIX} - 2\beta_c = \pm 10°$ and they are shown in table IV.

5. – Conclusions

This paper elucidates the time-dependent analysis of the D^0 mesons discussed in ref. [5]. We concentrated on the possible measurement of the $\beta_{c,eff}$ angle of the charm unitarity triangle, on the mixing phase ϕ_{MIX} and on the mixing parameters. We estimate our results and compare them for the experimental environments that we think could and should perform this analysis: Super$B$, LHCb and Belle II. We found that Super$B$ may perform better this analysis, but time is required before the collaboration will start data taking. LHCb will have to control the background levels to perform this measurement resulting then in a challenging analysis. However as referred to in the article the LHCb Collaboration has already available an amount of data to analyse. This same amount of data has already shown a first hint of direct CP violation in charm, we think it would be worth going through the time-dependent formalism. The Belle II Collaboration will start data taking in few years, and the background-clean environment will allow to perform a time-dependent analysis and an evaluation of the mixing phase and of the $\beta_{c,eff}$ at high precision.

TABLE IV. – *Combined sensitivities at SuperB.*

Parameter	Statistical sensitivity	Systematic sensitivity
σ_x $(D^0 \to \pi^+\pi^-)$	0.09%	–
σ_x $(D^0 \to K^+K^-)$	0.05%	–
$\sigma_{\phi_{\pi\pi}}$	1.62°	0.14°
$\sigma_{\phi_{KK}}$	1.05°	0.02°
$\sigma_{\beta_{c,eff}}$	0.92°	0.03°

* * *

This work has been supported by Queen Mary, University of London.

REFERENCES

[1] Christenson J. H. *et al.*, *Phys. Rev. Lett.*, **13** (1964) 138.
[2] Aubert B. *et al.* (BABAR Collaboration), *Phys. Rev. Lett.*, **93** (2004) 131801.
[3] Chao Y. *et al.* (Belle Collaboration), *Phys. Rev. Lett.*, **93** (2004) 191802.
[4] LHCb Collaboration, arXiv:1112.0938v1.
[5] Bevan A., Inguglia G. and Meadows B., *Phys. Rev. D*, **84** (2011) 114009, arXiv:1106.5075v2.
[6] Brod J., Kagan A. L. and Zupan J., arXiv:1111.5000 (2011).
[7] Cabibbo N., *Phys. Rev. Lett.*, **10** (1963) 531.
[8] Kobayashi M. and Maskawa T., *Prog. Theor. Phys.*, **49** (1973) 652.
[9] Buras A. J., Lautenbacher M. E. and Ostermaier G., *Phys. Rev. D*, **50** (1994) 3433, hep-ph/9403384.
[10] Nakamura K. *et al.*, *J. Phys.*, **37** (2010) 075021.
[11] O'Leary B. *et al.*, (SuperB) 1008.1541, (2010).
[12] Grauges E. *et al.*, (SuperB) 1007.4241, (2010).
[13] Biagini M. E. *et al.*, (SuperB) 1009.6178, (2010).
[14] Meadows B. *et al.*, (SuperB) 1109.5028, (2011).
[15] Belle II Collaboration, 1011.0352 (2012).
[16] HFAG, 1010.1589 (2011).

IL NUOVO CIMENTO Vol. 35 C, N. 6 Novembre-Dicembre 2012
DOI 10.1393/ncc/i2012-11381-7

Colloquia: LaThuile12

BSM Higgs searches in tau final states at DØ

L. Suter
The University of Manchester - Manchester, UK

ricevuto il 7 Settembre 2012

Summary. — We present a search for beyond the standard model (BSM) Higgs bosons in τ lepton final states at DØ. Data were collected by the DØ detector in proton-antiproton collisions at a center-of-mass energy of $\sqrt{s} = 1.96\,\text{TeV}$ during Run II at the Tevatron with up to $7.0\,\text{fb}^{-1}$ of integrated luminosity. The results are used to set 95% CL limits on the pair production cross section on these BSM Higgs bosons.

PACS 14.80.Fd – Other charged Higgs bosons.
PACS 13.85.Rm – Limits on production of particles.

1. – Introduction

Beyond the standard model (BSM) Higgs boson searches in τ final states are of specific interest as several BSM theories, such as Supersymmetry, predict enhanced couplings to τ leptons. Supersymmetry (SUSY) is an extension to the standard model (SM) that predicts an additional symmetry between bosons and fermions. SUSY has several advantages over the SM, such as the introduction of a dark matter candidate, a solution to the hierarchy problem and a potential for GUT scale unification. The minimal supersymmetric standard model, MSSM, [1] is the simplest version of a SUSY theory. It predicts, after symmetry breaking, five Higgs bosons of which three are neutral and two charged, denoted by h, H, A, H^+ and H^-. In the MSSM the coupling of the neutral Higgs to down-type quarks and leptons is enhanced by a factor of $\tan\beta$ and the corresponding coupling to the up-type quarks and leptons is suppressed. This means that decay modes to bottom quarks and tau leptons are dominant with a predicted decay rate of around 90% to bottom quarks and 10% to tau leptons. At a hadron collider, the bottom quark channel is background dominated from multijet production.

In other BSM theories, Higgs bosons with higher multiplicities of charge can be created. In Higgs triplet models, for example, Higgs bosons with a double charge, $H^{\pm\pm}$, can be produced. For these doubly-charged Higgs bosons various models predict the decay of the $H^{\pm\pm}$ to τ leptons to be of specific importance. The 3-3-1 model of ref. [2] predicts that the decays $H^{\pm\pm} \to \tau^\pm\tau^\pm$ are dominant. Assuming the normal hierarchy of neutrino masses in a seesaw neutrino mass mechanism leads to approximately equal branching fractions for $H^{\pm\pm}$ boson decays to $\tau\tau$, $\mu\tau$, and $\mu\mu$, if the mass of the lightest neutrino is less than 10 meV [3].

Left-right symmetric models can be considered to be a general Higgs triplet model. These predict both right-handed ($H_R^{\pm\pm}$) and left-handed states ($H_L^{\pm\pm}$). These are characterized through their coupling to right and left-handed fermions, respectively. The cross section for production of right-handed $H_R^{++}H_R^{--}$ pairs is about a factor of two smaller than for $H_L^{++}H_L^{--}$ because of the different coupling to the Z boson [4]. The mass limits for $H_R^{\pm\pm}$ bosons therefore tend to be weaker than for $H_L^{\pm\pm}$ bosons.

In this paper I summarize the first search for $H^{\pm\pm} \to \tau^\pm\tau^\pm$ decays at a hadron collider. This analysis is based on data collected with the DØ detector at the Fermilab Tevatron Collider which corresponds to an integrated luminosity of up to 7.0 fb^{-1} [5]. The decay of the $H^{\pm\pm}$ into tau leptons and muons was studied. Limits were set for left-handed and right-handed Higgs for three model independent cases, when $\mathcal{B}(H_L^{\pm\pm} \to \tau^\pm\tau^\pm) = 1$, $\mathcal{B}(H_L^{\pm\pm} \to \mu^\pm\tau^\pm) = 1$ and when the $\mathcal{B}(H_L^{\pm\pm} \to \tau^\pm\tau^\pm) + \mathcal{B}(H_L^{\pm\pm} \to \mu^\pm\tau^\pm) = 1$. Limits were in addition set for a left-handed Higgs for one model dependent case, with equal branching ratios to $\tau\tau$, $\mu\mu$ and $\tau\mu$ states as predicted by [3].

2. – The doubly charged Higgs

The analysis summarized here assumes that $H^{\pm\pm}$ Higgs bosons could be pair-produced through the mechanism $q\bar{q} \to Z/\gamma^* \to H^{++}H^{--} \to \ell^+\ell'^+\ell^-\ell'^-$ ($\ell, \ell' = e, \mu, \tau$), where the $H^{\pm\pm}$ decays to τ and μ leptons. Single production of $H^{\pm\pm}$ bosons through W exchange, leading to $H^{\pm\pm}H^{\mp}$ final states, is not considered in the analysis presented here to reduce the model dependency of the results [6]. The decay of $H^{\pm\pm}$ into electrons is also not considered [5]. This analysis also considers decays to mixed flavor lepton pairs, since all $H^{\pm\pm}$ decays violate lepton flavor number conservation.

The $H^{\pm\pm}$ bosons have been searched for previously at the LEP e^+e^- Collider at CERN [7] and at the HERA ep Collider at DESY [8]. Limits were set on the mass of the $H^{\pm\pm}$ boson between 95–100 GeV, for τ leptons, muons and electrons. Single $H^{\pm\pm}$ production was studied by the OPAL and H1 Collaborations in the processes $e^+e^- \to e^\mp e^\mp H^{\pm\pm}$ [9] and $e^\pm p \to \ell^\mp H^{\pm\pm} p$ [8]. In addition, OPAL also studied Bhabha scattering, $e^+e^- \to e^+e^-$ [9] which constrains the $H^{\pm\pm}$ boson's Yukawa couplings h_{ee} to electrons.

The DØ and CDF Collaborations at the Tevatron Collider set limits on the mass of the $H^{\pm\pm}$ in the range $M(H_L^{\pm\pm}) > 112$–150 GeV, assuming 100% decays into $\mu\mu$, ee, $e\tau$, and $\mu\tau$ final states [10-13].

3. – The DØ detector

The DØ detector [14] is a general purpose detector containing tracking detectors, calorimeters and a muon spectrometer. The tracking detector consists of a silicon microstrip detector and a scintillating fiber tracker which are used to reconstruct charged particle tracks within a 2 T solenoid. The calorimeter is uranium and liquid-argon based and used to measure particle energies. The selected events are required to pass triggers that select at least one muon candidate, which are identified by requiring both tracks in the central tracker and hits in the muon spectrometer.

All background and signal processes are simulated using Monte Carlo (MC) event generators, except the multijet background, which is determined from data. The W+jet, $Z/\gamma^* \rightarrow \ell^+\ell^-$, and $t\bar{t}$ processes are generated using ALPGEN [15] with showering and hadronization provided by PYTHIA [16]. Diboson production (WW, WZ, and ZZ) and signal events are simulated using PYTHIA. The τ lepton decays are simulated with TAUOLA [17], which includes a full treatment of the tau polarization. The signal and diboson processes are normalized to next-to-leading order (NLO) quantum chromodynamics calculations of their cross sections. Next-to-NLO calculations are used for all other processes.

The generated MC samples are processed through a GEANT [18] simulation of the detector and are overlaid with data from random beam crossings which account for the detector noise and additional $p\bar{p}$ interactions in the analyzed data. Efficiency corrections are applied to the simulated distributions, for the trigger efficiency in data as function of the instantaneous luminosity. They are also applied for the differences between data and simulation in the reconstruction efficiencies and in the distribution of the longitudinal coordinate of the interaction point along the beam direction.

At DØ tau leptons are categorized into three types depending on their decays and hence their signature in the detector. Type-1 tau lepton candidates consist of a calorimeter cluster, with one associated track and no subcluster in the EM section of the calorimeter. This signature corresponds mainly to $\tau^\pm \rightarrow \pi^\pm\nu$ decays. For type-2 tau lepton candidates, an energy deposit in the EM calorimeter is required in addition to the type-1 signature, as expected for $\tau^\pm \rightarrow \pi^\pm\pi^0\nu$ decays. For type-3 tau lepton candidates, an energy deposit in the EM calorimeter and the more than one reconstructed track is required, in addition to the type-2 requirements. This corresponds mainly to the decays $\tau^\pm \rightarrow \pi^\pm\pi^\pm\pi^\mp(\pi^0)\nu$ (3-prong).

A neural network, with an output variable NN_τ designed to discriminate τ_h from jets, is trained for each tau type. The input variables are based on jet isolation variables and on the spatial distribution of showers. A requirement of $NN_\tau > 0.75$ [19] for all tau types greatly reduces the jet background significantly [5].

4. – Event selection

The $H^{\pm\pm}$ analysis [5] requires events with at least one isolated muon and at least two τ_h candidates, where τ_h indicates a hadronically decaying tau lepton. The τ_h are restricted to type-1 or type-2 to reduce the contamination from jets misidentified as hadronically decaying tau leptons.

Each event must have a reconstructed $p\bar{p}$ interaction vertex with a longitudinal component located within 60 cm of the nominal center of the detector. The longitudinal coordinate $z_{\rm dca}$ of the distance of closest approach for each track is measured with respect to the nominal center of the detector. The differences between $z_{\rm dca}$ of the highest-p_T muon and the two highest-p_T τ_h (labeled τ_1 and τ_2), must be less than 2 cm. The pseudorapidity(1) of the selected muons, τ_1, and τ_2 must be $|\eta^\mu| < 1.6$ and $|\eta^{\tau_{1,2}}| < 1.5$, respectively, and for additional τ_h candidates we require $|\eta^\tau| < 2$. The transverse momenta must be $p_T^\mu > 15$ GeV and $p_T^{\tau_{1,2}} > 12.5$ GeV. All selected τ_h candidates and muons are required to be separated by $\Delta\mathcal{R}_{\mu\tau} > 0.5$, where $\Delta\mathcal{R} = \sqrt{(\Delta\phi)^2 + (\Delta\eta)^2}$ and ϕ is the

(1) The pseudorapidity is defined as $\eta = -\ln[\tan(\theta/2)]$, where θ is the polar angle with respect to the proton beam direction.

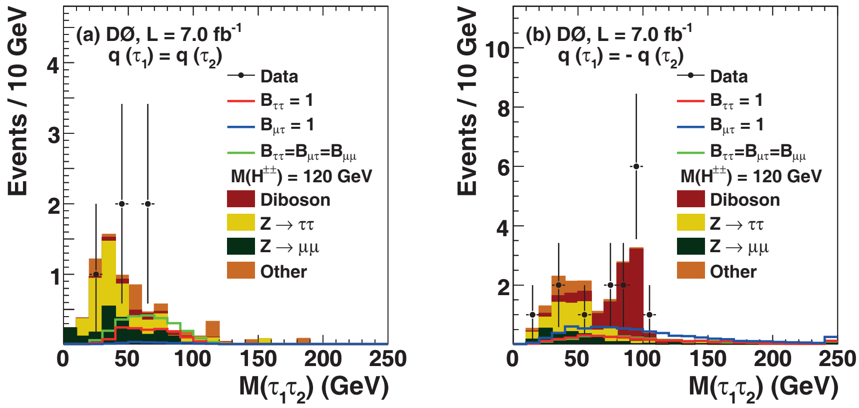

Fig. 1. – $M(\tau_1, \tau_2)$ distribution for the (a) $q_{\tau_1} = q_{\tau_2}$ and (b) $q_{\tau_1} = -q_{\tau_2}$ samples after all selections [5]. The data are compared to the sum of the expected background and to simulations of a $H_L^{\pm\pm}H_L^{\pm\pm}$ signal for $M(H^{\pm\pm}) = 120\,\text{GeV}$ and $\mathcal{B}(H_L^{\pm\pm} \to \tau^\pm\tau^\pm) = 1$, $\mathcal{B}(H_L^{\pm\pm} \to \mu^\pm\tau^\pm) = 1$, and $\mathcal{B}(H_L^{\pm\pm} \to \tau^\pm\tau^\pm) = \mathcal{B}(H_L^{\pm\pm} \to \mu^\pm\mu^\pm) = \mathcal{B}(H_L^{\pm\pm} \to \mu^\pm\tau^\pm) = 1/3$, normalized using the NLO calculation of the cross section. "Other" background comprises $W+\text{jet}$, $Z/\gamma^* \to e^+e^-$, and $t\bar{t}$ processes. All entries exceeding the range of the histogram are added to the last bin.

azimuthal angle, and the two leading τ_h must be separated by $\Delta\mathcal{R}_{\tau_1\tau_2} > 0.7$. The sum of the charges of the highest-p_T muon, τ_1, and τ_2 is required to be $Q = \sum_{i=\mu,\tau_1,\tau_2} q_i = \pm 1$ as expected for signal events. After all selections, the main background is from diboson production and $Z \to \tau^+\tau^-$, where an additional jet mimics a lepton.

The multijet background contribution is estimated from data using three independent data samples and identical selections, except with the NN_τ requirements reversed, by requiring that either one or both τ_h candidates have $NN_\tau < 0.75$. The expected background simulated as described in sect. **3** is subtracted before the samples are used to determine the differential distributions and normalization of the multijet background in the signal region. The total rate of expected multijet background events following all selections is negligible ($< 3\%$ of the total background).

The selected data, after all requirements are applied, are separated into four non-overlapping samples. As defined by the charges of the muon (q_μ) and the τ_h candidates (q_τ) and the number of muons (N_μ) and τ_h (N_τ) in the event. Two samples are defined where $N_\mu = 1$ and $N_\tau = 2$, and are further subdivided into the cases where both tau leptons have the same charge, $q_{\tau_1} = q_{\tau_2}$, and events with τ_1 and τ_2 of opposite charge, *i.e.*, $q_{\tau_1} = -q_{\tau_2}$, which implies that one of the τ leptons and the muon have the same charge. This separates the cases where the $H^{\pm\pm}$ decays into two tau leptons, from when it decays into a tau lepton and a muon. The third sample is defined by $N_\tau = 3$ and the fourth sample by $N_\mu = 2$, without any additional requirements on the charges.

Figures 1(a) and (b) show the distributions of the invariant mass of the two leading tau candidates, $M(\tau_1, \tau_2)$, for the like- and opposite-charge samples. The samples have different fractions of signal and background events the like-charge sample being dominated by background from $Z+$jets decays and the opposite-charge sample by background from diboson production. The diboson background has a significant contribution from $WZ \to \mu\nu e^+e^-$ events where the electrons are misidentified as tau leptons [5]. The

TABLE I. – *Numbers of events in data, predicted background, and expected signal for* $M(H_L^{\pm\pm}) =$ 120 GeV, *assuming the NLO calculation of the signal cross section for* $\mathcal{B}(H_L^{\pm\pm} \to \tau^\pm\tau^\pm) = 1$, $\mathcal{B}(H_L^{\pm\pm} \to \mu^\pm\tau^\pm) = 1$, *and* $\mathcal{B}(H_L^{\pm\pm} \to \tau^\pm\tau^\pm) = \mathcal{B}(H_L^{\pm\pm} \to \mu^\pm\mu^\pm) = \mathcal{B}(H_L^{\pm\pm} \to \mu^\pm\tau^\pm) = 1/3$. *The numbers are shown for the four samples separately, together with their total uncertainties.*

	All	$N_\mu = 1$, $N_\tau = 2$		$N_\mu = 1$, $N_\tau = 3$	$N_\mu = 2$, $N_\tau = 2$
		$q_{\tau_1} = q_{\tau_2}$	$q_{\tau_1} = -q_{\tau_2}$		
Signal					
$\tau^\pm\tau^\pm$	6.6 ± 0.9	1.4 ± 0.2	3.1 ± 0.4	1.6 ± 0.2	0.4 ± 0.1
$\mu^\pm\tau^\pm$	13.9 ± 1.9	0.3 ± 0.1	6.8 ± 0.9	0.4 ± 0.1	6.3 ± 0.9
Equal $\mathcal{B}$	9.5 ± 1.3	2.5 ± 0.3	3.1 ± 1.0	1.2 ± 0.2	2.6 ± 0.4
Background					
$Z \to \tau^+\tau^-$	8.2 ± 1.1	3.4 ± 0.5	4.8 ± 0.7	< 0.1	< 0.1
$Z \to \mu^+\mu^-$	5.1 ± 0.7	2.2 ± 0.3	2.5 ± 0.4	0.1 ± 0.1	0.2 ± 0.1
$Z \to e^+e^-$	0.3 ± 0.1	< 0.1	0.3 ± 0.1	< 0.1	< 0.1
W + jets	2.9 ± 0.4	1.1 ± 0.2	1.8 ± 0.3	< 0.1	< 0.1
$t\bar{t}$	0.6 ± 0.1	0.3 ± 0.1	0.3 ± 0.1	0.1 ± 0.1	< 0.1
Diboson	10.5 ± 1.7	0.5 ± 0.1	8.5 ± 1.4	0.4 ± 0.1	1.1 ± 0.2
Multijet	< 0.8	< 0.2	< 0.5	< 0.1	< 0.1
Background Sum	27.6 ± 4.9	7.5 ± 1.2	18.2 ± 3.3	0.6 ± 0.1	1.3 ± 0.2
Data	22	5	15	0	2

different background compositions in the separate samples increases the sensitivity to the signal. The expected number of background and signal events for the four samples and the observed numbers of events in data are shown in table I with the statistical uncertainties of the MC samples and systematic uncertainties added in quadrature.

As the data are described well by the background prediction, limits are set on the $H^{++}H^{--}$ production cross section using a modified frequentist approach [20]. A log-likelihood ratio (LLR) test statistic is formed using the Poisson probabilities for estimated background yields, the signal acceptance, and the observed number of events for different $H^{\pm\pm}$ mass hypotheses. The confidence levels are derived by integrating the LLR distribution in pseudo-experiments using both the signal-plus-background (CL_{s+b}) and the background-only hypotheses (CL_b). The excluded production cross section is taken to be the cross section for which the confidence level for signal, $CL_s = CL_{s+b}/CL_b$, equals 0.05. The $M(\tau_1, \tau_2)$ distribution was used to discriminate signal from background [5].

5. – Systematic uncertainties

Systematic uncertainties on both background and signal, including their correlations, are taken into account [5]. The theoretical uncertainty on background cross sections for

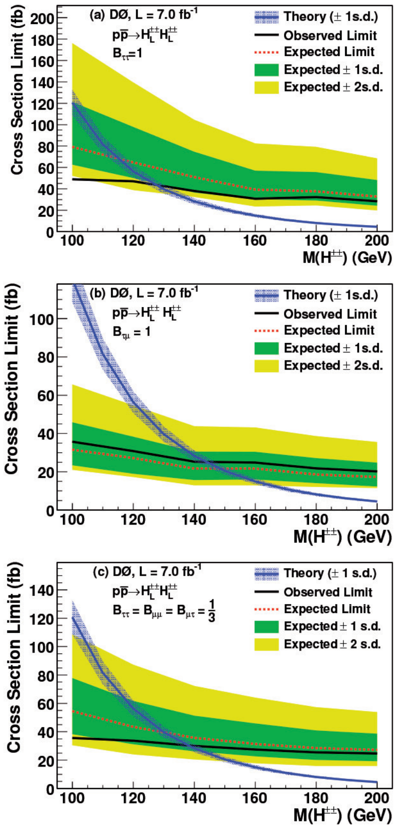

Fig. 2. – Upper limit on the $H_L^{\pm\pm}H_L^{\pm\pm}$ pair production cross section for (a) $\mathcal{B}(H_L^{\pm\pm} \to \tau^\pm\tau^\pm) = 1$, (b) $\mathcal{B}(H_L^{\pm\pm} \to \mu^\pm\tau^\pm) = 1$, and (c) $\mathcal{B}(H_L^{\pm\pm} \to \tau^\pm\tau^\pm) = \mathcal{B}(H_L^{\pm\pm} \to \mu^\pm\mu^\pm) = \mathcal{B}(H_L^{\pm\pm} \to \mu^\pm\tau^\pm) = 1/3$. The bands around the median expected limits correspond to regions of ±1 and ±2 standard deviation (s.d.), and the band around the predicted NLO cross section for signal corresponds to a theoretical uncertainty of $\pm10\%$ [5].

$Z/\gamma^* \to \ell^+\ell^-$, $W+$jets, $t\bar{t}$, and diboson production varies between 6%–10%. The uncertainty on the measured integrated luminosity is taken to be 6.1% [21]. The systematic uncertainty on muon identification is 2.9% per muon and the uncertainty on the identification of τ_h, including the uncertainty from applying a neural network to discriminate τ_h from jets, is 4% for each type-1 and 7% for each type-2 τ_h candidate. The trigger efficiency has a systematic uncertainty of 5%. The uncertainty on the signal acceptance from parton distribution functions is 4%.

6. – Limits

The upper limits on the cross sections are compared to the NLO signal cross sections for $H_L^{\pm\pm}H_L^{\pm\pm}$ pair production [4] in fig. 2, for the branching ratios (a) $\mathcal{B}(H_L^{\pm\pm} \to \tau^\pm\tau^\pm) = 1$, (b) $\mathcal{B}(H_L^{\pm\pm} \to \mu^\pm\tau^\pm) = 1$, and (c) $\mathcal{B}(H_L^{\pm\pm} \to \tau^\pm\tau^\pm) = \mathcal{B}(H_L^{\pm\pm} \to \mu^\pm\mu^\pm) = \mathcal{B}(H_L^{\pm\pm} \to \mu^\pm\tau^\pm) = 1/3$. The corresponding expected and observed limits are shown in table II.

TABLE II. – *Expected and observed limits on $M(H^{\pm\pm})$ (in GeV) for left-handed and right-handed $H^{\pm\pm}$ bosons. Only left-handed states exist in the model that assumes equality of branching fractions into $\tau\tau$, $\mu\tau$, and $\mu\mu$ final states. We only derive limits if the expected limit on $M(H^{\pm\pm})$ is ≥ 90 GeV.*

Decay	$H_L^{\pm\pm}$		$H_R^{\pm\pm}$	
	expected	observed	expected	observed
$\mathcal{B}(H^{\pm\pm} \to \tau^\pm\tau^\pm) = 1$	116	128		
$\mathcal{B}(H^{\pm\pm} \to \mu^\pm\tau^\pm) = 1$	149	144	119	113
Equal $\mathcal{B}$ into $\tau^\pm\tau^\pm, \mu^\pm\mu^\pm, \mu^\pm\tau^\pm$	130	138		
$\mathcal{B}(H^{\pm\pm} \to \mu^\pm\mu^\pm) = 1$	180	168	154	145

The $H^{\pm\pm}$ boson mass limits, assuming $\mathcal{B}(H^{\pm\pm} \to \tau^\pm\tau^\pm)+\mathcal{B}(H^{\pm\pm} \to \mu^\pm\mu^\pm) = 1$ are determined by combining signal samples generated with pure 4τ, $(2\tau/2\mu)$, and 4μ final states with fractions $\mathcal{B}^2$, $2\mathcal{B}(1-\mathcal{B})$, and $(1-\mathcal{B})^2$, respectively, where $\mathcal{B} \equiv \mathcal{B}(H^{\pm\pm} \to \tau^\pm\tau^\pm)$. As this analysis did not analyze a pure muon sample, a search for $H^{++}H^{--} \to 4\mu$, performed by the DØ Collaboration with $1.1\,\mathrm{fb}^{-1}$ of integrated luminosity [10] is included in the limit setting to account for this contribution. The invariant mass of the two highest p_T muons, including the systematic uncertainties and their correlations is used as the final discriminant. The determined mass limits are shown in fig. 3 for varying the branching ratio to tau leptons $\mathcal{B} = 0\%$–100% in steps of 10%.

7. – Summary

In summary, BSM Higgs searches with tau leptons may be of specific interest. The first search at a hadron collider for pair production of doubly charged Higgs bosons decaying exclusively into tau leptons has been summarized as a example of such a search. This

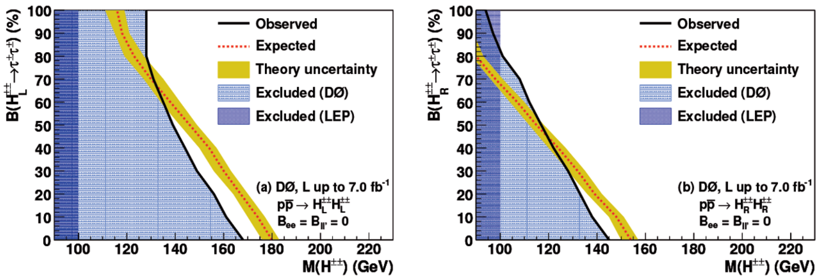

Fig. 3. – Expected and observed exclusion region at the 95% CL in the plane of $\mathcal{B}(H^{\pm\pm} \to \tau^\pm\tau^\pm)$ *versus* $M(H^{\pm\pm})$, assuming $\mathcal{B}(H^{\pm\pm} \to \tau^\pm\tau^\pm) + \mathcal{B}(H^{\pm\pm} \to \mu^\pm\mu^\pm) = 1$, for (a) left-handed and (b) right-handed $H^{\pm\pm}$ bosons. The band around the expected limit represents the uncertainty on the NLO calculation of the cross section for signal [5].

analysis set an observed (expected) lower limit of $M(H_L^{\pm\pm}) > 128$ (116) GeV for a 100% branching fraction of $H^{\pm\pm} \to \tau^{\pm}\tau^{\pm}$, $M(H_L^{\pm\pm}) > 144$ (149) GeV for a 100% branching fraction into $\mu\tau$, and $M(H_L^{\pm\pm}) > 130$ (138) GeV for a model with equal branching ratios into $\tau\tau$, $\mu\tau$, and $\mu\mu$.

REFERENCES

[1] Nilles H. P., *Phys. Rep.*, **110** (1984) 1; Haber H. E. and Kane G. L., *Phys. Rep.*, **117** (1985) 75.
[2] Ramirez Barreto E., Coutinho Y. A. and Sá Borges J., *Phys. Rev. D*, **83** (2011) 075001.
[3] Kadastik M., Raidal M. and Rebane L., *Phys. Rev. D*, **77** (2008) 115023; Hektor A. *et al.*, *Nucl. Phys. B*, **787** (2007) 198.
[4] Mühlleitner M. and Spira M., *Phys. Rev. D*, **68** (2003) 117701 and private communications.
[5] Abazov V. M. *et al.* (D0 Collaboration), *Phys. Rev. Lett.*, **108** (2012) 021801.
[6] Akeroyd A. G. and Aoki M., *Phys. Rev. D*, **72** (2005) 035011.
[7] Abbiendi G. *et al.* (OPAL Collaboration), *Phys. Lett. B*, **526** (2002) 221; Achard P. *et al.* (L3 Collaboration), *Phys. Lett. B*, **576** (2003) 18; Abdallah J. *et al.* (DELPHI Collaboration), *Phys. Lett. B*, **552** (2003) 127.
[8] Aktas A. *et al.* (H1 Collaboration), *Phys. Lett. B*, **638** (2006) 432.
[9] Abbiendi G. *et al.* (OPAL Collaboration), *Phys. Lett. B*, **577** (2003) 93.
[10] Abazov V. M. *et al.* (D0 Collaboration), *Phys. Rev. Lett.*, **101** (2008) 071803.
[11] Abazov V. M. *et al.* (D0 Collaboration), *Phys. Rev. Lett.*, **93** (2004) 141801.
[12] Acosta D. *et al.* (CDF Collaboration), *Phys. Rev. Lett.*, **93** (2004) 221802.
[13] Aaltonen T. *et al.* (CDF Collaboration), *Phys. Rev. Lett.*, **101** (2008) 121801.
[14] Abazov V. M. *et al.* (D0 Collaboration), *Nucl. Instrum. Methods Phys. Res. A*, **565** (2006) 463; Abolins M. *et al.*, *Nucl. Instrum. Methods Phys. Res. A*, **584** (2008) 75; Angstadt R. *et al.*, *Nucl. Instrum. Methods Phys. Res. A*, **622** (2010) 298.
[15] Mangano M. L. *et al.*, *JHEP*, **07** (2003) 1; we use version 2.11.
[16] Sjöstrand T., Mrenna S. and Skands P., *JHEP*, **05** (2006) 026; we use version 6.323.
[17] Waş Z., *Nucl. Phys. B Proc. Suppl.*, **98** (2001) 96; we use version 2.5.04.
[18] Brun R. and Carminati F., CERN Program Library Long Writeup W5013, 1993.
[19] Abazov V. M. *et al.* (D0 Collaboration), *Phys. Rev. D*, **71** (2005) 072004; erratum **77** (2008) 039901.
[20] Fisher W., FERMILAB-TM-2386-E (2006).
[21] Andeen T. *et al.*, FERMILAB-TM-2365 (2007).

IL NUOVO CIMENTO Vol. 35 C, N. 6 Novembre-Dicembre 2012
DOI 10.1393/ncc/i2012-11382-6

Colloquia: LaThuile12

Finding a $\mathrm{Z} \to 2$ jets signal in $\mathrm{W} + 3$ jets events at CDF

C. Vernieri

Scuola Normale Superiore - Pisa and INFN, Sezione di Pisa - Pisa, Italy

ricevuto il 7 Settembre 2012

Summary. — The observation of WZ associated production at the Tevatron in a final state with a lepton, missing transverse energy and jets is difficult since the signal rate is low and competes with a huge background. In an attempt to increase the acceptance, the sample where three high-energy jets are reconstructed is investigated. In this sample, which within our event selection cuts includes 1/3 of the diboson signal events, rather than choosing the two transverse energy (E_T) leading jets to detect a Z signal, the information carried by all jets is combined.

PACS `14.70.-e` – Gauge bosons.
PACS `13.85.Ni` – Inclusive production with identified hadrons.
PACS `13.85.Qk` – Inclusive production with identified leptons, photons, or other nonhadronic particles.
PACS `13.87.-a` – Jets in large-Q^2 scattering.

1. – Introduction

In the Standard Model (SM) of particle physics, the electroweak bosons are the gauge bosons of the local $SU(2)\otimes U(1)$ symmetry. All couplings of the W, Z bosons and photons are well defined within this symmetry, while the W- and Z-boson masses arise because of the spontaneous breaking of this symmetry.

The study of diboson (W,Z) production at hadron colliders provides a test of the electroweak sector of the SM, since any deviation from the predicted WWZ, WZZ couplings (TGC, Trilinear Gauge Couplings) would be indicative of new physics [1].

Diboson measurements are also instrumental for searches for the SM light Higgs boson. By choosing to focus on the final state where a Z-boson decays into $b\bar{b}$-pairs, the topology of WZ events would be the same as expected for associated production of a W and a light Higgs boson ($M_H < 135\,\mathrm{GeV}$). At the Tevatron, the process $\mathrm{WH} \to \mathrm{W}b\bar{b}$ has an expected cross section times branching ratio ($\sigma \cdot \mathrm{BR}$) about five times lower than $\mathrm{WZ} \to \mathrm{W}b\bar{b}$ for $M_H \simeq 120\,\mathrm{GeV}/c^2$. Therefore, observing that process would be a benchmark for the even more difficult light Higgs search in the $\mathrm{WH} \to \mathrm{W}b\bar{b}$ process.

2. – Motivations for the three-jets studies

Observing WZ associated production at the 1.96 TeV center-of-mass energy of the Fermilab proton-antiproton Tevatron collider is difficult since the event rate is extremely low. NLO calculations predict WZ production cross section to be about 3.22 pb [2]. Thus, one expects a handful of events per fb^{-1} of integrated luminosity in the $\ell\nu q\bar{q}$ final state, after allowing for trigger and kinematical selection efficiency. This statement remains valid even if the few accepted ZZ events with leptonic decay of one Z, where one lepton is not detected, are included.

Furthermore, the signal to background ratio is very poor, due primarily to the large background contributed by the production of W and associated jets. Since the main signal feature to be exploited to disentangle signal from background is the invariant mass of H-decay jets, the correct selection of the jets to be assigned to H decay and an optimal resolution in jet systems mass is of utmost importance.

In diboson analyses at CDF the standard kinematical cut requires two high-energy jets (*i.e.* $E_T > 20\,\mathrm{GeV}$) in the candidate sample (*two-jets region*). Since simulations show that if a third high-energy jet is allowed (*three-jets region*, as defined by our selection cuts on jet energy), the signal acceptance is increased by 33%, it would be important to be able to detect the Z signal also in events with more than two high-energy jets.

However, the issue is confused because in WZ events additional jets may be initiated by gluon(s) radiated from the interacting partons (Initial State Radiation, ISR) or from the Z-decay products (Final State Radiation, FSR). This work presents a method to overcome this difficulty and by making optimal use of the information on diboson production contained in the sample with 3 associated jets.

Extra-activity produced by spectator partons or by pile-up of events was found to be negligible in our studies.

2·1. *Event selection*. – The experimental signature involves the presence of a charged lepton (electron or muon), a neutrino (identified through the missing transverse energy, $\not{E}_T$) and large-E_T jets.

The offline event selection identifies jets using the JETCLU cone algorithm with radius $\sqrt{(\Delta\phi^2 + \Delta\eta^2)} = 0.4$, in the space of azimuthal angle ϕ and pseudorapidity η, corrected for detector effects as described in [3].

The sample we investigate is selected by the following cuts:

– exactly three jets([1]) with $E_T(J_1, J_2, J_3) > 25,\ 15,\ 15\,\mathrm{GeV}$ and $|\eta(J_1, J_2, J_3)| < 2,\ 2,\ 3.6$;

– an isolated triggered electron or muon with $|\eta| < 1.1$ and $E_T > 20\,\mathrm{GeV}$;

– $\not{E}_T > 20\,\mathrm{GeV}$;

– Multi-jet QCD veto:
  - $M_T^W > 10\ (30)\,\mathrm{GeV}$ if the triggered lepton is a muon (electron), M_T^W being the W-invariant mass in the transverse plane,
  - $\not{E}_T$-significance([2]) > 1.8 if the triggered lepton is an electron.

([1]) Events with a fourth jet with $E_T > 10\,\mathrm{GeV}$ are rejected.

([2]) $\not{E}_T$-significance $= (-\log_{10}(P(\not{E}_T^{fluct} > \not{E}_T)))$, where P is the probability and $\not{E}_T^{fluct}$ is the expected missing transverse energy arisen from fluctuations in the energy measurements [4].

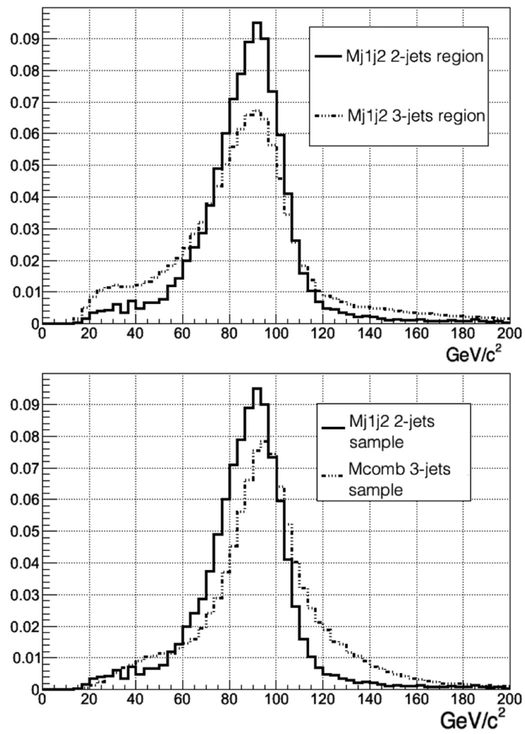

Fig. 1. – Top, $M(J_1J_2)$ in the *three-jets region* (dotted) is compared to $M(J_1J_2)$ in the *two-jets region*. Bottom, $M(J_1J_2)$ in the *two-jets region* is compared to MJJ_{COMB} (dotted) in the *three-jets region*.

Then, two different subsamples corresponding to an integrated luminosity of 6.6 fb^{-1} are studied separately. One, the tag sample, where two b-jets in the final state are required, represents the golden channel for the light SM Higgs boson search at Tevatron (WH → W$b\bar{b}$). In this analysis the b-tagger employed is the b-ness [5], which is a multivariate, neural network (NN) based tagger. It provides an output value serving as a figure of merit to indicate how b-like a jet appears to be. Jets with increasing b-ness are more b-like.

The second, the notag sample is the sub-sample of the pretag sample([3]) where the tag obtained by removing the tag sample. This makes the tag and no-tag samples independent of each other and allows combining the results obtained by analyzing the two samples.

In order to select the tag sample we require the two leading jets to have $b$ness $>$ 0.75, -0.2 respectively. These cuts have been optimized against the sensitivity of the measurement. In fig. 1 the invariant mass built using the two E_T leading jets $M(J_1J_2)$ for WZ MC events in the *two jets region* is compared with the same distribution built in the *three jets region*. In the three jets region, since jets due to initial or final state radiation confuse the choice of the jet system to be attributed to Z decay, $M(J_1J_2)$ has

([3]) Pretag sample is the one where no constrain on jets flavor are applied.

TABLE I. – *Predicted and observed number of events in the notag and tag samples. W+jets and QCD rates are estimated by fitting data. The expected rates are separated for different triggered lepton type. By construction the expected numbers are equal to the observed ones.*

NOTAG	Process	Rate (Electrons)	Rate (Muons)
	Signal (WZ/ZZ)	66.2 ± 0.9	69.5 ± 0.9
	WW	386.2 ± 3.0	311.1 ± 3.1
	$t\bar{t}$	333.0 ± 1.4	288.5 ± 1.2
	single-top	68.9 ± 0.4	57.8 ± 0.3
	Z+jets	350.0 ± 3.2	1167.8 ± 4.5
	W+jets	10304.2 ± 29.6	8275 ± 22.8
	QCD	1600.4 ± 60.0	352.3 ± 5.4
	Total Observed	13109.0 ± 114.5	10522.0 ± 102.6
TAG	Process	Rate (Electrons)	Rate (Muons)
	Signal (WZ/ZZ)	3.5 ± 0.2	3.6 ± 0.2
	WW	6.2 ± 0.4	4.7 ± 0.3
	$t\bar{t}$	146.4 ± 0.9	127.9 ± 0.8
	single-top	22.5 ± 0.2	18.7 ± 0.2
	Z+jets	8.0 ± 0.4	23.6 ± 0.6
	W+jets	212.0 ± 3.9	189.9 ± 3.2
	QCD	32.5 ± 0.3	5.7 ± 0.0
	Total Observed	431.0 ± 20.8	374.0 ± 19.3

a degraded resolution: high mass and low mass tails due to wrong combinations are present. It is reasonable to expect that choosing the correct jet combination MJJ_{COMB} (to be defined later) for building the Z mass would improve the resolution. (see fig. 1, bottom). This work builds on the analysis methods reported in [6].

2˙2. *Composition of the selected events*. – The following processes contribute to a data sample selected within our cuts:

– Electroweak and top (EW): WW, WZ, ZZ, Z+jets, $t\bar{t}$, single *top*. Each of these processes can mimick the signal signature, with one detected lepton, large $\not{E}_T$ and jets. The contamination of these processes in the selected data sample is estimated by using their accurately predicted cross sections [2]. The shapes (templates) of a number of observables are obtained from ALPGEN+Pythia [7], Pythia MC [8] after the simulation of the CDF detector.

– W($\rightarrow l\nu$)+jets, $l = e, \mu, \tau$. Due to the presence of real leptons and neutrinos, the $W+$ jets background is the hardest to be reduced. Templates are obtained from ALPGEN+Pythia MC, while the rate normalization is obtained from data [6].

– QCD: multi-jet production with a jet faking the lepton and fake $\not{E}_T$. Since the mechanism for a jet faking a lepton or for fake missing transverse energy is not expected to be well modeled in MC events, both rate normalization and templates are obtained from data.

In table I we show the estimated number of events for each process contributing for the $M(J_1J_2)$ distribution in the notag and tag samples.

3. – Adopted strategy

In order to simulate the WZ $\to \ell\nu jjj$ process we used the ALPGEN generator interfaced to the generator PYTHIA to include jet fragmentation.

Jets are ordered in decreasing E_T in the notag sample and in decreasing b-ness in the tag sample(4).

We started from studying the three jets sample in WZ MC in which jets are matched in direction to particles produced by the hadronization ("hadrons") of partons from Z. The matching algorithm implemented searches for hadrons rather than quarks in the jet cone and traces back the origin of the hadrons in order to understand if they were produced by a Z-decay. In this way the rate of matching reaches $\sim 99\%$(5) and it allow us to train NNs with a set of events as much as possible similar to the real data.

Since PYTHIA saves all the information related to stable hadrons produced by partons hadronization for each hadron shower we are able to state if it comes from a primary beam parton (ISR) or if it originates from Z (FSR). Then, we look for stable hadrons within the jet cone and for each of the 3 jets in the event, we ask that the total hadron energy originating from a single parton is $> 50\%$ than the jet energy. With this method we are able to label the 99% of jets as ISR or FSR.

Once the origin of each jet is well understood we know event-by-event which jet combination should be used to reconstruct the Z mass (named the right jet combination, RJC). In terms of the frequency of RJC the notag (tag) sample is composed as follows:

1. J_3 is from ISR, J_1 and J_2 from FSR $\mapsto$ RJC $= J_1J_2$: 33.5% (53.4%) of events
2. J_2 is from ISR, J_1 and J_3 from FSR $\mapsto$ RJC $= J_1J_3$: 21.4% (9.5%) of events
3. J_1 is from ISR, J_2 and J_3 from FSR $\mapsto$ RJC $= J_2J_3$: 10.8% (4.9%) of events
4. J_1, J_2, J_3 are from FSR $\mapsto$ RJC $= J_1J_2J_3$: 33.3% (31.2%) of events

Notice that in tag sample J_1J_2 is the RJC in the 53.4% of cases, since jets are ordered in b-ness and we require the two b-ness leading jets to satisfy some criterion. The greater contribution of $M(J_1J_2)$ in the whole sample is the reason why in the tag sample the resolution is already good for the distribution built with the two jets with highest b-ness. Still, even in this sample a better combination than J_1J_2 can be searched for in $\sim 47\%$ of events.

3·1. *Neural Networks.* – Four different Neural Networks (NNs) have been trained, using MLP method [9], in MC signal events to isolate each of the above cases: NN(J_1J_2), NN(J_1J_3), NN(J_2J_3) and NN($J_1J_2J_3$). These NNs combine kinematical information and some tools developed by CDF Collaboration for discriminating gluon-like and b-like jets from light-flavored jets [5, 10]. Inputs to NNs are:

1. Kinematical variables:
   - $\mathrm{d}\eta_{j_ij_k} = |\eta_{j_i} - \eta_{j_k}|$
   - $\mathrm{d}R_{j_ij_k}$

(4) J_1, J_2 would be the two with highest b-ness value, J_3 the one with highest E_T among the others.
(5) The rate of matching jets to quarks is about 60%.

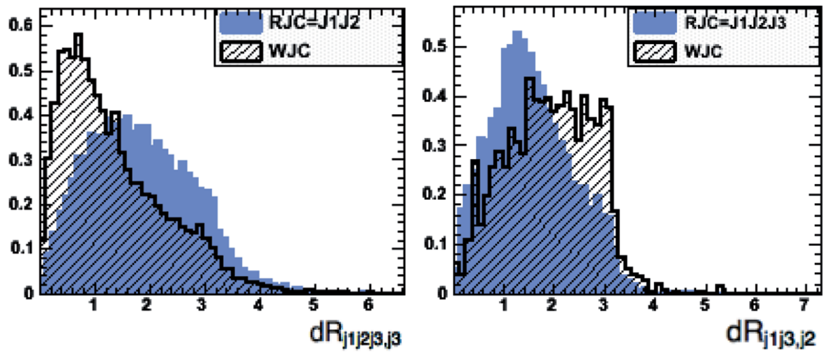

Fig. 2. – Some distributions of the variables used as input to NNs, built for the RJC sample and for the complementary one (shaded).

TABLE II. – *Parameters of the fits to the distributions of* $M(J_1J_2)$ *and* MJJ_{COMB} *in the tag and notag samples. A is the acceptance; p is the purity which is defined as the fraction of events where the corrected jets are selected;* σ *and* μ *are width and average of Gaussian fits to the distributions in the mass window* $[70, 110]\,\mathrm{GeV}/c^2$.

	Notag: $M(J_1J_2)$	MJJ_{COMB}	Tag: $M(J_1J_2)$	MJJ_{COMB}
A	100%	90%	100%	92%
p	35%	65%	53%	72%
σ/μ	0.25	0.13	0.22	0.14

- $\mathrm{d}R_{j_i\ell}$, $\mathrm{d}R_{j_kj_l,j_p}$, $\mathrm{d}R_{j_1j_2j_3,j_k}$ (6)

2. Variables related to the jet systems:
   - $m_{j_ij_k}/m_{j_1j_2j_3}$
   - $\gamma_{j_ij_k} = (E_{j_i} + E_{j_k})/m_{j_ij_k}$
   - $\gamma_{jjj} = (E_{j_1} + E_{j_2} + E_{j_3})/m_{j_1j_2j_3}$
   - "pt-imbalance" $= P_{Tj1} + P_{Tj2} - P_{T\ell} - \not{E}_T$
   - $\eta(j_i + j_k)/\eta(j_p)$, $p_T(j_i + j_k)/p_T(j_p)$
3. b/light quark discriminant, quark/gluon discriminant.

Based on the response of the four NNs, we determine the most likely jet combination for building the Z mass for each event. The method allows to use a different combination from J_1J_2 in about 65% (45%) of cases in the notag (tag) sample.

In fig. 2 some inputs are shown.

Combining by a set of subsequent optimal cuts(7) the information provided by the outputs of the four NNs, we build a MJJ_{COMB} Z-mass [6]. Using MJJ_{COMB} rather than $M(J_1J_2)$, the resolution improves by a factor ~ 2, see fig. 1 and table II.

(6) $i, k, p = 1, 2, 3$ are the indices of the jets. $\ell =$ highest E_T lepton.
(7) Cuts have been optimized against the sensitivity of the measurement.

TABLE III. – *Sensitivity of the fits considering only the three jets region.*

Fit Method	$P_{2\sigma}$	$P_{3\sigma}$
Fit signal $WZ/ZZ/WW$ (pretag)		
$M(J_1J_2)$	51.2%	6.4%
MJJ_{COMB}	66.7%	25.9%
	p-value	
Fit signal WZ/ZZ (notag+tag)		
$M(J_1J_2)$	0.44σ	
MJJ_{COMB}	0.54σ	

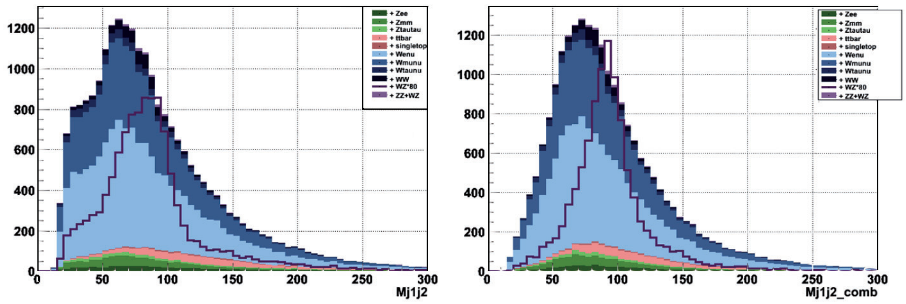

Fig. 3. – Simulation of signal+background for the notag sample. Left, $M(J_1J_2)$. Right, MJJ_{COMB}. The horizontal scale is in GeV/c^2. The signal is multiplied by 80.

We apply the method also to the main sources of background of a typical diboson analysis at CDF (W+jets, Z+ jets, $t\bar{t}$ and single top) and compare the result to WZ events. In figs. 3 and 4 and in table II one observes that MJJ_{COMB} allows a better separation of the WZ/ZZ signal from background in both notag and tag samples.

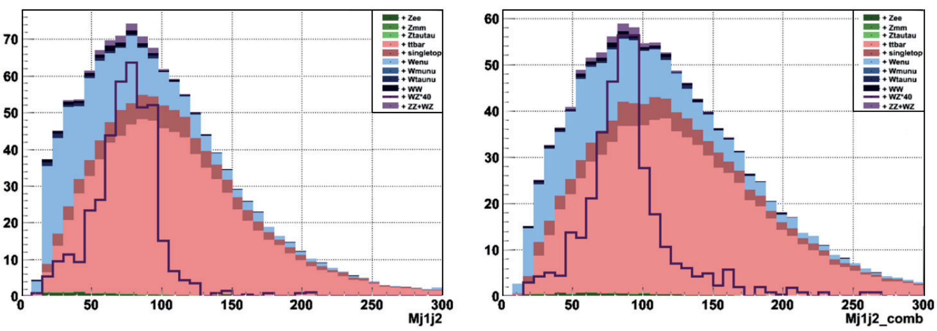

Fig. 4. – Simulation of signal+background for the tag sample. Left, $M(J_1J_2)$. Right, MJJ_{COMB} built with the criterion described in the text. The horizontal scale is in GeV/c^2 and the signal is multiplied by 40.

4. – Tests of the method

To qualify the potential of the method we have studied an experimental data sample accepting events with an isolated large E_T (p_T) lepton, large missing E_T and three large transverse-momentum jets. The selection cuts accept jets of all flavors (*pretag* sample), and all diboson events including WW besides WZ, ZZ may pass the cuts. We estimate the probability at three standard deviations level to extract an inclusive diboson signal. After our procedure for building the Z mass is applied, $P_{3\sigma}$ is about 4 times greater than when building the Z mass "by default" with the two E_T leading jets, as reported in table III.

This attempt represents just a check of our technique. A diboson signal has been observed at CDF using W events with exclusive two jets [11], we performed a test to gauge the probability of revealing a diboson signal also in the pretag three jets sample([8]).

In order to discriminate WZ against the WW contribution we apply our technique considering only WZ/ZZ as the signal. We decide to treat separately the notag and tag three jets regions and then combine the results in order to reach a greater sensitivity. The sensitivity increases when MJJ_{COMB} rather than the standard $M(J_1J_2)$ is used: the expected p-value is about 20% greater in the former case (see table III).

In conclusion, our technique allows including the three jets sample in the WZ/ZZ search in order to increase acceptance and sensitivity in the search for the hadronically decaying Z boson.

* * *

The author is grateful to M. Trovato, Prof. G. Bellettini, Dr. G. Latino and Dr. V. Rusu for many fruitful discussions and suggestions.

REFERENCES

[1] Hagiwara K. *et al.*, *Phys. Rev. D*, **41** (1990) 2113.
[2] Campbell J. M. and Ellis R. K., *Phys. Rev. D*, **65** (2002) 113007.
[3] Bhatti A. *et al.*, *Nucl. Instrum. Methods A*, **566** (2006) 375.
[4] Culbertson R. *et al.*, CDF Public Note, 9184 (2008).
[5] Freeman J. *et al.*, *Nucl. Instrum. Methods A*, **663** (2012) 37.
[6] Vernieri C., CDF Public Note (Thesis), 10675 (2011).
[7] Mangano M. *et al.*, *JHEP*, **07** (2001) 001.
[8] Sjöstrand T. *et al.*, *Computer Phys. Commun.*, **135** (2001) 238.
[9] Hoecker A. *et al.*, `http://tmva.sourceforge.net` (2009).
[10] Ketchum W. *et al.*, CDF Public Note, 10643 (2011).
[11] Aaltonen T. *et al.*, *Phys. Rev. Lett. A*, **104** (2010) 101801.

([8]) We expect the ZZ contribution to be negligible due to the requirement on $\not{E}_T$.

SESSION IX - PERSPECTIVES

IL NUOVO CIMENTO Vol. 35 C, N. 6 Novembre-Dicembre 2012
DOI 10.1393/ncc/i2012-11392-4

Colloquia: LaThuile12

Galileo, the European GNSS program, and LAGEOS

S. Berardi([1]), S. Dell'Agnello([1]), G. Delle Monache([1]), A. Boni([1]), C. Cantone([1]), M. Garattini([1]), C. Lops([1]), M. Martini([1]), G. Patrizi([1]), M. Tibuzzi([1]), R. Vittori([2]), G. Bianco([3]), S. Zerbini([4]), N. Intaglietta([1]) and E. Ciocci([1])

([1]) *Laboratori Nazionali di Frascati (LNF) of INFN - Via E.Fermi 40, 00040 Frascati (RM) Italy*
([2]) *Aeronautica Militare Italiana (AMI) - Viale dell'Università 4, 00185 Rome, Italy and ESA-HSO-U*
([3]) *Centro di Geodesia Spaziale G. Colombo (CGS) of ASI - Località Terlecchia P.O. Box ADP, 75100 Matera, Italy*
([4]) *Department of Physics Sector of Geophysics, University of Bologna Viale Berti Pichat 8 40127 Bologna, Italy*

ricevuto il 7 Settembre 2012

Summary. — With the ASI-INFN project "ETRUSCO-2 (Extra Terrestrial Ranging to Unified Satellite COnstellations-2)" we have the opportunity to continue and enhance the work already done with the former ETRUSCO INFN experiment. With ETRUSCO (2005-2010) the SCF_LAB (Satellite/lunar laser ranging Characterization Facility LABoratory) team developed a new industry-standard test for laser retroreflectors characterization (the SCF-Test). This test is an integrated and concurrent thermal and optical measurement in accurately laboratory-simulated space environment. In the same period we had the opportunity to test several flight models of retroreflectors from NASA, ESA and ASI. Doing this we examined the detailed thermal behavior and the optical performance of LAGEOS (Laser GEOdynamics Satellites) cube corner retroreflectors and many others being used on the Global Navigation Satellite System (GNSS) constellations currently in orbit, mainly GPS, GLONASS and GIOVE-A/GIOVE-B (Galileo In Orbit Validation Element) satellites, which deploy old-generation aluminium back-coated reflectors; we also SCF-Tested for ESA prototype new-generation uncoated reflectors for the Galileo IOV (In-Orbit Validation) satellites, which is the most important result presented here. ETRUSCO-2 inherits all this work and a new lab with doubled instrumentation (cryostat, sun simulator, optical bench) inside a new, dedicated $85\,\mathrm{m}^2$ class 10000 (or better) clean room. This new project aims at a new revision of the SCF-Test expressly conceived to dynamically simulate the actual GNSS typical orbital environment, a new, reliable Key Performance Indicator for the future GNSS retroreflectors payload. Following up on this and using LAGEOS as a reference standard target in terms of optical performances, the SCF_LAB research team led by S. Dell'Agnello is designing, building and testing a new generation of GNSS retroreflectors array (GRA) for the new European GNSS constellation Galileo.

PACS 42.30.-d – Imaging and optical processing.
PACS 95.10.Eg – Orbit determination and improvement.
PACS 95.30.sf – Relativity and gravitation.

1. – Introduction

An improvement of positioning accuracy, stability and precision with respect to the ITRF [1](1) of modern GNSS constellations is highly recommended by ILRS(2) in order to strengthen determination and stability of the ITRF [2]. Space and ground colocation of SLR and MW(3) techniques would make possible to align a GNSS reference frame to the ITRF, whose origin and scale are mostly determined with the SLR technique. In order to achieve these results, Laser Retroreflector Arrays (LRAs) deployed on these satellites, should guarantee an adequate level of effective cross section coming back at the stations, as defined by ILRS [2, 3]. Hence LRAs performance must be improved. The INFN, with experiment ETRUSCO, started to build, in 2005 a facility (SCF) and developed a standard test (SCF-Test) in order to characterize and validate the optical performance of GNSS LRAs, with particular attention on Galileo [1]. During the years we tested prototypes and flight models of first generation retroreflectors (coated) and LRAs for GNSS [1]. Those types of retroreflectors, both from actual SLR measurements and our SCF-Tests, proved to have problems that cause a low return rate to SLR stations and signal strength drop in certain parts of the orbit. New generation GNSS constellations are moving to uncoated retroreflectors, which with a proper mounting design can minimize thermal degradation of optical performance. Uncoated reflectors are deployed on one of the standard SLR target: the LAGEOS satellite. So in order to show a calibration of our SCF-Test, we tested in 2009 an engineering model of the LAGEOS satellite, lent by NASA-GSFC(4). In sect. **2** we report the results of these tests. Moreover with Galileo's atomic clocks and LRAs the measurement of the gravitational redshift will be improved and LAGEOS is being used to measure the $\mathrm{G} \cdot M_{\oplus}$ (gravitational constant times Earth mass), to test the inverse-square force law [4], to investigate the Lense-Thirring effect [5] and to costrain spacetime torsion [6, 7].

2. – SCF-Test of the LAGEOS engineering model

The LAGEOS engineering model, LAGEOS Sector, is an aluminum spherical sector of the whole satellite which includes 37 CCRs (Cube Corner Retroreflectors) [8] in total, one on the pole and 36 on three successive rings (as in fig. 1a). The test we performed on this prototype pointed out the excellent mounting design of the CCR inside the cylindrical cavities of the aluminium body. This mounting allows a good thermal insulation of the CCR fused silica body from the bulk aluminium body of the satellite. A good insulation leads to minimal degradation of laser return intensity when the body is exposed to sun heat and, consequently the CCR are subject to strong thermal gradients that can change the refractive index along the light path inside the CCR volume. The intensity of the light return in the transition from sunlight exposition to shadow showed a decrease of less than 20% compared to the unperturbed CCR (fig. 1b). The light return stability is particularly remarkable when compared to that offered by the main competing technology for CCR uncoated arrays, the coated ones. This kind of CCR are currently installed on several orbiting bodies (GPS/GLONASS/GIOVE-A/B) and we had the opportunity to test some of them. Coated CCR showed a light return degradation of about 87%. This

(1) International Terrestrial Reference Frame.
(2) International Laser Ranging Service.
(3) Satellite Laser ranging and MicroWave.
(4) NASA-Goddard Space Flight Center.

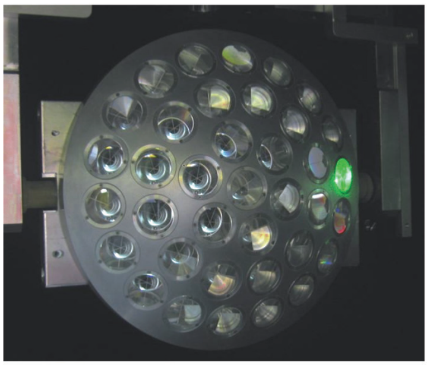

a

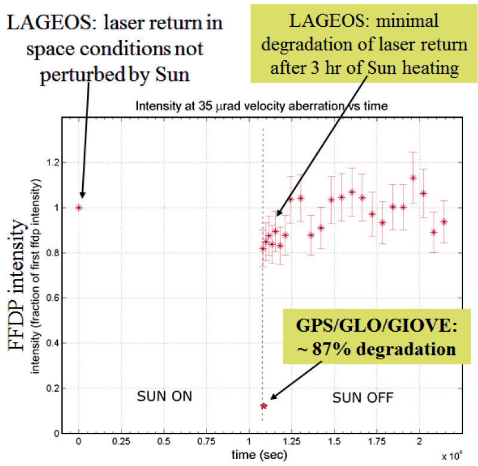

b

Fig. 1. – LAGEOS sector inside the SCF cryostat (a) and the SCF-Test plot of LAGEOS sector uncoated CCR compared to coated CCR (b).

data has been included in the plot of fig. 1b in order to have an immediate comparison between the different levels of performance.

Concerning the LAGEOS sector SCF-Test, as described in [1], it consists of a first phase in which prototypes, reached a stationary state, are heated under the sun simulator (SS) beam and then cooled down. From the thermal analysis point of view, the output is the thermal relaxation time, τ_{CCR}, of the CCR, based on IR measurements of the variation of the CCRs front face temperature. τ_{CCR} is taken from the following formula:

$$T_1 = T_0 \pm \Delta T(1 - \exp(t/\tau)).$$

We decided to SCF-Test all the retroreflectors of the prototype. Numbering them from the polar one to the outers we plotted the τ_{CCR} of each CCR for three different temperature setpoints of the bulk aluminium body. This plot is reported in fig. 2, showing the average relaxation times, between heating and cooling phases, of the first nineteen thermally analyzed CCRs. The first important outcome of the measurements is that τ_{CCR} decreases as the temperature of the aluminum increases. The ratio between the average values of all the relaxation times, at each temperature, is close to the following:

$$\frac{\tau_{T_1}}{\tau_{T_2}} \simeq \left(\frac{T_2}{T_1}\right)^3.$$

For the left part of the plot (polar CCR and first ring) the time constant of the retroreflectors shows a typical behavior that is consistent with computer simulations and, thus, with the formula mentioned above. In the right part of the plot (from CCR 8 to 19) the behaviour is not so clear since the outer retroreflectors (second and third ring) have an inclination that exceeds the capacity of the CCR to avoid the sun radiation to enter the cavity. This phenomenon, conventionally called breakthrough, leads to a behaviour that is unpredictable for mathematical models and computer simulations.

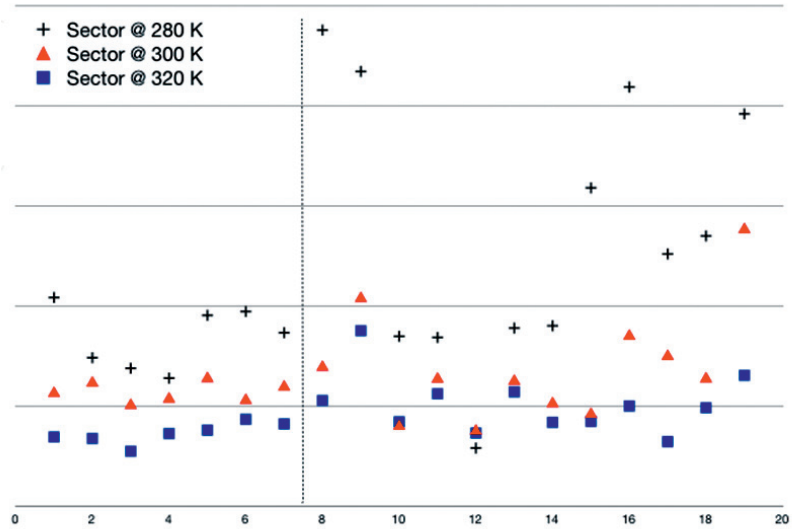

Fig. 2. – Average τ_{CCR} at different temperatures setpoints for the LAGEOS Sector aluminium bulk body.

3. – First GCO SCF-Test of a prototype uncoated CCR for Galileo-IOV satellites provided by ESA

Galileo is the European GNSS constellation named after Galileo Galilei, the famous Italian astronomer. The main goal of Galileo is to provide a non-military navigation system to rely on even during political disagreements with other countries that already owns a GNSS system. The entire system is being built by the European Union (EU) and European Space Agency (ESA) and will ensure better coverage at high latitudes and with high buildings with interoperability with GPS and GLONASS. The first two satellites were launched in October 2011 and the estimated end of phase 2 (30 satellites and ground segment operational) is 2020.

Galileo represents a great opportunity for the scientific community too, since each satellite of the constellation will be equipped with a retroreflector array, allowing the SLR network to remarkably increase the amount of measurements and, thus, the orbit determination precision. This is the starting point to improve several fundamental physics measurements such as gravitational redshift or the determination of the terrestrial reference system. This opportunity has been underlined by an issue published on Advances in Space Research [9].

In summer 2010 we had the opportunity to test an uncoated CCR prototype designed for Galileo-IOV satellites and provided by ESA (fig. 3a). We decided to study a new test procedure in order to simulate the most stressing conditions for an optical payload onboard a typical GNSS satellite. This happens when the nodal line is parallel to the sun-earth direction as shown in fig. 3b. We call this particular orbit and the related test the "GNSS Critical half-Orbit" (GCO). This is only a half of the complete orbit since in the symmetrical part the incidence angle of the sun rays on the retroreflectors front face is more than 90°. Shifting from sunlight to shadow and back, critical aspects of the thermal and optical behavior of the CCR occurs, including breakthrough: depending on

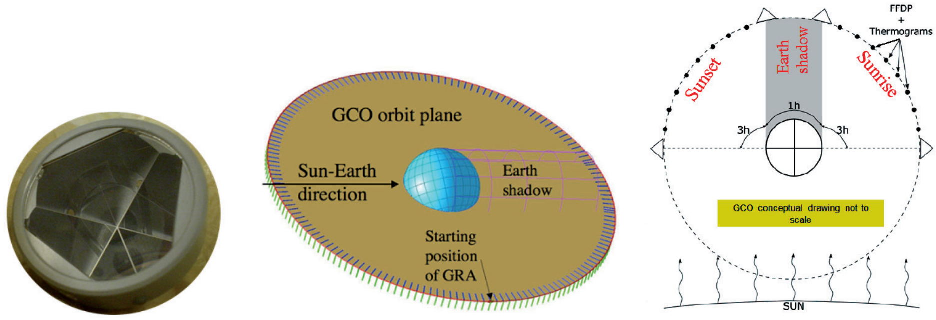

a b c

Fig. 3. – The Galileo-IOV uncoated retroreflector (a), a GNSS Critical half-Orbit conceptual drawing (b) and a scheme of the GCO test sequence (c).

the orientation of the CCR with respect to the SS beam, there are cases in which total internal reflection is broken and rays pass through the CCR heating the internal surfaces of the housing (breakthrough (BT)). For uncoated CCRs this occurs when a light ray is tilted with respect to the symmetry axis above 17°.

The retroreflector tested at the SCF, inside its housing, was installed inside an Al enclosure built at LNF, to replicate the condition of a CCR inside the array surrounded by other CCR housings (fig. 4a). The Al housing was suspended with a G10 screw to the payload support/positioning system rotating around the vertical direction. We positioned a circular aluminum plate behind the CCR housing in order to simulate the presence of the satellite body. This aluminum plate was thermally controlled, but just to bring the CCR to the right starting temperature, indicated by ESA; afterwards the object was left floating, as it is in orbit. When the CCR temperature reached 244 K, we

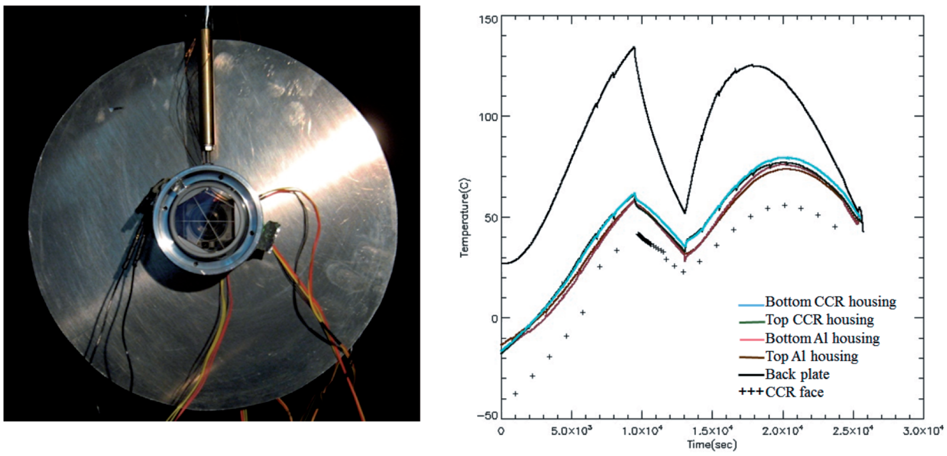

a b

Fig. 4. – Galileo-IOV CCR mounted inside the SCF for the GCO (a) and the temperatures of the IOV CCR assembly during the GCO (b).

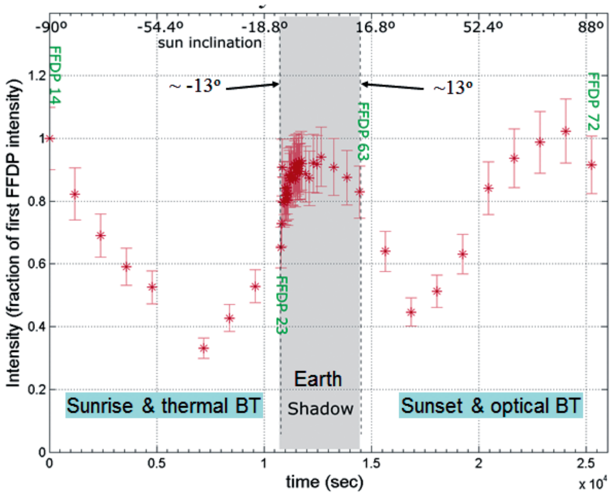

Fig. 5. – Average relative FFDP intensity at 24 μrad.

started simulating the GCO. One of the physical edges of the retroreflector was positioned horizontally. Along the GCO the inclination of the sun rays with respect to the CCR front face changes from $-90°$ to $+90°$. These conditions are reproduced in laboratory by rotating the LRA inside the cryostat, at discrete angle steps, for the proper GCO period. Galileo satellites have a quasi-circular orbit with a semi-major axis of about 29600 Km, which corresponds to an orbital period of about 14 hs.

We simulated half of the orbit, from the moment in which sun rays rise above CCRs front face till they fall on the other side, corresponding to a period of about 7 hrs. A conceptual drawing of this simulated orbit is in fig. 3c. In the SCF the GCO is the horizontal plane, so starting with the SS beam parallel to the CCRs front face we rotated the CCR, at regular angle steps, with respect to the SS, therefore simulating the sunrise phase, the passage through the Earth shadow and afterwards the sunset. The CCR was oriented with an edge horizontal in a direction such that optical BT could occur only during the sunset. The temperatures trend during the GCO is shown in fig. 4b. Bottom/Top CCR housing are temperatures taken with temperature probes on two points of the CCR housing. Bottom/Top Al housing are taken on two points of the auxiliary Al cavity. Back plate is the temperature of the plate. CCR face is the temperature of the CCR front face measured with the IR camera. Note the large temperature excursion of more than 100 K and the asymmetrical behavior due to the BT phenomena. After the completion of the orbital simulation the data acquired in the lab were post-processed with a MATLAB® script in order to obtain several analysis on the light return behavior. The main output of this analysis is fig. 5, a summary plot of the intensity, in optical cross section (OCS) units, over time at the velocity aberration (VA) of 24 μrad (design VA for Galileo-IOV CCRs, according to info from ESA). In this plot is shown the fluctuation of the OCS during the GCO. Plotted data have an estimated error of 10% on the average relative intensity, due to instrument, statistics, and residual systematic fluctuations of the SCF environment.

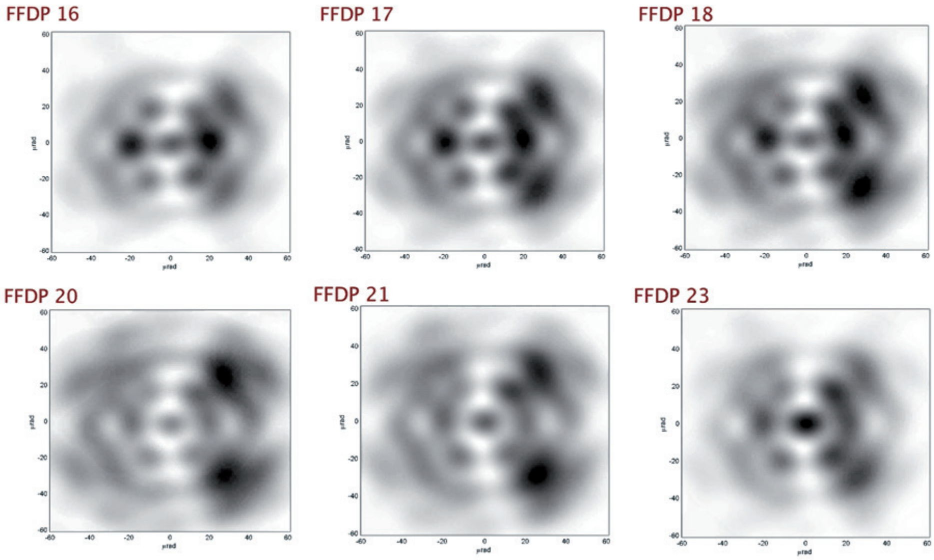

Fig. 6. – Galileo-IOV measured FFDP during the GCO. Grid dimensions are $[-60; 60]\,\mu$rad. Intensity grey-scale levels are scaled to 100.

Figure 6 shows some of the key FFDPs(5) of the GCO simulated orbit. The basic SCF-Test showed a degradation of about 25% on optical performance, compared to the much larger one (about 87%) of old GPS/GLONASS/GIOVE ones. Averaging over the entire GCO, which is a half orbit, the measured IOV CCR average intensity at $24\,\mu$rad VA had a degradation of about 35%. The prototype IOV CCR shows the expected FFDP degradation due to optical BT during sunset, but also for almost symmetric sun inclinations during sunrise, when there is no optical BT. We call this effect "thermal breakthrough". Thermal BT could be due to an IOV CCR mounting scheme with relatively large thermal conductance, as the standard SCF-Test described earlier seemed to point out.

4. – Conclusions

For the ETRUSCO-2 project the original SCF-Test has been improved and fine-tuned on the specific GNSS space environment and, furthermore, the SCF_LAB team had the chance to apply this new procedure to a first prototype of the Galileo-IOV CCRs.

This opportunity confirmed our former SCF-Test conclusions on the uncoated CCR good thermo-optical behaviour compared to the coated technology. The metallic coating on the back faces of the retroreflectors has been removed, finally, on modern GNSS, after 30 years, thanks to our SCF-Test results. Now it is very important to SCF-Test more IOV retroreflectors and, especially, reflectors of FOC (Full Orbit Capability) satellites, which are different from IOV (different makers).

In the next months in our test facility, during the next SCF-Tests, we will be able to perform concurrent wavefront interferograms of the retroreflectors inside the cryostat

(5) Far Field Diffraction Patterns.

and, as the ultimate goal, we will develop and SCF-Test a new Galileo-optimized GRA for FOC-2, with a pan-European effort, to reduce the dependence of Europes flagship programme from non-European laser retroreflector technologies. Moreover, discussions are underway for GPS-3 and other GNSS constellations like IRNSS([6]), COMPASS([7]) & QZSS([8]).

REFERENCES

[1] DellAgnello S. *et al.*, *Adv. Space Res.*, **47** (2011) 822.
[2] `http://lrs.gsfc.nasa.gov/docs/retroreflector_specification_070416.pdf`.
[3] Pearlman M. R., *Technological challenges of SLR tracking of GNSS constellations*, in *International Technical Laser Workshop on SLR Tracking of GNSS Constellations, Metsovo, Greece, 2009*.
[4] Lucchesi D. and Peron R., *Phys. Rev. Lett.*, **105** (2010) 231103.
[5] Ciufolini I. and Pavlis E. C., *Nature*, **431**, no. 7011 (2004) 958.
[6] March R., Bellettini G., Tauraso R. and Dell'Agnello S., *Phys. Rev. D*, **83** (2011) 104008.
[7] March R., Bellettini G., Tauraso R. and Dell'Agnello S., *Gen. Relativ. Gravit.*, **43** (2011) 3099; DOI 10.1007/s10714-011-1226-2.
[8] Boni A. *et al.*, *Optical Far Field Diffraction Pattern test of laser retroreflectors for space applications in air and isothermal conditions at INFN-LNF*, INFN-LNF Report LNF-08/26(IR) 2008.
[9] `http://www.sciencedirect.com/science/article/pii/S0273117710007143`.

([6]) Indian Regional Navigational Satellite System.
([7]) Chinese Regional Navigational Satellite System.
([8]) Quasi-Zenith Satellite System.

IL NUOVO CIMENTO Vol. 35 C, N. 6 Novembre-Dicembre 2012
DOI 10.1393/ncc/i2012-11393-3

Colloquia: LaThuile12

CTA: The Cherenkov Telescope Array

D. Mazin(*) on behalf of the CTA Consortium
IFAE, Edifici Cn, Campus UAB - E-08193 Bellaterra, Spain

ricevuto il 7 Settembre 2012

Summary. — Ground-based gamma-ray astronomy has had a major breakthrough with the impressive results obtained using systems of imaging atmospheric Cherenkov telescopes. Ground-based gamma-ray astronomy has a huge potential in astrophysics, particle physics and cosmology. CTA is an international initiative to build the next generation instrument, with a factor of 5–10 improvement in sensitivity in the 100 GeV to 10 TeV range and the extension to energies well below 100 GeV and above 100 TeV. CTA will consist of two arrays (one in the Northern hemisphere and one in the Southern hemisphere) for full sky coverage and will be operated as an open observatory. This paper briefly reports on the status and presents the major design concepts of CTA.

PACS 95.55.Ka – X- and gamma-ray telescopes and instrumentation.
PACS 95.85.Pw – Gamma-ray.

1. – Introduction

In the field of very-high-energy gamma-ray astronomy (VHE, energies > 100 GeV(1)), the instruments H.E.S.S. [1], MAGIC [2] and VERITAS [3] have been driving the development in recent years. The spectacular astrophysics results from the current Cherenkov instruments have generated considerable interest in both the astrophysics and particle physics communities and have created the desire for a next-generation, more sensitive and more flexible facility, able to serve a larger community of users. The proposed CTA [4] is a large array of Cherenkov telescopes of different sizes, based on proven technology and deployed on an unprecedented scale (fig. 1). It will allow significant extension of our current knowledge in high-energy astrophysics. CTA is a new facility, with capabilities well beyond those of conceivable upgrades of existing instruments such as H.E.S.S., MAGIC or VERITAS. The CTA project unites the main research groups in this field in a common strategy, resulting in an unprecedented convergence of efforts, human resources,

(*) E-mail: mazin@ifae.es
(1) 1 GeV = 10^9 eV; 1 TeV = 10^{12} eV; 1 PeV = 10^{15} eV.

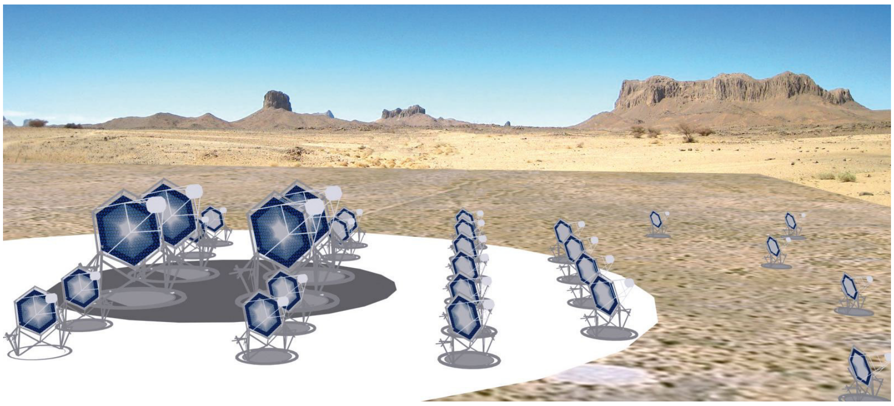

Fig. 1. – Conceptual layout of a possible Cherenkov Telescope Array (not to scale).

and know-how. Interest in and support for the project is coming from scientists around the world, all of whom wish to use such a facility for their research and are willing to contribute to its design and construction. CTA will offer worldwide unique opportunities to users with varied scientific interests. In particular, the number of young scientists working in the still evolving field of gamma-ray astronomy is growing at a steady rate, drawing from other fields such as nuclear and particle physics. In addition, there is increased interest by other parts of the astrophysical community, ranging from radio to X-ray and satellite-based gamma-ray astronomers. CTA will, for the first time in this field, provide open access via targeted observation proposals and generate large amounts of public data, accessible using Virtual Observatory tools. CTA aims to become a cornerstone in a networked multi-wavelength, multi-messenger exploration of the high-energy non-thermal universe. Details on the science cases and on technical implementations of CTA can be found in [5]. This article gives a brief overview and updates on the status of the project.

2. – Status of the field

Radiation at gamma-ray energies differs fundamentally from that detected at lower energies and hence longer wavelengths: GeV to TeV gamma rays cannot conceivably be generated by thermal emission from hot celestial objects. The energy of thermal radiation reflects the temperature of the emitting body, and apart from the Big Bang there is and has been nothing hot enough to emit such gamma rays in the known Universe. Instead, we find that high-energy gamma rays probe a non-thermal Universe, where other mechanisms allow the concentration of large amounts of energy onto a single quantum of radiation. In a bottom-up fashion, gamma rays can be generated when highly relativistic particles – accelerated for example in the shock waves of stellar explosions – collide with ambient gas, or interact with photons and magnetic fields. The flux and energy spectrum of the gamma rays reflects the flux and spectrum of the high-energy particles. They can therefore be used to trace these cosmic rays and electrons in distant regions of our own galaxy or even in other galaxies. High-energy gamma rays can also be produced in a top-down fashion by decays of heavy particles such as hypothetical dark matter particles or cosmic strings, both of which might be relics of the Big Bang. Gamma rays therefore provide a window on the discovery of the nature and constituents of dark matter.

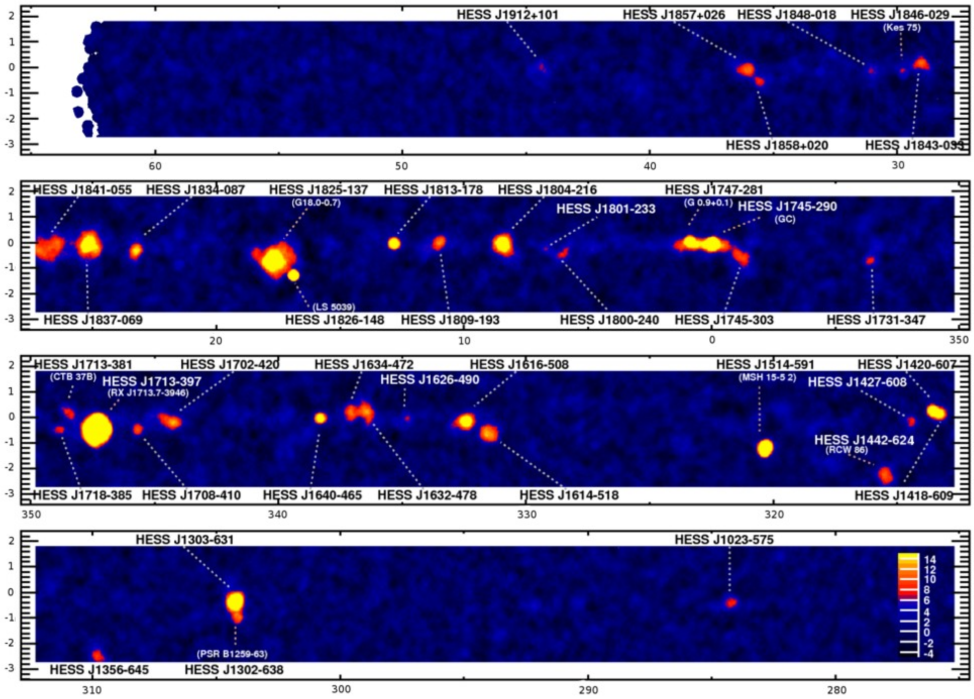

Fig. 2. – The Milky Way viewed in VHE gamma rays, in four bands of galactic longitude [8].

In the recent years, more than 150 galactic and extragalactic sources have been detected in VHE gamma rays. The H.E.S.S. galactic plane survey (see fig. 2) provided the first deep survey in VHE gamma rays of the Milky Way. Many pulsar wind nebulae have been found making them the most common objects to emit gamma rays in our galaxy. Deep observations of selected objects enabled detailed images of extended sources like the supernova remnant RX J1713.7-3946 or W51C. Several X-ray ray binaries have been identified to emit gamma rays. Another highlight of the galactic observations was a discovery of the Crab pulsar to emit gamma rays with energies up to at least 400 GeV. The sources of VHE gamma rays in the extragalactic sky are mostly blazars: the active galactic nuclei harboring super-massive black holes in their centers. In blazars, the ultra-relativistic jets point towards us boosting the VHE emission, which eases their detection. The furthest blazar to emit VHE gamma rays is 3C 279 at $z = 0.536$. Several radio galaxies have been observed to emit gamma rays: M 87, Cen A and NGC 1275. Very deep observations (more than 150 hrs per source) were done to also detect the starburst galaxies M 82 and NGC 253. These detections are important because these sources do not have strong jets. With the data available, not only source physics is being studied. The observed gamma rays also allow for studying fundamental physics such as the Lorentz Invariance Violation, search for dark matter as well as probing star and galaxy formation and cosmological models. The discovered source classes, their morphologies, observed time variability and spectral energy distributions cannot be more than the tip of the iceberg of a richer panorama that is yet to be discovered. For recent review of the status of the gamma-ray astronomy see, *e.g.*, [6, 7].

2˙1. *Detection technique*. – The recent breakthroughs in VHE gamma-ray astronomy were achieved with ground-based Cherenkov telescopes. When a VHE gamma ray enters the atmosphere, it interacts with atmospheric nuclei and generates a shower of secondary electrons, positrons and photons. Moving through the atmosphere at speeds higher than the speed of light in air, these electrons and positrons emit a beam of bluish light, the Cherenkov light. For near vertical showers this Cherenkov light illuminates a circle with a diameter of about 250 m on the ground. For large zenith angles the area can increase considerably. This light can be captured with optical elements and be used to image the shower, which vaguely resembles a shooting star. Reconstructing the shower axis in space and tracing it back onto the sky allows the celestial origin of the gamma ray to be determined. Measuring many gamma rays enables an image of the gamma-ray sky, such as that shown in fig. 2, to be created. Large optical reflectors with areas in the 100 m^2 range and beyond are required to collect enough light, and the instruments can only be operated in dark nights at clear sites. With Cherenkov telescopes, the effective area of the detector is about the size of the Cherenkov pool at ground. As this is a circle with 250 m diameter this is about $10^5\times$ larger than the size that can be achieved with satellite-based detectors. Therefore much lower fluxes at higher energies can be investigated with Cherenkov Telescopes, enabling the study of short time scale variability.

2˙2. *Existing facilities*. – The Imaging Atmospheric Cherenkov Technique was pioneered by the Whipple Collaboration in the United States. After more than 20 years of development, the Crab Nebula, the first source of VHE gamma rays, was discovered in 1989. The Crab Nebula is among the strongest sources of very high energy gamma rays, and is often used as a "standard candle". Modern instruments, using multiple telescopes to track the cascades from different perspectives and employing fine-grained photon detectors for improved imaging, can detect sources down to 1% of the flux of the Crab Nebula, see, *e.g.*, [6].

At the moment, three big installation are in operation: The H.E.S.S. Collaboration operates four 12 m diameter Cherenkov telescopes in Namibia, near the Gamsberg mountain since 2003. The MAGIC Collaboration operates two 17 m diameter Cherenkov telescopes on La Palma, Canary Islands. The mono observations started in 2004 while the second telescope and the stereo observations came into operation in October 2009. The VERITAS Collaboration operates four 12 m diameter Cherenkov telescopes in southern Arizona, USA since 2007. Both, MAGIC and VERITAS telescopes operate in the Northern hemisphere, whereas the H.E.S.S. array is in the Southern hemisphere. Given the relatively small field of view of the instruments (3.5 to 5°), the instruments are mainly complementary to each other while, at the same time, it is possible to cross-calibrate them by observing steady gamma-ray sources visible from both hemispheres [9].

3. – Physics drivers

The aims of the CTA (as well as of the current generation instruments) can be roughly grouped into three main themes, serving as key science drivers:

Understanding the origin of cosmic rays and their role in the Universe: This comprises the study of the physics of galactic particle accelerators, such as pulsars and pulsar wind nebulae, supernova remnants, and gamma-ray binaries. It deals with the impact of the accelerated particles on their environment (via the emission from particle interactions with the interstellar medium and radiation fields), and the cumulative effects seen at various scales, from massive star forming regions to starburst galaxies.

Understanding the nature and variety of particle acceleration around black holes: This concerns particle acceleration near super-massive and stellar-sized black holes. Objects of interest include microquasars at the galactic scale, and blazars, radio galaxies and other classes of AGN that can potentially be studied in high-energy gamma rays. The fact that CTA will be able to detect a large number of these objects enables population studies which will be a major step forward in this area. Extragalactic background light (EBL), galaxy clusters and gamma-ray burst (GRB) studies are also connected to this topic.

Searching for the ultimate nature of matter and physics beyond the Standard Model: This covers what can be called "new physics", with searches for dark matter through possible annihilation signatures, tests of Lorentz invariance, and any other observational signatures that challenge our current understanding of fundamental physics.

CTA will be able to generate significant advances in all these areas.

4. – Realizing CTA

4·1. *General concept.* – The key elements of the CTA array are:

– Two observatories, one in the Southern hemisphere and one in the Northern hemisphere to cover the whole sky.

– Much (a factor of 5–10) improved sensitivity compared to the current instruments. The goal is to achieve a mCrab integral sensitivity (*i.e.* to detect a clear signal from a source with a flux of 0.1% of the Crab Nebula flux in 50 h of observations) or better.

– Wide energy range. The Cherenkov technique allows one to detect gamma rays with energies from tens of GeV (using few large telescopes to collect as much light from a single shower as possible) up to hundreds of TeV (using many small telescopes to cover as much area as possible).

– Superb angular resolution. To study morphology of galactic sources an improved angular resolution down to arcmin scale is required and can be achieved by using fine pixelized cameras.

– Temporal resolution. With its large detection area, CTA will resolve flaring and time-variable emission on sub-minute time scales, which are currently not accessible.

– Survey capability. One of the main goals of CTA will be to produce a detailed GeV-TeV map of our galaxy. This is achievable by constructing a flexible in configuration array of telescopes with 6–8° field-of-view cameras.

4·2. *Monte Carlo simulations and layout studies.* – A particular size of Cherenkov telescope is only optimal for covering about 1.5 to 2 decades in energy. Three sizes of telescope are therefore needed to cover the large energy range CTA proposes to study (from a few tens of GeV to above 100 TeV). The current baseline design consists of three telescope types: SST: Small size telescopes of 5–8 m diameter, both single-mirror and dual-mirror designs are considered; MST: Medium size telescopes of 10–12 m diameter, both single-mirror and dual-mirror designs are considered; and LST: Large size single-mirror telescopes of 23 m diameter.

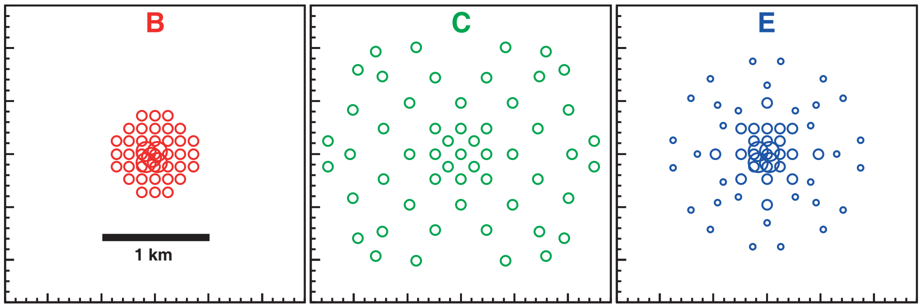

Fig. 3. – Three example candidate arrays (B, C and E) are among the studied configurations that would have an approximately similar construction cost.

Several different telescope configurations have been investigated in simulation studies for CTA so far. The first simulations were used to cross-check the different simulation packages and to begin the investigation of the dependence of performance on telescope and array parameters. The evaluation of the performance of these candidate arrays is a first step towards the optimisation of the CTA design. Figure 3 shows some of the telescope layouts used. All systems assume conventional technology for mirrors, PMTs and read-out electronics. Standard analysis techniques are used in general, with the results from more sophisticated methods shown for comparison in specific cases. Preliminary results as illustrated for the integral sensitivity and angular resolution in fig. 4 show that the ambitious goals of CTA are within the reach.

4·3. *CTA telescope technology*. – The CTA telescope technology is mainly based on known concepts and makes a heavy use of the experience in the field of Cherenkov telescopes. Several designs of different telescope types (SST, MST and LST, see above) are being developed with an optimal cost/performance ratio.

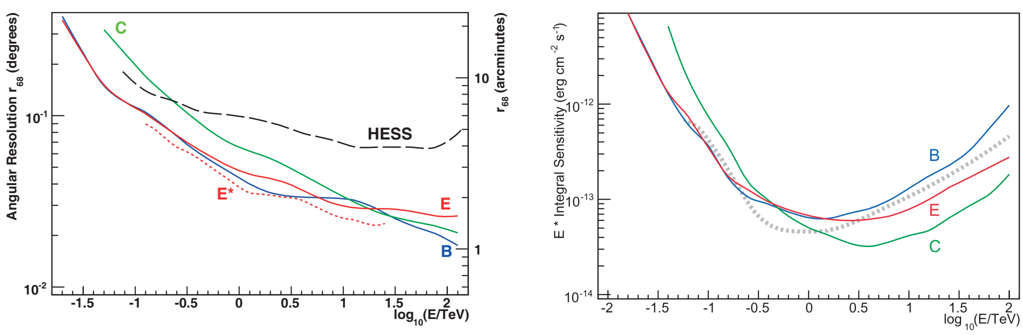

Fig. 4. – Left: Angular resolution (68% containment radius of the gamma-ray PSF) *versus* energy for the candidate configurations B, C and E. The resolution for a more sophisticated shower axis reconstruction method for configuration E is shown for comparison (dashed red line—E*). Right: Integral sensitivity (multiplied by E) for the candidate configurations B, C and E, for point sources observed for 50 hours at a zenith angle of 20°. The goal curve for CTA (dashed line) is shown for comparison.

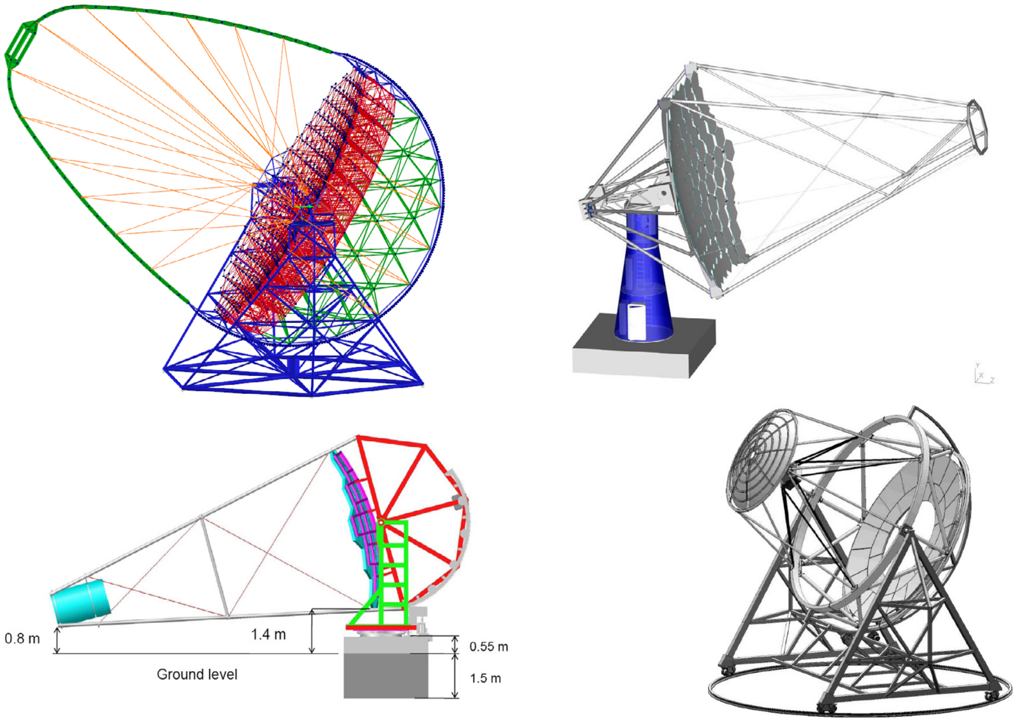

Fig. 5. – Top left: concept of a 23 m diameter LST with parabolic dish and $f/d = 1.2$. Top right: concept of a 12 m diameter MST with a Davies-Cotton dish and $f/d = 1.4$. Bottom left: concept of a 6 m diameter SST with a Davies-Cotton dish and $f/d = 1.4$. Bottom right: concept of a dual mirror Schwarzschild-Couder MST telescope.

Concepts of different telescope structures are illustrated in fig. 5. Schwarzschild-Couder telescopes with their dual optic are more difficult to construct because of the precision of the optical surface needed but if realized they would offer a possibility for a smaller (more compact and less expensive) cameras combined with a large field of view. The other designs assume a single reflector telescopes allowing for adequate fields of view for the costs of larger cameras. Imaging is improved by choosing relatively large f/d values, in the range of 1.2 to 1.5. A second variable is the dish shape: a Davies-Cotton layout provides good imaging over wide fields, but introduce a time dispersion. For small dish diameters this dispersion is smaller than the intrinsic width of the photon distribution, and therefore insignificant. For large dish diameters, the difference in photon path length from different parts of the reflector becomes larger than the intrinsic spread of photon arrival times, broadening the light pulse.

As the photosensor photomultiplier tubes (PMTs) are planned to be used. PMTs are very linear devices with a large (4 orders of magnitude) dynamic range and they allow the detection of single Cherenkov photons. Moreover PMTs are fast (photoelectrons signal widths below 3 ns duration), which is important to suppress background in the images. The camera of a CTA telescope will consist of 500 to 2000 PMTs depending on the telescope type and has strict limits on the weight and needed cooling power. To read out the signals from the cameras several concepts exist. The readout system must ensure a large bandwidth and low noise in order not to degrade the signal quality. It must also have small dead time and a sufficient buffer to allow for a trigger decision. The leading concepts use analogue sampling memory based recording systems. An alternative design using a 250 MSample/s system is based on a commercial low-cost FADC.

Hardware prototyping is under way for most of the parts to confirm simulated or expected results. The prototyping is also needed to confirm the costs estimates for the array construction and maintenance.

4˙4. *CTA as an open observatory*. – Unlike current ground-based gamma-ray instruments, CTA will be an open observatory, with a Science Data Centre (SDC) which provides pre-processed data to the user, as well as the tools necessary for the most common analyses. The software tools will provide an easy-to-use and well-defined access to data from this unique observatory. CTA data will be accessible through the Virtual Observatory, with varying interfaces matched to different levels of expertise. The required toolkit is being developed by partners with experience in SDC management from, for example, the INTEGRAL space mission.

5. – Conclusions

The CTA observatory is the logical next step in the exploration of the high-energy Universe, and will promote VHE observations as a public tool for modern astronomy. CTA will explore the VHE domain from several tens of GeV up to more than 100 TeV with unprecedented sensitivity and angular resolution, enabling a comprehensive understanding of cosmic particle acceleration physics at various scales, distances and time scales. Major advances are expected in understanding the origin of galactic cosmic rays, their propagation within galaxies, and their impact on their environment. Particle acceleration in the vicinity of black holes will be explored in a large variety of sources, and interactions and feedback effects of the particles on their surroundings will be explored. CTA will also probe physics beyond the established horizon, holding promise for a better understanding of the ultimate laws that govern the Universe. The CTA project started a preparatory phase in 2011, and array deployment could begin as early as 2016, with a full observatory operational before the end of this decade. Early science may be optimistically expected from 2017–2018 on.

* * *

We gratefully acknowledge support from the agencies and organisations listed in this page: `http://www.cta-observatory.org/?q=node/22`.

REFERENCES

[1] `http://www.mpi-hd.mpg.de/hfm/HESS`.
[2] `http://magic.mppmu.mpg.de`.
[3] `http://veritas.sao.arizona.edu`.
[4] `http://www.cta-observatory.org`.
[5] Actis M. *et al.* (CTA Consortium), *Exp Astron*, **32** (2011) 193.
[6] Hinton J. A. and Hofmann W., *Annu. Rev. Astron. Astrophys.*, **47** (2009) 523.
[7] Funk S., *32nd ICRC, China, 2011* (2012) arXiv:1204.4529.
[8] See, *e.g.*, Aharonian F. A., *Astrophys. J.*, **636** (2006) 777 (and subsequent presentations in conferences).
[9] See, *e.g.*, Meyer M. *et al.*, *Astron. Astrophys.*, **523** (2010) A2.

PARTICIPANTS

Aldaya Maria	DESY	Hamburg	Germany
Ali Murat Guler	METU	Ankara	Turkey
Altmannshofer Wolfgang	Fermilab	Batavia	USA
Apresyan Artur	Caltech	Pasadena	USA
Arbuzova Elena	Dubna University	Dubna	Russia
Arcidiacono Roberta	INFN-Torino	Torino	Italy
Barbieri Riccardo	SNS-Pisa	Pisa	Italy
Bellettini Giorgio	INFN-Pisa	Pisa	Italy
Bendavid Josh	MIT	Cambridge, MA	USA
Berardi Simone	INFN-LNF	Frascati	Italy
Bernagozzi Andrea	Fondazione C. Fillietroz	Aosta	Italy
Bertolini Enzo	Fondazione C. Fillietroz	Aosta	Italy
Bertolucci Sergio	CERN	Geneva	Switzerland
Bilokon Halina	INFN-LNF	Frascati	Italy
Brunelière Renaud	University of Freiburg	Freiburg	Germany
Brunetti Giulia	LHEP-Bern University	Bern	Switzerland
Carbognani Albino	Fondazione C. Fillietroz	Aosta	Italy
Cavaliere Viviana	University of Illinois	Urbana Champaign	USA
Cavoto Gianluca	INFN-Roma	Roma	Italy
Chiarelli Giorgio	INFN-Pisa	Pisa	Italy
Cirelli Marco	CERN	Geneva	Switzerland
Dar Arnon	Technion	Haifa	Israel
Davidson Sacha	CNRS	Villeurbanne	France
De Palma Francesco	INFN-Bari	Bari	Italy
De Rújula Alvaro	CERN	Geneva	Switzerland
Degrassi Giuseppe	Università di Roma Tre	Roma	Italy
Desai Satish	Fermilab	Batavia	USA
Deschamps Olivier	LPC	Clermont-Ferrand	France
Di Canto Angelo	INFN-Pisa	Pisa	Italy
Dokuchaev Vyacheslav	RAS	Moscow	Russia
Dorosti Hasankiadeh Qader	Groningen University	Groningen	The Netherlands
Doršner Ilja	University of Sarajevo	Sarajevo	Bosnia
Enari Yuji	LPNHE Paris	Paris	France
Falkowski Adam	LPT Orsay	Orsay	France
Flood Kevin	Caltech	Pasadena	USA
Fortin Dominique	TRIUMF	Vancouver	Canada
Galanti Mario	University of Cyprus	Nicosia	Cyprus
Gastaldi Ugo	INFN-LNL	Legnaro	Italy
Gentile Simonetta	INFN-Roma	Roma	Italy
Gervino Gianpiero	INFN-Torino	Torino	Italy

Giammarchi Marco Giulio	INFN-Milano	Milano	Italy
Giovannella Simona	INFN-LNF	Frascati	Italy
Giunti Carlo	INFN-Torino	Torino	Italy
Glazov Sasha	DESY	Hamburg	Germany
Greco Mario	Università di Roma Tre	Roma	Italy
Grohsjean Alexander	DESY	Hamburg	Germany
Hemmer Sabine Elisabeth	INFN-Padova	Padova	Italy
Henderson Stuart	Fermilab	Batavia	USA
Inguglia Gianluca	Queen Mary University of London	London	UK
Isidori Gino	INFN-LNF	Frascati	Italy
Jayatilaka Bodhitha	Duke University	Durham	USA
Kamenik Jernej	Jozef Stefan Insitute	Ljubljana	Slovenia
Kazakov Dmitry	JINR/ITEP	Moscow	Russia
Kirk Julie	Rutherford Appleton Laboratory	Oxford	UK
Korytov Andrey	University of Florida	Gainesville	USA
Košnik Nejc	Lab. Accélérateur Linéaire	Orsay	France
Kravchenko Ilya	University of Nebraska	Lincoln	USA
Krokovny Pavel	BINP	Novosibirsk	Russia
Lindquist Brian	SUNY	Stony Brook	USA
López Mateos David	Harvard University	Cambridge	USA
Maccarrone Giovanni	INFN-LNF	Frascati	Italy
Magana-Villalba Ricardo	Cinvestav	Mexico D.F.	Mexico
Mahn Kendall	TRIUMF	Vancouver	Canada
Maiani Luciano	INFN-Roma	Roma	Italy
Masiero Antonio	INFN-Padova	Padova	Italy
Maurice Emilie	CPPM	Marseille	France
Mazin Daniel	IFAE	Barcelona	Spain
Merlo Luca	TUM	Garching	Germany
Mijović Liza	DESY	Hamburg	Germany
Minkowski Peter	University of Bern	Bern	Switzerland
Miyake Hideki	University of Tsukuba	Tsukuba	Japan
Moed Sher Shulamit	Fermilab	Batavia	USA
Mohapatra Debabrata	Virginia Tech	Blacksburg	USA
Nardecchia Marco	CP3-Origins	Odense	Denmark
Natoli Paolo	Università di Ferrara	Ferrara	Italy
Nisati Aleandro	INFN-Roma	Roma	Italy
Nocera Emanuele	Università di Milano	Milano	Italy
Novikov Victor	ITEP	Moscow	Russia
Paoletti Riccardo	Università di Siena	Siena	Italy
Punzi Giovanni	INFN-Pisa	Pisa	Italy
Qian Wenbin	CERN	Geneva	Switzerland
Ramello Luciano	Universita del Piemonte Orientale	Torino	Italy
Reinhold Bernd	MPIK	Heidelberg	Germany
Rolandi Luigi	CERN	Geneva	Switzerland
Romano Angela	University of Birmingham	Birmingham	UK
Rossi Paolo	Università di Zurigo	Zurigo	Switzerland
Salam Gavin	CERN	Geneva	Switzerland
Sanchez Ariel	MPI	Garching	Germany
Santoni claudio	LPC	Clermont-Ferrand	France

Santovetti Emanuele	INFN-Roma	Roma	Italy
Stamou Emmanuel	Technical University Munich	Munich	Germany
Stdenis Richard	University of Glasgow	Glasgow	UK
Stoye Markus	CERN	Geneva	Switzerland
Studenikin Alexander	Moscow State University	Moscow	Russia
Suter Louise	University of Manchester	Manchester	UK
Tanaka Junichi	University of Tokyo	Tokyo	Japan
Tenchini Roberto	INFN-Pisa	Pisa	Italy
Thorne Felicitas	HEPHY	Vienna	Austria
Trott Michael	CERN	Geneva	Switzerland
Truc Fabio		Aosta	Italy
Turini Nicola	INFN-Siena	Siena	Italy
Valencia German	Iowa State University	Ames	USA
Van der Leeuw Robin	Nikhef	Amsterdam	The Netherlands
Veres Gabor	CERN	Geneva	Switzerland
Vernieri Caterina	INFN-Pisa	Pisa	Italy
Wang Haichen	University of Wisconsin	St. Genis	USA
Warsinsky Markus	Albert-Ludwigs-Universität	Freiburg	Germany
Wolfe Homer	The Ohio State University	Batavia	USA

FRASCATI PHYSICS SERIES VOLUMES

Volume I
Heavy Quarks at Fixed Target
Eds.: S. Bianco and F.L. Fabbri
Frascati, May 31–June 2, 1993
ISBN 88-86409-00-1

Volume II – Special Issue
Les Rencontres de Physique de la Vallée d'Aoste – Results and Perspectives in Particle Physics
Ed.: M. Greco
La Thuile, Aosta Valley, March 5 –11, 1995
ISBN 88-86409-03-6

Volume III
Heavy Quarks at Fixed Target
Ed.: B. Cox
University of Virginia, Charlottesville
October 7–10, 1994, 11
ISBN 88-86409-04-4

Volume IV
Workshop on Physics and Detectors for DAΦNE
Eds.: R. Baldini, F. Bossi, G. Capon, G. Pancheri
Frascati, April 4–7, 1995
ISBN 88-86409-05-2

Volume V – Special Issue
Les Rencontres de Physique de la Vallée d'Aoste – Results and Perspectives in Particle Physics
Ed.: M. Greco
La Thuile, Aosta Valley, March 3–9, 1996
ISBN 88-86409-07-9

Volume VI
Calorimetry in High Energy Physics
Eds.: A. Antonelli, S. Bianco, A. Calcaterra, F.L. Fabbri
Frascati, June 8–14, 1996
ISBN 88-86409-10-9

Volume VII
Heavy Quarks at Fixed Target
Ed.: L. Kőpke
Rhinefels Castle, St. Goar, October 3–6, 1996
ISBN 88-86409-11-7

Volume VIII
ADONE a milestone on the particle way
Ed.: V. Valente 1997
ISBN 88-86409-12-5

Volume IX – Special Issue
Les Rencontres de Physique de la Vallée d'Aoste – Results and Perspectives in Particle Physics
Ed.: M. Greco
La Thuile, Aosta Valley, March 2–8, 1997
ISBN 88-86409-13-3

Volume X
Advanced ICFA Beam Dynamics Workshop on Beam Dynamics Issue for e^+e^- Factories
Eds.: L. Palumbo, G. Vignola
Frascati, October 20–25, 1997
ISBN 88-86409-14-1

Volume XI
Proceedings of the XVIII International Conference on Physics in Collision
Eds.: S. Bianco, A. Calcaterra, P. De Simone, F. L. Fabbri
Frascati, June 17–19, 1998
ISBN 88-86409-15-X

Volume XII – Special Issue
Les Rencontres de Physique de la Vallée d'Aoste – Results and Perspectives in Particle Physics
Ed.: M. Greco
La Thuile, Aosta Valley, March 1–7, 1998
ISBN 88-86409-16-8

Volume XIII
Bruno Touschek and the Birth of thee^+e^-
Ed.: G. Isidori
Frascati, 16 November, 1998
ISBN 88-86409-17-6

Volume XIV – Special Issue
Les Rencontres de Physique de la Vallée d'Aoste – Results and Perspectives in Particle Physics
Ed.: M. Greco
La Thuile, Aosta Valley, February 28–March 6, 1999
ISBN 88-86409-18-4

Volume XV
Workshop on Hadron Spectroscopy
Eds.: T. Bressani, A. Feliciello, A. Filippi
Frascati, March 8–12 1999
ISBN 88-86409-19-2

Volume XVI
Physics and Detectors for DAΦNE
Eds.: S. Bianco, F. Bossi, G. Capon, F.L. Fabbri,
P. Gianotti, G. Isidori, F. Murtas
Frascati, November 16–19, 1999
ISBN 88-86409-21-4

Volume XVII – Special Issue
Les Rencontres de Physique de la Vallée d'Aoste –
Results and Perspectives in Particle Physics
Ed.: M. Greco
La Thuile, Aosta Valley, February 27 – March 4, 2000
ISBN 88-86409-23-0

Volume XVIII
LNF Spring School
Ed.: G. Pancheri
Frascati, 15–20 May, 2000
ISBN 88-86409-24-9

Volume XIX
XX Physics in Collision
Ed.: G. Barreira
Lisbon June 29–July 1st. 2000
ISBN 88-86409-25-7

Volume XX
Heavy Quarks at Fixed Target
Eds.: I. Bediaga, J. Miranda, A. Reis
Rio de Janeiro, Brasil, October 9–12, 2000
ISBN 88-86409-26-5

Volume XXI
IX International Conference on Calorimetry in
High Energy Physics
Eds.: B. Aubert, J. Colas, P. Nédélec, L. Poggioli
Annecy Le Vieux Cedex, France, October 9–14, 2000
ISBN 88-86409-27-3

Volume XXII – Special Issue
Les Rencontres de Physique de la Vallée d'Aoste –
Results and Perspectives in Particle Physics
Ed.: M. Greco
La Thuile, Aosta Valley, March 4–10, 2001
ISBN 88-86409-28-1

Volume XXIII
XXI Physics in Collision
Ed.: Soo-Bong Kim
Seoul, Korea, June 28–30, 2001
ISBN 88-86409-30-3

Volume XXIV
International School of Space Science – 2001 Course on:
Astroparticle and Gamma-ray Physics in Space
Eds.: A. Morselli, P. Picozza
L'Aquila, Italy, August 30 – September 7, 2000
ISBN 88-86409-31-1

Volume XXV
TRDs for the 3rd Millennium Workshop on
Advanced Transition Radiation Detectors for
Accelerator and Space Applications
Eds. N. Giglietto, P. Spinelli
Bari, Italy, September 20–23, 2001
ISBN 88-86409-32-X

Volume XXVI
KAON 2001 International Conference on CP Violation
Eds.: F. Costantini, G. Isidori, M. Sozzi
Pisa Italy, June 12th – 17th, 2001
ISBN 88-86409-33-8

Volume XXVII – Special Issue
Les Rencontres de Physique de la Vallée d'Aoste –
Results and Perspectives in Particle Physics
Ed.: M. Greco
La Thuile, Aosta Valley, March 3–9, 2002
ISBN 88-86409-34-6

Volume XXVIII
Heavy Quarks at Leptons 2002
Eds.: G. Cataldi, F. Grancagnolo, R. Perrino, S. Spagnolo
Vietri sul mare (Italy), May 27th – June 1st, 2002
ISBN 88-86409-35-4

Volume XXIX
Workshop on Radiation Dosimetry: Basic Technologies,
Medical Applications, Environmental Applications
Ed.: A. Zanini
Rome, Italy, February 5–6, 2002
ISBN 88-86409-36-2

Volume XXIX – Suppl.
Workshop on Radiation Dosimetry: Basic Technologies, Medical Applications, Environmental Applications
Ed.: A. Zanini
Rome, Italy, February 5–6, 2002
ISBN 88-86409-36-2

Volume XXX – Special Issue
Les Rencontres de Physique de la Vallée d'Aoste – Results and Perspectives in Particle Physics
Ed.: M. Greco
La Thuile, Aosta Valley, March 9–15, 2003
ISBN 88-86409-39-9

Volume XXXI
Frontier Science 2002 – Charm, Beauty and CP, First International Workshop on Frontier Science
Eds.: L. Benussi, R. de Sangro, F.L. Fabbri, P. Valente
Frascati, October 6–11, 2002
ISBN 88-86409-37-0

Volume XXXII
19th International Conference on x-ray and Inner-Shell Processes
Eds.: A. Bianconi, A. Marcelli, N.L. Saini
Universitá di Roma "La Sapienza" June 24–28, 2002
ISBN 88-86409-39-07

Volume XXXIII
Bruno Touschek Memorial Lectures
Ed.: M. Greco, G. Pancheri
Frascati, May 11, 1987
ISBN 88-86409-40-0

Volume XXXIV – Special Issue
Les Rencontres de Physique de la Vallée d'Aoste – Results and Perspectives in Particle Physics
Ed.: M. Greco
La Thuile, Aosta Valley, February 29 – March 6, 2004
ISBN 88-86409-42-7

Volume XXXV
Heavy Quarks And Leptons 2004
Ed.: A. López
San Juan, Puerto Rico, 1–5 June 2004
ISBN 88-86409-43-5

Volume XXXVI
DAΦNE 2004: Physics At Meson Factories
Eds.: F. Anulli, M. Bertani, G. Capon, C. Curceanu-Petrascu, F.L. Fabbri, S. Miscetti
Frascati, June 7–11, 2004
ISBN 88-86409-53-2

Volume XXXVII
Frontier Science 2004, Physics and Astrophysics in Space
Eds.: A. Morselli, P. Picozza, M. Ricci
Frascati, 14–19 June, 2004
ISBN 88-86409-52-4

Volume XXXVIII
II Workshop Italiano sulla Fisica di ATLAS e CMS
Eds.: Gianpaolo Carlino and Pierluigi Paolucci
Napoli, October 13 – 15, 2004
ISBN 88-86409-44-3

Volume XXXIX – Special Issue
Les Rencontres de Physique de la Vallée d'Aoste – Results and Perspectives in Particle Physics
Ed.: M. Greco
La Thuile, Aosta Valley, February 27 – March 5, 2005
ISBN 88-86409-45-1

Volume XL
Frontier Science 2005 – New Frontiers in Subnuclear Physics
Eds.: A. Pullia, M. Paganoni
Milano, September 12 - 17, 2005
ISBN 88-86409-46-X

Volume XLI
Discoveries in Flavour Physics at e^+e^- Colliders
Eds.: L. Benussi, S. Bianco, C. Bloise, R. de Sangro, C. Gatti, G. Isidori, M. Martini, F. Mescia, S. Miscetti
Frascati, February 28th - March 3rd, 2006
ISBN 88-86409-51-6

Volume XLII – Special Issue
Les Rencontres de Physique de la Vallée d'Aoste – Results and Perspectives in Particle Physics
Ed.: M. Greco
La Thuile, Aosta Valley, March 5 – March 11, 2006
ISBN 88-86409-47-8

Volume XLIII – Special Issue
Neutral Kaon Interferometry at A Phi-Factory: from Quantum Mechanics to Quantum Gravity
Ed.: A. Di Domenico
Frascati, March 24th 2006
ISBN 978 88-86409-50-8

Volume XLIV – Special Issue
Les Rencontres de Physique de la Vallée d'Aoste – Results and Perspectives in Particle Physics
Ed.: M. Greco
La Thuile, Aosta Valley, February 28th - March 5th, 2007
ISBN 978 88-86409-49-4

Volume XLV *Frontier Science – Science with the New Generation High Energy Gamma-ray Experiments*
Eds.: A. Lionetto, A. Morselli
Villa Mondragone, Monteporzio, Italy, June 18 -20, 2007
ISBN 978 88-86409-54-0

Volume XLVI
XII International Conference on Hadron Spectroscopy
Eds.: L. Benussi, M. Bertani, S. Bianco, C. Bloise, R. de Sangro, P. de Simone, P. di Nezza, P. Giannotti, S. Giovanella, M.P. Lombardo, S. Pacetti
Laboratori Nazionali di Frascati, October 7-13, 2007
ISBN 978-88-86409-55-1

Volume XLVII – Special Issue
Les Rencontres de Physique de la Vallée d'Aoste – Results and Perspectives in Particle Physics
Ed.: M. Greco
La Thuile, Aosta Valley, February 24^{th} - March 1^{st}, 2008
ISBN 978-88-86409-56-8

Volume XLVIII
The XIV LNF Spring School "Bruno Touschek" in Nuclear, Subnuclear and Astroparticle Physics
Young Researchers Workshop "Physics Challenges in the LHC Era"
Ed.: E. Nardi
Laboratori Nazionali di Frascati, Frascati, May 11th - May 14th, 2009
ISBN 978-88-86409-57-5

Volume XLIX
Workshop on Monte Carlo's, Physics and Simulations at the LHC
Ed. P. Nason
Laboratori Nazionali di Frascati, Frascati, February 27-28, 2006
ISBN 978-88-86409-58-2

Volume L – Special Issue
Les Rencontres de Physique de la Vallée d'Aoste –
Results and Perspectives in Particle Physics
Ed.: M. Greco
La Thuile, Aosta Valley, March 1^{st} - 7^{th}, 2009
ISBN 978-88-7438-053-4

Volume LI
Second Young Researchers Workshop
"Physics Challenges in the LHC Era" 2010
Ed. E. Nardi
Laboratori Nazionali di Frascati, Frascati, May 10-13, 2010
ISBN 978-88-86409-60-5

Volume LII – Special Issue
Les Rencontres de Physique de la Vallée d'Aoste –
Results and Perspectives in Particle Physics
Ed.: M. Greco
La Thuile, Aosta Valley, February28th - March 6^{th}, 2010
ISBN 978-88-7438-060-2

Volume LIII – Special Issue
Les Rencontres de Physique de la Vallée d'Aoste –
Results and Perspectives in Particle Physics
Ed.: M. Greco
La Thuile, Aosta Valley, February27th - March 5^{th}, 2011
ISBN 978-88-7438-068-8

Volume LIV
LC11 Workshop: understanding QCD at linear colliders
in searching for old and new physics
Villazzano (TN), 12-16 September 2011
ISBN 978-88-86409-60-5

Volume LV
Third Young Researchers Workshop "Physics Challenges in the LHC Era" 2012
Ed. E. Nardi
Frascati, May 7th and May 10th, 2012
ISBN 978-88-86409-59-9

Volume LVI
DARK2012
Dark Forces at Accelerators
Ed. F. Bossi
Frascati, October 16th and 19th 2012
ISBN 978-88-86409-62-9

FRASCATI PHYSICS SERIES VOLUMES – Italian Collection

Collana: Scienza Aperta Vol. I (2006) - ComunicareFisica2005
Atti 1° Convegno "Comunicare Fisica e altre Scienze",
Frascati, 24-27 Ottobre, 2005
Eds: Franco L. Fabbri, Piero Patteri
ISBN 88-86-409-48-6

Finito di stampare
nel mese di Gennaio 2013
Compositori Industrie Grafiche - Bologna